

**Probing Thermodynamics, Correlations, and  
Transport of the 2D Fermi-Hubbard Model Under a  
Fermi Gas Microscope**

by

Matthew Alan Nichols

B.A., University of California, Berkeley (2012)

Submitted to the Department of Physics  
in Partial Fulfillment of the Requirements for the Degree of

Doctor of Philosophy

at the

MASSACHUSETTS INSTITUTE OF TECHNOLOGY

June 2019

© Massachusetts Institute of Technology 2019. All rights reserved.

Author .....  
Department of Physics  
May 24, 2019

Certified by .....  
Martin W. Zwierlein  
Thomas A. Frank Professor of Physics  
Thesis Supervisor

Accepted by .....  
Nergis Mavalvala  
Associate Department Head



# Probing Thermodynamics, Correlations, and Transport of the 2D Fermi-Hubbard Model Under a Fermi Gas Microscope

by

Matthew Alan Nichols

Submitted to the Department of Physics  
on May 24, 2019, in partial fulfillment of the  
requirements for the degree of  
Doctor of Philosophy

## Abstract

Ultracold fermionic atoms in optical lattices offer a pristine platform for quantum simulation of materials with strong electron correlations. With the advent of quantum gas microscopy, we now have the abilities to observe and manipulate these systems at the level of single atoms and lattice sites. In this thesis, I will describe how we perform fluorescence microscopy on fermionic  $^{40}\text{K}$  using Raman sideband cooling, and how we realize the two-dimensional Fermi-Hubbard model on a square lattice, a paradigm believed to capture the essence of high- $T_c$  superconductivity in the cuprates. I will then discuss several experiments we have performed with this system aimed at improving our current understanding of both the equilibrium and transport properties of this strongly correlated many-body Hamiltonian.

The first part of this thesis discusses measurements of thermodynamic properties of different states of the Fermi-Hubbard model in equilibrium, including metallic, Mott-insulating, and band-insulating states. With the single-site resolution afforded by our quantum gas microscope, we examine spatial spin and charge correlations in a fermionic Mott insulator as a function of the filling in the lattice. At half-filling, we observe antiferromagnetic spin correlations in the presence of doublon-hole bunching. Upon doping, these spin correlations weaken monotonically, and an interaction-enhanced Pauli-hole emerges, a real-space manifestation of Pauli-blocking.

The second part of this thesis describes near-equilibrium transport experiments we performed with ultracold fermionic atoms, which allowed us to measure both the spin diffusion coefficient and the spin conductivity of a homogeneous Mott insulator at half-filling, transport coefficients that are difficult to measure in the cuprates, and which are highly challenging to calculate theoretically. In the strongly interacting regime, we observe diffusive spin transport that is driven by super-exchange and doublon-hole-assisted tunneling, and which violates the quantum limit of charge diffusion.

Thesis Supervisor: Martin W. Zwierlein  
Title: Thomas A. Frank Professor of Physics



*To my family*



## Acknowledgments

The time that I have spent at MIT working towards my PhD has been one of the most difficult, yet fulfilling and rewarding periods in my life, and there are many people that I must thank, who not only inspired me and helped me to achieve my academic goals, but who also enriched my graduate school experience, and made my time here so fun and enjoyable. I would like to start by thanking my research advisor, Martin Zwierlein, for his constant support and guidance, both in and out of the lab, throughout the past seven years. I have learned so much from Martin during my time here: his ability to take complex concepts and problems and distill them into simple, easy to understand ideas has taught me so much about physics, from his lectures in the atomic physics courses and his chalkboard talks during our weekly group seminars, to his explanations of experimental and technological ideas in the lab. Whenever we encountered obstacles in the lab that seemed insurmountable, he was always able to come up with fresh ideas, and to inspire us to keep pushing through the tough times. It was such a joy building one of the world's first quantum gas microscopes for fermionic atoms with him, and such an amazing experience that we shared seeing single potassium atoms in the lattice for the first time. His sheer passion for physics, and his ability to positively motivate those around him has been a true inspiration throughout my PhD, and I would not be where I am today without him.

I would also like to thank all of those people with whom I have worked directly over the past few years, especially the many students and post docs of Fermi 2, who spent so many long hours with me in the lab, working together to achieve something truly amazing. I am indebted to Thomas Gersdorf and David Reens for laying the groundwork of the experiment, and assembling a large portion of the apparatus before I arrived, including the vacuum chamber and the magnetic field coils. Waseem Bakr, the first post doc I worked with when I began, and Vinay Ramasesh, a master's student on the experiment, were not only crucial in the original design and construction of the machine, but also quickly caught me up to speed on the basics of ultracold

atomic physics, a brand new field to me at the time, and provided invaluable guidance and friendship in the early years of my PhD. I must also extend my gratitude to Hao Zhang, Melih Okan, and Lawrence Cheuk, the Fermi 2 team members that worked me throughout the majority of my time at MIT, and who were invaluable throughout the construction process of the machine, as well as the design and implementation of the numerous experiments we performed using the quantum gas microscope. Lawrence, the senior graduate student on the experiment when I first started, was not only an amazing physicist with a great intuition for both the experimental and theoretical aspects of the field, but he was also extremely passionate and dedicated to the research, and his drive and leadership made the success of our experiment possible. While I was still learning the ropes, he never once looked down on me for asking silly questions, and he always went out of his way to help me sort through and understand problems. Having spent so many years together, we have become very close friends, which made the many long hours in lab working together a very enjoyable experience. Melih, the graduate student on the experiment between Lawrence and I, played a major role in the construction of the machine, as well as the implementation of all the different research projects we pursued. His calm and collected attitude in the lab always helped ease my constant stress, and his simple approaches to problems were a great balance to my typically overly meticulous ones. He has also been a great friend in addition to a great teammate, and he has provided me with a valuable perspective on life, both in and out of the lab, that has really inspired me throughout my time at MIT. Hao, the post doc that spent the most time working with me during my PhD, has been a great friend throughout the years, and his unyielding curiosity and fascination with physics has really inspired me to pursue and understand problems on a much deeper level than I ever would have otherwise. I would also like to thank the other Fermi 2 team members who worked with me during my time at MIT, and who made many significant contributions towards the research, including Thomas Lompe, Katherine Lawrence, Enrique Mendez, Thomas Hartke, and Ningyuan Jia. Thomas Hartke and Jia, the newest generation of Fermi 2 team members, are both incredible physicists with amazing work ethics, and I am sure that the experiment could not be left in

better hands. I wish them the best of luck for all of their future endeavors with the fermionic quantum gas microscope.

I want to extend my thanks to the many theorists with whom we have collaborated over the years, including Thereza Paiva and Nandini Trivedi, who performed the DQMC calculations which we used to compare with our equilibrium measurements of spatial spin and charge correlations in the 2D Fermi-Hubbard model, as well as Ehsan Khatami and Marcos Rigol, who performed the corresponding NLCE calculations. I would especially like to thank Ehsan, who also found a way to calculate transport properties of the Fermi-Hubbard model using NLCE, which gave us something concrete to compare our transport measurements with, and also allowed us to better interpret our results. He has been a great and incredibly friendly collaborator, and we have had many fruitful discussions over the years that have really helped connect the experiment with the theory. I am also very grateful to Senthil Todadri for the many discussions that have allowed us to better understand transport within the Fermi-Hubbard model: his perspective has been extremely valuable, and he has helped us more thoroughly understand the impact of our work with ultracold atoms within the broader context of condensed matter physics research as a whole.

I am also very grateful to all the other wonderful members of Martin's research group whom I have interacted with over the years, including Biswaroop Mukherjee, Parth Patel, Zhenjie Yan, Julian Struck, Tarik Yefsah, Yiqi Ni, Carsten Robens, Richard Fletcher, Airlia Shaffer-Moag, Cedric Wilson, Zoe Yan, Elmer Guardado-Sanchez, Wenjie Ji, Mark Ku, Jennifer Schloss, Sebastian Will, Ariel Sommer, Cheng-Hsun Wu, Huanqian Loh, and Jeewoo Park. Everyone has been so amazing and supportive, and the group has truly fostered a work environment that is both intellectually stimulating and fun. I would also like to thank my academic advisor, Dave Pritchard, and all of the amazing physics, CUA, and RLE staff members, including Cathy Modica, Al McGurl, Joanna Welch, and Paula Sack, who made our research, as well as my academic path through MIT, possible. Additionally, I would like to extend my gratitude to all the other members of the CUA, especially the research group of Wolfgang Ketterle, who provided many fruitful discussions about research

and technical expertise over the years, and who also assisted us in times of need by generously sharing essential lab equipment. I learned so much from the academic environment created by the CUA, and I am so grateful to all those who helped make the CUA such a great place to do research.

Finally, I would like to thank my whole family, especially my parents and my brother, whose unending support gave me the strength I needed to make it all the way through to the end of the long road that is graduate school. I also want to thank my uncle, Alan Nichols, who encouraged me to pursue my dreams, regardless of the cost, and without whom I would never have been able to make it to where I am today. I am also incredibly grateful to the following people, whose friendship has meant so much to me over the years, and who have significantly added to my life during graduate school, especially outside of the lab: Zach Smithwick, Ian Counts, Lawrence Cheuk, Yaray Ku, Jeewoo Park, Sebastian Will, Julian Struck, Tarik Yefsah, Niki Jepsen, Timur Rvachov, Jesse Amato-Grill, Parth Patel, Waseem Bakr, Zoe Yan, Katherine Lawrence, Zhenjie Yan, Hao Zhang, Colin Kennedy, Ivana Dimitrova, Vinay Ramasesh, Zak Vendeiro, Elisa Soave, Lee Liu, Elmer Guardado-Sanchez, Sepehr Ebadi, Cody Burton, Tom Cooper, Holing Yip, Yiqi Ni, Biswaroop Mukherjee, Alan Jamison, Sherry Chu, Melih Okan, Aaron Buikema, Shing Shing Ho, and Keaton Burns.

# Contents

|  |            |
|--|------------|
| <b>1 Overview</b>  | <b>21</b>  |
| 1.1 Thesis Outline . . . . .   | 25         |
| <b>2 Ultracold Atoms in Optical Lattices</b>   | <b>29</b>  |
| 2.1 Non-Interacting Fermions . . . . .   | 30         |
| 2.1.1 Band Structure, the Fermi Surface, and the Tight Binding Model                 | 31         |
| 2.1.2 Density Correlation Functions for the Non-Interacting System                   | 37         |
| 2.1.3 Spin Correlation Function for the Non-Interacting System . .                   | 45         |
| 2.2 Fermi-Hubbard Model . . . . .  | 46         |
| 2.2.1 Double-Well Hubbard Model . . . . .  | 52         |
| 2.2.2 Theoretical Approaches to the Fermi-Hubbard Model . . . .                      | 59         |
| 2.2.3 Equation of State and Basic Phenomenology of the Fermi-Hubbard Model . . . . . | 70         |
| 2.3 Transport Properties . . . . .   | 84         |
| 2.3.1 Drude Theory of the Conductivity . . . . .                                     | 86         |
| 2.3.2 Linear Response Theory . . . . .   | 89         |
| 2.3.3 Features of the Conductivity and Sum Rules . . . . .                           | 102        |
| <b>3 Quantum Gas Microscopy of Fermionic <math>^{40}\text{K}</math></b>              | <b>107</b> |
| 3.1 Experimental Apparatus . . . . .   | 108        |
| 3.1.1 Magnetic Field Coils . . . . .   | 112        |
| 3.1.2 Optical Traps . . . . .  | 119        |
| 3.1.3 Single-Site Imaging Lasers and Beam Paths . . . . .                            | 129        |

|          |  |            |
|----------|--|------------|
| 3.1.4    | High-Resolution Imaging System . . . . .   | 133        |
| 3.2      | Single-Site Imaging . . . . .  | 135        |
| 3.2.1    | Imaging a Different Vertical Layer of the Optical Lattice . . .  | 147        |
| 3.3      | Summary of Experimental Sequence . . . . .   | 152        |
| 3.4      | Spin-Resolved Single-Site Imaging . . . . .  | 157        |
| 3.4.1    | Experimental Sequence . . . . .  | 159        |
| 3.4.2    | Calibrating the Parameters of the Spin Imaging . . . . .   | 164        |
| 3.4.3    | Imaging the Total Density of One Spin State . . . . .  | 171        |
| <b>4</b> | <b>Measuring Thermodynamic Properties and Correlations of the Fermi-Hubbard Model</b>                    | <b>177</b> |
| 4.1      | Previous Studies of the Fermi-Hubbard Model Using Ultracold Atoms  | 179        |
| 4.2      | Experimental Realization in our Quantum Gas Microscope . . . . .   | 181        |
| 4.2.1    | Calibrating the Hubbard Parameters . . . . .   | 187        |
| 4.2.2    | The Local Moment and its Properties . . . . .  | 193        |
| 4.3      | Observing Metallic, Mott-Insulating, and Band-Insulating States <i>In Situ</i>                           | 204        |
| 4.3.1    | Imaging Metallic, Mott-Insulating, and Band-Insulating States  | 205        |
| 4.3.2    | Radial Profiles of the Observed Local Moment and its Fluctuations . . . . .                              | 206        |
| 4.3.3    | Comparing Measured Profiles to Theory . . . . .  | 210        |
| 4.3.4    | Melting a Mott Insulator: Studying the Effects of Temperature  | 214        |
| 4.3.5    | The Local Moment as a Probe of Equilibrium Properties of the Hubbard Model and its Limitations . . . . . | 219        |
| 4.4      | Spatial Charge and Spin Correlations . . . . .   | 223        |
| 4.4.1    | Definitions of the Spin and Charge Correlation Functions . . .   | 225        |
| 4.4.2    | Spin-Resolved Imaging . . . . .  | 233        |
| 4.4.3    | Measurements of the Spatially Resolved Spin and Charge Correlation Functions . . . . .                   | 242        |
| <b>5</b> | <b>Measuring Transport Properties of the Half-Filled Fermi-Hubbard Model</b>                             | <b>279</b> |

|          |   |            |
|----------|---|------------|
| 5.1      | Introduction and Summary of Previous Studies . . . . .  | 280        |
| 5.2      | Experimental Implementation . . . . .   | 284        |
| 5.2.1    | Calibrating the Hubbard Parameters . . . . .  | 293        |
| 5.2.2    | Calibrating the Magnetic Gradient Strength . . . . .  | 294        |
| 5.2.3    | Calibrating the Harmonic Trapping Frequencies . . . . .   | 300        |
| 5.2.4    | Spin-Dependent Imaging Errors . . . . .   | 304        |
| 5.3      | Thermoelectric Effects . . . . .  | 306        |
| 5.4      | Results . . . . .   | 310        |
| 5.4.1    | Equilibrium Properties of the Tilted Potential . . . . .  | 314        |
| 5.4.2    | Measuring the Spin Diffusion Coefficient . . . . .  | 322        |
| 5.4.3    | Examining the Dynamics as a Function of the System Size .   | 333        |
| 5.4.4    | Measurement of the Conductivity . . . . .   | 337        |
| 5.4.5    | Comparing the Experimental Data to Theory . . . . .   | 343        |
| 5.4.6    | Effects of Heating . . . . .  | 350        |
| 5.5      | Outlook . . . . .   | 353        |
| <b>6</b> | <b>Summary and Outlook</b>  | <b>361</b> |
| <b>A</b> | <b>Isothermal and Isentropic Numerical Calculations of the Hole-Hole, Hole-Doublon, and Doublon-Doublon Correlation Functions at Half-Filling Versus <math>U/t</math></b> | <b>367</b> |
| <b>B</b> | <b>Observation of 2D Fermionic Mott Insulators of <math>^{40}\text{K}</math> with Single-Site Resolution</b>  | <b>371</b> |
| <b>C</b> | <b>Observation of Spatial Charge and Spin Correlations in the 2D Fermi-Hubbard Model</b>  | <b>377</b> |
| <b>D</b> | <b>Spin Transport in a Mott Insulator of Ultracold Fermions</b>   | <b>383</b> |



# List of Figures

|     |   |     |
|-----|---|-----|
| 2-1 | Illustration of the <i>in situ</i> particle distribution for different paradigmatic states of the Fermi-Hubbard model . . . . . | 71  |
| 2-2 | $\langle \hat{n} \rangle$ versus $\mu/t$ for fixed $U/t$ and $k_B T/t$ . . . . .  | 73  |
| 2-3 | $\langle \Delta \hat{n}^2 \rangle$ versus $\mu/t$ for fixed $U/t$ and $k_B T/t$ . . . . .                                       | 75  |
| 2-4 | Average doublon density at half-filling and fixed $U/t$ versus $k_B T/t$ . .  | 76  |
| 2-5 | Entropy per site, $s/k_B$ , at half-filling and fixed $U/t$ versus $k_B T/t$ . .  | 78  |
| 2-6 | Uniform spin susceptibility, $\chi t a^2$ , at half-filling and fixed $U/t$ versus $k_B T/t$ . . . . .                          | 79  |
| 2-7 | Schematic phase diagram for the cuprate high- $T_c$ superconductors . . . . .   | 83  |
| 3-1 | Top view of the vacuum chamber, along the $-z$ -direction . . . . .   | 110 |
| 3-2 | Illustration of the magnetic field coils used for generating homogeneous magnetic fields and magnetic field gradients . . . . . | 116 |
| 3-3 | Side-view along the $x$ -direction of the optical traps and the solid immersion lens . . . . .                                  | 121 |
| 3-4 | Side-view along the $-y$ -direction of the optical traps and the solid immersion lens . . . . .                                 | 123 |
| 3-5 | Offset-lock laser system for the $D1$ optical pumping light . . . . .   | 131 |
| 3-6 | High-resolution imaging setup and illustration of the Raman sideband cooling scheme . . . . .                                   | 139 |
| 3-7 | Site-resolved fluorescence image of $^{40}\text{K}$ atoms in a square optical lattice   | 144 |
| 3-8 | Measuring the point spread function of the imaging system and the intensity histogram of the observed fluorescence . . . . .    | 145 |

|      |   |     |
|------|---|-----|
| 3-9  | Identification of occupied lattice sites from a raw fluorescence image . . . . .  | 147 |
| 3-10 | Calibrating the duration of the light pulse used to remove atoms for spin-resolved imaging . . . . .  | 166 |
| 3-11 | Imaging doubly-occupied sites through spin-dependent imaging . . . . .  | 174 |
| 4-1  | Calibration of the on-site interaction energy $U$ using lattice modulation spectroscopy . . . . .   | 188 |
| 4-2  | Lattice modulation spectroscopy to measure the band gap between the ground and first excited bands . . . . .  | 192 |
| 4-3  | Average local moment at half-filling and fixed temperature versus $U/t$   | 196 |
| 4-4  | Average local moment at half-filling and fixed entropy per particle versus $U/t$ . . . . .  | 198 |
| 4-5  | Average local moment at half-filling and fixed $U/t$ versus $k_B T/t$ . . . . .   | 200 |
| 4-6  | $\langle \hat{m}_{z,i}^2 \rangle$ and $\langle \Delta \hat{m}_{z,i}^2 \rangle$ versus $\mu/t$ for fixed $U/t$ and $k_B T/t$ . . . . .                                     | 202 |
| 4-7  | Observation of metallic, Mott-insulating, and band-insulating states of the 2D Fermi-Hubbard model . . . . .  | 207 |
| 4-8  | Radially averaged profiles of the in-trap local moment and its variance for metallic, Mott-insulating, and band-insulating states of the 2D Fermi-Hubbard model . . . . . | 208 |
| 4-9  | Comparing two methods for measuring the variance of the local moment  | 210 |
| 4-10 | Radially averaged local entropy per site . . . . .  | 213 |
| 4-11 | Examining the effects of temperature on the average local moment, and its variance, for Mott- and band-insulating samples . . . . .                                       | 215 |
| 4-12 | Temperature dependence of the average local moment, $\langle \hat{m}_z^2 \rangle$ , at fixed $U/t$ and $\mu/U$ . . . . .  | 218 |
| 4-13 | Spin-resolved single-site fluorescence imaging of a fermionic Mott insulator . . . . .  | 234 |
| 4-14 | Site-resolved average local moment and average nearest-neighbor charge and spin correlations of a 2D fermionic Mott insulator . . . . .                                   | 242 |

|   |     |
|---|-----|
| 4-15 Nearest-neighbor charge and spin correlations as functions of $\langle \hat{m}_z^2 \rangle$ and $k_B T/t$ , for $U/t = 7.2(1)$ . . . . .   | 249 |
| 4-16 The average moment corresponding to the zero-crossing of the nearest-neighbor moment correlation function, $C_m(1)$ , versus $U/t$ . . . . .   | 252 |
| 4-17 The average total density corresponding to the zero-crossing of the nearest-neighbor moment correlation function, $C_m(1)$ , versus $U/t$ . . . . .  | 253 |
| 4-18 The average moment corresponding to the minimum value of the nearest-neighbor moment correlation function, $C_m(1)$ , versus $U/t$ . . . . .   | 254 |
| 4-19 The average total density corresponding to the minimum value of the nearest-neighbor moment correlation function, $C_m(1)$ , versus $U/t$ . . . . .  | 255 |
| 4-20 Temperature $k_B T/t$ of Mott-insulating samples at $U/t = 7.2(1)$ , as a function of time held in equilibrium in an optical lattice . . . . .   | 256 |
| 4-21 $g_2(1)$ and $\bar{g}_2(1)$ as functions of the average local moment for $U/t = 7.2(1)$ and fixed temperature . . . . .  | 261 |
| 4-22 Relative contributions to $C_m(1)$ as functions of the average local moment at $U/t = 7.2$ and $k_B T/t = 1.22$ . . . . .  | 265 |
| 4-23 Charge and spin spatial correlation matrices as functions of $\langle \hat{m}_z^2 \rangle$ at $U/t = 7.2(1)$ . . . . .   | 268 |
| 4-24 Spin and charge correlation functions of the 2D Fermi-Hubbard model versus filling, $\langle \hat{n} \rangle = \langle \hat{n}_\uparrow + \hat{n}_\downarrow \rangle$ , for different values of the spatial separation between lattice sites, at $U/t = 7.2$ . . . . . | 270 |
| 4-25 Nearest-neighbor spin and charge correlation functions versus $U/t$ at half-filling and fixed temperature, $k_B T/t$ . . . . .   | 272 |
| 4-26 Nearest-neighbor spin and charge correlation functions versus $U/t$ at half-filling and fixed entropy per particle, $S/k_B N$ . . . . .  | 273 |
| 4-27 Charge and spin correlation functions of the half-filled 2D Fermi-Hubbard model versus temperature, $k_B T/t$ , for different values of the spatial separation between lattice sites, at $U/t = 7.2$ . . . . .   | 275 |

|      |   |     |
|------|---|-----|
| 4-28 | Hole-hole, hole-doublon, and doublon-doublon correlation functions of the half-filled 2D Fermi-Hubbard model versus temperature, $k_B T/t$ , for different values of the spatial separation between lattice sites, at $U/t = 7.2$ | 277 |
| 5-1  | Creating stripes in a large, dilute sample of $^{40}\text{K}$ atoms to calibrate an applied magnetic gradient   | 297 |
| 5-2  | Calibration of the applied magnetic gradient using microwave spectroscopy   | 298 |
| 5-3  | Calibration of the applied magnetic gradient using lattice modulation spectroscopy  | 299 |
| 5-4  | Calibration of the harmonic trapping frequency of the underlying potential of the optical lattice   | 302 |
| 5-5  | Spin thermoelectric susceptibility and spin Seebeck Coefficient versus polarization, $(\hat{n}_\uparrow - \hat{n}_\downarrow)/(\hat{n}_\uparrow + \hat{n}_\downarrow)$ , of the half-filled 2D Fermi-Hubbard model                | 308 |
| 5-6  | Separating the two spin states in a homogeneous 2D Fermi-Hubbard system   | 316 |
| 5-7  | Measured temperature, $k_B T/t$ , and uniform spin susceptibility, $\chi ta^2$ , versus $t/U$   | 319 |
| 5-8  | Relaxation dynamics after removing the tilt of the lattice potential  | 324 |
| 5-9  | $D_s$ of the half-filled homogeneous 2D Fermi-Hubbard model versus $t/U$  | 329 |
| 5-10 | Average doublon density at half-filling and fixed entropy per particle versus $U/t$   | 333 |
| 5-11 | Dependence of the relaxation time, $\tau_D$ , on the system size $L$  | 335 |
| 5-12 | Time dependence of the imbalance in the box after quenching the magnetic gradient to a finite value from zero   | 339 |
| 5-13 | DC spin conductivity of the half-filled 2D Fermi-Hubbard model versus $t/U$   | 341 |

|   |     |
|---|-----|
| 5-14 NLCE calculations of real-time spin current-current correlation functions and the AC spin conductivity . . . . .   | 345 |
| 5-15 AC response of the spin density imbalance under a sinusoidal drive . .   | 359 |
| <br>  |     |
| A-1 Nearest-neighbor hole-hole correlation function versus $U/t$ at half-filling<br>for fixed temperature and fixed entropy per particle, $S/k_B N$ . . . . . | 368 |
| A-2 Nearest-neighbor hole-doublon correlation function versus $U/t$ at half-filling<br>for fixed temperature and fixed entropy per particle, $S/k_B N$ . .    | 368 |
| A-3 Nearest-neighbor doublon-doublon correlation function versus $U/t$ at<br>half-filling for fixed temperature and fixed entropy per particle, $S/k_B N$     | 369 |



# Chapter 1

## Overview

In recent decades, ultracold atomic gases have emerged as pristine, isolated, and highly-controllable quantum platforms for experimentally studying the myriad of interesting phenomena which arise in quantum many-body systems [22]. For instance, the first realization of Bose-Einstein condensation (BEC) of a dilute vapor of bosonic atoms [3, 50] enabled experimental probes into the nature of degenerate bosonic quantum matter. This, in turn, provided much insight into the interplay between the quantum statistics of bosonic particles, whereby a macroscopic number of particles may enter the same quantum state under the correct conditions, and inter-particle interactions [118]. With these experimental systems, it became possible, for example, to study the connection between superfluidity and Bose-Einstein condensation [170, 185], as well as to examine the excitation spectrum of the system in the presence of interactions [215, 231]. Soon after the creation of the first Bose-Einstein condensates with ultracold atoms, it became possible to experimentally produce quantum degenerate samples of ultracold Fermi gases [51, 207, 227, 113, 75, 84]. This achievement represented a major milestone for the field, because it allowed for the experimental study of quantum systems of particles that obey fermionic statistics, and which must therefore conform to the Pauli exclusion principle, a rule that prevents two fermionic particles from occupying the same quantum state, in a highly-controllable and clean setting. Such fermionic systems can be found throughout nature, and the collective behavior of these systems dictate, for instance, the structure of the periodic table

of elements, the properties of electrical conduction in many materials, and even the inner workings of nuclear matter.

One extremely appealing aspect of this new experimental platform lies in the fact that these ultracold Fermi gases inherently resemble the behavior of a large variety of natural physical systems, from the electrons in a metal to the neutrons in a neutron star. It is thus possible to use these ultracold gases of fermionic atoms, that can be created and observed in a controllable lab environment, to simulate the properties of physically similar, but generally more complex quantum systems, a concept commonly referred to as quantum simulation [65]. Having the ability to simulate the physics of strongly interacting many-body systems using a separate, highly controllable and clean quantum system is extremely powerful, given that the fermionic character of the constituent particles generally makes a complete theoretical understanding of these systems using classical computers highly challenging, a phenomenon known as the fermionic sign problem [144, 226].

The power of ultracold Fermi gases as quantum simulators became apparent when it was realized that, by adjusting a magnetic field near a Feshbach resonance [106, 48, 41], one could tune both the strength and the sign of the *s*-wave interactions between fermions in different spin states, allowing one to freely explore the smooth crossover from a BEC of tightly bound molecules, to a superfluid of loosely bound BCS pairs of fermionic atoms [189, 247, 246, 119, 81]. The experimental realization of the BEC-BCS crossover represented a major achievement in the field of many-body physics, because it provided significant insight into the nature of superfluidity in bulk fermionic systems. Because of the strong interactions present in the middle of the crossover region, this new type of fermionic superfluid also allowed for incredibly high critical temperatures for the transition to superfluidity, relative to the Fermi temperature, compared to other superfluids observed in nature, such as Helium-3 or the high- $T_c$  superconductors.

Around the same time as the experimental realization of the BEC-BCS crossover in bulk Fermi gases, a different technique was being applied to degenerate Fermi gases which would allow for the simulation of electronic systems in condensed mat-

ter [156, 183, 124, 42, 63]. This technique, which confined the Fermi gas in a periodic potential formed from a far-detuned optical lattice, was motivated by the idea that strongly interacting ultracold fermionic atoms in a lattice potential could be used to simulate the Fermi-Hubbard model [101], a paradigmatic model of strong electron correlations in solid state systems believed to capture the essential physics underlying the behavior observed in the high- $T_c$  superconducting cuprates [5, 6, 201, 49, 139], materials whose unconventional superconductivity cannot be explained by BCS theory alone. The strong experimental push to simulate this Hamiltonian using ultracold fermionic atoms was also riding on the recent successes that had come from studying ultracold bosonic optical lattice systems [52, 80, 218]. This, combined with the fact that the Fermi-Hubbard model had not been (and still is not) solved theoretically (except in several specific limiting cases), because of the fermion sign problem, led to the hope that, through the experimental simulation of the Fermi-Hubbard model with ultracold atoms, it would become possible to understand the behavior of this strongly correlated many-body Hamiltonian in theoretically intractable regimes, which could then shed light on the physical mechanism(s) underlying superconductivity in the cuprates. As a side note, in recent years another interesting platform has been developed, magic-angle twisted graphene, which also shows evidence of correlated insulator and unconventional superconducting behavior [32, 31].

Significant progress towards the ultimate goal of understanding high- $T_c$  superconductivity in the cuprates using ultracold atoms was achieved when signatures of the Mott-insulating state, an interaction driven insulator, were observed for the first time via a reduction in the density of doubly-occupied sites in the lattice with increasing on-site interactions [114], as well as through a suppression of the compressibility of the system [205]. Shortly thereafter, another major milestone was achieved through the observation of short-range antiferromagnetic spin correlations in the Mott-insulating state [78, 105, 76, 89]. However, even though these results represented significant breakthroughs in the field, due to the lack of high-resolution *in situ* imaging in these experiments, many of the interesting properties of this strongly interacting fermionic lattice system had to be probed by somewhat indirect means (e.g. using Bragg

scattering or through dimerized lattices). Fortunately, while there was a significant experimental effort pushing the frontier of fermionic atoms in optical lattices, a new tool was developed for bosonic atoms, the quantum gas microscope, which allowed for both the observation [16, 209], and control [236] of single atoms on single lattice sites in two-dimensional systems. This proved an extremely powerful tool for bosonic gases, because it made it possible to directly observe spatial structure and ordering in bosonic Mott insulators [15, 209], at the level of the smallest length scale in the system, a single lattice site. Additionally, it enabled measurements of spatial correlations and dynamics in two-dimensional Bose-Hubbard systems [60, 35, 61, 108], which would not have been accessible otherwise. There was therefore a strong push to develop this technology for two-dimensional fermionic systems [40, 85, 179, 169, 58, 27], since it was clear that the ability to observe and manipulate samples at the single atom and single lattice site level could not only give one the ability to examine local, spatial structure in these strongly correlated many-body fermionic states, but it would also provide ultimate control over these systems, which was desirable, for instance, in order to push ultracold fermionic lattice experiments into regimes which are highly challenging to describe with current theoretical tools [20, 99].

The work presented in this thesis is concerned precisely with this topic, and describes the concept of quantum gas microscopy with fermionic  $^{40}\text{K}$  atoms in a square optical lattice in two dimensions. The different experiments performed using this tool, which are covered in this thesis, can be divided into two main areas of focus. The first concerns the use of our quantum gas microscope to probe thermodynamic properties of the 2D Fermi-Hubbard model in equilibrium, including the site-resolved occupation of metallic, Mott-insulating, and band-insulating states in the lattice, as well as locally resolved spatial spin and charge correlations within a Mott-insulating sample. The second area of focus is concerned with non-equilibrium, transport properties of the 2D Fermi-Hubbard model, and uses the single-site resolution of the quantum gas microscope to measure the linear response spin transport coefficients of the system at half-filling. These transport coefficients are inherent properties of the 2D Fermi-Hubbard Hamiltonian, which are highly challenging to calculate at relatively

low temperatures using current theoretical techniques. Analogous measurements in the cuprates are also very difficult to perform, because the ability to control and manipulate spin currents in these materials is heavily impeded.

## 1.1 Thesis Outline

This thesis is organized as follows.

Chapter 2 provides some theoretical background for the work discussed in this thesis. We discuss the basic principles of non-interacting fermions in a periodic potential, including Bloch states and the corresponding band structure, and then motivate a single-band tight binding description of the system in the deep lattice limit. Because this topic is heavily discussed in previous theses and text books, we generally provide the relevant results, without going into too much detail. From the tight binding picture of the Hamiltonian, we examine the eigenstates and corresponding dispersion relation, and subsequently take a look at the spatial density and spin correlations which are present in the non-interacting Fermi gas in two dimensions on a square lattice. After gaining some intuition from the non-interacting case, we motivate the tight binding Hamiltonian for the case where there are repulsive interactions between opposite spin states, which ultimately leads to a description of the system via the 2D Fermi-Hubbard model. We then examine some of the basic phenomenology of the Fermi-Hubbard model by studying the limiting case of a double well system, and we also describe some of the essential features of different paradigmatic states which exist in larger systems, to provide some general intuition for the thermodynamic properties of this Hamiltonian. Finally, at the end of chapter 2, we examine the electrical conductivity, a transport coefficient which characterizes the linear response of the system to an external perturbation. We then derive a Kubo formula for the conductivity, which relates this transport property to the underlying Fermi-Hubbard Hamiltonian in the absence of the external perturbation, and we subsequently examine some basic features of the conductivity which are relevant for the transport experiments discussed in later chapters.

In chapter 3, we provide a technical description of the experimental apparatus, including the relevant optical traps and magnetic coils, with sufficient detail for the reader to understand most of the technical aspects and experimental details of subsequent chapters. Further information about the apparatus itself and its construction can be found in previous theses. We then describe our fluorescence imaging technique based on Raman sideband cooling, which allows us to detect single atoms on single lattice sites with high fidelity, and we discuss how we are able to reconstruct the *in situ* parity-projected site occupation from these fluorescence images. After discussing the single-site imaging process, we provide a short description of the basic experimental sequence used to create degenerate samples of fermionic  $^{40}\text{K}$ , while leaving the details specific to particular experiments for subsequent chapters. At the end of chapter 3, we examine the details of our spin-dependent imaging technique, which was developed to allow us to separately observe the different spin states in the lattice through single-site imaging. This technique is used heavily in later chapters for measurements of the spin correlation function, to examine antiferromagnetic correlations in the 2D Fermi-Hubbard model, as well as the spin current, to obtain the spin conductivity from transport experiments.

In chapter 4, we begin with a short introduction to previous experiments that have been performed with ultracold fermionic atoms in optical lattices in order to examine different aspects of the Fermi-Hubbard model. We then describe how this Hamiltonian is realized in our fermionic quantum gas microscope, and we introduce the local moment, a quantity that describes the density of singly occupied sites in the system, and which acts as our experimental observable. After discussing some basic properties of the local moment itself, we describe our experimental results which examine metallic, Mott-insulating, and band-insulating states of the 2D Fermi-Hubbard model *in situ*. We then take a look at the effects of temperature on the local moment of Mott and band insulators, and we show how the insulating behavior melts away with increasing temperature. Subsequently, we examine more closely the behavior of the Mott insulator, and describe our experimental results which locally study the spatial spin and charge correlations present in a trapped sample. This allows us to

measure these correlation functions, using the single-site resolution of our quantum gas microscope, as functions of the local doping in the system. We then examine more thoroughly the non-trivial behavior observed in the nearest-neighbor charge correlator as a function of doping: near half-filling, singly-occupied sites are found to tend to bunch together, due to correlated doublon-hole pairs in the system that are associated with antiferromagnetic spin correlations. At low densities, however, the effects of repulsive interactions between particles, combined with Pauli blocking between like-spin atoms, dominates and leads to an effective repulsion, or anti-bunching behavior between singly occupied sites, which changes the character of the charge correlation function. We compare our experimental results for both the spin and charge correlations as functions of doping to numerical calculations of these quantities, and generally find good quantitative agreement.

In chapter 5, we provide a brief introduction to the concept of using ultracold atoms in optical lattices for the purpose of studying transport, and describe several previous experiments that have been performed specifically with fermionic atoms for this purpose. We then give a technical description of the experimental technique which we developed to study near-equilibrium spin transport in the 2D Fermi-Hubbard model using our quantum gas microscope. Subsequently, we present our experimental results which measure the DC spin diffusion coefficient, the uniform spin susceptibility, and the DC spin conductivity of a homogeneous Mott-insulating sample at half-filling, as functions of the ratio between the on-site interaction energy and the nearest-neighbor tunneling amplitude. We compare the experimentally measured transport coefficients with independent numerical calculations, and motivate the many theoretical challenges associated with calculating the transport properties of the Hamiltonian in the DC limit. Finally, at the end of chapter 5, we give a detailed outlook of these results, and provide a description of several ways this work can be readily extended in the future, including a look at ongoing work in the lab that involves measuring the full frequency dependent response of the AC spin conductivity for the 2D Fermi-Hubbard model at half-filling.

Finally, chapter 6 concludes the thesis with a short summary of the results, and

a brief outlook towards future research directions which are possible using our quantum gas microscope for fermionic  $^{40}\text{K}$ . The appendices at the end include isothermal and isentropic numerical calculations from NLCE of the nearest-neighbor hole-hole, hole-doublon, and doublon-doublon correlation functions versus the Hubbard parameters  $U/t$ , which were generated by our theory collaborators for the spin and charge correlation work discussed in chapter 4, and which are provided for future reference. Also included in the appendices are the publications which are most relevant to the research discussed in this thesis, and in which I was involved during the course of my PhD.

# Chapter 2

## Ultracold Atoms in Optical Lattices

In this chapter, we present some of the basic theoretical background for the work described in this thesis. We begin the chapter in section 2.1 with a short description of the principles which dictate the behavior of non-interacting fermions in a square optical lattice. We relate the depth of the lattice potential to the tunneling matrix element in the tight-binding limit, and discuss the behavior of spatial density and spin correlations for the non-interacting two component system in this regime. Subsequently in section 2.2, we discuss the effects of on-site interactions between opposite spin states, and introduce the 2D Fermi-Hubbard Hamiltonian as the model system that appropriately depicts the behavior of an interacting two-component gas of ultracold atoms in an optical lattice. We then examine the behavior of this Hamiltonian in the limiting case of two lattice sites (a double well) in section 2.2.1, followed by an introduction, in section 2.2.2, to several theoretical approaches which have been developed to study this Hamiltonian in its more general form. In section 2.2.3, we discuss some of the basic phenomenology and thermodynamic properties of the 2D Fermi-Hubbard model, which we then relate to electronic and thermodynamic properties that have been observed in the high- $T_c$  cuprate superconductors, a class of materials for which the 2D Fermi-Hubbard model has been proposed as a model system. Finally, in section 2.3, we discuss the concept of electrical (and spin) transport, and introduce the conductivity, a transport coefficient which describes the linear response of the system to an applied external perturbation, such as an electric field. We

relate the conductivity to the intrinsic properties of the unperturbed Hamiltonian, and discuss some of its basic features.

## 2.1 Non-Interacting Fermions

In this section we provide a brief review of the physics of non-interacting fermionic atoms in a periodic potential formed from an optical lattice, a cold atoms analog of the electrons in a crystalline material. In this system, the potential formed by the periodic arrangement of positive ions in the crystal that the electrons experience is replaced by a periodic potential, for neutral fermionic atoms, of interfering laser beams. Because this topic has been described in great detail in previous theses [79, 241, 37, 168], and can also be found in numerous textbooks [12], we quote here most of the relevant results, rather than re-deriving them, and refer the reader to the cited resources for more information. We focus instead in this section on the behavior of spatial correlations between non-interacting fermionic atoms in the lattice, in order to gain some intuition for the behavior of these correlations in the more complicated case of the fully interacting, 2D Fermi-Hubbard model studied throughout the rest of this thesis. This will allow us to better understand, for instance, the extent to which the spatial correlations we observe experimentally, in both the charge and spin degrees of freedom, can be attributed to the effects of interactions between opposite spin states in the lattice, versus the effects of the Pauli exclusion principle and the fermionic statistics of the constituent particles. In section 2.1.1, we discuss relevant results regarding the tight binding description of atoms in a deep optical lattice, as well as its associated band structure and eigenstates. Then in sections 2.1.2 and 2.1.3, we discuss spatial density and spin correlations, respectively, for a two component gas of fermionic atoms in a square lattice, which will be relevant for the experimental correlation measurements of the interacting system described in section 4.4.

### 2.1.1 Band Structure, the Fermi Surface, and the Tight Binding Model

In an optical lattice formed from two counter-propagating, red-detuned laser beams which interfere with one another, the potential experienced by the atoms confined to the lattice has the form

$$V(x) = V_0 \sin^2 \left( \frac{k_L x}{2} \right), \quad (2.1)$$

where  $V_0$  characterizes the depth of the lattice,  $k_L \equiv 2\pi/a$ , and  $a$  is the lattice spacing along the  $x$ -direction. Since the lattice considered in this thesis is square, the potential is separable along the two spatial dimensions, so that the eigenstates can be calculated separately for each axis, and the final single-particle energy is simply a sum of the eigenvalues along the two orthogonal axes. We thus consider, for the moment, only the potential along, for example, the  $x$ -direction (Eq. 2.1). In such a potential, the single-particle Hamiltonian in first-quantized notation becomes,

$$\hat{H}_{\text{single}} = \frac{-\hbar^2}{2m} \nabla^2 + V_0 \sin^2 \left( \frac{k_L x}{2} \right), \quad (2.2)$$

where  $m$  is the mass of the atom. Because the potential, Eq. 2.1, is periodic in the lattice spacing,  $V(x+a) = V(x)$ , we can apply Bloch's theorem to write the single-particle eigenstates of Eq. 2.2 in the form,

$$\psi_{n,q}(x) = e^{iqx} u_{n,q}(x), \quad (2.3)$$

where  $e^{iqx}$  is a simple plane wave with momentum  $q$ , and  $u_{n,q}(x)$  is some function that is periodic in the lattice potential,  $u_{n,q}(x+a) = u_{n,q}(x)$ . The labels  $n$  and  $q$  here represent the band index and the quasi-momentum state, respectively, of the eigenstate  $\psi_{n,q}(x)$ . For a large crystalline lattice with  $N$  sites along the  $x$ -direction, so that  $N = L/a$ , where  $L$  is the length of the crystal along  $\hat{x}$ , we can apply Born-von Karman boundary conditions to the Bloch states in Eq. 2.3, which requires  $\psi(x+Na) = \psi(x)$  for the wave function in the crystal. Plugging this boundary condition

into Eq. 2.3 then gives,

$$\begin{aligned}\psi_{n,q}(x + Na) &= e^{iqNa} e^{iqx} u_{n,q}(x + Na) = e^{iqNa} e^{iqx} u_{n,q}(x) \\ &= \psi_{n,q}(x) = e^{iqx} u_{n,q}(x).\end{aligned}\quad (2.4)$$

One must therefore have that  $e^{iqNa} = 1$ , so that,

$$q = \frac{2\pi}{a} \frac{j}{N} = k_L \frac{j}{N}, \quad (2.5)$$

where  $j$  is some integer. Additionally, because the potential is spatially periodic in  $a$ , the reciprocal lattice must be spatially periodic in the reciprocal lattice vector  $k_L = 2\pi/a$ . This means that we can restrict our analysis to values of  $q$  that lie within the first Brillouin zone,  $q \in [-\pi/a, \pi/a] = [-k_L/2, k_L/2]$ , and that we can index the states with the band indices  $n$  in such a way that, for a fixed value of  $n$ , if we consider the Bloch states as functions of  $q$ , then they are periodic in the reciprocal lattice vector,  $\psi_{n,q+k_L}(x) = \psi_{n,q}(x)$ . Therefore, for each value of  $q$ , there are an infinite (albeit discrete) number of bands  $n$  corresponding to different eigenstates, with the same quasi-momentum, that have distinct eigen energies,  $\epsilon_n(q)$ . Here,  $\epsilon_n(q)$  is also periodic in the reciprocal lattice vector, so that  $\epsilon_n(q + k_L) = \epsilon_n(q)$ .

To obtain the band structure of the optical lattice system,  $\epsilon_n(q)$ , corresponding to the eigenvalues of the Bloch eigenstates, one can rewrite the Bloch states in the plane wave basis,

$$\psi_{n,q}(x) = e^{iqx} \sum_j c_j(n) e^{ijk_L x}, \quad (2.6)$$

where the  $c_j(n)$  are the complex coefficients of the expansion. Note that only integer multiples of  $k_L$  are included in the Fourier decomposition of the Bloch states, since these states are periodic in the reciprocal lattice wave vector. One can also Fourier transform the lattice potential, Eq. 2.1, which, neglecting the overall energy offset and adjusting the lattice phase for convenience, contains only the Fourier components,  $V_0 e^{ik_L x}/4$  and  $V_0 e^{-ik_L x}/4$ . The lattice potential can therefore only couple Fourier components which differ by  $k_L$ . The kinetic energy,  $-\hbar^2 \nabla^2 / 2m$ , on the other hand, is

diagonal in the plane wave basis, with energy  $\hbar^2(q + jk_L)^2/2m$  for a plane wave with quasi-momentum  $q + jk_L$ . One can therefore break up the single-particle Hamiltonian, Eq. 2.2, into a series of terms labeled by  $q$  within the first Brillouin zone, which individually only act on momentum states in the family  $q + jk_L$ , for integer values of  $j$ . That is, one can write,

$$\hat{H}_{\text{single}} = \sum_q \hat{H}(q), \quad (2.7)$$

where the matrix elements of the term  $\hat{H}(q)$  in the series are given by,

$$\hat{H}_{n,p}(q) = \frac{\hbar^2}{2m}(q + nk_L)^2 \delta_{n,p} + \frac{V_0}{4}(\delta_{n+1,p} + \delta_{n-1,p}). \quad (2.8)$$

For convenience of notation, in the remainder of this thesis we will write the depth of the optical lattice in units of the recoil energy,

$$E_R = \frac{\hbar^2 \pi^2}{2ma^2}, \quad (2.9)$$

which represents the single-particle kinetic energy for a state whose quasi-momentum lies at the edge of the first Brillouin zone. Additionally, we can express things in terms of the unit-less quasi-momentum  $q/k_L$ . With this notation, Eq. 2.8 becomes simply,

$$\frac{\hat{H}_{n,p}(q)}{E_R} = 4(q + n)^2 \delta_{n,p} + \frac{s}{4}(\delta_{n+1,p} + \delta_{n-1,p}), \quad (2.10)$$

where  $s \equiv V_0/E_R$  is the lattice depth in units of recoil energies, and  $q$  here is understood to be the unit-less quasi-momentum. One can then diagonalize the matrix defined by Eq. 2.10 numerically to obtain the discrete set of eigenvalues  $\epsilon_n(q)$  for all of the different energy levels  $n$  corresponding to the quasi-momentum  $q$  in the first Brillouin zone. Once this band structure,  $\epsilon_n(\mathbf{q})$ , is known (we temporarily write  $\mathbf{q}$  in vector notation for the case of multiple spatial dimensions), one can easily obtain different quantities which characterize the eigenstates  $\psi_{n,\mathbf{q}}(\mathbf{r})$ , including the mean velocity,

$$\mathbf{v}_n(\mathbf{q}) = \frac{1}{\hbar} \nabla_{\mathbf{q}} \epsilon_n(\mathbf{q}), \quad (2.11)$$

where  $\nabla_{\mathbf{q}}$  represents the gradient with respect to  $\mathbf{q}$ , or the effective band mass tensor,

$$[\mathbf{M}_n^{-1}(\mathbf{q})]_{i,j} = \frac{1}{\hbar^2} \frac{\partial^2 \epsilon_n(\mathbf{q})}{\partial q_i \partial q_j}. \quad (2.12)$$

When the optical lattice is relatively deep, so that the band gap  $\Delta$  between the lowest energy band and the first excited band, which characterizes the minimal energy separation between the two bands as a function of quasi-momentum  $q$ , is large relative to all other energy scales, including the temperature and the total chemical potential of the sample,  $k_B T \ll \Delta$  and  $\mu \ll \Delta$ , we can describe the system using a single-band model, since only one band is effectively occupied. To do this, we can first write the single-particle Hamiltonian in second-quantized notation as,

$$\hat{H}_0 = \int dx \hat{\psi}^\dagger(x) \hat{H}_{\text{single}} \hat{\psi}(x) = \int dx \hat{\psi}^\dagger(x) \left( \frac{-\hbar^2}{2m} \nabla^2 + V(x) \right) \hat{\psi}(x), \quad (2.13)$$

where  $\hat{\psi}^\dagger(x)$  ( $\hat{\psi}(x)$ ) are the fermionic field creation (annihilation) operators. When the lattice is deep, it is convenient to change bases from the delocalized Bloch state basis, to one which describes states that are localized to individual sites. This will allow us to make a tight-binding approximation for our single-band, model system. We can therefore change to the Wannier basis, where the Wannier function in the first (lowest energy) band, which describes a particle localized at site  $i$ , is given in terms of the Bloch states as,

$$w_{n=1}(x - x_i) = \frac{1}{\sqrt{N}} \sum_{q \in FBZ} e^{-iqx_i} \psi_{n=1,q}(x), \quad (2.14)$$

where the summation runs over all quasi-momenta in the first Brillouin zone (FBZ). Writing the fermionic field operators in this Wannier basis, and ignoring contributions from all bands beyond the lowest energy band (the single band approximation), then

gives,

$$\begin{aligned}\hat{\psi}(x) &= \sum_j w_{n=1}(x - x_j) \hat{c}_j \\ \hat{\psi}^\dagger(x) &= \sum_j w_{n=1}^*(x - x_j) \hat{c}_j^\dagger,\end{aligned}\quad (2.15)$$

where  $\hat{c}_j^\dagger$  ( $\hat{c}_j$ ) is the fermionic creation (annihilation) operator for a particle in the Wannier function  $w_{n=1}(x - x_j)$ , which is localized at a position  $x_j$  corresponding to site  $j$ . If we then plug Eq. 2.15 into the second quantized Hamiltonian, Eq. 2.13, we obtain,

$$\hat{H}_0 = \sum_{i,j} \hat{c}_i^\dagger \hat{c}_j \int dx \left[ w_{n=1}^*(x - x_i) \left( \frac{-\hbar^2}{2m} \nabla^2 + V(x) \right) w_{n=1}(x - x_j) \right]. \quad (2.16)$$

When the optical lattice is deep, which means the different Wannier functions are well localized to individual sites, with little overlap with neighboring sites, we can ignore contributions to the summation in Eq. 2.16 where the overlap integral,

$$\int dx \left[ w_{n=1}^*(x - x_i) \left( \frac{-\hbar^2}{2m} \nabla^2 + V(x) \right) w_{n=1}(x - x_j) \right], \quad (2.17)$$

contains Wannier functions that are separated by more than one site. When we do this, we arrive at the tight-binding approximation for the single-band system,

$$\hat{H}_{TB} = -t \sum_{\langle i,j \rangle} \left[ \hat{c}_i^\dagger \hat{c}_j + h.c. \right], \quad (2.18)$$

where the summation is performed over all pairs of nearest-neighbor sites  $i$  and  $j$ , denoted by  $\langle i,j \rangle$ , and  $t$  is the nearest-neighbor tunneling amplitude,

$$t = - \int dx \left[ w_{n=1}^*(x) \left( \frac{-\hbar^2}{2m} \nabla^2 + V(x) \right) w_{n=1}(x + a) \right]. \quad (2.19)$$

Physically, the tight binding Hamiltonian, Eq. 2.18, describes particles hopping between nearest-neighbor sites in the lattice at a rate set by  $t$ . If we were to ex-

plicitly include higher-order terms from the full single-band Hamiltonian, Eq. 2.16, such as terms where the overlap integral contains Wannier functions separated by next-nearest-neighbor sites, these would appear as higher-order (e.g. next-nearest-neighbor and beyond) tunneling terms in the final tight-binding Hamiltonian. The overlap integrals (Eq. 2.17), which characterize the different tunneling amplitudes (i.e. nearest-neighbor versus next-nearest-neighbor, etc...), can be calculated directly using numerical calculations, however, and for typical lattice depths used in the experiment ( $s = V_0/E_R > 6$ ), the higher-order tunneling amplitudes are negligible relative to the nearest-neighbor amplitude  $t$  (see, for example, Fig. 2-3 of [37]). We are therefore justified, in the deep lattice limit where we operate experimentally, in using the approximate tight binding Hamiltonian, Eq. 2.18, which only takes into account tunneling between neighboring sites, to describe the behavior of our optical lattice system in the single band regime [110].

We can understand the eigenstates and eigenvalues of the tight binding Hamiltonian, Eq. 2.18, by transforming the position operators  $\hat{c}_j^\dagger$  and  $\hat{c}_j$  to Fourier space via,

$$\hat{c}_j = \frac{1}{\sqrt{N}} \sum_{k \in FBZ} e^{-ikaj} \hat{b}_k, \quad (2.20)$$

where  $\hat{b}_k^\dagger$  ( $\hat{b}_k$ ) is the fermionic creation (annihilation) operator for a particle with quasi-momentum  $k$  in the first Brillouin zone. In this basis, the Hamiltonian is diagonal and becomes,

$$\begin{aligned} \hat{H}_{TB} &= -t \sum_{k \in FBZ} [e^{ika} + e^{-ika}] \hat{b}_k^\dagger \hat{b}_k \\ &= \sum_{k \in FBZ} [-2t \cos(ka)] \hat{b}_k^\dagger \hat{b}_k. \end{aligned} \quad (2.21)$$

It follows then that the eigenstates of this system are delocalized states with well-defined quasi-momentum  $k$ , where the corresponding dispersion relation is given by,

$$\epsilon(k) = -2t \cos(ka). \quad (2.22)$$

The bandwidth of this lowest energy band is therefore  $4t$ , and the mean velocity and effective mass of the band can be calculated directly from Eq. 2.22 using Eqs. 2.11 and 2.12, respectively. Generalizing this result to higher spatial dimensions is relatively straightforward, and for the two dimensional situation studied in this thesis, the dispersion relation in the ground band becomes,

$$\epsilon(k) = -2t [\cos(k_x a) + \cos(k_y a)], \quad (2.23)$$

where  $k_x$  is the quasi-momentum along the  $x$ -direction, and  $k_y$  is the quasi-momentum along the  $y$ -direction. Because of these two degrees of freedom,  $k_x$  and  $k_y$ , in the 2D case, the single particle bandwidth increases from  $4t$  in 1D to  $8t$  in 2D. The energy scale for the kinetic energy of the system, which is set by the single-particle bandwidth, is therefore  $8t$  for the 2D case. This will become important in later chapters, when we want to compare the relative strength of the interaction energy to the kinetic energy in the system. One final note about the 2D system is that, because we utilize a square lattice potential, with corresponding lattice vectors  $a\hat{x}$  and  $a\hat{y}$ , the reciprocal lattice vectors are  $\hat{G}_x = (2\pi/a)\hat{x}$  and  $\hat{G}_y = (2\pi/a)\hat{y}$ , which means that the first Brillouin zone is a square region that is comprised of all points  $(k_x, k_y)$  where  $k_x, k_y \in [-\pi/a, \pi/a]$ . At half-filling then, where the band is filled up exactly halfway with particles, the Fermi surface corresponds to a diamond within this square region, where the four corners of the diamond are located at the points  $(\pm\pi/a, 0)$  and  $(0, \pm\pi/a)$ .

### 2.1.2 Density Correlation Functions for the Non-Interacting System

In section 2.1.1, we discussed the behavior of non-interacting fermions in an optical lattice potential, and described a tight binding model for the system (Eq. 2.18) in the single band limit, where the eigenstates were found to be delocalized states with well-defined quasi-momentum  $k$ , and corresponding dispersion relation  $\epsilon(k)$  (Eq. 2.23). In that context, we found it extremely useful, and rather convenient, to examine the system in quasi-momentum space, where the Hamiltonian was easily diagonalized.

However, one of the biggest strengths of a quantum gas microscope experiment lies in its ability to examine the system in real space, rather than in momentum space. For this reason, we are motivated to examine the spatial correlations present in a non-interacting gas of fermionic atoms in an optical lattice. Such correlations are non-trivial due to the formation of a Fermi surface in quasi-momentum space that singles out a particular wave vector, the Fermi wave vector,  $k_F$ . We can first gain some intuition about the spatial correlations in the lattice system by examining the free Fermi gas with dispersion  $\epsilon(k) = \hbar^2 k^2 / 2m$ . We consider then the two-point correlator,

$$G(\mathbf{x}_2, \mathbf{x}_1) \equiv \langle \hat{\psi}^\dagger(\mathbf{x}_2) \hat{\psi}(\mathbf{x}_1) \rangle, \quad (2.24)$$

which describes the spatial correlation between removing a particle at position  $\mathbf{x}_1$  and creating a particle at  $\mathbf{x}_2$ , where  $\hat{\psi}^\dagger(\mathbf{x})$  ( $\hat{\psi}(\mathbf{x})$ ) are the fermionic field creation (annihilation) operators. We can simplify things since the system is uniform and translationally invariant, which means that  $G(\mathbf{x}_2, \mathbf{x}_1)$  can only depend on the spatial separation  $\mathbf{r} = \mathbf{x}_2 - \mathbf{x}_1$ , so that  $G(\mathbf{x}_2, \mathbf{x}_1) = G(\mathbf{r})$ . Additionally, because there is no preferred spatial direction,  $G(\mathbf{r})$  can only depend on  $r = |\mathbf{r}|$ , allowing us to write  $G(\mathbf{x}_2, \mathbf{x}_1) = G(r) = \langle \hat{\psi}^\dagger(\mathbf{r}) \hat{\psi}(\mathbf{0}) \rangle$ , where we have chosen one point as the origin for simplicity. We can then move to Fourier space, and take the Fourier transform of the field operators,

$$\begin{aligned} \hat{\psi}(\mathbf{x}) &= \frac{1}{V} \sum_{\mathbf{k}} \hat{c}_{\mathbf{k}} e^{-i\mathbf{k}\cdot\mathbf{x}} \\ \hat{\psi}^\dagger(\mathbf{x}) &= \frac{1}{V} \sum_{\mathbf{k}} \hat{c}_{\mathbf{k}}^\dagger e^{i\mathbf{k}\cdot\mathbf{x}}, \end{aligned} \quad (2.25)$$

where  $V$  is the volume of the system, and  $\hat{c}_{\mathbf{k}}^\dagger$  ( $\hat{c}_{\mathbf{k}}$ ) is the fermionic creation (annihilation) operator for a particle with momentum  $\mathbf{k}$ . Plugging Eq. 2.25 into  $G(r)$  and simplifying then gives,

$$G(\mathbf{r}) = \frac{1}{V} \sum_{\mathbf{k}} e^{i\mathbf{k}\cdot\mathbf{r}} \langle \hat{c}_{\mathbf{k}}^\dagger \hat{c}_{\mathbf{k}} \rangle = \frac{1}{V} \sum_{\mathbf{k}} e^{i\mathbf{k}\cdot\mathbf{r}} \langle \hat{n}_{\mathbf{k}} \rangle, \quad (2.26)$$

where  $\langle \hat{n}_{\mathbf{k}} \rangle$  represents the average occupation of momentum state  $\mathbf{k}$ . It is clear then that  $G(r)$ , which physically represents a two point spatial correlation function, is equivalent to the Fourier transform of the momentum occupation function  $\langle \hat{n}_{\mathbf{k}} \rangle$ . It therefore makes sense that when there is a well-defined Fermi surface in momentum space, such as at zero temperature in 1D, when  $\langle \hat{n}_{\mathbf{k}} \rangle$  resembles a step function, the Fourier transform of the momentum occupation function will exhibit non-trivial features, including oscillations, which appear in the spatial two-point correlator  $G(r)$ . For the free Fermi gas at zero temperature in  $d$  dimensions, one can calculate  $G(r)$  directly from Eq. 2.26, using  $\sum_{\mathbf{k}} \rightarrow \frac{V}{(2\pi)^d} \int d^d \mathbf{k}$  and the fact that  $\langle \hat{n}_{\mathbf{k}} \rangle = 1$  for  $|\mathbf{k}| < k_F$  and  $\langle \hat{n}_{\mathbf{k}} \rangle = 0$  for  $|\mathbf{k}| > k_F$ . In 1D and 2D one thus obtains,

$$\begin{aligned} G_{1D}(r) &= \frac{1}{\pi} \frac{\sin(k_F r)}{r} = n \left( \frac{\sin(k_F r)}{k_F r} \right) \\ G_{2D}(r) &= \frac{k_F}{2\pi} \frac{J_1(k_F r)}{r} = n \left( \frac{2J_1(k_F r)}{k_F r} \right), \end{aligned} \quad (2.27)$$

where  $n$  is the total density, and  $J_1(r)$  is a Bessel function of the first kind. Taking the limit  $r \rightarrow 0$  in both  $G_{1D}$  and  $G_{2D}$  in Eq. 2.27 gives  $n$ , as one would expect from the fact that  $n = n(\mathbf{x}) = \langle \hat{\psi}^\dagger(\mathbf{x}) \hat{\psi}(\mathbf{x}) \rangle = G(0)$ . Additionally, from the form of  $G_{1D}$  and  $G_{2D}$  in Eq. 2.27, it is clear that  $G(r)$  oscillates as a function of  $r$  with a period set by  $1/k_F$  (as one might expect from the Fourier transform of a step function), and also decays with increasing distance as  $1/r^d$ , where  $d = 1, 2$  for 1D and 2D, respectively.

From the two point correlation function, Eq. 2.24 and Eq. 2.27, one can also calculate higher-order spatial correlations, such as the  $g_2$  correlation function for the total density,

$$g_2(r) \equiv \frac{1}{n^2} \langle \hat{\psi}^\dagger(\mathbf{r}) \hat{\psi}(\mathbf{r}) \hat{\psi}^\dagger(\mathbf{0}) \hat{\psi}(\mathbf{0}) \rangle. \quad (2.28)$$

For the non-interacting system, one can apply Wick's theorem [240, 64] to the correlator in Eq. 2.28 to obtain, for  $r > 0$ ,

$$\begin{aligned} \langle \hat{\psi}^\dagger(\mathbf{r}) \hat{\psi}(\mathbf{r}) \hat{\psi}^\dagger(\mathbf{0}) \hat{\psi}(\mathbf{0}) \rangle &= \langle \hat{\psi}^\dagger(\mathbf{r}) \hat{\psi}(\mathbf{r}) \rangle \langle \hat{\psi}^\dagger(\mathbf{0}) \hat{\psi}(\mathbf{0}) \rangle + \langle \hat{\psi}^\dagger(\mathbf{r}) \hat{\psi}(\mathbf{0}) \rangle \langle \hat{\psi}(\mathbf{r}) \hat{\psi}^\dagger(\mathbf{0}) \rangle \\ &= n^2 - |G(r)|^2, \end{aligned} \quad (2.29)$$

where we have made use of the identities  $n = \langle \hat{\psi}^\dagger(\mathbf{r})\hat{\psi}(\mathbf{r}) \rangle$  and  $\langle \hat{\psi}(\mathbf{r})\hat{\psi}^\dagger(\mathbf{0}) \rangle = -G(-\mathbf{r}) = -G^*(\mathbf{r})$ . It follows therefore that,

$$g_2(r) = 1 - \frac{|G(r)|^2}{n^2}, \quad (2.30)$$

so that for the 1D and 2D systems at zero temperature, we have,

$$\begin{aligned} g_2^{1D}(r) &= 1 - \left( \frac{\sin(k_F r)}{k_F r} \right)^2 \\ g_2^{2D}(r) &= 1 - \left( \frac{2J_1(k_F r)}{k_F r} \right)^2. \end{aligned} \quad (2.31)$$

Taking the  $r \rightarrow 0$  limit of  $g_2^{1D}(r)$  and  $g_2^{2D}(r)$  in Eq. 2.31 gives  $g_2^{1D,2D}(r) \rightarrow 0$ , which means there is zero probability of two fermions occupying the same location in space, something which is completely consistent with what we would expect from the Pauli exclusion principle. Additionally, due to the oscillatory nature of the functions in Eq. 2.31, the strong suppression of  $g_2(r)$  below 1 near the origin extends over a finite distance, from  $r = 0$  to  $r \sim 1/k_F$ , which describes roughly the inter-particle spacing. This is an effect known as the Pauli hole, and represents a real space manifestation of the Pauli exclusion principle. A second important feature of Eq. 2.31 is the oscillatory behavior itself, for the  $g_2$  function, which occurs with a spatial period set by  $1/k_F$ . This is an effect commonly known as Friedel oscillations [68, 193], which appears in the real space correlation functions due to the sharp Fermi surface in momentum space.

At finite temperature,  $k_B T > 0$ , the real space Pauli hole and Friedel oscillations in the  $g_2$  function survive, but become washed out with increasing temperature, due to the effect of finite temperature smearing out the Fermi surface, which removes the sharpness of the features in momentum space. To see this, we note that the general form for the  $g_2$  function, Eq. 2.30, as well as the form for the two point correlation function  $G(r)$ , from Eq. 2.26, remain unchanged, except that the momentum space

occupation  $\langle \hat{n}_{\mathbf{k}} \rangle$  must be generalized to take into account the finite temperature,

$$\langle \hat{n}_{\mathbf{k}} \rangle = \frac{1}{1 + e^{\beta(\epsilon(\mathbf{k}) - \mu)}}, \quad (2.32)$$

which is just the Fermi-Dirac distribution, where  $\beta = 1/k_B T$ ,  $\mu$  is the chemical potential, which sets the total particle number, and  $\epsilon(\mathbf{k}) = \hbar^2 k^2 / 2m$  is the dispersion relation for the free Fermi gas. Thus, at finite temperature the momentum occupation is no longer a step function, where  $\langle \hat{n}_{\mathbf{k}} \rangle = 1$  for  $|\mathbf{k}| < k_F$  and  $\langle \hat{n}_{\mathbf{k}} \rangle = 0$  for  $|\mathbf{k}| > k_F$ . Instead, the Fermi surface is smoothed out by the finite value of  $\beta$ , which allows some states above  $k_F$  to become occupied, and suppresses the occupation of some states below  $k_F$ . The amount that the Fermi surface is smeared out is set by the ratio of the temperature,  $k_B T$ , to the Fermi energy  $\epsilon_F \sim k_F^2$ . For the  $g_2$  function, the effect of finite temperature then is to reduce the width of the Pauli hole, i.e. the region where  $g_2$  is suppressed below 1 centered around  $r = 0$  (the limit  $r \rightarrow 0$  of  $g_2^{1D,2D}(r)$  is still 0 by Pauli exclusion, however), as well as to suppress the amplitude of the Friedel oscillations. As the temperature  $k_B T$  approaches the Fermi energy, these oscillations become extremely suppressed. One can calculate  $g_2^{1D,2D}(r)$  directly, with numerical methods for instance, using Eq. 2.32, Eq. 2.30, and Eq. 2.26, and the interested reader can find such finite temperature plots of the  $g_2$  function for a free, non-interacting Fermi gas in Fig. 2-2 of [37].

From the results for the non-interacting free Fermi gas, we should expect, in the case of non-interacting fermions in the lattice, that there will still be a suppression in the spatial density correlations of the system at short distances due to the Pauli hole, a real-space manifestation of the Pauli exclusion principle, and that this effect should still extend over a distance set by the inter-particle spacing, which scales as  $1/k_F$ . This is because the constituent particles are still fermionic atoms, and the basic effect of the lattice is to introduce a second length scale into the system, the lattice spacing, which might quantitatively change the strength of the density correlations as a function of spatial separation, but should not completely alter our intuition from the free fermion case. For the lattice system, we consider the case where there

are two spin states,  $|\uparrow\rangle$  and  $|\downarrow\rangle$ , with corresponding densities  $\langle\hat{n}_\uparrow\rangle = \langle\hat{n}_\downarrow\rangle$  (the spin-balanced case), where the total density at site  $i$  is given by  $\langle\hat{n}_i\rangle = \langle\hat{n}_{\uparrow,i} + \hat{n}_{\downarrow,i}\rangle$ . We can examine, then, spatial correlations in the total density by defining the density correlation function,

$$C_n(\mathbf{r}) = \langle\hat{n}_i\hat{n}_{i+\mathbf{r}}\rangle - \langle\hat{n}_i\rangle\langle\hat{n}_{i+\mathbf{r}}\rangle, \quad (2.33)$$

where we have subtracted off the trivial part of the correlations in Eq. 2.33,  $\langle\hat{n}_i\rangle\langle\hat{n}_{i+\mathbf{r}}\rangle$ , since we would like to examine deviations from the totally uncorrelated case,  $\langle\hat{n}_i\hat{n}_{i+\mathbf{r}}\rangle = \langle\hat{n}_i\rangle\langle\hat{n}_{i+\mathbf{r}}\rangle$ . For simplicity of notation, we write  $\langle\hat{A}\hat{B}\rangle_c$  to represent  $\langle\hat{A}\hat{B}\rangle - \langle\hat{A}\rangle\langle\hat{B}\rangle$  for two operators  $\hat{A}$  and  $\hat{B}$ . Plugging  $\langle\hat{n}_i\rangle = \langle\hat{n}_{\uparrow,i} + \hat{n}_{\downarrow,i}\rangle$  into Eq. 2.33, and using the fact that the two spin states are non-interacting and are therefore uncorrelated, so that  $\langle\hat{n}_{\uparrow,i}\hat{n}_{\downarrow,j}\rangle = \langle\hat{n}_{\uparrow,i}\rangle\langle\hat{n}_{\downarrow,j}\rangle$  (where  $\langle\hat{n}_{\uparrow,i}\rangle = \langle\hat{n}_{\downarrow,j}\rangle$ ) for any two sites  $i$  and  $j$ , one obtains,

$$C_n(\mathbf{r}) = \sum_{\sigma} \langle\hat{n}_{\sigma,i}\hat{n}_{\sigma,i+\mathbf{r}}\rangle_c, \quad (2.34)$$

where the summation is performed over the two spin states,  $\sigma = (\uparrow, \downarrow)$ . Because the system is symmetric with respect to the two spin states, we must have that  $\langle\hat{n}_{\uparrow,i}\hat{n}_{\uparrow,i+\mathbf{r}}\rangle_c = \langle\hat{n}_{\downarrow,i}\hat{n}_{\downarrow,i+\mathbf{r}}\rangle_c$ , so that  $C_n(\mathbf{r}) = 2\langle\hat{n}_{\uparrow,i}\hat{n}_{\uparrow,i+\mathbf{r}}\rangle_c$ . It is therefore sufficient to examine the density correlations for a single spin state ( $|\uparrow\rangle$  for example),  $\langle\hat{n}_{\uparrow,i}\hat{n}_{\uparrow,i+\mathbf{r}}\rangle_c$ . In the single-band tight binding limit, we can write  $\hat{n}_{\uparrow,i} = \hat{c}_{\uparrow,i}^\dagger\hat{c}_{\uparrow,i}$ , where  $\hat{c}_{\uparrow,i}^\dagger$  ( $\hat{c}_{\uparrow,i}$ ) is the fermionic creation (annihilation) operator for an  $|\uparrow\rangle$  particle at site  $i$ . We can then apply Wick's theorem for the non-interacting system to obtain,

$$\begin{aligned} \langle\hat{n}_{\uparrow,i}\hat{n}_{\uparrow,i+\mathbf{r}}\rangle &= \left\langle\hat{c}_{\uparrow,i}^\dagger\hat{c}_{\uparrow,i}\hat{c}_{\uparrow,i+\mathbf{r}}^\dagger\hat{c}_{\uparrow,i+\mathbf{r}}\right\rangle \\ &= \left\langle\hat{c}_{\uparrow,i}^\dagger\hat{c}_{\uparrow,i}\right\rangle\left\langle\hat{c}_{\uparrow,i+\mathbf{r}}^\dagger\hat{c}_{\uparrow,i+\mathbf{r}}\right\rangle + \left\langle\hat{c}_{\uparrow,i}^\dagger\hat{c}_{\uparrow,i+\mathbf{r}}\right\rangle\left\langle\hat{c}_{\uparrow,i}\hat{c}_{\uparrow,i+\mathbf{r}}^\dagger\right\rangle, \end{aligned} \quad (2.35)$$

so that  $\langle\hat{n}_{\uparrow,i}\hat{n}_{\uparrow,i+\mathbf{r}}\rangle_c = \left\langle\hat{c}_{\uparrow,i}^\dagger\hat{c}_{\uparrow,i+\mathbf{r}}\right\rangle\left\langle\hat{c}_{\uparrow,i}\hat{c}_{\uparrow,i+\mathbf{r}}^\dagger\right\rangle = -\left|\left\langle\hat{c}_{\uparrow,i}^\dagger\hat{c}_{\uparrow,i+\mathbf{r}}\right\rangle\right|^2$ . It follows then that,

$$C_n(r) = -2\left|\left\langle\hat{c}_{\uparrow,i}^\dagger\hat{c}_{\uparrow,i+\mathbf{r}}\right\rangle\right|^2, \quad (2.36)$$

where  $\left\langle\hat{c}_{\uparrow,i}^\dagger\hat{c}_{\uparrow,i+\mathbf{r}}\right\rangle$  is the tight binding lattice analog of the two point correlator,

Eq. 2.24. From Eq. 2.36, it immediately follows that the density correlations in the non-interacting fermionic system on a lattice are always negative (indicative of anti-bunching behavior), which is exactly what we expected from real space Pauli blocking, and the results for the free fermion case. To see the relation of  $\langle \hat{c}_{\uparrow,i}^\dagger \hat{c}_{\uparrow,i+r} \rangle$  to  $G(r)$ , we can Fourier transform the tight binding creation and annihilation operators according to Eq. 2.20, and plug this into  $\langle \hat{c}_{\uparrow,i}^\dagger \hat{c}_{\uparrow,i+r} \rangle$  to obtain,

$$\langle \hat{c}_{\uparrow,i+r}^\dagger \hat{c}_{\uparrow,i} \rangle = \frac{1}{N} \sum_{\mathbf{k}_{\text{occ}} \in FBZ} e^{i\mathbf{k}\cdot\mathbf{r}} \langle \hat{b}_\mathbf{k}^\dagger \hat{b}_\mathbf{k} \rangle, \quad (2.37)$$

where  $\mathbf{k}_{\text{occ}} \in FBZ$  represents the occupied momentum states in the first Brillouin zone,  $N$  is the total number of lattice sites, and  $\langle \hat{b}_\mathbf{k}^\dagger \hat{b}_\mathbf{k} \rangle = \langle \hat{n}_\mathbf{k} \rangle$  is the average occupation of states with quasi-momentum  $\mathbf{k}$ . At finite temperature,  $\langle \hat{n}_\mathbf{k} \rangle$  is given by Eq. 2.32, where the correct dispersion relation to use in the Fermi-Dirac distribution is Eq. 2.23 (for the 2D case). Eq. 2.37 is therefore the lattice analog of the free space two point correlator, Eq. 2.26, so that for simplicity of notation we write simply  $C_n(r) = -2|G(r)|^2$ , where we have defined

$$G(r) \equiv \langle \hat{c}_{\uparrow,i+r}^\dagger \hat{c}_{\uparrow,i} \rangle \quad (2.38)$$

for the tight binding lattice system.

For a 1D lattice at zero temperature, we can evaluate  $C_n(r) = -2|G(r)|^2$  analytically using Eq. 2.37. We assume that the lattice has a filling factor of  $f$  for the  $|\uparrow\rangle$  atoms, so that the total number of  $|\uparrow\rangle$  atoms is  $Nf$ , where  $f = 1/2$  for the half-filled case. Because the first Brillouin zone consists of all  $k$  vectors contained in the region  $[-\pi/a, \pi/a]$ , and the periodic boundary conditions (Eq. 2.5) discretize the possible values those  $k$ -vectors within the first Brillouin zone can take, so that they have the form  $k = (2\pi/a)(j/N)$ , for some integer  $j$ , the occupied  $k$  states in the first Brillouin zone at zero temperature are those satisfying  $-f\pi/a < k < f\pi/a$ . It follows then that the occupied  $k$  states, which we can label by  $j$  for  $k = (2\pi/a)(j/N)$ , can be indexed with  $j$  running from  $-Nf/2$  to  $+Nf/2$ . Because  $\langle \hat{n}_\mathbf{k} \rangle = 1$  for these states,

and  $\langle \hat{n}_{\mathbf{k}} \rangle = 0$  otherwise, we can write Eq. 2.37 as,

$$\begin{aligned} \left\langle \hat{c}_{\uparrow, i+\mathbf{r}}^\dagger \hat{c}_{\uparrow, i} \right\rangle &= \frac{1}{N} \sum_{k_{\text{occ}} \in FBZ} e^{ikr} \left\langle \hat{b}_k^\dagger \hat{b}_k \right\rangle \\ &= \frac{1}{N} \sum_{j=-Nf/2}^{Nf/2} \left( e^{i \frac{2\pi}{a} \frac{r}{N}} \right)^j. \end{aligned} \quad (2.39)$$

If we then let  $r = aR$ , where  $R$  represents the spatial separation in units of lattice sites, and if we shift the index of summation by an amount  $Nf/2$ , then Eq. 2.39 becomes,

$$G(R) = \frac{e^{-i\pi Rf}}{N} \sum_{j=0}^{Nf} \left( e^{i2\pi R/N} \right)^j. \quad (2.40)$$

We can sum this geometric series and simplify the equations after taking the magnitude squared to obtain,

$$|G(R)|^2 = \frac{1}{N^2} \frac{\sin^2(R\pi(\frac{Nf+1}{N}))}{\sin^2(\frac{\pi R}{N})}. \quad (2.41)$$

We then take the limit  $N \rightarrow \infty$ , and arrive at the final equation for  $|G(R)|^2$ ,

$$|G(R)|^2 = \frac{\sin^2(\pi Rf)}{\pi^2 R^2}. \quad (2.42)$$

This is exactly analogous to the value for the two point correlator at zero temperature in free space, Eq. 2.27. For the non-interacting two-component gas in a 1D lattice at zero temperature and filling fraction  $f$ , then, the total density correlation function, Eq. 2.33, can be written as

$$C_n(R) = -2 |G(R)|^2 = -2 \frac{\sin^2(\pi Rf)}{\pi^2 R^2}, \quad (2.43)$$

where  $R$  is an integer representing the number of sites of spatial separation. The filling fraction  $f$  can also be written as  $f = n/2$ , where  $n$  is the total number of

particles per site (the total density), where  $n = 1$  is half-filling, so that

$$C_n(R) = -2 \frac{\sin^2\left(\frac{\pi R n}{2}\right)}{\pi^2 R^2}. \quad (2.44)$$

This implies that the density correlations for the non-interacting two-component gas are negative at all values of  $R$ , and decay with increasing separation as  $1/R^2$ . Additionally, these correlations display oscillations with a spatial period given by  $2/n$  sites. Overall, this is the same behavior observed in the free space case, and agrees with our intuition about Pauli blocking in real space.

### 2.1.3 Spin Correlation Function for the Non-Interacting System

We can also examine the spin correlations present in the two-component non-interacting Fermi gas on a lattice. We define the spin correlation function as,

$$C_S(\mathbf{r}) = \left\langle \hat{S}_{z,i+\mathbf{r}} \hat{S}_{z,i} \right\rangle_c, \quad (2.45)$$

where,

$$\hat{S}_{z,i} = \frac{\hat{n}_{\uparrow,i} - \hat{n}_{\downarrow,i}}{2} \quad (2.46)$$

represents the  $z$ -component of the spin at site  $i$  for this spin-1/2 system. For a spin balanced system where  $\langle \hat{n}_{\uparrow,i} \rangle = \langle \hat{n}_{\downarrow,i} \rangle$ , we can plug Eq. 2.46 into Eq. 2.45, and use the fact that opposite spin states are uncorrelated to obtain,

$$C_S(\mathbf{r}) = \frac{1}{4} \sum_{\sigma} \langle \hat{n}_{\sigma,i} \hat{n}_{\sigma,i+\mathbf{r}} \rangle_c = \frac{1}{4} C_n(\mathbf{r}). \quad (2.47)$$

We can therefore apply all the results discussed in section 2.1.2 for the density correlation function of the non-interacting two-component gas (Eq. 2.33) to the spin correlation function, so that we have,

$$C_S(r) = -\frac{1}{2} |G(r)|^2, \quad (2.48)$$

where  $G(r)$  is defined in Eq. 2.38, and is evaluated using Eq. 2.37. We therefore find that, even in the absence of interactions between particles, the two-component Fermi gas demonstrates antiferromagnetic spin correlations, since  $C_S(r)$  is negative at all values of  $r$ , which means that the spins  $\hat{S}_{z,i}$  separated by a distance  $r$  prefer to be oppositely aligned. This will become important when we discuss our experimental measurements of antiferromagnetic nearest-neighbor spin correlations in the 2D Fermi-Hubbard model in section 4.4, because we can compare our measurements to the expected correlations for the non-interacting system (at the correct temperature), in order to understand how much of the observed spin correlations arise from the presence of on-site interactions between opposite spin states, compared to how much we would expect just from the effects of Pauli blocking. For the non-interacting two component gas in a 1D lattice at zero temperature, we can use the exact result for  $|G(r)|^2$  derived in section 2.1.2 to write the spin correlation function as,

$$C_S(R) = -\frac{1}{2} \frac{\sin^2\left(\frac{\pi R n}{2}\right)}{\pi^2 R^2}, \quad (2.49)$$

where  $R$  is the separation in units of lattice sites. At half-filling,  $n = 1$ , the spin correlations oscillate with a spatial period of 2 sites, consistent with antiferromagnetic correlations that are commensurate with the lattice spacing. A calculation of  $|G(r)|^2$  (and therefore of  $C_s(r)$  and  $C_n(r)$ ) at zero temperature, for a two-component Fermi gas on a two-dimensional square lattice, can be found in Fig. 2-5 of [37].

## 2.2 Fermi-Hubbard Model

We have thus far only considered the case of non-interacting fermions in a periodic potential formed from an optical lattice. In real experiments, however, when there are two fermionic spin states present at low temperatures, opposite spins can interact with each other through *s*-wave collisions. At such low temperatures, when the collisional momentum  $k$  is sufficiently small that the associated de Broglie wavelength,  $\lambda_{dB} = 2\pi/k$ , is much larger than the range of the actual interatomic potential, the fine

details of the interaction are not important for the *s*-wave scattering properties, and we can approximate the complicated interatomic interaction potential with a pseudo-potential that correctly reproduces the *s*-wave scattering [198, 30]. For our purposes, it is sufficient to use a pseudo-potential of the form,

$$V(r) = \frac{4\pi\hbar^2 a_0}{m} \delta(r), \quad (2.50)$$

where  $a_0$  is the *s*-wave scattering length,  $m$  is the mass of a  ${}^{40}\text{K}$  atom, and  $\delta(r)$  represents a Delta-function. Given this form for the interaction between opposite spin states written in first quantized notation, we can write down the interaction energy term for the two-component fermionic system in second quantized form as,

$$\begin{aligned} \hat{V} &= \frac{1}{2} \sum_{\sigma,\sigma'} \int dx dx' \hat{\psi}_\sigma^\dagger(x) \hat{\psi}_{\sigma'}^\dagger(x') V(x - x') \hat{\psi}_{\sigma'}(x') \hat{\psi}_\sigma(x) \\ &= \frac{g}{2} \sum_{\sigma,\sigma'} \int dx dx' \hat{\psi}_\sigma^\dagger(x) \hat{\psi}_{\sigma'}^\dagger(x') \delta(x - x') \hat{\psi}_{\sigma'}(x') \hat{\psi}_\sigma(x) \\ &= \frac{g}{2} \sum_{\sigma,\sigma'} \int dx \hat{\psi}_\sigma^\dagger(x) \hat{\psi}_{\sigma'}^\dagger(x) \hat{\psi}_{\sigma'}(x) \hat{\psi}_\sigma(x), \end{aligned} \quad (2.51)$$

where we have defined  $g$  as  $g = 4\pi\hbar^2 a_0/m$ . In the spirit of a tight binding description of the interaction, similar to the tight binding approximation for the tunneling energy (Eq. 2.18), we can expand the fermionic creation and annihilation field operators in the ground band Wannier basis, Eq. 2.15. Taking into account the spin degree of freedom for the operators, and assuming we operate in the single band limit, where the band gap  $\Delta$  is much larger than  $k_B T$ ,  $\mu$ , or the energy scale of the interactions themselves, we have that

$$\begin{aligned} \hat{\psi}_\sigma(x) &= \sum_j w(x - x_j) \hat{c}_{\sigma,j} \\ \hat{\psi}_\sigma^\dagger(x) &= \sum_j w^*(x - x_j) \hat{c}_{\sigma,j}^\dagger, \end{aligned} \quad (2.52)$$

where  $x_j$  represents the position of site  $j$ , and where we assume that the Wannier functions in the ground band are independent of spin, given that the two spin states used in the experiment experience the same lattice potential from the linearly-polarized, far red-detuned optical lattice. Note that we have also dropped the band index from the Wannier functions in Eq. 2.52 for simplicity, but we implicitly assume that they are defined for the ground band (Eq. 2.14). Plugging Eq. 2.52 into the second quantized form of the interaction energy operator, Eq. 2.51, gives,

$$\hat{V} = \frac{g}{2} \sum_{\sigma, \sigma'} \sum_{i, j, k, l} \left[ \int dx w^*(x - x_i) w^*(x - x_j) w(x - x_k) w(x - x_l) \right] \hat{c}_{\sigma, i}^\dagger \hat{c}_{\sigma', j}^\dagger \hat{c}_{\sigma', k} \hat{c}_{\sigma, l}. \quad (2.53)$$

In the deep lattice limit, we can make the same approximation we made in deriving the tight binding form of the kinetic energy, Eq. 2.18, and assume that the overlap between the Wannier functions on different sites is small, so that the dominant contribution to the interaction energy comes from the on-site term,  $i = j = k = l$ , due to the fact that the overlap integral,

$$\int dx w^*(x - x_i) w^*(x - x_j) w(x - x_k) w(x - x_l), \quad (2.54)$$

in the summation of Eq. 2.53 is small otherwise. In the tight binding limit then, we include only the terms where  $i = j = k = l$ , so that the interaction energy operator becomes,

$$\begin{aligned} \hat{V} &= \frac{g}{2} \sum_{\sigma, \sigma'} \sum_i \left[ \int dx |w(x)|^4 \right] \hat{c}_{\sigma, i}^\dagger \hat{c}_{\sigma', i}^\dagger \hat{c}_{\sigma', i} \hat{c}_{\sigma, i} \\ &= U \sum_i \hat{n}_{\uparrow, i} \hat{n}_{\downarrow, i}, \end{aligned} \quad (2.55)$$

where we have defined the on-site interaction energy  $U$  as,

$$U = \frac{4\pi\hbar^2 a_0}{m} \int dx |w(x)|^4. \quad (2.56)$$

Including higher order terms in the series, such as those terms where  $i = j = k$ , and  $l$  is a nearest-neighbor site, or where  $i = j$  and  $k = l$  are nearest-neighbor sites of one another, leads to higher order terms in the tight binding Hamiltonian, such as density-dependent tunneling, and nearest-neighbor interaction terms, respectively. However, in the deep lattice limit where we operate experimentally ( $V_0 > 6E_R$ ), these higher order terms are negligible compared to the on-site interaction term and can be safely ignored. A calculation of the ratio of the on-site interaction energy  $U$  to the nearest-neighbor interaction energy, as a function of the lattice depth, can be found in Fig. 2-8 of [37]. We therefore arrive at the final version of the tight binding Hamiltonian, which includes the effects of on-site interactions between opposite spin states, given by the sum of the tunneling energy operator, Eq. 2.18, and the on-site interaction energy operator, Eq. 2.55,

$$\hat{H} = \hat{T} + \hat{V} = -t \sum_{\langle i,j \rangle, \sigma} \left[ \hat{c}_{\sigma,i}^\dagger \hat{c}_{\sigma,j} + h.c. \right] + U \sum_i \hat{n}_{\uparrow,i} \hat{n}_{\downarrow,i}. \quad (2.57)$$

If we include a chemical potential  $\mu_\sigma$  for atoms with spin  $\sigma = (\uparrow, \downarrow)$ , we obtain a form for the Hamiltonian that accurately depicts the behavior of our fermionic ultracold atomic system in a single band of an optical lattice, with two spin components,

$$\hat{H}_{\text{FH}} = -t \sum_{\langle i,j \rangle, \sigma} \left[ \hat{c}_{\sigma,i}^\dagger \hat{c}_{\sigma,j} + h.c. \right] + U \sum_i \hat{n}_{\uparrow,i} \hat{n}_{\downarrow,i} - \sum_{\sigma,i} \mu_\sigma \hat{n}_{\sigma,i}, \quad (2.58)$$

where  $\hat{n}_{\sigma,i} = \hat{c}_{\sigma,i}^\dagger \hat{c}_{\sigma,i}$  is the number operator at site  $i$ , and  $\mu_\uparrow = \mu_\downarrow$  represents the situation where the system is spin-balanced. This Hamiltonian, Eq. 2.58, represents what is often referred to as the single band Fermi-Hubbard model.

While this model provides a good description of our ultracold atomic system in an optical lattice, it has significantly broader applications in the field of physics, and has been proposed, for instance, as a simple, paradigmatic lattice model that is believed to capture much of the essential aspects of the strongly correlated electron systems in the cuprate high-temperature superconductors [139]. These materials, such as hole doped  $\text{La}_{2-x}\text{Sr}_x\text{CuO}_4$ , or electron doped  $\text{Nd}_{2-x}\text{Ce}_x\text{CuO}_4$ , where  $x$  repre-

sents the dopant concentration, have critical temperatures for superconductivity,  $T_c$ , that are much higher than the conventional BCS type superconductors. It is known that BCS theory alone cannot explain the superconducting behavior of these complex materials, but it is still uncertain what the exact physical mechanism is behind this unconventional form of superconductivity. Although the Fermi-Hubbard model has been proposed as an extremely simplified description of the behavior of the electrons in these complex materials, it is also currently unclear the extent to which the Fermi-Hubbard model captures the many interesting thermodynamic and transport phenomena that have been observed in these materials. Much of this uncertainty about the properties of the Fermi-Hubbard model, and its relation to the cuprates, arises because this Hamiltonian, while appearing deceptively simple, has only been solved in specific, limiting cases. This is where our ultracold atomic system becomes important, because we have the ability to simulate the Fermi-Hubbard model directly, with full control over all the Hamiltonian parameters. In this sense, one of the major goals of our experiment is to ask nature about the properties of this Hamiltonian directly, especially in theoretically intractable regimes, by simulating it with ultracold atoms in an optical lattice.

In this section, we will discuss some of the general properties of this Hamiltonian. We will use, for instance, the exactly solvable two-site version of the model in section 2.2.1 to illustrate some of the basic physical concepts, and will then discuss, in section 2.2.2, some of the different theoretical approaches which have been developed to better understand this Hamiltonian. Finally, in section 2.2.3, we will discuss some of the general phenomenology of the model on a 2D square lattice, and will describe some of the properties of different paradigmatic states which arise in various parameter regimes. We will support this with calculations from a numerical technique, NLCE, obtained from the data provided in [120], for the thermodynamic properties and equation of state of this system, in order to provide some intuition about the behavior of this complex, strongly interacting Hamiltonian, and to give a backdrop for the discussion in later chapters of this thesis.

One of the fundamental symmetries of this Hamiltonian, which will assist us in

our understanding of its properties in the remainder of this thesis, is the fact that it is particle-hole symmetric on a 2D square lattice. This is a property that arises from the bi-partite nature of the square lattice, which means that the lattice can be decomposed into independent A and B square sub-lattices, where an A lattice site is neighbored by four B lattice sites, and visa versa. We can then perform a sub-lattice dependent particle-hole transformation of the form,

$$\begin{aligned}\hat{c}_{\sigma,i}^\dagger &\rightarrow (-1)^{\alpha(i)} \hat{c}_{\sigma,i} \\ \hat{c}_{\sigma,i} &\rightarrow (-1)^{\alpha(i)} \hat{c}_{\sigma,i}^\dagger,\end{aligned}\quad (2.59)$$

where  $\alpha(i) = 0$  if site  $i$  is contained in the A sub-lattice, and  $\alpha(i) = 1$  if site  $i$  is contained in the B sub-lattice. Such a transformation changes the relevant operators in the Hamiltonian as,

$$\begin{aligned}\hat{n}_{\sigma,i} &\rightarrow 1 - \hat{n}_{\sigma,i} \\ \hat{c}_{\sigma,i}^\dagger \hat{c}_{\sigma,j} + \hat{c}_{\sigma,j}^\dagger \hat{c}_{\sigma,i} &\rightarrow \hat{c}_{\sigma,i}^\dagger \hat{c}_{\sigma,j} + \hat{c}_{\sigma,j}^\dagger \hat{c}_{\sigma,i},\end{aligned}\quad (2.60)$$

for nearest-neighbor sites,  $i$  and  $j$ , on different sub-lattices. Under this particle-hole transformation then, the Hamiltonian, Eq. 2.58, where we assume  $\mu_\uparrow = \mu_\downarrow = \mu$  for simplicity, is mapped to (ignoring overall energy offsets),

$$\hat{H}_{\text{FH}} \rightarrow -t \sum_{\langle i,j \rangle, \sigma} \left[ \hat{c}_{\sigma,i}^\dagger \hat{c}_{\sigma,j} + h.c. \right] + U \sum_i \hat{n}_{\uparrow,i} \hat{n}_{\downarrow,i} - \mu' \sum_{\sigma,i} \hat{n}_{\sigma,i}, \quad (2.61)$$

where  $\mu' = U - \mu$ . The particle-hole transformation, Eq. 2.59, thus converts the Fermi-Hubbard model with chemical potential  $\mu$  to the same Hamiltonian, but with a new chemical potential,  $U - \mu$ . It is clear then that there is a symmetry point,  $\mu = U/2$ , where the Hamiltonian is mapped back onto itself by the transformation. In this case, the average density of each spin state at each site, given by  $\langle \hat{n}_{\sigma,i} \rangle$ , must remain unchanged, because the Hamiltonian itself is unchanged, so that we must have  $\langle \hat{n}_{\sigma,i} \rangle = \langle 1 - \hat{n}_{\sigma,i} \rangle$ , which is obtained from Eq. 2.60. At  $\mu = U/2$ , it follows then that

$\langle \hat{n}_{\sigma,i} \rangle = 1/2$  for both spin states, so that the total density is  $\langle \hat{n}_{\uparrow,i} + \hat{n}_{\downarrow,i} \rangle = 1$ , which means that the system is half-filled. We therefore see that  $\mu < U/2$  corresponds to hole doping,  $\mu > U/2$  corresponds to particle doping, and that any thermodynamic property of the system at a filling  $\mu$  on one side of half-filling, can be determined by its value at  $U - \mu$ , once it is known how that property changes under the particle hole transformation, Eq. 2.59.

### 2.2.1 Double-Well Hubbard Model

One simple limit where the Hubbard model is analytically solvable is the situation where the system size is finite, and there are exactly two sites: the double well model. By examining the behavior of this simpler system, we can gain some qualitative intuition about this complex Hamiltonian that will elucidate some of the physical principles which dictate the behavior in larger systems. In this sense, one can think of this simplified model as the basic component, or fundamental building block, upon which larger Hubbard type systems are built. Experimentally, this simple model has been studied in depth using  $^6\text{Li}$  atoms confined in an optical double well potential [162]. Here, we consider the case of a spin-balanced system at half-filling (i.e. two particles), so that there is one  $|\uparrow\rangle$  atom and one  $|\downarrow\rangle$  atom. We first examine the case when these atoms are fermions, where we will find that the ground state of the system is a spin singlet, with some admixture of neighboring doublon-hole pairs. Thus, as we will see, the two site Fermi-Hubbard system already qualitatively captures the physics of anti-ferromagnetic spin correlations arising from super-exchange, as well as the associated doublon-hole bunching coming from the admixture of correlated doublon-hole pairs in the wave function. We explore this physics in more detail in section 4.4, when we discuss our results regarding the observation of spatial spin and charge correlations in a large 2D Fermi-Hubbard system using our quantum gas microscope for  $^{40}\text{K}$ . After we describe the behavior of the fermionic double well, we then discuss the situation when the atoms are bosonic. This will provide an interesting comparison with the fermionic case because, as we will see, the ground state of the two site Bose-Hubbard model is a spin triplet, rather than a spin singlet, with some admixture of neighboring

doublon-hole pairs. As we will show, for the particular triplet state comprising the ground state of the spin-balanced, two site Bose-Hubbard model at half-filling, the spin correlations are also antiferromagnetic.

## Fermi-Hubbard Model

We begin with the spin-balanced, two site Fermi-Hubbard model at half-filling. We label the two sites of the double well by  $L$  and  $R$ , representing the left and right sites, respectively. We can then write the Hamiltonian for this simplified system as,

$$\hat{H} = -t \sum_{\sigma} \left( \hat{c}_{\sigma,L}^{\dagger} \hat{c}_{\sigma,R} + \hat{c}_{\sigma,R}^{\dagger} \hat{c}_{\sigma,L} \right) + U (\hat{n}_{\uparrow,L} \hat{n}_{\downarrow,L} + \hat{n}_{\uparrow,R} \hat{n}_{\downarrow,R}) . \quad (2.62)$$

We then use the following four basis states, which span the Hilbert space of the half-filled, spin-balanced system, to express the Hamiltonian in matrix form, which is determined by how it acts on the respective states in the basis,

$$\begin{aligned} |\uparrow, \downarrow\rangle &= \hat{c}_{\uparrow,L}^{\dagger} \hat{c}_{\downarrow,R}^{\dagger} |0\rangle \\ |\downarrow, \uparrow\rangle &= \hat{c}_{\downarrow,L}^{\dagger} \hat{c}_{\uparrow,R}^{\dagger} |0\rangle \\ |\uparrow\downarrow, 0\rangle &= \hat{c}_{\uparrow,L}^{\dagger} \hat{c}_{\downarrow,L}^{\dagger} |0\rangle \\ |0, \uparrow\downarrow\rangle &= \hat{c}_{\uparrow,R}^{\dagger} \hat{c}_{\downarrow,R}^{\dagger} |0\rangle . \end{aligned} \quad (2.63)$$

Here,  $|0\rangle$  represents the vacuum state. In this basis,  $\{|\uparrow, \downarrow\rangle, |\downarrow, \uparrow\rangle, |\uparrow\downarrow, 0\rangle, |0, \uparrow\downarrow\rangle\}$ , the  $4 \times 4$  Hamiltonian matrix can be written as,

$$\hat{H} = \begin{pmatrix} 0 & 0 & -t & -t \\ 0 & 0 & t & t \\ -t & t & U & 0 \\ -t & t & 0 & U \end{pmatrix} . \quad (2.64)$$

Diagonalizing this matrix yields eigenvalues, in order from lowest energy to highest energy, of,

$$\begin{aligned} E_1 &= \frac{U}{2} - \frac{1}{2}\sqrt{16t^2 + U^2} \\ E_2 &= 0 \\ E_3 &= U \\ E_4 &= \frac{U}{2} + \frac{1}{2}\sqrt{16t^2 + U^2}, \end{aligned} \quad (2.65)$$

with corresponding eigenvectors,

$$\begin{aligned} |1\rangle &= \frac{\cos\theta}{\sqrt{2}}(|\uparrow,\downarrow\rangle - |\downarrow,\uparrow\rangle) + \frac{\sin\theta}{\sqrt{2}}(|\uparrow\downarrow,0\rangle + |0,\uparrow\downarrow\rangle) \\ |2\rangle &= \frac{|\uparrow,\downarrow\rangle + |\downarrow,\uparrow\rangle}{\sqrt{2}} \\ |3\rangle &= \frac{|\uparrow\downarrow,0\rangle - |0,\uparrow\downarrow\rangle}{\sqrt{2}} \\ |4\rangle &= \frac{\sin\theta}{\sqrt{2}}(|\uparrow,\downarrow\rangle - |\downarrow,\uparrow\rangle) - \frac{\cos\theta}{\sqrt{2}}(|\uparrow\downarrow,0\rangle + |0,\uparrow\downarrow\rangle). \end{aligned} \quad (2.66)$$

The angle  $\theta$  here is defined by,

$$\tan\theta = \frac{4t}{U + \sqrt{16t^2 + U^2}}. \quad (2.67)$$

Upon examination of the ground state wave function,  $|1\rangle$ , given in Eq. 2.66, it is clear that the state is a combination of a spin singlet,  $|\uparrow,\downarrow\rangle - |\downarrow,\uparrow\rangle$ , whose relative amplitude in the wave function is  $\cos\theta$ , and an admixture of neighboring doublon-hole pairs,  $|\uparrow\downarrow,0\rangle + |0,\uparrow\downarrow\rangle$ , with a relative amplitude of  $\sin\theta$ . We can then calculate the nearest-neighbor spin correlation function,

$$4\left\langle \hat{S}_{z,L}\hat{S}_{z,R} \right\rangle = \langle (\hat{n}_{\uparrow,L} - \hat{n}_{\downarrow,L})(\hat{n}_{\uparrow,R} - \hat{n}_{\downarrow,R}) \rangle, \quad (2.68)$$

where  $\hat{S}_{z,i} = (\hat{n}_{\uparrow,i} - \hat{n}_{\downarrow,i})/2$ , for  $i = (L, R)$ , for the ground state  $|1\rangle$ , which gives

$$4 \left\langle \hat{S}_{z,L} \hat{S}_{z,R} \right\rangle = 4 \langle | \hat{S}_{z,L} \hat{S}_{z,R} | 1 \rangle = -\cos^2 \theta. \quad (2.69)$$

It is therefore evident that, for all values of  $U/t$ , the ground state of the two-site Fermi-Hubbard model demonstrates antiferromagnetic spin correlations.

We can also examine correlations in the charge degree of freedom for the ground state, and look at, for instance, the total density correlations,

$$\langle \hat{n}_L \hat{n}_R \rangle - \langle \hat{n}_L \rangle \langle \hat{n}_R \rangle = \langle (\hat{n}_{\uparrow,L} + \hat{n}_{\downarrow,L}) (\hat{n}_{\uparrow,R} + \hat{n}_{\downarrow,R}) \rangle - \langle (\hat{n}_{\uparrow,L} + \hat{n}_{\downarrow,L}) \rangle \langle (\hat{n}_{\uparrow,R} + \hat{n}_{\downarrow,R}) \rangle. \quad (2.70)$$

Plugging in the wave function  $|1\rangle$  then gives,

$$\langle \hat{n}_L \hat{n}_R \rangle - \langle \hat{n}_L \rangle \langle \hat{n}_R \rangle = -\sin^2 \theta, \quad (2.71)$$

which means that the density correlations in the ground state are always negative, consistent with the fact that fermionic particles tend to anti-bunch. We can, however, capture the doublon-hole bunching behavior in the ground state by examining, instead, the doublon-hole correlation function,

$$\left\langle \hat{h}_L \hat{d}_R \right\rangle - \left\langle \hat{h}_L \right\rangle \left\langle \hat{d}_R \right\rangle = \langle (2 - \hat{n}_L) (\hat{n}_{\uparrow,R} \hat{n}_{\downarrow,R}) \rangle - \langle (2 - \hat{n}_L) \rangle \langle (\hat{n}_{\uparrow,R} \hat{n}_{\downarrow,R}) \rangle, \quad (2.72)$$

where  $\hat{h}_L = (1 - \hat{n}_{\uparrow,L}) + (1 - \hat{n}_{\downarrow,L})$  is the total hole operator on site  $L$ , and  $\hat{d}_R = \hat{n}_{\uparrow,R} \hat{n}_{\downarrow,R}$  is the doublon operator on site  $R$ . Plugging the wave function  $|1\rangle$  into Eq. 2.72 then gives,

$$\left\langle \hat{h}_L \hat{d}_R \right\rangle - \left\langle \hat{h}_L \right\rangle \left\langle \hat{d}_R \right\rangle = \frac{\sin^2 \theta}{2}, \quad (2.73)$$

which is always positive for non-zero values of  $\theta$ , indicating that doublons and holes tend to bunch together in the ground state. We thus find that, for the ground state,  $|1\rangle$ , of the two site Fermi-Hubbard model, antiferromagnetic spin correlations go hand in hand with doublon-hole bunching.

In the limiting case where the on-site interactions are much greater than the

tunneling strength,  $U \gg t$ , we have that,

$$\tan \theta \approx \theta \approx \frac{2t}{U}, \quad (2.74)$$

and the energy of the ground state becomes,

$$E_1 \approx -\frac{4t^2}{U}. \quad (2.75)$$

The different correlation functions in this limit, on the other hand, are

$$\begin{aligned} 4 \left\langle \hat{S}_{z,L} \hat{S}_{z,R} \right\rangle &= -1 \\ \langle \hat{n}_L \hat{n}_R \rangle - \langle \hat{n}_L \rangle \langle \hat{n}_R \rangle &= -4 \left( \frac{t}{U} \right)^2 \\ \left\langle \hat{h}_L \hat{d}_R \right\rangle - \left\langle \hat{h}_L \right\rangle \left\langle \hat{d}_R \right\rangle &= 2 \left( \frac{t}{U} \right)^2. \end{aligned} \quad (2.76)$$

Therefore, in this Heisenberg or strongly interacting limit, the system can lower its energy by an amount  $-4t^2/U$  in the ground state (relative to the second lowest lying energy state,  $|2\rangle$ ), when the spins are antiferromagnetically aligned. This property represents the two-site equivalent of super-exchange, a virtual hopping process of particles between neighboring sites which produces an effective antiferromagnetic spin-spin interaction with a coupling strength set by  $4t^2/U$  [54]. Furthermore, in this limit the doublon-hole fluctuations in the system, which represent the virtual states in the language of super-exchange, are suppressed by an amount  $(t/U)^2$ , since the amplitude of the doublon-hole states in the wave function,  $|\uparrow\downarrow, 0\rangle + |0, \uparrow\downarrow\rangle$ , is proportional to  $\sin \theta \approx \theta$ . We therefore have, for large but finite values of  $U/t$ , strong antiferromagnetic spin correlations in the ground state of the two site Fermi-Hubbard model, coinciding with positive doublon-hole and negative density-density correlations, whose magnitudes are suppressed, relative to the spin correlations, by a factor of  $(t/U)^2$ , due to the overall suppression of doublon-hole fluctuations when  $U \gg t$ . As we will discuss in more detail in section 4.4, this intuition carries over to larger system sizes as well (and also to 2D), and is (at least partially) the origin

of the antiferromagnetic spin correlations which we observe experimentally in large 2D Fermi-Hubbard systems, in the presence of strong doublon-hole bunching [38]. A more detailed discussion of the fermionic double well model, including a generalization of the system described here aimed at preserving the  $SU(2)$ -symmetry of the Fermi-Hubbard Hamiltonian, as well as a generalization to finite doping, can be found in section 6.3.3 of [37].

### Bose-Hubbard Model

To elucidate the behavior of the ground state of the two site Fermi-Hubbard model, Eq. 2.66, we can also examine the spin-balanced, double well system at half-filling when the constituent particles are bosons instead of fermions, a system that was investigated experimentally in [225]. In this case, the form of the Hamiltonian, Eq. 2.62, and the basis states we use to span the relevant Hilbert space, Eq. 2.63, remain unchanged, but the fermionic creation and annihilation operators,  $\hat{c}_{\sigma,i}^\dagger$  and  $\hat{c}_{\sigma,i}$ , respectively, which respect the fermionic anti-commutation relation  $\{\hat{c}_{\sigma,i}, \hat{c}_{\sigma',j}^\dagger\} = \delta_{\sigma,\sigma'}\delta_{i,j}$ , are transformed to corresponding bosonic creation and annihilation operators, which satisfy the bosonic commutation relation,  $[\hat{c}_{\sigma,i}, \hat{c}_{\sigma',j}^\dagger] = \delta_{\sigma,\sigma'}\delta_{i,j}$ . We can then write the matrix form of the Hamiltonian, where all the operators have been converted to bosonic operators satisfying bosonic commutation relations, in the basis  $\{| \uparrow, \downarrow \rangle, | \downarrow, \uparrow \rangle, | \uparrow \downarrow, 0 \rangle, | 0, \uparrow \downarrow \rangle\}$ , analogous to Eq. 2.64, which gives,

$$\hat{H} = \begin{pmatrix} 0 & 0 & -t & -t \\ 0 & 0 & -t & -t \\ -t & -t & U & 0 \\ -t & -t & 0 & U \end{pmatrix}. \quad (2.77)$$

Although this looks extremely similar to Eq. 2.64, the one subtle difference, the fact that all the tunneling matrix elements have the same sign in the bosonic case, which arises directly from the bosonic commutation relations, turns out to be the key to changing the singlet/triplet character of the ground state of this two site Hubbard system. Solving for the eigenvalues of this matrix gives, in order from lowest energy

to highest energy,

$$\begin{aligned}
E_1 &= \frac{U}{2} - \frac{1}{2}\sqrt{16t^2 + U^2} \\
E_2 &= 0 \\
E_3 &= U \\
E_4 &= \frac{U}{2} + \frac{1}{2}\sqrt{16t^2 + U^2},
\end{aligned} \tag{2.78}$$

exactly the same as the fermionic case. The corresponding eigenvectors, however, are not the same, but are instead given by,

$$\begin{aligned}
|1\rangle &= \frac{\cos\theta}{\sqrt{2}}(|\uparrow,\downarrow\rangle + |\downarrow,\uparrow\rangle) + \frac{\sin\theta}{\sqrt{2}}(|\uparrow\downarrow,0\rangle + |0,\uparrow\downarrow\rangle) \\
|2\rangle &= \frac{|\uparrow,\downarrow\rangle - |\downarrow,\uparrow\rangle}{\sqrt{2}} \\
|3\rangle &= \frac{|\uparrow\downarrow,0\rangle - |0,\uparrow\downarrow\rangle}{\sqrt{2}} \\
|4\rangle &= \frac{\sin\theta}{\sqrt{2}}(|\uparrow,\downarrow\rangle + |\downarrow,\uparrow\rangle) - \frac{\cos\theta}{\sqrt{2}}(|\uparrow\downarrow,0\rangle + |0,\uparrow\downarrow\rangle).
\end{aligned} \tag{2.79}$$

We therefore find that the ground state  $|1\rangle$  has a triplet character,  $(|\uparrow,\downarrow\rangle + |\downarrow,\uparrow\rangle)/\sqrt{2}$ , in addition to a doublon-hole admixture,  $(|\uparrow\downarrow,0\rangle + |0,\uparrow\downarrow\rangle)/\sqrt{2}$ , whereas the lowest lying excited state,  $|2\rangle$ , has a singlet character,  $(|\uparrow,\downarrow\rangle - |\downarrow,\uparrow\rangle)/\sqrt{2}$ . The angle  $\theta$  in this case is defined in the same way as Eq. 2.67. The observed ground state  $|1\rangle$  is consistent with the Lieb-Mattis theorem [141], which says that the ground state of two bosonic atoms must be a spin triplet. It is thus interesting to find that the statistics of the constituent particles manifest themselves very subtly in the ground state of the two site Hubbard model, as a single sign change in the wave function. We can then go through the same procedure we performed in the fermionic case, and calculate the spin correlations, as well as the density-density and doublon-hole correlations for the bosonic ground state wave function. Plugging the wave function  $|1\rangle$  into the definitions of the correlation functions, Eqs. 2.68, 2.70, and 2.72, with all

operators replaced by bosonic operators, yields,

$$\begin{aligned} 4 \left\langle \hat{S}_{z,L} \hat{S}_{z,R} \right\rangle &= -\cos^2 \theta \\ \left\langle \hat{n}_L \hat{n}_R \right\rangle - \left\langle \hat{n}_L \right\rangle \left\langle \hat{n}_R \right\rangle &= -\sin^2 \theta \\ \left\langle \hat{h}_L \hat{d}_R \right\rangle - \left\langle \hat{h}_L \right\rangle \left\langle \hat{d}_R \right\rangle &= \frac{\sin^2 \theta}{2}. \end{aligned} \quad (2.80)$$

As Eq. 2.80 shows, the correlation behavior for the ground state of the two site Bose Hubbard model is exactly the same as the fermionic Hubbard model, independent of the triplet character of the bosonic state. Given that the ground state must be a spin triplet from the Lieb-Mattis theorem, and the fact that we restricted the system to be spin-balanced and half-filled, however, it is maybe not so surprising that the spin correlations are antiferromagnetic, since we did not allow for the possibility of generating ferromagnetism in the system by extending the Hilbert space [54]. One potential way to distinguish the triplet character of the bosonic ground state from the fermionic singlet, however, is through, for instance, dynamics experiments, as demonstrated in [225].

### 2.2.2 Theoretical Approaches to the Fermi-Hubbard Model

Due to the theoretical intractability of the 2D Fermi-Hubbard model arising from the fermion sign problem away from half-filling [144], many theoretical approaches have been developed, both numerical and series-expansion based, which are aimed at furthering our understanding of the behavior this strongly interacting, many-body Hamiltonian. Unfortunately, many of the series-expansion methods rely on the presence of some small parameter about which to expand, the existence of which is not always guaranteed in this complex system, meaning that many of the approximations made with such a technique can run completely uncontrolled in many parameter regimes. The numerical approaches tend to have similar issues, and, while many are essentially exact around half-filling (a highly symmetric point in the model) for a large range of temperatures and values of the Hubbard parameters  $U/t$ , they often run into convergence issues when there is finite doping, due to the fermion sign prob-

lem, at which point the numerical predictions also become uncontrolled. This is one of the major reasons why quantum gas microscopy of the 2D Fermi-Hubbard model is so important, because it allows us, in the sense of quantum simulation, to directly benchmark many of the theoretical predictions, and to better understand the parameter regimes where the theoretical approaches break down. Additionally, it allows us to examine the system in regimes that are currently inaccessible to theory.

A third, slightly different theoretical approach to understanding the 2D Fermi-Hubbard model actually involves mapping the full Hubbard Hamiltonian onto an approximate, yet simpler model that is more theoretically tractable, such as the 2D Heisenberg or  $t - J$  models, and which ideally captures some of the essential physics of the full Hamiltonian in certain parameter regimes. It is then interesting to compare the experimental results for the full 2D Fermi-Hubbard system with theoretical predictions from these approximate Hamiltonians, and to look for deviations between the two, in order to better understand the physical contributions from the elements of the full system which are left out in the approximate models. For example, by comparing experimental measurements with predictions from the 2D Heisenberg model, which projects out doubly-occupied sites at half-filling, one might hope to gain a clearer understanding of the role doublons and holes play in determining the physical properties of the system, including both the equilibrium and transport properties (see, for example, section 5.4.2). In this section, we describe several theoretical approaches that we use to compare with the experimental data discussed in this thesis (see chapters 4 and 5). Specifically, we describe the High-Temperature Series Expansion (HTSE) in the tunneling strength  $t$ , the Numerical Linked Cluster Expansion (NLCE), Determinant Quantum Monte Carlo (DQMC), and the mapping of the 2D Fermi-Hubbard model onto the 2D Heisenberg and  $t - J$  models. While there are many other theoretical techniques which have been applied to understanding the properties of the 2D Fermi-Hubbard system (e.g. dynamical mean field theory, dynamical cluster approximation, and multi-reference projected Hartree-Fock methods, to name a few [136]), we limit this short discussion to those particular methods which are mentioned directly in the results of the work described in this thesis.

## High-Temperature Series Expansion

The High-Temperature Series Expansion (HTSE) technique is an expansion of the partition function and grand canonical potential for the homogeneous Fermi-Hubbard model into an infinite series using the expansion parameter  $t/k_B T = \beta t$  [165], where  $\beta = 1/k_B T$ . This approach is typically valid when the temperature is relatively high compared to  $t$ ,  $t < k_B T < U$ , and breaks down for temperatures  $k_B T < t$ , i.e. when  $\beta t$  is no longer a small parameter to expand with. From the approximate form of the partition function and grand canonical potential of the system obtained by truncating the series expansion at some finite order in the expansion parameter  $\beta t$ , one can directly obtain approximate expressions for all of the relevant thermodynamic quantities, such as the entropy or density, as functions of  $\beta$ ,  $U$ , and  $\mu$ , for the homogeneous system. These thermodynamic variables can then be compared to the trapped samples realized experimentally using the local density approximation (LDA), where the chemical potential  $\mu$  is replaced with a spatially varying, local chemical potential  $\mu(r) = \mu_0 - V(r)$  [203]. Here,  $\mu_0$  is the global chemical potential in the center of the trap, and  $V(r)$  is the underlying potential associated with the shape of the trap. For instance, for an underlying harmonic potential typically encountered in optical lattice experiments, with trap frequency  $\omega$ ,  $V(r) = 0.5m\omega^2r^2$ , and the local chemical potential  $\mu(r)$  decreases quadratically with increasing distance from the center of the trap.

The expansion begins with the atomic limit, where each lattice site is essentially isolated from all others, which occurs when  $U \gg t$ , and particles tunneling in the lattice can be ignored. In this limit, one can examine the partition function of each individual site in the grand canonical ensemble. Specifically, at any given site there are only four possible states: occupation by a hole, occupation by a single particle of either of the two spin states, or occupation by a doublon, which incurs an energy cost of  $U$ . The partition function of the single lattice site is then,

$$z_0 = 1 + 2\zeta + \zeta^2 w, \quad (2.81)$$

where  $\zeta \equiv \exp(\beta\mu)$  and  $w \equiv \exp(-\beta U)$ . The partition function for the  $N$  particle system in this atomic limit is then simply,

$$\mathcal{Z}(\beta, \mu, U) = (1 + 2\zeta + \zeta^2 w)^N = z_0^N, \quad (2.82)$$

from which one can directly extract, for instance, the total density  $n(\beta, \mu, U)$ , the double occupancy  $d(\beta, \mu, U)$ , and the entropy per site  $s(\beta, \mu, U)$ . That is, the total density is given by,

$$n(\beta, \mu, U) = \frac{\zeta}{N} \frac{\partial \ln(\mathcal{Z})}{\partial \zeta} = \frac{1}{N\beta} \frac{\partial \ln(\mathcal{Z})}{\partial \mu}, \quad (2.83)$$

the doublon density is obtained from,

$$d(\beta, \mu, U) = \frac{w}{N} \frac{\partial \ln(\mathcal{Z})}{\partial w} = -\frac{1}{N\beta} \frac{\partial \ln(\mathcal{Z})}{\partial U}, \quad (2.84)$$

and the entropy per site can be found through,

$$s(\beta, \mu, U) = \frac{1}{N} \frac{\partial}{\partial T} (k_B T \ln(\mathcal{Z})). \quad (2.85)$$

From the atomic limit, one can then perform perturbation theory in the small parameter  $\beta t$ , when the value of  $t$  is finite and non-zero, and incorporate the leading order effects of tunneling into the grand canonical potential per site,  $\Omega$ . The details of this procedure can be found in [165], and we quote here the result that includes the first non-vanishing (second order) term in the series beyond the atomic limit, for an isotropic square lattice,

$$-\beta\Omega(\beta, \mu, U) = \ln(z_0) + \frac{2}{z_0^2} (\beta t)^2 \left[ 2\zeta(1 + \zeta^2 w) + \frac{4\zeta^2}{\beta U}(1 - w) \right]. \quad (2.86)$$

From the grand canonical potential per site,  $\Omega(\beta, \mu, U)$ , in Eq. 2.86, one can directly obtain the density, double-occupancy, and entropy per site through  $n(\beta, \mu, U) = -\partial\Omega/\partial\mu$ ,  $d(\beta, \mu, U) = \partial\Omega/\partial U$ , and  $s(\beta, \mu, U) = -\partial\Omega/\partial T$ , respectively. This is sufficient then to obtain, for instance, the average local moment,  $m_z^2 = n - 2d$ , which

measures the density of singly-occupied sites, and is the quantity actually accessed directly in the experiment. The next non-vanishing term in the series that can be included in the expansion for  $\Omega(\beta, \mu, U)$  is the fourth order term,  $(\beta t)^4$ , which is written out explicitly in section 2.3.3 of [37]. For the HTSE fits to the data shown in section 4.3.3, however, we typically only include terms up to second order in the expansion for  $\Omega(\beta, \mu, U)$ , Eq. 2.86. A generalization of this equation to anisotropic square lattices can be found in [78].

## Numerical Approaches

The two numerical techniques that we use to compare with experimental results are the Numerical Linked Cluster Expansion (NLCE) and Determinant Quantum Monte Carlo (DQMC), both of which directly simulate properties of the 2D Fermi-Hubbard Hamiltonian. The theoretical calculations from the two different techniques which are presented in this thesis are produced by two separate theory research groups (one for the NLCE and one for the DQMC), with whom we have collaborated significantly throughout the course of the various experiments discussed here. We briefly describe in this section the basic concepts of how these two techniques work, and refer the interested reader to one of the many resources cited subsequently for further details.

The first numerical technique, NLCE, expresses extensive properties of a given lattice model (e.g. the 2D Fermi-Hubbard model), directly in the thermodynamic limit, as a sum over contributions from all finite sized clusters, up to the largest cluster size used in the simulations, which can be directly embedded within the lattice [194, 195, 120, 121, 223]. Specifically, one can express some extensive property  $P$  per site as,

$$P = \sum_c M(c) W_P(c), \quad (2.87)$$

where the summation is performed over all distinct clusters  $c$  (i.e. those which are not related through some symmetry of the lattice),  $M(c)$  is a counting pre-factor which represents the number of ways each distinct cluster type  $c$  appears per site, and  $W_P(c)$  denotes the contribution of that particular cluster type to the property

of interest,  $P$ . The contribution of cluster type  $c$  to property  $P$  is calculated via the inclusion-exclusion principle,

$$W_P(c) = p(c) - \sum_{s \subset c} W_P(s), \quad (2.88)$$

where  $p(c)$  represents the value of property  $P$  calculated for cluster type  $c$ , and the summation is carried out over all sub-clusters  $s$  of  $c$ , which have a smaller number of lattice sites, and which can be embedded within the larger cluster  $c$ . To calculate  $p(c)$ , NLCE makes use of the same basis used in the HTSE, but does not rely on the same perturbative expansion in powers of  $\beta t$  that the HTSE requires. Instead, NLCE calculates  $p(c)$  directly using exact diagonalization, which is valid for all orders of  $\beta t$ , and which provides the exact value (with no approximations) for  $p(c)$ , at least to within the machine precision. Of course, because it relies on exact diagonalization of finite clusters, which can be computationally costly, there is a practical limit to the largest cluster size one can use in Eq. 2.87 for calculating property  $P$  per site. At some point, the summation must be truncated at the largest accessible cluster size, which ultimately determines the convergence of the numerics. For most of the work discussed in this thesis, the calculations are typically carried out to either 8<sup>th</sup>- or 9<sup>th</sup>-order, which means that the maximum cluster used in the series has a size of either 8 or 9, respectively. As long as the various correlations within the system are sufficiently short range (i.e. smaller than the size of the maximum cluster used in the expansion), then because of the exact treatment of the system by the numerics at the level of finite clusters, the summation in Eq. 2.87 can converge and subsequently provides an accurate prediction for  $P$ . However, as the temperature is lowered, the correlations in the system typically grow longer range. This is true, for instance, for the spin correlations in the system, whose correlation length can quickly grow larger than the size of the biggest cluster used in the expansion, Eq. 2.87, at sufficiently low temperatures (see Eq. 4.16). When this occurs, i.e. when the correlations in the system (in whichever form) at low temperatures become larger than the biggest cluster size used in the calculations, the numerics can no longer converge, and the prediction

for property  $P$  by Eq. 2.87 ceases to be accurate. Practically speaking, by comparing the NLCE results with both the experimental data and the DQMC predictions, we find that the NLCE calculations of relevant equilibrium, thermodynamic properties of the Hamiltonian remain accurate down to temperatures of roughly  $k_B T \sim 0.3t$ , over all fillings, at  $U/t = 8$ . The minimal convergence temperature also typically improves with increasing  $U/t$ . Compared to the typical temperatures realized experimentally ( $k_B T \sim t$ ), this minimal temperature limit to the convergence of the numerics is sufficiently low that, for all practical purposes, the NLCE predictions can be used for reliable comparisons to the experimental data, which allows us to estimate, for instance, the temperature of prepared samples, by comparing experimentally measured quantities (like the local moment or the nearest-neighbor spin correlation strength) to the NLCE predictions at different temperatures.

The second numerical technique made use of in this thesis is Determinant Quantum Monte Carlo (DQMC) [21, 239, 143, 161, 53, 174]. DQMC is a numerical algorithm which provides unbiased and statistically exact predictions for the different thermodynamic properties of a system, like the energy or the strength of different correlations, as functions of the system temperature,  $k_B T$ . To do this, it first separates the Hamiltonian into a single particle part and an interacting part,  $\hat{H} = \hat{T} + \hat{V}$ , where the single particle energy is given by,

$$\hat{T} = -t \sum_{\langle i,j \rangle, \sigma} \left[ \hat{c}_{\sigma,i}^\dagger \hat{c}_{\sigma,j} + h.c. \right] - \mu \sum_{i,\sigma} \hat{n}_{\sigma,i}, \quad (2.89)$$

and the interacting part of the Hamiltonian is given by,

$$\hat{V} = U \sum_i (\hat{n}_{\uparrow,i} - 1/2) (\hat{n}_{\downarrow,i} - 1/2). \quad (2.90)$$

The thermodynamic calculations are then performed using the partition function for this Hamiltonian, which is calculated by evolving the system in imaginary time over the interval  $[0, \beta = 1/k_B T]$ . To approximate the partition function, this imaginary time interval can be broken up into  $M$  discrete segments of duration  $\delta\tau = \beta/M$ . A

Trotterized separation of the operators  $\hat{T}$  and  $\hat{V}$  in the Hamiltonian, which do not commute, can then be performed for each segment of time  $\delta\tau$ , which incurs errors on the order of  $\sim tU(\delta\tau)^2$ , to approximate the term  $e^{-\beta\hat{H}}$  as,

$$e^{-\beta\hat{H}} = \left[ e^{-\delta\tau(\hat{T}+\hat{V})} \right]^M \approx \left[ e^{-\delta\tau\hat{T}} e^{-\delta\tau\hat{V}} \right]^M. \quad (2.91)$$

Subsequently, one can factorize the quartic terms in the interaction energy, Eq. 2.90, into a quadratic form which can be integrated exactly in a path integral representation of the partition function of the system in imaginary time. To do this, however, one must introduce an auxiliary field at each point in space and time,  $S(\mathbf{x}, \tau)$ . Typically, for the DQMC calculations shown in this thesis, an Ising auxiliary field,  $S = \pm 1$ , is used at each space-time point. Once  $S(\mathbf{x}, \tau)$  is introduced, the interaction term in Eq. 2.91 can be written in a quadratic form as,

$$e^{-\delta\tau U(\hat{n}_{\uparrow,i}-1/2)(\hat{n}_{\downarrow,i}-1/2)} = \frac{1}{2} e^{-\delta\tau U/4} \sum_{S(\mathbf{x}, \tau) = \pm 1} e^{-\delta\tau \lambda S(\mathbf{x}, \tau)(\hat{n}_{\uparrow,i} - \hat{n}_{\downarrow,i})}, \quad (2.92)$$

where  $\lambda$  here is the solution of  $\cosh(\delta\tau\lambda) = e^{\delta\tau U/2}$  (one can easily verify this expression by plugging in the four possible combinations of values of  $\hat{n}_{\uparrow,i}$  and  $\hat{n}_{\downarrow,i}$ ). Eq. 2.92 essentially allows one to reduce the path integral for the fully interacting system into an effectively non-interacting problem, where the action for the path integral now describes the propagation of a fermionic particle through a fluctuating configuration of auxiliary fields given by,

$$-t \sum_{\langle i,j \rangle, \sigma} \left[ \hat{c}_{\sigma,i}^\dagger \hat{h}_\sigma(\overline{S}(\tau)) \hat{c}_{\sigma,j} \right] = -t \sum_{\langle i,j \rangle, \sigma} \left[ \hat{c}_{\sigma,i}^\dagger \hat{c}_{\sigma,j} + h.c. \right] + \sum_{i, \sigma} [-\mu + \sigma \lambda S(i, \tau)] \hat{n}_{\sigma,i}, \quad (2.93)$$

where  $\sigma = \pm 1$ , and where the right-hand side of this equation is obtained by plugging Eq. 2.92 into Eq. 2.91, using Eq. 2.90. Since the fermion contributions are now quadratic in Eqs. 2.92 and 2.93 (at the expense of having to integrate over the auxiliary fields), they can be integrated out exactly (i.e. both spin states), leaving a partition function for the system, which is more accessible numerically, of the form [21, 143,

161, 53],

$$\mathcal{Z} = \sum_{\{S\}} \text{DetM}_{\uparrow}(S) \text{DetM}_{\downarrow}(S), \quad (2.94)$$

where the summation is carried out over all configurations of the auxiliary field, and  $\text{DetM}_{\sigma}(S)$  represents the determinant of  $M_{\sigma}(S)$ , which is given by,

$$M_{\sigma}(S) = \left[ I + \prod_{\tau} e^{-\delta\tau \hat{h}_{\sigma}(\bar{S}(\tau))} \right]. \quad (2.95)$$

The Monte Carlo portion of the algorithm comes in here, via the sampling of the different configurations of the auxiliary field. From the partition function in Eq. 2.94, one can then obtain all of the relevant thermodynamic variables. For the DQMC data discussed in section 4.4, regarding the experimental measurements of spin and charge correlations in the 2D Fermi-Hubbard model, the simulations were performed on an  $8 \times 8$  lattice with  $t\delta\tau = 0.05$ , where each DQMC data point utilized 200 independent runs with 20000 sweeps through the lattice for each run.

The parameter regime where this DQMC technique produces accurate predictions for the thermodynamic properties of the system is ultimately determined by the negative sign or complex phase of the determinants in Eq. 2.94, which lies at the origin of the infamous fermion sign problem [144], since away from half-filling these determinants are not necessarily positive-definite. As the temperature of the system decreases, away from half-filling, thereby increasing  $\beta$ , this fermion sign problem becomes more significant, which ultimately limits the ability of DQMC to make accurate predictions for the thermodynamic properties of the Hamiltonian at low temperatures away from half-filling. Practically speaking, we find, through comparisons of the DQMC predictions with experimental data and NLCE calculations, that the DQMC predictions of relevant equilibrium, thermodynamic properties of the Hamiltonian remain reliable down to temperatures of at least  $k_B T \sim 0.3t$ , over all fillings, at  $U/t = 8$ . The DQMC calculations are therefore more than adequate for the comparison of thermodynamic observables with the experimental data, which typically reach temperatures around  $k_B T \sim t$ .

## Heisenberg and t-J Models

Another approach to understanding the intricacies of the complex many-body Hamiltonian of the 2D Fermi-Hubbard model is to map the Hamiltonian, in certain parameter regimes, onto a simpler model which is more theoretically tractable, and which (ideally) captures the essential physics of the Hubbard model in that parameter regime [13]. The simplest example is that of the mapping of the 2D Fermi-Hubbard model at half-filling, low temperatures  $k_B T \ll U$ , and strong interactions  $U \gg t$ , onto the 2D isotropic Heisenberg model with antiferromagnetic interactions, given by,

$$H_{\text{Heisenberg}} = \frac{4t^2}{U} \sum_{\langle i,j \rangle} \mathbf{S}_i \cdot \mathbf{S}_j, \quad (2.96)$$

where  $\mathbf{S}_i = \hat{S}_{x,i}\hat{x} + \hat{S}_{y,i}\hat{y} + \hat{S}_{z,i}\hat{z}$  is a spin-1/2 operator, and

$$\begin{aligned} \hat{S}_{x,i} &= \frac{\hat{c}_{\uparrow,i}^\dagger \hat{c}_{\downarrow,i} + \hat{c}_{\downarrow,i}^\dagger \hat{c}_{\uparrow,i}}{2} \\ \hat{S}_{y,i} &= -i \left( \frac{\hat{c}_{\uparrow,i}^\dagger \hat{c}_{\downarrow,i} - \hat{c}_{\downarrow,i}^\dagger \hat{c}_{\uparrow,i}}{2} \right) \\ \hat{S}_{z,i} &= \frac{\hat{n}_{\uparrow,i} - \hat{n}_{\downarrow,i}}{2}. \end{aligned} \quad (2.97)$$

The  $\hat{S}_{x,i}$ ,  $\hat{S}_{y,i}$ , and  $\hat{S}_{z,i}$  components of the spin, as they are defined in Eq. 2.97, obey the normal spin-1/2 Pauli commutation relations, meaning that this Hamiltonian truly acts as a pure spin model on a square lattice in two dimensions. The details of this mapping will not be derived here, but can be found in numerous textbooks and publications. For the interested reader, see, for example, [4, 13, 54]. It is important to note, however, that to arrive at the Heisenberg model, Eq. 2.96, one must project out any charge fluctuations across the Mott gap, which produce doublons and holes in the system, in order to obtain a uniformly filled system with exactly one particle per site. In this sense, the Heisenberg model is designed to capture the physics of the antiferromagnetic spin interactions which are also present in the Hubbard model, as well as the energetically low-lying spin excitations. It cannot, however, account

for any effects related to quantum or thermal charge fluctuations in the system at half-filling, which are certainly present, even at extremely low temperatures, at finite values of the Hubbard parameters, e.g.  $U/t = 8$  (see, for example, the ground state of the Fermi-Hubbard double well in section 2.2.1). Thus, while it can describe the spin degree of freedom in the Hubbard model at extremely large interactions  $U \gg t$  and low temperatures  $k_B T \ll U$ , where double-occupancies are negligible, the Heisenberg model cannot capture the physics of, for example, the dynamics of doublon-hole correlations at half-filling and intermediate interactions (e.g.  $U/t = 8$ ), nor does it take into account any coupling between the spin and charge degrees of freedom which can exist in the Hubbard model.

A second model which is commonly examined is the  $t - J$  model [88, 222, 147, 13, 216, 191, 139], a slight generalization of the Heisenberg model that takes into account the interactions and dynamics of doped holes in the immediate vicinity of half-filling. The  $t - J$  model can be written as,

$$H_{tJ} = -t \sum_{\langle i,j \rangle, \sigma} \left[ \hat{c}_{\sigma,i}^\dagger \hat{c}_{\sigma,j} + h.c. \right] + \frac{4t^2}{U} \sum_{\langle i,j \rangle} \left[ \mathbf{S}_i \cdot \mathbf{S}_j - \frac{\hat{n}_i \hat{n}_j}{4} \right], \quad (2.98)$$

where the kinetic energy term is the normal Hubbard tunneling energy, the spin operators  $\mathbf{S}_i$  are defined in the same way as they are for the Heisenberg model (Eq. 2.97), and  $\hat{n}_i = \hat{n}_{\uparrow,i} + \hat{n}_{\downarrow,i}$  is the total density at site- $i$ . Implicit to Eq. 2.98 is a projection operator, which restricts the full Hilbert space of the Hubbard model to the subspace where there are no double-occupancies on any site (although holes are allowed) [13, 165, 139]. In this sense, the  $t - J$  model sits somewhere between the general case of the full 2D Hubbard model, which allows for doublons, holes, and single-occupancies at any value of  $U/t$ , and the Heisenberg model, which is restricted to half-filling and does not allow for either holes or doublons. When there are no holes in the system (e.g. half-filling), the  $t - J$  model once again becomes the Heisenberg model, Eq. 2.96, and therefore acts as an effective extension of the simple Heisenberg system. Because it does not allow for doublons, however, the model is once again only applicable at strong interactions,  $U \gg t$ , relatively low temperatures  $k_B T \ll U$ , and

in the hole-doped vicinity of half-filling, where the effects of doublons in the Hubbard model are small. We will not go into detail about the specifics of either the  $t - J$  or Heisenberg models here, since the purpose of this thesis is to focus on experimental studies of the full 2D Fermi-Hubbard system, but the interested reader can find a detailed review of  $t - J$  physics relevant to the Hubbard model and the cuprates in [13, 139]. It was worth noting though, that through comparisons of experimental measurements performed on the full 2D Fermi-Hubbard system, with Heisenberg and  $t - J$  predictions, one could potentially hope to elucidate the specific roles that doublons and holes, and any correlations between them, play in the thermodynamic and transport properties of the Hubbard model.

### 2.2.3 Equation of State and Basic Phenomenology of the Fermi-Hubbard Model

In this section, we describe some of the basic phenomenology of the spin-balanced 2D Fermi-Hubbard model, in order to provide some background for subsequent discussions in the remaining chapters of this thesis. Specifically, the Hubbard Hamiltonian, Eq. 2.58, with  $\mu_\uparrow = \mu_\downarrow = \mu$ , essentially has three degrees of freedom for varying the relative strengths of the different energy scales, once the overall energy is normalized by one of the parameters, typically the tunneling strength  $t$ . In this case, the available parameters are the relative strength of the on-site interaction energy term in the Hamiltonian,  $U/t$ , the relative chemical potential term,  $\mu/t$ , and the temperature of the system,  $k_B T/t$ . In these normalized units, the half-filling point, where  $\langle \hat{n} \rangle = \langle \hat{n}_\uparrow + \hat{n}_\downarrow \rangle = 1$ , occurs at  $\mu/t = \frac{1}{2}(U/t)$ . By varying the strength of these different energy scales in the Hamiltonian, one can realize different paradigmatic states of the 2D Fermi-Hubbard model, including metallic, Mott-insulating, and band-insulating states. We can first consider the situation where the on-site interactions are relatively weak, so that  $U/t \ll 1$ . In this case, the system is essentially non-interacting, and our intuition from the non-interacting system, section 2.1, and more generically single-particle band theory, applies. That is, when the chemical

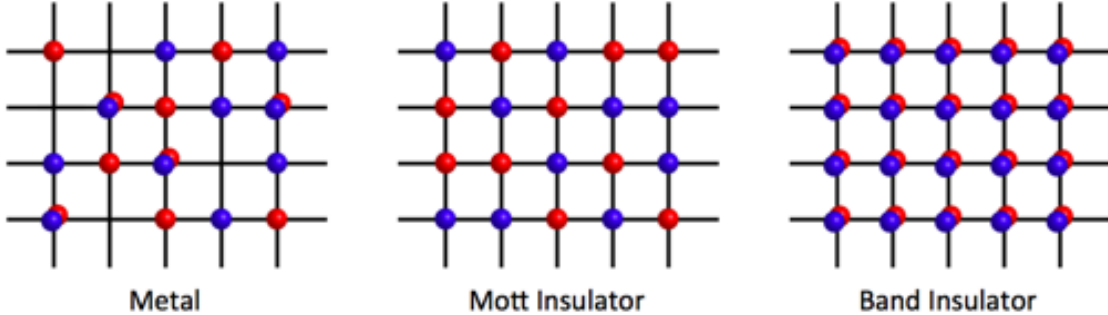


Figure 2-1: Illustration of the *in situ* particle distribution for different paradigmatic states of the Fermi-Hubbard model. Shown are representative "images" which illustrate the characteristic distribution of particles for these states, after projecting the system onto real space in the lattice. The left-most image represents a metallic state, which shows significant particle fluctuations, and a large fraction of sites that are either empty or occupied with doublons. The middle figure represents a Mott-insulating state with strong on-site interactions and one particle per site (half-filling). The interactions suppress particle fluctuations in the system, so that the atoms are effectively localized, which leads to insulating behavior for this state. Additionally, due to effects such as super-exchange, there are significant antiferromagnetic spin correlations present at low temperatures. The right most image shows a band-insulating state, where all of the single-particle states are filled, so that each site is maximally occupied with two atoms of opposite spin. This occurs when the chemical potential is large compared to the other energy scales, and sits within the bandgap. Because there are no single particle states to scatter into in this case, this state is also an insulator. Figure reproduced from [37].

potential  $\mu$  lies somewhere within the lowest energy band, there are unfilled single-particle states, and the system behaves like a metal, a conducting state characterized by delocalized particles, and therefore significant on-site particle fluctuations. This is illustrated in the left-most image of Fig. 2-1. However, when the chemical potential is larger than the highest-energy state in the 2D single-particle dispersion relation, Eq. 2.23, so that  $\mu > 4t$ , it sits within the band gap, and all of the single-particle states are filled. In this situation, the system has become a band-insulator, because there are no single-particle states left for atoms to scatter into, so that it can no longer conduct. In real space, this means that each site is maximally occupied by one particle of each spin state, so that every site is filled with a doublon. This is illustrated in the right-most image of Fig. 2-1.

Even when the on-site interactions  $U/t$  are finite, if the chemical potential is

large enough that all of the states are completely filled, and each site is doubly-occupied in real space, the system remains in the band-insulating state. Additionally, if the chemical potential lies below the half-filling point  $\frac{1}{2}(U/t)$ , when there are non-zero interactions present, so that the total density is fairly dilute,  $\langle \hat{n} \rangle < 1$ , and the temperature lies in the intermediate temperature regime,  $4t^2/U \lesssim k_B T \lesssim U$ , the metallic character of the system persists. This is because there is a suppressed likelihood of two particles encountering one another at low densities, meaning that the effects of the on-site interactions are also suppressed in this regime. Therefore, one should expect enhanced particle fluctuations, consistent with metallic behavior, even with a finite interaction energy,  $U/t > 1$ , when the chemical potential is small enough that the total density per site is low,  $\langle \hat{n} \rangle < 1$ . Because of the particle-hole symmetry of the 2D Fermi-Hubbard model on a square lattice about the half-filling point, Eq. 2.61, this must also be true for the case where the chemical potential sits above half-filling,  $\mu > U/2$ , so that the total density per site is large, but not quite in the band-insulating regime,  $1 < \langle \hat{n} \rangle < 2$ . In this region, the state still behaves like a metal, with enhanced particle fluctuations, but these fluctuations occur on top of a background of doubly-occupied sites. That is, the state is a metal composed of holes, or missing particles, in a sea of doublons, rather than a metal of single particles in a sea of empty sites, which occurs in the low density regime.

Another insulating state can be realized when the system is half-filled,  $\mu = U/2$ , and the on-site interactions are large,  $U/t \gg 1$ . Although single-particle band theory would tell us that this state is metallic, when the on-site interactions are large enough, the creation of doubly-occupied sites in the system is energetically suppressed by the large repulsive energy gap of order  $U$  associated with doublons. Since the repulsive interactions suppress the formation of doublons in this regime where the average total density is one particle per site, and because Pauli blocking prevents two particles of the same spin from ever occupying the same site, this means atoms must be localized in space to individual sites, and cannot easily tunnel around. Thus, the strong interactions at half-filling create a uniform background of singly occupied sites in real space, which is illustrated in the middle figure of Fig. 2-1. In this sense, the large charge

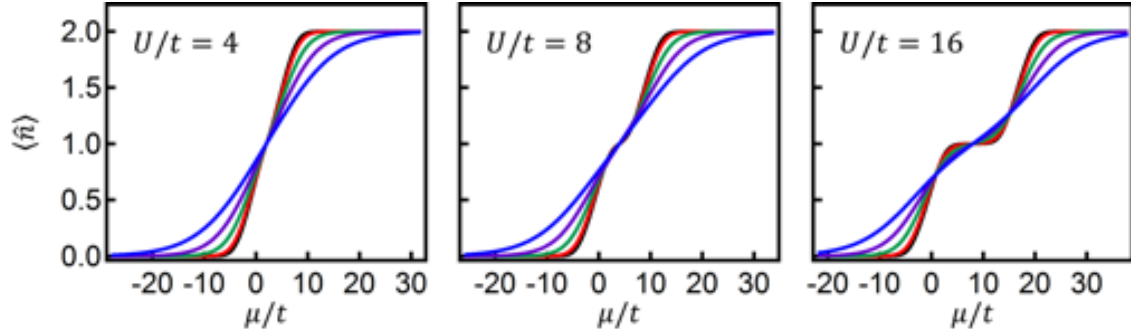


Figure 2-2:  $\langle \hat{n} \rangle$  versus  $\mu/t$  for fixed  $U/t$  and  $k_B T/t$ . The different curves represent isothermal 9<sup>th</sup>-order NLCE predictions for the average total density per site,  $\langle \hat{n} \rangle$ , as a function of the global chemical potential  $\mu/t$ , for several different temperatures  $k_B T/t$  and values of the Hubbard parameters  $U/t = (4, 8, 16)$ , where each figure represents a different value of  $U/t$ . The black curves in the figures represent  $k_B T/t = 0.82$ , the red curves are  $k_B T/t = 1.13$ , the green curves are  $k_B T/t = 1.97$ , the purple curves are  $k_B T/t = 3.19$ , and the blue curves are  $k_B T/t = 5.16$ . The half-filling point in each graph is determined by the location of  $\mu = U/2$ . In the sense of the LDA, the profiles shown here are directly related to the in-trap total density distributions that can be observed in the experiment. These plots are generated using the NLCE data provided in the supplement of [120].

gap of order  $U$  drives the system into an insulating state, known as a Mott insulator, where charge fluctuations are suppressed. How good of an insulating state this is, and how much these charge fluctuations are suppressed, depends on the exact value of  $U/t$ . As we saw in the double well system in section 2.2.1, finite (i.e. not infinite) values of  $U/t \gg 1$  still allow for a quantum mechanical admixture of doublon-hole pairs (even at zero temperature) into the system, whose amplitude is suppressed as  $\sim t/U$ . Additionally, at finite values of the temperature  $k_B T/U \sim 1$ , doublon-hole fluctuations can be thermally excited, which also suppresses the insulating character of this state, making it more metallic. As the temperature is lowered, however, such that  $k_B T \ll U$ , these thermal doublon-hole fluctuations can be effectively frozen out, so that the insulating nature of the Mott insulator is restored, and single atoms are again localized to individual sites, at least up to what is quantum mechanically allowed by the finite value of the Hubbard parameters  $U/t$ .

In Figs. 2-2 and 2-3, we support these qualitative arguments for the behavior of the 2D Fermi-Hubbard system in different parameter regimes by showing numerical cal-

culations from NLCE. These plots are generated using the data from [120], and show the total density  $\langle \hat{n} \rangle$ , and its associated variance,  $\langle \Delta \hat{n}^2 \rangle \equiv \langle \hat{n}^2 \rangle - \langle \hat{n} \rangle^2$ , respectively, where the variance characterizes the particle fluctuations in the system, as functions of the chemical potential  $\mu$ , for different temperatures  $k_B T/t$ , and three different values of the Hubbard parameters,  $U/t$ . From the density plot in Fig. 2-2, it is clear that, even for reasonably strong on-site interactions,  $U/t = 16$ , a band-insulating state with  $\langle \hat{n} \rangle = 2$  can be realized for large enough chemical potentials,  $\mu/t$ . The threshold chemical potential where this occurs increases with increasing temperature, due to thermal fluctuations, as can be seen from the different temperature curves in Fig. 2-2 at a fixed value of  $U/t$ . In this regime, when the density is very nearly maximized at two particles per site, the corresponding particle fluctuations shown in Fig. 2-3 are strongly suppressed, due to the insulating behavior of the band-insulator. At or near half-filling, on the other hand, a plateau in the density forms around  $\langle \hat{n} \rangle = 1$  when the interactions are large, e.g.  $U/t = 16$ , as can be seen in Fig. 2-2, representative of the Mott-insulating state. The appearance of the Mott, or charge gap, of order  $U$  in this state, which suppresses particle fluctuations in the system, corresponds to a suppression of the density variance at half-filling, as shown in Fig. 2-3. As the interactions become stronger, the suppression of the particle variance is enhanced, and extends over a finite region in  $\mu$  around half-filling. The effect of finite temperature can also be seen from these plots, in that the Mott plateau, where  $\langle \hat{n} \rangle = 1$ , is suppressed with increasing temperature, which increases the admixture of thermally excited doublon-hole pairs in the system. In the variance plots, this can be seen as an enhanced variance due to the thermal doublon-hole fluctuations, with increasing temperature. The metallic states, meanwhile, correspond to those regions where the particle fluctuations and density variance are large, which can occur either from large temperatures, which thermally excite density fluctuations, weak interactions, where the Mott gap is ill-formed, or intermediate densities on either side of half-filling.

From density versus chemical potential plots, such as those in Fig. 2-2, one can

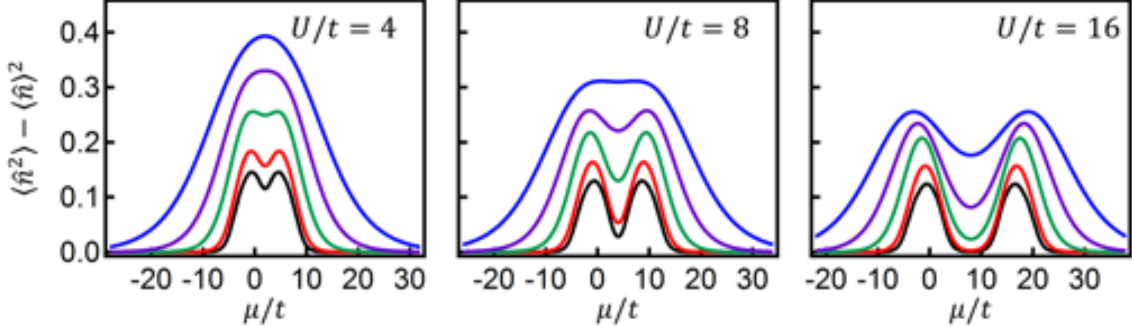


Figure 2-3:  $\langle \Delta \hat{n}^2 \rangle$  versus  $\mu/t$  for fixed  $U/t$  and  $k_B T/t$ . The different curves represent isothermal 9<sup>th</sup>-order NLCE predictions for the on-site variance in the total density,  $\langle \Delta \hat{n}^2 \rangle = \langle \hat{n}^2 \rangle - \langle \hat{n} \rangle^2$ , as a function of the global chemical potential  $\mu/t$ , for several different temperatures  $k_B T/t$  and values of the Hubbard parameters  $U/t = (4, 8, 16)$ , where each figure represents a different value of  $U/t$ . The black curves in the figures represent  $k_B T/t = 0.82$ , the red curves are  $k_B T/t = 1.13$ , the green curves are  $k_B T/t = 1.97$ , the purple curves are  $k_B T/t = 3.19$ , and the blue curves are  $k_B T/t = 5.16$ . The half-filling point in each graph is determined by the location of  $\mu = U/2$ . In the sense of the LDA, the profiles shown here are directly related to the in-trap local density fluctuations that can occur in the experiment. These plots are generated using the NLCE data provided in the supplement of [120].

directly read off the isothermal compressibility of the system, given by,

$$\frac{1}{n^2} \left( \frac{\partial n}{\partial \mu} \right) \Big|_T, \quad (2.99)$$

which can also be used to characterize different states of the Hubbard model, similar to the density variance. Since the compressibility is directly related to the local slope of the curves in Fig. 2-2, one can immediately see that the isothermal compressibility is suppressed where the state is insulating. For instance, in the band-insulating state, where a plateau in the density forms around  $\langle \hat{n} \rangle = 2$ , there is a minimal slope as a function of  $\mu$ , corresponding to a strong suppression of the compressibility, which occurs simultaneously with the suppression in the particle variance. This also holds for the Mott-insulating state, when a plateau in the density forms around  $\langle \hat{n} \rangle = 1$  for strong interactions and low temperatures. Such a suppression of the compressibility has been used in previous experimental studies of ultracold fermionic lattice systems to characterize and observe the Mott-insulating state itself [205, 55]. In contrast, the conducting metallic regions correspond to those areas in Fig. 2-2 where the slope as a

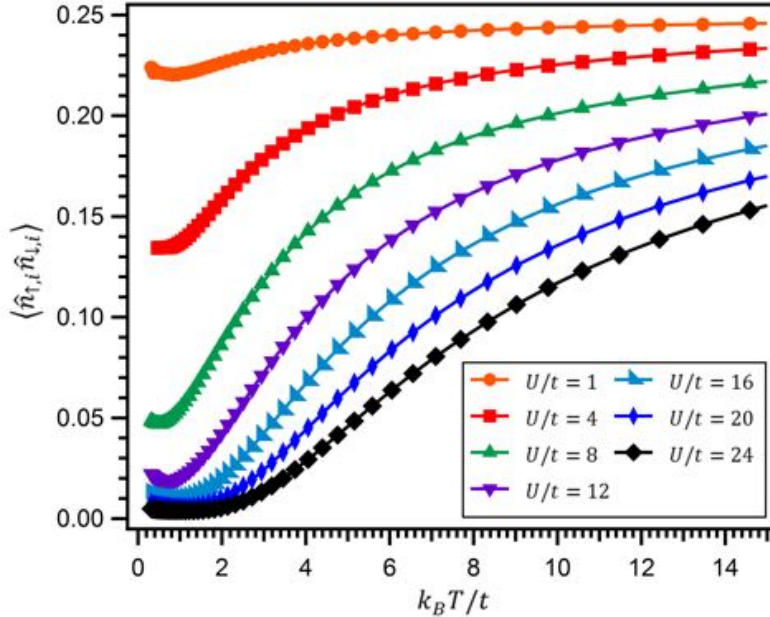


Figure 2-4: Average doublon density at half-filling and fixed  $U/t$  versus  $k_B T/t$ . Plotted are 9<sup>th</sup>-order NLCE predictions for the average density of doubly-occupied sites,  $\langle \hat{n}_{\uparrow,i} \hat{n}_{\downarrow,i} \rangle$ , at half-filling ( $\mu = U/2$ ), as a function of the system temperature  $k_B T/t$ , for several different values of the Hubbard parameters  $U/t$  in the range  $1 \leq U/t \leq 24$ . This range of Hubbard parameters covers most of the typical values used in the experimental data discussed in this thesis. For intermediate temperatures,  $4t^2/U < k_B T < U$ ,  $\langle \hat{n}_{\uparrow,i} \hat{n}_{\downarrow,i} \rangle$  decreases with decreasing temperature, for all of the  $U/t$  values shown, as the thermally excited doublon-hole fluctuations are gradually frozen out when the temperature is lowered relative to  $U$ . At lower temperatures,  $k_B T < 4t^2/U$ ,  $\langle \hat{n}_{\uparrow,i} \hat{n}_{\downarrow,i} \rangle$  shows non-monotonic behavior (see e.g. the curve for  $U/t = 12$ ), which is related to an enhanced delocalization of particles, which can arise in the presence of strong antiferromagnetic correlations [173]. The curves are generated using the NLCE data provided in the supplement of [120].

function of  $\mu$  is large, such as when the temperature is relatively high, the interactions are weak, or the density is in an intermediate regime away from half-filling.

Another way to characterize the Mott-insulating state is through the reduction of double occupancies at half-filling when the interactions are large,  $U/t \gg 1$ , and the temperature is low,  $k_B T/U \ll 1$ . In Fig. 2-4, we show NLCE numerical calculations of the density of doubly occupied sites, corresponding to the quantity  $\langle \hat{n}_{\uparrow} \hat{n}_{\downarrow} \rangle$ , which are generated using the data from [120], as a function of temperature,  $k_B T/t$ , at half-filling, for several different values of the Hubbard parameters  $U/t$ . This figure shows that, at a fixed value of the temperature, the density of doubly-occupied sites

at half-filling decreases with increasing  $U/t$ , consistent with our intuition from the double well Hubbard system, and the idea that doublons are energetically suppressed due to the Mott gap at large values of  $U/t$ . Additionally, for a fixed value of the Hubbard parameters  $U/t$ , the doublon density decreases with decreasing temperature, consistent with the idea that thermally excited doublon-hole fluctuations are suppressed, or frozen out, as the temperature is lowered relative to  $U$ . However, even at very low temperatures,  $k_B T \ll U$ , the density of doubly occupied sites is non-zero when the Hubbard parameters are finite, due to the quantum mechanical admixture of doublon-hole pairs at large, but not infinite values of  $U/t$  (see e.g. section 2.2.1). For example, at  $U/t = 8$ , the doublon density reaches a minimum of  $\sim 5\%$  at the lowest temperatures shown in the plot, which also means that, because the system is half-filled, the corresponding density of empty sites (holes) is also  $\sim 5\%$ . Characterizing the fraction of doubly occupied sites in the system has been used in [114, 221], for instance, for experimental verification of Mott-insulating behavior in ultracold fermionic optical lattice systems.

For reference, we also show in Figs. 2-5 and 2-6 the entropy per site,  $s/k_B$ , and the uniform spin susceptibility,  $\chi ta^2$ , of the 2D Fermi-Hubbard model at half-filling, as functions of the temperature,  $k_B T/t$ , for different values of the Hubbard parameters  $U/t$ . These plots are both generated using the NLCE numerical data from [120]. At half-filling, where there is, on average, one particle per site, the entropy per site corresponds to the entropy per particle,  $S/k_B N$ . The isothermal uniform spin susceptibility, on the other hand, is given by,

$$\chi = \left( \frac{\partial \langle \hat{S}_z \rangle}{\partial \Delta\mu} \right)_{n,T}, \quad (2.100)$$

where  $\Delta\mu = \mu_\uparrow - \mu_\downarrow$  and  $\hat{S}_z = (\hat{n}_\uparrow - \hat{n}_\downarrow)/2$ . It is, in some sense, the analog of the isothermal compressibility, applied to the spin density  $\langle \hat{S}_z \rangle$  rather than the total density  $\langle \hat{n} \rangle$ . We will discuss the uniform spin susceptibility in significantly more detail in section 5.4.1, but it is worth mentioning here that an experimental measurement of

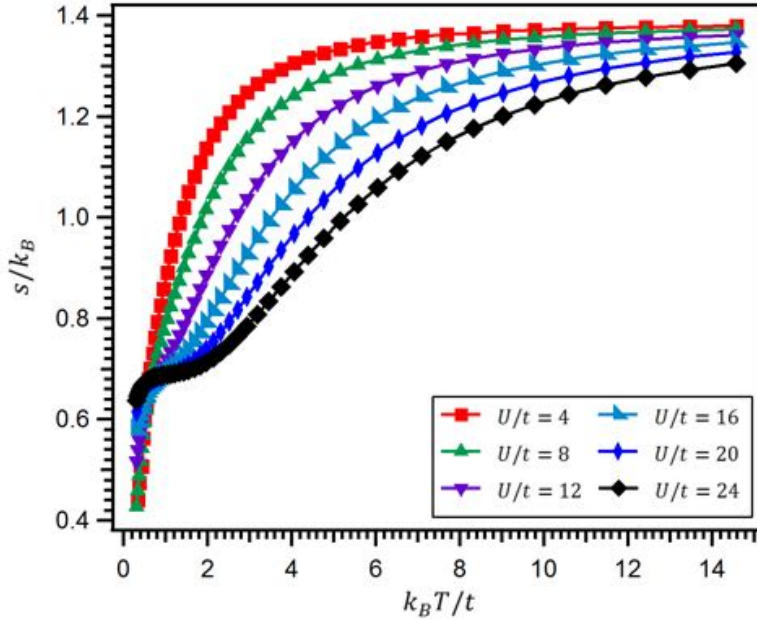


Figure 2-5: Entropy per site,  $s/k_B$ , at half-filling and fixed  $U/t$  versus  $k_BT/t$ . Plotted are 9<sup>th</sup>-order NLCE predictions for the entropy per site at half-filling ( $\mu = U/2$ ), which is equivalent to the total entropy per particle,  $S/k_B N$ , at this filling, as a function of the system temperature  $k_BT/t$ , for several different values of the Hubbard parameters  $U/t$  in the range  $4 \leq U/t \leq 24$ . This range of Hubbard parameters covers most of the typical values used in the experimental data discussed in this thesis. For strong interactions (e.g.  $U/t = 24$ ), a plateau can be observed in the entropy as a function of temperature around approximately  $s/k_B = \ln(2)$ , which occurs in the temperature region where the entropy associated with charge fluctuations has been frozen out,  $k_BT \ll U$ , but the temperature has not quite reached  $4t^2/U$ , where significant antiferromagnetic correlations develop, and where the entropy can be further lowered by freezing out the low-energy spin excitations. The curves are generated using the NLCE data provided in the supplement of [120].

the uniform spin susceptibility at half-filling and known Hubbard parameters  $U/t$  can be used, through a comparison with the NLCE data shown in Fig. 2-6, for instance, to obtain the temperature  $k_BT/t$  of the system, especially for intermediate temperatures in the range  $4t^2/U < k_BT < U$ , where  $\chi ta^2$  is relatively sensitive to, and monotonic in, changes in the temperature. This can then be combined with the NLCE entropy data in Fig. 2-5 to obtain the experimental entropy per site at half-filling. The entropy itself, in the temperature range  $4t^2/U < k_BT < U$ , resembles somewhat the behavior of the doublon density,  $\langle \hat{n}_\uparrow \hat{n}_\downarrow \rangle$ , as a function of temperature at half-filling. This is simply because, as the temperature is lowered relative to  $U$ , the entropy stored in

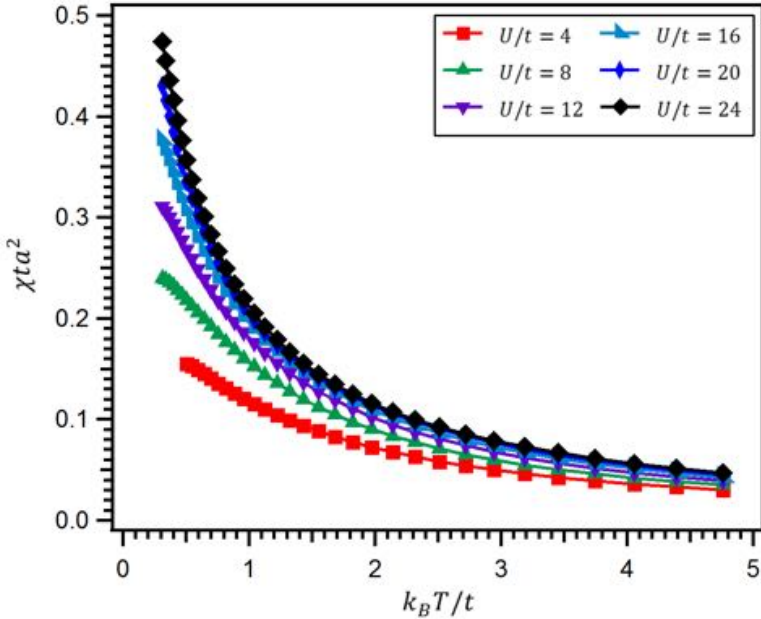


Figure 2-6: Uniform spin susceptibility,  $\chi ta^2$ , at half-filling and fixed  $U/t$  versus  $k_B T/t$ . Plotted are 9<sup>th</sup>-order NLCE predictions for the uniform spin susceptibility at half-filling ( $\mu = U/2$ ), as a function of the system temperature  $k_B T/t$ , for several different values of the Hubbard parameters  $U/t$  in the range  $4 \leq U/t \leq 24$ . This range of Hubbard parameters covers most of the typical values used in the experimental data discussed in this thesis. The curves are generated using the NLCE data provided in the supplement of [120].

the charge fluctuations of the system is removed. Similarly, at a fixed temperature, the entropy per site decreases with increasing  $U/t$ , due to the fact that less entropy can be stored in thermal doublon-hole fluctuations when the Mott gap of order  $U$  is enhanced, which, for fixed  $k_B T$ , suppresses the thermal doublon fraction.

One of the things which makes the 2D Fermi-Hubbard model so interesting is that there is a residual degree of freedom beyond the charge fluctuations, the spin degree of freedom, which we have not yet mentioned in our discussion of the phenomenology of the model in this section, but which can play an important role in the physical properties of the system at low temperatures. For example, within the uniform background of singly occupied sites in the Mott-insulating regime at half-filling, the system can further lower its energy at low temperatures through antiferromagnetic alignment of the spins. One can understand this through second order perturbation theory, whereby the system can lower its energy by an amount  $4t^2/U$  when the spins

are antiferromagnetically aligned, due to a virtual hopping process between neighboring sites occupied with opposite spin states known as super-exchange. This virtual hopping process produces a perturbative admixture of doublon-hole pairs into the wave function of the system with an amplitude set by  $t/U$ . Such behavior is exemplified in the Fermi-Hubbard double well discussed in section 2.2.1, where, in the limit  $U/t \gg 1$ , the singlet ground state can lower its energy by an amount  $4t^2/U$  relative to the first excited state, and the doublon-hole admixture in the ground state has an amplitude of  $\sim t/U$ . This super-exchange physics is also at the heart of the mapping of the half-filled Hubbard model at low temperatures  $k_B T \ll U$  and strong interactions,  $U/t \gg 1$ , to the antiferromagnetic, isotropic Heisenberg model (Eq. 2.96) [13, 54]. Generally speaking, as the temperature is lowered towards the super-exchange energy scale,  $4t^2/U$ , and below at half-filling, the antiferromagnetic spin correlations present in the system are enhanced, as the low-lying thermal spin excitations are gradually frozen out. On the square lattice, there is an additional geometric effect which makes the system susceptible to the formation of antiferromagnetic spin correlations, known as Fermi surface nesting. We will discuss this effect in more detail in section 4.4.3, when we describe our experimental measurements of antiferromagnetic spin correlations in our cold atom 2D Fermi-Hubbard system, but essentially the effect arises because of the geometric shape of the Fermi surface at half-filling, a diamond with corners located at the points  $(\pm\pi/a, 0)$  and  $(0, \pm\pi/a)$  in the first Brillouin zone. There is therefore a unique wave vector, the antiferromagnetic wave vector,  $\mathbf{Q} = (\pi/a, \pi/a)$ , which connects large segments of the Fermi surface, and thus makes the system susceptible to spin ordering along the direction of  $\mathbf{Q}$  in the presence of interactions between opposite spin states. Interestingly, however, even in the absence of interactions, as we discussed in section 2.1.3, the real space manifestation of Pauli blocking between like-spins, which can extend over a finite range in the spatial separation between the particles, can generate antiferromagnetic spin correlations in the system at low temperatures.

Some of the physical consequences of antiferromagnetic ordering of the spins at half-filling and low temperatures can be observed in the numerical data shown in

Figs. 2-4 and 2-5. In the plot of  $\langle \hat{n}_\uparrow \hat{n}_\downarrow \rangle$  versus temperature in Fig. 2-4, for instance, non-monotonic behavior can be observed in the doublon fraction at half-filling and strong interactions (e.g.  $U/t \geq 8$ ) as a function of temperature, in the region  $k_B T \sim 4t^2/U$ . Specifically, there is a minimum which occurs in the doublon density in this temperature regime. In the intermediate temperature region,  $4t^2/U < k_B T < U$ , as the temperature is lowered, thermally excited doublon-hole fluctuations are gradually frozen out, which causes the doublon fraction to decrease. Eventually, once the charge fluctuations are essentially completely removed at temperatures  $k_B T \ll U$ , what remains are energetically low-lying spin excitations in the system. Such thermal spin excitations enhance the likelihood of encountering atoms in the same spin state on neighboring sites. When this occurs, Pauli blocking prevents these particles from delocalizing through nearest-neighbor virtual hopping. However, once the temperature reaches the super-exchange scale  $\sim 4t^2/U$ , and the antiferromagnetic spin correlations are significantly enhanced, particles can once again delocalize in the super-exchange sense, because the ferromagnetic spin excitations have been frozen out. When this occurs, the doublon fraction actually increases slightly with decreasing temperature, because the system can more effectively generate correlated doublon-hole pairs through super-exchange [173]. The effect of strong antiferromagnetic spin correlations also manifests itself in the entropy per site at half-filling shown in Fig. 2-5, as a plateau in the entropy around  $s/k_B \sim \ln(2)$  as a function of temperature, at large interactions, e.g.  $U/t = 24$ . That is, as the temperature is lowered in the intermediate temperature regime,  $4t^2/U < k_B T < U$ , the entropy decreases because the thermally excited doublon-hole fluctuations are frozen out, and entropy can no longer be stored there. However, once the temperature is well below the Mott gap,  $k_B T \ll U$ , this degree of freedom has been effectively eliminated, and the entropy plateaus around  $\ln(2)$ , corresponding to a random distribution of spins in the lattice. Not until the temperature reaches the super-exchange energy scale  $k_B T \sim 4t^2/U$ , which is energetically well separated from the Mott gap energy scale  $U$  at large values of  $U/t$ , can the system continue to lower its entropy by removing low-lying, thermally excited spin excitations, thereby enhancing the antiferromag-

netic spin order present. The entropy per site therefore plateaus in the region where the thermal doublon-hole charge fluctuations have been frozen out, but the temperature has not quite reached the super-exchange energy scale, which itself decreases with increasing  $U/t$ , and which therefore becomes more energetically separated from the Mott gap. Once the temperature reaches the super-exchange scale, however, the entropy can continue to decrease below  $\sim \ln(2)$  by removing spin excitations, as the temperature is lowered further [120].

These arguments regarding antiferromagnetism in the Hubbard model and its physical effects all generally apply to the half-filled case, which has been well studied and is accessible theoretically due to the symmetry in the Hamiltonian at this point. As one moves away from half-filling, however, and dopes the system with either holes or particles in this very low temperature regime,  $k_B T < 4t^2/U$ , the general behavior of the 2D Fermi-Hubbard system and its thermodynamic properties are not well understood, an issue that arises from the fermion sign problem, which makes accessing this region of the phase diagram theoretically and numerically challenging. It is therefore currently unclear what the exact relationship is between the 2D Fermi-Hubbard model and the real system for which it has been proposed as a simplified description, the strongly correlated electrons within the high- $T_c$  cuprates.

## Phases Observed in the Cuprates

One of the major motivations for examining the 2D Fermi-Hubbard model experimentally is to better understand whether this reasonably simple model contains enough physics to explain the unconventional high-temperature superconductivity and pseudogap behavior observed in the cuprate materials, a task that is extremely challenging from a theoretical perspective. In fact, it is currently not well understood in general just how much of the cuprate phase diagram, or how much of the associated thermodynamic or transport properties observed in the cuprates, are captured by the 2D Fermi-Hubbard model [49, 139]. This is, of course, exacerbated by the fact that the 2D Fermi-Hubbard model has not been solved except in very specific, limiting cases [142]. What is known, however, is that there are many similarities between those regimes

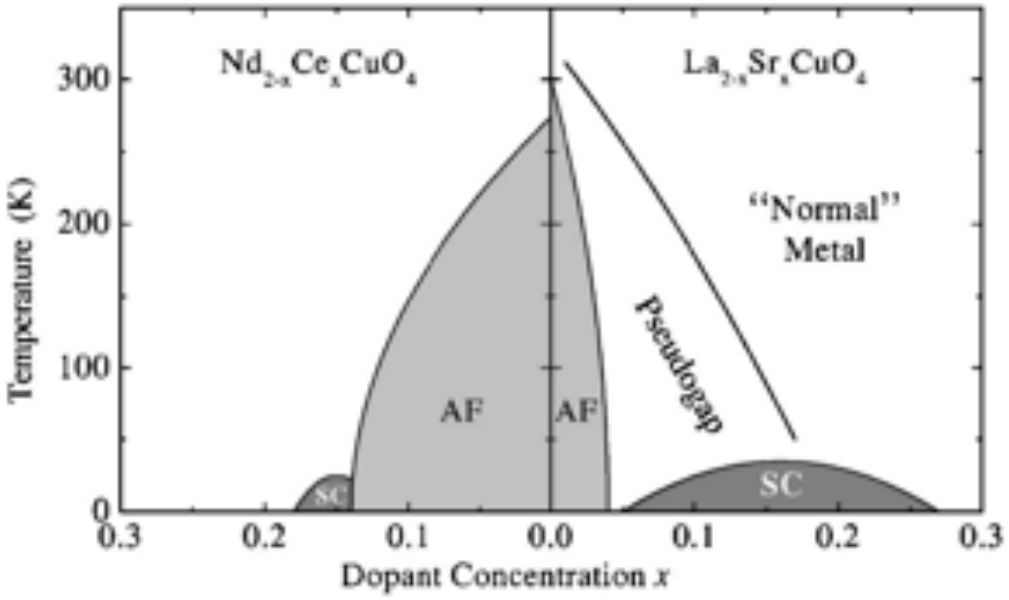


Figure 2-7: Schematic phase diagram for the cuprate high- $T_c$  superconductors. The plot shows the observed phases in the parent compounds  $La_2CuO_4$  and  $Nd_2CuO_4$ , as a function of temperature and doping. The  $La_2CuO_4$  compound is hole doped by substituting trivalent La with divalent Sr, whereas the  $Nd_2CuO_4$  compound is electron doped by substituting Nd with Ce. The doping axis thus represents hole doping on the right half of the diagram, and electron or particle doping on the left half of the diagram, where  $x = 0$  denotes the half-filling point. This figure shows a clear particle-hole asymmetry, unlike the 2D Fermi-Hubbard model, where the more robust antiferromagnetic region on the electron-doped side hides, in some sense, the other interesting phases observed on the hole-doped side, like the pseudogap state. Such particle-hole asymmetry can arise, for instance, from non-zero next-nearest-neighbor tunneling in the material [210]. Figure reproduced from [49].

of the Hubbard phase diagram that are theoretically well understood, and certain regimes within the cuprate phase diagram. Fig. 2-7 shows an example schematic phase diagram for the doped cuprate parent compounds  $La_2CuO_4$  and  $Nd_2CuO_4$  [49]. Plotted are the observed phases as a function of temperature and dopant concentration, where the right half of the figure represents the hole doped regime, and the left half of the figure represents the electron or particle doped regime. At half-filling (i.e. zero dopants), the cuprate system is Mott-insulating, and demonstrates antiferromagnetic ordering of spins at sufficiently low temperatures, similar to the Hubbard model. At temperatures slightly above the antiferromagnetic ordering temperature, or Néel temperature (roughly  $\sim 300K$  in Fig. 2-7), however, the parent compounds at

half-filling still show significant antiferromagnetic spin correlations, but whose magnitude weakens with increasing temperature. Upon doping with holes at temperatures below the N  el temperature, the antiferromagnetic order is suppressed and eventually gives way to pseudogap and novel metallic states. At even lower temperatures, the antiferromagnetic Mott insulator, upon doping with either holes or electrons at fixed temperature, transitions into an unconventional superconducting state that demonstrates  $d_{x^2-y^2}$  symmetry, something indicative of a pairing mechanism that cannot be explained by conventional BCS theory. On the hole doped side, the superconducting dome extends from  $\sim 5\%$  dopant concentration to  $\sim 26\%$  at the lowest temperatures [49, 139]. On the electron doped side, however, the superconducting dome begins around  $\sim 14\%$  dopant concentration, and ends around  $\sim 18\%$  dopant concentration. This particle-hole asymmetry in the phase diagram does not occur naturally in the particle-hole symmetric 2D Fermi-Hubbard model on a square lattice, but can arise, for instance, if one introduces longer range (next-nearest-neighbor) tunneling to the system [210]. Neglecting these additional complexities, however, it is still a subject of current investigation exactly how much of this interesting and strongly-correlated phase diagram can be explained by predictions from the standard 2D Fermi-Hubbard model. That is, it is uncertain (although we are hopeful) whether such a simplistic description of these extremely complex materials is sufficient to support the plethora of atypical and exciting phenomena observed there.

## 2.3 Transport Properties

Much of the interest in the high- $T_c$  cuprate materials arises from their unusual transport properties, and the fact that a lot of the observed transport phenomena, even in the normal state, cannot be explained using conventional theoretical tools. In the bad or strange metallic regime of these materials, for instance, the resistivity demonstrates an anomalous scaling with temperature that is inconsistent with the predictions of Fermi liquid theory and the Boltzmann kinetic equation [46], theoretical tools which can successfully explain the transport properties of many more

conventional materials at low temperatures, like standard metals. Of course, there is also the high-critical temperature superconducting state of these cuprates, which reveals a pairing gap with  $d_{x^2-y^2}$  symmetry, something that cannot be explained through conventional BCS theory. One approach towards understanding the physical mechanisms underlying the myriad of interesting transport phenomena observed in the cuprates is to examine and explain the transport properties of a simple model system, like the Fermi-Hubbard model, which is believed to capture the essential behavior of the electrons in these complex materials. Unfortunately, due to the complications associated with the strong correlations present in a fermionic many-body system like the Fermi-Hubbard model, which significantly impact our theoretical understanding of even the equilibrium properties of this Hamiltonian, there is still much that we do not understand about its charge and spin transport properties. In this section, we will discuss one method of characterizing transport within an electronic system, the conductivity, a transport coefficient that determines the linear response of the system to an external perturbation, such as an electric field. In section 2.3.1, we will discuss a simple model for the conductivity, the Drude model, which applies kinetic theory to phenomenologically describe the behavior of many simple materials, like conventional metals, near room temperature. We will then, in section 2.3.2, relate the conductivity to properties of the (equilibrium) Fermi-Hubbard Hamiltonian, in the absence of an external perturbation, through a Kubo formula, which will allow us to understand the conductivity, in linear response theory, as the current response function, a property that is intrinsic to the underlying Hamiltonian itself. From this form for the conductivity, it will become apparent why it is so theoretically challenging to calculate directly using, for instance, numerical tools like DQMC or NLCE, and why, therefore, there is still so much that we do not understand about transport within the Hubbard model. Finally, in section 2.3.3, we will discuss some useful properties of the conductivity itself, including sum rules, which relate the conductivity to the average kinetic energy of the unperturbed system.

### 2.3.1 Drude Theory of the Conductivity

One simple model for the electrical conductivity of a metal is the Drude model, which relates the AC and DC electrical conductivities to the relaxation time  $\tau$ , a phenomenological parameter that characterizes the average time an electron experiences between collisions. The Drude model assumes that any interactions of a given electron with other electrons, or with the ion cores forming the periodic lattice potential in the crystal, that occur between collisions, can be ignored. Additionally, it assumes that the collision process itself is relatively instantaneous, so that it can rapidly change the velocity of an electron. When the electron emerges from the collision, the model then assumes that it emerges with a velocity that is randomly oriented, and whose magnitude is determined by the local temperature where the collision occurred. The relaxation time  $\tau$  then is defined such that  $1/\tau$  is the probability per unit time that an electron experiences a collision, so that the probability an electron experiences a collision in an infinitesimal period of time  $dt$  is  $dt/\tau$ . We will assume for the moment (although this can in principle be relaxed) that  $\tau$  is independent of the electron's velocity, but we will not make any assumptions about the physical origin of  $\tau$  (for now).

The conductivity then, which acts as the proportionality constant between the induced electrical current and the electric field, can be written as  $\mathbf{J} = \sigma \mathbf{E}$ , where  $\mathbf{E}$  is the electric field in the metal,  $\mathbf{J}$  is the current density, and  $\sigma$  is the conductivity. The current density itself can be expressed as,

$$\mathbf{J} = -nev\mathbf{v}, \quad (2.101)$$

where  $n$  is the electron density,  $e$  is the charge, and  $\mathbf{v}$  is the average electronic velocity in the material. In the absence of an applied electric field, the velocities of the individual electrons are randomly oriented, so that the average velocity  $\mathbf{v}$  is zero, meaning the net current density is also zero. However, an electric field  $\mathbf{E}$  will induce a net drift velocity for the electrons in the material, which will result in a non-zero current density.

If we examine a single electron immediately after a collision, where it emerges with some outgoing velocity  $\mathbf{v}_0$ , it will be accelerated by the electric field in the material for a time  $t$  since that last collision occurred. The electron's velocity at time  $t$  would then be,

$$\mathbf{v}_{\text{electron}} = \mathbf{v}_0 - \frac{e}{m} \mathbf{E}t, \quad (2.102)$$

where  $m$  is the electron mass, and  $-e\mathbf{E}t/m$  is the velocity gained by the acceleration from the electric field. If we then take the average electronic velocity, the contribution from  $\mathbf{v}_0$  will be zero, since we have assumed that the velocity with which an electron emerges from a collision is randomly oriented. The average velocity is then purely determined by the velocity gained through acceleration by the electric field. Because the average time electrons can be accelerated by  $\mathbf{E}$  before they undergo another collision is  $\tau$ , the average electron drift velocity is then simply  $\mathbf{v}_{\text{avg}} = -e\mathbf{E}\tau/m$ . Plugging this into the current density, Eq. 2.101, then gives,

$$\mathbf{J} = \frac{ne^2\tau}{m} \mathbf{E}, \quad (2.103)$$

so that the DC conductivity is given by,

$$\sigma = \frac{ne^2\tau}{m}. \quad (2.104)$$

This tells us that the conductivity is linearly proportional to the density, and to the average time between collisions, a physically reasonable result. The relaxation time  $\tau$  can also be used to construct the mean free path  $l$ , which represents the average distance traveled between collisions, via  $l = v\tau$ , where  $v$  is the average speed. Although this Drude result provides a relatively simple form for the DC conductivity, it does not tell us what  $\tau$  is, or how it is related to the underlying Hamiltonian. In this sense, it is a sort of phenomenological parameter within the model.

Given the existence of some effective relaxation time  $\tau$ , however, we can write the equation of motion for the average electronic momentum, which we will then be able to use to obtain the Drude result for the AC conductivity. We will let  $\mathbf{p}(t)$  represent

the average electron momentum at time  $t$ . In the absence of collisions, Newton's laws of motion tell us that  $d\mathbf{p}/dt = \mathbf{F}(t)$ , where  $\mathbf{F}(t)$  is the average force per electron due to, for example, an applied electric field. With a finite relaxation rate  $1/\tau$  due to collisions, however, this equation is modified so that,

$$\frac{d\mathbf{p}}{dt} = -\frac{\mathbf{p}}{\tau} + \mathbf{F}(t), \quad (2.105)$$

where the relaxation rate  $1/\tau$  has introduced an effective damping term into the equation of motion for the electronic momentum. If we then apply an AC electric field of the form  $E(t) = E_0 e^{-i\omega t}$ , where  $\omega$  is the frequency of the applied field and  $E_0$  is the amplitude, the force term in Eq. 2.105 becomes  $F(t) = -eE_0 e^{-i\omega t}$ . We can then look for steady state solutions to Eq. 2.105 of the form  $p(t) = p(\omega)e^{-i\omega t}$ , so that,

$$\begin{aligned} \frac{dp}{dt} &\rightarrow -i\omega p(\omega)e^{-i\omega t} \\ -\frac{p}{\tau} &\rightarrow -\frac{p(\omega)e^{-i\omega t}}{\tau}. \end{aligned} \quad (2.106)$$

The equation of motion then simplifies to,

$$-i\omega p(\omega) = -\frac{p(\omega)}{\tau} - eE_0. \quad (2.107)$$

Solving for  $p(\omega)$ , and plugging this into the current density using  $J(\omega) = -nep(\omega)/m$  (Eq. 2.101), then gives,

$$J(t) = J(\omega)e^{-i\omega t} = \frac{(ne^2\tau/m) E_0 e^{-i\omega t}}{1 - i\omega\tau} = \frac{(ne^2\tau/m) E(t)}{1 - i\omega\tau}, \quad (2.108)$$

so that we can directly read off the AC Drude conductivity as,

$$\sigma(\omega) = \frac{(ne^2\tau/m)}{1 - i\omega\tau} = \frac{\sigma_{DC}}{1 - i\omega\tau}, \quad (2.109)$$

where  $\sigma_{DC}$  is the DC Drude conductivity given by Eq. 2.104. It follows then that the

real part of the conductivity,  $\text{Re}[\sigma(\omega)]$ , is simply,

$$\text{Re}[\sigma(\omega)] = \frac{\sigma_{DC}}{1 + \omega^2\tau^2}. \quad (2.110)$$

The Drude model thus predicts a Lorentzian profile for the frequency dependent conductivity that is peaked at the DC value, and that has a HWHM, as a function of  $\omega$ , of  $1/\tau$ . While this Drude prediction may seem very crude, given that we do not know, *a priori*, what  $\tau$  is or how it can be calculated, and even though it might appear not to have any bearing on the complex dynamics in a strongly interacting system like the Fermi-Hubbard model, a very similar result can be obtained by modeling the Fermi-Hubbard dynamics hydrodynamically, with a finite momentum relaxation rate  $\Gamma$  that damps the current in the system, the equivalent of  $1/\tau$ , and which arises from weak umklapp scattering with the lattice. Such a description was used in [26], for instance, without the assumption of quasi-particle based transport, to model the low-frequency response of the charge conductivity that was measured there in a doped Fermi-Hubbard system with strong interactions,  $U/t = 7.2$ , and low temperatures,  $0.3t < k_B T < 8t$ . We will discuss such a hydrodynamic description of the Fermi-Hubbard dynamics in more detail in section 5.4.5, when we describe a comparison of our experimental measurements of the spin conductivity of the 2D Fermi-Hubbard model at half-filling with independent theoretical predictions. Thus, the general form predicted by the Drude result, Eq. 2.110, is more widely applicable than one might naively expect, and many complex details of the physical mechanisms governing the transport dynamics can be incorporated into the effective relaxation time  $\tau$ , as well as the effective quasi-particle mass  $m^*$  for the charge carriers (the equivalent of  $m$  in Eq. 2.104), if such quasi-particles exist.

### 2.3.2 Linear Response Theory

In this section we will derive a Kubo formula for the conductivity, which is a linear response relationship that connects it to intrinsic properties of the underlying, unperturbed Hamiltonian (i.e. the 2D Fermi-Hubbard model at finite temperature). We

do this to help de-mystify the electrical conductivity, which, to some, might initially appear as a very experimental, almost phenomenological parameter, but is, in reality, an intrinsic property of the equilibrium system itself. We will derive the formula for the electrical charge conductivity at zero temperature, but this is easily generalizable to the spin conductivity, as well as finite temperature, as we will see. More detailed derivations and descriptions can be found in a variety of textbooks, including [148]. For the remainder of this section, we will work in units where  $\hbar = a = k_B = 1$ , and where  $a$  is the lattice spacing. We assume there is a time-dependent electric field in the solid, which we write as,

$$E_\alpha(\mathbf{r}, t) = \Theta_\alpha e^{i(\mathbf{q} \cdot \mathbf{r} - \omega t)}, \quad (2.111)$$

where  $\Theta_\alpha$  is the amplitude of the  $\alpha$  component of the electric field, for  $\alpha = (x, y, z)$ . The conductivity is then defined as the proportionality constant (or tensor), in linear response, between the total electric field in the solid, and the induced current,

$$J_\alpha(\mathbf{r}, t) = \sum_\beta \sigma_{\alpha\beta}(\mathbf{q}, \omega) E_\beta(\mathbf{r}, t), \quad (2.112)$$

where  $J_\alpha(\mathbf{r}, t)$  represents the  $\alpha$  component of the induced current at position  $\mathbf{r}$  and time  $t$ , and  $\sigma_{\alpha\beta}(\mathbf{q}, \omega)$  is the electrical conductivity tensor for response at momentum  $\mathbf{q}$  and frequency  $\omega$ . In general, the induced current need not be parallel to the electric field, hence the tensorial form of the conductivity.

We will work in the Coulomb gauge, where the vector potential  $\mathbf{A}$  satisfies  $\nabla \cdot \mathbf{A} = 0$ , and we will take the vector and electric potentials to be transverse, so that the scalar potential can be set to zero. In this case, the electric field can be written in terms of the vector potential as,

$$\frac{1}{c} A_\alpha(\mathbf{r}, t) = \frac{-i}{\omega} E_\alpha(\mathbf{r}, t). \quad (2.113)$$

In the presence of such a vector potential, the kinetic energy term of the original

Hamiltonian is modified, and becomes

$$\hat{T} = \frac{1}{2m} \sum_i \left[ \mathbf{p}_i - \frac{e}{c} \mathbf{A}(\mathbf{r}_i) \right]^2, \quad (2.114)$$

where  $\mathbf{p}_i$  represents the momentum operator for particle  $i$ ,  $\mathbf{r}_i$  is its position, and the summation is carried out over all particles in the system. If we expand the equation in brackets in Eq. 2.114, and keep only those terms that are linear in  $\mathbf{A}$  (for linear response purposes), and are therefore linear in the electric field, we obtain, after expressing things in terms of the electric field,

$$\hat{T} = \hat{T}_0 + \frac{ie}{2m\omega} \sum_j [\mathbf{p}_{\alpha,j} e^{i\mathbf{q}\cdot\mathbf{r}_j} + e^{i\mathbf{q}\cdot\mathbf{r}_j} \mathbf{p}_{\alpha,j}] \Theta_\alpha e^{-i\omega t}, \quad (2.115)$$

where  $\hat{T}_0$  represents the kinetic energy of the unperturbed Hamiltonian,

$$\hat{T}_0 = \frac{1}{2m} \sum_j \mathbf{p}_j^2, \quad (2.116)$$

which, for the Fermi-Hubbard system, takes the tight-binding form of Eq. 2.18, and where we have assumed, for simplicity of notation, that there is an unwritten summation over the repeated indices  $\alpha$ . The overall Hamiltonian in the presence of the electric field can therefore be written as  $H = H_0 + H'$ , where  $H_0$  denotes the total unperturbed Hamiltonian, including both the kinetic and the interaction energy terms (i.e. Eq. 2.58 for the 2D Fermi-Hubbard model), and  $H'$  represents the perturbing Hamiltonian (the second term in Eq. 2.115),

$$H' = \frac{i}{\omega} j_\alpha(\mathbf{q}) \Theta_\alpha e^{-i\omega t}. \quad (2.117)$$

Here,  $j_\alpha(\mathbf{q})$  denotes the  $\mathbf{q}$  component of the current operator,

$$j_\alpha(\mathbf{q}) = \frac{e}{2m} \sum_j [\mathbf{p}_{\alpha,j} e^{i\mathbf{q}\cdot\mathbf{r}_j} + e^{i\mathbf{q}\cdot\mathbf{r}_j} \mathbf{p}_{\alpha,j}]. \quad (2.118)$$

The induced current density that is actually measured,  $J_\alpha(\mathbf{r}, t)$ , from Eq. 2.112, on

the other hand, can be expressed as a sum of the average velocities of all the particles in the system, divided by the total volume  $V$  (analogous to Eq. 2.101),

$$J_\alpha(\mathbf{r}, t) = \frac{e}{V} \sum_j \langle \mathbf{v}_{\alpha,j} \rangle, \quad (2.119)$$

where  $\mathbf{v}_{\alpha,j}$  is the  $\alpha$  component of the velocity operator for particle  $j$ , given (in the presence of a vector potential  $\mathbf{A}$ ) by,

$$\mathbf{v}_j = \frac{1}{m} \left[ \mathbf{p}_j - \frac{e}{c} \mathbf{A}(\mathbf{r}_j) \right]. \quad (2.120)$$

Plugging Eq. 2.120 into Eq. 2.119 gives,

$$J_\alpha(\mathbf{r}, t) = \frac{e}{mV} \sum_j \langle \mathbf{p}_{\alpha,j} \rangle - \frac{e^2}{mcV} \sum_j A_\alpha(\mathbf{r}_j). \quad (2.121)$$

For the second term in Eq. 2.121, we will assume that the perturbation is relatively long-wavelength, so that we can evaluate  $A_\alpha(\mathbf{r}_j)$  at  $\mathbf{r}$ , and pull it out of the summation, which then simply gives the total number of particles  $N$ . Expressing things in terms of the electric field, this then becomes,

$$\frac{e^2}{mcV} \sum_j A_\alpha(\mathbf{r}_j) = i \frac{ne^2}{m\omega} E_\alpha(\mathbf{r}, t), \quad (2.122)$$

where  $n = N/V$  is the particle density. The first term in Eq. 2.121, on the other hand, is given by the average of the current operator in real space (the Fourier transform of Eq. 2.118),

$$j_\alpha(\mathbf{r}, t) = \frac{e}{mV} \sum_j \mathbf{p}_{\alpha,j}, \quad (2.123)$$

so that,

$$J_\alpha(\mathbf{r}, t) = \langle j_\alpha(\mathbf{r}, t) \rangle + i \frac{ne^2}{m\omega} E_\alpha(\mathbf{r}, t). \quad (2.124)$$

The total induced current is therefore given by a sum of two different current contributions,  $J_\alpha(\mathbf{r}, t) = J_\alpha^{(1)}(\mathbf{r}, t) + J_\alpha^{(2)}(\mathbf{r}, t)$ , where  $J_\alpha^{(1)}(\mathbf{r}, t) = i \frac{ne^2}{m\omega} E_\alpha(\mathbf{r}, t)$  is already explicitly proportional to the electric field, and  $J_\alpha^{(2)}(\mathbf{r}, t) = \langle j_\alpha(\mathbf{r}, t) \rangle$  is the current we

must solve for, which, in the end, will also turn out to be proportional to the electric field.

We now seek to evaluate the term  $J_\alpha^{(2)}(\mathbf{r}, t) = \langle j_\alpha(\mathbf{r}, t) \rangle$  in the zero-temperature limit. Let  $|\psi'\rangle$  denote the ground state wave function of the total Hamiltonian,  $H = H_0 + H'$ , in the Heisenberg picture. The expectation value  $\langle j_\alpha(\mathbf{r}, t) \rangle$  can then be evaluated as,

$$\langle j_\alpha(\mathbf{r}, t) \rangle = \langle \psi' | e^{i(H_0+H')t} j_\alpha(\mathbf{r}) e^{-i(H_0+H')t} | \psi' \rangle. \quad (2.125)$$

We can then switch to the interaction representation, where  $H'$  becomes the perturbation term, and write,

$$e^{-i(H_0+H')t} = e^{-iH_0t} U(t), \quad (2.126)$$

where  $U(t)$  is given by,

$$U(t) = e^{iH_0t} e^{-i(H_0+H')t}. \quad (2.127)$$

Plugging this back into Eq. 2.125 then tells us that,

$$\langle j_\alpha(\mathbf{r}, t) \rangle = \langle \psi' | U^\dagger(t) e^{iH_0t} j_\alpha(\mathbf{r}) e^{-iH_0t} U(t) | \psi' \rangle. \quad (2.128)$$

The time evolution operator  $U(t)$  in the interaction picture can be expressed as,

$$U(t) = T \exp \left[ -i \int_0^t dt' H'_I(t') \right], \quad (2.129)$$

where  $H'_I(t') = e^{iH_0t'} H' e^{-iH_0t'}$  is the perturbation Hamiltonian in the interaction representation, and  $T$  represents the time ordering operator which, when acting on a selection of time-dependent operators, arranges them in order from latest times on the left to earliest times on the right. For example,  $T[\hat{A}(t_1)\hat{B}(t_2)\hat{C}(t_3)] = \hat{C}(t_3)\hat{A}(t_1)\hat{B}(t_2)$  if  $t_3 > t_1 > t_2$ . Written explicitly, the integral form of the time evolution operator  $U(t)$  is given by,

$$U(t) = 1 + \sum_{n=1}^{\infty} \frac{(-i)^n}{n!} \int_0^t dt_1 \int_0^{t_1} dt_2 \dots \int_0^{t_{n-1}} dt_n T [H'_I(t_1) H'_I(t_2) \dots H'_I(t_n)]. \quad (2.130)$$

We can also write the current operator  $j_\alpha(\mathbf{r})$  in Eq. 2.128 in the interaction representation as,  $j_\alpha^{(I)}(\mathbf{r}, t) \equiv e^{iH_0t} j_\alpha(\mathbf{r}) e^{-iH_0t}$ , so that  $\langle j_\alpha(\mathbf{r}, t) \rangle = \langle \psi' | U^\dagger(t) j_\alpha^{(I)}(\mathbf{r}, t) U(t) | \psi' \rangle$ . The issue now, however, is that the expectation value  $\langle j_\alpha(\mathbf{r}, t) \rangle$  is taken using the ground state  $|\psi'\rangle$  of the total Hamiltonian,  $H = H_0 + H'$ , which we don't know a priori, and we would like to evaluate it strictly in terms of the ground state  $|\psi\rangle$  of the unperturbed Hamiltonian  $H_0$ , which is, in principle, known. It can be shown [72] that these two ground states are related to one either via

$$|\psi'\rangle = T \exp \left[ -i \int_{-\infty}^0 dt' H'_I(t') \right] |\psi\rangle, \quad (2.131)$$

so that,

$$U(t) |\psi'\rangle = T \exp \left[ -i \int_{-\infty}^t dt' H'_I(t') \right] |\psi\rangle. \quad (2.132)$$

Because we are ultimately only interested in terms which are linear in the electric field (and are therefore linear in the perturbation term  $H'$ ) for linear response purposes, we can expand the exponential operator in Eq. 2.132, and keep only the terms up to linear order in  $H'_I$ ,

$$U(t) |\psi'\rangle = T \exp \left[ -i \int_{-\infty}^t dt' H'_I(t') \right] |\psi\rangle \rightarrow \left[ 1 - i \int_{-\infty}^t dt' H'_I(t') \right] |\psi\rangle. \quad (2.133)$$

From this it also follows that the Hermitian conjugate becomes,

$$\langle \psi' | U^\dagger(t) \rightarrow \langle \psi | \left[ 1 + i \int_{-\infty}^t dt' H'_I(t') \right]. \quad (2.134)$$

We can therefore express the expectation value  $\langle j_\alpha(\mathbf{r}, t) \rangle = \langle \psi' | U^\dagger(t) j_\alpha^{(I)}(\mathbf{r}, t) U(t) | \psi' \rangle$ , which represents the current  $J_\alpha^{(2)}(\mathbf{r}, t)$ , as,

$$J_\alpha^{(2)}(\mathbf{r}, t) = \langle \psi | \left[ 1 + i \int_{-\infty}^t dt' H'_I(t') \right] j_\alpha^{(I)}(\mathbf{r}, t) \left[ 1 - i \int_{-\infty}^t dt' H'_I(t') \right] |\psi\rangle. \quad (2.135)$$

Expanding this out and again dropping non-linear terms in the perturbation  $H'_I$  gives,

$$J_\alpha^{(2)}(\mathbf{r}, t) = \langle \psi | \left[ j_\alpha^{(I)}(\mathbf{r}, t) - i \int_{-\infty}^t dt' [j_\alpha^{(I)}(\mathbf{r}, t) H'_I(t') - H'_I(t') j_\alpha^{(I)}(\mathbf{r}, t)] \right] |\psi\rangle. \quad (2.136)$$

The first term in Eq. 2.136,  $\langle \psi | j_\alpha^{(I)}(\mathbf{r}, t) | \psi \rangle$ , we can take to be zero since there is no current in the unperturbed system without an electric field. The second term in Eq. 2.136, on the other hand, is non-zero in general, and we can simplify the expression using the commutator  $[j_\alpha^{(I)}(\mathbf{r}, t), H'_I(t')] = j_\alpha^{(I)}(\mathbf{r}, t)H'_I(t') - H'_I(t')j_\alpha^{(I)}(\mathbf{r}, t)$ , so that

$$J_\alpha^{(2)}(\mathbf{r}, t) = -i \int_{-\infty}^t dt' \langle \psi | [j_\alpha^{(I)}(\mathbf{r}, t), H'_I(t')] | \psi \rangle. \quad (2.137)$$

We can simplify this even further using the fact that  $H'_I(t') = e^{iH_0 t'} H' e^{-iH_0 t'}$ , where  $H' = \frac{i}{\omega} j_\alpha(\mathbf{q}) \Theta_\alpha e^{-i\omega t'}$  (from Eq. 2.117), so that  $H'_I(t') = \frac{i}{\omega} j_\alpha^{(I)}(\mathbf{q}, t') \Theta_\alpha e^{-i\omega t'}$ , where  $j_\alpha^{(I)}(\mathbf{q}, t') = e^{iH_0 t'} j_\alpha(\mathbf{q}) e^{-iH_0 t'}$  is the spatial Fourier transform of  $j_\alpha^{(I)}(\mathbf{r}, t')$ . In writing this expression for  $H'_I(t')$ , we are again assuming that there is an implicit summation over the repeated indices  $\alpha$ . This allows us to write the commutator  $[j_\alpha^{(I)}(\mathbf{r}, t), H'_I(t')]$  as,

$$\begin{aligned} [j_\alpha^{(I)}(\mathbf{r}, t), H'_I(t')] &= \frac{i}{\omega} \Theta_\beta e^{-i\omega t'} [j_\alpha^{(I)}(\mathbf{r}, t), j_\beta^{(I)}(\mathbf{q}, t')] \\ &= \frac{i}{\omega} E_\beta(\mathbf{r}, t) e^{-i\mathbf{q} \cdot \mathbf{r}} e^{i\omega(t-t')} [j_\alpha^{(I)}(\mathbf{r}, t), j_\beta^{(I)}(\mathbf{q}, t')]. \end{aligned} \quad (2.138)$$

Plugging Eq. 2.138 into Eq. 2.137 then yields,

$$J_\alpha^{(2)}(\mathbf{r}, t) = \frac{1}{\omega} E_\beta(\mathbf{r}, t) e^{-i\mathbf{q} \cdot \mathbf{r}} \int_{-\infty}^t dt' e^{i\omega(t-t')} \langle \psi | [j_\alpha^{(I)}(\mathbf{r}, t), j_\beta^{(I)}(\mathbf{q}, t')] | \psi \rangle. \quad (2.139)$$

We now have an expression for  $J_\alpha^{(2)}(\mathbf{r}, t)$  which is proportional to the electric field. Combining Eq. 2.139 with the other contribution to the induced current,  $J_\alpha^{(1)}(\mathbf{r}, t) = i \frac{ne^2}{m\omega} E_\alpha(\mathbf{r}, t)$ , finally gives us an expression for the conductivity by comparing with Eq. 2.112,

$$\sigma_{\alpha\beta}(\mathbf{q}, \omega) = \frac{1}{\omega} e^{-i\mathbf{q} \cdot \mathbf{r}} \int_{-\infty}^t dt' e^{i\omega(t-t')} \langle \psi | [j_\alpha^{(I)}(\mathbf{r}, t), j_\beta^{(I)}(\mathbf{q}, t')] | \psi \rangle + i \frac{ne^2}{m\omega} \delta_{\alpha\beta}. \quad (2.140)$$

We can eliminate the  $\mathbf{r}$ -dependence on the right hand side of Eq. 2.140 by integrating both sides of the equation over all space and dividing by the total volume  $V$ . The left hand side of the equation remains unaffected, but the right hand side gets spatially

Fourier transformed due to the  $e^{-i\mathbf{q}\cdot\mathbf{r}}$  pre-factor, so that  $j_\alpha^{(I)}(\mathbf{r}, t)$  in the commutator becomes  $j_\alpha^{(I)}(-\mathbf{q}, t) = \left(j_\alpha^{(I)}\right)^\dagger(\mathbf{q}, t)$ . Additionally, because everything is now expressed in terms of the unperturbed Hamiltonian  $H_0$  (i.e. both the expectation value in the integral as well as the operator time evolution), we simplify our notation and write  $j_\alpha^{(I)}(\mathbf{q}, t) = j_\alpha(\mathbf{q}, t)$ , where it is understood that now  $j_\alpha(\mathbf{q}, t) = e^{iH_0 t} j_\alpha(\mathbf{q}) e^{-iH_0 t}$ , in the Heisenberg sense of the operator time evolution for the unperturbed Hamiltonian. We can simplify things even further since the commutator expectation value in Eq. 2.140 can only depend on the time difference  $t - t'$ , which allows us to change integration variables to  $t - t'$ , and evaluate one of the operators in the commutator at time  $t' = 0$ . The final expression for the conductivity thus becomes,

$$\sigma_{\alpha\beta}(\mathbf{q}, \omega) = \frac{1}{\omega} \int_0^\infty dt e^{i\omega t} \langle [j_\alpha^\dagger(\mathbf{q}, t), j_\beta(\mathbf{q}, 0)] \rangle + i \frac{ne^2}{m\omega} \delta_{\alpha\beta}, \quad (2.141)$$

where we have replaced the expectation value with respect to the ground state wave function  $|\psi\rangle$  of the unperturbed Hamiltonian  $H_0$  with generic averaging notation. Written in this way, it is thus clear how to generalize the final result for the conductivity, Eq. 2.141, derived at zero temperature, to the finite temperature expression: simply replace the expectation value of the commutator at zero temperature with a thermal average, so that Eq. 2.141 still holds at finite temperature, if we understand  $\langle [j_\alpha^\dagger(\mathbf{q}, t), j_\beta(\mathbf{q}, 0)] \rangle$  to represent a thermal average in the general case. This expression for the conductivity, Eq. 2.141, is the Kubo formula [133, 134, 148, 115]. As is evident from the form of the equation, it expresses the conductivity purely in terms of properties of the unperturbed Hamiltonian  $H_0$ , as the Fourier transform of the current-current correlation function, revealing the fact that the conductivity is truly an intrinsic part of the unperturbed, equilibrium system in linear response, and not simply a phenomenological parameter.

For the transport experiment discussed in this thesis (see chapter 5), we examine the spatially uniform, or long-wavelength limit of the conductivity,  $\mathbf{q} \rightarrow 0$ , as well as the DC or zero-frequency limit  $\omega \rightarrow 0$ . However, in taking these limits in Eq. 2.141, it is important to first take  $\mathbf{q} \rightarrow 0$ , and then  $\omega \rightarrow 0$ , and not the other way around [202].

Physically, this is because if you were to first take  $\omega \rightarrow 0$ , then for  $\mathbf{q} \neq 0$ , the result would describe a static electric field which is spatially periodic. However, in such a static field, once the charges have rearranged themselves into their new equilibrium positions, current will stop flowing, and the system will come to rest, which is not the situation we would like to describe. Thus, if we take the  $\mathbf{q} \rightarrow 0$  limit of Eq. 2.141, we obtain

$$\sigma_{\alpha\beta}(\omega) = \frac{1}{\omega} \int_0^\infty dt e^{i\omega t} \langle [j_\alpha(t), j_\beta(0)] \rangle + i \frac{ne^2}{m\omega} \delta_{\alpha\beta}, \quad (2.142)$$

where we have written  $\sigma_{\alpha\beta}(\omega) \equiv \sigma_{\alpha\beta}(\mathbf{q} = 0, \omega)$ , and  $j_\beta(t) \equiv j_\beta(\mathbf{q} = 0, t) = j_\beta^\dagger(\mathbf{q} = 0, t)$ . In the DC limit, we are only interested in the real part of the conductivity,  $\text{Re}[\sigma_{\alpha\beta}(\omega)]$ , and so we take the real part of both sides of Eq. 2.142. The second term on the right-hand side of Eq. 2.142 is purely imaginary, and therefore does not contribute to  $\text{Re}[\sigma_{\alpha\beta}(\omega)]$ , unless there is a delta function response at  $\omega = 0$ . Such a response would correspond to a non-zero Drude weight [202], arising from current-current correlations,  $\langle [j_\alpha^\dagger(t), j_\beta(0)] \rangle$ , that extend out to infinite time. At the temperatures accessed in the experiment, however, we will assume that the correlation function decays to zero after sufficient time, so that the Drude weight can be ignored [115]. Thus, we need only take the real part of the first term on the right hand side of Eq. 2.142. This gives,

$$\text{Re}[\sigma_{\alpha\beta}(\omega)] = \frac{1}{\omega} \int_0^\infty dt \text{Re} [e^{i\omega t} \langle [j_\alpha(t), j_\beta(0)] \rangle]. \quad (2.143)$$

If we apply an electric field along one of the lattice axes in the square lattice used in the experiment, as we do in chapter 5, we can consider just the diagonal terms of the conductivity, which determine the current along the direction of interest. We can thus examine just  $\sigma_{\alpha\alpha}(\omega)$ , which we write as  $\sigma(\omega)$  for simplicity. We also drop the index notation of the current operator, and write  $j_\alpha(t) \equiv j(t)$ . Note here that  $\langle [j(t), j(0)] \rangle = \langle j(t)j(0) \rangle - \langle j(0)j(t) \rangle = \langle j(t)j(0) \rangle - \langle j(t)j(0) \rangle^* = 2i\text{Im}[\langle j(t)j(0) \rangle]$ , so that

$$\text{Re}[\sigma(\omega)] = \frac{-2}{\omega} \text{Im} \left[ \int_0^\infty dt e^{i\omega t} \text{Im} [\langle j(t)j(0) \rangle] \right]. \quad (2.144)$$

This is the form of the AC conductivity used to perform the theoretical calculations of spin transport within the 2D Fermi-Hubbard model at half-filling, which is discussed in detail in section 5.4.5. For completion, we include here the general ( $\mathbf{q}$ -dependent) form of the current operators in a tight-binding model like the Fermi-Hubbard model,

$$\begin{aligned} j_\alpha^{(C)}(\mathbf{q}) &= -it \sum_{\sigma,l} e^{i\mathbf{q}\cdot\mathbf{r}_l} \left( \hat{c}_{\sigma,l}^\dagger \hat{c}_{\sigma,l+\Delta_\alpha} - \hat{c}_{\sigma,l+\Delta_\alpha}^\dagger \hat{c}_{\sigma,l} \right) \\ j_\alpha^{(S)}(\mathbf{q}) &= -it \sum_{\sigma,l} \sigma e^{i\mathbf{q}\cdot\mathbf{r}_l} \left( \hat{c}_{\sigma,l}^\dagger \hat{c}_{\sigma,l+\Delta_\alpha} - \hat{c}_{\sigma,l+\Delta_\alpha}^\dagger \hat{c}_{\sigma,l} \right), \end{aligned} \quad (2.145)$$

where  $j_\alpha^{(C)}(\mathbf{q})$  and  $j_\alpha^{(S)}(\mathbf{q})$  represent the charge and spin current operators, respectively, at momentum  $\mathbf{q}$ ,  $\mathbf{r}_l$  represents the spatial location of site  $l$ , and  $l + \Delta_\alpha$  represents a shift by one lattice site from site  $l$  along the direction of  $\alpha$ . These forms for the current operators can be derived using the respective continuity equation for either the total density (the charge),  $\hat{n} = \hat{n}_\uparrow + \hat{n}_\downarrow$ , or the spin density (the spin),  $\hat{S}_z = (\hat{n}_\uparrow - \hat{n}_\downarrow)/2$ . For a derivation of the spin current, for instance, see section 5.4.2. Depending upon which of these current operators is used in Eq. 2.144, one can obtain either the charge conductivity  $\sigma_C(\omega)$  (using  $j_\alpha^{(C)}(\mathbf{q} = \mathbf{0})$ ), or the spin conductivity  $\sigma_S(\omega)$  (using  $j_\alpha^{(S)}(\mathbf{q} = \mathbf{0})$ ), since the Kubo formula (Eq. 2.141) can be applied generally to either case using the correct operator, even though we derived it here for the specific case of the charge current.

We can derive another expression for the conductivity which is equivalent to Eq. 2.144, and which will become relevant in section 5.4.5, where we discuss numerical estimates of the conductivity, as a second method of calculating the conductivity numerically that can be compared to calculations based on Eq. 2.144, in order to check the validity of the numerics. To do this, we use the retarded Green's function for the current correlator,

$$\Lambda(\mathbf{q}, t - t') \equiv -i\Theta(t - t') \langle [j^\dagger(\mathbf{q}, t), j(\mathbf{q}, t')] \rangle, \quad (2.146)$$

where  $\Theta(t - t')$  denotes the Heaviside step function, and where we have put back the  $\mathbf{q}$  dependence of the current operators, although we still drop the spatial coordinate

$\alpha$ , assuming that we are considering only the diagonal terms. Taking the Fourier transform of  $\Lambda(\mathbf{q}, t - t')$  gives,

$$\Lambda(\mathbf{q}, \omega) = -i \int_{-\infty}^{\infty} dt e^{i\omega t} \Theta(t) \langle [j^\dagger(\mathbf{q}, t), j(\mathbf{q}, 0)] \rangle, \quad (2.147)$$

so that (from Eq. 2.143 generalized to non-zero  $\mathbf{q}$ ),

$$\text{Re}[\sigma(\mathbf{q}, \omega)] = -\frac{1}{\omega} \text{Im}[\Lambda(\mathbf{q}, \omega)]. \quad (2.148)$$

Here,  $\text{Im}[\Lambda(\mathbf{q}, \omega)]$  can be interpreted as the spectral function of the current operator. We then work within the Matsubara formalism, and use the equivalent Green's function for the current correlator (Eq. 2.146) in imaginary time  $\tau$  [148], where  $\tau \in [0, \beta]$ ,

$$\Lambda(\mathbf{q}, \tau) = -\langle T_\tau j^\dagger(\mathbf{q}, \tau) j(\mathbf{q}, 0) \rangle, \quad (2.149)$$

where  $T_\tau$  represents the imaginary time ordering operator (defined similarly to the real time ordering operator). We again take the  $\mathbf{q} \rightarrow 0$  limit, and write  $j(\tau) \equiv j(\mathbf{q} = 0, \tau) = j^\dagger(\mathbf{q} = 0, \tau)$ , and  $\Lambda(\tau) \equiv \Lambda(\mathbf{q} = 0, \tau)$ , so that  $\Lambda(\tau) = -\langle T_\tau j(\tau) j(0) \rangle$ . Fourier transforming  $\Lambda(\tau)$  to Matsubara frequency space, we obtain,

$$\Lambda(i\omega_n) = - \int_0^\beta d\tau e^{i\omega_n \tau} \langle j(\tau) j(0) \rangle, \quad (2.150)$$

where  $\omega_n = 2\pi n/\beta$  are the Matsubara frequencies. We can then evaluate the correlator  $\langle j(\tau) j(0) \rangle$  using the fact that  $j(\tau) = e^{\tau H_0} j(0) e^{-\tau H_0}$ , and by expressing the thermal average of an operator  $\hat{O}$  as  $\langle \hat{O} \rangle = \frac{1}{Z} \text{Tr} [\hat{O} e^{-\beta H_0}]$ , where  $Z$  denotes the partition function,

$$Z = \sum_m e^{-\beta \epsilon_m}. \quad (2.151)$$

The summation over  $m$  in Eq. 2.151 runs over all states of the system, where the  $\epsilon_m$

are the corresponding energies. The thermally averaged correlator then becomes,

$$\begin{aligned}\langle j(\tau)j(0) \rangle &= \langle e^{\tau H_0} j(0) e^{-\tau H_0} j(0) \rangle \\ &= \frac{1}{Z} \sum_{m,m'} e^{-\beta \epsilon_m} e^{\tau \epsilon_m} e^{-\tau \epsilon_{m'}} |\langle m | j(0) | m' \rangle|^2.\end{aligned}\quad (2.152)$$

Plugging this into Eq. 2.150, we find,

$$\begin{aligned}\Lambda(i\omega_n) &= -\frac{1}{Z} \sum_{m,m'} e^{-\beta \epsilon_m} |\langle m | j(0) | m' \rangle|^2 \int_0^\beta d\tau e^{\tau(\epsilon_m - \epsilon_{m'} + i\omega_n)} \\ &= -\frac{1}{Z} \sum_{m,m'} e^{-\beta \epsilon_m} |\langle m | j(0) | m' \rangle|^2 \frac{e^{\beta(\epsilon_m - \epsilon_{m'})} - 1}{\epsilon_m - \epsilon_{m'} + i\omega_n}.\end{aligned}\quad (2.153)$$

We can then perform an analytic continuation to obtain the results in the real frequency domain, using the transformation  $i\omega_n \rightarrow \omega + i\delta$  (with  $\delta \rightarrow 0$ ) [148], so that we obtain,

$$\Lambda(\omega) \equiv \Lambda(\mathbf{q} = 0, \omega) = -\frac{1}{Z} \sum_{m,m'} e^{-\beta \epsilon_m} |\langle m | j(0) | m' \rangle|^2 \frac{e^{\beta(\epsilon_m - \epsilon_{m'})} - 1}{\epsilon_m - \epsilon_{m'} + \omega + i\delta}. \quad (2.154)$$

Using Eq. 2.148 to obtain the real part of the conductivity from the imaginary part of  $\Lambda(\omega)$ , and using the fact that  $\text{Im} \left[ \frac{1}{\epsilon_m - \epsilon_{m'} + \omega + i\delta} \right] = -\pi\delta(\epsilon_m - \epsilon_{m'} + \omega)$ , we have that

$$\text{Re} [\sigma(\omega)] \equiv \text{Re} [\sigma(\mathbf{q} = 0, \omega)] = \frac{\pi (1 - e^{-\beta\omega})}{\omega Z} \sum_{m,m'} e^{-\beta \epsilon_m} |\langle m | j(0) | m' \rangle|^2 \delta(\epsilon_m - \epsilon_{m'} + \omega). \quad (2.155)$$

In the form given by Eq. 2.155, it is potentially even more striking, relative to Eq. 2.144 at least, how directly connected the electrical conductivity is to the underlying properties of the unperturbed Hamiltonian in thermal equilibrium. The operator  $j(0)$  in this equation can be either the spin or charge current operators defined in Eq. 2.145, allowing one to obtain either the spin or the charge conductivities, respectively.

To express Eq. 2.155 in terms of real-time current-current correlations, in a form

that is analogous to Eq. 2.144, we consider the integral,

$$\gamma(\omega) \equiv \lim_{\delta \rightarrow 0} \frac{1}{\omega} \text{Re} \left[ \int_0^\infty dt e^{it(\omega+i\delta)} \langle j(t)j(0) \rangle \right]. \quad (2.156)$$

If we then express the correlator  $\langle j(t)j(0) \rangle$  using the real-time equivalent of Eq. 2.152,

$$\langle j(t)j(0) \rangle = \frac{1}{Z} \sum_{m,m'} e^{-\beta\epsilon_m} e^{it\epsilon_m} e^{-it\epsilon_{m'}} |\langle m| j(0) |m' \rangle|^2, \quad (2.157)$$

we can plug this into Eq. 2.156 for  $\gamma(\omega)$  to obtain,

$$\begin{aligned} \gamma(\omega) &= \lim_{\delta \rightarrow 0} \frac{1}{\omega Z} \sum_{m,m'} e^{-\beta\epsilon_m} |\langle m| j(0) |m' \rangle|^2 \text{Re} \left[ \int_0^\infty dt e^{it(\epsilon_m - \epsilon_{m'} + \omega + i\delta)} \right] \\ &= \lim_{\delta \rightarrow 0} \frac{1}{\omega Z} \sum_{m,m'} e^{-\beta\epsilon_m} |\langle m| j(0) |m' \rangle|^2 \text{Re} \left[ \frac{i}{\epsilon_m - \epsilon_{m'} + \omega + i\delta} \right] \\ &= \frac{\pi}{\omega Z} \sum_{m,m'} e^{-\beta\epsilon_m} |\langle m| j(0) |m' \rangle|^2 \delta(\epsilon_m - \epsilon_{m'} + \omega) \\ &= \frac{\text{Re} [\sigma(\omega)]}{1 - e^{-\beta\omega}}, \end{aligned} \quad (2.158)$$

where the last line follows from Eq. 2.155, and where we have used the fact that  $\text{Re} \left[ \frac{i}{\epsilon_m - \epsilon_{m'} + \omega + i\delta} \right] = \pi\delta(\epsilon_m - \epsilon_{m'} + \omega)$ . We therefore obtain a second equation for the conductivity in terms of real-time current-current correlators,

$$\text{Re} [\sigma(\omega)] = \frac{1 - e^{-\beta\omega}}{\omega} \text{Re} \left[ \int_0^\infty dt e^{i\omega t} \langle j(t)j(0) \rangle \right]. \quad (2.159)$$

This equation is completely equivalent to Eq. 2.144, and is discussed in section 5.4.5 as a second method (in addition to Eq. 2.144) of calculating the conductivity of the 2D Fermi-Hubbard model at finite temperature numerically using NLCE, which can directly access the real-time current-current correlation function,  $\langle j(t)j(0) \rangle$ , in order to compare with our experimental measurements of the DC spin conductivity,  $\text{Re} [\sigma_S(\omega = 0)]$ , at half-filling, obtained using our fermionic quantum gas microscope. These spin transport experiments are described in detail in chapter 5.

### 2.3.3 Features of the Conductivity and Sum Rules

In this section we will describe some basic features of the frequency-dependent conductivity at  $\mathbf{q} = 0$ . Further details about the spin (charge) conductivity, and its relationship to other transport coefficients, such as the spin (charge) diffusion coefficient, and the spin-density (total density) response function can be found in chapter 5 in sections 5.4 and 5.5. We begin by relating the integral of the conductivity over all frequencies to the imaginary-time retarded current-current correlation function,  $\Lambda(\tau)$ . This is generally a useful thing to do, because many theoretical and numerical techniques, like DQMC for instance, cannot calculate the current-current correlation functions directly in real time, but can only access imaginary time correlation functions, and must therefore express all relevant quantities through these. We therefore consider the following integral,

$$\Pi(i\omega_n) \equiv \frac{1}{\pi} \int_{-\infty}^{\infty} \frac{\omega}{i\omega_n - \omega} \text{Re} [\sigma(\omega)] d\omega, \quad (2.160)$$

where  $\omega_n = 2\pi n/\beta$ . We can then plug Eq. 2.155 for  $\text{Re} [\sigma(\omega)]$  into Eq. 2.160 for  $\Pi(i\omega_n)$  to obtain,

$$\begin{aligned} \Pi(i\omega_n) &= \frac{1}{Z} \sum_{m,m'} e^{-\beta\epsilon_m} |\langle m | j(0) | m' \rangle|^2 \int_{-\infty}^{\infty} \frac{1 - e^{-\beta\omega}}{i\omega_n - \omega} \delta(\epsilon_m - \epsilon_{m'} + \omega) d\omega \\ &= -\frac{1}{Z} \sum_{m,m'} e^{-\beta\epsilon_m} |\langle m | j(0) | m' \rangle|^2 \frac{e^{\beta(\epsilon_m - \epsilon_{m'})} - 1}{i\omega_n + \epsilon_m - \epsilon_{m'}} \\ &= \Lambda(i\omega_n), \end{aligned} \quad (2.161)$$

where the last line follows from Eq. 2.153. We therefore have that,

$$\Lambda(i\omega_n) = \frac{1}{\pi} \int_{-\infty}^{\infty} \frac{\omega}{i\omega_n - \omega} \text{Re} [\sigma(\omega)] d\omega. \quad (2.162)$$

We may then inverse Fourier transform  $\Lambda(i\omega_n)$  in Eq. 2.162 from Matsubara frequency space to imaginary time space using the relation  $\Lambda(\tau) = \frac{1}{\beta} \sum_n e^{-i\omega_n \tau} \Lambda(i\omega_n)$ , which

gives

$$\begin{aligned}\Lambda(\tau) &= \frac{1}{\pi\beta} \sum_n e^{-i\omega_n\tau} \int_{-\infty}^{\infty} \frac{\omega}{i\omega_n - \omega} \text{Re}[\sigma(\omega)] d\omega \\ &= \frac{1}{\pi\beta} \int_{-\infty}^{\infty} \omega \text{Re}[\sigma(\omega)] d\omega \sum_n \frac{e^{-i\omega_n\tau}}{i\omega_n - \omega}.\end{aligned}\quad (2.163)$$

The summation  $\sum_n \frac{e^{-i\omega_n\tau}}{i\omega_n - \omega}$  can be evaluated using the fact that  $\omega_n = 2\pi n/\beta$ , which gives,

$$\sum_n \frac{e^{-i\omega_n\tau}}{i\omega_n - \omega} = \beta \frac{e^{-\tau\omega}}{1 - e^{-\beta\omega}}. \quad (2.164)$$

Plugging this into Eq. 2.163 yields,

$$\Lambda(\tau) = \frac{1}{\pi} \int_{-\infty}^{\infty} \frac{\omega e^{-\omega\tau}}{1 - e^{-\beta\omega}} \text{Re}[\sigma(\omega)] d\omega. \quad (2.165)$$

We thus have a direct relationship between an integral of  $\text{Re}[\sigma(\omega)]$  over all frequencies, and  $\Lambda(\tau)$ . This equation helps partially elucidate why it can be very challenging to calculate transport properties of a system numerically if one cannot access real-time correlation functions: while  $\text{Re}[\sigma(\omega)]$  is the desired quantity, for some specific frequency  $\omega$  (e.g. the DC limit,  $\text{Re}[\sigma(\omega = 0)]$ ),  $\Lambda(\tau)$  represents the quantity that is numerically accessible, through Eq. 2.149. While there are techniques to try to perform a numerical analytic continuation [111], in order to extract a unique  $\text{Re}[\sigma(\omega)]$  which satisfies the numerical calculations of  $\Lambda(\tau)$ , in general such a procedure is made extremely challenging by the fact that there are many different  $\text{Re}[\sigma(\omega)]$  which can satisfy Eq. 2.165.

An approximate expression for the DC limit of the conductivity,  $\text{Re}[\sigma(\omega = 0)]$ , can be obtained by setting  $\tau = \beta/2$  in Eq. 2.165. In this case we have,

$$\begin{aligned}\Lambda(\beta/2) &= \frac{1}{\pi} \int_{-\infty}^{\infty} \frac{\omega e^{-\beta\omega/2}}{1 - e^{-\beta\omega}} \text{Re}[\sigma(\omega)] d\omega \\ &= \frac{1}{2\pi} \int_{-\infty}^{\infty} \frac{\omega}{\sinh(\beta\omega/2)} \text{Re}[\sigma(\omega)] d\omega.\end{aligned}\quad (2.166)$$

To estimate  $\text{Re}[\sigma(\omega = 0)]$  from this, one assumes that, at the temperature  $\beta$  of in-

terest, the function  $\frac{1}{2\pi} \frac{\omega}{\sinh(\beta\omega/2)}$  decays to zero much more rapidly, as a function of  $\omega$ , than  $\text{Re}[\sigma(\omega)]$ . That is, one assumes that  $\text{Re}[\sigma(\omega)]$  is a much more slowly varying function of  $\omega$  at temperature  $\beta$ . In this case, one can approximate  $\text{Re}[\sigma(\omega)]$  in the integral using its DC value,  $\text{Re}[\sigma(0)]$ , since it is assumed to be roughly constant over the frequency range in which the other function decays to zero, so that it may therefore be pulled out of the integral. With such an approximation, one thus obtains,

$$\begin{aligned}\Lambda(\beta/2) &\approx \frac{\text{Re}[\sigma(0)]}{2\pi} \int_{-\infty}^{\infty} \frac{\omega}{\sinh(\beta\omega/2)} d\omega \\ &= \frac{\pi}{\beta^2} \text{Re}[\sigma(0)],\end{aligned}\tag{2.167}$$

so that

$$\text{Re}[\sigma(0)] \approx \frac{\beta^2}{\pi} \Lambda(\beta/2).\tag{2.168}$$

Generally speaking, this approximation for the DC limit of the conductivity is valid only if  $\text{Re}[\sigma(\omega)]$  remains roughly constant over a frequency range that is significantly larger than  $1/\beta$ , which sets the scale over which  $\frac{1}{2\pi} \frac{\omega}{\sinh(\beta\omega/2)}$  decays to zero. Whether or not this is valid for the 2D Fermi-Hubbard model at experimentally accessible temperatures is not entirely clear. For a comparison of the DC spin conductivity of the half-filled 2D Fermi-Hubbard model obtained from Eq. 2.168, with calculations based on real-time current-current correlation functions (Eqs. 2.144 and 2.159), see, for instance, the supplemental material of [164].

We end this discussion by providing one final useful relation for the conductivity, which connects the integral of the conductivity over all frequencies to the average kinetic energy in the system along the direction of interest. Such a relation is often called an *f*-sum rule for the conductivity, and can be used, for instance, to check the validity of a numerical calculation, or an approximate analytic form for  $\text{Re}[\sigma(\omega)]$ . In the charge degree of freedom, where the charge current,  $j_x^{(C)}(\mathbf{q})$ , defined in Eq. 2.145, is used to calculate the diagonal element of the charge conductivity,  $\text{Re}[\sigma_C(\omega)]$ , along, for instance, the  $x$ -direction (one of the lattice axes), the *f*-sum rule can be stated

as,

$$\int_0^\infty \text{Re} [\sigma_C(\omega)] d\omega = -\frac{\pi}{2} \langle \hat{T}_x \rangle. \quad (2.169)$$

Here,  $\hat{T}_x$  represents the Hubbard model kinetic energy operator (Eq. 2.18), which only includes hoping terms along the  $x$ -direction, so that  $\langle \hat{T}_x \rangle$  is the thermally averaged kinetic energy along  $\hat{x}$ . This relationship given by Eq. 2.169 is particularly useful because  $\langle \hat{T}_x \rangle$  is a static, thermodynamic quantity that can be calculated independently using various numerical techniques, including NLCE and DQMC, at least in regions of the phase diagram where the fermion sign problem does not pose too much of an issue. In the spin degree of freedom, where the spin current,  $j_x^{(S)}(\mathbf{q})$ , is also given in Eq. 2.145, the  $f$ -sum rule for the spin conductivity,  $\text{Re} [\sigma_S(\omega)]$ , is modified slightly from Eq. 2.169, and becomes,

$$\int_0^\infty \text{Re} [\sigma_S(\omega)] d\omega = -\frac{\pi}{8} \langle \hat{T}_x \rangle. \quad (2.170)$$

The extra factor of  $1/4$  in the spin conductivity  $f$ -sum rule is really a matter of convention, and arises from our definition of  $j_x^{(S)}(\mathbf{q})$ , that contains a pre-factor given by the total spin of the system, which we have defined to be  $S = 1/2$ . There is then an extra factor of  $1/2$  in the definition of the spin current, that, when carried through to the spin conductivity, which scales like the current-current correlation function  $\langle j(t)j(0) \rangle$ , becomes a factor of  $1/4$ , that must then be applied to both sides of the  $f$ -sum rule. We will not derive the different conductivity  $f$ -sum rules here, but a derivation for the case of the spin conductivity can be found in [66].



# Chapter 3

## Quantum Gas Microscopy of Fermionic $^{40}\text{K}$

In this chapter, we briefly describe our experimental apparatus used for quantum gas microscopy of fermionic  $^{40}\text{K}$ . We summarize those aspects of the experiment which are most relevant for the results discussed in chapters 4 and 5, and refer the interested reader to the following theses, where the apparatus is described in much more depth, including details of the vacuum chamber, the magnetic field coils, the laser systems for both  $^{40}\text{K}$  and  $^{23}\text{Na}$ , the DMD system and optical dipole traps, the optical lattices, and the single-site imaging [73, 186, 187, 37, 168]. We will provide here any relevant changes which have been made to the apparatus since these previous theses were written, and will describe in more detail how we implement spin-dependent single-site imaging, which is used for the spin correlation measurements of chapter 4, as well as the spin transport measurements of chapter 5. A description of how we implement site-resolved (spin-independent) fluorescence imaging of  $^{40}\text{K}$  using Raman sideband cooling in this experiment is also provided in the following publication:

*L. W. Cheuk, M. A. Nichols, M. Okan, T. Gersdorf, V. V. Ramasesh, W. S. Bakr, T. Lompe, and M. W. Zwierlein, “Quantum-Gas Microscope for Fermionic Atoms,” Phys. Rev. Lett. **114**, 193001 (2015) [40].*

We begin the chapter with a summary and description of the experimental appara-

tus itself, including the relevant magnetic field coils, the optical traps used to transport the atoms to the focal plane of the imaging system below the substrate, the DMD used to project optical potentials onto the atoms through the microscope objective, the optical lattices, the lasers used for Raman sideband cooling-based fluorescence imaging, and the high-resolution imaging system. We then summarize the basics of the site-resolved fluorescence imaging scheme, and describe how we have recently changed the vertical position of the single layer of the optical lattice which we use for studying the 2D Fermi-Hubbard model, a change which required re-optimization of the single-site imaging. Subsequently, we give a short summary of the basic experimental sequence, and how we prepare quantum degenerate samples of  $^{40}\text{K}$  in the focal plane of the high-resolution imaging system. Details of the sequence which are relevant and specific to different experiments can also be found in sections 4.2 and 5.2. Finally, we discuss in detail our experimental implementation of spin-resolved single-site imaging for  $^{40}\text{K}$ , and how we calibrate the various steps required to make this imaging technique work. At the end of the chapter, we summarize the results of a recent attempt to generalize this spin-dependent imaging technique, which, as it stands, allows us to measure the singles densities of the individual spin states which make up the sample, in order to allow us, instead, to directly measure the total density of any individual spin state. This generalized spin-dependent imaging, which is still a work in progress, is based on the selective removal of atoms in the undesired spin state, including those residing on doubly-occupied sites, before both atoms which make up a doublon are lost due to light-assisted collisions.

### 3.1 Experimental Apparatus

In this section we provide a general description of the experimental apparatus. Section 3.1.1 describes the relevant magnetic field coils, section 3.1.2 provides a description of the various optical traps and potentials used in the experiment, section 3.1.3 describes the lasers used for single-site imaging, and section 3.1.4 provides a description of the high-resolution imaging system, which allows us to image single atoms

on single lattice sites. Specific details about the design and construction of the apparatus can be found in [73, 186, 187]. The experiment, as it is used for the work in this thesis, utilizes two separate atomic species, bosonic  $^{23}\text{Na}$  and fermionic  $^{40}\text{K}$  (there is the additional possibility to use  $^6\text{Li}$ , which is also in the dual Na/Li oven), and is based on a simple design with a single vacuum chamber. An illustration of the chamber design, with all the viewports where the relevant laser beams and optical traps, as well as the two atomic sources, enter the chamber is given in Fig. 3-1. There are three relevant locations in the main vacuum chamber which are used throughout the experiment: the location where the Na and K 3D MOTs are loaded, which is depicted by the black circle in the center of the chamber in Fig. 3-1, the location of the plugged magnetic quadrupole trap, where the K atoms are sympathetically cooled through collisions with Na atoms that are evaporated directly, which is represented by the cross in Fig. 3-1, and finally the location where the K atoms are prepared in a square optical lattice and are subsequently imaged with single-site resolution, at the center of the solid immersion lens' super-polished substrate surface (see section 3.1.4). This final location, for the single-site imaging of K, sits on the same axis in the  $x-y$  plane (axes defined in Fig. 3-1) as the plugged magnetic quadrupole trap, and is therefore also represented by the cross in Fig. 3-1, but is displaced vertically along the  $+z$ -axis by  $\sim 2$  mm from the plug trap. The 3D MOT location, on the other hand (black dot in Fig. 3-1), is offset from the plugged quadrupole trap and the high-resolution imaging location by  $\sim +12$  mm along the  $x$ -axis, and sits approximately 9.5 mm vertically below the surface of the substrate. The chamber itself has two large re-entrant viewports along the  $z$ -axis (in addition to all the view ports orthogonal to the  $z$ -axis shown in Fig. 3-1), which form a bucket shape for the vacuum chamber in this direction, where the vacuum windows sit relatively close to the atoms, and where the magnetic field coils shown in Fig. 3-2, as well as the microscope objective, sit within the bucket region outside of the windows (see Fig. 4-6 of [73]). The in-vacuum RF antenna, which is generally used for addressing the Na and K atoms with RF and microwave fields, including for the forced RF evaporation of Na in the plugged quadrupole trap, as well as for creating spin mixtures of K with Landau-Zener sweeps,

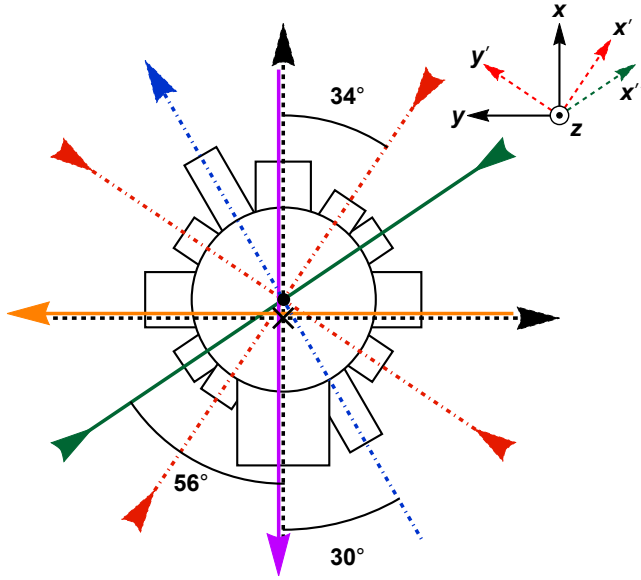


Figure 3-1: Top view of the vacuum chamber, along the  $-z$ -direction (the direction of gravity). The black circle is the center of the chamber, and the  $x - y$  location of the 3D MOTs, which sits 9.5 mm below the substrate surface. The cross is the high-resolution imaging axis, as well as the  $x - y$  position of the plugged quadrupole trap, which sits 2 mm below the substrate surface. The MOTs and the high-resolution imaging axis are offset by 12 mm along the  $x$ -direction. The different arrows represent different beam paths, including the MOT beams (red dot-dashed arrows) along  $\hat{x}'$  and  $\hat{y}'$ , the Na slower beam (blue dot-dashed arrow), the K 2D MOT push (along  $-\hat{x}''$ ) and the Na dark spot re-pumper (along  $+\hat{x}''$ ) beams (green solid arrows), the mag trap optical pumping, shallow angle, and incoming  $x$ -lattice beams (vertical black dotted arrow), the optical plug,  $y$ -ODT, and  $y$ -Raman beams (solid orange arrow), the incoming  $y$ -lattice beam (horizontal black dotted arrow), and the accordion,  $x$ -ODT,  $D1$  optical pumping, and  $x$ -Raman beams (solid purple arrow). Figure adapted from [37].

consists of two loops of oxygen-free copper wire inside the vacuum chamber (a picture of this antenna can be found in Fig. 6-12 of [73]). The direction orthogonal to the horizontal planes formed by the antenna loops points along the  $y$ -axis.

The Na MOT is loaded from a Zeeman slower whose source is a dual Na-Li oven (the Li is currently unused), and which is attached to one side of the vacuum chamber (the port where the blue dot-dashed arrow in Fig. 3-1, which represents the Na Zeeman slowing laser beam, exits the chamber). The Na atomic beam is controlled with an atomic beam shutter (Fig. 4-8 of [73]) that can be closed to prevent the beam from

hitting the cold cloud after the MOT has been loaded. A detailed description of the laser system used for laser cooling and trapping cold  $^{23}\text{Na}$  clouds can be found in Fig. B-4 of [37]. The MOT beams, for both Na and K, are represented by the red dot-dashed arrows in Fig. 3-1 (the  $x'$  and  $y'$  axes in this figure), where the two wavelengths of the two atomic species are combined on a dichroic before entering the chamber. Each axis has its own dual-wavelength quarter-wave plate for generating the circular polarization required for the MOTs. The vertical MOT beams, not shown in Fig. 3-1, enter the chamber from the bottom, pass through and exit the vacuum chamber, and subsequently pass through a dual-wavelength quarter-wave plate on the opposite side of the chamber, where they are then retro-reflected by a mirror sitting on top and outside of the upper vertical window (near the microscope objective), so that they pass back through the dual-wavelength quarter-wave plate and re-enter the vacuum chamber. In this experiment, we use a dark-spot MOT for the Na 3D MOT, where the re-pumper light (with the dark spot) enters the chamber along the direction of the green solid arrow in Fig. 3-1 (the  $+x''$ -axis in the figure), from the viewport in the lower left quadrant of this figure. The K MOT, on the other hand, is loaded from a 2D MOT source, which also enters the chamber along the direction of the green solid arrow in Fig. 3-1, but from the opposite direction of the Na re-pumper light (the port in the upper right quadrant in the figure). The cold K beam is pushed into the main chamber from the 2D MOT glass cell using a so-called "push" beam, and the K source is shut-off, once the 3D MOT is loaded, by simply turning off all the beams used for the 2D MOT (including the push beam). The re-pumper light for the K 3D MOT is combined with the regular MOT light on a separate laser table, and uses the same optical fibers as the K MOT beams. A detailed description of the laser system used for laser cooling and trapping  $^{40}\text{K}$  in this experiment is given in appendix B.1 of [37]. The optical pumping beams for both atomic species, which are used after the 3D MOT stage of the experiment, are combined on a dichroic and enter the chamber along the  $x$ -axis. These beams are represented by the black dotted arrow along the  $x$ -axis in Fig. 3-1. The 532 nm optical plug beam used in the plugged quadrupole trap enters the chamber along the  $y$ -direction, and is represented by the solid orange

arrow in Fig. 3-1. The remaining optical traps, including the lattices, the different ODTs, the DMD potential, and the dimple beam are discussed in section 3.1.2.

For debugging purposes, and for calibration of the atom numbers and temperatures of the two atomic species, we also have several absorption imaging paths set up to image the Na or K atoms in various locations of the chamber. The first path allows one to image the Na or K MOTs (or the magnetic traps in the MOT position), and the imaging beam propagates along the same axis as the optical pumping beams. This path is represented by the black dotted arrow along the  $x$ -axis in Fig. 3-1. The second path allows one to image the atoms in the location of the plugged quadrupole trap (in either the plug trap itself or the crossed ODTs, once the atoms have been transferred there from the plug trap), and the imaging beam for this path propagates along the  $-y$ -direction, represented by the black dotted arrow along the  $y$ -axis in Fig. 3-1. The third and fourth absorption imaging paths allow one to image the atoms, from the side, at the surface of the high-resolution imaging system. These beams are also represented by the black dotted arrows along the  $x$  and  $y$  axes in Fig. 3-1, although they are angled vertically (at a  $10.8^\circ$  angle with respect to the  $x - y$  plane) to access the substrate surface, which they reflect off of, so that they then exit the chamber on the opposite side. The final absorption imaging path is not shown in Fig. 3-1, but enters the chamber from below, and propagates along the  $z$ -direction, allowing one to image the atoms at the surface of the high-resolution imaging system from the vertical direction. Details of the different absorption imaging paths can be found in section 4.6 of [37].

### 3.1.1 Magnetic Field Coils

In this section, we briefly describe the magnetic field coils which are most relevant to the experiments described in chapters 4 and 5. We do not, however, discuss the field coils used in, for example, the  $^{40}\text{K}$  2D MOT or the  $^{23}\text{Na}$  Zeeman slower, since these are described in detail in previous theses [73, 186, 187], and have not changed over time. Also, for the interested reader, more detailed and precise descriptions of the different coils, how they were designed, how they are used in various parts of the

experimental sequence, how they are powered, and how they are positioned relative to the atoms in the vacuum chamber, are given in section 4.1 and appendix A of [37], and section 6.1 of [73].

There are eight magnetic field coils which are particularly important for the work described in this thesis: a Feshbach coil, two clover-leaf coils, a MOT coil, a curvature coil for magnetic trapping, and three bias field coils. Fig. 3-2 provides a cartoon illustration of the relative positions of these coils, which are all located within the bucket of the vacuum chamber, except for the bias field coils (not shown in this figure), which are all run in a Helmholtz configuration and are attached to the outside of the vacuum chamber to provide small bias fields in the  $x$ ,  $y$ , and  $z$ -directions. There is an additional coil run in Helmholtz configuration, which is wound around the top and bottom of the entire apparatus to apply a vertical field that can be used to actively stabilize the ambient magnetic field fluctuations in the vertical direction near the experiment. Such fluctuations, which vary within a range of approximately  $\pm 10$  mG in our experiment, arise from, for example, three nearby elevators. Although we do not make use of these coils to actively stabilize the ambient field in the majority of the work described here, they can be used in future experiments to achieve offset fields in the vertical direction (produced by, for instance, the Feshbach coil) with better fractional stability, by reducing the ambient field fluctuations from a  $\pm 10$  mG range, to approximately a  $\pm 0.5$  mG range near the atoms. These coils, as well as the ambient field cancelation scheme, are described in detail in section 5.4.1 of [37]. We now go through each of the eight coils which are most relevant for the work discussed in this thesis, and describe how they are used in the experiment.

The bias coil along the  $x$ -direction, probably the most important bias coil, is used in several stages of the experiment. It is a hand-wound coil attached to the outside of the vacuum chamber, and it provides a small magnetic field along the propagation direction of the  $x$  lattice, which can be used to zero the magnetic field along this direction. During the MOT loading stages, it is generally used for fine positioning of the quadrupole field produced by the MOT coil, and is powered by an Agilent E3614A power supply run in constant current operation mode. The connection of

this power supply to the coil is controlled by a MOSFET. After the MOT loading, the MOT light and MOT coil are turned off, and the  $x$  bias coil is used to provide a quantization axis for the optical pumping stage. In order to quickly apply a strong quantization field along the  $x$ -direction for this optical pumping, we swap to a different power supply using MOSFETs, a Sorensen DLM 20-30, which is also run in constant current mode. After both species are optically pumped, the coils are powered only by the Sorensen, and the Agilent is not used again. During the magnetic trapping section of the experimental sequence, in the plugged quadrupole trap, the  $x$  bias coil is used to finely tune the zero of the quadrupole trap. During the remainder of the sequence, it is generally used to apply a finite quantization offset field in the optical traps which we use for both the single-site imaging, as well as for spin state preparation/manipulation with RF and microwave Landau-Zener sweeps, such as the  $|F = 9/2, m_F = 9/2\rangle \rightarrow |F = 9/2, m_F = -9/2\rangle$  sweep for K, and the microwave sweep used in the spin-dependent imaging. We also use this coil to provide the quantization field along the  $x$ -direction for absorption imaging along this axis, for instance when we align the  $y$  ODT beam, or if we need to image the MOT. When we apply a strong vertical offset field using the Feshbach coil to go to  $\sim 150$  G, we typically leave the field produced by this coil on at a small, but non-zero value (usually less than 1 G), which does not significantly affect the magnitude of the magnetic field (it adds in quadrature to the Feshbach field), but allows us to ensure that the overall applied field never goes to zero during the various field ramps.

The other two bias coils, the  $y$  and  $z$  bias coils, are also hand-wound coils run in Helmholtz configuration, which are attached to the outside of the vacuum chamber (not shown in Fig. 3-2), and provide offset fields along the  $y$  and  $z$ -directions, respectively. The  $y$  bias coil is powered by a Delta Elektronika SM 18-50 power supply run in constant current mode, and the connection of this supply to the coil is controlled with a MOSFET. This coil is typically only used for fine positioning of the MOT and magnetic trap quadrupole field zeros. However, we can also use this coil to apply a quantization axis along the  $y$  direction for absorption imaging when we need to image the atoms in the plugged magnetic trap position (2 mm below the substrate surface),

such as when the atoms have been transferred into the crossed ODTs, but before they have been transported to the substrate surface, or when we image the atoms at the surface with absorption imaging for alignment of the various optical traps (the  $x$  ODT, the accordion, and the shallow angle beam). The  $z$  bias coil, on the other hand, is powered by an Agilent E3614A power supply run in constant current mode, and the connection of the supply to the coil is also controlled by a MOSFET. This coil is also used to tune the zero field position in the MOT and magnetic trap, and provides a quantization axis for the removal light pulse that is applied during the spin-dependent imaging. In principle it can also be used to provide a quantization axis for low-field absorption imaging in the vertical direction, but in recent years we typically align the various optical traps using high-field absorption imaging, where the field is provided by the Feshbach coil instead.

The MOT coils are shown in green in Fig. 3-2, and are displaced by 12 mm along the  $x$ -direction relative to the central axis of the high-resolution imaging system. These coils are run in an anti-Helmholtz configuration in order to provide a quadrupole field for both the Na and K 3D MOTs, as well as the magnetic catch and initial magnetic trapping of both species. From the initial magnetic trap provided by these coils, the atoms are subsequently magnetically transferred to the plugged magnetic quadrupole trap (provided by the curvature coils), which is centered below the high-resolution imaging system. During the Na MOT loading, these coils are powered by a Delta Elektronika SM 30-200 with high-speed programming (option P167), whose current is actively stabilized using feedback to the power supply programming in constant voltage mode. The current measurement for the feedback is done using a Danfysik LEM IT 200-S current transducer, whose output is read out with temperature stabilized, ultra-high precision Vishay VPR221Z, Z-foil power resistors. The connection of this power supply to the MOT coil is controlled with an IGBT. For the magnetic catch of the Na after the Na MOT, as well as for the K 3D MOT and the K magnetic catch, the MOT coils are powered by a Delta Elektronika SM66-AR-110, which is simply run in constant current mode (no active current stabilization). The connection of the MOT coil to this supply is also controlled with an IGBT. Once the

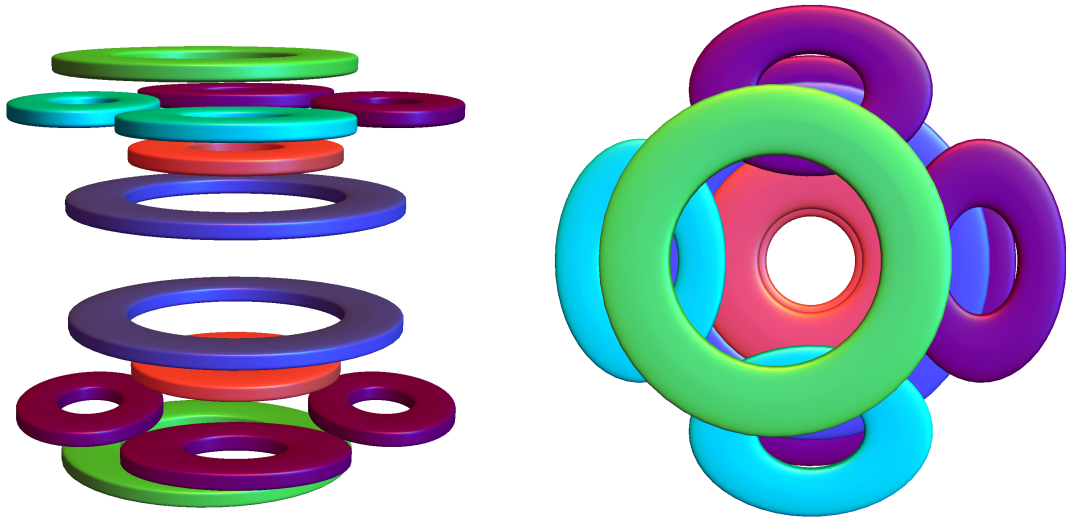


Figure 3-2: Illustration of the relevant magnetic field coils used for generating homogeneous magnetic fields and magnetic field gradients. The left image is a view of the coils looking down the  $-y$ -direction, and the right image is a view of the coils from above, looking down the  $-z$ -direction. The MOT coils, run in anti-Helmholtz configuration, are shown in green, and are offset from the high-resolution imaging axis along the  $+x$ -direction by 12 mm. These coils are centered on the center of the vacuum chamber. The Feshbach coils, run in Helmholtz configuration to generate homogeneous offset fields, are shown in blue, and are centered on the high-resolution imaging axis. Concentric with the Feshbach coils are the curvature coils, which are shown in red, and which are run in an anti-Helmholtz configuration to generate magnetic quadrupole fields. The purple coils are clover-leaf coils which are unused in the experiments described in this thesis. The cyan coils are the clover  $x$  and clover  $y$  coils which are used to generate magnetic gradients along the  $x$  and  $y$  directions, respectively. Not shown here are the three bias coils along the  $x$ ,  $y$ , and  $z$ -directions.

atoms have been transferred to the plugged quadrupole trap after the K magnetic catch in this coil, the MOT coils are no longer used, and the IGBTs connecting the power supplies to the MOT coil are turned off.

The curvature, or slicer coil (we use both names throughout this thesis) are shown in red in Fig. 3-2, and are centered around the axis of the high-resolution imaging system. These coils are run in an anti-Helmholtz configuration, and provide the main quadrupole field for the plugged magnetic trap centered  $\sim 2$  mm below the substrate. For the spin transport work discussed in chapter 5, the vertical gradient produced by these coils is used to compensate the vertical gradients arising from

the Feshbach coils when we operate at  $\sim 150$  G. In previous work, including [40], these coils were used to provide a large vertical gradient, which could be used to select a single vertical 2D layer of an optical lattice for single-site imaging using the spatially dependent Zeeman shift from the gradient to shelve a single layer of K atoms in the  $F = 7/2$  manifold with a microwave sweep, while the other layers were removed using a resonant light pulse (similar to the spin-dependent imaging technique described in section 3.4). This technique, called "slicing", is how these coils came to be occasionally called the slicer coils. We no longer use these coils for this purpose, however, since we now prepare a single 2D layer of atoms using an accordion lattice. When these coils are used to provide the magnetic quadrupole field for the plugged quadrupole trap, they are powered by a Lambda ESS-30-500 power supply, whose connection to the coils is controlled by an IGBT. Because the center of these coils is actually located approximately 9.5 mm below the substrate, but we run the plugged quadrupole trap approximately 2 mm below the substrate using an offset field provided by the Feshbach coil, any current noise in this coil can shift the center of the quadrupole trap, which directly leads to heating of the atoms (see section 6.1.1 of [37]). We therefore actively stabilize the current output of the Lambda ESS-30-500 power supply as it powers the curvature coil for the plugged quadrupole trap. The current output of the Lambda supply is measured with a Danisense DS600IDSA current transducer, whose output is read out with ultra-high precision Vishay VPR221Z, Z-foil power resistors. This signal is then fed back to the Lambda using the voltage programming of the supply run in constant voltage mode. When we use the curvature coil to cancel the vertical gradients of the Feshbach coil, such as when we operate with offset fields around  $\sim 150$  G, we change the power supply controlling the curvature coil, and power it instead with a Delta Elektronika SM 18-220, whose connection to the coil is controlled with a high-power MOSFET. We also actively stabilize the current output of this power supply, but in this case, we measure the current output using a Danfysik LEM IT 200-S current transducer. As with the other current stabilization setups, the output of this transducer is read with ultra-high precision Vishay VPR221Z, Z-foil power resistors, and the signal is fed

back to the Delta power supply with the supply's voltage programming in constant voltage mode.

The clover-leaf coils are shown in both purple and cyan in Fig. 3-2. There are eight clover-leaf coils in total, which were originally designed to make up part of a Ioffe-Pritchard magnetic trap, whose trap center is centered around the high-resolution imaging axis, and which is vertically located approximately 9.5 mm below the substrate. We do not, however, use all eight coils currently in the experiment, since we do not make use of the Ioffe-Pritchard trap. The coils which we do not use are shown in purple in Fig. 3-2. The coils we do use in the experiment are shown in cyan in Fig. 3-2, and are used to apply magnetic gradients along the  $x$  and  $y$ -directions. Each coil is powered by its own Delta Elektronika SM 18-50 power supply run in constant current mode (no active current stabilization), and the connections of these supplies to the coils are controlled with high power MOSFETs. The Delta power supply controlling the clover coil that produces a gradient along the  $y$ -direction also has high-speed programming (option P251) for fast modulation of the current in this coil. For the purposes of the experiments discussed in this thesis, we only use one clover coil, which sits in the upper half region of the chamber, per axis: a clover  $x$  coil and a clover  $y$  coil (as we refer to them). This produces sufficient gradient strengths for the work described here, but future experiments could in principle make use of additional clover-leaf coils to generate larger gradients. During the experimental sequence, these coils are generally used for canceling the horizontal gradients produced by the Feshbach coil when we operate at large magnetic offset fields, in conjunction with the slicer coil which cancels the vertical gradients. Additionally, the two coils are used together for the creation of a magnetic gradient along the  $y$ -lattice direction (see section 5.2.2), which we make use of for the spin transport measurements discussed in chapter 5. During the final stage of optical evaporation in the combined shallow angle and dimple beams, before we prepare the atoms in the optical lattice, the clover  $x$  coil alone is also used to provide a magnetic gradient which pushes the atoms out of the trap along the propagation direction of the shallow angle beam, as the optical powers in the two beams are lowered.

The final coil that we actively use in the experiment is the Feshbach coil, which is shown in blue in Fig. 3-2 and is run in a Helmholtz configuration. This coil is also centered horizontally around the high-resolution imaging axis, and is centered vertically approximately 9.5 mm below the substrate surface. During the experiment, we use this field for two main purposes: shifting the zero of the plugged magnetic quadrupole trap from 9.5 mm below the substrate surface to approximately 2 mm below the substrate surface, and providing a large offset field in the vertical direction which can, for instance, be used for accessing Feshbach resonances between the different hyperfine states in  $^{40}\text{K}$ . When this coil is operated, it is powered by a Delta Elektronika SM 30-200 power supply with high-speed programming (the same power supply used for the Na MOT), whose current is actively stabilized (see discussion of the MOT coil). The connection of this power supply to the Feshbach coil is controlled with an IGBT. After the atoms have been transferred from the plugged quadrupole trap (where we use the Feshbach coil to position the trap zero), we typically use the large field provided by this coil as an offset field in the optical traps during the remainder of the sequence. For example, we use the homogeneous field generated by this coil (typically  $\sim 150$  G) to create the various spin mixtures of K in the crossed ODTs through a series of RF sweeps. We also use this large offset field as a quantization axis for high-field absorption imaging along the vertical direction, which we utilize for the alignment of various optical traps, including the shallow angle beam, the accordion, and the incoming (not retro-reflected) lattice beams. The Feshbach coil also provides the offset field utilized for the spin transport measurements discussed in chapter 5. Although we do not make use of any Feshbach resonances in this thesis, in principle the Feshbach coil is perfectly suited for this purpose.

### 3.1.2 Optical Traps

In this section, we describe the various optical traps and how they are used during the experimental sequence, including the crossed ODTs, the accordion, the dimple beam, the shallow angle beam, the  $x$ ,  $y$ , and  $z$  optical lattices, and the repulsive potential projected onto the atoms in the lattice using a digital micro-mirror device (DMD).

More detailed descriptions of the 1064 nm optical traps and the dimple beam, and their corresponding optics setups, can be found in sections 4.3 and 4.5, and appendix B of [37], and a detailed description of the DMD projected potential can be found in section 4.3 of [168]. The  $x$  and  $y$  crossed ODTs, the accordion, the shallow angle beam, and the  $x$ ,  $y$ , and  $z$  optical lattices are all formed with 1064 nm light, which is sourced by a total of three different Nufern NuAmp SUB-1174-25, 50 W output fiber amplifiers. These amplifiers are all seeded by a single Coherent Mephisto laser with 1 W CW output and  $\sim 1$  kHz line-width. We label the three different Nufern amplifiers as the  $x$  Nufern, the  $y$  Nufern, and the  $z$  Nufern. The dimple and DMD light, on the other hand, are sourced by separate lasers at different wavelengths, and are described subsequently. Each of the beams described here is independently intensity stabilized using its own photodiode, which monitors the beam power on the experiment table, before the light enters the vacuum chamber, and whose signal is fed back to a servo controller, which controls the power sent to the experiment table for that particular beam through an optical fiber using an AOM in the beam path (see, for example, appendix B.4 of [37]). The 1064 nm beams are monitored using Thorlabs PDA10CS, switchable gain, InGaAs amplified photodiodes, and the dimple and DMD beams are monitored using Thorlabs PDA36A, switchable gain, Si amplified photodiodes.

The  $x$  and  $y$  crossed ODTs are 1064 nm dipole traps which are used to optically transport the atoms vertically from the location of the plugged magnetic quadrupole trap (the cross in Figs. 3-1, 3-3, and 3-4) located 2 mm below the surface, to a position approximately 40  $\mu$ m below the surface of the super-polished substrate, at the center of the high-resolution imaging axis. This transport process is conducted over a period of 900 ms, where the position of each ODT at the atoms is independently controlled using its own IntraAction DTD-274HA6 shear mode acousto-optic deflector (AOD), which is placed in the Fourier plane (see Fig. 4-9 of [37]) of the beam path. By sweeping the RF frequency controlling the AOD, which tunes the angle of the beam exiting the AOD crystal, and therefore (because the AOD is in the Fourier plane) the vertical position of the beam at the atoms, we can translate the position of the atoms

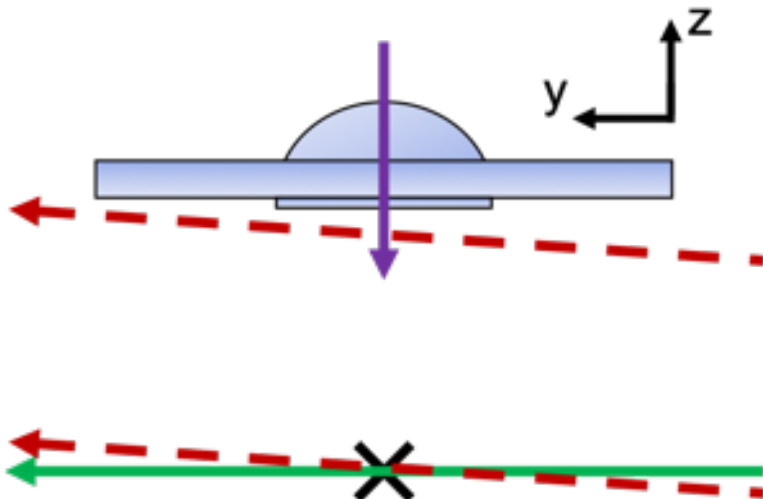


Figure 3-3: Side-view along the  $x$ -direction of the optical traps and the solid immersion lens. The cross represents the position of the plugged magnetic quadrupole trap, located 2 mm below the substrate surface. The green arrow pointing along  $+\hat{y}$  indicates the position and propagation direction of the optical plug. The lower dashed red arrow represents the initial vertical position and propagation direction of the  $y$  ODT, where the atoms are transferred after evaporation in the plugged quadrupole trap. The upper dashed red arrow indicates the final vertical position of the  $y$  ODT after the atoms are optically transported along the high-resolution imaging axis to a position  $\sim 40 \mu\text{m}$  below the substrate surface. The purple arrow represents the high-resolution imaging axis, and also indicates the propagation direction of both the dimple beam and the DMD light. The spherical cap, vacuum window, and substrate, which form the solid immersion lens, are shown in blue.

in the crossed ODT, without altering the incident angle of the beams with respect to the  $x - y$  plane. Note that the photodiodes used for the intensity stabilization of these beams are placed before the AODs, where the beam positions are fixed on the experiment table. In addition to this first stage of optical transport, we also use the 1064 nm crossed ODTs for manipulating the internal spin states of the atoms. For example, this trap is where we put the K atoms in the lowest energy hyperfine state,  $|F = 9/2, m_F = -9/2\rangle$ , as well as where we make the various K spin mixtures used in the experiments described in chapters 4 and 5. Both the  $x$  and  $y$  ODT beams are sourced from the  $y$  Nufern amplifier, and are transported from the Nufern source to the experiment table using Thorlabs P3-980PM-FC FC/APC fibers. The  $x$  ODT propagates along the  $-x$ -direction, as shown by the red dashed arrows in Fig. 3-

4 and the purple solid arrow in Fig. 3-1, has a beam waist of  $40\ \mu\text{m}$ , and has an incident angle at the atoms of approximately  $+1.2^\circ$  with respect to the  $x - y$  plane, to mode match the ODT with the accordion beam, and to minimize the number of vertical layers formed when this beam reflects from the substrate surface at the end of this beam's optical transport stage. The initial and final positions of the  $x$  ODT during the optical transport, located approximately 2 mm below the surface and approximately  $40\ \mu\text{m}$  below the surface, respectively, are represented by the lower and upper dashed red arrows in Fig. 3-4, respectively. The  $y$  ODT, on the other hand, propagates along the  $+y$ -direction, as shown by the red dashed arrows in Fig. 3-3 and the orange solid arrow in Fig. 3-1, has an elliptical cross section with a beam waist of  $40\ \mu\text{m} \times 90\ \mu\text{m}$  ( $40\ \mu\text{m}$  vertical,  $90\ \mu\text{m}$  horizontal), and has an incident angle at the atoms of approximately  $+5.4^\circ$  with respect to the  $x - y$  plane, to avoid hitting the in-vacuum RF antenna as the beam moves in the vacuum chamber during transport. The initial and final positions of the  $y$  ODT during the optical transport, located approximately 2 mm below the surface and approximately  $40\ \mu\text{m}$  below the surface, respectively, are represented by the lower and upper dashed red arrows in Fig. 3-3, respectively.

The accordion beam [103] is a 1064 nm beam which is used to transfer the atoms from the final position of the crossed ODTs to a single layer of a vertical optical lattice. The vertical lattice is formed from the reflection of the accordion from the surface of the super-polished substrate at an initial incident angle with respect to the  $x - y$  plane of approximately  $1.1^\circ$ , which places the second layer of the accordion lattice at approximately  $40\ \mu\text{m}$ . The incident angle of this beam on the substrate surface can be tuned dynamically using a Thorlabs GVS311 galvo mirror that is imaged directly onto the substrate (see Fig. 4-8 of [37]). To make sure that the position (in the  $x - y$  plane) where the accordion reflects from the substrate surface does not change as the galvo mirror is varied (due to, for example, imperfect imaging of the galvo onto the substrate surface), an additional galvo with a 3 mm thick fused silica glass plate is placed in the beam path ( $\sim 30\ \text{mm}$  after the galvo mirror), which can finely tune the position, in the  $x - y$  plane, where the accordion hits the substrate. By increasing

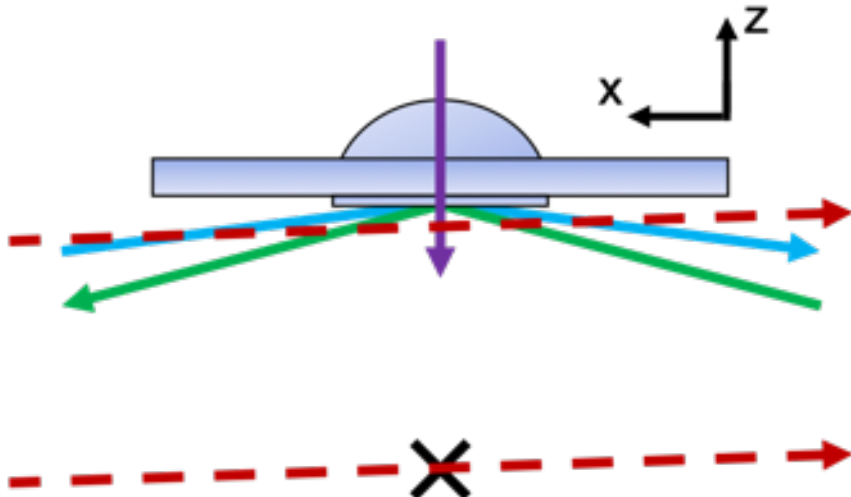


Figure 3-4: Side-view along the  $-y$ -direction of the optical traps and the solid immersion lens. The cross represents the position of the plugged magnetic quadrupole trap, located 2 mm below the substrate surface. The lower dashed red arrow represents the initial vertical position and propagation direction of the  $x$  ODT, where the atoms are transferred after evaporation in the plugged quadrupole trap. The upper dashed red arrow indicates the final vertical position of the  $x$  ODT after the atoms are optically transported along the high-resolution imaging axis to a position  $\sim 40 \mu\text{m}$  below the substrate surface. The cyan arrow indicates the propagation of the accordion beam, which initially reflects from the surface at an angle of approximately  $1.1^\circ$ , and whose incident angle can be tuned dynamically to further transport the atoms from  $\sim 40 \mu\text{m}$  below the surface to the final vertical position at the focus of the high-resolution imaging system. The green arrow represents the shallow angle beam, which reflects from the surface at an angle of  $5.8^\circ$ , propagates in the opposite direction of the  $x$  ODT and accordion, and is used for the final stage of optical evaporation. The purple arrow represents the high-resolution imaging axis, and also indicates the propagation direction of both the dimple beam and the DMD light.

the incident angle of the accordion beam from its initial  $1.1^\circ$  value using the galvo mirror, the vertical position of the second layer of this vertical lattice, which holds all of the atoms, can be moved from  $\sim 40 \mu\text{m}$  to any desired final position closer to the substrate surface. In this way, we can move the atoms to the final vertical location below the substrate where they can be prepared in the optical lattice and imaged with single-site resolution. Additionally, as the incident angle of the accordion increases, the confinement in the  $z$ -direction for the single layer of atoms becomes tighter, so that the system becomes more two-dimensional. Note that the photodiode used for the intensity stabilization of this beam on the experiment table is placed before the

beam hits either galvo, where the beam position remains fixed. The source of the accordion light is the  $z$  Nufern amplifier, which is brought to the experiment table from the Nufern using a Thorlabs P3-980PM-FC FC/APC fiber. The beam itself propagates along the  $-x$  direction, represented by the cyan solid arrow in Fig. 3-4 and the purple solid arrow in Fig. 3-1, and has a waist of  $72\ \mu\text{m}$  at the atoms.

The dimple beam is an 830 nm red-detuned optical dipole trap which is sent through the microscope objective and focused onto the atoms near the focal point of the single-site imaging. To avoid interference fringes arising from, for example, reflections off of the many glass surfaces in the microscope objective or the solid immersion lens, which can distort the optical potential of the dimple at the location of the atoms, we use a broadband light source for this beam. When the line-width of the light is broad enough, the coherence length becomes sufficiently short that interference fringes due to reflections in the objective are strongly suppressed. Here, we use a Thorlabs SLD830S-A20 superluminescent diode with 22 mW output and a 20 nm FWHM optical spectrum centered at 830 nm. To increase the power in this beam, the superluminescent diode seeds a tapered amplifier (TA) which boosts the total power to several hundred mW. The output of the TA is then sent through two long-pass Semrock filters, which remove any resonant light from the TA's amplified spontaneous emission (ASE) pedestal near the  $^{40}\text{K } D_1$  and  $D_2$  lines. The light then goes through an AOM for intensity stabilization, after which it is fiber coupled and sent to the experiment table with a Thorlabs P3-780PM-FC FC/APC fiber. On the experiment table, the dimple is focused onto the atoms near the substrate surface with the microscope objective, so that it has a waist of  $30\ \mu\text{m}$  and propagates in the  $-z$ -direction, as represented by the solid purple arrows in Figs. 3-3 and 3-4, with linear polarization parallel to the substrate surface. The purpose of the dimple beam is generally to provide additional confinement within the  $x - y$  plane while the atoms are trapped in a single layer of either the accordion or the shallow angle beams, since these beams are weakly confining along their respective directions of propagation. Such additional confinement is also useful for the final stage of optical evaporation in the shallow angle beam, since it significantly increases the density in the trap, which

increases the thermalization rate for efficient evaporative cooling. The dimple can also be used to add additional harmonic confinement in the  $x - y$  plane while the atoms are in the optical lattice, in order to increase the density in the center of the trap, and therefore to increase the global chemical potential of the 2D Fermi-Hubbard system.

The shallow angle beam is a 1064 nm optical dipole trap which is used for the final stage of optical evaporation (in conjunction with the dimple), after transferring the atoms to a single vertical layer of this beam from a single vertical layer of the accordion. Once the two-dimensional optical evaporation of the atoms has finished, the atoms are subsequently transferred from the shallow angle beam to the  $x$  and  $y$  optical lattice, where the system realizes the 2D Fermi-Hubbard model and where it can be imaged with single-site imaging. The source of the shallow angle beam light is the  $z$  Nufern amplifier, which is brought to the experiment table using a Thorlabs P3-980PM-FC FC/APC fiber. In the experiment, it propagates along the  $+x$ -direction with linear polarization, as represented by the solid green arrow in Fig. 3-4 and the vertical black dotted arrow in Fig. 3-1, and reflects from the substrate surface at a fixed  $5.8^\circ$  angle with respect to the  $x - y$  plane, which forms a vertical lattice with spacing  $5.26 \mu\text{m}$ . When the  $x$  and  $y$  optical lattices used to simulate the 2D Fermi-Hubbard system are shallow (e.g.  $\lesssim 4E_R$ ), this beam can also be used to provide additional vertical confinement in order to prevent atoms from tunneling along the  $z$ -direction.

The  $x$  and  $y$  optical lattice beams are 1064 nm retro-reflected beams which are used to simulate the 2D Fermi-Hubbard model, and which are also used to pin the atoms for single-site imaging. The atoms are transferred to the  $x$  and  $y$  lattices after the final stage of optical evaporation in the shallow angle and dimple beams. Due to the retro-reflection, these lattice beams form a square optical lattice in the  $x - y$  plane with a lattice spacing of 541 nm. However, they also reflect from the surface of the substrate at an angle of  $10.8^\circ$  with respect to the  $x - y$  plane, so that, in addition to the in-plane lattice, they also form a vertical lattice with a lattice spacing of  $2.84 \mu\text{m}$ . When the atoms are transferred to these beams from the shallow angle beam, only

a single vertical layer is populated. The incoming  $x$  lattice propagates along the  $+x$ -direction, as indicated by the vertical black dotted arrow in Fig. 3-1, so that the retro-reflection propagates along the  $-x$ -direction. This is illustrated in Fig. 3-6(a). The beam shape of the  $x$ -lattice is elliptical, and has a vertical waist of  $40\ \mu\text{m}$ , and a horizontal waist of  $135\ \mu\text{m}$ , whereas the polarization is linear and perpendicular to the surface of the substrate. The  $x$  lattice beam source is the  $x$  Nufern, and the light is brought to the experiment through a NKT Photonics LMA-25 single mode photonic crystal fiber with  $25\ \mu\text{m}$  core size that is connectorized by AlphaNov. The incoming  $y$  lattice, on the other hand, propagates along the  $-y$  direction, as indicated by the horizontal black dotted arrow in Fig. 3-1, so that the retro-reflected light propagates along the  $+y$ -direction. The retro-reflection setup for the  $y$  lattice is the same as the  $x$  lattice, represented in Fig. 3-6(a). The beam shape of the  $y$ -lattice is also elliptical, with a vertical waist of  $40\ \mu\text{m}$  and a horizontal waist of  $135\ \mu\text{m}$ , whereas the polarization is linear and parallel to the surface of the substrate. The source of the  $y$  lattice light is the  $y$  Nufern, which is brought to the experiment through the same type of photonic crystal fiber as the  $x$  lattice. Because the dynamic range for the optical power in these beams can be very large due to the significant difference between the lattice depths used for simulating the Hubbard model ( $\sim 2 - 20E_R$ ), and the depths used for single site imaging ( $\sim 1000E_R$ ), and because the power must be intensity stabilized over this entire range to prevent heating, we use a combination of two photodiodes, for each lattice beam, for the intensity stabilization feedback. Specifically, we use one photodiode which is sensitive to the optical power for lattice depths in the range of  $0 - 100E_R$ , but which saturates after approximately  $100E_R$ , and a second photodiode which is sensitive to the optical power for lattice depths greater than  $\sim 100E_R$ , and which does not saturate at the imaging depth,  $\sim 1000E_R$ . The outputs of these two photodiodes are then added together (when the low power photodiode saturates, the voltage of this signal path is set to rail to a fixed  $10\ \text{V}$  reference to prevent voltage drift issues) and divided by two before they are fed into the servo for intensity stabilization. In this way, we can dynamically tune the power of the optical lattice beams between the physics depths and the imaging depths, with

good sensitivity and intensity stabilization over the full range of powers.

The  $z$  lattice beam is another 1064 nm retro-reflected beam which is used to provide extra vertical confinement (along the  $z$ -direction) during the single-site imaging. After the atomic distribution of the sample of interest has been frozen in the  $x$  and  $y$  lattice beams at  $\sim 100E_R$ , the depths of the  $x$  and  $y$  lattice beams are increased to  $\sim 1000E_R$  in the horizontal direction for single-site imaging, while the  $z$  lattice beam is simultaneously increased to bring the lattice depth in the  $z$ -direction to  $\sim 1000E_R$  as well. For the work described in this thesis, the  $z$  lattice is only used for this purpose, although in future experiments it could act as a more versatile tool. The source of the  $z$  lattice light is the  $z$  Nufern amplifier, which is brought to the experiment table using a Thorlabs P3-980PM-FC FC/APC fiber. The incoming beam propagates vertically in the  $+z$ -direction, where it is retro-reflected at normal incidence by the super-polished substrate, returning back along the  $-z$ -direction. This is illustrated in Fig. 3-6(a). Because of the retro-reflection at normal incidence, the lattice spacing formed by this beam is 532 nm. At the atoms, the beam is circular with a waist of  $60\ \mu\text{m}$ , and the polarization of the light is linear and parallel to the surface of the substrate.

The final optical potential used in the experiments described in this thesis is the DMD repulsive (blue-detuned) potential. This light is projected onto the atoms in the lattice through the microscope objective, and is used to locally shape, in a site-resolved way, the potential landscape experienced by the atoms. It is used, for instance, to create the box potential in the spin transport studies of chapter 5, which prevents atoms in the isolated system from escaping during the spin dynamics, and simultaneously keeps out atoms from the surrounding environment. It could also be used, in principle, to generate other interesting potential landscapes/geometries for transport studies, as well as for creating site-resolved disorder for the study of many-body localization [44]. For the work described in this thesis, the light source for the DMD potential is a Gigajet 20C femtosecond oscillator that is pumped by a 532 nm Verdi V18. The central wavelength of the Gigajet output is 739 nm (blue-detuned with respect to the  $D1$  and  $D2$  lines of  ${}^{40}\text{K}$ ), with a  $\sim 1\ \text{nm}$  FWHM line-width. Because

this light is projected through the microscope objective, like the dimple light, we sought a light source with a large enough line-width to reduce the coherence length ( $\sim 170\mu\text{m}$  in this case) sufficiently that we could avoid interference fringes at the atoms due to reflections from the surfaces of the optics in the high-resolution imaging system. Before being sent to the experiment table through a Thorlabs P3-630PM-FC FC/APC fiber, however, the output of the Gigajet is sent through a 3 nm wide Semrock notch filter centered at 739 nm, in order to suppress any light in the optical spectrum resonant with the  $D1$  and  $D2$  lines of  $^{40}\text{K}$ . After the spin transport data described in chapter 5 was taken, we have since replaced the light source for the DMD, because the Gigajet required significant daily maintenance in order to generate and output the correct optical spectrum. As of the writing of this thesis, we are currently using an Eagleyard Photonics EYP-BAL-0740-01000-2010-CMT02-0000 broad area laser. This laser outputs approximately 1 W of light at 739 nm with a 1 nm FWHM line-width, and has no mechanical parts required to adjust the optical spectrum (there are only the current and the temperature degrees of freedom). Although the output is spatially multi-mode, the mode is cleaned up by coupling the light into a single mode optical fiber before sending it to the experiment. To ensure there is no light resonant with the  $D1$  and  $D2$  lines of  $^{40}\text{K}$ , we send the output of this laser through the same Semrock 3 nm wide notch filter before sending it to the experiment through an optical fiber. On the experiment table, the light illuminates a digital micromirror device (DMD) in the image plane of the beam path, before entering the microscope objective where it is focused onto the atoms in the optical lattice. It thus propagates in the  $-z$ -direction, represented by the solid purple arrow in Figs. 3-3 and 3-4, and has a linear polarization parallel to the substrate surface. For a detailed description of how the DMD is imaged onto the atoms, and how the light is combined with the dimple light to pass through the microscope objective, see section 4.3 and Figs. 4-8 and 4-9 of [168]. For reference, the magnification for the imaging system which images the surface of the DMD onto the atoms is roughly  $\sim 125$ . The DMD itself, which is a Texas Instruments DLP4500 0.45 WXGA DMD and Chipset, has  $912 \times 1140$  pixels, where each pixel is square with a  $10.8\mu\text{m}$  diagonal length. Based on the packing of the

micromirrors onto the DMD chip (Fig. 4-3 of [168]), the imaging magnification gives us approximately  $6 \times 12$  micromirrors per lattice site, which provides us with enough bits per site to perform a significant amount of gray scaling of the DMD potential if so desired [67]. To program the DMD with the computer in order to generate the desired arbitrary optical potential, we use a Keynote Photonics FlexLight LC4500 controller with a plug-in BeagleBone board. For a thorough description of how we stop the flickering of the DMD mirrors in our experimental setup, as well as a detailed analysis of the box potential generated by the DMD for the spin transport studies of chapter 5, see chapter 4 of [168].

### 3.1.3 Single-Site Imaging Lasers and Beam Paths

There are four relevant single-site imaging lasers used in the experiment: three lasers for the optical pumping and one laser which generates the light for the two-photon Raman transitions in the Raman sideband cooling. The first optical pumping laser is a Photodigm PH770DBR 770 nm DBR laser which is locked to the crossover feature of the  $^{39}\text{K}$   $D1$  line. This laser acts as a frequency reference to which we independently offset-lock two separate Toptica DL-Pro ECDL lasers operating at 770 nm for the  $F$  and  $m_F$  pumping in the single-site imaging. The independent offset-lock of the  $F$  and  $m_F$  pumping lasers gives us a simple method to independently adjust the absolute frequency of these two beams, without significantly altering the power at the experiment table. For the single-site imaging, the  $F$  pumping laser is  $-80$  MHz detuned from the  $F = 7/2 \rightarrow F' = 9/2$  stark-shifted (by the optical lattice)  $D1$  transition, and the  $m_F$  pumping laser is  $-80$  MHz detuned from the  $F = 9/2 \rightarrow F' = 7/2$  stark-shifted  $D1$  transition. The outputs of the  $F$  and  $m_F$  pumping lasers are combined on a non-polarizing beamsplitter cube with the same polarization, and are then sent to the experiment table through the same optical fiber, where they pass through quarter- and half-wave plates for polarization control. They are then combined with the  $x$  Raman beam on another non-polarizing beamsplitter cube, and are subsequently sent through the retro-reflection mirror of the  $x$ -lattice, into the vacuum chamber and to the atoms, propagating in the  $-x$ -direction. The optical

pumping beams are co-aligned with the  $x$ -lattice beam, and reflect from the surface of the substrate at an angle of  $10.8^\circ$  from the  $x - y$  plane. The optical pumping and  $x$  Raman beams, as they enter the vacuum chamber and hit the atoms at the substrate, are depicted in blue in Fig. 3-6(a). The quarter- and half-wave plates which independently control the polarization of the optical pumping light are adjusted to minimize the amount of  $\hat{\sigma}^+$  polarization seen by the atoms at the surface. A detailed description of the  $D1$  optical pumping optics setup, including all the relevant locking frequencies, is given in appendix B.3 of [37]. For reference, we provide here, in Fig. 3-5, the diagram of the optics setup for the offset-lock of the two Toptica DL-Pro lasers to the  $D1$  master laser, which is missing from Fig. B-6 of [37]. As a side note, we have briefly attempted to replace the two DL-Pro ECDLs in the offset-lock setup with Photodigm PH770DBR 770 nm DBR lasers, for better locking stability, but found that the average single-site imaging loss rate increased from  $\sim 5\%$  with the ECDLs, to  $\sim 13\%$  with the DBR lasers. It is currently unclear why the DBR lasers produced a higher single-site imaging loss rate compared to the ECDLs, so for now we continue to operate using the ECDLs.

For the work described in this thesis, the Raman light source used is an M Squared SolsTiS continuous-wave Ti:Sapphire laser operating at 766.857 nm (vacuum wavelength), which is pumped by a Lighthouse Photonics Sprout-G-10W DPSS 10 W, 532 nm laser, and which is detuned from the  $D2$  transition in  ${}^{40}\text{K}$  by approximately  $-80$  GHz. The output of the Ti:Sapph is sent through several optical isolators, and then through a single 80 MHz AOM for controlling the total power (in both the  $x$  and  $y$  Raman beams) of the Raman light. After this AOM, the light is fiber coupled and sent to a separate laser table, where it is split into two paths: one for the  $x$ -Raman light and one for the  $y$ -Raman light. The relative frequencies of the two paths are controlled using multiple AOMs. The  $x$ -Raman light, which controls the first leg of the two-photon transition from  $|F = 9/2, m_F = -9/2\rangle$  to  $|F = 7/2, m_F = -7/2\rangle$ , the two states used in the single-site imaging scheme, has multiple frequency components in order to address the different motional sidebands along the different lattice axes. These multiple frequencies are generated by inputting multiple RF tones into an

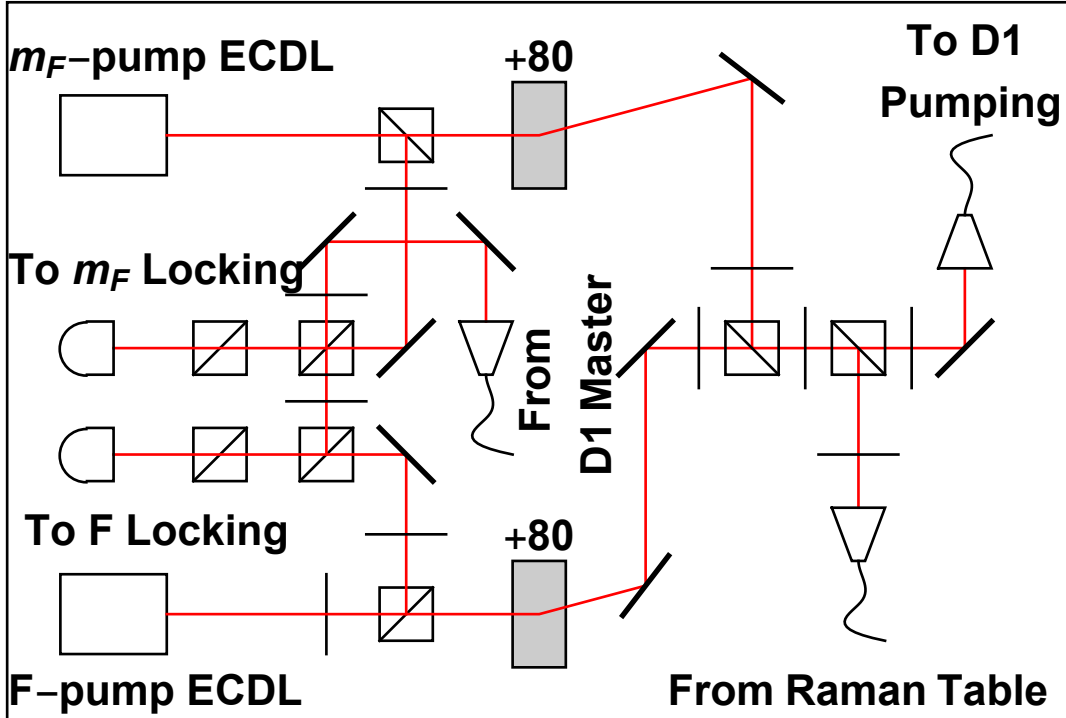


Figure 3-5: Offset-lock laser system for the  $D1$  optical pumping light. Shown is a diagram of the system used to generate the  $F$  and  $m_F$  pumping light for single-site imaging. The two ECDLs are offset-locked to the  $D1$  master, which itself is locked to the cross-over feature of the  $^{39}\text{K}$   $D1$  line. The  $F$  pumping laser is  $-80\text{ MHz}$  detuned from the  $F = 7/2 \rightarrow F' = 9/2$  stark-shifted (by the optical lattice)  $D1$  line in  $^{40}\text{K}$ , and the  $m_F$  pumping laser is  $-80\text{ MHz}$  detuned from the  $F = 9/2 \rightarrow F' = 7/2$  stark-shifted  $D1$  line. The fiber from the Raman table can be used to put Raman light at  $766.857\text{ nm}$  into the optical pumping fiber for alignment of the optical pumping path in the experiment. During normal operation, however, the output of the Raman fiber in this setup is blocked. Frequencies are in MHz. This is the missing Fig. B-6 of [37].

80 MHz double-pass AOM in this path. The output of this double-pass AOM is then fiber coupled, and sent to the experiment table. The other path, for the  $y$ -Raman light, controls the second leg of the two-photon transition from  $|F = 9/2, m_F = -9/2\rangle$  to  $|F = 7/2, m_F = -7/2\rangle$ , and only has a single frequency. This path is approximately 1.3 GHz red detuned relative to the  $x$ -Raman light, in order to address the  $F = 9/2 \rightarrow F = 7/2$  hyperfine splitting in  $^{40}\text{K}$ , and the frequency of this path is controlled with a series of two separate double-pass AOMs. After the frequency is set by these AOMs, this  $y$  Raman path is coupled into a separate fiber, and is also sent to the experiment table. A detailed schematic of the optics setup for the generation

of the Raman light frequencies is given in Fig. B-8 of [37]. On the experiment table, the  $x$  Raman light is combined on a non-polarizing cube with the  $D1$  optical pumping light, and is sent through the retro-reflection mirror of the  $x$  lattice, propagating along the  $-x$ -direction. This is illustrated by the blue solid arrow in Fig. 3-6(a), which demonstrates that this beam reflects from the substrate surface at an angle of  $10.8^\circ$  with respect to the  $x - y$  plane. The polarization of the  $x$ -Raman beam is linear, and parallel to the substrate surface, pointing along the  $y$ -direction, which is orthogonal to the quantization field used for single-site imaging. The  $y$ -Raman beam on the experiment table, on the other hand, is not combined with any light, and simply transmits through the  $y$ -lattice retro-reflection mirror, propagating along the  $+y$ -direction (the same direction as the  $y$  ODT). The way that this beam enters the vacuum chamber and hits the atoms is analogous to the  $x$ -Raman beam (although it enters from an orthogonal axis), which is depicted in blue in Fig. 3-6(a). Just like the  $x$ -Raman beam, the  $y$ -Raman light also reflects from the substrate surface at an angle of  $10.8^\circ$  with respect to the  $x - y$  plane. The polarization of this beam is also linear and parallel to the substrate surface, and points along the  $x$ -axis, parallel to the quantization field used for single-site imaging.

After taking the data for the work described in this thesis (chapters 4 and 5), we decided to replace the Raman light source with a laser that is simpler and easier to work with. Specifically, we replaced the M Squared Ti:Sapph with an interference filter based, Radiant Dyes NarrowDiode ECDL, that operates at the same wavelength (766.857 nm). To increase the optical power emitted from this laser, the light, after passing through an optical isolator, seeds a tapered amplifier (TA) which increases the power to  $\sim 500$  mW. The output of this TA is then sent through another optical isolator, after which it goes through an 80 MHz AOM, which is simply used to control the total optical power in all the Raman beams (just like the setup for the Ti:Sapph). To suppress the broadband amplified spontaneous emission (ASE) from the output of the TA, especially any light at the 766.7 nm  $D2$  resonance, we send the output of the AOM through a heated K vapor cell, which absorbs and suppresses any light near the  $D2$  line. We obtain further suppression of the ASE pedestal after the vapor cell

by sending the beam through an Ondax ASE suppression filter (ASE-766.84) with  $< 0.1$  nm FWHM bandwidth. After the filter, the light is fiber coupled and sent to the other laser table described previously (Fig. B-8 in [37]), where it is split into the  $x$  and  $y$  Raman paths, and where the relative frequencies between the two paths are set by AOMs. Experimentally, we found no detectable difference in the single-site imaging fidelity (in either the average loss rate or the average hopping rate) between this new source for the Raman light, and the previous Ti:Sapph source. Practically speaking, however, it is typically easier to work with, and requires negligible daily maintenance. During operation, we simply let the ECDL free run (no locking) at the desired wavelength, which is sufficiently stable for the purpose of driving two-photon Raman transitions with  $\sim 80$  GHz single-photon detuning from the  $D_2$  line (it does not matter if the laser drifts by  $\sim 1$  GHz for example).

### 3.1.4 High-Resolution Imaging System

The high-resolution imaging system used in our experiment to achieve single-site imaging consists of a large numerical aperture ( $NA$ ) microscope objective combined with an integrated solid immersion lens, which helps eliminate imaging aberrations that can arise from a planar vacuum window. The combination of these two components in the experimental setup is illustrated in Fig. 3-6(a). The solid immersion lens consists of three separate pieces: a fused silica spherical cap with a 9 mm radius of curvature that is optically contacted to the outside of the vacuum window, the 5 mm thick fused silica vacuum window itself, and a 1.8 mm thick, fused silica super-polished substrate which is optically contacted to the inside (the ultra-high vacuum side) of the vacuum window. Each of the three components of the solid immersion lens is also illustrated in Fig. 3-6(a). Together, the spherical cap, the vacuum window, and the super-polished substrate form a hemispheric solid immersion lens that enhances the effective  $NA$  of the imaging system, and minimizes the refraction of light at the air-to-glass interface, which minimizes imaging aberrations. That is, the refraction of light at the vacuum-to-glass interface, which is emitted by atoms located near the surface of the substrate (in reality,  $\sim 13$   $\mu\text{m}$  from the surface), and at the center of the

hemispheric lens, increases the overall light collection angle of the imaging system, which increases the effective  $NA$  by a pre-factor determined by the index of refraction of fused silica,  $n_{FS} \approx 1.46$ . Thus, for a microscope objective with  $NA = 0.6$ , the effective  $NA$  of the imaging system with the solid immersion lens is enhanced and becomes  $NA \approx 0.87$ . Additionally, the light rays, after entering the glass of the solid immersion lens from the atoms at the center of the substrate, exit the lens at the glass-to-air interface with near normal incidence, due to the hemispheric design of the lens, so that the light rays at this interface experience minimal refraction, thereby reducing the aberrations which would normally arise from a planar window. Of course, in the real experiment, the atoms are not touching the surface of the substrate itself, but are actually  $7.1\text{ }\mu\text{m}$  (or  $12.8\text{ }\mu\text{m}$  for the spin transport data of chapter 5) away in order to reduce the effects of surface potentials on the atoms. This finite distance of the atoms from the center of the solid immersion lens increases the imaging aberration due to finite refraction at the glass-to-air interface, but is necessary in order to isolate the ultracold system from the glass material itself. The substrate is coated with an anti-reflective coating which is optimized for transmission at normal incidence of the wavelengths  $589\text{ nm}$ ,  $671\text{ nm}$ , and  $767\text{ nm}$ , in order to reduce loss of the emitted light at the glass surface, and is simultaneously coated with a high-reflectivity coating that is optimized to reflect the lattice laser beams at  $1064\text{ nm}$  for both normal incidence, and  $10^\circ$  incidence relative to the substrate surface.

The microscope objective we utilize in our experiment is a commercial (non-custom) objective from Edmund Optics, an EO 20X HR Infinity Corrected Objective, with  $NA = 0.6$ , a  $10\text{ mm}$  effective focal length, a  $13\text{ mm}$  working distance, and a  $\approx 2.1\text{ }\mu\text{m}$  depth of focus at  $770\text{ nm}$  (which is reduced to  $\approx 1\text{ }\mu\text{m}$  depth of focus with the enhanced  $NA$  of the solid immersion lens). This objective is mounted to the vacuum chamber above the solid immersion lens, and is attached to a Newport three-axis steel translation stage that is controlled by Newfocus Picomotor piezo actuators, which allows for fine tuning of the focusing of the objective (the  $z$ -axis), as well as the  $x$  and  $y$  positioning of the objective, in order to center it, in the horizontal plane, on the center of the solid immersion lens. The tilt of the objective with respect to the

surface of the substrate is not adjustable, and is mechanically fixed by the mounting of the objective to the vacuum chamber. Because the effective  $NA$  of the imaging system is enhanced by the fused silica solid immersion lens, we achieve an improvement in the diffraction limit of the imaging,  $d \approx 0.61\lambda/(NA)$ , which, for  $NA \approx 0.87$  and  $\lambda = 770\text{ nm}$  (the  $D1$  line of  $^{40}\text{K}$ ) is  $d \approx 540\text{ nm}$ , as well as an improvement in the overall collection efficiency of the emitted light (we achieve approximately a 25% collection efficiency), which increases the signal-to-noise ratio in a given image.

The light emitted by the atoms near the surface of the substrate at 770 nm, which is collected by the solid immersion lens and the high- $NA$  objective, is imaged onto an Andor iXon Ultra 897 EMCCD camera, which is thermoelectrically cooled to  $-70^\circ\text{C}$ , with a magnification of  $\approx 89$ . The pixel size of the camera is  $16\text{ }\mu\text{m}$  per pixel (the camera chip has  $512 \times 512$  pixels), which, when combined with the magnification of the imaging system, yields approximately  $3 \times 3$  camera pixels per 541 nm lattice site. Taking into account the finite quantum efficiency of the camera ( $\approx 0.85$  at 770 nm), and the light which is lost throughout the remainder of the imaging path, the overall collection efficiency of the imaging system is approximately 20%. For the imaging process itself, we run the camera in frame transfer mode without electron multiplication, which allows us to take many images in quick succession (without waiting for the full read-out time of the entire chip), in order to characterize the detection fidelity of the imaging through, for example, the number of sites where atoms are lost between subsequent frames. For a more detailed description of the high-resolution imaging system, including specifics of the coatings/flatness of the solid immersion lens, the optical contacting and assembly process, and diagrams of the optics involved in the final imaging setup onto the Andor camera, see chapter 7 of [73] and sections 4.2 and 4.6 of [37].

## 3.2 Single-Site Imaging

In order to detect single atoms in the lattice during the imaging process, in a way that allows us to reliably reconstruct the *in situ* occupation of each lattice site, we must si-

multaneously laser cool the atoms at each site while performing fluorescence imaging, to counteract the recoil heating that arises from the spontaneous emission of photons during the fluorescence process. For different atomic species used in other quantum gas microscope experiments, including  $^{87}\text{Rb}$  and Yb, it is possible to collect fluorescence for imaging while laser cooling the atoms using an optical molasses [16, 209, 154]. However,  $^{40}\text{K}$  has several issues regarding its internal structure in a deep 1064 nm optical lattice that makes laser cooling via an optical molasses extremely challenging. The first is the fact that both the  $D1$  and  $D2$  electronic excited states,  $4P_{1/2}$  and  $4P_{3/2}$ , respectively, experience an anti-trapping potential in the 1064 nm optical lattice that is approximately 5.1 times stronger than the trapping potential experienced by atoms in the ground state,  $4S_{1/2}$ . Such a strong anti-trapping potential arises from the  $4P_{3/2} \rightarrow 3D_{3/2}$ ,  $4P_{3/2} \rightarrow 3D_{5/2}$ , and  $4P_{3/2} \rightarrow 5S_{1/2}$  transitions for the  $4P_{3/2}$  excited state, which lie at 1177.29 nm, 1177.61 nm, and 1243.57 nm, respectively, as well as the  $4P_{1/2} \rightarrow 3D_{3/2}$  and  $4P_{1/2} \rightarrow 5S_{1/2}$  transitions for the  $4P_{1/2}$  excited state, which lie at 1169.34 nm and 1252.56 nm, respectively. Because of the presence of these lines, the optical lattice is only  $\sim 100$  nm blue-detuned with respect to these transitions, which, on top of the usual anti-trapping arising from the coupling to the ground state  $4S_{1/2}$  by the 1064 nm light (the  $D1$  and  $D2$  transitions lie at 770.11 nm and 767.7 nm, respectively), leads to the approximately 5.1 times stronger anti-trapping potential experienced by atoms in  $4P_{1/2}$  and  $4P_{3/2}$ , relative to the trapping potential experienced by atoms in  $4S_{1/2}$ . Such a strong anti-trapping potential in the 1064 nm optical lattice can cause issues during an optical molasses, which requires atoms to spend significant time in the excited state. Specifically, an anti-trapping potential can cause heating and diffusion of the atoms in the lattice any time they enter the excited state, which can destroy the information one is trying to obtain, the *in situ* density distribution of the original quantum system. Because the lattice depths required to prevent atoms from moving around over the time it takes to acquire an image lead to highly stark shifted excited states, on the order of 60 MHz for the depths used in this experiment, such heating caused by dispersion of the wave packet while in the excited state can become extremely significant, and so a typical optical molasses

becomes ineffective.

The second issue regarding  $^{40}\text{K}$  in a 1064 nm optical lattice that renders an optical molasses challenging is the strong mixing between hyperfine states in the  $4P_{3/2}$  electronic excited state manifold. This arises from the fact that the stark shift experienced by atoms in the  $4P_{3/2}$  state at the imaging depth of the optical lattice, which can reach nearly 60 MHz, is comparable to, or even larger than, the hyperfine splitting between different  $F$  manifolds in the  $4P_{3/2}$  state, which is at most 45 MHz, for the  $F' = 11/2 \leftrightarrow F' = 9/2$  splitting. Thus, the  $D2$  excited state can become highly mixed in a deep lattice, such that even different  $F$  manifolds can be mixed together. This means that neither  $F$  nor  $m_F$  are good quantum numbers in the deep lattice, so that the normal selection rules for  $F$  and  $m_F$  changing transitions no longer apply. Therefore, the effectiveness of an optical molasses (and even normal optical pumping on the  $D2$  line), which requires a certain degree of selectivity in the allowed transitions that can be driven by the molasses beams, can be severely impacted due to the presence of the deep lattice. A more detailed discussion of the effects of the 1064 nm lattice on  $^{40}\text{K}$  can be found in section 5.2 of [37].

Because we could not change the lattice wavelength used for single-site imaging without making significant alterations to the experiment (for example, the substrate is only designed with a high-reflectivity coating for 1064 nm), we decided to use 3D Raman sideband cooling [157, 86, 233, 117, 87, 163, 116, 224, 181, 245] as the laser cooling technique utilized for single-site imaging, which allows one to circumvent the issues which impact the effectiveness of an optical molasses. This is not the only available option, however, since a separate laser cooling technique, EIT cooling, has also been used successfully for single-site imaging of  $^{40}\text{K}$  in a 1064 nm lattice [85, 58]. For Raman sideband cooling in a deep optical lattice, where the optical potential experienced by the atoms at each site is approximately harmonic in all directions, two Raman beams drive vibrationally lowering transitions between two internal states of the atom through a coherent two-photon process. When combined with optical pumping that brings the atom back to the original internal state, without altering the vibrational quantum number in the lattice potential, this technique cools the atom

towards its motional ground state in the harmonic potential of the lattice site, while scattering photons during the optical pumping process which can be collected for single-site imaging. Although one could use this, in principle, to achieve near unity occupancy of the 3D motional ground state in the lattice potential with sufficient cooling power, the atoms would become dark to the imaging light once they reach the ground state, which would mean that the photon scattering rate would drop, so that the imaging would no longer work well. We thus optimize the Raman sideband cooling/imaging in our experiment for imaging fidelity, which requires photon scattering, rather than for pure cooling. Regardless of this, however, by measuring the ground state fraction after performing single-site imaging, we still find that approximately 72(3)% of the atoms occupy the 3D motional ground state of their respective lattice site [40].

The details of our Raman sideband cooling based fluorescence imaging technique are described in detail in [40], and have been discussed in previous theses [37, 168], so we only give here a short summary of how we implement the technique in the experiment, and how we can use the resulting images to reconstruct the parity-projected *in situ* occupation of each lattice site. To conduct the single-site imaging, we increase the depths of the lattices along the  $x$ ,  $y$ , and  $z$ -directions to  $\sim 1000E_R$  each. We do this using the depths of the  $x$  and  $y$  lattice beams, shown in red in Fig. 3-6(a), which predominately control the lattice depths in the  $x$  and  $y$ -directions (with some contribution to the depth in the  $z$ -direction as well). To provide tighter confinement in the vertical direction during imaging, we turn on an additional vertical lattice beam, the  $z$ -lattice beam, which is not present during the Hubbard simulation portion of the sequence, and which is also shown in red in Fig. 3-6(a). At such deep lattice depths, the potential experienced by the atoms at each lattice site is approximately harmonic, with harmonic trapping frequencies in each direction given by  $(\omega_x, \omega_y, \omega_z) = 2\pi \times (280, 300, 260)$  kHz for our experimental parameters. While the lattices are ramping up, we simultaneously apply a 4.2 G bias field along the  $x$ -direction using the bias  $x$  coil, which allows us to isolate a single two-level system for the Raman sideband cooling, formed from two different internal hyperfine states

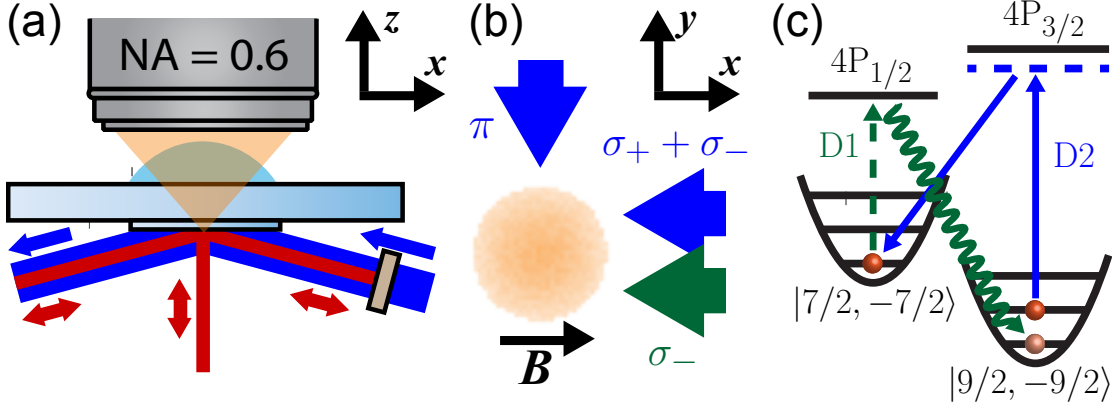


Figure 3-6: High-resolution imaging setup and illustration of the Raman sideband cooling scheme. (a) Illustration of the high-resolution imaging setup, including the  $NA = 0.6$  commercial microscope objective and the solid immersion lens, which is formed from a spherical cap and a super-polished substrate that are optically contacted to opposing sides of the vacuum window. The solid immersion lens enhances the effective  $NA$  of the imaging system from 0.6 to 0.87. The optical lattice beams used for single site imaging are shown in red: the vertical red beam represents the  $z$ -lattice and the horizontal red beam, which reflects from the substrate at a shallow angle before being retro-reflected, is the  $x$ -lattice. The optical pumping and  $x$ -Raman beams, which transmit through the  $x$ -lattice retro-reflection mirror, are shown in blue. (b) View of the Raman and optical pumping beams (and their respective polarizations) from the top. The blue arrows represent the Raman beams, the green arrow denotes the optical pumping beam, and the black arrow is the direction of the magnetic bias field. (c) Illustration of the Raman sideband cooling scheme used for single-site imaging. The Raman light (blue) is tuned near the  $D_2$  line, and coherently drives vibrationally lowering transitions in the deep lattice, while simultaneously changing the atom's internal state. The  $F$ -pumping beam (dashed green line) is tuned near the  $D_1$  line, and recycles the atom back to the original internal state without altering its vibrational quantum number. The  $m_F$ -pumping beam is not shown in this diagram. Figure reproduced from [40].

of  $^{40}\text{K}$ ,  $|F = 9/2, m_F = -9/2\rangle$  and  $|F = 7/2, m_F = -7/2\rangle$ . The energy separation between these two hyperfine states is non-degenerate with other hyperfine transitions because of the 4.2 G field, so that we can effectively address only these two levels. Additionally, this bias field, which is shown in Fig. 3-6(b), provides a quantization axis for the Raman sideband cooling and optical pumping.

Once the lattices have reached their final depth, and the magnetic field has stabilized, we turn on the single-site imaging beams, which consist of two Raman beams, and one optical pumping beam with multiple frequencies. For our Raman sideband

cooling scheme, both the optical pumping and Raman beams are on continuously, and are turned on simultaneously. The optical pumping beam is combined on a non-polarizing beamsplitter cube with one of the Raman beams, and both propagate along the  $-x$ -direction. These two beams transmit through the retro-reflection mirror of the  $x$ -lattice beam, and are co-aligned with this beam. They therefore reflect from the substrate surface at a  $10.8^\circ$  angle with respect to the  $x - y$  plane. The second Raman beam propagates along the  $y$ -direction (the same direction as the plug and the  $y$  ODT), and transmits through the  $y$ -lattice retro-reflection mirror: it is co-aligned with the  $y$ -lattice beam and therefore also reflects from the substrate at a  $10.8^\circ$  angle with respect to the  $x - y$  plane. The imaging beams are represented in blue in Fig. 3-6(a). We send the Raman and optical pumping light through the lattice retro-reflection mirrors to avoid back-reflections from the surface of this mirror, which can create an in-plane lattice for the imaging light, which is not commensurate with the pinning lattice. The Raman light used in our experiment, which couples the two internal states  $|F = 9/2, m_F = -9/2\rangle$  and  $|F = 7/2, m_F = -7/2\rangle$ , by driving vibrationally lowering transitions from  $|F = 9/2, m_F = -9/2\rangle$  to  $|F = 7/2, m_F = -7/2\rangle$ , has a typical single-photon detuning of  $-80$  GHz with respect to the  $D2$  line of  ${}^{40}\text{K}$  (this is an updated value which is slightly larger in magnitude than the previous number provided in [40]). Specifically, we typically run the Raman light at a wavelength (in vacuum) of  $766.857$  nm. This is illustrated in Fig. 3-6(c) with blue arrows. Using two-photon Raman transitions for cooling allows us to avoid the issues of the anti-trapping potentials, as well as the strong mixing of hyperfine states in the  $4P_{3/2}$  manifold, since the admixture of the excited states during the coherent two-photon transition scales as  $1/\Delta^2$ , where  $\Delta = -80$  GHz is the single-photon detuning of the Raman light. The two-photon Rabi frequency, on the other hand, scales as  $1/\Delta$ , so that, by increasing the Raman beam powers to maintain a fixed two-photon Rabi frequency, one can essentially eliminate the excited state admixture during the two-photon transition by increasing the single-photon detuning of the Raman light, which therefore makes the deleterious effects of the excited state in the lattice negligible during this process. In the experiment, the  $x$  Raman beam drives the first leg of

the two-photon transition from  $|F = 9/2, m_F = -9/2\rangle$  to  $|F = 7/2, m_F = -7/2\rangle$  in Fig. 3-6(c), and contains multiple frequencies (controlled by sending multiple RF tones into an AOM which shifts the frequency of this beam) to address the different motional sideband frequencies along the different axes. We currently use two frequencies in this beam: one to address the  $x$  and  $y$  sideband frequencies, and one to address the  $z$  sideband frequency. We make up the difference between the  $x$  and  $y$  sidebands by modulating this sideband frequency using triangle wave frequency modulation at 10 kHz modulation frequency and 40 kHz amplitude. Such a modulation also allows us to increase the region where the single-site imaging works well, by making up for variations in the single-site trapping frequencies across a large cloud arising from spatial intensity variation of the lattice beams themselves across the cloud. We thus also modulate the  $z$ -sideband frequency with the same modulation parameters to achieve a similar purpose. The beam intensity of the  $x$  and  $y$  frequency components of the  $x$  Raman beam is approximately five times larger than that of the  $z$  frequency component, and is roughly  $1.46 \text{ W/cm}^2$ , whereas the  $z$  frequency component is roughly  $0.29 \text{ W/cm}^2$ . The  $y$  Raman beam, on the other hand, has only a single frequency, and addresses the second leg of the two-photon transition from  $|F = 9/2, m_F = -9/2\rangle$  to  $|F = 7/2, m_F = -7/2\rangle$ , while the intensity of this beam is roughly  $2.0 \text{ W/cm}^2$ . The polarizations of both the  $x$  and  $y$  Raman beams are linear, and are parallel to the surface of the substrate: the  $x$  Raman beam is linearly polarized along the  $y$ -direction, orthogonal to the quantization axis, which means it has both a  $\hat{\sigma}^+$  and a  $\hat{\sigma}^-$  component, whereas the  $y$  Raman beam is linearly polarized along the  $x$ -direction, meaning it has  $\hat{\pi}$  polarization. This is illustrated in Fig. 3-6(b). The  $\hat{\sigma}^+$  component of the  $x$  Raman beam is necessary to drive the  $\Delta m_F = +1$  transition required to bring the atom from  $|F = 9/2, m_F = -9/2\rangle$  to  $|F = 7/2, m_F = -7/2\rangle$ , since the  $\hat{\pi}$  leg of the  $y$  Raman beam does not change  $m_F$ , whereas the  $\hat{\sigma}^-$  component of the  $x$  Raman beam is off-resonant with the transition, and essentially does nothing. It is useful to work with linear polarizations for the Raman beams, however, since circularly polarized light would create a differential effective magnetic field for the  $|F = 9/2, m_F = -9/2\rangle$  and  $|F = 7/2, m_F = -7/2\rangle$  states due to vector light shifts. For reference, given the

on-site trapping frequencies along the three axes, combined with the wavelength and incident angles of the Raman beams, we can determine the Lamb-Dicke parameter, which acts as a proportionality factor in determining the two-photon Rabi coupling for a transition between hyperfine states that lowers the vibrational quantum number by one, and is given by,

$$\eta = \Delta k \sqrt{\frac{\hbar}{2m\omega}}, \quad (3.1)$$

where  $\hbar\Delta k$  is the momentum transferred by the two Raman beams during the two-photon process. For our experimental parameters, the Lamb-Dicke parameters along the three axes are given by  $(\eta_x, \eta_y, \eta_z) = (0.17, 0.17, 0.068)$ .

Once the Raman beams have lowered the vibrational quantum number along some axis by one, and have simultaneously changed the hyperfine state of the atom, the cycle must be completed by optically pumping the atom back from  $|F = 7/2, m_F = -7/2\rangle$  to  $|F = 9/2, m_F = -9/2\rangle$ , so that the Raman cooling may continue. Here, we optically pump on the *D*1 line of  ${}^{40}\text{K}$ , which is 3 nm away from the *D*2 Raman light, and which is illustrated in Fig. 3-6(c). This is useful for two reasons: the first is that because of the different wavelengths between the *D*1 and *D*2 lines, we can spectrally separate any scattered Raman light before it hits the imaging camera using dichroic filters that transmit 770 nm light, but reject 767 nm light. Thus, when we collect the spontaneously emitted photons on the *D*1 line from the optical pumping step of the Raman sideband cooling process for single-site imaging, we can significantly reduce the background in the image caused by the Raman light which is scattered from the substrate surface, and which could reach the camera. The second reason it is beneficial to optically pump on the *D*1 line is that it avoids the issue associated with the coupling between different hyperfine states in the  $4P_{3/2}$  level (arising from tensor light shifts from the intense lattice beams), which affects the selection rules for different transitions, and which therefore impacts the efficacy of the optical pumping. For the  $J = 1/2$  case of the *D*1 state  $4P_{1/2}$ , one can avoid such coupling between hyperfine states by using linear polarizations for the lattice beams, which eliminates any effective magnetic field which could arise in the presence of the lattice beam

light field, so that the usual transition selection rules still apply. Of course, optically pumping on the  $D1$  line still has the issue of strong anti-trapping in the excited state, due to the fact that atoms must occupy the excited state during the optical pumping process, before they can spontaneously decay back to the desired state. To avoid this issue, one can detune the optical pumping light away from resonance, which selectively enhances the rate of transitions into trapped, rather than un-trapped, states, and also minimizes the steady-state population in these un-trapped states. The physical reasoning behind this is explained in detail in the supplementary material of [40] and section 5.3.2 of [37]. In our experiment, the optical pumping light, which propagates in the  $-x$ -direction with the  $x$  Raman beam, is optimized to have mostly  $\hat{\sigma}^-$  polarization, as shown in Fig. 3-6(b), and has two frequencies, one to bring the atoms from  $F = 7/2$  to  $F = 9/2$  (the  $F$ -pumping light) and one to change the  $m_F$  state of the atom to  $m_F = -9/2$  (the  $m_F$ -pumping light). Experimentally, we find that the optimal optical pumping parameters are such that the  $F$ -pumping light is detuned by  $-80$  MHz from the stark-shifted  $F = 7/2 \rightarrow F' = 9/2$  resonance (the detuning is to avoid the anti-trapped excited state issue), whereas the  $m_F$ -pumping light is detuned by  $-80$  MHz from the stark-shifted  $F = 9/2 \rightarrow F' = 7/2$  resonance. The logic behind these choices for the  $F$ -pumping and  $m_F$ -pumping transitions is explained in detail in section 5.4.2 of [37]. The intensities of the two beams used in the experiment are roughly  $5.8\text{ mW/cm}^2$  for the  $F$ -pumping light, and  $1.6\text{ mW/cm}^2$  for the  $m_F$ -pumping light, where each beam has a waist of approximately  $200\text{ }\mu\text{m}$ . The Lamb-Dicke parameter for the optical pumping is  $\eta = 0.18$  for all directions. Further details regarding the single-site imaging scheme, including diagrams of the optics setups for the Raman and optical pumping light, and specifics about the locking of the  $D1$  optical pumping lasers can be found in chapter 5 and appendix B of [37].

With these roughly optimized imaging parameters, we can collect the spontaneously emitted photons from the  $D1$  optical pumping on our Andor camera to take high-quality single-site fluorescence images of atoms in the lattice. An example image is shown in Fig. 3-7. For a  $1\text{ s}$  exposure, we collect roughly 1000 photons per atom, which, with the 20% light collection efficiency of the high-resolution imaging setup,

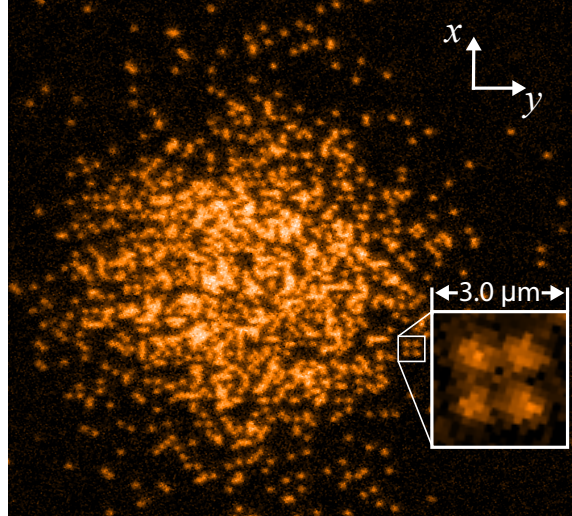


Figure 3-7: Site-resolved fluorescence image of  $^{40}\text{K}$  atoms in a square optical lattice. The image shown here is a fluorescence image of atoms in a square lattice with spacing 541 nm, taken using Raman sideband cooling for an exposure time of 2 s. The parameters associated with the imaging and cooling process are optimized for high-fidelity read-out of the *in situ* atomic density distribution. The inset shows a magnified view of four atoms sitting on the corners of a square  $3 \times 3$  grid. The empty sites between the atoms can be observed clearly, demonstrating the high-spatial resolution of the imaging, and its ability to detect single atoms. Figured reproduced from [40].

corresponds to a photon scattering rate of roughly 5000 photons per second per atom. During typical operation, we use a 2.5 s exposure, which does not significantly affect the overall imaging fidelity, but improves the measured signal, and therefore reduces the probability of reconstruction errors. We can measure the point spread function (PSF) of the imaging system using isolated atoms in dilute samples in order to estimate the imaging resolution. The inset to Fig. 3-8(a) shows the average image of several such isolated atoms, and the main part of Fig. 3-8(a) shows the radial average of this image, which represents the radially averaged PSF. From the full-width at half-maximum of Fig. 3-8(a), one can estimate the imaging resolution, which we measure to be 640 nm, slightly larger than the 541 nm lattice spacing. However, because we do not need to determine the exact location of neighboring atoms (we know exactly how the space is divided up into a grid by the square lattice), but simply whether a site is occupied by an atom or not, this imaging resolution is sufficient,

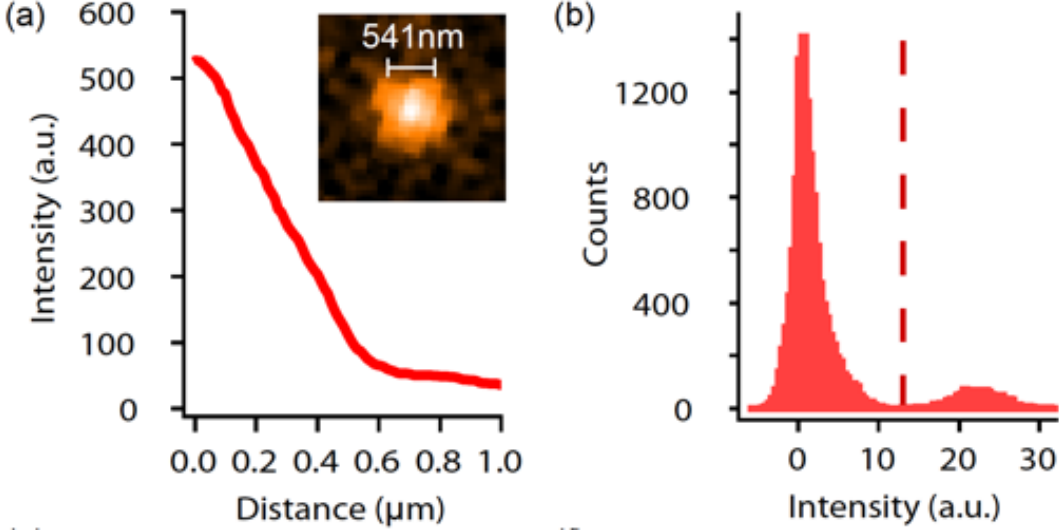


Figure 3-8: Measuring the point spread function of the imaging system and the intensity histogram of the observed fluorescence. (a) Inset: Averaged point spread function obtained from the fluorescence of isolated atoms in dilute samples. The main figure is the radial average of the PSF shown in the inset. This radial average is fit to a double Gaussian distribution, which is used to extract the PSF FWHM of 640 nm. (b) Fluorescence intensity histogram obtained by binning the deconvoluted image into the individual lattice sites. The intensity threshold used in the reconstruction process to determine whether or not a site is occupied is represented by the vertical dashed red line. The exposure time for the plots in (a) and (b) is 1 s, and the images used to generate them are taken in the vertical layer which sits 7.1  $\mu\text{m}$  from the substrate surface. Figured reproduced from [40].

with a large enough signal-to-noise ratio, to achieve single lattice site resolution after deconvolution of the image with the measured PSF (Fig. 3-8(a) inset). Specifically, we first deconvolve a given fluorescence image (which itself can be used to determine the lattice axes and the lattice spacings on the camera) by the measured PSF using a Weiner deconvolution algorithm [37], from which we can then determine the phases of the lattices in the  $x$  and  $y$ -directions. Once the lattice phase is determined, we can bin the intensity of the deconvolved image into each lattice site, which allows us to form a histogram of the counts in each bin. This is shown in Fig. 3-8(b), which reveals a clear bimodal distribution. The large peak near zero intensity corresponds to no atoms, or empty sites, and the smaller peak at finite intensity represents sites occupied by single atoms. From such histograms, we find no evidence of a third peak which would correspond to doubly occupied sites. We also find no evidence of the recapture of

atoms in the Raman sideband cooling, which have been ejected via light-assisted collisions during the imaging process, and are subsequently re-cooled and imaged before they can escape the trap (see, for example, section 4.3 of [235]). The imaging thus effectively removes doubly-occupied sites via light-assisted collisions [52], without the necessity of a push-out light pulse, so that we image only singly-occupied sites, and doublons and holes both appear as empty sites. Once we have the histogram of a given image, we can set a threshold at the minimum between the empty and occupied histogram peaks, such that any site whose binned image counts lie above the threshold is considered occupied, and any site whose counts lie below the threshold is considered empty. This process is illustrated in Fig. 3-9, which shows the raw image (with the reconstructed lattice superimposed), the deconvolved image, and the sites which have been determined to be occupied using the threshold in the corresponding histogram. Therefore, because we can measure the lattice phase from the deconvolved image, and we can also determine the occupation of each site from the binned histogram, we can fully reconstruct the site-resolved, parity-projected (due to the loss of doubly occupied sites during the imaging), *in situ* density distribution of the system. Details of the image deconvolution process, the determination of the lattice angles and spacings, and the determination of the lattice phase can be found in section 5.5 of [37]. To determine the single-site imaging fidelity, we take many subsequent images of the same sample, and record any changes in the detected site-occupations. For example, if a site was occupied in one frame, and is empty in a subsequent frame, we can consider this as an event where an atom is lost. If, on the other hand, a site becomes occupied in one frame, where it was previously empty, we can classify this as an event where an atom hopped between sites. We can therefore estimate the loss and hopping rates which occur during the imaging process by determining the number of occurrences of each type of event between neighboring images, and normalizing by the total detected atom number. For typical exposure times of 2.5 s, we measure average loss rates of < 5%, and average hopping rates of < 1%. Given these rates, which also include any reconstruction errors, we can estimate the overall detection fidelity of the single-site imaging to be  $\sim 95\%$  for our optimized imaging parameters.

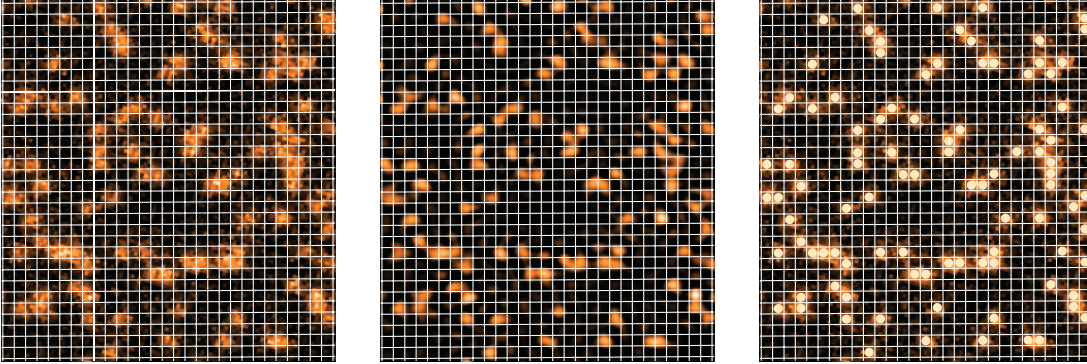


Figure 3-9: Identification of occupied lattice sites from a raw fluorescence image. The left-most figure shows a raw fluorescence image, with a 1 s exposure time, of a dilute sample of atoms in a single vertical layer of a square optical lattice, which is located vertically  $7.1 \mu\text{m}$  from the substrate surface. The underlying square lattice, whose phase is determined from the deconvoluted image, is overlaid on top of the raw fluorescence image, and is illustrated by the white grid lines. The middle figure is the same image of the same sample, but after the raw image has been deconvolved with the PSF (Fig. 3-8(a)). After binning the deconvoluted image into each lattice site, the occupation of a given site is determined by a threshold in the intensity histogram (Fig. 3-8(b)). The right-most figure shows the same raw fluorescence image as the left-most figure, with the overlaid square lattice, where a white dot has been placed in the center of each site that has been identified by the reconstruction algorithm as occupied by an atom. Figure reproduced from [40].

From the finite exposure time, we expect that roughly  $1 - 2\%$  of the residual loss rate arises from collisions with background gas in the vacuum chamber.

### 3.2.1 Imaging a Different Vertical Layer of the Optical Lattice

Due to the presence of strong surface potentials observed in the layer of the vertical lattice located  $7.1 \mu\text{m}$  from the surface of the substrate (see appendix A of [168]), we decided to change the vertical layer in which we prepare and image the atoms, so that the atoms were further away from the surface. This was done between the equilibrium spin correlation work of [38], and the spin transport work of [164], in April and May of 2017. The surface patch potentials, which could severely affect the shape of the atomic distribution in the lattice, so that the cloud was no longer radially symmetric (nor even elliptical for that matter), and which could also affect the final temperatures we could reach, by impacting the efficiency of the final stage

of optical evaporation, were temporarily mitigated by applying UV light for several minutes to the substrate surface. Specifically, we used a Thorlabs M365LP1, 365 nm, 1150 mW UV LED, collimated to a diameter of  $\sim 40$  mm, which we sent from the bottom of the chamber, along the same path as the vertical 1064 nm  $z$ -lattice, to illuminate the entire substrate surface. We did this in the same spirit as the UV desorption technique used to increase the flux from the K 2D MOT [2, 123], which desorbs K atoms that have been adsorbed to the glass surface of the 2D MOT cell (see section 3.3), thinking that the source of the surface potentials was atoms (either Na or K atoms, or possibly even atoms that were accidentally oblated from the in-vacuum RF antenna by the high power 1064 nm ODTs or the 10 W 532 nm plug) stuck to the substrate surface. After shining the UV light on the substrate surface for several minutes, and subsequently re-imaging the atoms in the lattice at a particular value of the Hubbard parameters  $U/t$ , we found that the radially symmetric cloud shape was restored (at least temporarily), and that the temperature of the cloud (based on the average local moment at half-filling) had also improved. However, as time progressed, we found that the UV cure (which we typically needed to apply 1 – 2 times per day) became less and less effective, and required longer and longer UV exposures to fix the cloud shape, until eventually the UV light no longer seemed to sufficiently fix the problem. At this point, we decided to move the atoms further away from the substrate surface, to a different vertical layer of the optical lattice, where the effects of the surface potentials would be significantly smaller. It was (and still is) unclear, however, whether the potentials were due to atoms on the substrate surface, which might produce a Van der Waals, or  $1/r^6$  type potential, or if they were due to something worse, like surface charges or magnetic particles stuck to the surface, which could produce longer range potentials.

When moving to a different vertical layer of the optical lattice, there are several considerations to keep in mind. First is the fact that the physics lattice, formed by the retro-reflected  $x$  and  $y$  lattice beams, which both reflect from the substrate at a  $10.8^\circ$  incident angle, form a vertical lattice themselves (due to the substrate reflection) of spacing  $2.84\ \mu\text{m}$ . Second, the shallow angle beam, which is used for the final stage

of optical evaporation before transferring the atoms to a single vertical layer of the  $x$  and  $y$  lattice beams, forms its own vertical lattice (which provides the vertical confinement during the final stage of optical evaporation), due to the reflection of this beam from the substrate surface at a  $5.8^\circ$  angle. The spacing of the shallow angle beam vertical lattice is  $5.26\ \mu\text{m}$ . One must therefore choose a vertical layer of the  $x$  and  $y$  lattice beams for physics and imaging which has good overlap with a layer of the shallow angle beam. We can easily control which layer of the shallow angle beam we populate using the accordion beam, by adjusting how close to the surface we move the atoms in the final stage of vertical optical transport using the galvo mirror of the accordion. A third consideration in choosing the location of the vertical layer is the fact that the single-site imaging beams, the  $x$  and  $y$  Raman beams and the optical pumping beam, also reflect from the substrate surface at a  $10.8^\circ$  angle, and can therefore also form vertical lattices with spacing  $2.05\ \mu\text{m}$  and  $2.06\ \mu\text{m}$  for the Raman and optical pumping light, respectively. One must therefore make sure that the layer chosen for imaging does not sit at a minimum in the intensity of either of the imaging beams. Finally, one cannot move the atoms arbitrarily far from the substrate surface because the imaging aberrations become worse the further away the atoms are from the substrate. Additionally, the power of all of the optical beams, including the lattices and the shallow angle beam, decreases with increasing distance from the substrate, due to the finite size of these beams, so that more optical power is required to achieve, for example, the same lattice depth in the  $x$  and  $y$  lattices for single-site imaging. Thus, one can also be limited in how far away one can move from the surface by the available power in these different beams.

With these different considerations in mind, we decided to use the layer of the  $x$  and  $y$  lattice beams located  $12.8\ \mu\text{m}$  from the substrate surface. This layer has good overlap with a layer of the shallow angle beam, located  $13.16\ \mu\text{m}$  from the surface, making the transfer between these two beams straight forward. It also has good overlap with any vertical lattice formed by the Raman and optical pumping beams for single-site imaging, whose intensity maximum is located  $13.3\ \mu\text{m}$  from the surface. However, once we successfully populated this single layer of the optical lattice, we

quickly found that we had to re-optimize the parameters of the single-site imaging. Specifically, we first had to move the focus of the microscope objective down by  $5.7\text{ }\mu\text{m}$ , which is controlled by the vertical translation stage where the objective is mounted, and the picomotor piezo actuators that alter the position of this stage. This brought the atoms back in to focus, but the loss rate for the imaging was also abnormally high. We then had to slightly increase the powers of the  $x$ ,  $y$ , and  $z$  lattice beams during the single-site imaging to compensate for the slight decrease in power at the new position further from the surface, and to bring the on-site trapping frequencies in the imaging lattice back to their original values, where the single-site imaging parameters were previously optimized. We also had to adjust slightly the powers of the Raman beams and the optical pumping beams to account for the slightly different vertical position of the atoms in the imaging lattice relative to the intensity maximum of the Raman and optical pumping vertical lattices (meaning the atoms saw a slightly different intensity of these beams compared to the previous layer). In this case, we only needed to adjust the overall powers of the Raman and pumping beams (in reality, the final optimized values of both sets of beams are very similar to the optimized values in the previous layer), where the relative power between the different Raman sidebands, and between the  $F$  and  $m_F$  pumping light remained fixed. Additionally, neither the single photon detuning of the Raman light, nor the detuning of the optical pumping light from resonance needed to be changed. Other than the lattice beam powers, which fixed the on-site trapping frequencies to be their original values,  $(\omega_x, \omega_y, \omega_z) = 2\pi \times (280, 300, 260)\text{ kHz}$ , and the small changes to the Raman and optical pumping beam powers, the main alteration which was necessary to reduce the single-site imaging loss rate was a re-optimization of the optical pumping light polarization to minimize the amount of  $\hat{\sigma}^+$  polarization at the new location of the atoms. Such a re-optimization of the polarization, which was done using a combination of quarter- and half-wave plates specific to the optical pumping light path, was necessary because of the reflection of the optical pumping light from the substrate surface, where the polarization of the reflected light at the  $10.8^\circ$  incident angle is not purely  $\hat{\sigma}^-$ , even if the incoming light is, due to the different reflection

coefficients of the dielectric coating on the substrate for polarizations parallel and perpendicular to the surface. Therefore, due to the different polarizations, intensities, and phases between the incoming and reflected beams at this  $10.8^\circ$  angle, and the interference of these beams at the position of the atoms, the actual polarization experienced by the atoms can change significantly with vertical distance from the substrate, and so the incoming polarization must be adjusted to compensate for this fact, and to minimize the amount of  $\hat{\sigma}^+$  optical pumping light seen by the atoms.

After adjusting these imaging parameters, the single-site imaging fidelity previously achieved in the  $7.1\ \mu\text{m}$  layer was restored, so that we again observed average loss rates of  $< 5\%$ , and average hopping rates of  $< 1\%$  between neighboring images taken of the same sample in succession, in the new  $12.8\ \mu\text{m}$  layer. However, because of the new vertical position of the imaging, we had to re-calibrate the rotation angle of the image on the camera, to properly identify the angles of the lattice axes with respect to the camera, as well as to measure the new magnification, determined by the observed lattice spacing (after properly rotating the image to align with the lattice axes) in the raw fluorescence image. An outline of this procedure is given in section 5.5.1 of [37]. The new rotation angles for the  $12.8\ \mu\text{m}$  layer are measured to be  $17.498(0.002)^\circ$  for the  $x$ -lattice, with a corresponding lattice spacing of 3.0494 pixels on the camera, and  $17.084(0.0066)^\circ$  for the  $y$  lattice, with a corresponding lattice spacing of 3.0508 pixels on the camera. For comparison, the previous values in the  $7.1\ \mu\text{m}$  layer were  $17.511(0.04)^\circ$  for the  $x$ -lattice, with a corresponding lattice spacing of 3.0486 pixels on the camera, and  $17.24(0.07)^\circ$  for the  $y$ -lattice, with a corresponding lattice spacing of 3.0447 pixels on the camera. Once the angle and magnification were properly calibrated, we could then measure the PSF of the imaging system in the new vertical position using an average of several isolated atoms in a dilute sample (analogous to Fig. 3-8(a)). An updated PSF in the new imaging layer was necessary for the Weiner deconvolution algorithm used in the reconstruction of the *in situ*, parity-projected site occupation. Radially averaging the measured PSF, we find that the new FWHM is approximately 675 nm, slightly larger than the previous 640 nm observed in the  $7.1\ \mu\text{m}$  layer. A slight increase in the measured FWHM of the PSF is not

unexpected, however, since the imaging aberrations are slightly worse as one moves further from the substrate. Additionally, the observed resolution is sufficient for us, after deconvolution of the raw image with the PSF, to achieve single-site resolution, and to accurately reconstruct the *in situ*, parity-projected site occupation.

### 3.3 Summary of Experimental Sequence

We provide here a general description of the experimental sequence used to create an initial ultracold cloud of  $^{40}\text{K}$  in the crossed ODTs  $\sim 2\text{ mm}$  below the surface of the super-polished substrate. Details of the sequence which are specific to particular experiments can be found in sections 4.2 and 5.2, for the equilibrium correlation measurements and the dynamic spin transport measurements, respectively. The preparation scheme is centered around the fact that our experiment has a single vacuum chamber, where we create the initial 3D MOTs of K and Na, as well as perform the final single-site imaging of K [73, 186, 187, 37, 168]. We begin by loading a 3D dark-spot MOT of  $^{23}\text{Na}$  atoms for 5 s from a Zeeman slower that is fed from a Na oven. For reference, the Na oven temperatures used during operation of the experiment are  $360^\circ\text{C}$  for the Na nozzle,  $345^\circ\text{C}$  for the Na flange, and  $320^\circ\text{C}$  for the Na cup. The center of the MOT, which is determined by the zero of the quadrupole field generated by the MOT coils (see Figs. 3-1 and 3-2), is located along the central axis of the vacuum chamber, which is offset along the  $+x$ -direction from the high-resolution imaging axis by 12 mm. Due to light-assisted collisions between the Na and K atoms in the presence of the MOT light from both species, we found that we cannot prepare both MOTs simultaneously, but must prepare them sequentially for the best atom numbers, in agreement with [177, 242]. Once we have loaded the Na MOT, we close the atomic beam shutter, which blocks the beam of Na atoms through the Zeeman slower, and we simultaneously turn off both the Na MOT light and the MOT quadrupole field. We then quickly turn on a homogeneous bias field along the  $x$ -direction using the bias  $x$  coil, by swapping the power supply controlling the bias  $x$  coil during operation of the MOT (see section 3.1.1) to one which is pre-charged,

and ready to quickly supply sufficient current to create a strong quantization field of 4.2 G along this direction. We subsequently apply a  $\sim 100 \mu\text{s}$  pulse of  $\hat{\sigma}^+$ -polarized light traveling along the  $+x$ -direction, which is resonant with the  $F = 2 \rightarrow F' = 3$  D2 transition in  $^{23}\text{Na}$  (for  $m_F$  pumping), simultaneously with  $\hat{\sigma}^+$ -polarized light traveling along  $+\hat{x}$  which is resonant with the  $F = 1 \rightarrow F' = 2$  D2 transition in  $^{23}\text{Na}$  (for  $F$  pumping), in order to optically pump the atoms into the magnetically trapped  $|F = 2, m_F = 2\rangle$  state. We then catch the optically pumped Na atoms in a magnetic trap formed from the quadrupole field of the MOT coils, by quickly ramping up current in the MOT coils using a pre-charged power supply that is separate from the supply used for the Na MOT stage (the same technique which we use for the optical pumping quantization field with the bias  $x$  coil). To further purify the spin states of the magnetically trapped Na atoms, we decrease the strength of the initial magnetic gradient used to catch the atoms, until any residual atoms in the  $|F = 2, m_F = 1\rangle$  state, which are present in the magnetic trap due to imperfect optical pumping, can no longer be held against gravity and escape from the trap, since this state has a smaller magnetic moment than the  $|F = 2, m_F = 2\rangle$  atoms, and therefore experiences a weaker magnetic trapping potential. We perform this additional step of state purification for Na, because any remaining  $|F = 2, m_F = 1\rangle$  atoms can lead to atom loss when we load the K MOT, due to spin-changing collisions [177, 242].

At this weaker gradient, where the  $|F = 2, m_F = 1\rangle$  atoms are not trapped, and where the remaining  $|F = 2, m_F = 2\rangle$  atoms are hidden in a purely magnetic trap (with no Na MOT light on), we then load the 3D MOT of  $^{40}\text{K}$  for  $\approx 700 \text{ ms}$  from a K 2D MOT source. For reference, we heat the K 2D MOT ampule source to  $88^\circ\text{C}$ . While the K 2D MOT light is turned on, we simultaneously apply 455 nm UV light from a Thorlabs M455D2 LED to the 2D MOT glass cell, which helps to desorb any K atoms that have been adsorbed to the glass surface, thereby increasing the flux of K atoms to the 3D MOT region [2, 123]. When the K MOT has finished loading, we switch off the 2D MOT light, the 3D MOT light, and the magnetic quadrupole field to release both the Na and K atoms. We then again apply a 4.2 G field along the  $x$ -direction using the bias  $x$  coil, and, after a  $400 \mu\text{s}$  delay for the fields to stabilize, subsequently

apply a  $\sim 100 \mu\text{s}$  pulse of  $\hat{\sigma}^+$ -polarized light traveling along the  $+x$ -direction, which is resonant with the  $F = 9/2 \rightarrow F' = 11/2$  D2 transition in  ${}^{40}\text{K}$  (for  $m_F$  pumping), to optically pump the atoms into the magnetically trappable  $|F = 9/2, m_F = 9/2\rangle$  state. The  $F$ -pumping light resonant with the  $F = 7/2 \rightarrow F' = 9/2$  D2 transition in  ${}^{40}\text{K}$  is provided during this optical pumping step by the 3D MOT re-pumper beams, which are left on during this time (only the regular 3D MOT light is turned off). Once the K atoms have been optically pumped to the  $|F = 9/2, m_F = 9/2\rangle$  state, we then quickly ramp up current in the MOT coils to magnetically catch the freely floating Na and K atoms in a magnetic quadrupole trap. At this stage of the sequence, both atoms are trapped in a purely magnetic trap formed by the MOT coils (12 mm horizontally offset from the high-resolution imaging axis, and approximately 9.5 mm below the substrate surface) in their respective stretched states:  $|F = 2, m_F = 2\rangle$  for Na and  $|F = 9/2, m_F = 9/2\rangle$  for K.

After magnetically trapping both species, we magnetically transport the atoms to the location of the plugged quadrupole trap, which sits on the high-resolution imaging axis approximately 2 mm below the substrate surface, by adiabatically ramping down the current in the MOT coil, while simultaneously increasing the current in the curvature coil (red coils in Fig. 3-2), which transports the atoms along the  $x$ -direction, as well as the current in the Feshbach coil (blue coils in Fig. 3-2), which generates a homogeneous field that determines the vertical position of the magnetic trap (this provides the transport along the  $z$ -direction). When the magnetic transport is complete, we turn off the IGBT to the MOT coils, and turn on a 532 nm optical plug which propagates along the  $+y$ -direction, and intersects the magnetic field zero of the magnetic quadrupole trap formed by the curvature coil quadrupole field and Feshbach coil offset field. This laser light acts as a repulsive potential for both the Na and K atoms, which prevents atoms from accessing the region around the magnetic field zero, in order to suppress Majorana losses. The waist of the plug beam at the center of the magnetic trap is  $30 \mu\text{m}$ , and we typically use 9 – 10 W of power, which is derived from a Lighthouse Photonics Sprout-G-10W diode-pumped solid-state (DPSS) laser. In the plugged magnetic trap, we then perform forced RF evaporation of the

Na atoms by applying microwave radiation to the cloud using an in-vacuum RF antenna, which drives transitions between the initial trapped  $|F = 2, m_F = 2\rangle$  state, and the magnetically un-trapped  $|F = 1, m_F = 1\rangle$  state. The RF evaporation begins with an applied microwave frequency which is very blue-detuned with respect to the zero-field  $|F = 2, m_F = 2\rangle \leftrightarrow |F = 1, m_F = 1\rangle$  resonance frequency. This higher-frequency radiation can then only address those atoms which sit far away from the magnetic field zero, where the absolute field strength is stronger, which Zeeman shifts the  $|F = 2, m_F = 2\rangle \leftrightarrow |F = 1, m_F = 1\rangle$  transition into resonance with the radiation. We then slowly sweep the frequency of the applied microwave radiation from its initial large blue-detuning towards the zero-field resonance value, which transfers those atoms (in the sense of a Landau-Zener sweep) whose spatial location in the magnetic trap puts them in resonance with the applied radiation, to the un-trapped  $|F = 1, m_F = 1\rangle$  state, so that they can escape and leave the trap. Since the atoms which are selectively removed by the microwave sweep in the outer regions of the trap also happen to be the hotter atoms, the remaining cloud re-thermalizes through collisions and becomes colder. Thus, as we evaporate the Na atoms, and the cloud becomes colder, so too do the K atoms via collisions with the Na, a technique often called sympathetic cooling. Because the in-trap density of both species of atoms increases significantly as the system becomes colder during the forced evaporation, we must decompress the magnetic gradient strength during the middle of the evaporation, in order to avoid significant three-body losses. That is, once the in-trap density becomes too high, we slowly lower the current in both the curvature coil and the Feshbach coil in such a way that the trap zero remains in the same location, but the gradient strength of the magnetic trap is reduced by a factor of  $\sim 6$ , in order to significantly reduce the in-trap atomic density. During this decompression stage, small bias fields are applied along all three axes using the bias  $x$ , bias  $y$ , and bias  $z$  coils to ensure the magnetic field zero remains in the correct location. Once the magnetic trap has been decompressed, we continue sweeping the microwave radiation frequency (whose value has been adjusted to account for the different in-trap distribution and field strength in the decompressed trap) to remove Na atoms and sympathetically

cool the K. At the end of the evaporation, we sweep the microwave radiation all the way through the zero-field  $|F = 2, m_F = 2\rangle \leftrightarrow |F = 1, m_F = 1\rangle$  resonance to remove all the  $^{23}\text{Na}$  atoms, so that we are left with a cold cloud of approximately 3 million  $^{40}\text{K}$  atoms in  $|F = 9/2, m_F = 9/2\rangle$  at  $\approx 10\ \mu\text{K}$ .

When all of the Na atoms have been removed, we transfer the K atoms from the plugged magnetic trap to a 1064 nm optical trap formed by the crossed ODT beams, which propagate along the  $-x$  and  $+y$  directions. The initial location of the crossed ODT trap is centered along  $y$  and  $z$  with respect to the center of the magnetic trap, but is displaced slightly along the  $x$ -direction from the magnetic field zero in order to avoid the optical plug, and to transfer as many atoms as possible into the optical trap. We thus slowly increase the optical power in the ODT beams to transfer the atoms into this trap, and subsequently slowly ramp down the currents in the Feshbach and curvature coils to reduce the magnetic trapping. As the magnetic trap is turned off, the bias fields must be continuously adjusted in proportion to keep the magnetic field zero in the same location throughout the ramp down. This is very important, since otherwise the magnetic trap can move around significantly as the fields ramp down, which can cause significant heating and loss of atoms in the final crossed ODT. Upon ramping down the currents in the Feshbach and curvature coils, and turning off the IGBTs to these coils, we leave a 4.2 G bias field turned on along the  $x$ -direction using the bias  $x$  coil, to provide a non-zero quantization field. At this stage, in the purely optical trap, we transfer the atoms from  $|F = 9/2, m_F = 9/2\rangle$  to the lowest energy state,  $|F = 9/2, m_F = -9/2\rangle$ , using a 10 ms Landau-Zener RF sweep. We do this state transfer at fairly low fields, where the Zeeman splitting between neighboring  $m_F$  states is relatively small, so that is easier to transfer the atoms across all the  $m_F$  sub-levels using an RF sweep with reasonable duration and frequency span. After the atoms have been transferred to the lowest energy spin state in the crossed ODT, which is initially located at the position of the plugged quadrupole trap, we can form a spin mixture of K atoms using a series of short RF sweeps, so that the cloud can thermalize via  $s$ -wave collisions in the trap, which allows us to subsequently optically transport the spin mixture, from the position of the magnetic trap, vertically 2 mm

to the focus of the high-resolution imaging system. We then prepare the atoms in a single two-dimensional layer of a vertical optical lattice below the substrate, and in the ground band of a square in-plane optical lattice, where we can simulate and study the 2D Fermi-Hubbard model. Details of this remaining portion of the experimental sequence, including the spin mixture creation (which depends on the specific experiment we would like to perform), and the subsequent optical transport to the substrate surface and preparation within the ground band of the optical lattice, as well as the lattice ramps for single-site imaging, can be found in sections 3.4.1, 4.2, and 5.2.

## 3.4 Spin-Resolved Single-Site Imaging

In this section, we describe the experimental details underlying our spin-dependent imaging scheme, which allows us to resolve the sign of the spin of the atoms in the lattice, and is based on the selective removal of one spin state from the lattice prior to single-site imaging. This is a slight generalization of the normal single-site fluorescence imaging described in section 3.2, which is insensitive to the spin of the atoms, and only allows us to measure the parity-projected occupation of each lattice site. In other words, the normal single-site imaging allows us to measure the local moment at each site (see section 4.2.2), but the spin-dependent imaging technique allows us to isolate each spin state individually, and to measure the density of singly occupied sites for atoms only in that particular spin state. Because the spin-dependent imaging scheme suffers from the same parity-projected effects which remove doubly occupied sites via light-assisted collisions that the normal single-site imaging experiences, we cannot access the total density of either spin-state, but we image only those atoms in the desired spin state that are located on singly-occupied lattice sites. However, this is sufficient to allow us to measure, for example, in a site-resolved manner, the spin-spin correlations between sites with arbitrary separation (see section 4.4.1), with which we can probe the 2D Fermi-Hubbard model for signs of antiferromagnetic ordering of spins (see section 4.4.3). A similar spin-dependent imaging technique, applied to  ${}^6\text{Li}$ ,

is used in [180, 152] for the same purpose. We discuss the details of the experimental sequence we use to image the different spin states in section 3.4.1, and we describe how to calibrate the various steps of the spin-dependent imaging in section 3.4.2. A detailed analysis of the effects of finite fidelity for the detection of the individual spin states, and the impact of this fidelity on various measurable quantities, is given in sections 4.4.2 and 5.2.4, as well as details of the spin-dependent imaging sequence which are specific to those experiments. Although the technique discussed in this section does not allow one to access the site-resolved total density of either spin state, since only the singlons of a particular spin state are imaged due to the effects of parity projection, it was shown in the work of [27, 155], which operates with  ${}^6\text{Li}$ , that single atoms of the undesired spin state which reside on doubly occupied sites can be selectively removed before both atoms in the doublon are lost via light-assisted collisions. Thus, it was possible in that case to directly measure the total density of either spin state,  $\hat{n}_{\sigma,i}$ , for  $\sigma = (\uparrow, \downarrow)$ , in a single image. This, of course, also allows one to directly measure the total average density,  $\langle \hat{n}_{\uparrow,i} + \hat{n}_{\downarrow,i} \rangle$ , by imaging the different spin states in different experimental realizations. In section 3.4.3, we briefly discuss recent progress towards achieving the same result in our experiment operating with  ${}^{40}\text{K}$ .

One negative aspect of the spin-dependent imaging technique described here, which also applies to [180, 152, 27, 155], is that different experimental realizations are required to image the different spin states, which means that correlations between the densities of the two spin states cannot be accessed in a single shot. This also means that if one observes an empty site within a single image after removing one spin state, it is impossible to know whether that site was occupied by a hole, a doublon, or a single atom of the opposite spin state. Although this does not affect the measurement of the spin correlation function (Eq. 4.10), it can significantly affect one's ability to measure other types of two-point correlators (e.g. correlations between the densities of the two spin states,  $\langle \hat{n}_{\uparrow,i} \hat{n}_{\downarrow,j} \rangle$ ), as well as various higher order correlators (beyond two-point correlations). One potential solution to this issue was demonstrated in [23], where a super-lattice was used to split each individual lattice

site used during the physics stage of the sequence into multiple separate sites prior to imaging. By combining this super-lattice splitting with an applied magnetic gradient for Stern-Gerlach separation of the different spin states, it was shown that it is possible to access the full information regarding the occupation of any given site, i.e. whether a site is occupied by a hole, a doublon, or a single atom of either spin state (which were also resolved). With such simultaneous spin- and density-resolved single-site imaging, it was possible in that experiment to study previously inaccessible correlators, such as string correlators, and to study new effects, like incommensurate magnetism, in Hubbard systems [96, 199].

### 3.4.1 Experimental Sequence

We describe here the sequence used in our experiment to selectively image the different spin states of  $^{40}\text{K}$  in the lattice. Details of the other parts of the experimental sequence, including the initial preparation of quantum degenerate samples within a single two-dimensional plane underneath the substrate in the square optical lattice, as well as other aspects of the sequence specific to particular experiments, can be found in sections 3.3, 4.2, and 5.2, as well as sections 4.1 and 6.1.2 of [37]. For the normal single-site imaging, which allows us to measure the local moment, or equivalently the total singles density, of each lattice site, we first freeze the atomic distribution of whatever sample we have initially prepared by rapidly increasing the depth of the lattices in the  $x$  and  $y$ -directions from their initial depth to  $\sim 100E_R$  in less than 2 ms. At this depth, the motion of the atoms is negligible (i.e. the tunneling strength is  $t/\hbar < 0.001 \text{ Hz}$ , corresponding to a tunneling time  $\hbar/t > 160 \text{ s}$ ), so that the atoms are effectively pinned and localized at specific lattice sites. We subsequently increase the depth of the lattice in the  $x$  and  $y$ -directions to  $\sim 1000E_R$  over 20 ms using a two-point cubic spline (or s-shaped) ramp, while simultaneously turning on and increasing the power of an additional vertical lattice beam to  $\sim 1000E_R$  in the  $z$ -direction using a 40 ms two-point cubic spline ramp. As the lattices are increasing in depth, we also perform a 40 ms two-point cubic spline ramp of the magnetic field by increasing the current in the bias coil in the  $x$  direction, while ramping down the current in the

other bias coils (if they are on) in order to bring the field to a value of 4.2 G. We then turn on the Raman sideband cooling beams 5 ms after the lattices have reached  $\sim 1000E_R$  in all directions, and perform site-resolved fluorescence imaging to measure the parity-projected site occupation, which does not contain information about the sign of the spin of the atoms.

To detect the spin state of the atoms, we perform several steps between the lattice freezing ramp to  $\sim 100E_R$ , and the single-site imaging ramp to  $\sim 1000E_R$ . Specifically, once the atomic motion is frozen at  $\sim 100E_R$ , we first ramp the magnetic fields in order to apply a  $\approx 4.2$  G field along the  $x$ -direction using the  $x$  bias coil. This involves decreasing the Feshbach field, the slicer field, and the clover  $x$  and clover  $y$  fields to zero using a 40 ms two-point cubic spline ramp of the currents in those coils, while simultaneously increasing the current in the bias coil along the  $x$ -direction with the same 40 ms two-point cubic spline ramp in order to create the 4.2 G field. At this point in the sequence, there is typically no field applied using the  $y$  or  $z$  bias coils. After these current ramps, we let the fields stabilize for 60 ms before proceeding, since the initial Feshbach fields can, in principle, be large (150 – 250 G), and it is worth making sure that any transient fields from the 40 ms ramp have died out. Subsequently, we turn off the MOSFETs and IGBTs which allow current to run through the Feshbach, slicer, clover  $x$ , and clover  $y$  coils over a 10 ms period, so that these coils are effectively disconnected from their respective power supplies. Once these MOSFETs and IGBTs are off, we apply a 100 ms Landau-Zener microwave sweep with 100 kHz span, using the in-vacuum RF antenna, which selectively transfers one of the  $^{40}\text{K}$  hyperfine states in the lattice from the  $F = 9/2$  hyperfine manifold to the  $F = 7/2$  hyperfine manifold. For instance, we can selectively transfer atoms in the  $|F = 9/2, m_F = -9/2\rangle$  hyperfine state to  $|F = 7/2, m_F = -7/2\rangle$ , while leaving the atoms in other spin states, such as  $|F = 9/2, m_F = -7/2\rangle$ , untouched. The 4.2 G field in this case is sufficiently large that we are able to address each spin state individually using its specific microwave resonance frequency. Additionally, because this field is also not too strong (it is in the low field regime), so that the different microwave resonances used to address the different hyperfine states are separated by, roughly,

several MHz, the efficiency of the microwave transfer during the Landau-Zener sweep is relatively insensitive to the original  $m_F$  state of the atom.

Having shelved one spin state (the one we will end up imaging) in the  $F = 7/2$  hyperfine manifold, we subsequently perform another ramp of the magnetic field. In this case, we increase the current in the bias coil along the  $z$ -axis from zero using a 10 ms two-point cubic spline ramp to apply a small, several Gauss field along the vertical direction. Once the field created by this bias coil supplies a sufficient quantization axis (in reality, 5 ms after the beginning of the current ramp in this coil), we decrease the current in the bias coil along the  $x$ -axis linearly in time to zero over 10 ms. We then wait for an additional 5 ms to ensure the magnetic fields have settled. The purpose of this second field ramp is simply to provide a quantization field along an axis with convenient optical axis (in this case the  $z$ -direction), and which is orthogonal to the plane of the atoms, so that it is relatively straight forward to apply a light pulse with a reasonably uniform intensity across the sample, and a clean circular polarization. The latter condition is more difficult to achieve with either the  $x$  or  $y$  directions, since these require the beam to propagate with a non-zero angle (typically  $10.8^\circ$ ) with respect to the quantization axis, in order to reflect from the substrate surface. At the end of the field ramp, we apply a 5 ms pulse of light to the atoms in the lattice which is resonant with the  $F = 9/2 \rightarrow F' = 11/2$  transition on the  $D2$  line of  ${}^{40}\text{K}$ . The light from this pulse propagates along the  $+z$ -direction with  $\hat{\sigma}^-$  polarization, and is the same  $D2$  light source and optical path used for vertical absorption imaging (see section 4.6 and Fig. 4-10 of [37]). Specifically, the light in this path originates from a separate laser that is offset-locked to the  ${}^{40}\text{K}$   $D2$  master laser, which allows for great flexibility in the frequency tuning of this light without changing the optical power. This offset-locked light source is described in detail in Fig. B-3 of [37], although we have since replaced the ECDL beat-lock laser described there with a Photodigm PH767DBR080T8, 767 nm, 80 mW output, DBR laser. Upon application of this resonant light to the sample, the atoms which were not transferred to the  $F = 7/2$  hyperfine manifold by the microwave sweep (so everything remaining in  $F = 9/2$ ) are heated out of the trap by resonant photon

scattering, while the atoms in  $F = 7/2$  remain relatively unaffected since they are detuned from this light by  $\approx 1.29$  GHz. At low magnetic fields, where this blast is applied, the efficiency with which the atoms are removed by the light pulse is relatively insensitive to the original  $m_F$  state of the atoms in the  $F = 9/2$  manifold, at least for those  $m_F$  states typically used in the experiment. This is because the atoms can continue to scatter photons from the light as long as they remain in the  $F = 9/2$  manifold, since the Zeeman shift of the different  $\Delta m_F = -1$  resonances in the  $F = 9/2 \rightarrow F' = 11/2$  transition at low fields is relatively small compared to the natural line-width of the  $D2$  line ( $\Gamma/2\pi \approx 6$  MHz). Additionally, because the atoms return back to the  $F = 9/2$  manifold after scattering on the  $F = 9/2 \rightarrow F' = 11/2$  transition, they can continue to scatter photons from this manifold as long as the likelihood of off-resonantly scattering on the  $F = 9/2 \rightarrow F' = 9/2$  transition, which is detuned by  $\approx 44$  MHz, and falling back down to the  $F = 7/2$  manifold, where they are dark to the light, is relatively low over the time it takes to heat the atoms out of the trap. For the cycling transition, this effect is negligible, and for initial  $m_F$  values greater than  $m_F = -9/2$ , this effect remains small as long as the atoms are optically pumped relatively quickly to the cycling state (or simply escape the trap). This is the case for the  $m_F$  values near  $m_F = -9/2$  used in the experiments here. Of course, at larger values of  $m_F$ ,  $m_F = +9/2$  for instance, if such a state is ever used in the future, both of these effects can become more significant, and one must check that the blast efficiency is not severely affected. For the hyperfine states used in this thesis to study the Fermi-Hubbard model, we have checked, using spin polarized samples, that the blast is equally effective for each state.

Once the unwanted spin state has been successfully removed from the lattice, we then proceed with the usual lattice ramps from the initial  $\sim 100E_R$  pinning depth to the  $\sim 1000E_R$  imaging depth in all directions, as described previously. Subsequently, we perform the Raman sideband cooling fluorescence imaging, as we would in the normal single-site imaging, and image the atoms remaining after the removal pulse, which, in the ideal world, are only the atoms we wanted to image by hiding them in the  $F = 7/2$  manifold. Note that we do not need to transfer the atoms back to

$F = 9/2$  from the  $F = 7/2$  manifold in order to image them, since these states are not dark to the single-site imaging, and simply require a stage of optical pumping before the first vibrationally lowering Raman transition can be applied (although in reality, both the optical pumping and Raman light are on continuously for the imaging). We also do not observe a noticeable difference in the single-site imaging fidelity (the loss rate or the hoping rate) between the case where the atoms begin in the  $F = 7/2$  manifold prior to imaging, and the case where they begin in the  $F = 9/2$  manifold. As a final side note, because this method is extremely sensitive to the presence of different hyperfine states in the sample, and is relatively insensitive to the actual hyperfine state we would like to image (neither the microwave sweep nor the blast are particularly sensitive to the original  $m_F$  value), we can easily check, using this technique, the total spin balance of the sample (i.e. the ratio between the total number of atoms in each spin state), to ensure that we have prepared the correct 50:50 mixture (or whichever ratio is desired). This also allows us to check that there are no other spin states present in the sample, to make sure that we did not accidentally create a three spin mixture, for instance.

Overall, the total time it takes to perform the magnetic field ramps, the microwave sweep, and the resonant removal pulse before the single-site imaging stage, all of which are conducted at the  $100E_R$  lattice depth, is 235 ms. This is much shorter than the tunneling time at this lattice depth,  $\sim 160$  s, as well as the vacuum lifetime ( $\sim 100$  s), and so we can safely neglect any motion of the atoms during this period of time, which could affect the observed local site occupations. To confirm this, we have also explicitly checked that there are no noticeable affects on the observed particle distribution due to a 235 ms hold time at  $100E_R$  after the lattice freezing ramp. That is, we can monitor, for example, the average local moment at half filling with and without the 235 ms hold time after the freezing ramp, with no microwave sweep or blasting pulse applied, and we observe no effect of the hold time. We can also extend the hold time by roughly a factor of 2, to 500 ms, in order to make sure there is a reasonable region of time where the density distribution is unaffected by tunneling, and we again observe no effect of the hold time.

### 3.4.2 Calibrating the Parameters of the Spin Imaging

In this section, we describe how we experimentally calibrate the different sequence parameters used for the spin-selective imaging technique described in section 3.4.1. These include the microwave sweep, which shelves the spin state to be imaged in the  $F = 7/2$  manifold, and the resonant light pulse, which removes any atoms remaining in the  $F = 9/2$  manifold. The calibration of the microwave transfer is fairly straight forward since the value of the magnetic field is known, 4.2 G, which points along the  $x$ -direction. This known field determines the resonance frequency (via a Breit-Rabi calculation for instance) of the different hyperfine changing transitions, for example for the  $|F = 9/2, m_F = -9/2\rangle \rightarrow |F = 7/2, m_F = -7/2\rangle$  transition used to hide and images atoms originally in  $|F = 9/2, m_F = -9/2\rangle$ . We can, however, finely tune the applied microwave resonance frequency used for the shelving process by taking advantage of the good signal-to-noise ratio provided by the spin-dependent imaging. For instance, we can vary the center frequency of the Landau-Zener microwave sweep used to address a particular spin state and hide it in  $F = 7/2$ , and, after removing the remaining atoms in  $F = 9/2$  with the push-out pulse, we can take a single-site fluorescence image of the remaining atoms, and count the total number of detected atoms remaining. One can thus observe a peak in the detected atom number when the center frequency of the Landau-Zener sweep is resonant with the correct hyperfine changing transition (e.g.  $|F = 9/2, m_F = -9/2\rangle \rightarrow |F = 7/2, m_F = -7/2\rangle$ ). To become more sensitive to this resonance frequency value, one can reduce the span of the microwave sweep, which allows one to narrow in on the resonance value to the desired precision. The value of the resonance obtained in this way uniquely determines the value of the magnetic field seen by the atoms, which uniquely determines the resonance frequencies of the other hyperfine changing transitions. Of course, one can also measure these directly by changing which state is addressed with the applied microwave radiation, to make sure the field calibrations obtained from different resonance frequencies agree with each other. Once the field, and therefore the resonance frequencies for the different spin states are determined with the desired accuracy, one

can also vary both the Landau-Zener sweep span and sweep duration to optimize the transfer process, and to maximize the percentage of the population of a given spin state in the  $F = 9/2$  manifold which is successfully transferred to the  $F = 7/2$  manifold.

In this experiment, the microwave transfer efficiency is approximately 95%. The imperfect fidelity of this transfer can affect the final fidelity of the spin-dependent imaging process, since a small percentage ( $\sim 5\%$ ) of the atoms which are to be imaged remain in  $F = 9/2$  after the microwave sweep, and are therefore subsequently removed by the resonant light pulse. Thus, inefficiency in the microwave transfer can reduce the detection fidelity of a given spin state, since those atoms which are not transferred successfully are lost before they can be detected with the single-site imaging. The impact of this effect on the detection fidelity of the singles density of a given spin state is quantified in depth in sections 4.4.2 and 5.2.4. However, one can get a reasonable idea of the microwave transfer efficiency for the spin-dependent imaging by applying two separate microwave sweeps to address each of the two spin states in the lattice, and to shelve both states in  $F = 7/2$  before subsequently applying the resonant light pulse to remove the remaining atoms. In principle, if the sweeps were perfect, one would then measure the same atomic distribution one would have obtained without performing any spin-dependent imaging. One can therefore compare the averaged parity projected site-occupations obtained through the normal imaging, and through the two microwave sweeps with the resonant push-out pulse. Any difference between the two measured distributions (for example the average value at half-filling) is due predominantly to inefficiencies in the microwave transfer, assuming the removal pulse is relatively efficient and that off-resonant scattering of the push-out light in the  $F = 7/2$  manifold is negligible. In this way, we find that our microwave sweep efficiency is approximately 95%, which agrees with other independent calibrations of the general microwave transfer efficiency obtained in the experiment.

To calibrate the parameters of the resonant light pulse, we first determine the resonance of the  $F = 9/2 \rightarrow F' = 11/2$  transition in the lattice at the several gauss magnetic field applied in the  $z$ -direction. Specifically, after the atomic distribution

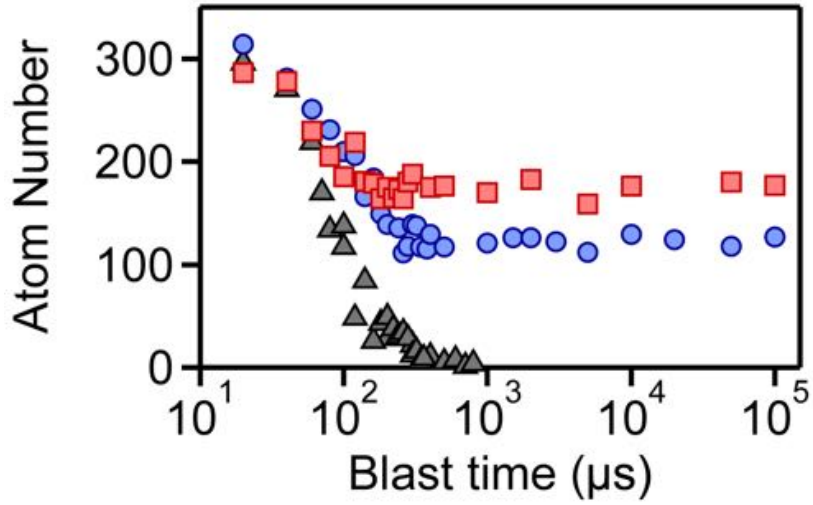


Figure 3-10: Calibrating the duration of the light pulse used to remove atoms for spin-resolved imaging. Plotted is the total atom number observed through site-resolved fluorescence imaging after applying a resonant light pulse to remove atoms in  $F = 9/2$ , once the atomic distribution is frozen at  $\sim 100E_R$ , for a sample of atoms initially in  $|9/2, -9/2\rangle$  and  $|9/2, -7/2\rangle$ , as a function of the duration of the pulse, called the blast time. The gray triangles show the total atom number when neither spin state is transferred to  $F = 7/2$  before the blast, so that they are both affected by the light pulse. At the particular blast power used here, all the atoms are effectively removed after  $\sim 1000\ \mu\text{s}$ . The red squares (blue circles) show the remaining atom number when the  $|9/2, -7/2\rangle$  ( $|9/2, -9/2\rangle$ ) atoms are first transferred to  $F = 7/2$  before the blast, where they are dark to the applied light. After  $\sim 1000\ \mu\text{s}$ , the un-transferred atoms remaining in  $F = 9/2$  are completely removed by the resonant light, but the atoms hidden in  $F = 7/2$  remain relatively unaffected, even out to 100 ms of pulse duration. During normal operation of the spin-dependent imaging, the blast is applied for 5 ms.

has been frozen in the  $\sim 100E_R$  deep lattice, and the bias field points along the  $z$ -direction, we apply a short ( $\sim 100\ \mu\text{s}$ ) light pulse with intensity well below the saturation intensity, without using the microwave transfer technique, in order to remove a small fraction of the atoms from the lattice before performing the normal single-site imaging process. We can then count the total number of detected atoms remaining after applying the light pulse, and measure this number as a function of the laser frequency of the applied pulse (very similar to how one would normally find the imaging resonance frequency for standard absorption imaging). When the laser hits the  $F = 9/2 \rightarrow F' = 11/2$  transition resonance, the fraction of atoms removed by the light pulse is maximized, so that one observes a dip in the remaining detected atom

number as a function of the laser frequency. By fitting such a curve to, for example, a Lorentzian profile, one can obtain the blast pulse resonance frequency from the minimum of the fit. We can then fix the frequency of the light to the measured resonance, and calibrate the atom removal efficiency as a function of the duration of the applied light pulse (for a fixed intensity below the saturation intensity). A typical calibration curve of this type is represented by the gray triangles in Fig. 3-10, which shows the total detected atom number measured through single-site imaging after applying the resonant light pulse for a given duration of time (with no microwave sweep to shelve the atoms in  $F = 7/2$ ) to a small sample of roughly  $\sim 300$  atoms in the initial spin states  $|F = 9/2, m_F = -9/2\rangle$  and  $|F = 9/2, m_F = -7/2\rangle$ . This curve demonstrates that after approximately 1 ms, at the given optical power, nearly all the initial atoms have been heated out of the  $\sim 100E_R$  trap. To be sure that all the atoms are removed, and that the removal efficiency is not sensitive to small drifts in the optical power of the applied light, during normal operation of the spin-dependent imaging we apply the light pulse for 5 ms, safely in the regime, according to Fig 3-10, where the atoms in  $F = 9/2$  are efficiently removed. Any atoms which are not removed from  $F = 9/2$  by the light pulse, however, can affect the detection fidelity of the singles densities of the different spin states, since atoms of the incorrect spin state remain in the lattice after the removal pulse, where they are subsequently imaged by the single-site imaging, and are therefore falsely detected as atoms in the desired spin state. We can quantify the efficiency of the removal pulse by examining the ratio between the final detected atom number after applying the light pulse on resonance for 5 ms, and the initial atom number without applying the light pulse. Through such a measurement, we find that the light pulse typically removes  $> 95\%$  of the atoms in  $F = 9/2$ . The impact of this effect on the spin-dependent imaging fidelity is discussed in further detail in sections 4.4.2 and 5.2.4.

We can also examine the effect of the blast on the spins that have been shelved in the  $F = 7/2$  manifold. Specifically, after the atomic distribution has been frozen at  $\sim 100E_R$ , we can hide one spin state in  $F = 7/2$  using a microwave sweep, and subsequently apply the removal light pulse on the  $F = 9/2 \rightarrow F' = 11/2$

transition resonance for a fixed intensity below the saturation intensity, and for a variable duration. We can then measure the total detected atom number remaining after the light pulse is applied, through single-site imaging. The red squares (blue circles) in Fig. 3-10 show the total remaining detected atom number for a small initial sample of  $\sim 300$  atoms in a spin mixture of the states  $|F = 9/2, m_F = -9/2\rangle$  and  $|F = 9/2, m_F = -7/2\rangle$ , after the  $|F = 9/2, m_F = -7/2\rangle$  ( $|F = 9/2, m_F = -9/2\rangle$ ) atoms have been transferred to  $|F = 7/2, m_F = -5/2\rangle$  ( $|F = 7/2, m_F = -7/2\rangle$ ) using the microwave sweep, and the remaining atoms in  $F = 9/2$  are addressed with the resonant light pulse for a given duration of time. At short pulse times, when the light pulse has a minimal effect, the detected atom number is comparable to the initial atom number measured through normal single-site imaging. For intermediate pulse durations between  $10\ \mu\text{s}$  and  $1000\ \mu\text{s}$ , the total detected atom number decreases, in the same way as the curve (gray triangles) where no atoms are hidden in  $F = 7/2$ . However, in this case, once all the atoms remaining in  $F = 9/2$  have been removed, the total detected atom number flattens out as a function of the pulse time, because the remaining atoms in  $F = 7/2$  are dark to the applied removal light. The residual difference between the absolute levels of the long-time tails of the  $|F = 9/2, m_F = -7/2\rangle$  and  $|F = 9/2, m_F = -9/2\rangle$  curves in Fig. 3-10 is due simply to an initial spin imbalance in the prepared sample. The curves for the blue circles and the red squares in Fig. 3-10 demonstrate a clear separation of time scales for the spin removal process: after the fast initial decay of the detected atom number due to the removal of the spin state remaining in  $F = 9/2$ , the atoms hidden from the removal light in  $F = 7/2$  show a significantly slower decay due to the off-resonant scattering of the light on the  $F = 9/2 \rightarrow F' = 11/2$  transition, which is detuned by  $\sim 1.3\ \text{GHz}$  with respect to the atoms in  $F = 7/2$ . We can measure the lifetime of the atoms remaining in  $F = 7/2$  in the presence of the  $F = 9/2 \rightarrow F' = 11/2$  light by measuring the significantly longer timescale of the decay of these atoms, relative to the fast initial decay of the  $F = 9/2$  atoms. By comparing this measured lifetime (from the long-time tails of the curves in Fig. 3-10) to the total pulse duration used for the actual spin-dependent imaging (5 ms), we estimate that  $< 0.03\%$  of the atoms

which were successfully transferred to  $F = 7/2$  are removed by the applied light pulse. It then follows that, when it comes to the unintended loss of atoms in the spin state which is to be imaged through spin-dependent imaging, the finite microwave transfer efficiency for bringing atoms from  $F = 9/2$  to  $F = 7/2$  of  $\sim 95\%$  is the dominant loss mechanism (since un-transferred atoms remaining in  $F = 9/2$  are subsequently removed), rather than off-resonant scattering of the removal light by atoms hidden in  $F = 7/2$ .

Once the frequency and duration of the removal pulse are fixed, as well as the parameters of the Landau-Zener microwave sweep, the only major remaining question is whether the spin-dependent imaging technique successfully removes double occupancies from the system, so that the measured quantities are in fact the densities of singly-occupied sites of either spin state (see Eq. 4.11). For example, the resonant light pulse could selectively heat one of the atoms on a doubly occupied site out of the trap before the two atoms could undergo a light-assisted collision [27, 155]. In this case, a single atom would remain after the removal pulse, which would be subsequently imaged during the single-site imaging, and would therefore be falsely detected as an atom in the desired spin state originating from a singly-occupied site in the original atomic distribution. To address this issue, we specifically apply the spin-dependent imaging to samples with a band-insulating core, where there is a high density of doubly-occupied sites. We can then measure the average detected densities of the two different spin states obtained through the spin-dependent imaging procedure, and compare their sum to the total average detected density (the average local moment) obtained through the normal single-site imaging alone, which does remove doublons via light-assisted collisions. By comparing these three types of measurements (the average local moment, and the average detected densities of the two spin states) in the band-insulating regions, we observe experimentally that the spin-imaging technique predominantly removes doubly-occupied sites, and that  $< 1(3)\%$  of the doubly-occupied sites in a sample are accidentally converted to singly-occupied sites, which are subsequently detected. We discuss this effect and its impact on the spin-dependent imaging fidelity in more detail in sections 4.4.2 and 5.2.4. It is worth

noting here though that one potential reason that the doublon removal efficiency is so high for this spin-dependent imaging technique is that spin-relaxation can occur between an atom in  $F = 7/2$  and an atom in  $F = 9/2$  on a doubly-occupied site (see section 2.1.2 of [119]). That is, because the density in the doubly-occupied site is rather high at the  $\sim 100E_R$  depth, the two atoms can quickly collide through an  $s$ -wave collision in such a way that the total  $m_F$  is conserved,

$$m_{F,initial}^{atom,1} + m_{F,initial}^{atom,2} = m_{F,final}^{atom,1} + m_{F,final}^{atom,2}, \quad (3.2)$$

where  $m_{F,initial}^{atom,i}$  is the initial  $m_F$  state of atom  $i$  and  $m_{F,final}^{atom,i}$  is the final  $m_F$  state of atom  $i$  after a collision, but the initial  $\sim h \times 1.3$  GHz of energy stored in the internal state of the atom initially transferred to  $F = 7/2$  can be released to kinetic energy if this atom decays to the  $F = 9/2$  manifold during the collision, at which point both atoms easily escape from the trap. For instance, two atoms initially in  $|F = 7/2, m_F = -7/2\rangle$  and  $|F = 9/2, m_F = -7/2\rangle$  after the microwave transfer can quickly decay to  $|F = 9/2, m_F = -9/2\rangle$  and  $|F = 9/2, m_F = -5/2\rangle$  through collisions, which would eject both atoms from the trap due to the release of the hyperfine energy splitting. Due in part to this effect, and the fact that the spin-dependent imaging relies on the storage of atoms in  $F = 7/2$ , it can be extremely difficult to accidentally convert a doublon to a singly-occupied site that is subsequently detected, using the current technique. In section 3.4.3, we discuss an attempt to generalize the spin-dependent imaging technique in such a way that it no longer requires one to shelve atoms in  $F = 7/2$ , in order to avoid the spin-relaxation doublon loss, allowing one to try to selectively remove single atoms from doubly-occupied sites using photon scattering from the applied light pulse, before the atoms can undergo light-assisted collisions. If such a technique were implemented with sufficiently high fidelity, we could access the total density of a particular spin state, rather than the (slightly more obscure) density of singly-occupied sites of that spin state [27, 155].

### 3.4.3 Imaging the Total Density of One Spin State

The spin-resolved single-site imaging technique discussed previously in this section provides access to the density of singly-occupied sites of a particular spin-state, Eq. 4.11. For many experiments, this somewhat limited information is actually sufficient to measure the desired quantities, including the spin correlation function (Eq. 4.10), as described in chapter 4, or the spin current (Eq. 5.16), for spin transport studies, as described in chapter 5. However, in some instances it is desirable, or even necessary, to measure the total density of a particular spin state (or of both spin states), which provides more information than the density of singly-occupied sites for that spin state alone. For instance, such information could be used to measure the total charge current in the sample during a transport measurement [26], or to access correlation functions or other thermodynamic quantities which are otherwise inaccessible [23, 96, 155, 199]. One potential solution to this issue is to perform the spin-resolved imaging in such a way that one spin state is removed from the lattice with a resonant light pulse, while the other spin state remains completely unaffected [27, 155, 26]. For the case of a doubly occupied site, this would mean that the resonant light pulse would heat the unwanted spin state out of the trap through photon scattering, before both atoms forming a doublon can be lost through light-assisted collisions [52, 234, 69]. For the spin-resolved imaging technique developed here for  $^{40}\text{K}$ , which was discussed in sections 3.4, 3.4.1, and 3.4.2, where the spin state which is to be imaged is transferred via a microwave sweep to the  $F = 7/2$  manifold, where it is dark to the light pulse that removes the other spin state, there is the additional issue of spin relaxation between atoms on doubly-occupied sites. In this case, when one of the atoms in a doublon is in  $F = 7/2$ , and the other is in  $F = 9/2$ , the two atoms can collide within their single lattice site in such a way that both atoms end up in  $F = 9/2$ , and the internal energy set by the hyperfine splitting is converted to the atoms' kinetic energy, so that they both subsequently escape from the trap before either can be imaged.

To solve the latter issue of spin-relaxation of doublons, in order to eventually try

to image atoms on doubly occupied sites, one cannot rely on a microwave sweep which transfers atoms to the  $F = 7/2$  manifold. One must then find a different method to make sure that the atoms in the spin state to be imaged can remain dark to any applied light which is used to remove the other spin state. One solution is to simply remove the unwanted spin state at relatively high magnetic fields, e.g.  $> 150$  G, where the strong Zeeman splitting between different  $m_F$  sub-levels is sufficiently large that one spin state is completely out of resonance with light applied in order to address the other spin state. For example, at large fields, atoms in  $|F = 9/2, m_F = -7/2\rangle$  can be effectively dark to light resonant with the  $|F = 9/2, m_F = -9/2\rangle \rightarrow |F' = 11/2, m_{F'} = -11/2\rangle$  transition used to remove atoms originally in the  $|F = 9/2, m_F = -9/2\rangle$  state, when the Zeeman shift of the imaging resonance is large compared to the natural line-width. We can use this effect in the experiment then to try to image a sample comprised of a 50:50 spin mixture of atoms in  $|F = 9/2, m_F = -9/2\rangle$  and  $|F = 9/2, m_F = -7/2\rangle$ . Specifically, we can alter the spin-imaging sequence in the following way: once the sample has been prepared in the square optical lattice at the desired value of the Hubbard parameters  $U/t$ , and at a reasonably large magnetic offset field (e.g. 150 G) applied in the  $z$ -direction with the Feshbach coil, we can freeze the atomic distribution by quickly ramping the lattice depths in the  $x$  and  $y$  directions to  $\sim 100E_R$  in less than 2 ms. For the normal spin-resolved imaging, we would at this point ramp down the 150 G Feshbach field, and apply a 4.2 G field along the  $x$ -direction using the bias  $x$  coil, where we could then easily drive a microwave transition to shelve one spin state in  $F = 7/2$ . In this new method, however, we leave the Feshbach field on at 150 G in the  $z$ -direction, and simply skip the microwave step. We then send in a short light pulse with  $\hat{\sigma}^-$  polarization propagating along the  $+z$ -direction (the same beam used for the normal spin-dependent imaging removal pulse), which resonantly addresses the atoms in the  $|F = 9/2, m_F = -9/2\rangle$  state at this 150 G field. Because the  $|F = 9/2, m_F = -7/2\rangle$  atoms are not completely dark to this light, however, and can experience off-resonant scattering, we must apply a relatively short light pulse ( $\sim 100\ \mu\text{s}$ ), which ideally leaves the atoms in  $|F = 9/2, m_F = -7/2\rangle$  relatively unaffected, but removes all the atoms

in  $|F = 9/2, m_F = -9/2\rangle$  from the lattice. After applying this light pulse, we then increase the lattice depth to  $\sim 1000E_R$  in all directions, as we would normally do for single-site imaging, and simultaneously ramp down the Feshbach field (which in this case does not sweep across any Feshbach resonances during the ramp down) to zero. As the Feshbach field is turned off, we apply a 4.2 G bias field along the  $x$ -direction using the bias  $x$  coil, where we subsequently perform the normal single-site fluorescence imaging to image the remaining  $|F = 9/2, m_F = -7/2\rangle$  atoms. To image the  $|F = 9/2, m_F = -9/2\rangle$  atoms instead, we can first apply a Landau-Zener RF sweep between the two states, after the distribution has been frozen at  $\sim 100E_R$ , which swaps them,  $|F = 9/2, m_F = -9/2\rangle \leftrightarrow |F = 9/2, m_F = -7/2\rangle$ , before applying the light pulse resonant with the  $|F = 9/2, m_F = -9/2\rangle \rightarrow |F' = 11/2, m_{F'} = -11/2\rangle$  transition to heat out those atoms which are now in the  $|F = 9/2, m_F = -9/2\rangle$  state. We would then follow through with the remaining single-site imaging procedure to image what is left, which should be the atoms which were originally in  $|F = 9/2, m_F = -9/2\rangle$  in the initial sample.

While such a procedure worked relatively well for imaging the two spin states in initially dilute samples, albeit with worse fidelity than the normal spin-resolved single-site imaging technique described in sections 3.4.1 and 3.4.2, due to the relatively short duration of the spin removal light pulse, the main motivation for pursuing this technique was to image the total density, including doubly-occupied sites, of a particular spin state. We thus prepared initial samples at 152.047 G (away from any Feshbach resonances), in a 50:50 spin mixture of  $|9/2, -9/2\rangle$  and  $|9/2, -7/2\rangle$ , with large band-insulating cores. The first image in Fig. 3-11 illustrates a site-resolved fluorescence image of such a sample, obtained through the usual, non-spin-resolved single-site imaging, where the measured center filling is approximately 15%. We then applied this generalized spin-dependent imaging technique, where we removed the atoms in  $|9/2, -9/2\rangle$ , once the distribution was frozen at  $\sim 100E_R$ , using a  $100\mu\text{s}$  light pulse, and subsequently imaged the remaining atoms. The second image in Fig. 3-11 shows the resulting distribution of atoms in  $|9/2, -7/2\rangle$ . This image reveals that many of the sites in the band-insulating core, which appeared empty in the first

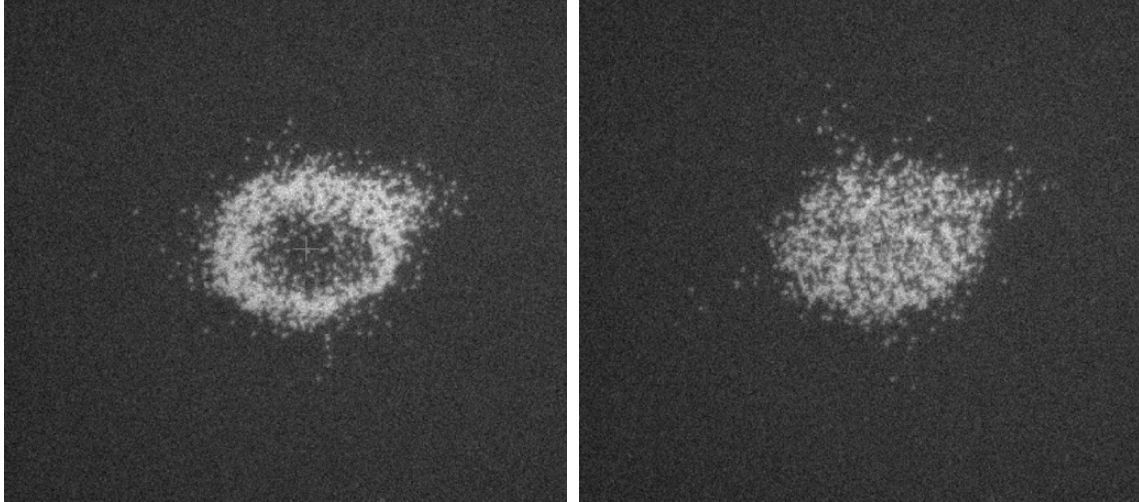


Figure 3-11: Imaging doubly-occupied sites through spin-dependent imaging. The left figure is a raw fluorescence image of the local moment for a band-insulating sample of atoms formed from a balanced mixture of the states  $|9/2, -9/2\rangle$  and  $|9/2, -7/2\rangle$ . The average moment in the central band-insulating core is approximately 0.15, so that 15% of the sites are singly-occupied, while the remaining 85% are predominantly occupied by doublons, since the likelihood of finding a hole in this high-density region is extremely low (analogous to the likelihood of finding a doublon in a low density region). The right figure is a raw fluorescence image of a different experimental realization with the same configuration as the left image, but after removing the  $|9/2, -9/2\rangle$  atoms, once the atomic distribution is frozen at  $\sim 100E_R$ , using a resonant light pulse on the cycling transition and a 152.047 G vertical offset field. The  $|9/2, -7/2\rangle$  are relatively dark to this light due to the Zeeman shift at 152.047 G, which pushes them out of resonance. After the  $|9/2, -9/2\rangle$  atoms are removed, the remaining atomic distribution is imaged with single-site imaging, which yields an average filling in the band-insulating core of 61%, higher than the 15% observed in the average moment. The additional atoms observed in the core arise from  $|9/2, -7/2\rangle$  atoms on doubly-occupied sites which remain in the lattice after the  $|9/2, -9/2\rangle$  atoms are removed.

image of the local moment, due to the significant number of doubly-occupied sites in this region, contain single atoms after removing one spin state. What this means is that many of the  $|9/2, -9/2\rangle$  atoms on doubly occupied sites were removed by the light pulse through photon scattering, before the two atoms within a given doublon could be simultaneously lost through light-assisted collisions. This also supports the hypothesis stated in section 3.4.2, that one of the reasons the doublon removal efficiency of the normal spin-dependent imaging is so high could be because of the spin-relaxation mechanism between atoms in  $F = 7/2$  and  $F = 9/2$ . However, it is

also possible, based on these observations, that the blast light simply couples more strongly to a molecular transition when one atom is in  $F = 7/2$  and the other is in  $F = 9/2$ , leading to an enhancement in the rate of light-assisted collisions in this case, relative to the situation where both atoms are in  $F = 9/2$ . Thus, it could also be that the light-assisted collision rate is suppressed when both atoms are in  $F = 9/2$ , due to weaker coupling to molecular transitions with this configuration in the presence of the blast light, which would allow us to selectively remove single atoms from doubly-occupied sites in this configuration (which was not the case in the other configuration) if the single-atom heating rate were larger than the light-assisted collision rate. In either case, we find that, with this initial attempt to measure the total density of a single spin state, it is possible to image atoms of that spin which were originally on doubly-occupied sites. However, as is evident from Fig. 3-11, the filling in the center of the sample, after applying the spin removal pulse, is not 100% (which one would expect for a perfect band insulator, where a single atom is perfectly removed from each site), but is, in reality, only approximately 61%. Thus, if we assume that, in the original sample, all 85% of the observed empty sites in the band-insulating core were doubly-occupied (a rough approximation), and that half of the observed 15% of singly-occupied sites were originally  $|9/2, -9/2\rangle$  atoms, which we then assume to be perfectly removed by the light pulse (again a rough approximation), then based on the observed 61% filling in the core of the sample after applying the light pulse, approximately 63% of the  $|9/2, -7/2\rangle$  atoms which were originally on doubly-occupied sites have been imaged through this technique. While this is not perfect, and the spin-dependent imaging fidelity is not as high (due to the shorter duration of the blast) as the spin-resolved imaging technique used throughout the rest of the work discussed in this thesis, it is a first step towards imaging doublons in  $^{40}\text{K}$ , and can be further refined in future work. However, it is currently unclear what is limiting this  $\sim 63\%$  conversion of doubly-occupied sites. The most likely culprit is the finite ratio between the single-particle photon scattering rate from the applied removal light, which heats a single spin state out of the trap, and the rate at which light-assisted collisions can occur within a single site at the  $\sim 100E_R$  depth. By

optimizing different experimental parameters, including the lattice depth where the spin removal is performed (shallower depths than  $\sim 100E_R$  could lower the density at a given site, which could affect the light-assisted collision rate), or by making use of a Feshbach resonance to tune the scattering length between the atoms within a doubly-occupied site [155], one might hope to increase the single-particle heating rate from the blast relative to the light-assisted collision rate, and improve the detection fidelity of atoms, in a particular spin state, on doubly-occupied sites.

# Chapter 4

## Measuring Thermodynamic Properties and Correlations of the Fermi-Hubbard Model

In this chapter, we discuss our experimental research regarding the equilibrium properties of the 2D Fermi-Hubbard model. Specifically, we probe low entropy metallic, Mott-insulating, and band-insulating states in order to better understand and characterize the low-temperature phase diagram and thermodynamics of the Fermi-Hubbard system. The results are summarized in the following publications:

*L. W. Cheuk, M. A. Nichols, K. R. Lawrence, M. Okan, H. Zhang, and M. W. Zwierlein, “Observation of 2D Fermionic Mott Insulators of  $^{40}\text{K}$  with Single-Site Resolution,” Phys. Rev. Lett. **116**, 235301 (2016) [39]. Included in Appendix B.*

*L. W. Cheuk\*, M. A. Nichols\*, K. R. Lawrence, M. Okan, H. Zhang, E. Khatami, N. Trivedi, T. Paiva, M. Rigol, and M. W. Zwierlein, “Observation of Spatial Charge and Spin Correlations in the 2D Fermi-Hubbard Model,” Science **353**, 1260 (2016) [38]. Included in Appendix C.*

We begin the chapter with a brief introduction to the state of the field prior to the advent of fermionic quantum gas microscopy, and discuss what previous ex-

periments without single-site resolution had observed regarding the Fermi-Hubbard model. We then summarize how we realize low entropy, equilibrium states of the 2D Fermi-Hubbard model in our experiment, and how we image these states with single-site resolution. Subsequently, we introduce the site-resolved quantity we have access to with our parity-projected imaging, the local moment, and discuss some of its properties. After describing this site-resolved observable, we review an experiment where we used this quantity to observe and probe *in situ* properties of metallic, Mott-insulating, and band-insulating states of the Hubbard model. Having realized these different equilibrium states, we then explore the effect of temperature in the system, and, upon observing the melting of a Mott insulator with increasing temperature, discuss the use of the average local moment as a thermometer in the lattice.

Next, we describe an extension of our single-site imaging which allows us to resolve the spin of the individual atoms. With this generalized imaging technique, we have access to spatial correlations in both the charge and spin degrees of freedom. We then review an experiment where we measure simultaneous spatial spin and charge correlations in a Mott-insulating state, and explore how these correlations change as a function of filling in the lattice. At half-filling, we observe short-range antiferromagnetic spin correlations in the presence of nearest-neighbor doublon-hole bunching. Upon doping, the antiferromagnetic spin correlations weaken monotonically, and an interaction-enhanced Pauli hole emerges in the charge sector, a real-space manifestation of Pauli-blocking. Finally, we examine the effect of temperature on these spin and charge correlations, and discuss the use of the nearest-neighbor spin correlator as a local thermometer which operates effectively in temperature regimes significantly below what can be accurately measured using the average local moment alone. Throughout this chapter, we compare our experimental results to theoretical predictions from the high temperature series expansion (HTSE), and to numerical calculations from the numerical linked cluster expansion (NLCE) and determinant quantum Monte Carlo (DQMC). We generally find good agreement between the predictions from theory and the experimental data throughout all the parameter regimes which we explore here.

## 4.1 Previous Studies of the Fermi-Hubbard Model Using Ultracold Atoms

The experimental realization of low entropy states of the Fermi-Hubbard model has been a longstanding goal in ultracold atomic physics [119, 22, 63]. This is due in part to the paradigmatic role played by this model in understanding the behavior of strongly correlated electronic systems such as the high-critical temperature superconducting cuprates [6, 139]. It is also due to the fact that, despite the apparent simplicity of the Fermi-Hubbard model, it is theoretically intractable because of the fermion sign problem away from half-filling [144, 226], and has only been solved in special limiting cases. In this sense, one of the major goals of ultracold atom optical lattice experiments has been to realize and study interesting regimes of the Fermi-Hubbard model which cannot be described by current theories [136]. A reasonable first step towards this goal was to realize and probe a Fermionic Mott insulator, a strongly correlated insulating state which requires temperatures low compared to the on-site interaction energy  $U$ , and densities near one particle per lattice site. Due to the lack of high-resolution imaging in experiments prior to the advent of quantum gas microscopy, however, these states had to be examined via somewhat indirect means. For example, several experiments observed Mott-insulating behavior via a reduction in the density of doubly-occupied sites as the strength of the on-site interactions was increased [114, 221]. Others examined the compressibility of the system, and found that the compressibility was strongly suppressed in the Mott-insulating regime [205, 55]. As the experimental field progressed, other properties of the Mott-insulating state were observed, including short-range antiferromagnetic spin correlations above the Néel temperature, which were studied using Bragg scattering [89] and dimerized lattices [78, 105, 76]. Subsequently, as the imaging resolution in these fermionic optical lattice experiments improved, it became possible to measure the equation of state (EOS) for the spin-1/2 Fermi-Hubbard model in two-dimensions [45], as well as for the 3D Fermi-Hubbard model with higher spin values [100], using high-resolution *in situ* imaging. While this work was being conducted in the realm of fermionic

Hubbard systems, a new experimental tool was developed for bosonic atoms, the quantum gas microscope, which enabled *in situ* imaging of single bosonic atoms in Hubbard-type lattice systems with high enough resolution to encompass the shortest relevant length scale, a single lattice site [16, 209]. This new tool allowed for the direct probing and observation of spatial structure and ordering [15, 209], as well as of interesting correlations and dynamics in these strongly interacting Bose-Hubbard systems [60, 35, 61, 108]. In addition to this single-atom imaging, however, the high spatial resolution afforded by these experiments also allowed for the control and manipulation of individual atoms on single lattice sites [236]. Because of the incredible level of control demonstrated in these bosonic experiments, as well as the ability to examine previously inaccessible observables for characterizing the system, it became clear that the power of quantum gas microscopy could make significant contributions to the study of the Fermi-Hubbard model. Thus, significant effort was made to develop the first fermionic quantum gas microscopes allowing for single-site imaging of atoms in 2D Fermi-Hubbard systems [40, 85, 179, 169, 58]. Since the development of this technology, experiments (including those discussed here) have directly observed 2D fermionic Mott insulators, metallic states, and band insulators for the first time [77, 39], and measured spatially and density resolved spin and charge correlations in these systems [23, 38, 180]. With the ability to locally shape the underlying potentials experienced by the atoms, these microscopes have even allowed experiments to push the lower bounds of accessible temperatures into previously unattainable regimes, where the spin correlation length approaches the size of the system [152, 43]. In the subsequent sections, we discuss several experimental results [39, 38], obtained using our fermionic quantum gas microscope, which highlight the strengths of our *in situ* single-site imaging, and its application to the study of the equilibrium and thermodynamic properties of the 2D Fermi-Hubbard model.

## 4.2 Experimental Realization in our Quantum Gas Microscope

We briefly summarize here how we experimentally realize and image low entropy states of the 2D Fermi-Hubbard model. A more complete description of the experimental setup is given in chapter 3 of this thesis, and is discussed in detail in chapter 4 and appendices A and B of [37], as well as chapter 4 of [168]. The latter two theses also show complete diagrams of all optical setups used in the experiments described here.

To prepare low entropy, two-dimensional systems of two-component fermionic atoms below our high-resolution imaging system, we first sympathetically cool fermionic  $^{40}\text{K}$  atoms in the  $|F = 9/2, m_F = 9/2\rangle$  state using bosonic  $^{23}\text{Na}$  atoms in an optically plugged magnetic quadrupole trap in the  $|F = 2, m_F = 2\rangle$  state. This magnetic trap is centered  $\sim 2$  mm below the in-vacuum substrate which forms the bottom surface of a solid immersion lens in our high-resolution imaging system (see section 3.1.4). The optical plug is formed from a 10 W 532 nm laser focused to a waist of  $30\ \mu\text{m}$  at the center of the magnetic trap. To cool the K atoms, we evaporatively cool the Na atoms in the quadrupole trap using a radio-frequency (RF) sweep which transfers the Na atoms from the magnetically trapped  $|F = 2, m_F = 2\rangle$  state to the un-trapped  $|F = 1, m_F = 1\rangle$  state. Using the RF sweep, we remove all the remaining Na atoms from the trap, at which point we have roughly  $2 - 3 \times 10^6$   $^{40}\text{K}$  atoms in  $|F = 9/2, m_F = 9/2\rangle$  at  $\sim 10\ \mu\text{K}$ . These atoms are subsequently transferred from the magnetic trap into a 1064 nm crossed optical dipole trap (ODT) formed from two separate beams propagating along the  $-x$  and  $y$ -directions, respectively (see section 3.1.2). Once the atoms have been transferred into the optical trap, we apply a short resonant light pulse designed to remove any remaining Na atoms which were not removed by the RF. This is done to avoid three-body loss of K atoms arising from the presence of excess Na and the high densities in the optical trap.

At this point, we transfer the K atoms from the  $|F = 9/2, m_F = 9/2\rangle$  state to the lowest energy  $|F = 9/2, m_F = -9/2\rangle$  state using a Landau-Zener RF sweep. Subsequently, we apply a series of ten non-adiabatic RF sweeps to create a 50:50 two-

component spin mixture of atoms in the  $|9/2, -9/2\rangle$  and  $|9/2, -7/2\rangle$  states, which allows the system to thermalize via s-wave collisions. For the magnetic fields used in the work discussed in this thesis (< 150 G), which are not located in the vicinity of any relevant Feshbach resonances, the s-wave scattering length between these two states is only slightly modified from the background value of approximately  $174 a_0$  [190], where  $a_0$  is the Bohr radius. This spin mixture is then evaporated directly in the crossed ODT by simultaneously lowering the powers of the two dipole trap beams. At this stage, we typically have approximately  $2 - 3 \times 10^5$  total atoms at a temperature of  $\sim 600$  nK. Once the spin mixture is sufficiently cold, we optically transport the atoms from  $\sim 2$  mm below the substrate to  $\sim 40\ \mu\text{m}$  below the substrate by moving the position of the crossed ODT. That is, the physical location at the atoms of each ODT beam is independently varied by adjusting the RF frequencies which control acousto-optic deflectors (AODs) in the Fourier plane of each beam path (see section 3.1.2). Thus, by sweeping the frequency of each AOD over a period of 900 ms, we can move the location of the crossed ODT to  $\sim 40\ \mu\text{m}$  below the substrate, without changing the incident angle, with respect to the atoms, of either beam. We are physically limited in how close we can bring the atoms to the substrate using the crossed ODT because the finite beam waist and non-zero angle with respect to the  $x-y$  plane of the ODTs means that the beams will eventually reflect from the surface of the substrate if they are moved too close. In doing so, a vertical lattice would form which would prevent further transport to the desired location.

Because of this, once the atoms are  $\sim 40\ \mu\text{m}$  from the surface, we ramp down the ODT along the  $-x$ -direction, and simultaneously ramp up a 1064 nm accordion beam which also propagates along the  $-x$ -direction (see section 3.1.2). This dipole trap is designed to reflect from the surface of the substrate at an incident angle of  $\approx 1.2^\circ$ . At this angle of incidence, the accordion forms a vertical lattice of spacing  $\approx 26.5\ \mu\text{m}$ , so that the second layer of this lattice corresponds to the  $\sim 40\ \mu\text{m}$  position of the atoms. In this way, we can capture the atoms in a single (albeit fluffy) layer of a vertical optical lattice. To provide confinement along the propagation direction of the accordion, we leave the ODT beam propagating along the  $y$ -direction turned on,

and also ramp up the dimple beam simultaneously with the accordion ramp. The dimple consists of an 830 nm beam with waist  $20 \mu\text{m}$  focused onto the atoms through the microscope objective, which propagates along the  $-z$ -direction (see section 3.1.2). At this stage, we can tune the angle of incidence of the accordion beam with respect to the  $x - y$  plane using a galvo mirror that is imaged onto the center of the substrate surface. This allows us to dynamically change the vertical location of the lattice layer confining the atoms (by varying the lattice spacing), without changing the horizontal position of the atom cloud within the  $x - y$  plane. Thus, we transport the single layer of atoms vertically from  $\sim 40 \mu\text{m}$  to  $\sim 7 \mu\text{m}$  by changing the incident angle of the accordion from  $\approx 1.2^\circ$  to  $\approx 5.8^\circ$  over 250 ms. In addition to bringing the atoms to their final vertical position for studying the 2D Fermi-Hubbard model and single-site imaging, this transport step also compresses the cloud vertically by increasing the trap frequency along this direction, ultimately bringing the system closer to the two-dimensional regime.

Once the accordion has moved the single layer of atoms to a position  $\sim 7 \mu\text{m}$  below the substrate, we ramp down the accordion and the ODT propagating along the  $y$ -direction, and simultaneously ramp up a shallow angle 1064 nm ODT beam which propagates along the  $+x$ -direction, and which reflects from the substrate at the same angle as the final position of the accordion,  $\approx 5.8^\circ$  from the surface (see section 3.1.2). Here, the shallow angle beam provides all of the vertical confinement for the single layer of atoms, and the dimple provides the majority of the radial confinement in the  $x - y$  plane. Because this whole process of preparing a single two-dimensional layer of atoms  $\sim 7 \mu\text{m}$  below the surface can cause some heating of the cloud, we perform a final stage of evaporative cooling on the spin mixture by lowering the powers of both the dimple and shallow angle beams. During this final stage of evaporation, we apply a small magnetic gradient along the  $x$ -direction to help the atoms escape radially (rather than in the tightly confined vertical direction), and improve the efficiency of the evaporation.

After the final evaporation in the shallow angle and dimple beams, the atomic cloud is relatively cold (although we do not have a precise estimate of the phase

space density at this stage, prior to turning on the lattice) and two-dimensional. To study Fermi-Hubbard physics in a square lattice, we subsequently transfer the atoms into an optical lattice formed by two separate retro-reflected beams propagating along the  $x$  and  $-y$  directions, respectively (see section 3.1.2). Each lattice beam is formed from a 1064 nm beam which reflects from the surface at an angle of  $\approx 10.8^\circ$ , and is subsequently retro-reflected. The  $\approx 10.8^\circ$  reflection creates a vertical lattice of spacing  $\approx 2.8 \mu\text{m}$ , whose third layer corresponds to the  $\sim 7 \mu\text{m}$  vertical position of the atoms, thus providing additional vertical confinement. The retro-reflection, on the other hand, creates a lattice along the propagation direction of the beam, which, due to the shallow angle of incidence with the surface, has a spacing of 541 nm in the horizontal plane. To adiabatically transfer the atoms into the lattice, we first increase the lattice depths along both the  $x$  and  $y$  directions over 40 ms to  $1.5E_R$ , where  $E_R = (\hbar^2/2m)(\pi/a)^2$ ,  $m$  is the mass of  $^{40}\text{K}$ , and  $a = 541 \text{ nm}$  is the lattice spacing. This is done in order to open a small band gap, and to ensure that only the lowest energy band is populated [241]. Subsequently, we increase both the  $x$  and  $y$  lattice depths to  $6E_R$  over 100 ms. Simultaneously during this 100 ms lattice ramp, we ramp the power of the dimple beam to a desired value in order to adjust the harmonic confinement in the final lattice configuration. This allows us to either increase or decrease the density in the center of the underlying trapping potential, and therefore change the final global chemical potential of the system. For the data discussed in section 4.3, we use this ramp of the dimple power to adjust the final density of the lattice system in order to realize different states of the Fermi-Hubbard model. For the correlation data discussed in section 4.4, on the other hand, we turn off the dimple during this stage, and rely on the lattice beams and shallow angle beam alone to provide the necessary confinement. The final density in this case is controlled by the depth of the final stage of evaporative cooling in the shallow angle and dimple beams. Once this is finished, we then perform one last ramp of the  $x - y$  lattice over 150 ms from  $6E_R$  to the final depth which produces the desired Hubbard parameters  $U/t$  (section 4.2.1). Of course, to ensure this ramp is adiabatic, the speed can be adjusted depending on the final lattice depth. Typically, for final depths below  $12E_R$ , we use

150 ms ramps, but for higher depths we increase the ramp time to 250 ms. By the end of this final ramp, the system realizes the 2D Fermi-Hubbard model on a square lattice at the desired Hubbard parameters  $U/t$  and the desired density, which we can then probe using our single-site imaging. To ensure the system is truly 2D, however, we can perform modulation spectroscopy (section 4.2.1) to measure the bandgap in the vertical direction (the bandgaps in the other directions are typically much larger than the vertical due to the tighter confinement). For typical lattice depths between, for example,  $6E_R$  and  $18E_R$ , we measure that the vertical trapping frequency ranges from  $2\pi \times 4$  kHz to  $2\pi \times 8$  kHz. For typical on-site interaction energies  $U/h \sim 1$  kHz, the chemical potential of a half-filled system,  $\mu = U/2$ , is  $\mu/h \sim 500$  Hz, so that  $\mu/\hbar\omega_z$  satisfies  $\mu/\hbar\omega_z < 0.15$ , where  $\omega_z$  is the vertical trap frequency in the physics lattice. This means that the chemical potential is much smaller than the bandgap to the first-excited state along the vertical direction, so that the system is effectively 2D. This must also hold for the temperature, and we discuss thermometry in subsequent sections, where we find temperatures on the order of the tunneling strength  $t$ , which is also much smaller than  $\omega_z$ .

To prepare the atoms for imaging, we first freeze the atomic distribution by quickly ramping the  $x$  and  $y$  lattice powers from their physics depth, corresponding to the desired value of  $U/t$ , to  $\sim 100E_R$  in less than 2 ms. At this high depth, the tunneling amplitude  $t$  between neighboring sites is small,  $t/h < 10^{-3}$  Hz (compared to  $t/h \sim 100$  Hz at the physics depth), so that the atoms are indeed effectively frozen. The spin dependent imaging technique described in sections 3.4 and 4.4.2 is performed at this point. Specifically, a 100 ms microwave Landau-Zener sweep transfers atoms from the  $F = 9/2$  manifold to the  $F = 7/2$  manifold in a spin-selective manner, while a subsequent 5 ms resonant light pulse removes unwanted atoms remaining in  $F = 9/2$ . In this way, only the atoms which were transferred to  $F = 7/2$  are imaged. If instead one would like to image both spin states simultaneously, as is done for the data described in section 4.3 for example, one simply skips both the microwave sweep and the resonant light pulse, and images the entire distribution. After this stage, the lattices are further increased to  $\sim 1000E_R$  over 40 ms, while the shallow

angle beam and dimple beam (if it is used) are simultaneously ramped down. During this final 40 ms imaging ramp, an additional 1064 nm lattice beam propagating along the  $z$ -direction, which is retro-reflected at normal incidence by the substrate, is also ramped up to  $\sim 1000E_R$  (see section 3.1.2). This additional vertical lattice beam is necessary to provide a sufficiently large vertical trapping frequency for the single-site imaging, which cannot be done with the vertical confinement from the  $x$  and  $y$  lattice beams alone. Finally, we turn on the Raman imaging light (both the optical pumping and Raman beams), described in section 3.1.3, 5 ms after the three lattice directions have reached  $\sim 1000E_R$ . The two Raman beams propagate along the  $-x$  and  $y$  directions, respectively, transmit through the respective lattice retro-reflection mirrors, and overlap with the retro-reflected lattice beams. The optical pumping beam is combined with the  $-x$  propagating Raman beam prior to transmission through the lattice retro-mirror. Because these imaging beams overlap with the retro-reflected lattice beams, they also reflect from the surface at a  $\approx 10.8^\circ$  angle, and therefore also create a vertical lattice. One must therefore be careful to ensure that neither the Raman nor the optical pumping beams destructively interfere at the vertical location of the atoms.

Once the imaging beams have been turned on, we collect fluorescence emitted during the optical pumping process on an EMCCD camera (see section 3.1.4). Typically we image for 1 – 2 seconds, depending on the imaging scattering rate. We then use these fluorescence images to reconstruct the parity-projected site occupation in the lattice. Details of the image reconstruction process can be found in chapter 5 of [37]. If we did not perform spin-dependent imaging, this image tells us the total density of singly occupied sites. If we did perform spin-dependent imaging, however, we measure the singles density of the desired spin state. We typically take multiple images of the same atomic distribution from a single experimental realization, with negligible time delay between images, in order to estimate the imaging fidelity, discussed in sections 3.2 and 4.4.2, in each experimental run. This is not necessary from a data taking perspective, since it does add significant time to the experimental sequence, but it is useful for debugging purposes.

### 4.2.1 Calibrating the Hubbard Parameters

In order to make any quantitative comparison of our experimental data with predictions from theory, or even to qualitatively understand the behavior of the system, we must calibrate the Hubbard parameters  $U$  and  $t$ , which are determined by the depth of the optical lattice used in the final lattice configuration, and the scattering length for collisions between opposite spin states. To calibrate the on-site interaction energy  $U$ , we prepare relatively small Mott-insulating samples ( $\sim 300 - 500$  atoms) using a two-component, balanced spin mixture, at a lattice depth where  $U \gg t$ . Using small samples ensures that the calibration spectra are not artificially broadened by spatial variation of the lattice intensity over the region of the atomic cloud, and also prevents the formation of a band-insulating core. We then perform modulation spectroscopy on these samples by modulating the laser power of one of the lattice axes, and observing the response of the system as a function of the modulation frequency [114, 221]. Specifically, by modulating the beam power, we can modulate the depth of one of the optical lattice beams according to the form  $V(\tau) = V(0) + \delta V \sin(2\pi f\tau)$ , where  $V(0)$  represents the lattice depth we are using to measure  $U$ ,  $\delta V$  is the amplitude of the modulation,  $f$  is the modulation frequency, and  $\tau$  is the time. In order to avoid power broadening the spectrum, we pick modulation parameters that produce as small a perturbation to the system as possible, while maintaining sufficient signal to accurately determine  $U$ . Typically we modulate the lattice depth with an amplitude  $\delta V$  that is  $\sim 2 - 3\%$  of the lattice depth  $V(0)$ , and for a time  $\tau = N/f$ , where  $N \sim 200 - 500$  (depending on the depth  $V(0)$ ). In a given modulation spectrum, we keep the number of modulation cycles  $N$  constant for each frequency  $f$  to ensure that each frequency is given equal weight. We then vary the frequency  $f$  for each independent experimental realization and observe the frequency dependent response.

We can understand the frequency-dependent response from the fact that, in the deep lattice limit where  $U \gg t$ , there is a well formed Mott gap of strength  $U$ , corresponding approximately to the energy difference between a neighboring doublon-hole pair (with doublon interaction energy  $U$ ), and neighboring sites which contain

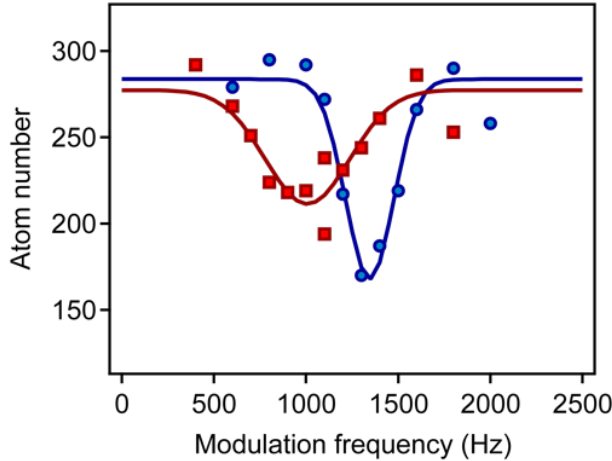


Figure 4-1: Calibration of the on-site interaction energy  $U$  using lattice modulation spectroscopy. Plotted is the detected atom number, which represents the total number of atoms on singly-occupied sites in the sample, after intensity modulation of one of the lattice beams, as a function of the intensity modulation frequency. The modulation spectra shown are performed on Mott insulating samples composed of atoms in the states  $|9/2, -9/2\rangle$  and  $|9/2, -7/2\rangle$ , with the background scattering length,  $174 a_0$ . The minimum detected atom number corresponds to the frequency of the on-site interaction energy,  $U/h$ , due to the resonant creation of doublons and holes within the original Mott-insulating sample at this modulation frequency. The blue circles represent modulation at a lattice depth of  $18E_R$  in both the  $x$  and  $y$  directions, with 10% intensity modulation amplitude, and 1000 modulation cycles. The red squares represent modulation at a lattice depth of  $12E_R$ , with 5% intensity modulation amplitude, and 500 modulation cycles. The actual modulation is performed by sinusoidally modulating the analog set point of the intensity stabilization on one of the lattice beams, which directly controls the optical power in this beam via an AOM. The solid lines are Gaussian fits to the data, whose peak location determines  $U/h$ . For the  $18E_R$  lattice depth, we measure  $U/h = 1350(50)$  Hz, and for the  $12E_R$  lattice depth, we measure  $U/h = 1007(40)$  Hz. Figure adapted from [39].

opposite spin atoms. In this regime, when the filling is sufficiently high that there is, on average, one particle per site for the total density, and when the temperature is low compared to  $U$ ,  $k_B T < U$ , the strong on-site interactions ensure that there are few inherent doublons and holes in the system, and that most sites are occupied by a single atom (see sections 4.2.2 and 4.3.2). When the depth of the optical lattice is then modulated, this predominantly modulates the tunneling amplitude  $t$ , which is significantly more sensitive to the lattice depth than the on-site interactions  $U$  [241]. Thus, when the tunneling amplitude is modulated at a frequency corresponding to

the energy difference between a doublon-hole configuration and a neighboring singly-occupied site configuration, one can drive resonant tunneling between sites which were initially singly-occupied by opposite spin atoms to create doublon-hole pairs. Here, the resonant drive makes up the energy difference  $U$  between the two configurations, allowing us to directly probe the Mott gap. Because the initial state in this case is a Mott insulator with a roughly uniform background of singly occupied sites, when the drive frequency  $f$  is resonant, i.e.  $f = U/h$ , many of these sites are converted to doublons and holes. Our single-site imaging, however, can only detect singly-occupied sites, and cannot distinguish between sites which are doubly-occupied and those which are empty, both appear empty in the final image (see section 4.2.2). Therefore, we can detect the frequency resonance as an onset of detected-atom loss. Two example frequency spectra are shown in Fig. 4-1. These spectra show the total detected atom number, corresponding to the total number of singly-occupied sites, measured as a function of the modulation frequency  $f$  at two different initial lattice depths,  $V(0) = 18E_R$  and  $V(0) = 12E_R$ , where  $E_R = (\hbar^2/2m)(\pi/a)^2$ ,  $m$  is the mass of  $^{40}\text{K}$ , and  $a = 541 \text{ nm}$  is the lattice spacing. When the drive frequency  $f$  equals  $U/h$  at a given lattice depth, there is a dip in the total detected-atom number, as shown in the figure. If, however, there are some experimental atom number instabilities, such as significant shot to shot fluctuations in the total detected-atom number, one can instead radially average the detected parity-projected site-occupation in a given image, to obtain the average local moment (section 4.2.2) as a function of position in the trap. One can then examine just the peak average moment (or maximum average singles density) as a function of modulation frequency, which is generally less sensitive to atom number fluctuations, and which shows the same resonance behavior at  $U/h$ . This is because the peak average moment, which is initially near unity in the Mott insulator, decreases significantly upon the creation of doublons and holes. In either case, we can then fit the observed resonance to a Gaussian (also shown in Fig. 4-1) to obtain the peak resonance location,  $U/h$ .

For the experimental results shown in this thesis, we typically work in the vicinity of the background scattering length  $174 a_0$  [190], which, at typical lattice depths used,

$V(0) \sim 6 - 18E_R$ , corresponds to an on-site interaction energy  $U/h \sim 600 - 1400$  Hz. This strength of the on-site interactions is approximately an order of magnitude smaller than the bandgap between the ground and first excited bands along all three orthogonal lattice axes ( $x$ ,  $y$ , and  $z$ ), at the typical lattice depths used here. One must keep in mind, however, that using this technique to directly measure  $U$  only works well near the atomic limit,  $U \gg t$ . At lower lattice depths, where this condition breaks down, the modulation transfer spectra are broadened significantly, by an amount approximately equal to the finite tunneling strength  $t/h$ , which corresponds to the finite width of the Hubbard bands ( $\sim t$ ) growing relative to the size of the Hubbard gap ( $\sim U$ ). In this situation, it becomes difficult to accurately measure the interaction energy directly using modulation spectroscopy, so we rely on tight-binding calculations which use the calibrated lattice depths (discussed subsequently) to determine  $U$  in this regime. At the background scattering length, this must typically be done for lattice depths below  $\sim 10E_R$ .

To calibrate the depth of the optical lattices, we also use modulation spectroscopy. That is, by modulating the power of the desired lattice beam (both lattice beams must be calibrated independently), we modulate the depth of the lattice along this direction according to the form  $V(\tau) = V(0) + \delta V \sin(2\pi f\tau)$ , as we did to calibrate  $U$ . For the lattice depth calibration, however, we typically modulate the depth with an amplitude  $\delta V$  that is 2 – 3% of  $V(0)$ , and for  $N \sim 2000$  modulation cycles, where  $\tau = N/f$ , in order to obtain a reasonable signal. As we do for the calibration of  $U$ , we prepare small samples of roughly 200 – 500 atoms, so that the extent of the cloud size is small relative to the lattice beam waist. This allows us to minimize the variation of the lattice intensity over the sample, which can artificially broaden the calibration spectra. Additionally, in contrast to the  $U$  calibration, we try to prepare cold, small samples which are highly spin-polarized. Typically we prepare samples where 85% of the atoms are in one spin state, and 15% are in the other. We do this in order to minimize the possible effects of interactions on the calibration of the depth [62].

Modulating the depth of the desired lattice beam at a frequency corresponding to the bandgap between the ground and first-excited bands allows us to resonantly

excite atoms, which are initially all in the ground band, into the first-excited band. When this happens, we observe a slight increase in the width of the cloud due to the energy injected into the system by the modulation, and the faster tunneling rate in the first-excited band relative to the ground band. Thus, we can measure the transition frequency between the two lowest energy bands by measuring the cloud width as a function of the modulation frequency. Fig. 4-2 shows an example lattice depth calibration spectrum, where we measure the cloud width in a given image using the root mean square (RMS) distance of each detected-atom from the center of mass of the cloud. At the frequency resonance corresponding to the bandgap between the two lowest energy bands, there is a peak in the RMS width of the cloud, as shown in the figure. If shot-to-shot atom number fluctuations are an issue, which translate directly into shot-to-shot RMS cloud width fluctuations, we can normalize the measured RMS width by the square root of the detected atom number to partially normalize-out these fluctuations. This is not shown in Fig. 4-2, but has recently proven to be a more stable metric for these spectra in the presence of experimental instabilities, and is now the typical quantity we examine.

Once we have measured the transition frequencies between the ground and first-excited band using this technique, we can compare our measurements to a full band structure calculation, and extract the corresponding lattice depth  $V(0)$ . When the depth  $V(0)$  is known, we perform a tight-binding calculation to obtain the tunneling amplitude  $t$  along this lattice direction (see section 2.1.1, or section 2.1.2 of [37]). This becomes slightly more complicated by the fact that the energy bands of the lattice potential are not flat, but contain inherent quasi-momentum dependence [241, 37]. Specifically, this means that the excitation resonance between the two lowest energy bands develops a width associated with different transition frequencies at different quasi-momentum [241, 37]. Because fermionic atoms occupy a large range of quasi-momentum states in the ground band due to the Pauli exclusion principle, this directly translates into an inherent width of our modulation spectra. This effect is most significant at low lattice depths, where the band curvature is strongest (the energy bands tend to flatten out at higher lattice depths), meaning the spectra can

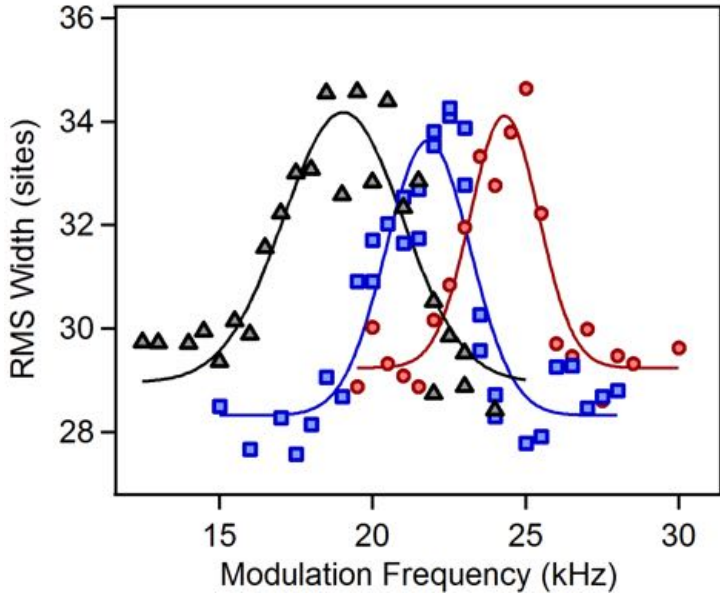


Figure 4-2: Lattice modulation spectroscopy to measure the lattice band gap. Plotted is the RMS width in the  $y$ -direction of the observed parity-projected *in-situ* density distribution after sinusoidally modulating the intensity of the  $y$  lattice for 2000 modulation cycles with 3% intensity modulation amplitude, as a function of the modulation frequency. The intensity modulation spectra shown here are performed on an initially cold, spin-imbalanced sample of  $\sim 500$  atoms, where  $\approx 85\%$  of the atoms are in the  $|9/2, -3/2\rangle$  state, and the remaining  $\approx 15\%$  are in the  $|9/2, 1/2\rangle$  state. When the intensity modulation frequency is resonant with the band gap between the ground band (which the atoms initially occupy) and the first excited band, energy is injected into the system, leading to an expansion of the cloud size. We can thus measure this band gap at a given lattice depth from the shape and position of these spectra. The red circles represent the response at an initial lattice depth of  $11E_R$  in the  $x$  and  $y$ -directions, the blue squares represent  $9.3E_R$ , and the black triangles represent  $7.7E_R$ . The solid lines are Gaussian fits to the data in order to guide the eye.

become fairly broad at low depths. When the spectra become too broad, the lattice calibration becomes challenging since it is difficult to accurately determine a resonance location. Because of this, we typically calibrate the lattices at larger depths ( $V(0) \gtrsim 6E_R$ ) using the modulation spectroscopy technique, where the frequency broadening is sufficiently weak, and scale the calibrated depths according to the lattice beam intensities when lower lattice depths are desired. The fact that we drive transitions between the ground and first-excited bands also mitigates broadening due to the finite bandwidth, because, although the coupling to the first-excited band via intensity modulation is weaker than that to the second-excited band, the broadening

due to the finite bandwidths of the ground band and first-excited band is smaller than that due to the finite bandwidths of the ground band and second-excited band (see supplementary material of [77] and section 6.2.2 of [37]). Thus, the widths of our measured modulation spectra are significantly smaller than they would be if we were to drive transitions to the second-excited band.

### 4.2.2 The Local Moment and its Properties

For a Fermi gas with two spin states residing in the lowest energy band of an optical lattice, the occupation of a given lattice site is restricted to three possible values: no particles, one particle (of either  $|\downarrow\rangle$  or  $|\uparrow\rangle$ ), or two particles (one of each spin state). This follows from the fact that the Pauli exclusion principle prevents the possibility of two or more particles of the same spin state inhabiting the same lattice site. In other words,  $\hat{c}_{\sigma,i}^\dagger \hat{c}_{\sigma,i}^\dagger = 0$  at each site  $i$  for  $\sigma = (\uparrow, \downarrow)$ . Combined with the fact that the imaging process removes all doubly occupied sites, or doublons, from the system prior to detection [52], the resulting site-resolved images reveal only those sites which were occupied by a single particle, and cannot distinguish between doublons and empty sites. Therefore, the quantity which we have access to in our experiment is the density of singly-occupied sites, something which is also sometimes called the local moment,  $\hat{m}_{z,i}^2$ , of a lattice site  $i$ . The local moment is a reasonable name, given that our images detect whether a site had a single  $|\uparrow\rangle$  or a single  $|\downarrow\rangle$  particle, corresponding to the presence of a localized magnetic moment at that site. Although the detection scheme cannot determine the sign of the localized moment, i.e. whether it was spin up or spin down (for this we need spin-resolved imaging, discussed in section 4.4.2), it can determine its magnitude, since the presence of either a hole or a doublon at a site represents the absence of a magnetic moment.

Because the occupation of each lattice site is fundamentally limited, it is possible to write down a simple explicit equation for the local moment at a particular site  $i$ ,

$$\hat{m}_{z,i}^2 = \hat{n}_{\uparrow,i} + \hat{n}_{\downarrow,i} - 2 \hat{n}_{\uparrow,i} \hat{n}_{\downarrow,i}. \quad (4.1)$$

Given that the only possible values  $\hat{n}_{\sigma,i}$  can take are 0 and 1, it is relatively apparent that this equation successfully describes the effect of parity-projection on the experimentally measured particle density. It also makes sense intuitively because  $\hat{n}_{\uparrow,i}\hat{n}_{\downarrow,i}$  represents the density of doublons in the system. Since doublons are lost during the imaging process, corresponding to a loss of two atoms per doublon, the detected density at each site is simply the total density  $\hat{n}_{\uparrow,i} + \hat{n}_{\downarrow,i}$  minus the number of atoms lost through light-assisted collisions,  $2\hat{n}_{\uparrow,i}\hat{n}_{\downarrow,i}$ . Using the fact that  $\hat{n}_{\sigma,i}^2 = \hat{n}_{\sigma,i}$  for fermionic particles, Eq. 4.1 can be re-written as

$$\hat{m}_{z,i}^2 = (\hat{n}_{\uparrow,i} - \hat{n}_{\downarrow,i})^2 = 4\hat{S}_{z,i}^2, \quad (4.2)$$

which makes the connection of this quantity to localized magnetic moments more apparent.

We can use Eq. 4.1 to derive two important properties of the local moment operator. The first is that fluctuations of the local moment about its average value, or its variance, reveal no fundamentally new information beyond what can be obtained from the average itself. This follows, using  $\hat{n}_{\sigma,i}^2 = \hat{n}_{\sigma,i}$  and  $[\hat{n}_{\uparrow,i}, \hat{n}_{\downarrow,i}] = 0$ , from the fact that  $(\hat{m}_{z,i}^2)^2 = (\hat{n}_{\uparrow,i} + \hat{n}_{\downarrow,i} - 2\hat{n}_{\uparrow,i}\hat{n}_{\downarrow,i})^2 = \hat{n}_{\uparrow,i} + \hat{n}_{\downarrow,i} - 2\hat{n}_{\uparrow,i}\hat{n}_{\downarrow,i} = \hat{m}_{z,i}^2$ . Explicitly, we have that

$$\langle (\hat{m}_{z,i}^2)^2 \rangle - (\langle \hat{m}_{z,i}^2 \rangle)^2 = \langle \hat{m}_{z,i}^2 \rangle (1 - \langle \hat{m}_{z,i}^2 \rangle), \quad (4.3)$$

which means that the variance of the local moment at a given site is simply a function of its average value. This will become important in section 4.3.2, when we discuss our experimental observation of metallic, Mott-insulating, and band-insulating states *in situ*, and how these states are distinguished through their local moment properties.

The second important property which can be derived from Eq. 4.1 is that the local moment operator remains invariant under a particle-hole transformation. That is, under the transformation  $\hat{c}_{\sigma,i}^\dagger \rightarrow \hat{c}_{\sigma,i}$  ( $\hat{c}_{\sigma,i} \rightarrow \hat{c}_{\sigma,i}^\dagger$ ), we have that  $\hat{n}_{\sigma,i} = \hat{c}_{\sigma,i}^\dagger \hat{c}_{\sigma,i} \rightarrow$

$1 - \hat{n}_{\sigma,i}$ , which implies

$$\begin{aligned}
\hat{m}_{z,i}^2 &= \hat{n}_{\uparrow,i} + \hat{n}_{\downarrow,i} - 2 \hat{n}_{\uparrow,i} \hat{n}_{\downarrow,i} \\
&\rightarrow (1 - \hat{n}_{\uparrow,i}) + (1 - \hat{n}_{\downarrow,i}) - 2(1 - \hat{n}_{\uparrow,i})(1 - \hat{n}_{\downarrow,i}) \\
&= \hat{n}_{\uparrow,i} + \hat{n}_{\downarrow,i} - 2 \hat{n}_{\uparrow,i} \hat{n}_{\downarrow,i} = \hat{m}_{z,i}^2.
\end{aligned} \tag{4.4}$$

In other words, the local moment operator is particle-hole symmetric. Physically, this means that the average local moment we measure in the experiment must be symmetric about the half-filling point  $\mu = U/2$ ; it cannot distinguish between a system which is hole-doped and one which is particle-doped. This provides us with a relatively simple way of determining the half-filling ( $\mu = U/2$ ) point experimentally if we make use of the underlying trapping potential associated with the spatial variation in the intensity of the optical lattice. This underlying potential creates a spatially varying chemical potential, which causes the average density to decrease monotonically with increasing distance from the center of the trap. Thus, if we purposefully prepare samples with average density  $\langle \hat{n}_{\uparrow,i} + \hat{n}_{\downarrow,i} \rangle > 1$  in the center of the trap (corresponding to  $\mu > U/2$  at the center), we can identify the trap radius corresponding to the half-filling point as the radius where the average local moment is maximal, since it decreases symmetrically from its maximal value upon doping on both the hole-doped ( $\mu < U/2$ ) and particle-doped ( $\mu > U/2$ ) sides of half-filling. We can therefore determine the location within the trapped system where  $\langle \hat{n}_{\uparrow,i} + \hat{n}_{\downarrow,i} \rangle = 1$  without requiring direct access to the total density at each lattice site. We make use of this in section 4.4.3 when we discuss our measurements of spin and charge correlations in the Fermi-Hubbard model.

Before discussing our experimental results which examine different equilibrium states of the Hubbard model using the site-resolved local moment, we first show here numerical calculations from NLCE of the average local moment and its fluctuations in order to provide more intuition about this somewhat atypical quantity, and to demonstrate how it functionally depends on the different parameters of the 2D Fermi-Hubbard model on a square lattice, including the Hubbard parameters  $U/t$ , the

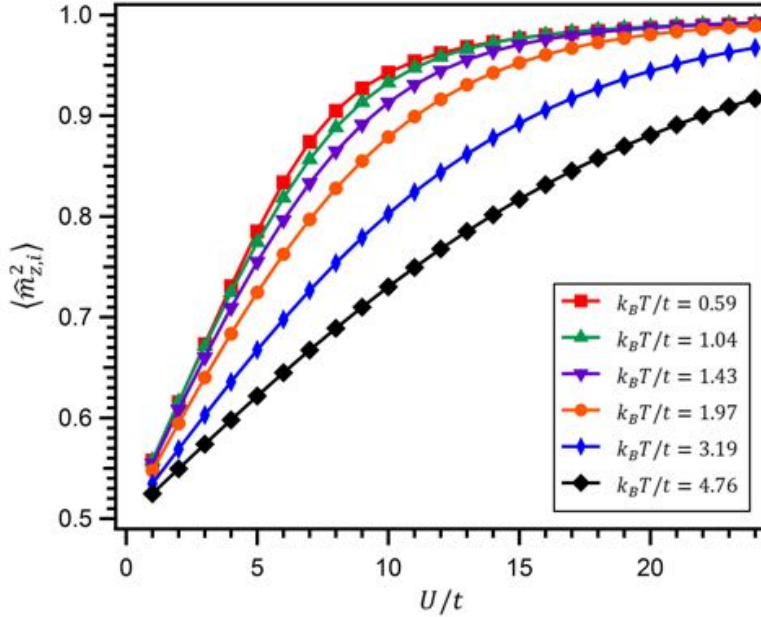


Figure 4-3: Average local moment at half-filling and fixed temperature versus  $U/t$ . The different curves represent isothermal, 9<sup>th</sup>-order NLCE predictions for the average local moment of the 2D Fermi-Hubbard model at half-filling ( $\mu = U/2$ ) as a function of the Hubbard parameters  $U/t$ , for several different temperatures in the range  $0.59 \leq k_B T/t \leq 4.76$ . This temperature range represents typical values of the temperature which are achieved in the experimental data discussed in this thesis. Generally, at a fixed temperature, the average local moment, which represents the average density of singly-occupied sites, increases with increasing  $U/t$ , due to the increasing repulsive interaction energy cost associated with the formation of doubly-occupied sites. At a finite value of  $U/t$  (e.g.  $U/t = 8$ ), however, even at very low temperatures, the average local moment does not reach the maximum possible value of one, meaning there is a finite density of doublons and holes present in the system. The curves are generated using the NLCE data provided in the supplement of [120].

temperature  $k_B T/t$ , and the chemical potential  $\mu$ . This introduction to the properties of the local moment will help facilitate subsequent discussions regarding experimental measurements, and will provide a backdrop which we can use to help interpret our results. The NLCE calculations shown here are from data provided in [120].

We first show the dependence of the average local moment at half-filling ( $\mu = U/2$ ) on the Hubbard parameters  $U/t$ . Fig. 4-3 shows the NLCE calculations of  $\langle \hat{m}_{z,i}^2 \rangle$  at this fixed filling and at a fixed temperature  $k_B T/t$ , for temperatures in the range  $0.59 \leq k_B T/t \leq 4.76$ . As we will discuss in more detail in sections 4.3.3 and 4.4.3, this is a typical temperature regime for our experimental parameters. There are two

important features of the average local moment at half-filling which Fig. 4-3 demonstrates. The first is that, at a fixed temperature, as the on-site interaction energy  $U$  increases relative to the tunneling amplitude  $t$ , the average local moment also increases, and eventually saturates at sufficiently large  $U/t$  at the maximum possible value  $\langle \hat{m}_{z,i}^2 \rangle$  can attain, one. The maximum value of one follows simply from the fact that  $\hat{m}_{z,i}^2$  can only take on two possible values, zero or one, so that  $0 \leq \langle \hat{m}_{z,i}^2 \rangle \leq 1$ . The saturation behavior with increasing  $U/t$  at fixed temperature can be understood intuitively from the fact that, when the on-site interactions are very large relative to the tunneling strength, it becomes very energetically costly to allow for doubly occupied sites in the system due to the repulsive nature of the interactions. Because  $\langle \hat{n}_{\uparrow,i} + \hat{n}_{\downarrow,i} \rangle = 1$  at half-filling, and because the density of doubly-occupied sites decreases, due to increasing interaction energy cost, as  $U/t$  increases, this means that the density of singly-occupied sites (or the average local moment) must increase. Consequently, this also means that particle fluctuations must be reduced as  $\langle \hat{m}_{z,i}^2 \rangle$  approaches one (Eq. 4.3), which, as we will discuss subsequently, is related to the insulating behavior of the system in this regime. The second important feature of  $\langle \hat{m}_{z,i}^2 \rangle$  demonstrated by Fig. 4-3 is that, at a fixed value of  $U/t$ , as the temperature in the system increases, the average local moment decreases. This is related to the previous argument, and is a result of the fact that, as the system gains more thermal energy, it can overcome the repulsive on-site interaction energy cost more effectively, and increase the density of doubly-occupied sites in the system. Thus, as the temperature increases, which increases the density of doublons, the density of singly occupied sites (or the average local moment) must decrease at a fixed filling,  $\langle \hat{n}_{\uparrow,i} + \hat{n}_{\downarrow,i} \rangle = 1$ . As we will discuss in section 4.3.5, this argument is overly simplistic, and actually breaks down at sufficiently low temperatures (not shown in Fig. 4-3). That is, as the temperature decreases and becomes comparable to the super-exchange energy scale  $4t^2/U$ , the energy scale of magnetic ordering, the average local moment at half-filling actually becomes a non-monotonic function of the temperature, and begins to decrease as the temperature is lowered further.

Fig. 4-3 shows NLCE data at fixed filling and fixed temperature, but we can also

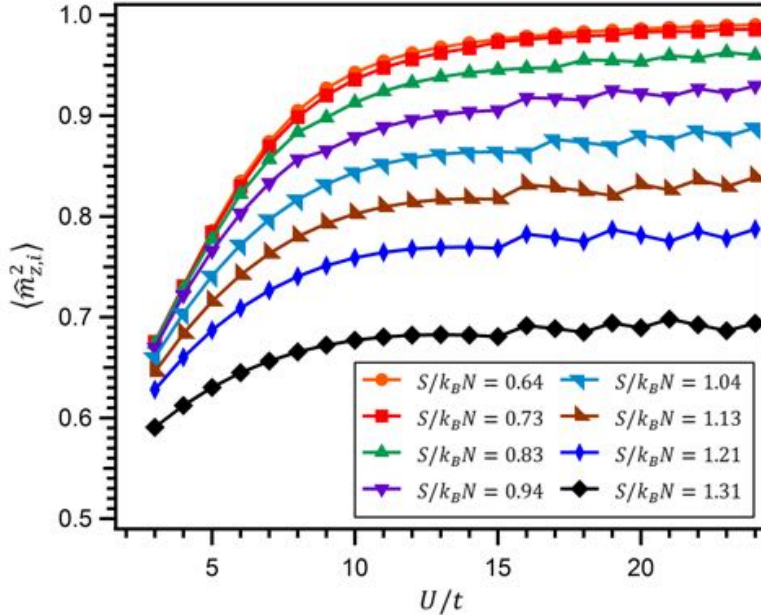


Figure 4-4: Average local moment at half-filling and fixed entropy per particle versus  $U/t$ . The different curves represent isentropic, 9<sup>th</sup>-order NLCE predictions for the average local moment of the 2D Fermi-Hubbard model at half-filling ( $\mu = U/2$ ) as a function of the Hubbard parameters  $U/t$ , for several different entropies per particle in the range  $0.64 \leq S/k_B N \leq 1.31$ . This entropy range represents typical values of the entropy which are achieved in the experimental data discussed in this thesis. The wiggles observed at large values of  $U/t$  are artifacts which arise from the fact that the NLCE calculations are performed at fixed temperature, rather than fixed entropy, and only a discrete set of temperatures on a logarithmically uniform grid are given in the NLCE calculations. The curves are generated using the NLCE data provided in the supplement of [120].

examine the dependence of  $\langle \hat{m}_{z,i}^2 \rangle$  on  $U/t$  at half-filling and at fixed entropy per particle,  $S/k_B N$ . Fig. 4-4 shows the NLCE data for the isentropic dependence of  $\langle \hat{m}_{z,i}^2 \rangle$  on  $U/t$ , for entropies per particle in the range  $0.64 \leq S/k_B N \leq 1.31$ , which is a typical experimentally attainable entropy range. The small wiggles visible in this figure at large values of  $U/t$  are artifacts, and arise because the NLCE calculations are actually performed at a fixed temperature rather than a fixed entropy. Since only a discrete set of temperatures are provided in the NLCE data of [120], and since the temperature changes significantly with  $U/t$  at fixed entropy per particle, the curves in Fig. 4-4 are only approximately isentropic, and can fluctuate slightly if the closest temperature available in the NLCE data set corresponds to a slightly

different entropy from the desired value. Despite this fact, however, the isentropic behavior of the average local moment can still be observed. Qualitatively at least, this behavior is not so different from the isothermal behavior. That is, at a fixed value of the entropy, the average local moment increases with increasing  $U/t$ . This simply follows from the same arguments applied to the isothermal case. The main difference here is that the saturation behavior observed in the isothermal case for increasing  $U/t$  is less obvious, even missing, for the isentropic curves. This comes about because the increased repulsive interaction energy cost of double-occupancies at larger values of  $U/t$  is partially compensated by the fact that the temperature  $k_B T/t$  also increases with increasing  $U/t$  (see section 2.2.3), which means that the system has more thermal energy to overcome the energy penalty associated with doublons (Fig. 4-3). If this compensation is strong enough, then the saturation behavior at the maximum value of one with increasing  $U/t$  is not observed over reasonable values of  $U/t$ .

Next, we can explore more closely the temperature dependence of the average local moment at half-filling for different Hubbard parameters  $U/t$ . This is shown, using the NLCE data, in Fig. 4-5 for  $1 \leq U/t \leq 24$ . As can be seen in the figure, at a fixed temperature, the average local moment increases with increasing  $U/t$ , in agreement with the NLCE calculations shown in Fig. 4-3, and our expectation that, at a given temperature and filling, the density of doublons should decrease as the interaction energy cost increases, meaning the density of singly-occupied sites should increase. However, Fig. 4-5 demonstrates a different feature of the average local moment which was not clearly shown in Fig. 4-3. Specifically, one can see that, at a given value of  $U/t$ , as the temperature decreases from large values,  $k_B T < U$ , the average local moment increases, since there is less thermal energy to help the system overcome the interaction energy cost. As the temperature is lowered further still, the average local moment increases less quickly with decreasing temperature, and eventually saturates around some peak value in a manner which depends on  $U/t$ . This can be understood from the fact that, once  $k_B T$  is sufficiently below  $U$ , it is no longer possible to thermally excite doublons in the system. In other words, the particle fluctuations due to thermal excitation of doublons are effectively frozen out at

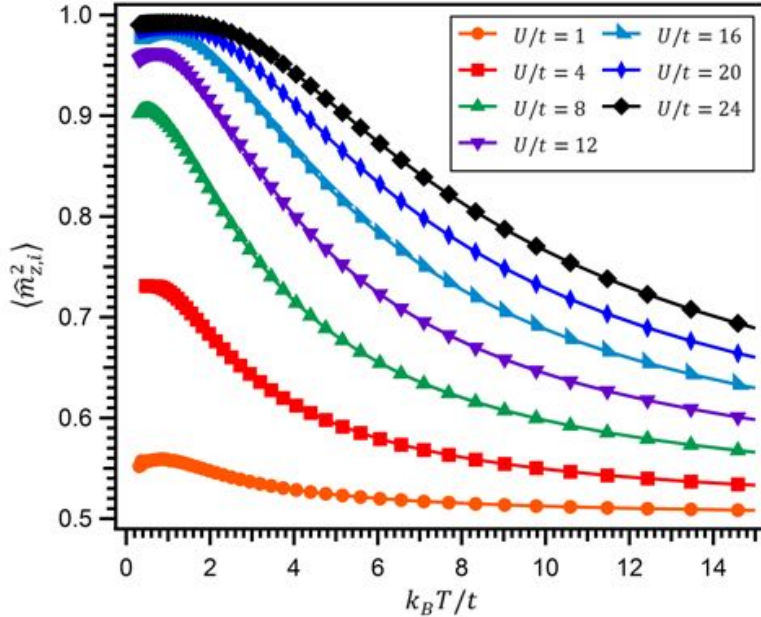


Figure 4-5: Average local moment at half-filling and fixed  $U/t$  versus  $k_B T/t$ . Plotted are 9<sup>th</sup>-order NLCE predictions for the average local moment of the 2D Fermi-Hubbard model at half-filling ( $\mu = U/2$ ) as a function of the system temperature  $k_B T/t$ , for several different values of the Hubbard parameters  $U/t$  in the range  $1 \leq U/t \leq 24$ . This range of Hubbard parameters covers most of the typical values used in the experimental data discussed in this thesis. For intermediate temperatures,  $4t^2/U < k_B T < U$ , the average local moment increases with decreasing temperature, for all of the  $U/t$  values shown, as the thermally excited doublon-hole fluctuations are gradually frozen out when the temperature is lowered relative to  $U$ . At lower temperatures,  $k_B T < 4t^2/U$ , the average local moment shows non-monotonic behavior (see e.g. the curve for  $U/t = 12$ ), which is related to an enhanced delocalization of particles which can arise in the presence of strong antiferromagnetic correlations. The curves are generated using the NLCE data provided in the supplement of [120].

temperatures  $k_B T \ll U$ , meaning the insulating character of the system is enhanced. Once these thermal charge excitations are frozen out, the average local moment is no longer sensitive to changes in the temperature and roughly saturates at some value which depends on the nature of the quantum state determined by the value of  $U/t$ . For example, in a perfect metallic state at half-filling, where  $U \ll t$  and the particles are totally delocalized, it is equally likely for a site to be occupied with either a hole, a single particle of either spin, or a doublon. In this case, one would expect the average density of singly-occupied sites (or the average moment) to be 0.5. If there are small, but finite interactions present, e.g.  $U = t$  (the orange curve in Fig. 4-5),

singly-occupied sites are slightly energetically favored above doubly-occupied sites, so that the average density of singly-occupied sites should increase beyond the non-interacting limit of 0.5, in agreement with the  $U/t = 1$  curve in the figure. In the opposite limit, where  $U/t \gg 1$ , doubly-occupied sites are essentially entirely blocked, so that the particles are effectively localized, and the average local moment approaches the maximum value of one. In this case, the strong on-site interactions have driven the system into an insulating state, otherwise known as a Mott insulator. For intermediate values of  $U/t$ , e.g.  $U/t = 8$ , the moment saturates in an intermediate regime, somewhere inbetween 0.5 and 1. In the case of  $U/t = 8$ , it saturates around 0.9, meaning that roughly 5% of the sites are doubly-occupied and roughly 5% are holes. It is also worth mentioning here that, as the temperature is lowered further at a given  $U/t$ , and approaches the super-exchange energy scale  $4t^2/U$ , the average local moment becomes non-monotonic, and actually decreases slightly from the peak saturated value. This can be clearly seen, for example, in the  $U/t = 12$  curve in Fig. 4-5. The non-monotonic behavior is related to the removal of thermal spin excitations at sufficiently low temperatures, which means that antiferromagnetic ordering in the system is enhanced in this regime. Such magnetic ordering of the spins actually allows particles to delocalize slightly because they are no longer Pauli blocked by neighboring atoms in the same spin state. This ultimately leads to a slight decrease in the average moment below the peak value, and will be discussed in more detail in section 4.3.5. We would also like to note here that the strong temperature dependence of the average local moment at half-filling, in the temperature regime where the moment has not yet saturated, can be used to determine a reasonable temperature of the system by measuring the value experimentally at a particular  $U/t$ , and comparing to the NLCE results shown in Fig. 4-5. This will be discussed in more detail in sections 4.3.4 and 4.3.5.

To round off this discussion regarding the behavior of the local moment in the 2D Fermi-Hubbard model, we finally explore the dependence of  $\langle \hat{m}_{z,i}^2 \rangle$  on the chemical potential  $\mu$ . NLCE calculations of the average local moment as a function of  $\mu$ , at several different fixed temperatures,  $0.82 \leq k_B T/t \leq 5.16$ , and several different fixed

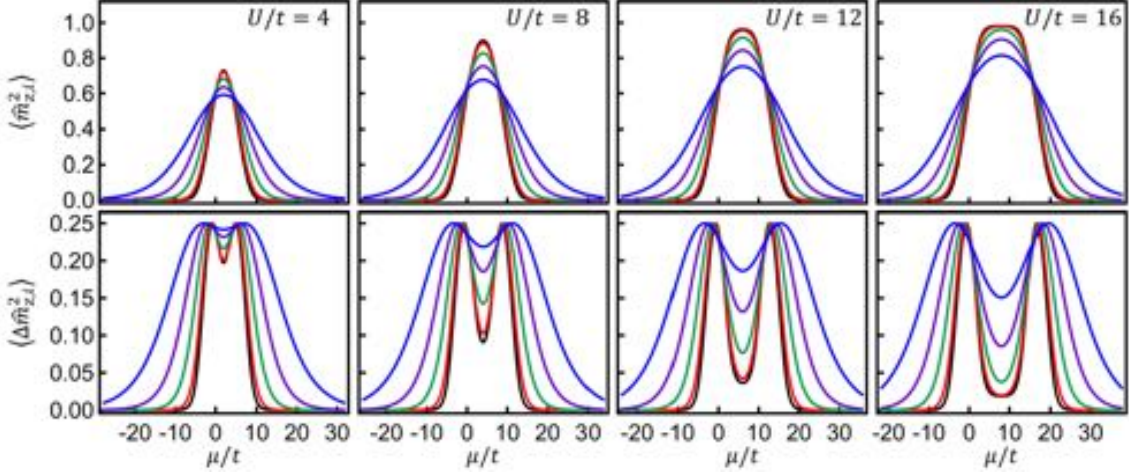


Figure 4-6:  $\langle \hat{m}_{z,i}^2 \rangle$  and  $\langle \Delta \hat{m}_{z,i}^2 \rangle$  versus  $\mu/t$  for fixed  $U/t$  and  $k_B T/t$ . The different curves represent isothermal 9<sup>th</sup>-order NLCE predictions for the average local moment  $\langle \hat{m}_{z,i}^2 \rangle$  (top row) and the variance in the local moment  $\langle \Delta \hat{m}_{z,i}^2 \rangle$  (bottom row) as a function of the global chemical potential  $\mu/t$ , for several different temperatures  $k_B T/t$  and values of the Hubbard parameters  $U/t = (4, 8, 12, 16)$ , where each column represents a different value of  $U/t$ . The black curves in the figures represent  $k_B T/t = 0.82$ , the red curves are  $k_B T/t = 1.13$ , the green curves are  $k_B T/t = 1.97$ , the purple curves are  $k_B T/t = 3.19$ , and the blue curves are  $k_B T/t = 5.16$ . The half-filling point in each graph is determined by the location of  $\mu = U/2$ . In the sense of the LDA, the profiles shown here are directly related to the in-trap distributions of the local moment, and its variance, that are observed in the experiment. These plots are generated using the NLCE data provided in the supplement of [120].

Hubbard parameters,  $4 \leq U/t \leq 16$ , are shown in the top row of Fig. 4-6. Also shown, in the bottom row of this figure, are the corresponding average fluctuations in the local moment (Eq. 4.3) as functions of the chemical potential  $\mu$ , which sets the density of particles in the system. Immediately apparent from this figure is the particle-hole symmetry of the local moment operator (Eq. 4.4) about the half-filling point  $\mu = U/2$ : the average moment takes the same value for a hole doped system ( $\mu < U/2$ ) as it does for a particle doped system ( $\mu > U/2$ ). The fact that  $\mu = U/2$  represents half-filling,  $\langle \hat{n}_{\uparrow,i} + \hat{n}_{\downarrow,i} \rangle = 1$  follows simply from the reflection symmetry of the Hubbard model about this point: under a particle-hole transformation,  $\langle \hat{n}_{\uparrow,i} + \hat{n}_{\downarrow,i} \rangle$  becomes  $\langle (1 - \hat{n}_{\uparrow,i}) + (1 - \hat{n}_{\downarrow,i}) \rangle = 2 - \langle \hat{n}_{\uparrow,i} + \hat{n}_{\downarrow,i} \rangle$ . At the symmetry point, however, where the particle-hole transformation has no effect, we must have that these two quantities are equal, so that  $\langle \hat{n}_{\uparrow,i} + \hat{n}_{\downarrow,i} \rangle = 2 - \langle \hat{n}_{\uparrow,i} + \hat{n}_{\downarrow,i} \rangle$ , which means  $\langle \hat{n}_{\uparrow,i} + \hat{n}_{\downarrow,i} \rangle = 1$ . The

curves in Fig. 4-6 also demonstrate three points of relevance. First, at a fixed chemical potential and fixed temperature, the average local moment increases with increasing  $U/t$ , a behavior which we discussed previously for the specific case of half-filling, but which, as this figure shows, also holds for chemical potential values away from half-filling. Second, at a fixed value of  $U/t$ , as the temperature of the system increases, the peak moment at half-filling decreases, as we discussed in Fig. 4-5, but the width of the distribution also increases substantially. This increase in the width of the average moment is strongly reminiscent of the behavior of the density distribution of a trapped ideal Fermi gas in the classical limit [119], where the width is set by the temperature of the system. Thus, not only does the peak moment at half-filling give an estimate of the temperature, but also the sharpness of the moment distribution in the trap. The final point that Fig. 4-6 demonstrates is that, at a fixed, large value of  $U/t$ , for example  $U/t = 16$ , and at low temperatures, the average moment distribution flattens out at the top of the distribution. At larger values of  $U/t$ , the width of this flat top region increases. Ultimately this is a manifestation of the incompressibility of the Mott insulator [205, 55], and the opening of a Mott gap in the density of states. That is, because the strong interactions reduce the density of double-occupancies at half-filling, which means there is a high density of singly-occupied sites, adding particles to the system by increasing  $\mu$  necessarily increases the double occupancy, which is energetically costly. Thus, the system would prefer to maintain one particle per site, and requires a larger increase of the chemical potential in order to overcome the interaction energy penalty and increase the density. Another way to say this is that the compressibility,  $\frac{1}{n^2} \left( \frac{\partial n}{\partial \mu} \right) \Big|_T$ , where  $n$  is the total density, decreases around half-filling as  $U/t$  increases: the Mott insulator is incompressible. Because of this, the density distribution flattens out around half-filling as a function of  $\mu$ , and therefore so too does the average local moment. We will discuss the variance of the local moment as a function of  $\mu$ , shown in the bottom row of Fig. 4-6, in more detail in section 4.3, when we discuss properties of the different states of the Hubbard model. For now we simply note that the variance, which describes particle fluctuations, reaches a local minimum value at half-filling, where the moment is peaked, which indicates insulating

behavior for large  $U/t$ . The variance peaks, on the other hand, at a value of 0.25, where the moment is 0.5. This peak variance indicates significant particle fluctuations and therefore metallic behavior of the system at this chemical potential.

### 4.3 Observing Metallic, Mott-Insulating, and Band-Insulating States *In Situ*

With access to the local moment at each site, and the ability to prepare cold samples with control over all parameters in the Hamiltonian (including the relative strengths of  $t$ ,  $U$ ,  $\mu$ , and to some extent  $T$ ), we can directly observe different states of the Hubbard model *in situ*, and characterize them through the properties of their local moments in real-space. For example, when the on-site interactions in the system are weak ( $U < 8t$ ), or the density is sufficiently low ( $\langle \hat{n}_{\uparrow,i} + \hat{n}_{\downarrow,i} \rangle \ll 1$ ), the system behaves like a metal, and is characterized by large fluctuations in the occupation of each lattice site arising from the presence of itinerant particles. Such fluctuations in the site occupation are evident in both the variance of the total density of the system and the variance of the local moment. When the chemical potential is increased sufficiently such that  $\mu \gg U, t, T$ , but  $\mu$  still lies within the single particle bandgap, all of the states within the lowest energy band become filled, corresponding to one particle of each spin state per site, and the system enters a band-insulating state. The Pauli exclusion principle is the driving force behind this insulating behavior, because there are no empty states available for particles to scatter into in order to conduct, or tunnel around in the lattice. In real-space, this property manifests itself in the form of a strongly suppressed variance in the density at each site, since every site is doubly occupied (the maximum possible filling). In terms of the what we can observe in the experiment, the local moment must vanish in the band insulator since  $\langle \hat{n}_{\uparrow,i} + \hat{n}_{\downarrow,i} \rangle = 2$ , a striking signature of this state.

Another type of insulator emerges when the system is at half-filling and the on-site interactions are strong ( $U \gg 8t$ ). In this situation, and when the temperature

is low enough ( $k_B T \ll U$ ), the strong interactions present make the possibility of creating doubly occupied sites very unlikely due to the significant energy cost this would incur. Because the density is such that  $\langle \hat{n}_{\uparrow,i} + \hat{n}_{\downarrow,i} \rangle = 1$ , and the creation of doublons is fundamentally limited by this charge gap, this means that on-site particle fluctuations are strongly suppressed, and the only configuration available to the system is one where each particle is well localized to its respective site and cannot tunnel around in the lattice. In contrast to the band-insulating state whose insulating behavior arises from Pauli blocking, this insulating behavior is driven by strong interactions, and is called a Mott insulator. In terms of local moments, such a state manifests itself through an average local moment very near the maximal value of 1 ( $\langle \hat{m}_{z,i}^2 \rangle \sim 1$ ), which follows from the fact that the system is at half-filling and  $\langle \hat{m}_{z,i}^2 \rangle \approx \langle \hat{n}_{\uparrow,i} + \hat{n}_{\downarrow,i} \rangle$  when the density of doublons is small. Thus, it is apparent that each of these states can reveal itself through its local moment, a measure of the charge degree of freedom. The spin degree of freedom associated with these states also exhibits interesting behavior, and is discussed in detail in section 4.4.3.

### 4.3.1 Imaging Metallic, Mott-Insulating, and Band-Insulating States

We can realize these states experimentally by varying the relative strengths of the different energy scales,  $U$ ,  $t$ , and  $\mu$ , using the depth of the optical lattice and the strength of the external confinement provided by the dimple. The lattice depth controls the ratio  $U/t$ , and the external confinement changes the density, and therefore  $\mu$ , at the center of the trap. We can then take fluorescence images of these states *in situ* using our quantum gas microscope, which allows us to detect the parity-projected occupation of each lattice site. Fig. 4-7 shows exemplary raw images of each of the metallic, Mott-insulating, and band-insulating states, as well as the corresponding reconstructed parity-projected site occupation we obtain after analyzing these images. As expected from the previous arguments, the metallic state shows significant density fluctuations across the sample. In contrast, the Mott insulator displays a fairly

uniform moment near unity (one particle per site), and the band insulator reveals a vanishing moment in the center where the density approaches two particles per site. Because an underlying trapping potential is present (due to the light intensity variation from both the optical lattice and the dimple), the local density decreases monotonically with increasing distance from the trap center, which means that metallic, Mott-insulating, and band-insulating states can actually coexist within the same sample. This effect is most apparent in the image of the band insulator, where the band-insulating core is surrounded by an annular Mott insulator region with one particle per site. Because the density must change smoothly between the Mott insulator (one particle per site) and the vacuum (no particles), the region surrounding the Mott insulator, where the density is low but non-zero, is metallic and therefore shows larger particle fluctuations. Due to the particle-hole symmetry of the Fermi-Hubbard model on a bi-partite lattice about the half-filling point  $\mu = U/2$ , which in this case lies within the annular Mott insulator region, the boundary region connecting the band insulator (two particles per site) to the Mott insulator, where  $1 < \langle \hat{n}_{\uparrow,i} + \hat{n}_{\downarrow,i} \rangle < 2$ , is also generically metallic, and shows particle fluctuations comparable to the outer metallic region.

#### 4.3.2 Radial Profiles of the Observed Local Moment and its Fluctuations

Because of the (approximate) radial symmetry of the underlying trapping potential associated with the intensity variation of the optical lattice and the dimple, we can perform a more quantitative analysis of the images shown in Fig. 4-7(a-c) by radially averaging the reconstructed parity-projected site occupations of Fig. 4-7(d-f). The results of this are shown in Fig. 4-8(a-c), respectively. To generate these curves, we first compute the center of mass of each of the reconstructed local moment maps, Fig. 4-7(d-f), then calculate the distance of each site from the corresponding center of mass, along with the value of the local moment at that site (either zero or one). We then bin the measured radii uniformly and take the average value of the local

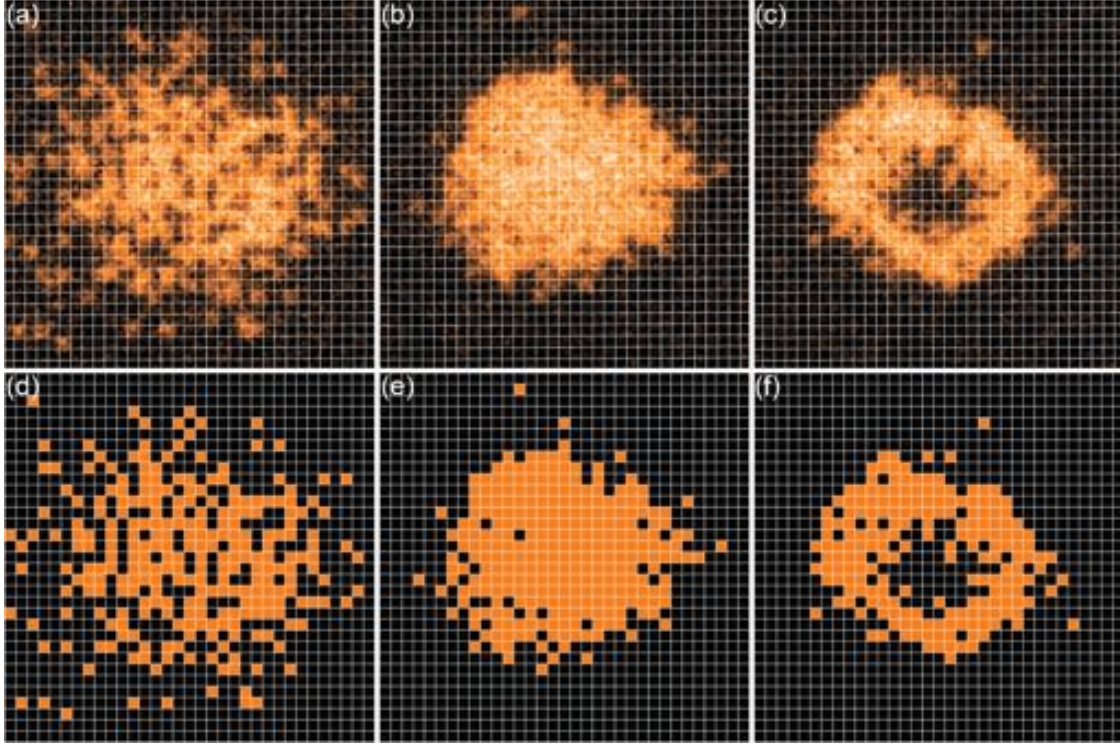


Figure 4-7: Observation of metallic, Mott-insulating, and band-insulating states of the 2D Fermi-Hubbard model. Site-resolved fluorescence images taken *in situ* (top row), and their corresponding reconstructed site occupations (bottom row), of different paradigmatic states of the 2D Fermi-Hubbard model, realized with  $^{40}\text{K}$  atoms in a square optical lattice. (a),(d) represent a metallic state, with  $U/t = 2.6(3)$ ,  $\mu_0/U = 0.52(9)$ ,  $k_B T/U = 0.55(9)$ ,  $\hbar\omega/U = 0.21(2)$ , and  $U/h = 540(60)$  Hz. (b),(e) represent a Mott-insulating state, with  $U/t = 98(6)$ ,  $\mu_0/U = 0.46(2)$ ,  $k_B T/U = 0.09(1)$ ,  $\hbar\omega/U = 0.085(4)$ , and  $U/h = 1350(50)$  Hz. (c),(f) represent a band-insulating state (at the core), with  $U/t = 20.8(8)$ ,  $\mu_0/U = 1.44(7)$ ,  $k_B T/U = 0.18(2)$ ,  $\hbar\omega/U = 0.18(1)$ , and  $U/h = 1007(40)$  Hz. Figures reproduced from [39].

moment within each radial bin. Simultaneously, we can compute the variance of the local moment about its average value within each bin, and this is shown in Fig. 4-8(d-f), respectively.

For the metallic state with  $U/t = 2.6(3)$ , Fig. 4-8(a),(d), the observed local moment reaches a peak value of  $\sim 0.7$ , less than the maximum possible value of 1, and a peak variance of  $\sim 0.25$ . The suppressed value of the peak moment is consistent with the notion that particles are relatively free to move around due to the weak interactions, so that doublons and holes can occur with reasonably high probabil-

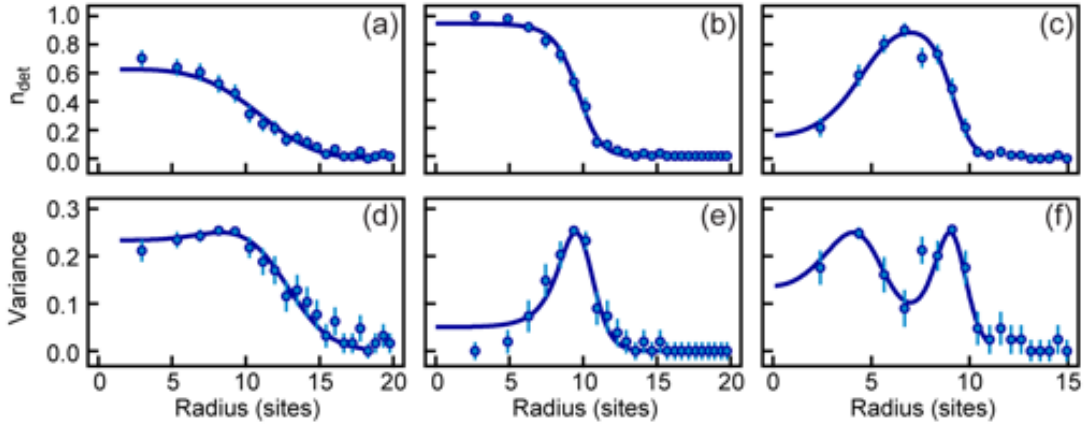


Figure 4-8: Radially averaged profiles of the in-trap local moment and its variance for metallic, Mott-insulating, and band-insulating states of the 2D Fermi-Hubbard model. The top row represents the radially averaged, detected density,  $n_{det}$ , of different states of the Hubbard model, which is equivalent to the average local moment,  $\langle \hat{m}_z^2 \rangle$ , whereas the bottom row represents the corresponding variance of the local moment,  $\langle \Delta \hat{m}_z^2 \rangle$ , measured from the fluctuations around the average value. The solid curves represent theoretical fits to the experimentally measured in-trap profiles. (a),(d) represent the metallic state of Fig. 4-7(a),(d), with  $U/t = 2.6(3)$ ,  $\mu_0/U = 0.52(9)$ ,  $k_B T/U = 0.55(9)$ ,  $\hbar\omega/U = 0.21(2)$ , and  $U/h = 540(60)$  Hz, which is fit to NLCE data with  $U/t = 3$ . (b),(e) represent the Mott-insulating state of Fig. 4-7(b),(e), with  $U/t = 98(6)$ ,  $\mu_0/U = 0.46(2)$ ,  $k_B T/U = 0.09(1)$ ,  $\hbar\omega/U = 0.085(4)$ , and  $U/h = 1350(50)$  Hz, which is fit to HTSE. (c),(f) represent the band-insulating state of Fig. 4-7(c),(f), with  $U/t = 20.8(8)$ ,  $\mu_0/U = 1.44(7)$ ,  $k_B T/U = 0.18(2)$ ,  $\hbar\omega/U = 0.18(1)$ , and  $U/h = 1007(40)$  Hz, which is fit to NLCE data with  $U/t = 21$ . Figures reproduced from [39].

ity, even around half-filling, thereby reducing the observed density of singly occupied sites. This argument also supports the large variance observed for this state. In fact, for a perfect metal at half-filling, one would expect a variance of exactly 0.25, since it is equally probable that a site is empty, doubly occupied, or occupied by a single particle of either spin state. The metallic state observed in the experiment contains finite on-site interactions however, which tend to lower the density of doubly occupied sites in the system, thereby increasing the measured local moment relative to what one would expect for a perfect metal. From Eq. 4.3, a variance of 0.25 should occur at an observed moment of 0.5. The effect of finite interactions in the metallic state then is to cause the maximum variance in the local moment to occur at a density slightly below half-filling.

In contrast, the Mott insulating state with  $U/t = 98(6)$ , Fig. 4-8(b),(e), shows an

enhanced local moment that reaches a peak value of 0.98(2), close to the maximum possible value. This is exactly what one would expect of a Mott insulator, where  $U/t \gg 1$  and the density is at or near half-filling, since the strong interactions localize particles to individual sites and suppress the probability of doublons in the system. The insulating effect also manifests itself in a strong suppression of the variance of the local moment, which is observed experimentally to drop below 0.03, in stark contrast to the metallic state. The band insulator with  $U/t = 20.8(8)$  shown in Fig. 4-8(c),(f) demonstrates a depletion of the local moment at the center of the trap, with a corresponding suppression of the variance, consistent with insulating behavior arising from Pauli blocking and the presence of two particles per lattice site. Moving away from the trap center, the variance peaks in the metallic region connecting the band insulator with the annular Mott insulator, then decreases and reaches a local minimum in the Mott-insulating region, where the moment reaches its peak value. Going past the Mott-insulating annulus, the variance peaks once again in the metallic region between the Mott insulator and the vacuum, and finally drops to zero as the particle density vanishes, along with the local moment.

Because we measured both the variance and the average from the moment values contained within each radial bin produced during the averaging process, we can perform an independent check of Eq. 4.3 using the experimental data. That is, we can compare the values of the variance obtained directly from the data with the variance calculated using Eq. 4.3 and the measured average moment. The results of this check on the band-insulating data of Fig. 4-8(c),(f) are shown in Fig. 4-9. We find that, well within the experimental error, these two methods of calculating the variance of the local moment agree with each other. This appears to hold even in the presence of slight deviations of the trap geometry from perfect radial symmetry that could potentially effect the measured average or variance differently. It is also worth noting that the behavior of the variance given by Eq. 4.3 does not generally hold for the total density itself  $\langle \hat{n}_i \rangle = \langle \hat{n}_{\uparrow,i} + \hat{n}_{\downarrow,i} \rangle$ . That is because  $\langle \hat{n}_i^2 \rangle - \langle \hat{n}_i \rangle^2 = \langle \hat{n}_i \rangle (1 - \langle \hat{n}_i \rangle) + 2 \langle \hat{n}_{\uparrow,i} \hat{n}_{\downarrow,i} \rangle$ . Thus, if our imaging process did not efficiently remove doublons for example, so that the quantity measured was not actually that defined by Eq 4.1, we might expect

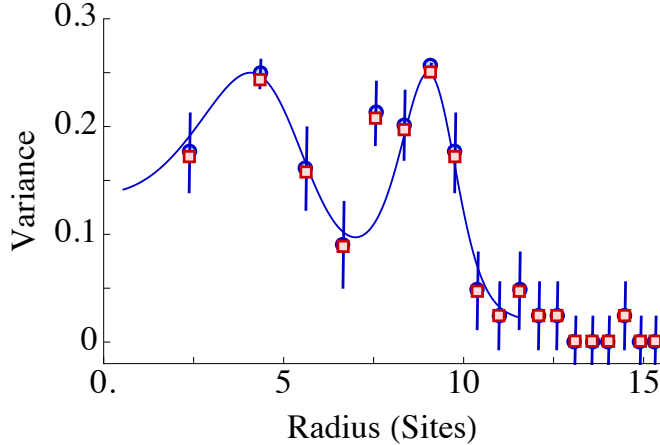


Figure 4-9: Comparing two methods for measuring the variance of the local moment. Plotted is the radial profile of the variance of the local moment about its average value for the site-resolved band insulator image of Fig. 4-7(c),(f). The blue circles represent the experimentally measured variance of the local moment,  $\langle \Delta \hat{m}_z^2 \rangle$ , about its radially averaged value,  $\langle \hat{m}_z^2 \rangle$ , which itself is shown in Fig. 4-8(c). The error bars represent the  $1\sigma$  statistical uncertainty in the measurement. These are the same data points shown in Fig. 4-8(f). The red squares represent a measurement of the radial profile of  $\langle \Delta \hat{m}_z^2 \rangle$  for the band-insulator image of Fig. 4-7(c),(f), which is obtained using the radially averaged local moment,  $\langle \hat{m}_z^2 \rangle$ , from Fig. 4-8(c), and the equation for the variance of the local moment expressed in terms of the average value, Eq. 4.3. The error bars for the red squares are not shown. As is evident in the plot, the two methods of obtaining  $\langle \Delta \hat{m}_z^2 \rangle$  agree with each other well to within the experimental uncertainty in the measurement. The solid line represents the NLCE fit to the data, from Fig. 4-8(c),(f), with  $U/t = 20.8(8)$ ,  $\mu_0/U = 1.44(7)$ ,  $k_B T/U = 0.18(2)$ , and  $\hbar\omega/U = 0.18(1)$ . Figure reproduced from [37] and adapted from [39].

possible discrepancies between the two methods of calculating the variance of the observed signal, which we do not see.

### 4.3.3 Comparing Measured Profiles to Theory

We can obtain an estimate of the temperature,  $k_B T/U$ , and chemical potential,  $\mu_0$ , of the prepared samples by fitting the radially averaged profiles shown in Fig. 4-8 to theoretical predictions for the average local moment made using either NLCE or the HTSE in  $t/k_B T$  (see section 2.2.2). Although the shapes of the measured radial profiles depend strongly on various experimental details including the trap shape and strength of the underlying harmonic confinement arising from the dimple beam and

the optical lattice beams, a comparison between the experimental data and the theoretical predictions is made possible through the use of the local density approximation (LDA). Under this approximation, the effect of the underlying trapping potential is encompassed within a spatially varying local chemical potential  $\mu(r) = \mu_0 - V(r)$ , where  $\mu_0$  is the global chemical potential and  $V(r)$  is the underlying trapping potential [203, 174]. For our experiment, where the trapping potential arises from the intensity variation of the dimple and optical lattice beams,  $V(r)$  can be approximated as a harmonic trapping potential, so that  $V(r) = \frac{1}{2}m\omega^2r^2$ , where  $\omega$  is the harmonic trapping frequency and  $m$  is the mass of  $^{40}\text{K}$ . Using this form for the chemical potential, we can then easily convert the predictions of theory, which typically give the density or local moment as functions of the chemical potential at fixed  $U/t$  and  $k_B T/U$ , to functions of radius from the center of the trap at fixed  $U/t$  and  $k_B T/U$ .

For the fitting process, we leave  $\mu_0$ ,  $k_B T$ , and  $\omega$  as free parameters, and  $U$ ,  $t$  are determined independently in the experiment, as discussed in section 4.2.1, for each of the various states. Because the periodic lattice potential can significantly affect the interpretation of dipole oscillation measurements typically used for determining the trap frequency  $\omega$ , we found it simplest to leave this as a free parameter in the fit, rather than trying to determine it independently in the experiment. In Ch. 5, we discuss a different method of determining  $\omega$  using an applied magnetic field gradient of known gradient magnitude. Next, we fit the measured radial profiles of the moment with the equation of state data from either NLCE or the HTSE in  $t/k_B T$ , and minimize the difference between the data and the fit using the free fit parameters, in the least squares sense. The metallic and band-insulating data shown in Fig. 4-8(a),(c) are fit using NLCE, and the Mott-insulating data of Fig. 4-8(b) is fit using the HTSE in  $t/k_B T$ , where it is expected to describe the system well. The results of this process are shown as the solid lines in Fig. 4-8(a),(b),(c), which demonstrate good agreement between the data and the predictions from theory. The fits for the average local moment can be directly converted to radial profiles for the variance of the local moment using Eq. 4.3, and these are the solid lines shown in Fig. 4-8(d),(e),(f), which also demonstrate good agreement with the data. From the fits we find that, for the

metallic state with  $U/t = 2.6(3)$  and  $U/h = 540(60)$  Hz,  $\mu_0/U = 0.52(9)$ ,  $k_B T/U = 0.55(9)$ , and  $\hbar\omega/U = 0.21(2)$ . For the Mott-insulating state with  $U/t = 98(6)$  and  $U/h = 1350(50)$  Hz, we find  $\mu_0/U = 0.46(2)$ ,  $k_B T/U = 0.09(1)$ , and  $\hbar\omega/U = 0.085(4)$ , and for the band-insulating state with  $U/t = 20.8(8)$  and  $U/h = 1007(40)$  Hz, we find  $\mu_0/U = 1.44(7)$ ,  $k_B T/U = 0.18(2)$ , and  $\hbar\omega/U = 0.18(1)$ .

For the band-insulating case, we can perform an additional check that the data and the resulting values obtained for  $\mu_0$  and  $\omega$  from the fits are reasonable. This comes from the particle-hole symmetry of the local moment operator, Eq. 4.4, that is discussed in section 4.2.2. That is, because the average local moment reaches a global maximum at half-filling,  $\mu = U/2$ , we can directly relate  $\mu_0$  to  $\omega$  using the LDA,  $\mu(r) = \mu_0 - \frac{1}{2}m\omega^2r^2$ , if we can find the radial location of the peak value of the average moment,  $r_{peak}$ . Specifically, we must have that  $\mu_0 = U/2 + \frac{1}{2}m\omega^2r_{peak}^2$ . For this sample,  $U/h = 1007(40)$  Hz, the  $\omega$  obtained from the fit is  $\omega = 2\pi \times 181(3)$  Hz, and the peak average moment is found to occur at  $r_{peak} = 7a$ , where  $a = 541$  nm is the lattice spacing. Putting these numbers into the formula yields a prediction for the global chemical potential of  $\mu_0/h = 1433$  Hz, which is consistent within the experimental uncertainty with the value obtained from the fit,  $\mu_0/h = 1450(40)$  Hz.

We can use the results for the temperature  $k_B T/U$  and the local chemical potential  $\mu(r)$  of each of the samples, along with the equation of state data from NLCE or the HTSE in  $t/k_B T$ , to obtain a local entropy per site,  $s(r)/k_B$ , and a local average total density per site,  $n(r)$ , for each of the states in Fig. 4-7. The resulting local entropies per site are shown in Fig. 4-10. Comparing these radial entropy profiles with the average moment and variance profiles of Fig. 4-8, it is immediately apparent that entropy is not distributed homogeneously throughout the sample. In fact, the local entropy peaks in the metallic regions where the variance of the local moment simultaneously reaches a maximum value, and decreases in the Mott-insulating region, where the strong on-site interactions reduce particle fluctuations, and therefore the number of states that are locally accessible to the system. This suppression of the local entropy is even more drastic in the band-insulating region, where the number of accessible states is further reduced due to the relatively large chemical potential,

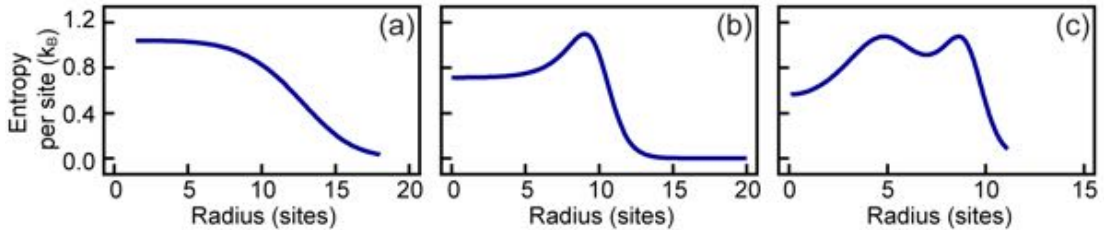


Figure 4-10: Radially averaged local entropy per site. The curves represent the theoretical predictions from NLCE, for figures (a) and (c), and HTSE, for figure (b), for the local entropy per site,  $s(r)/k_B$ , of the in-trap profiles shown in Figs. 4-7 and 4-8. These plots are obtained using the thermodynamic parameters extracted from the corresponding fits to the experimental data in Fig. 4-8, the local density approximation (LDA), and the equation of state data from the corresponding theoretical technique (NLCE or HTSE), which relates the extracted thermodynamic parameters (temperature, global chemical potential, etc...) to the entropy per site. (a) represents the metallic state of Fig. 4-7(a),(d), with  $U/t = 2.6(3)$ ,  $\mu_0/U = 0.52(9)$ ,  $k_B T/U = 0.55(9)$ ,  $\hbar\omega/U = 0.21(2)$ , and  $U/h = 540(60)$  Hz, which is fit to NLCE data with  $U/t = 3$ . (b) represents the Mott-insulating state of Fig. 4-7(b),(e), with  $U/t = 98(6)$ ,  $\mu_0/U = 0.46(2)$ ,  $k_B T/U = 0.09(1)$ ,  $\hbar\omega/U = 0.085(4)$ , and  $U/h = 1350(50)$  Hz, which is fit to HTSE. (c) represents the band-insulating state of Fig. 4-7(c),(f), with  $U/t = 20.8(8)$ ,  $\mu_0/U = 1.44(7)$ ,  $k_B T/U = 0.18(2)$ ,  $\hbar\omega/U = 0.18(1)$ , and  $U/h = 1007(40)$  Hz, which is fit to NLCE data with  $U/t = 21$ . Figures reproduced from [39].

which causes many of the sites to be doubly occupied. Integrating the local entropy per site over space,  $\int s(r)dr/k_B$ , and dividing by the integral of the local total density per site,  $\int n(r)dr$ , which is simply the total particle number  $N$ , yields a value for the trap-averaged entropy per particle  $S/k_B N$ . Doing this for each of the metallic, Mott-insulating, and band-insulating samples yields average entropies per particle of  $1.7(1)k_B$ ,  $1.23(6)k_B$ , and  $0.99(6)k_B$ , respectively, for the three different states.

In principle, one can combine this spatial redistribution of entropy with local manipulation of the underlying trapping potential in order to controllably further reduce the entropy within certain regions of the sample [20, 99]. This was demonstrated experimentally in [152], where the underlying trapping potential was purposefully shaped to extend the size of the metallic regions of the sample, which could locally store entropy, thereby removing entropy from within a central Mott-insulating core. A similar technique was also used to demonstrate the preparation of ultra-low entropy band-insulators, with the intention of utilizing them as initial quantum states that

could be adiabatically converted into other desirable many-body quantum states [43].

#### 4.3.4 Melting a Mott Insulator: Studying the Effects of Temperature

We can observe the effect of temperature on the average local moment and its variance by preparing initial band-insulating samples with  $U/t = 20.8(8)$  and  $\hbar\omega/U = 0.18(1)$ , which provide access to a range of densities within the trapped system, and holding them in the optical lattice for a variable amount of time, up to several seconds. Heating of the sample occurs during this hold time, and arises from various effects including noise on the intensity of the laser light used to form the optical lattice, pointing noise of the lattice laser beams (or the retro-reflected beams), and possible off-resonant scattering of lattice laser photons. By imaging the sample after some amount of hold time, we can access a large range of temperatures above the lowest initial temperature achieved for this configuration,  $k_B T/U = 0.18(2)$  (see section 4.3.3). Fig. 4-11(a) shows the measured parity-projected site occupation for samples held in the lattice for several different times, corresponding to several different temperatures. As was discussed in section 4.3.2, we can radially bin these site-resolved images in order to obtain the average moment and its variance as functions of distance from the trap center for each of the different hold times. The results of this are shown in Fig. 4-11(b),(c). By fitting the radial profiles of the average moment in Fig. 4-11(b) to the HTSE in  $t/k_B T$ , we can obtain the temperature,  $k_B T/U$ , and the global chemical potential,  $\mu_0$ , for each of the samples, as discussed in detail in section 4.3.3. The resulting best fit distributions for each of the samples are shown as the solid lines in Fig. 4-11(b),(c), and correspond to fitted temperatures in the range  $k_B T/U = 0.18(2)$  to  $0.55(8)$ .

Comparing the fitted temperatures with the corresponding images in Fig. 4-11(a), it is evident that, as the temperature increases relative to the on-site interaction energy  $U$ , more imaged holes, corresponding to either real holes or doublons, appear in the Mott-insulating annular region around the band-insulating core. This degra-

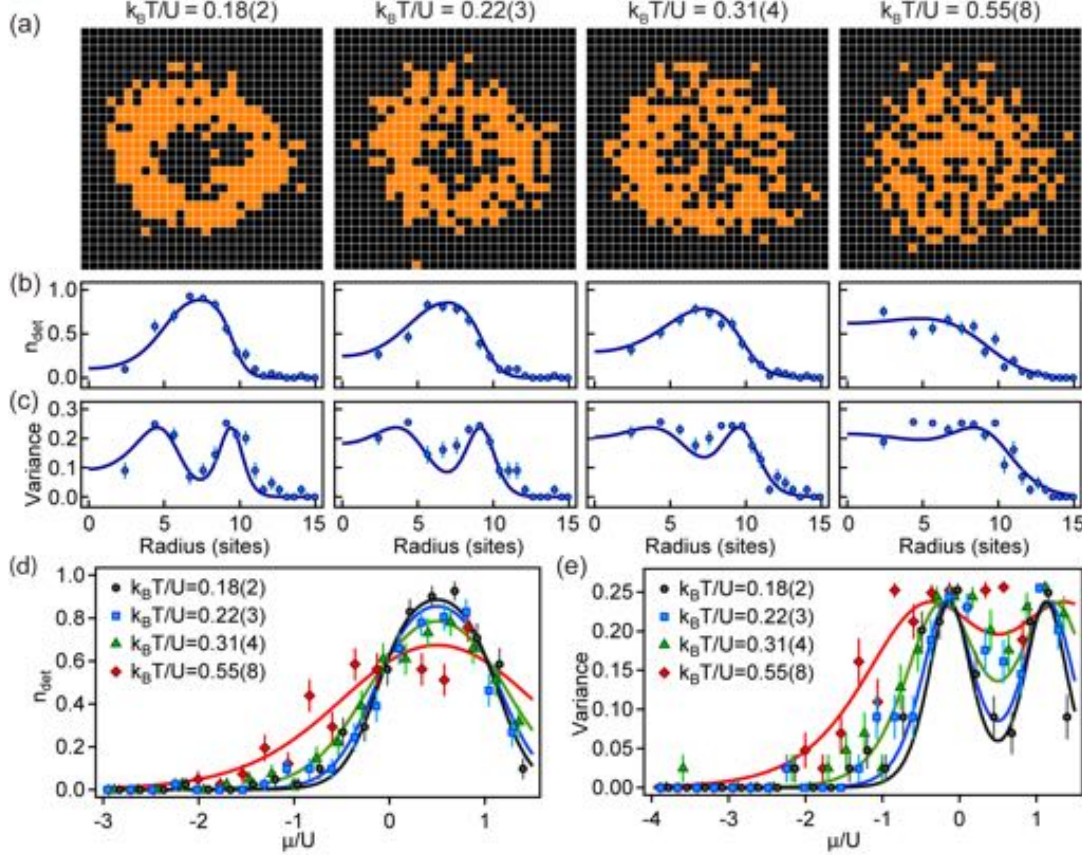


Figure 4-11: Examining the effects of temperature on the average local moment, and its variance, for Mott- and band-insulating samples. (a) The reconstructed site-occupations of samples with  $U/t = 20.8(8)$  and  $\hbar\omega/U = 0.18(1)$ , prepared at different temperatures,  $k_B T/U$ . The corresponding radial averages (b) of the local moment (denoted  $n_{det}$ ), and its variance (c), from the images shown in (a). The solid lines represent fits of the experimental data to the HTSE to obtain  $\mu_0$ ,  $\hbar\omega/U$ , and  $k_B T/U$ . (d),(e) The average moment and its variance, respectively, plotted versus  $\mu/U$  for the different values of the temperature. Figure reproduced from [39].

dation of the near unity occupation within the Mott insulator occurs because strong on-site interactions can no longer suppress the creation of doubly occupied sites (and corresponding holes) at half-filling once the temperature in the system becomes comparable in magnitude to the interaction energy  $U$ . For the sample with the highest temperature,  $k_B T/U = 0.55(8)$ , the site-resolved image is nearly indistinguishable from that of the metallic state shown in Fig. 4-7, which tells us that the temperature must actually be several times lower than  $U$  in order to observe Mott-insulating behavior. Similarly, as the temperature approaches the chemical potential,  $\mu_0$ , it be-

comes possible to create excitations in the system in the form of singly occupied sites within the high-density band-insulating region in the core of the sample. From the images shown in Fig. 4-11(a), this effect is directly observable. As the temperature increases, local moments, corresponding to singly occupied sites, appear within, and eventually fill in the band-insulating central core that was previously empty due to the enhanced density of double occupancies in this region. This qualitative behavior is quantitatively described by the radial profiles of the average moment and its variance. As the temperature increases, the peak average moment, which occurs at half-filling in the Mott insulator, decreases from  $\sim 0.9$  to  $\sim 0.7$ , while the average moment at the center of the sample increases from  $\sim 0.1$  to  $\sim 0.6$ . Simultaneously, the variance, which is initially suppressed in both the Mott- and band-insulating regions, increases significantly as the temperature increases, eventually reaching a value near  $\sim 0.25$  at  $k_B T/U = 0.55(8)$ , consistent with metallic behavior and enhanced particle fluctuations in the system.

Since we also have access to the global chemical potential  $\mu_0$  from the fits to the HTSE in  $t/k_B T$ , and under the LDA the local chemical potential obeys  $\mu(r) = \mu_0 - \frac{1}{2}m\omega^2r^2$ , we can convert both the experimental data and the HTSE fits in Fig. 4-11(b),(c) from functions of the radius from the trap center to functions of the chemical potential  $\mu/U$ . Doing this allows us to directly compare the four different samples with different temperatures and different global chemical potentials in a trap-independent manner. Fig. 4-11(d),(e) shows the data and the HTSE fits for the average moment and its variance, respectively, as functions of  $\mu/U$  for the four samples at different temperatures. These curves not only show that the peak average moment decreases as the temperature increases, but also that the width of the average moment distribution increases significantly with increasing temperature. This is related to the idea that, with more thermal energy in the system, the particles can more easily access regions of the trap which are further from the center, and are therefore at slightly higher potential energy. It is also related to the fact that the total particle number is roughly constant within each of the samples, so that a drop in the peak density must occur simultaneously with an increase in the width of the distribution. This is extremely

useful in the lab, because one can get an idea of the sample temperature, using either the peak average moment at half-filling or the sharpness of the features in the average moment distribution, from a single experimental realization. One can therefore use these quantities, at least for temperatures in the range  $t < k_B T < U$ , to quickly optimize various parameters in the experimental sequence.

For the purpose of thermometry, we can directly measure the temperature dependence of the average local moment at a fixed value of  $U/t$  and a fixed chemical potential,  $\mu/U$ . We do this using the same configuration of parameters that was used in Fig. 4-11, with  $U/t = 20.8(8)$  and  $\hbar\omega/U = 0.18(1)$ . To obtain a large range of different temperatures, we run many different iterations of the experiment with various amounts of time held in the lattice, to selectively heat the samples. We then radially average the parity-projected site occupation we measure for each sample, as discussed in section 4.3.2, to obtain the average local moment as a function of distance from the trap center. To determine the temperature,  $k_B T/t$ , and global chemical potential,  $\mu_0$ , we fit the radial profile of the average moment to the HTSE in  $t/k_B T$ , similar to what was done in sections 4.3.3 and 4.3.4. In this case, however, we fit only the wings of the moment distribution, where the average density is low, and the measured average moment satisfies  $\langle \hat{m}_{z,i}^2 \rangle < 0.25$ . We do this to obtain  $k_B T/t$  and  $\mu_0$  for a given sample, in such a way that the fit does not know about the experimentally measured average local moment near the center of the trap, so that these values may be independently compared to theoretical predictions at the correct chemical potential. Once the temperature and global chemical potential are known for each sample, one can extract the measured average moment at a particular chemical potential within a sample using the LDA,  $\mu(r) = \mu_0 - \frac{1}{2}m\omega^2r^2$ . Using many different realizations of the experiment at different temperatures, one can therefore access the average moment, at a given chemical potential, as a function of temperature,  $k_B T/t$ . Fig. 4-12 shows the results of this procedure for two chemical potentials,  $\mu = U/2$  (half-filling) and  $\mu = -U/4$ . The latter chemical potential value was chosen because it describes the metallic region below half-filling, where the density is low but non-zero,  $0 < \langle \hat{n}_{\uparrow,i} + \hat{n}_{\downarrow,i} \rangle < 1$ . Due to the particle-hole symmetry about  $\mu = U/2$  of

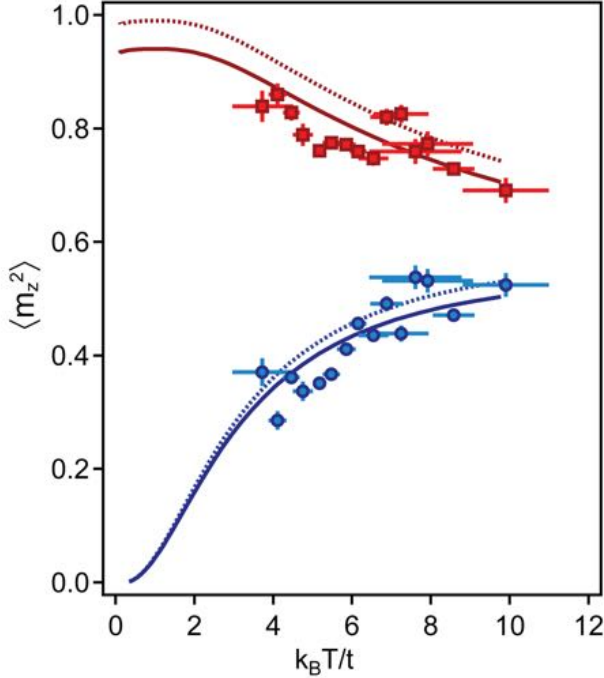


Figure 4-12: Temperature dependence of the average local moment,  $\langle \hat{m}_z^2 \rangle$ , at fixed  $U/t$  and  $\mu/U$ . The data represent  $\langle \hat{m}_z^2 \rangle$  as a function of  $k_B T/t$ , extracted from 117 independent experimental realizations prepared at  $U/t = 20.8(8)$ , for half-filling,  $\mu = U/2$  (red squares), and  $\mu = -U/4$  (blue circles). The temperature and global chemical potential of each sample are obtained by fitting the wings of the radially averaged moment distribution of the sample (with  $\langle \hat{m}_z^2 \rangle < 0.25$ ) to HTSE. From the HTSE fit and the LDA, one can obtain the radial location in the sample corresponding to the desired chemical potential, which, when combined with the extracted temperature for that sample, gives the experimental data shown in the figure. The solid (dotted) lines represent independent NLCE predictions for  $\langle \hat{m}_z^2 \rangle$  as a function of temperature at  $U/t = 21$ , for  $\mu = U/2$  (red curves), and  $\mu = -U/4$  (blue curves), which are (are not) corrected for the finite experimental imaging fidelity. Figure reproduced from [39].

both the moment operator and the Fermi-Hubbard model on a bi-partite lattice, the behavior of the local moment at  $\mu = -U/4$  also describes the corresponding metallic region above half-filling, where  $1 < \langle \hat{n}_{\uparrow,i} + \hat{n}_{\downarrow,i} \rangle < 2$ . Both sets of data agree with the behavior observed in Fig. 4-11(d), where the average moment at half-filling decreased with increasing temperature, and the average moment at both low and high fillings was found to increase with increasing temperature, corresponding to an increase in the overall width of the moment distribution.

Because this experimental data was obtained with minimal assumptions, using

only a fit of the wings of the moment distribution to the HTSE, we can compare it directly with the predictions of NLCE for the temperature dependence of the local moment at a fixed  $\mu/U$ . This allows us to independently verify the numerical predictions with experimental data that is obtained using other means. We can therefore check that the NLCE does in fact capture the behavior of the system in the experimentally attainable temperature and density ranges. The NLCE predictions for  $\langle \hat{m}_{z,i}^2 \rangle$  at  $\mu = U/2$  and  $\mu = -U/4$  are shown as the solid and dotted lines in Fig. 4-12. The dotted curves are the bare NLCE predictions, and the solid curves are the same predictions adjusted for the finite experimental detection fidelity of 95%. As shown in the figure, we find good agreement between the NLCE predictions and our experimental data. This suggests that the average local moment measured at half-filling, for example, can be used for thermometry by comparing the value with NLCE predictions. This allows one to obtain the temperature without having to fit the full radial profile to theory, which requires significant assumptions about the trap shape (e.g. that it is harmonic), as well as the validity of the LDA. This is especially useful, because the half-filling point can be found systematically in the experimental data, without any other assumptions, by purposefully preparing samples whose central density is above half-filling and simply determining the radial location of the peak moment (section 4.2.2).

### 4.3.5 The Local Moment as a Probe of Equilibrium Properties of the Hubbard Model and its Limitations

So far in this chapter, the discussion has focused strictly on the local moment and what it can teach us about various properties of the system. Practically speaking, this is because the moment is, in some sense, the most natural, and therefore the simplest quantity that our quantum gas microscope experiment can measure. In sections 4.3.1 and 4.3.2, for example, we discussed how different paradigmatic states of the 2D Fermi-Hubbard model, such as metallic, Mott-insulating, and band-insulating states, can be distinguished through the manifestly different behavior of the average

and variance of their local moments. We also found in section 4.3.4 that the average moment at half-filling, which reflects the density of thermal doublon-hole excitations in the system, can be used as a relatively sensitive thermometer to measure the temperature of the sample. This is supported by Fig. 4-5, which shows NLCE predictions for the temperature dependence of the average moment at half-filling for several values of  $U/t$ , in the temperature range  $0.3t < k_B T < 15t$ . This is a temperature regime where the NLCE predictions for the average moment are essentially exact at half-filling, so that by comparing these predictions with the experimentally measured values, we can obtain a reasonable estimate of the temperature of the system.

However, this technique for measuring the temperature is practical only when the average moment at half-filling shows a relatively strong temperature-dependence, so that small changes in the temperature lead to large, experimentally detectable changes in the moment. Examining Fig. 4-5, this is really only the case for a temperature range  $t < k_B T < U$ . For temperatures  $k_B T \gg U$ , there is enough thermal energy in the system that the on-site repulsive interactions no longer have a significant effect on the suppression of doubly occupied sites, meaning that particle fluctuations in the system are enhanced, and the moment at half-filling approaches the high-temperature limiting value of 0.5, where doublons, holes, and singly occupied sites are equally probable configurations. Thus, as the average moment at half-filling saturates towards this high-temperature limit, it loses much of its sensitivity to temperature changes. Similarly, for temperatures  $k_B T \ll U$  (typically  $k_B T \sim t$ ), thermally excited doublon-hole fluctuations (which require an energy of  $\sim U$ ) are essentially frozen out, and the average moment at half-filling again loses its sensitivity to temperature. This is evident from the NLCE predictions shown in Fig. 4-5, where the average moment flattens out, in a manner which depends on  $U/t$ , as the temperature is lowered sufficiently.

This saturation of the average moment at half-filling with decreasing temperature, as well as the distinguishing behavior of the average moment and its variance for the different states of the Hubbard model discussed in previous sections, are characteristics which most closely reflect the density, or charge degree of freedom of the Fermi-Hubbard model. That is, in the discussion so far regarding experimental re-

sults, the observations were mostly explained using the language of charge or density, without much reference to the spin degree of freedom of the Hubbard model. The presence of spin physics in this system, however, can lead to many exciting physical properties, including antiferromagnetic spin ordering, which can interact and possibly compete with properties tied to the charge degree of freedom. It is therefore worthwhile to try to study effects in both the spin and charge sectors, in order to better understand how they are interconnected within the Hubbard model. The practical issue with this idea, however, is that spin-related effects become most significant when the temperature of the system drops below the super-exchange energy scale,  $k_B T < 4t^2/U$ , when  $U/t \gtrsim 8$  (see sections 2.2.1 and 2.2.3), which is several times lower than the experimental temperatures discussed in section 4.3.3. Fortunately, precursory signs of physics at this energy scale, including short-range antiferromagnetic spin correlations, can occur at experimentally attainable temperatures. Thus, we are motivated to move beyond measurements of the local moment alone, and to study short-range correlation functions in both the spin and charge sectors using the site-resolved capabilities of our experiment. This will allow us to probe physics related to this super-exchange energy scale, and to better examine the interplay between the spin and charge degrees of freedom. We will discuss our measurements of these correlations in detail in section 4.4.

This does not mean, however, that the average local moment is devoid of physics related to super-exchange. In fact, it is exactly the difference between the local moment (Eq. 4.1) and the total density,  $\hat{n}_{\uparrow,i} + \hat{n}_{\downarrow,i}$  (i.e. the doublon density  $\hat{n}_{\uparrow,i}\hat{n}_{\downarrow,i}$ ), that allows the local moment to reflect some of this spin physics. Ultimately, this arises from the connection between correlated doublon-hole pairs, which affect the density of doublons, and antiferromagnetic spin correlations present in the system due to super-exchange related effects (see the discussion in section 2.2.1). We will explore this connection in more detail in section 4.4 when we discuss our experimental observations of spin and charge correlations. It is worth pointing out though that this connection is reflected in the behavior of the average moment at half-filling when the temperature approaches the super-exchange energy scale,  $k_B T \sim 4t^2/U$  [173]. This

can be seen directly in the NLCE predictions shown in Fig. 4-5 as a global maximum of the local moment attained at a small but finite temperature  $k_B T \neq 0$ . This peak comes about because the ground state of the system at half-filling, in the limit of strong interactions, is antiferromagnetic, a consequence of super-exchange interactions arising from virtual hopping of particles. This virtual hopping process, which goes hand in hand with antiferromagnetic order in the system, favors the delocalization of particles due to an admixture of correlated doublon-hole pairs into the ground state wave function (see sections 2.2.1 and 2.2.3). The resulting delocalization leads to a reduction of the average local moment at low temperatures. As the temperature increases from zero, the antiferromagnetic order in the system decays, as it becomes possible to induce spin excitations in the form of neighboring particles that are ferromagnetically aligned. However, the presence of these thermal ferromagnetic spin excitations ultimately increases the localization of particles relative to the ground state, because Pauli blocking prevents virtual hopping of neighboring particles that are in the same spin state. Thus, the value of the average local moment increases slightly as the temperature increases from zero. As the temperature increases further though, and approaches the on-site interaction energy,  $k_B T \sim U$ , it becomes possible to thermally excite doublons in the system. This decreases the localization of particles, and therefore again lowers the average local moment. Consequently, the local moment reaches a maximum value at a non-zero temperature, which can be seen clearly, for example, in the purple curve of Fig. 4-5, representing  $U/t = 12$ . Unfortunately, observing this effect can be difficult, both because it occurs at low temperatures  $k_B T \sim 4t^2/U$ , and because the strength of the signal is relatively weak, owing to the rather indirect connection between the average moment and antiferromagnetic spin correlations in the system. It is therefore desirable to study these effects more directly through, for example, the observation of spatial correlations of both the spin and charge.

## 4.4 Spatial Charge and Spin Correlations

In this section, we explore the connection between the spin and charge degrees of freedom of the Fermi-Hubbard model using spatially resolved two-point correlations. Because our high-resolution imaging system provides us with the ability to detect particles on neighboring lattice sites, we can leverage the strength of our quantum gas microscope to study how these correlations change as functions of separation between the sites. We focus specifically on a separation of a single lattice site, where the magnitude of these two-point spin and charge correlations are expected to be maximal. Although the temperature of the data which we will discuss in section 4.4.3,  $k_B T/t = 1.16(16)$  at  $U/t = 7.2(1)$ , is roughly a factor of two larger than the super-exchange energy scale  $4t^2/U$  which we hope to probe, the nearest-neighbor spin and charge correlation functions already demonstrate, even at this slightly elevated temperature, significant signatures of the physics of super-exchange. Using the local variation in the particle density arising from the underlying curvature of the optical lattice beam intensities, we study how these nearest-neighbor correlations change over the full range of dopings at a fixed temperature, from full doping (zero density) to zero doping (half-filling). Understanding how the interplay between spin and charge evolves under finite doping is important because the Fermi-Hubbard model, at low temperatures and away from half-filling, is theoretically intractable due to the fermion sign problem [144]. Thus, by studying doped systems experimentally, not only can we provide benchmarks for comparison with theoretical calculations, but we can provide new insight into the Fermi-Hubbard model, in the spirit of quantum simulation. Such insight is relevant to the study of high- $T_c$  cuprate superconductors, which, upon doping of the Mott insulating state, can exhibit strange metal and pseudogap phases, and, at even lower temperatures, an unconventional  $d$ -wave superconducting phase [6, 49, 139].

Prior to the advent of quantum gas microscopy for fermions, short-range anti-ferromagnetic spin correlations had been observed in Fermi-Hubbard systems using singlet-triplet oscillations [78, 76], and spin-sensitive Bragg scattering [89]. However,

due to the lack of high-resolution imaging in these previous experiments, the spin correlations that were obtained using these techniques had to be averaged over the entire in-trap density distribution. Not only did this mean that the density dependence of the correlations was inaccessible for these experiments, but also that a clean comparison between the data and theory was complicated by assumptions regarding the distribution of particles within the trap. Here, because we have access to the full spatial information of the system, we can study these correlations as functions of density (or doping) in a clean and controllable manner, down to a separation of a single lattice site, without performing a trap average of the correlations, and with minimal assumptions about the trap geometry. Specifically, using a spin-sensitive imaging technique, we observe antiferromagnetic spin correlations that are strongest (most negative) at half-filling, and that weaken monotonically as the doping in the system increases. Observations of antiferromagnetic spin correlations were also realized by other microscope experiments using fermionic  ${}^6\text{Li}$  in both 2D [180, 27, 152] and 1D [23]. In addition to the spin, we have access to the local moment, which describes the density of singly occupied sites in the system, and is therefore closely related to the charge degree of freedom. We can therefore study spatial correlations of this quantity as well. Examining the nearest-neighbor local moment correlator, we observe negative correlations at low density (large doping), corresponding to an anti-bunching behavior that arises from a combination of repulsive interactions between particles of opposite spin with real-space Pauli blocking that occurs between fermions in the same spin state. At half-filling (zero doping) on the other hand, we observe positive nearest-neighbor moment correlations which correspond to bunching of correlated doublon-hole pairs, whose presence in the system is ultimately related to the physics of super-exchange (sections 4.3.5 and 2.2.1), and is therefore connected to the antiferromagnetic spin correlations observed at half-filling.

We begin this section by defining the spin and charge correlation functions of interest, and describing qualitatively what these two-point correlations can teach us about the interplay between spin and charge in the Hubbard model. We then provide a detailed discussion of how we are able to measure these correlations experimentally

through the implementation of spin-sensitive imaging. Finally, we discuss our experimental measurements of these two-point correlation functions with variable filling at  $U/t = 7.2(1)$ , and compare these results to calculations made using DQMC and NLCE. We use this particular ratio of the Hubbard parameters,  $U/t \approx 8$ , because it represents the parameter regime where the magnitudes of the correlation signals are expected to be maximal at a given temperature. Intuitively, this is because it is at this ratio where the on-site interaction energy  $U$ , which tends to localize particles and reduce particle fluctuations in the system, is of the same magnitude as the kinetic energy, set by the single-particle bandwidth  $8t$ , which favors the delocalization of particles and enhanced particle fluctuations (section 4.3.2).

#### 4.4.1 Definitions of the Spin and Charge Correlation Functions

We first define the correlation functions that we examine in the experiment, and relate them to quantities which we can measure directly. We then provide some general intuition about what these correlation functions mean, and how they can be used to probe physical properties of the Fermi-Hubbard model.

As discussed in section 4.2.2, the simplest quantity which we can access using our quantum gas microscope is the site-resolved local moment,  $\hat{m}_{z,i}^2 = \hat{n}_{\uparrow,i} + \hat{n}_{\downarrow,i} - 2 \hat{n}_{\uparrow,i} \hat{n}_{\downarrow,i}$ . We can thus examine two-point correlations of this quantity between different lattice sites. For simplicity, we define here the local moment correlation function for nearest-neighbor lattice sites, although this is easily generalizable to arbitrary separations. The nearest-neighbor local moment correlation function is defined as,

$$C_m(1) = \frac{1}{4} \sum_{j \in nn_i} (\langle \hat{m}_{z,i}^2 \hat{m}_{z,j}^2 \rangle - \langle \hat{m}_{z,i}^2 \rangle \langle \hat{m}_{z,j}^2 \rangle), \quad (4.5)$$

where the summation is performed over the four nearest-neighbors  $j$  of a particular lattice site  $i$ , denoted by  $nn_i$ , and the pre-factor  $1/4$  is included because we want to average the symmetric contributions from each of the four neighbors. To gener-

alize this definition to correlations beyond nearest-neighbor, one simply calculates the correlation  $\langle \hat{m}_{z,i}^2 \hat{m}_{z,j}^2 \rangle - \langle \hat{m}_{z,i}^2 \rangle \langle \hat{m}_{z,j}^2 \rangle$ , where  $i$  and  $j$  are separated by the desired distance, then averages over all equivalent equidistant sites  $j$ . As it is written, Eq. 4.5 is technically defined as an average correlation at a particular lattice site  $i$ . We can therefore measure a value for this correlation function at each lattice site in the system by averaging over many different iterations of the experiment to obtain the equivalent of the brackets,  $\langle \rangle$ , in the equation, as we will discuss in section 4.4.3. However, because different lattice sites  $i$  which are equidistant from the trap center are symmetric and are therefore equivalent, we suppress the index in the definition. This does not presume that the correlator is independent of the density, and therefore of the radial location in the trap, but suppression of the site index preemptively assumes that we will radially average the correlations at equivalent lattice sites, similar to what was done in section 4.3.2, so that it is clear that Eq. 4.5 is dependent on the doping, and is not specific to a particular site. Additionally, in the definition of the nearest-neighbor moment correlator, Eq. 4.5, we subtract off the trivial contribution to the correlation signal,  $\langle \hat{m}_{z,i}^2 \rangle \langle \hat{m}_{z,j}^2 \rangle$ , so that any signal we observe represents a deviation from the uncorrelated case,  $\langle \hat{m}_{z,i}^2 \hat{m}_{z,j}^2 \rangle = \langle \hat{m}_{z,i}^2 \rangle \langle \hat{m}_{z,j}^2 \rangle$ . This is often called the connected part of the correlator, and is generally defined, for two observables  $\hat{A}$  and  $\hat{B}$ , as,

$$\langle \hat{A} \hat{B} \rangle_c \equiv \langle \hat{A} \hat{B} \rangle - \langle \hat{A} \rangle \langle \hat{B} \rangle, \quad (4.6)$$

a form which we will use often to simplify notation.

To physically interpret the meaning of the moment correlation function, Eq. 4.5, we define four new quantities,

$$\begin{aligned} \hat{n}_i &\equiv \hat{n}_{\uparrow,i} + \hat{n}_{\downarrow,i} \\ \hat{d}_i &\equiv \hat{n}_{\uparrow,i} \hat{n}_{\downarrow,i} \\ \hat{h}_{\sigma,i} &\equiv 1 - \hat{n}_{\sigma,i} \\ \hat{h}_i &\equiv \hat{h}_{\uparrow,i} + \hat{h}_{\downarrow,i} = 2 - \hat{n}_i. \end{aligned} \quad (4.7)$$

Here,  $\hat{n}_i$  represents the total particle density at lattice site  $i$ ,  $\hat{d}_i$  represents the density of doublons,  $\hat{h}_{\sigma,i}$  is the hole density representing a missing particle of spin  $\sigma = (\uparrow, \downarrow)$ , and  $\hat{h}_i$  is the total hole density. Using these definitions, we can rewrite the local moment operator as,  $\hat{m}_{z,i}^2 = \hat{n}_i - 2\hat{d}_i$ . We can then express the connected part of the moment correlator as,

$$\begin{aligned}\langle \hat{m}_{z,i}^2 \hat{m}_{z,j}^2 \rangle_c &= \langle \hat{m}_{z,i}^2 \hat{m}_{z,j}^2 \rangle - \langle \hat{m}_{z,i}^2 \rangle \langle \hat{m}_{z,j}^2 \rangle \\ &= \left\langle \left( \hat{n}_i - 2\hat{d}_i \right) \left( \hat{n}_j - 2\hat{d}_j \right) \right\rangle_c \\ &= \langle \hat{n}_i \hat{n}_j \rangle_c - 4 \langle \hat{n}_i \hat{d}_j \rangle_c + 4 \langle \hat{d}_i \hat{d}_j \rangle_c.\end{aligned}\quad (4.8)$$

To arrive at the last line, we made use of the fact that  $\langle \hat{n}_i \hat{d}_j \rangle_c = \langle \hat{d}_i \hat{n}_j \rangle_c$ , which follows from symmetry and the fact that the density operators representing different sites commute. Eq. 4.8 tell us that the moment correlation function, which physically represents correlations between the density of singles on different sites, actually contains contributions from three different terms. The first term represents correlations of the total density at different sites, which we expect to be negative due to repulsive interactions and Pauli blocking between fermions of the same spin state, both of which lead to anti-bunching behavior between particles. The presence of this term is reasonable, as the local moment is just a measure of the total density when there are no double occupancies in the system. At low total densities then, when the density of doubly occupied sites is also low, the moment correlations approximately represent the total density correlations. However, in the presence of doublons, such as at densities at or around half-filling, the moment correlations are slightly more complex than the total density correlations alone. This is because the moment correlations contain two other terms which represent correlations between doublons,  $\langle \hat{d}_i \hat{d}_j \rangle_c$ , and correlations between particles and doublons,  $\langle \hat{n}_i \hat{d}_j \rangle_c$ . Intuitively, one might expect that the contribution from  $\langle \hat{d}_i \hat{d}_j \rangle_c$  is relatively weak, as it is, in some sense, a higher-order correlation which contains four density operators and therefore eight fermion creation/annihilation operators. Additionally, because doublons are fermionic in character, we expect the sign of this correlator to be negative due to

Pauli blocking, which leads to anti-bunching between particles (see section 2.1.2). In section 4.4.3, we discuss this in more detail, and verify our intuition about this correlator using results from NLCE.

The final contribution to the moment correlator,  $\langle \hat{n}_i \hat{d}_j \rangle_c$ , can be interpreted more easily if we re-express the density operators in terms of hole operators,  $\hat{h}_i = 2 - \hat{n}_i$ . With this notation, Eq. 4.8 becomes,

$$\begin{aligned} \langle \hat{m}_{z,i}^2 \hat{m}_{z,j}^2 \rangle_c &= \langle \hat{n}_i \hat{n}_j \rangle_c - 4 \langle \hat{n}_i \hat{d}_j \rangle_c + 4 \langle \hat{d}_i \hat{d}_j \rangle_c \\ &= \langle \hat{h}_i \hat{h}_j \rangle_c + 4 \langle \hat{h}_i \hat{d}_j \rangle_c + 4 \langle \hat{d}_i \hat{d}_j \rangle_c, \end{aligned} \quad (4.9)$$

where  $\langle \hat{h}_i \hat{h}_j \rangle_c = \langle \hat{n}_i \hat{n}_j \rangle_c$  and  $\langle \hat{n}_i \hat{d}_j \rangle_c = -\langle \hat{h}_i \hat{d}_j \rangle_c$ . It is then apparent that the final contribution to the moment correlation function is actually due to correlations between doublons and holes. At low densities, this is expected to be small, as the doublon density itself is relatively low. At half-filling on the other hand, we expect that this correlator can be non-zero, and that it can in fact make a significant positive contribution to the moment correlation. This intuition comes from the fact that we expect antiferromagnetic spin correlations in this system at half-filling. From the double-well Hubbard model discussed in section 2.2.1, we know that these antiferromagnetic spin correlations are accompanied by an admixture of neighboring doublon-hole pairs into the wave function, which occurs with a probability  $\approx 4(t/U)^2$ . We therefore expect significant bunching between neighboring doublons and holes at half-filling when there are antiferromagnetic spin correlations present, and thus a positive contribution to the moment correlator arising from  $4 \langle \hat{h}_i \hat{d}_j \rangle_c$ , which could be potentially comparable in magnitude to  $\langle \hat{h}_i \hat{h}_j \rangle_c = \langle \hat{n}_i \hat{n}_j \rangle_c$ . Due to the contributions of these three competing terms, it is apparent that the local moment correlation function represents a charge correlator, in that it is insensitive to the spin, which can detect effects due to both super-exchange, through the doublon-hole correlations, as well as Pauli blocking, through the doublon-doublon and hole-hole (or density-density) correlations.

Of course, we would also like to independently probe spin physics within the

Fermi-Hubbard model, and the potential presence of antiferromagnetic correlations between spins, and for this we define and examine the nearest-neighbor spin correlation function,

$$C_s(1) = \sum_{j \in nn_i} \left( \langle \hat{S}_{z,i} \hat{S}_{z,j} \rangle - \langle \hat{S}_{z,i} \rangle \langle \hat{S}_{z,j} \rangle \right), \quad (4.10)$$

where  $\hat{S}_{z,i} = (\hat{n}_{\uparrow,i} - \hat{n}_{\downarrow,i})/2$  is the  $z$ -component of the spin. The definition is missing the factor of  $1/4$  that was present in the definition of the moment correlator, Eq. 4.5. This is simply a matter of convention, and comes from the implicit presence of the pre-factor  $1/S^2$ , where  $S = 1/2$  is the value of a particle's total spin, multiplying the average over the four neighboring lattice sites. Thus, to generalize this definition to distances beyond nearest-neighbor, one must be careful to include this pre-factor. At first glance, it is not immediately obvious how we could measure this quantity given that the imaging technique described so far is not sensitive to the spin of the particles in the lattice, and that it suffers from parity-projection, meaning that we can only measure the local moment at each site. However, as we will discuss in more detail in section 4.4.2, our imaging technique can be generalized in such a way that it is sensitive to the spin of the particles, allowing us access to two new quantities beyond the local moment. These quantities are,

$$\begin{aligned} \hat{n}_{\uparrow,i}^s &\equiv \hat{n}_{\uparrow,i} - \hat{n}_{\uparrow,i}\hat{n}_{\downarrow,i} \\ \hat{n}_{\downarrow,i}^s &\equiv \hat{n}_{\downarrow,i} - \hat{n}_{\uparrow,i}\hat{n}_{\downarrow,i}. \end{aligned} \quad (4.11)$$

Physically,  $\hat{n}_{\uparrow,i}^s$  ( $\hat{n}_{\downarrow,i}^s$ ) represents a measurement of the density of spin-up (spin-down) particles that are on singly occupied sites. Intuitively, this is because  $\hat{d}_i = \hat{n}_{\uparrow,i}\hat{n}_{\downarrow,i}$  denotes the number of particles of spin- $\sigma$  lost from parity-projection, so that the number of particles of spin- $\sigma$  which are actually imaged is simply  $\hat{n}_{\sigma,i} - \hat{n}_{\uparrow,i}\hat{n}_{\downarrow,i}$ , for  $\sigma = (\uparrow, \downarrow)$ . In other words, these quantities take the value one if there is a single particle with the correct spin on a site, and are zero otherwise. Additionally, it is worth noting that  $\hat{n}_{\uparrow,i}^s + \hat{n}_{\downarrow,i}^s = \hat{m}_{z,i}^2 = 4\hat{S}_{z,i}^2$  gives the total density of singly-occupied sites.

We can rewrite the spin correlation function, Eq. 4.10, in terms of the three quantities we can access, these two spin-sensitive quantities and the local moment. To see this, we note that,

$$\begin{aligned} 4 \left\langle \hat{S}_{z,i} \hat{S}_{z,j} \right\rangle_c &= \langle (\hat{n}_{\uparrow,i} - \hat{n}_{\downarrow,i}) (\hat{n}_{\uparrow,j} - \hat{n}_{\downarrow,j}) \rangle_c \\ &= \langle (\hat{n}_{\uparrow,i}^s - \hat{n}_{\downarrow,i}^s) (\hat{n}_{\uparrow,j}^s - \hat{n}_{\downarrow,j}^s) \rangle_c \\ &= \langle \hat{n}_{\uparrow,i}^s \hat{n}_{\uparrow,j}^s \rangle_c + \langle \hat{n}_{\downarrow,i}^s \hat{n}_{\downarrow,j}^s \rangle_c - \langle \hat{n}_{\uparrow,i}^s \hat{n}_{\downarrow,j}^s \rangle_c - \langle \hat{n}_{\downarrow,i}^s \hat{n}_{\uparrow,j}^s \rangle_c . \end{aligned} \quad (4.12)$$

In addition, we have that,

$$\begin{aligned} \langle \hat{m}_{z,i}^2 \hat{m}_{z,j}^2 \rangle_c &= \langle (\hat{n}_{\uparrow,i}^s + \hat{n}_{\downarrow,i}^s) (\hat{n}_{\uparrow,j}^s + \hat{n}_{\downarrow,j}^s) \rangle_c \\ &= \langle \hat{n}_{\uparrow,i}^s \hat{n}_{\uparrow,j}^s \rangle_c + \langle \hat{n}_{\downarrow,i}^s \hat{n}_{\downarrow,j}^s \rangle_c + \langle \hat{n}_{\uparrow,i}^s \hat{n}_{\downarrow,j}^s \rangle_c + \langle \hat{n}_{\downarrow,i}^s \hat{n}_{\uparrow,j}^s \rangle_c . \end{aligned} \quad (4.13)$$

Adding Eq. 4.12 to Eq. 4.13 and then rearranging terms gives

$$4 \left\langle \hat{S}_{z,i} \hat{S}_{z,j} \right\rangle_c = 2 \langle \hat{n}_{\uparrow,i}^s \hat{n}_{\uparrow,j}^s \rangle_c + 2 \langle \hat{n}_{\downarrow,i}^s \hat{n}_{\downarrow,j}^s \rangle_c - \langle \hat{m}_{z,i}^2 \hat{m}_{z,j}^2 \rangle_c , \quad (4.14)$$

from which it follows that

$$C_s(1) = \sum_{j \in nn_i} \frac{1}{2} \langle \hat{n}_{\uparrow,i}^s \hat{n}_{\uparrow,j}^s \rangle_c + \frac{1}{2} \langle \hat{n}_{\downarrow,i}^s \hat{n}_{\downarrow,j}^s \rangle_c - \frac{1}{4} \langle \hat{m}_{z,i}^2 \hat{m}_{z,j}^2 \rangle_c \quad (4.15)$$

We can therefore obtain the nearest-neighbor two-point spin correlation function (although this is true for all two-point correlation distances) experimentally by independently measuring the average nearest-neighbor correlations of the three quantities that we can image directly, and then taking a weighted sum of the resulting site-resolved correlations using Eq. 4.15. It is worth noting that the derivation of Eq. 4.15 did not require the assumption that the system was spin-balanced (i.e. a 50-50 mixture of spin-up and spin-down); the derivation simply made use of operator identities. One can therefore use this equation, along with Eq. 4.5, to measure both spin and charge correlations in the presence of finite spin-imbalance, which allows one to break the  $SU(2)$  symmetry inherent to the Fermi-Hubbard model [27]. As was the case for

the moment correlator, Eq. 4.15 gives the correlation strength at a particular site  $i$ , meaning we are able to produce a full 2D map of the site-resolved nearest-neighbor correlation strength in the lattice; we have just suppressed this site index in the equation for simplicity. Of course, obtaining such a 2D correlation map requires stability of the experiment and the lattice position over the time it takes to obtain the three independent data sets necessary to measure each of the correlators in Eq. 4.15 with a desired precision. This is true both for comparing individual experimental runs within a dataset to obtain one of the three average correlators at a single site, as well as for taking the weighted sum of the resulting average correlators at that site. We discuss this in more detail in section 4.4.3 when we describe our experimental results for the spin and charge correlation functions.

A basic intuition regarding the behavior of the spin correlation function can be obtained from the double-well system discussed in section 2.2.1. Due to the presence of super-exchange physics at large interactions  $U \gg t$ , we generally expect there to be antiferromagnetic spin correlations in this system at half-filling and low temperatures. As we showed in section 2.2.1, the ground state,  $|1\rangle$ , of the two site Fermi-Hubbard model is a spin singlet with a small doublon-hole admixture. We can directly calculate  $\langle \hat{S}_{z,1} \hat{S}_{z,2} \rangle_c = \langle 1 | \hat{S}_{z,1} \hat{S}_{z,2} | 1 \rangle$  for this state, and find that  $\langle \hat{S}_{z,1} \hat{S}_{z,2} \rangle_c = -(\cos^2 \theta)/4$ , where  $\tan \theta = 4t / (U + \sqrt{16t^2 + U^2})$  (see section 2.2.1). In the limit  $U \gg t$ ,  $\tan \theta \approx \theta$ , so that the correlator becomes simply  $\langle \hat{S}_{z,1} \hat{S}_{z,2} \rangle_c \approx -1/4$ . The total spin correlator is then  $C_s(1) = 4 \langle \hat{S}_{z,1} \hat{S}_{z,2} \rangle_c \approx -1$  in the limit  $U \gg t$ . We thus see that the spin correlation function reveals the antiferromagnetic behavior of the ground state of the two-site model.

We note, however, that the sign of the correlations does not depend on the actual value of  $t/U$ . That is,  $-(\cos^2 \theta)/4$  is less than zero for all values of  $\theta$ , so that the ground state is always antiferromagnetic at half-filling. On the other hand, the magnitude of these correlations does depend strongly on the ratio  $t/U$ . This is because the ratio  $t/U$  adjusts the amplitude of the singlet state,  $(|\uparrow, \downarrow\rangle - |\downarrow, \uparrow\rangle) / \sqrt{2}$ , relative to the doublon-hole pair state,  $(|\uparrow\downarrow, 0\rangle + |0, \uparrow\downarrow\rangle) / \sqrt{2}$ , in the ground state wave function, and the contribution to the spin correlator from the doublon-hole pair state is zero.

As  $t/U \rightarrow 0$ , the singlet nature of the ground state dominates and  $C_s(1)$  approaches the limiting, maximally negative value of  $-1$ . In the opposite limit, as  $U/t \rightarrow 0$ , the singlet state and doublon-hole pair state contribute equal weight to the ground state wave function, and  $C_s(1)$  approaches  $-0.5$ . Thus, even in the non-interacting limit, the ground state exhibits non-zero antiferromagnetic spin correlations. We will discuss this in more detail in section 4.4.3, where we compare our measurements of  $C_s(1)$  in a fully interacting system to what one would expect to see in the non-interacting case, allowing us to isolate the spin correlations due purely to the presence of interactions.

The real system, of course, has significantly more than two sites, and significantly more than two particles. Additionally, there is a non-zero temperature which affects the strength of the spin correlations. At low temperatures and in large systems, we know theoretically that the ground state of the Hubbard model at half-filling is antiferromagnetic with a nearest-neighbor spin correlator  $C_s(1) \approx 0.36$  [174, 180, 152]. Interestingly, the maximum strength of the nearest-neighbor spin correlator in the real system is not  $-1$ , but saturates before reaching this value, which we naively expected from the two-site Hubbard model. This is discussed in more detail in section 4.4.3. Additionally, in the zero-temperature limit of the 2D system, the spin correlations in the antiferromagnetic state are long range, and extend significantly beyond the nearest-neighbor separation. At finite temperature, however, there is no long range order in two dimensions [153], and the spatial length of the spin correlations, which we denote by  $\xi$ , decays exponentially with inverse temperature according to the form [33, 34, 150],

$$\xi(T) = C \exp\left(\frac{2\pi\rho_s}{T}\right), \quad (4.16)$$

where  $C$  is a constant and  $\rho_s$  is the spin stiffness. Even at a separation of one lattice site, one can discern the effects of finite temperature, because the nearest-neighbor spin correlations strongly decay as the temperature in the system increases. This makes sense intuitively because finite temperature tends to admix states nearby in energy which contain ferromagnetic spin excitations. The admixture of these states

then destroys the average antiferromagnetic correlations of the ground state, for all spatial separations, including nearest-neighbor.

#### 4.4.2 Spin-Resolved Imaging

In order to measure the spin correlation function, Eq. 4.10, we need to generalize the imaging technique described in section 3.2, which provides access to the local moment at each site  $\hat{m}_{z,i}^2$ , so that it can be sensitive to the spin of the atoms, allowing us to measure  $\hat{n}_{\uparrow,i}^s$  and  $\hat{n}_{\downarrow,i}^s$ , as defined in Eq. 4.11. The general experimental protocol used to implement this spin-resolved imaging is described in detail in section 3.4. For the measurement of spin and charge correlations described in section 4.4.3, we use a two-component spin mixture comprised of the states  $|F = 9/2, m_F = -9/2\rangle$  and  $|F = 9/2, m_F = -7/2\rangle$ . As described in section 3.4, the spin-resolved imaging technique requires shelving the spin state which is to be imaged in the  $F = 7/2$  hyperfine manifold, so that it is unaffected by the light pulse used to remove atoms remaining in the  $F = 9/2$  manifold. To implement this step for the particular spin mixture used here, we transfer atoms in state  $|F = 9/2, m_F = -9/2\rangle$  ( $|F = 9/2, m_F = -7/2\rangle$ ) to state  $|F = 7/2, m_F = -7/2\rangle$  ( $|F = 7/2, m_F = -5/2\rangle$ ) using a 100 ms microwave sweep with 100 kHz sweep span. Fig. 4-13 shows raw fluorescence images resulting from three independent realizations of the experiment that demonstrate the three types of images we can take using this generalized imaging scheme: the site-resolved local moment,  $\hat{m}_{z,i}^2$ , using the usual, spin-insensitive imaging protocol, and the individual spin-up and spin-down singles densities,  $\hat{n}_{\uparrow,i}^s$  and  $\hat{n}_{\downarrow,i}^s$ , using the spin-resolved imaging protocol. As a side note, this spin-sensitive imaging technique can be further generalized by applying it to three component mixtures, such as a balanced mixture of atoms in  $|F = 9/2, m_F = -9/2\rangle$ ,  $|F = 9/2, m_F = -7/2\rangle$ , and  $|F = 9/2, m_F = -5/2\rangle$ , states which are all mutually stable against spin changing collisions. This could then be used to measure spatial correlations between the various spin components, and to study magnetism in an  $SU(3)$ -symmetric Hubbard model [102, 36, 94]. In addition to exhibiting interesting new equilibrium and transport phenomena compared to the  $SU(2)$ -symmetric Hubbard model studied in this thesis, such a system could also

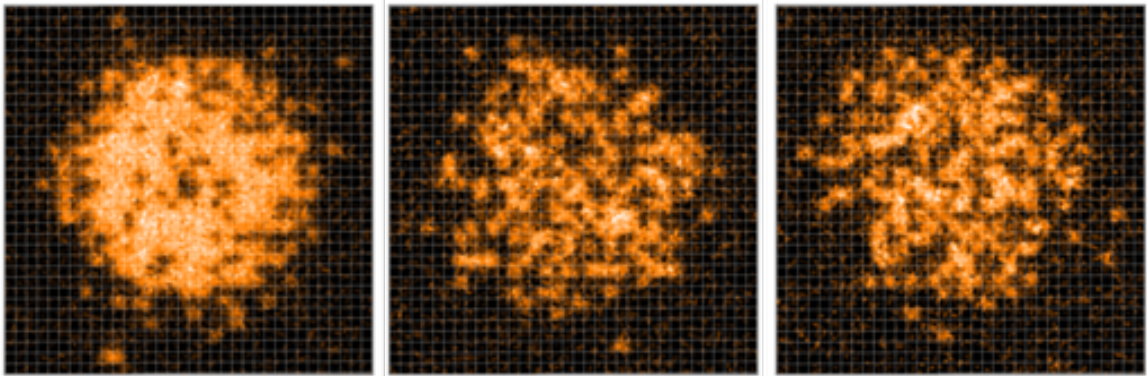


Figure 4-13: Spin-resolved single-site fluorescence imaging of a fermionic Mott insulator. Shown are raw single-site fluorescence images, with the underlying lattice overlaid, from three separate, independent experimental realizations of a 2D fermionic Mott insulator, prepared at  $U/t = 7.2(1)$  and  $k_B T/t = 1.1(1)$ . The left-most figure represents an image of the site-resolved local moment,  $\hat{m}_{z,i}^2$ , obtained through the usual single-site Raman sideband cooling imaging technique. The middle figure represents an image of the atoms in the state  $|F = 9/2, m_F = -9/2\rangle$  which sit on singly-occupied sites, denoted by the quantity  $\hat{n}_{\uparrow,i}^s$ , which was obtained through spin-resolved single-site imaging. The right-most figure represents an image of atoms in the state  $|F = 9/2, m_F = -7/2\rangle$  which sit on singly-occupied sites,  $\hat{n}_{\downarrow,i}^s$ , which is also obtained through spin-resolved single-site imaging. Figure adapted from [38].

benefit from Pomeranchuk cooling [192, 221], as well as provide a more accessible entropy per particle requirement to transition to a magnetically ordered state (i.e.  $\sim \ln(3)k_B$  per particle versus  $\sim \ln(2)k_B$  per particle for the  $SU(2)$ -symmetric case).

If the spin-resolved imaging were implemented perfectly, the quantities we could measurement experimentally would be  $\hat{n}_{\uparrow,i}^s$  and  $\hat{n}_{\downarrow,i}^s$ , providing us direct access to the site-resolved spin correlator through Eq. 4.15. However, in reality there are several sources of error that alter the value of the spin correlator we observe relative to its actual value. One major error is the overall imaging fidelity, which we denote as  $f$ , where  $f < 1$ , that is associated with the single-site imaging process itself, and is therefore common to all three types of images we can take (Fig. 4-13). The finite detection fidelity reduces the measured average moment  $\langle \hat{m}_{z,i}^2 \rangle$  by a factor of  $f$ , and reduces the average correlation signals (Eqs. 4.5 and 4.15) by a factor of  $f^2$ , but it does not introduce a systematic bias to our measurements. This imaging fidelity is the main source of error in our measurements of both the average moment and the moment correlations, but other sources of error are introduced during the spin-

resolved detection protocol, and are thus specific to our measurements of  $\hat{n}_{\uparrow,i}^s$  and  $\hat{n}_{\downarrow,i}^s$ .

We can quantify the errors specific to our spin-resolved detection scheme by transforming the ideal measurement operators  $\hat{n}_{\uparrow,i}^s$  and  $\hat{n}_{\downarrow,i}^s$  to observed measurement operators,  $\hat{\tilde{n}}_{\uparrow,i}^s$  and  $\hat{\tilde{n}}_{\downarrow,i}^s$ , where,

$$\hat{\tilde{n}}_{\sigma,i}^s = (1 - \epsilon_{1,\sigma}) \hat{n}_{\sigma,i} + \epsilon_{2,\sigma} \hat{n}_{-\sigma,i} - (1 - \epsilon_{1,\sigma} + \epsilon_{2,\sigma}) \hat{d}_i. \quad (4.17)$$

Here we have dropped the overall scaling factor,  $f$ , arising from the finite imaging fidelity for simplicity of notation, although it must be included in the final result for the measured quantities. The parameter  $0 \leq \epsilon_{1,\sigma} \leq 1$ , as it is used here, represents unintended loss of atoms in the desired spin state,  $\sigma = (\uparrow, \downarrow)$ , which occurs, for example, during the resonant light pulse intended to remove the opposite spins, so that  $\epsilon_{1,\sigma} = 0$  indicates zero unintentional loss, and  $\epsilon_{1,\sigma} = 1$  is complete loss. The second parameter,  $0 \leq \epsilon_{2,\sigma} \leq 1$ , represents error arising from imperfect removal of the unwanted spin state,  $-\sigma$ , during the push-out pulse, so that  $\epsilon_{2,\sigma} = 0$  means that all of the unwanted spins are removed, and  $\epsilon_{2,\sigma} = 1$  indicates that none of the unwanted spins have been removed. To a reasonably good approximation, these parameters are independent of the spin state,  $\sigma$ , being imaged, although we will examine the general case for now. Additionally, we neglect here the possibility of doubly-occupied sites being converted to singly-occupied sites during the resonant push-out pulse. That is, we are ignoring the possibility that the resonant light could remove one of the atoms on a doubly occupied site through photon scattering before the two atoms can undergo light-assisted collisions, so that a single atom would remain after the push-out pulse and would therefore appear in the final image. We will address this possibility subsequently, and keep, for now, only the effects of  $\epsilon_{1,\sigma}$  and  $\epsilon_{2,\sigma}$  on the doublon density,  $\hat{d}_i$ .

Given the form of the measured observables, Eq. 4.17, we can construct the connected correlators we can access using these observable operators,  $\langle \hat{\tilde{n}}_{\sigma,i}^s \hat{\tilde{n}}_{\sigma,j}^s \rangle_c$ . We can then calculate what the observed spin correlation function would be, given these

errors, using  $\left\langle \hat{n}_{\sigma,i}^s \hat{n}_{\sigma,j}^s \right\rangle_c$  instead of  $\left\langle \hat{n}_{\sigma,i}^s \hat{n}_{\sigma,j}^s \right\rangle_c$  in Eq. 4.15. We denote the resulting observed correlator as  $\tilde{C}_s(1)$ , and write this in the form,

$$\tilde{C}_s(1) = f^2 [C_s(1) + \Delta C_s(1)], \quad (4.18)$$

where we have explicitly now included the finite imaging fidelity,  $f$ ,  $C_s(1)$  is the actual value of the spin correlation signal that we would get if there were no errors, and  $\Delta C_s(1)$  is the deviation from the ideal spin correlation signal due to the spin-detection errors written in Eq. 4.17. Using the fact that

$$\tilde{C}_s(1) = f^2 \sum_{j \in nn_i} \frac{1}{2} \left\langle \hat{n}_{\uparrow,i}^s \hat{n}_{\uparrow,j}^s \right\rangle_c + \frac{1}{2} \left\langle \hat{n}_{\downarrow,i}^s \hat{n}_{\downarrow,j}^s \right\rangle_c - \frac{1}{4} \left\langle \hat{m}_{z,i}^2 \hat{m}_{z,j}^2 \right\rangle_c, \quad (4.19)$$

we can plug the definitions of  $\hat{n}_{\sigma,i}^s$  from Eq. 4.17 into Eq. 4.19 to obtain, to leading order in the error parameters  $\epsilon_{1,\sigma}$  and  $\epsilon_{2,\sigma}$ , an expression for  $\Delta C_s(1)$ ,

$$\Delta C_s(1) = \sum_{\sigma} \{ -(\epsilon_{1,\sigma} + \epsilon_{2,\sigma}) C_s(1) - (\epsilon_{1,\sigma} - \epsilon_{2,\sigma}) C_m(1) - (\epsilon_{1,\sigma} - \epsilon_{1,-\sigma}) [P_{\sigma}(1) - P_{-\sigma}(1)] \}. \quad (4.20)$$

Here,

$$P_{\sigma}(1) = \frac{1}{4} \sum_{j \in nn_i} \left\langle \hat{n}_{\sigma,i}^s \hat{n}_{\sigma,j}^s \right\rangle_c \quad (4.21)$$

represents the site-resolved, nearest-neighbor correlation signal of the singles density of a particular spin state,  $\sigma$ , which is one of the three terms forming the total spin correlation signal  $C_s(1)$  in Eq. 4.15. Interestingly, each error term that contributes to  $\Delta C_s(1)$  in Eq. 4.20 is proportional to a detectable correlation signal. We are of course ignoring here contributions to  $\Delta C_s(1)$  arising from terms proportional to  $\epsilon_{i,\sigma} \epsilon_{j,\sigma'}$ , where  $i, j \in \{1, 2\}$  and  $\sigma, \sigma' \in \{\uparrow, \downarrow\}$ , which are negligible relative to the first order contributions in Eq. 4.20 when the  $\epsilon_{i,\sigma}$  are small (which is the case here).

For the case where  $\epsilon_{1,\sigma} \approx \epsilon_{1,-\sigma}$  and  $\epsilon_{2,\sigma} \approx \epsilon_{2,-\sigma}$ , so that the error is approximately independent of the particular spin state being imaged, one can use  $\epsilon_1 \equiv (\epsilon_{1,\uparrow} + \epsilon_{1,\downarrow})/2$  and  $\epsilon_2 \equiv (\epsilon_{2,\uparrow} + \epsilon_{2,\downarrow})/2$  for the error parameters, and can estimate the size of these parameters using one of several possible experimental calibrations. To estimate  $\epsilon_2$  for

example, which essentially describes the efficiency of the resonant removal pulse, one can measure the ratio of the total number of atoms which remain after the pulse, when neither spin state is shelved in the  $F = 7/2$  manifold, to the total number of atoms in the system with no resonant light pulse applied. To carefully distinguish between  $\epsilon_{2,\uparrow}$  and  $\epsilon_{2,\downarrow}$ , one could, for example, prepare spin-polarized samples, and measure the removal efficiency for atoms in the  $|F = 9/2, m_F = -9/2\rangle$  and  $|F = 9/2, m_F = -7/2\rangle$  states separately, assuming that this removal efficiency is not strongly dependent on the initial band occupation of the state of the system, which can differ between the spin-polarized and spin-mixture samples. For the data shown in section 4.4.3 and for the spin transport data discussed in chapter 5, the difference between  $\epsilon_{2,\uparrow}$  and  $\epsilon_{2,\downarrow}$  is negligible compared to the average,  $\epsilon_2$ . This is because the spin removal is performed at low fields,  $\leq 4\text{G}$ , so that the resonant frequency of the  $F = 9/2 \rightarrow F' = 11/2$  transition used to remove atoms is approximately independent of their initial  $m_F$  state in the  $F = 9/2$  manifold. As long as off-resonant scattering on the  $F = 9/2 \rightarrow F' = 9/2$  transition, which is  $\approx +44\text{ MHz}$  detuned, is negligible during the pulse, atoms predominantly return to the  $F = 9/2$  manifold after scattering a photon from the applied light, and can therefore continue to scatter photons until they eventually escape from the trap. This is especially true for atoms initially in the  $|F = 9/2, m_F = -9/2\rangle$  and  $|F = 9/2, m_F = -7/2\rangle$  states, given that the applied push-out light uses  $\hat{\sigma}-$  polarization. Additionally, even though the different initial  $m_F$  states in the  $F = 9/2$  manifold have different matrix elements connecting them to the excited state, which in principle affects the scattering rate out of these states, as long as the number of photons scattered by atoms in the  $F = 9/2$  manifold during the push-out pulse is sufficient to heat them out of the trap, this effect is negligible.

To estimate  $\epsilon_1$ , we can compare the total singles density obtained by measuring the average local moment  $\langle \hat{m}_{z,i}^2 \rangle$ , which is not affected by the errors associated with the spin-dependent imaging, with the total singles density obtained independently by summing the average singles densities of spin-up and spin-down atoms,  $\langle \hat{n}_{\uparrow,i}^s \rangle + \langle \hat{n}_{\downarrow,i}^s \rangle$ . Because the latter method is sensitive to the errors related to the spin-dependent

imaging, we have, using Eq. 4.17,

$$\langle \hat{n}_{\uparrow,i}^s \rangle + \langle \hat{n}_{\downarrow,i}^s \rangle = (1 - \epsilon_1 + \epsilon_2) \langle \hat{m}_{z,i}^2 \rangle. \quad (4.22)$$

Thus, by measuring the ratio of  $\langle \hat{n}_{\uparrow,i}^s \rangle + \langle \hat{n}_{\downarrow,i}^s \rangle$  to  $\langle \hat{m}_{z,i}^2 \rangle$ , we can determine the difference  $\epsilon_1 - \epsilon_2$ . Because we know  $\epsilon_2$  from measuring the efficiency of the push-out pulse acting on both spin states, we can then obtain  $\epsilon_1$ . We can also independently calibrate  $\epsilon_1$  by shelving both spin states in the  $F = 7/2$  manifold using two separate microwave sweeps prior to the resonant push-out pulse, and then measuring the resulting total singles density. Comparing this to what one would obtain without the push-out pulse provides a direct measure of the unintended loss of atoms which are hidden in the  $F = 7/2$  manifold, and thus  $\epsilon_1$ . One can measure the spin-dependent nature of  $\epsilon_{1,\sigma}$  by applying this technique (with just a single microwave sweep required) to spin-polarized samples. However, again because the spin removal is performed at low fields, the difference between  $\epsilon_{1,\uparrow}$  and  $\epsilon_{1,\downarrow}$  is small compared to the average,  $\epsilon_1$ , which we have verified experimentally. This is essentially because the off-resonant scattering of the push-out light by atoms in the  $F = 7/2$  manifold, which is detuned by  $\approx 1.3$  GHz is very small over the light pulse duration. Experimentally, we find that  $< 0.03\%$  of the atoms in the  $F = 7/2$  manifold are lost due to this off-resonant scattering. So, even though different  $m_F$  states in the  $F = 7/2$  manifold might have different transition rates due to, for example, different transition matrix elements, the average scattering rate is sufficiently low that these effects are negligible compared to the dominant contribution to  $\epsilon_1$ , inefficiency in the microwave transfer from the  $F = 9/2$  to the  $F = 7/2$  manifold. That is,  $\epsilon_1$  and  $\epsilon_2$  not only capture imperfections in the removal process associated with the resonant light pulse, but they also encapsulate imperfect microwave transfer during the shelving process. In our experiment, this is the dominant contribution to  $\epsilon_1$ , because our microwave sweeps are not perfect, and typically transfer  $\gtrsim 95\%$  of the target atoms to the other hyperfine manifold. As long as the transfer efficiency of the microwave sweep doesn't depend strongly on the initial  $m_F$  state, which affects the resonant microwave transition frequency, then

$\epsilon_{1,\uparrow} - \epsilon_{1,\downarrow}$  will be negligible compared to the average,  $\epsilon_1$ . This is the case in our experiment, because these microwave transitions are performed at low magnetic fields, where the frequency differences between the different microwave transitions is sufficiently small,  $\sim 2\text{ MHz}$ , that the transfer efficiency is not strongly affected by, for example, differences in radiative power transmission of the RF antenna.

Using these experimental calibration techniques, we can bound the error contributions to Eq. 4.20 for the data shown in section 4.4.3 over all fillings in the lattice. We find experimentally that the first term in the equation is bounded by  $-0.2(1) \times C_s(1)$ , and the second error term by  $0.02(2) \times C_m(1)$ , corresponding to  $\epsilon_1 \sim 0.045$  and  $\epsilon_2 \sim 0.055$ . The third term, we find, is  $< 1 \times 10^{-4}$ , which is due to the fact that  $\epsilon_{1,\uparrow} - \epsilon_{1,\downarrow}$  is small compared to the average,  $\epsilon_1$ , as well as the fact that  $P_\uparrow(1) - P_\downarrow(1)$  is small because of the symmetry between the two spin states in the Hubbard model, as long as the system is approximately spin-balanced. For the data shown in section 4.4.3, the ratio of the populations of the two spin states was found to be  $1.02(1)$ . This was measured using the average atom number of each spin species obtained through spin-dependent imaging. We therefore find that  $-0.2(1) \times C_s(1)$  is the dominant contribution to the error, since, as we will discuss in section 4.4.3,  $C_m(1)$  is smaller in magnitude than  $C_s(1)$ . Given the bounded values of  $\epsilon_1$  and  $\epsilon_2$  that we measured, we also find that we were justified in neglecting contributions to the error,  $\Delta C_s(1)$ , which are higher order in these parameters. Finally, we estimate the imaging fidelity  $f = 95(1)\%$  by taking multiple, repeated images of a sample, and measuring the loss and hoping rates through a comparison of the site occupancy of subsequent images (see section 3.2).

The form for the deviation between the measured spin correlations and the ideal value of the spin correlations given by Eq. 4.20 assumes that doubly-occupied sites are efficiently removed during the spin-dependent imaging process, so that, other than the errors described by Eq. 4.17, the parity-projected measurable operators are  $\hat{n}_{\sigma,i}^s = \hat{n}_{\sigma,i} - \hat{d}_i$ . It is not necessarily true that this must be the case however. In fact, the opposite regime has been observed by other experiments using  ${}^6\text{Li}$  [27, 155, 26], where the push-out pulse efficiently removed one of the atoms on a doubly-occupied site that

was in the unwanted spin state, before both atoms were lost due to, for example, light-assisted collisions. Because of this, the removal pulse provided these experiments with direct access to the total density of either spin state,  $\hat{n}_{\sigma,i}$ . If, then, a fraction  $\epsilon_d$  of doublons are actually converted to singly-occupied sites during the push-out pulse, which subsequently appear in the final single-site image, we will have additional contributions to the deviation  $\Delta C_s(1)$  of the measured spin correlator relative to its ideal value  $C_s(1)$  that are not captured by Eq. 4.20. We can understand this, ignoring the other error contributions, as a transformation of the ideal measurement operator  $\hat{n}_{\sigma,i}^s = \hat{n}_{\sigma,i} - \hat{d}_i$  to an observable operator,

$$\hat{n}_{\sigma,i}^s = \hat{n}_{\sigma,i} - (1 - \epsilon_d) \hat{d}_i, \quad (4.23)$$

where  $\epsilon_d = 0$  corresponds to the situation where all doublons are removed during the spin-dependent imaging process, and  $\epsilon_d = 1$  corresponds to the situation where all doublons are converted to singly-occupied sites. Plugging Eq. 4.23 into the observable connected correlator  $\langle \hat{n}_{\sigma,i}^s \hat{n}_{\sigma,j}^s \rangle_c$  of this spin state in order to construct the nearest-neighbor observable spin correlator,  $\tilde{C}_s(1)$ , leads to a deviation,  $\Delta C_s(1)$ , as defined in Eq. 4.18, of  $\tilde{C}_s(1)$  from its ideal value  $C_s(1)$  given by,

$$\Delta C_s(1) = 4\epsilon_d \left( \langle \hat{n}_i \hat{d}_j \rangle_c - 2 \langle \hat{d}_i \hat{d}_j \rangle_c \right). \quad (4.24)$$

Here,  $\hat{n}_i = \hat{n}_{\uparrow,i} + \hat{n}_{\downarrow,i}$  is the total density operator. We can estimate the magnitude of this error by looking to NLCE calculations of this correlator,  $\langle \hat{n}_i \hat{d}_j \rangle_c - 2 \langle \hat{d}_i \hat{d}_j \rangle_c$ , at the approximate temperature of the samples comprising the data discussed in section 4.4.3,  $k_B T/t = 1.16(16)$ , and at half-filling. The NLCE predictions for the two relevant correlators,  $\langle \hat{n}_i \hat{d}_j \rangle_c$  and  $\langle \hat{d}_i \hat{d}_j \rangle_c$ , as functions of temperature at half-filling are shown in Fig. 4-28. From these numerical calculations, we can bound the contribution of imperfect non-detection of doubly-occupied sites to the error in  $C_s(1)$  by  $0.025\epsilon_d$ .

We can use two separate methods to bound the value of  $\epsilon_d$  itself. First, as we will discuss in detail in section 4.4.3, we can compare the density dependence of the ex-

perimentally measured nearest-neighbor spin correlator with predictions from NLCE calculations that are performed at a temperature that is independently determined using the value of the average moment at half-filling, a quantity which is not susceptible to these spin-dependent imaging errors. Based on the agreement of the NLCE calculations with our data, shown in Fig. 4-15, we estimate that  $\epsilon_d < 0.1$ . A second estimate of  $\epsilon_d$  can be made experimentally by comparing the average filling in a band-insulating region, where  $\langle \hat{n}_i \rangle \sim 2$ , as measured with the normal single-site imaging, to what one obtains by imaging both spin states separately using spin-dependent imaging. This is valid once  $\epsilon_1 - \epsilon_2$  is already calibrated, which can be done using a similar technique, as discussed previously, at lower densities,  $\langle \hat{n}_i \rangle < 1$ , where the doublon fraction is low, so that the local moment is approximately equal to the total density, and therefore the correction to the average moment due to imperfect non-detection of doublons is negligible. After correcting  $\langle \hat{n}_{\uparrow,i}^s \rangle + \langle \hat{n}_{\downarrow,i}^s \rangle$ , obtained from the spin-dependent imaging, by the pre-factor  $(1 - \epsilon_1 + \epsilon_2)$  (Eq. 4.22), one can obtain an estimate of  $\epsilon_d$ , assuming the total density is known (i.e.  $\langle \hat{n}_i \rangle \approx 2$  in the band-insulating region), by comparing to  $\langle \hat{m}_{z,i}^2 \rangle$ , measured at the same total density, using the normal single-site imaging. From this method, we find experimentally that the spin-dependent imaging efficiently converts doubly-occupied sites to empty sites, and that only  $\approx 1(3)\%$  of doubly-occupied sites are converted to detectable singly-occupied sites in the process. Thus, we estimate that  $\epsilon_d \leq 0.04$  from this calibration, in agreement with our other estimate that  $\epsilon_d < 0.1$  using the comparison to NLCE calculations. We therefore obtain an overall upper bound of  $2.5 \times 10^{-3}$  for the error correction to the spin correlation function given by Eq. 4.24. We discuss possible reasons for the high doublon to empty site conversion efficiency of our spin-dependent imaging technique in section 3.4.3, where we also describe ongoing experimental pursuits to enter the opposite regime, where doublons are efficiently converted to detectable singly-occupied sites, thereby allowing us to directly access the total density  $\hat{n}_{\sigma,i}$  of a given spin state.

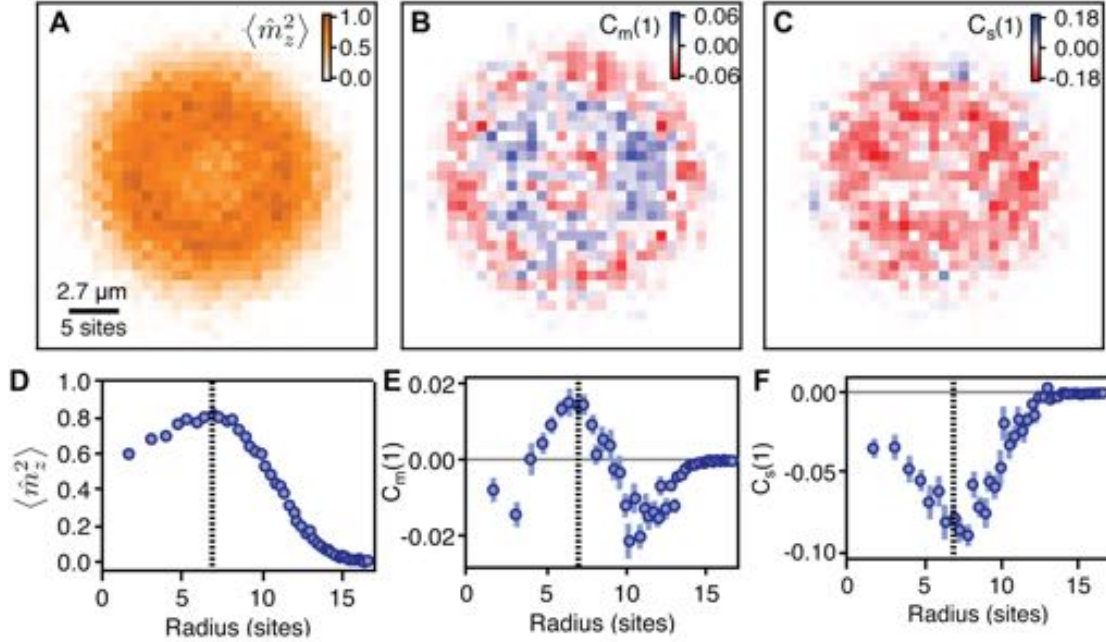


Figure 4-14: Site-resolved average local moment and average nearest-neighbor charge and spin correlations of a 2D fermionic Mott insulator. Site-resolved average of the in-trap local moment  $\langle \hat{m}_{z,i}^2 \rangle$  (a), and the in-trap nearest-neighbor charge correlation function  $C_m(1)$  (b), taken from  $\sim 90$  separate samples prepared at  $U/t = 7.2(1)$  and  $k_B T/t = 1.1(1)$ . (c) represents the site-resolved average of the in-trap nearest-neighbor spin correlation function,  $C_s(1)$ , taken from  $\sim 270$  separate samples prepared at  $U/t = 7.2(1)$  and  $k_B T/t = 1.1(1)$ , where  $\sim 90$  images were taken of  $\hat{m}_{z,i}^2$ ,  $\sim 90$  images were taken of  $\hat{n}_{\uparrow,i}^s$ , and  $\sim 90$  images were taken of  $\hat{n}_{\downarrow,i}^s$ . (d),(e),(f) represent radial averages of the data shown in (a),(b),(c), respectively. The spatial variation of these quantities arises from the spatial variation of the in-trap density caused by the underlying trapping potential of the optical lattice beams. The radial location of the half-filling point, denoted by the vertical dotted lines in (d-f), is found from the peak in the average local moment in (d). Figure reproduced from [38].

#### 4.4.3 Measurements of the Spatially Resolved Spin and Charge Correlation Functions

In this section, we discuss our experimental measurements of charge and spin correlations, Eqs. 4.5 and 4.10, as functions of doping in the lattice, with fixed Hubbard parameters  $U/t = 7.2(1)$ . We compare these results with numerical calculations from DQMC and NLCE , and find good agreement between the predictions from theory and the experimental results over the full range of doping, and over several different temperatures,  $k_B T/t$ . Details of the experimental sequence and sample preparation

are discussed in section 4.2; we use the same sample preparation protocol for these measurements as we did for the data discussed in section 4.3, where we studied properties of the site-resolved average local moment and its variance for different states of the Hubbard model. The only qualitative difference in this case is that, as we adiabatically increase the depth of the optical lattice to its final value, where  $U/t = 7.2(1)$ , we simultaneously lower the power of the dimple until it is completely off, so that in the final configuration, the lattice beams themselves form the dominant contribution to the underlying trapping potential. We do this because we found that we could achieve lower sample temperatures in the lattice with the dimple off, compared to the configuration used in section 4.3, where the dimple provides the dominant confinement in the plane of the lattice. The heating caused by the presence of the dimple could be due to several things, including off-resonant scattering of the dimple laser photons, intensity noise of the dimple light, which would modulate the harmonic confinement the atoms experience, or the possibility that the broadband SLED source used for the dimple hits a photoassociation resonance for the K atoms, which could ultimately also lead to heating. Regardless, we simply turn the dimple light off once the atoms are in the final lattice configuration, because we find that this slightly improves the final temperature of the sample.

We first measure the site-resolved average local moment,  $\langle \hat{m}_{z,i}^2 \rangle$ , at these Hubbard parameters using the usual single-site imaging technique, similar to what we discussed in section 4.3.1, and observed in Fig. 4-7. In this case, however, rather than immediately radially averaging the site-resolved occupation from a single experimental realization, we accumulate more statistics, and analyze the detected site-occupations from  $\sim 90$  independent experimental realizations which have, approximately, the same global chemical potential. This allows us to average the measured occupation at each site  $i$  over these  $\sim 90$  independent realizations of the experiment, so that we can form a full two-dimensional map of the average moment  $\langle \hat{m}_{z,i}^2 \rangle$  in a site-resolved manner. This is shown in Fig. 4-14(a). Performing this site-resolved averaging requires two different forms of experimental stability. First, the images which are averaged together must represent independent snapshots of the same quantum system. If, for

example, the atom number changes drastically between images, corresponding to a large change in the global chemical potential, then averaging the occupations of a particular lattice site between these images no longer makes sense, because that site is no longer equivalent between the two different realizations. Under the LDA, the spatial inhomogeneities of the underlying trapping potential, denoted by  $V(r)$ , where  $r$  is the distance from the center of the trap, lead to a spatially varying local chemical potential  $\mu(r) = \mu_0 - V(r)$ , where  $\mu_0$  is the global chemical potential (section 4.3.3). Thus, if site  $i$  is a distance  $r$  from the center of the trap, and the global chemical potential  $\mu_0$  changes between two realizations of the experiment, then site  $i$  is no longer at the same local chemical potential between the two images, and is therefore inequivalent for the purposes of averaging. Because of this, a reasonable degree of atom number stability is required for such an analysis. A second form of stability which is generally necessary for site-resolved averaging is stability of the sample location with respect to the imaged location on the camera. If, for some reason, the cloud location, with respect to the image, changes by ten or twenty lattice sites between different realizations, then again it no longer makes sense to average the occupations of a fixed lattice site  $i$ , as determined by the site location in the image, between these two different realizations. This is because this particular lattice site is no longer equivalent in the two images since it represents, for example, two different local chemical potentials. Such drift of the cloud with respect to the image can be caused by various things including pointing stability of both the incoming and retro-reflected lattice beams, which determine the trap center, or relative drift between the camera and the center of the vacuum chamber caused by potential environmental changes, such as changes in the temperature or humidity of the lab or the temperature of the magnetic field coils on top of the bucket window. The presence of a magnetic gradient whose magnitude is not stable can also lead to shifts of the cloud position, as well as imaging reconstruction errors, such as errors in the determination of the lattice phase [40], which can become significant if the single-site imaging is not working properly. In the ideal world of course, the sample location in the image is constant throughout the data set, but in the case of reasonable, slow drifts due to, for example, slow term

pointing drift of the lattice beams, one can compensate for this instability by referencing the lattice index  $i$  to the center of mass (COM) of each individual sample, rather than to the fixed frame of the camera. That is, one can calculate the COM of a given experimental realization from the measured site occupation, and then shift the relative location of the cloud in the image so that the COM of each sample in the data set overlaps. Then, one can average the observed local moment at each individual site once the different centers of mass are aligned. These stability requirements are not limited to the measurement of the site-resolved average local moment  $\langle \hat{m}_{z,i}^2 \rangle$ , but also apply to any site-resolved average quantity, including the spatial spin and charge correlations which we will discuss subsequently.

As can be seen in Fig. 4-14(a), the two-dimensional distribution of the average local moment is radially symmetric, due to the radial symmetry of the underlying confinement from the lattice beams. We can therefore simplify things by radially averaging this 2D map of  $\langle \hat{m}_{z,i}^2 \rangle$ , in the same way that was discussed in section 4.3.2, to obtain the average local moment as a function of distance from the center of the trap. The results of this are shown in Fig. 4-14(d). Similar to what we discussed in section 4.3.2, the average local moment demonstrates spatial variation in the trap, which can again be understood through the LDA, where the radial dependence of the local chemical potential  $\mu(r)$ , caused by the underlying trapping potential  $V(r)$ , leads to spatial variation in the average total density, which then affects the average local moment. For the data shown in Fig. 4-14, we purposely prepared samples which have a central density above half-filling,  $1 < \langle \hat{n}_i \rangle < 2$ , corresponding to a global chemical potential  $\mu(0) > U/2$ . Doing this ensures that we can observe a peak in the average local moment at a finite distance from the trap center, thereby providing an experimentally accessible way of determining the half-filling point ( $\mu = U/2$ ) from the radial location of this peak. The particle-hole symmetry of the local moment operator underlying this effect was discussed in section 4.2.2. We represent the radial location of the half-filling point in Fig. 4-14(d) as a vertical dotted line. As a side note, if the confining potential  $V(r)$  is harmonic with a known trap frequency  $\omega$ , the radial location of the half-filling point uniquely determines the global chemical

potential  $\mu(0)$ , as we discussed in section 4.3.3.

Since we have access to the average local moment at half-filling in this data set, we can use this value as a thermometer to determine the temperature of the sample in a fit-free manner, which does not require us to make any assumptions about the underlying trapping potential  $V(r)$ . This thermometry technique was discussed in detail in sections 4.3.4 and 4.3.5. After correcting the measured moment at half-filling for the finite imaging fidelity  $f = 95(1)\%$ , we can simply compare this value to predictions for the moment, at half-filling and  $U/t = 7.2$ , made using NLCE calculations, such as those shown in Fig. 4-5, to obtain a temperature of  $k_B T/t = 1.2(2)$ . For the temperature range of samples in this data set ( $4t^2/U \approx 0.56t < k_B T < U$ ), the local moment at half-filling is a monotonic function of the temperature, and therefore uniquely determines the temperature of the data. Of course, in this temperature regime, the moment begins to lose some of its sensitivity to changes in the temperature, as we discussed in section 4.3.5, because the charge fluctuations which affect the moment are effectively frozen out once  $k_B T$  is sufficiently below  $U$ , so that the peak moment is essentially saturated. However, as we will discuss subsequently, the value of the spin correlations at half-filling become a sensitive probe of temperature in this regime, and can take over the job of thermometer from the average moment once  $k_B T \sim t$  or lower, at this value of  $U/t$ .

From the  $\sim 90$  different snapshots of the local moment, in addition to measuring the average moment  $\langle \hat{m}_{z,i}^2 \rangle$  at each site, we can also obtain the site-resolved average nearest-neighbor moment correlator  $C_m(1)$ , as defined in Eq. 4.5. To do this, we first measure  $\hat{m}_{z,i}^2 \hat{m}_{z,j}^2$  from a single experimental realization by shifting the image of the reconstructed site-occupation by one site (although this changes if we consider further distance correlations) in the direction from site  $i$  to site  $j$ . We then multiply the resulting shifted image by the original, unshifted reconstructed site-occupation. This gives us the value of  $\hat{m}_{z,i}^2 \hat{m}_{z,j}^2$  for site  $i$  in this single sample, in the direction of  $i$  to  $j$ . We can do this for each of the  $\sim 90$  different experimental measurements of the local moment, and then average together each of the values measured for  $\hat{m}_{z,i}^2 \hat{m}_{z,j}^2$  at site  $i$  to obtain the site-resolved correlator  $\langle \hat{m}_{z,i}^2 \hat{m}_{z,j}^2 \rangle$ . The site-resolved averaging

procedure used here is the same as that used to obtain the site-resolved average moment  $\langle \hat{m}_{z,i}^2 \rangle$ . We then average  $\langle \hat{m}_{z,i}^2 \hat{m}_{z,j}^2 \rangle$  over the four nearest-neighbors of site  $i$ , and subsequently subtract off  $\langle \hat{m}_{z,i}^2 \rangle \langle \hat{m}_{z,j}^2 \rangle$ , averaged over the same four nearest-neighbors of site  $i$ , which we obtain from the site-resolved average local moment data shown in Fig. 4-14(a). From this, we then have the average nearest-neighbor moment correlation  $C_m(1)$  from Eq. 4.5, defined at site  $i$ . The final two-dimensional map of  $C_m(1)$  in the lattice resulting from this procedure is shown in Fig. 4-14(b).

As we did with the site-resolved average moment, we can radially average the site-resolved moment correlations in Fig. 4-14(b) to obtain  $C_m(1)$  as a function of distance from the trap center. This is shown in Fig. 4-14(e). The half-filling point,  $\mu = U/2$ , determined from the peak average moment in Fig. 4-14(d), is shown as the vertical dotted line in Fig. 4-14(e). From this figure, it is immediately apparent that  $C_m(1)$  displays a non-trivial and non-monotonic dependence on the radial location from the trap center, corresponding to different fillings (or dopings) in the system. That is, at half-filling we observe nearest-neighbor moment correlations which are positive, corresponding to a bunching behavior between moments. However, as we move past the half-filling location, further from the trap center, which corresponds to a decrease in the total density  $\langle \hat{n}_i \rangle < 1$  (or an increase in the hole doping of the system), we find that the nearest-neighbor moment correlations decrease, eventually cross zero, and finally become negative at sufficiently low filling. These negative correlations indicate an anti-bunching behavior which occurs between moments at low fillings. Thus, we observe a cross-over from bunching to anti-bunching behavior between moments as a function of doping in the system. We will investigate this interesting behavior of the moment correlations in more detail subsequently.

To measure the nearest-neighbor spin correlator,  $C_s(1)$ , defined by Eq. 4.10, we make use of Eq. 4.15, which expresses this correlator in terms of experimentally accessible quantities. From the images of the local moment of the system, obtained using normal single-site imaging, we have access to the connected moment correlator,  $\langle \hat{m}_{z,i}^2 \hat{m}_{z,j}^2 \rangle_c$ , which we used to obtain  $C_m(1)$ . To measure the other connected correlators in Eq. 4.15,  $\langle \hat{n}_{\sigma,i}^s \hat{n}_{\sigma,j}^s \rangle_c$ , we must separately measure the singles densities of the

two individual spin states,  $\hat{n}_{\sigma,i}^s$  (Eq. 4.11), which we can do using the spin-dependent imaging technique discussed in sections 3.4 and 4.4.2. We therefore take  $\sim 90$  images each, through independent experimental realizations, of the two spin states to measure  $n_{\uparrow,i}^s$  and  $n_{\downarrow,i}^s$ . Using the same correlation analysis and site-resolved averaging procedures applied to the site-resolved measurement of  $\langle \hat{m}_{z,i}^2 \hat{m}_{z,j}^2 \rangle_c$ , we can obtain the average connected correlators,  $\langle \hat{n}_{\sigma,i}^s \hat{n}_{\sigma,j}^s \rangle_c$  from these  $\sim 90$  spin-dependent images at each site  $i$ , in the direction of neighbor  $j$ . We then take the weighted sum of the different connected correlators obtained from the three independent data sets of the two spin states and the local moment, according to Eq. 4.15, and then sum over the resulting values of the four nearest-neighbors  $j$  of site  $i$  to obtain  $C_s(1)$  for site  $i$ . The final two-dimensional map of the nearest-neighbor spin correlator in the lattice resulting from this procedure is shown in Fig. 4-14(c). As was done for  $C_m(1)$  and  $\langle \hat{m}_{z,i}^2 \rangle$ , we can radially average the site-resolved average correlator in Fig. 4-14(c) to obtain  $C_s(1)$  as a function of distance from the trap center, which is shown in Fig. 4-14(f). The half-filling location is again indicated in this figure by a vertical dotted line. In contrast to the moment correlations of Fig. 4-14(e), the nearest-neighbor spin correlations shown in Fig. 4-14(f) are negative over the entire range of distances from the trap center, and are most negative (largest in magnitude) at half-filling. The negative sign of these correlations indicates that the spins prefer to be antiferromagnetically aligned, as we intuitively suspected from the double well model discussed in section 2.2.1, and as previously predicted theoretically for the 2D Fermi-Hubbard model [97, 120, 137]. Fig. 4-14(f) also shows that, as one moves away from the half-filling point in either direction, corresponding to doping the system with either particles or holes, these nearest-neighbor antiferromagnetic spin correlations weaken monotonically, and eventually go to zero far from the trap center, where the particle density also goes to zero.

Because we have access to both the average moment  $\langle \hat{m}_z^2 \rangle$  and the charge and spin correlations,  $C_m(1)$  and  $C_s(1)$ , as functions of distance from the trap center, we can eliminate the functional dependence on the trap radius, something which is specific to the experiment because of dependencies on properties like the underlying

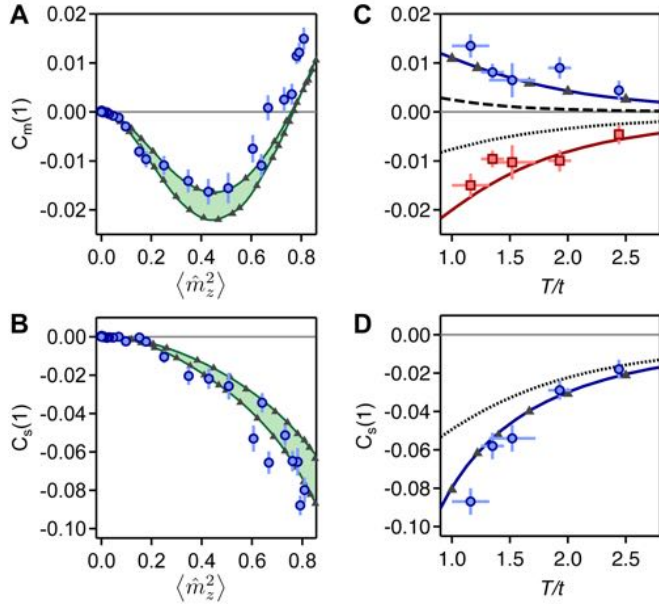


Figure 4-15: Nearest-neighbor charge and spin correlations as functions of  $\langle \hat{m}_z^2 \rangle$  and  $k_B T/t$ , for  $U/t = 7.2(1)$ .  $C_m(1)$  (a) and  $C_s(1)$  (b) plotted versus  $\langle \hat{m}_z^2 \rangle$ , obtained from the experimental data shown in Fig. 4-14 (blue circles). Green solid lines (gray triangles) represent isothermal predictions from NLCE (DQMC) for temperatures  $k_B T/t = 0.89$  (lower curves in the plots) and  $k_B T/t = 1.22$  (upper curves in the plots). The green shaded region represents the intermediate temperature range for the theoretical predictions. (c) The maximum (blue circles) and minimum (red squares) values of  $C_m(1)$ , as functions of  $k_B T/t$ . The blue and red solid lines are the corresponding NLCE predictions, the black dashed and dotted lines are predictions from the non-interacting two-component gas, and the gray triangles are predictions for the maximum value of  $C_m(1)$  from DQMC. (d)  $C_s(1)$  at half-filling (blue circles) as a function of  $k_B T/t$ . The solid blue line is the NLCE prediction, the gray triangles are DQMC, and the black dotted line is the two-component non-interacting gas. Theory curves not adjusted for experimental imaging fidelity. Figure reproduced from [38].

trapping potential  $V(r)$ , and examine the dependence of these correlators directly on the average moment itself. This is shown in Fig. 4-15(a),(b) for the charge and spin correlations, respectively. Such a method of plotting the charge and spin correlation functions provides us with a simple way to compare our experimental data to predictions from theory, with minimal assumptions about the experimental details. In this case, the average local moment acts as a thermodynamic quantity which is substituting for the usual role of the chemical potential,  $\mu$ . This thermodynamic substitution is totally reasonable for the Fermi-Hubbard model on a square lattice, because both the Hamiltonian and the local moment operator are symmetric under a particle-hole

transformation (see sections 2.2 and 4.2.2), meaning that all of the observable quantities, including the spin and charge correlation functions, are also symmetric under such a transformation. We can therefore conveniently parameterize the filling for our purposes using the average moment in place of the chemical potential,  $\mu$ , because such a parameterization contains the full information we need in a fit-free manner.

The data shown in Fig. 4-15(a),(b) are compared to predictions from both NLCE and DQMC for  $C_m(1)$  and  $C_s(1)$  at  $U/t = 7.2$  and fixed  $k_B T/t$ , as functions of the average moment. The NLCE and DQMC predictions are shown in the figure as green lines and gray triangles, respectively. We chose the temperature range that is shown for the numerical predictions,  $k_B T/t = 0.89$  to  $k_B T/t = 1.22$ , using the measured value of the nearest-neighbor spin correlation function at half-filling, and the associated error on the measurement. That is, because the numerics do not suffer from the fermion sign problem at half-filling, the predictions from NLCE and DQMC for  $C_s(1)$  are expected to be essentially exact at our experimental temperatures,  $k_B T/t = 1.2(2)$  (obtained from the average moment at half-filling). By comparing the measured value of  $C_s(1)$  at half-filling to theory for different temperatures then, we can obtain another estimate of the temperature of our system. Doing this, we find  $k_B T/t = 1.06(16)$ , in agreement with our previous temperature estimate based on the average moment at half-filling. Thus, having estimated the temperature  $k_B T/t$  using these two different methods, our technique for examining the charge and spin correlation functions shown in Fig. 4-15(a),(b) reveals its true strength, because it allows for a comparison of the experimental data with the theory predictions over the full range of doping, corresponding to the full range of the average moment, with no free fit parameters. Within the temperature range  $k_B T/t = 0.89$  to  $k_B T/t = 1.22$ , we find, as shown in Fig. 4-15(a),(b), that the two different numerical calculations, DQMC and NLCE, of  $C_m(1)$  and  $C_s(1)$ , which were performed specifically for this work, agree with each other almost exactly over the full range of doping. Additionally, we find that the numerical predictions and the experimental data agree with each other over the full range of doping, to within the experimental uncertainty, for both  $C_m(1)$  and  $C_s(1)$ . Thus, not only do the two different numerical techniques produce

the same result, but they also agree with the experimental data, thereby affirming the theoretical predictions, and demonstrating the ability of our quantum simulator to benchmark calculations made on a classical computer.

Examining the behavior of the spin correlation function,  $C_s(1)$ , in Fig. 4-15(b) more closely, it is clear that both the numerics and the experimental data demonstrate antiferromagnetic nearest-neighbor spin correlations which are strongest at half-filling, where the average moment is largest, and which weaken monotonically as the system becomes more dilute, as one would expect. The moment correlation function  $C_m(1)$  in Fig. 4-15(a), however, is positive at half-filling, where the average moment is largest, corresponding to bunching or an effective attraction between moments. As the filling in the system decreases, corresponding to a decrease in the average moment,  $C_m(1)$  decreases in magnitude, eventually crossing zero around an average moment of  $\langle \hat{m}_z^2 \rangle \approx 0.75$  (or a doping of  $x \approx 0.21$ , where  $x = 1 - \langle \hat{n}_i \rangle$ ), and becoming negative at sufficiently low fillings, representing anti-bunching or an effective repulsion between moments. These negative moment correlations become most negative around an average moment of  $\langle \hat{m}_z^2 \rangle \approx 0.45$ , and subsequently weaken in magnitude towards zero as the filling is lowered further.

Upon an initial inspection, there appears to be no clear physical significance of the value of the average moment where the zero-crossing of the moment correlation function occurs. Although it may be tempting to try to relate the location of the zero-crossing of  $C_m(1)$ , which occurs at a doping of  $x \approx 0.21$  for the data shown in Fig. 4-15(a), to the value of optimal doping,  $x_{opt} \sim 0.17$ , where the superconducting critical temperature is maximized in the cuprates [139], the similarity between the two doping values seems to be purely coincidental. In fact, the location of this moment correlation zero-crossing appears to depend strongly on both temperature and the value of  $U/t$ . For future reference, we show in Fig. 4-16 and Fig. 4-17 the value of the average moment and the corresponding average total density, respectively, where  $C_m(1)$  crosses zero, as a function of  $U/t$  for several different temperatures  $k_B T/t$ . These zero-crossing values were obtained using NLCE calculations that were performed for the data analysis in [38], and are expected to be essentially exact for

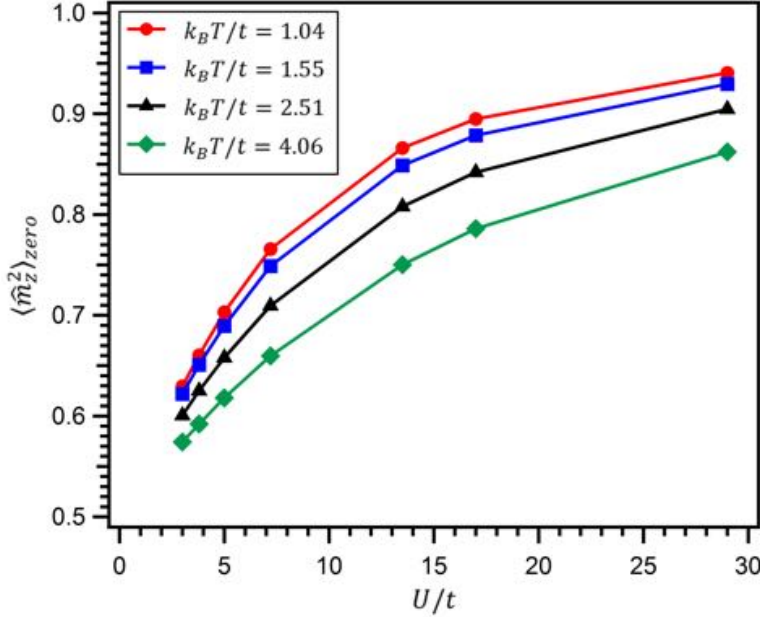


Figure 4-16: The average moment corresponding to the zero-crossing of the nearest-neighbor moment correlation function,  $C_m(1)$ , versus  $U/t$ . Plotted are isothermal 9<sup>th</sup>-order NLCE predictions for the value of the average local moment,  $\langle \hat{m}_z^2 \rangle$ , where the nearest-neighbor moment correlation function,  $C_m(1)$ , crosses zero as a function of  $\langle \hat{m}_z^2 \rangle$  within the 2D Fermi-Hubbard model (such as in Fig. 4-15(a), where  $C_m(1)$  is plotted as a function of the average moment at fixed  $U/t$  and fixed  $k_B T/t$ ), as a function of the Hubbard parameters  $U/t$ , for several different temperatures in the range  $1.04 \leq k_B T/t \leq 4.06$ . This temperature range represents typical values of the temperature which are achieved in the experimental data discussed in this thesis. The curves are generated using the NLCE data from [38].

the temperature range shown.

We can also ask about the value of the average moment or the average total density where the minimum value of  $C_m(1)$  occurs. Similar to the zero-crossing location, the minimum value location depends strongly on the Hubbard parameters  $U/t$ . However, unlike the zero-crossing location, the temperature dependence here is fairly weak. For the data shown in Fig. 4-15(a), the minimum in the moment correlator occurs at an average moment of  $\langle \hat{m}_z^2 \rangle \approx 0.45$ . Although the physical significance of the location of this minimum is not necessarily known, we show here, for future reference, the average moment and the average total density in Fig. 4-18 and Fig. 4-19, respectively, where  $C_m(1)$  is most negative (i.e. reaches its minimum value), as a function of  $U/t$ , and for several different temperatures  $k_B T/t$ . These values are also obtained using the

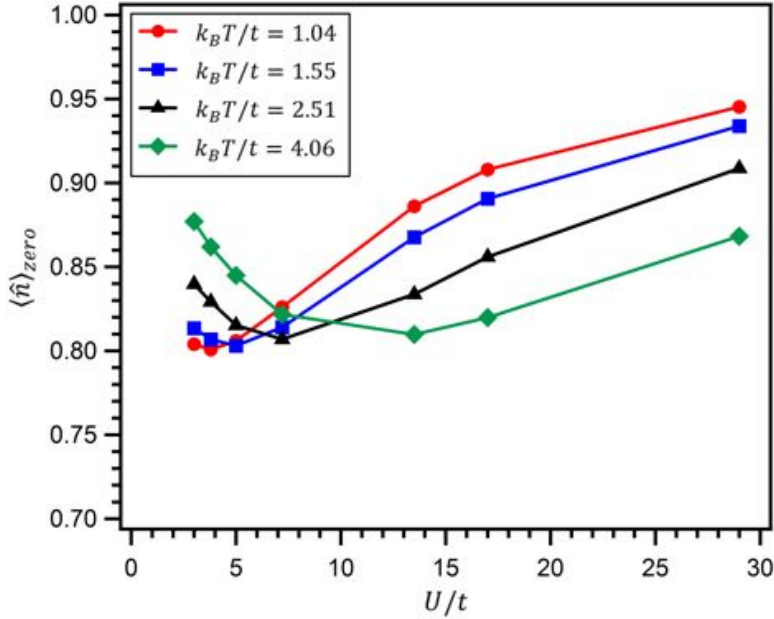


Figure 4-17: The average total density corresponding to the zero-crossing of the nearest-neighbor moment correlation function,  $C_m(1)$ , versus  $U/t$ . Plotted are isothermal 9<sup>th</sup>-order NLCE predictions for the value of the average total density,  $\langle \hat{n} \rangle = \langle \hat{n}_\uparrow + \hat{n}_\downarrow \rangle$ , where the nearest-neighbor moment correlation function,  $C_m(1)$ , crosses zero as a function of  $\langle \hat{m}_z^2 \rangle$ , within the 2D Fermi-Hubbard model (such as in Fig. 4-15(a), where  $C_m(1)$  is plotted as a function of the average moment at fixed  $U/t$  and fixed  $k_B T/t$ ), as a function of the Hubbard parameters  $U/t$ , for several different temperatures in the range  $1.04 \leq k_B T/t \leq 4.06$ . This temperature range represents typical values of the temperature which are achieved in the experimental data discussed in this thesis. The curves are generated using the NLCE data from [38].

same NLCE calculations performed for the data analysis in [38]. In contrast to this minimum value of  $C_m(1)$ , whose location varies depending on the temperature or the value of  $U/t$ , as seen in Fig. 4-18 and Fig. 4-19, the maximum value of  $C_m(1)$ , where it is most positive, occurs always at the half-filling point, and therefore occurs at a fixed doping value (zero doping).

In addition to examining the doping dependence of  $C_m(1)$  and  $C_s(1)$  at a fixed temperature, we can study the temperature dependence of these correlators at, for instance, a fixed doping. To vary the temperature of the sample, we simply hold the atoms for a variable time in the optical lattice at the final lattice configuration, where  $U/t = 7.2(1)$ , in order to heat the system. After this hold time, we measure the local moment and the singles densities of both spin states, as we did previously, in order to

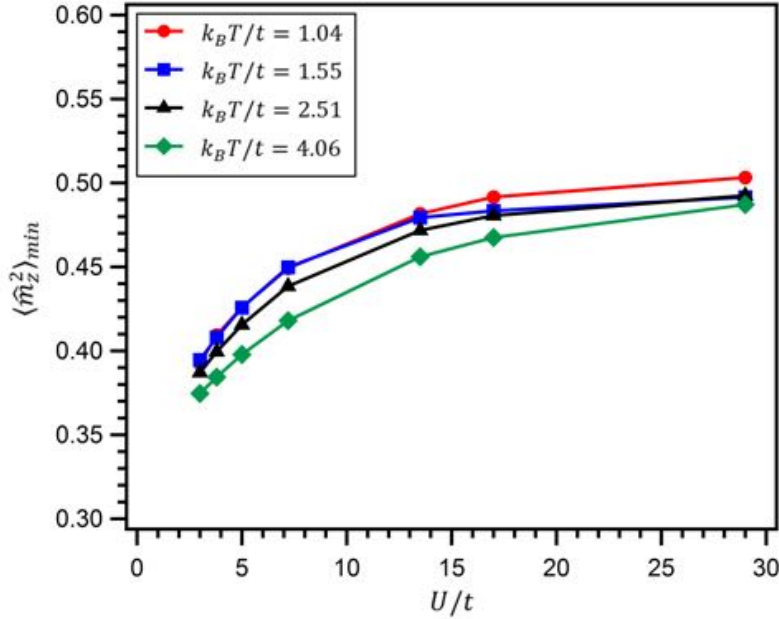


Figure 4-18: The average moment corresponding to the minimum value of the nearest-neighbor moment correlation function,  $C_m(1)$ , versus  $U/t$ . Plotted are isothermal 9<sup>th</sup>-order NLCE predictions for the value of the average local moment,  $\langle \hat{m}_z^2 \rangle$ , where the nearest-neighbor moment correlation function,  $C_m(1)$ , achieves its minimum value as a function of  $\langle \hat{m}_z^2 \rangle$  within the 2D Fermi-Hubbard model (such as in Fig. 4-15(a), where  $C_m(1)$  is plotted as a function of the average moment at fixed  $U/t$  and fixed  $k_B T/t$ ), as a function of the Hubbard parameters  $U/t$ , for several different temperatures in the range  $1.04 \leq k_B T/t \leq 4.06$ . This temperature range represents typical values of the temperature which are achieved in the experimental data discussed in this thesis. The curves are generated using the NLCE data from [38].

obtain both  $C_m(1)$  and  $C_s(1)$  for these different hold times. To determine the temperature of the system in a manner independent of the values of the correlation functions and which utilizes minimal assumptions, we measure the value of the average moment at the half-filling location, and compare this value to calculations from NLCE. As we discussed previously, this method gives a reasonable estimate of the temperature at the lowest temperatures achieved here,  $k_B T/t = 1.2(2)$ , and it agrees with estimates based on the nearest-neighbor spin correlations at half-filling. Additionally, at the higher temperatures we explore via lattice heating, where the likelihood of thermal charge fluctuations increases, this method becomes an even more sensitive thermometer (sections 4.3.4 and 4.3.5). Fig. 4-20 shows the calibrated temperature obtained in this way as a function of time held in the lattice at the final lattice configuration.

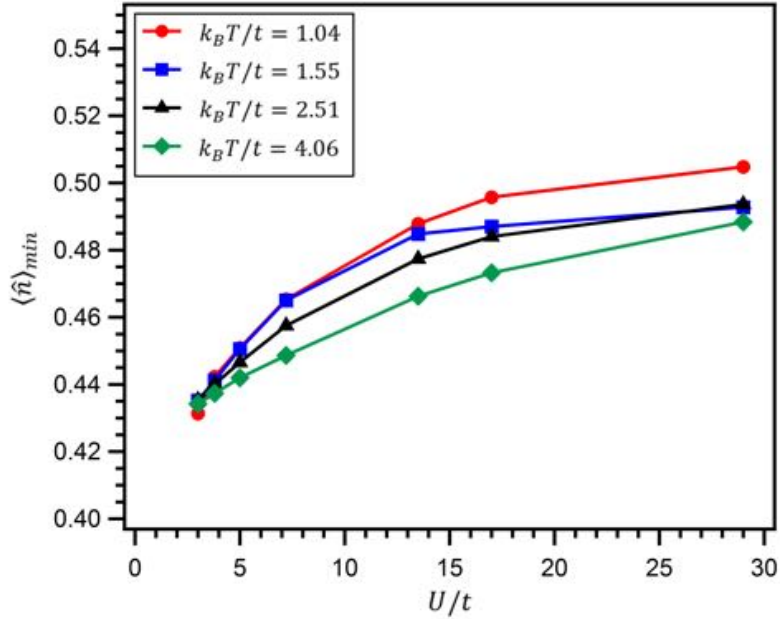


Figure 4-19: The average total density corresponding to the minimum value of the nearest-neighbor moment correlation function,  $C_m(1)$ , versus  $U/t$ . Plotted are isothermal 9<sup>th</sup>-order NLCE predictions for the value of the average total density,  $\langle \hat{n} \rangle = \langle \hat{n}_\uparrow + \hat{n}_\downarrow \rangle$ , where the nearest-neighbor moment correlation function,  $C_m(1)$ , achieves its minimum value as a function of  $\langle \hat{m}_z^2 \rangle$ , within the 2D Fermi-Hubbard model (such as in Fig. 4-15(a), where  $C_m(1)$  is plotted as a function of the average moment at fixed  $U/t$  and fixed  $k_B T/t$ ), as a function of the Hubbard parameters  $U/t$ , for several different temperatures in the range  $1.04 \leq k_B T/t \leq 4.06$ . This temperature range represents typical values of the temperature which are achieved in the experimental data discussed in this thesis. The curves are generated using the NLCE data from [38].

A linear fit to this curve provides us with information about the heating rate of the system, which we find to be  $0.64(5) t/s$  at this lattice depth.

Using the temperature calibration curve shown in Fig. 4-20, and the moment-dependence of the nearest-neighbor spin and charge correlations, analogous to Fig. 4-15(a),(b), measured at each hold time, we can extract the values of the correlators,  $C_m(1)$  and  $C_s(1)$ , at any filling, as functions of temperature  $k_B T/t$ . Fig. 4-15(c) shows the measured maximum value of  $C_m(1)$  (blue circles), which occurs at half-filling, and the measured minimum value (red squares), which occurs at an average moment  $\langle \hat{m}_z^2 \rangle \approx 0.45$  at  $U/t = 7.2(1)$  (Fig. 4-18), as functions of the calibrated temperature  $k_B T/t$ . These results are compared with calculations made using NLCE (solid lines

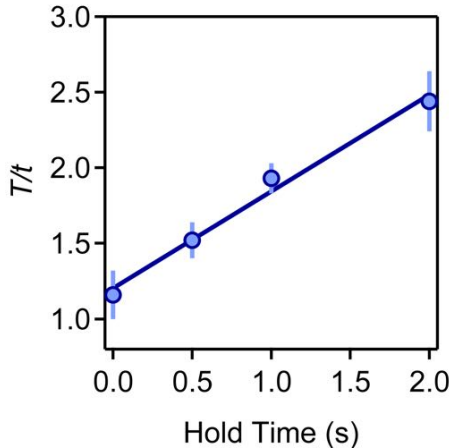


Figure 4-20: Temperature  $k_B T/t$  of Mott-insulating samples at  $U/t = 7.2(1)$ , as a function of time held in equilibrium in an optical lattice. An initially Mott-insulating sample is held at a fixed lattice depth corresponding to the Hubbard parameters  $U/t = 7.2(1)$  for a variable amount of time, and the temperature of the sample (blue circles) after the hold time is extracted from the value of the average local moment at half-filling. Specifically, the half-filling location in the sample is determined from the spatial position of the peak value of the average moment, and the temperature is obtained from a comparison of the experimentally measured value of  $\langle \hat{m}_z^2 \rangle$  at this half-filling location to a corresponding numerical prediction from NLCE. The error bars correspond to the  $1\sigma$  statistical uncertainty in the measurement of the average local moment at half-filling, after this uncertainty has been propagated into the corresponding uncertainty in the temperature. The blue solid line represents a linear fit to the experimental data, from which one can extract a heating rate for the sample at this lattice depth, from the slope of the fit, of  $0.64(5)t/s$ . Figure reproduced from [38].

in the figure) and DQMC (gray triangles) for  $C_m(1)$  at these different fillings and variable temperature, and we find good agreement between the experimental data and the numerical results. Both demonstrate that, as the temperature of the sample is lowered, the magnitude of both the maximum and minimum values of  $C_m(1)$  increases, consistent with the notion that temperature generally tends to wash out correlations (or order) in the system. We can also compare both the experimental data and the numerical results with the maximum and minimum values of  $C_m(1)$  one would expect to measure for a completely non-interacting spin mixture (black dashed and dotted lines, respectively, in the figure), which can be calculated directly as functions of temperature  $k_B T/t$  using the correct filling [37]. The minimum value of  $C_m(1)$  occurs at low values of the average moment, a regime where  $\langle \hat{m}_z^2 \rangle \approx \langle \hat{n} \rangle$  due to the

low density of doublons at low fillings. In this case, we can understand the non-interacting moment correlations in terms of density correlations, which one would expect to be negative due to Pauli blocking effects between like-spins. This is because Pauli blocking acts like an effective repulsion between same-spin atoms, whose extent persists to a distance of roughly the average inter-particle spacing. As the temperature is lowered, this effect becomes stronger, leading to an enhancement of the negative moment correlations. In our real system, however, the measured moment correlations at the minimum of  $C_m(1)$  are more negative than the non-interacting case would predict. This is because the presence of repulsive interactions between opposite spins further enhances the negative density correlations, as now there is effective repulsion between both same-spin and opposite spin atoms. We will examine this regime in more detail subsequently using the  $g_2$  function for moments. For the case of half-filling, where  $C_m(1)$  reaches its maximum value, the non-interacting moment correlations are weak compared to what we find for our real, interacting system. This is because, as we will discuss in more detail subsequently, the positive correlations are dominated by an effective attraction between neighboring doublons and holes at half-filling, which is ultimately connected to the presence of antiferromagnetic spin correlations arising from super-exchange, and a finite admixture of correlated doublon-hole pairs in the wave function (section 2.2.1). This super-exchange physics is absent for the non-interacting gas, leading to nearly vanishing moment correlations at half-filling.

We also examine the temperature dependence of the nearest-neighbor spin correlations,  $C_s(1)$ , at half-filling, where the correlations are most negative. This is shown in Fig. 4-15(d). The experimental data points (blue circles) are again compared to calculations of the nearest-neighbor spin correlator made using NLCE (solid blue line) and DQMC (gray triangles), and we find very good agreement between the experiment and the numerical predictions over the temperature range explored here. At the lowest temperatures achieved in the experiment, the nearest-neighbor spin correlations are most negative and reach a value of  $\approx -0.09$ . As the temperature of the system increases beyond the lowest value explored, the density of low energy spin excitations which are thermally excited increases, and the nearest-neighbor

spin correlations become washed out. At temperatures  $k_B T/t > 2.5$ , for example,  $|C_s(1)| \leq 0.02$ , and eventually approaches zero as the temperature increases further. As the temperature in the system decreases below the lowest temperatures achieved here, on the other hand, the magnitude of these correlations is expected to increase, as the spin order in the system becomes longer range and thermal spin excitations are frozen out. Eventually,  $C_s(1)$  saturates around a value of  $\sim -0.36$  in the  $k_B T/t \rightarrow 0$  limit [174, 180, 152]. This saturation arises from the differences between the classical Néel antiferromagnet on a square lattice and the fully quantum,  $SU(2)$  symmetric, 2D Hubbard model, which allows for superposition states, such as local singlet pairs between neighboring sites, that can lower the energy of the system relative to the classical Néel state. It also comes about from the quantum fluctuations present in the ground state of the 2D Hubbard model, and the finite admixture of doublon-hole pairs in the system at finite values of the Hubbard parameters  $U/t$ , which allows an antiferromagnetic configuration of spins to lower its energy through the delocalization of particles. The combination of these effects with the  $SU(2)$  symmetry of the Hubbard model, which randomizes the orientation of the antiferromagnetic alignment of the spins with respect to the measurement axis, leads to saturation of  $|C_s(1)| < 1$  at zero temperature.

To better understand the origin of the antiferromagnetic correlations at half-filling, we compare the experimental data and numerical calculations shown in Fig. 4-15(d) with the expected nearest-neighbor spin correlations of a non-interacting two-component gas at half-filling on a square lattice (black dotted line in the figure). Interestingly, even in the non-interacting case, there are significant antiferromagnetic spin correlations at a separation of one site, as can be seen in the figure. This is true even though, for a non-interacting system, opposite spin states are uncorrelated. That is, in this case, nearest-neighbor density correlations between opposite spin states are separable, so that  $\langle \hat{n}_{\sigma,i} \hat{n}_{-\sigma,j} \rangle = \langle \hat{n}_{\sigma,i} \rangle \langle \hat{n}_{-\sigma,j} \rangle$ . For the non-interacting system then,

we can rewrite the connected part of the nearest-neighbor spin correlator as,

$$\begin{aligned}
\left\langle \hat{S}_{z,i} \hat{S}_{z,j} \right\rangle_c &= \frac{1}{4} \langle (\hat{n}_{\uparrow,i} - \hat{n}_{\downarrow,i}) (\hat{n}_{\uparrow,j} - \hat{n}_{\downarrow,j}) \rangle_c \\
&= \frac{1}{4} [\langle \hat{n}_{\uparrow,i} \hat{n}_{\uparrow,j} \rangle_c + \langle \hat{n}_{\downarrow,i} \hat{n}_{\downarrow,j} \rangle_c - \langle \hat{n}_{\uparrow,i} \hat{n}_{\downarrow,j} \rangle_c - \langle \hat{n}_{\downarrow,i} \hat{n}_{\uparrow,j} \rangle_c] \\
&= \frac{1}{4} [\langle \hat{n}_{\uparrow,i} \hat{n}_{\uparrow,j} \rangle_c + \langle \hat{n}_{\downarrow,i} \hat{n}_{\downarrow,j} \rangle_c],
\end{aligned} \tag{4.25}$$

where the last line follows from the fact that  $\langle \hat{n}_{\sigma,i} \hat{n}_{-\sigma,j} \rangle_c = 0$ . Eq. 4.25 makes it apparent that  $C_s(1)$  contains the density correlations of each spin state separately. However, for a non-interacting gas Pauli exclusion means that density correlations within a single spin state are negative, due to the effective repulsion between same-spin atoms caused by the finite extent of Pauli blocking. It therefore follows from Eq. 4.25 that, because same-spin fermionic density correlations are negative,  $C_s(1)$  must also be negative, so that even the non-interacting gas shows antiferromagnetic correlations due to the Pauli exclusion principle.

Alongside Pauli suppression, there is an additional geometric effect for non-interacting fermions on a 2D square lattice that makes the system susceptible to antiferromagnetism. This is a property known as "nesting" of the Fermi surface at half-filling, and it occurs because the Fermi surface of each spin state in a 2D square lattice is a diamond whose vertices touch the edges of the first Brillouin zone in the directions of the reciprocal lattice vectors. Specifically, the vertices of the Fermi surface, in reciprocal space at half-filling, are located at  $\pm(\pi/a)\hat{x}$  and  $\pm(\pi/a)\hat{y}$ , where  $\hat{x}$  and  $\hat{y}$  are the axes of the 2D square lattice. Because this diamond shaped Fermi surface has multiple parallel segments, there is a nesting vector  $\mathbf{Q} = (\pi/a)\hat{x} + (\pi/a)\hat{y}$  which connects opposite edges of the surface together. Therefore, because many states of equal energy are connected by a single vector  $\mathbf{Q}$ , there is an enhancement in the density of states at a separation of  $\mathbf{Q}$ . Since many of the low temperature properties of a system are generally dominated by states near the Fermi surface, and the density of states is enhanced at a separation of  $\mathbf{Q}$ , in the presence of scattering between particles, such as that caused by a finite value of the on-site interaction energy  $U$  between opposite spin states, the system becomes susceptible to spin ordering along the direction of  $\mathbf{Q}$ . In

other words, due to nesting of the Fermi surface at the antiferromagnetic wavevector  $\mathbf{Q}$ , any finite repulsive interactions  $U$  between opposite spin states will produce an antiferromagnetic instability in the system. The combination of this Fermi surface nesting in the square lattice, Pauli-blocking between same-spin fermions, and the energetic effects of super-exchange discussed previously, all work together to enhance the antiferromagnetic nearest-neighbor spin correlations in the interacting system. For the data shown in Fig. 4-15(b),(d) at half-filling and at the lowest measured temperature,  $k_B T/t = 1.2(2)$ , the observed value of  $C_s(1)$  is approximately a factor of two larger than that of the non-interacting Fermi system, which we can therefore attribute to the effects of on-site interactions. As can be observed in Fig. 4-15(d), the difference between  $C_s(1)$  of the non-interacting system and that of the interacting system at  $U/t = 7.2(2)$  increases significantly as the temperature decreases and approaches the energy scale  $4t^2/U$ , where super-exchange physics becomes more significant.

To better understand why the nearest-neighbor moment correlation function,  $C_m(1)$ , changes sign from positive to negative as a function of filling, we examine two new quantities which separately capture the observed behavior in a particular filling regime. Isolating the behavior in both the low-filling and half-filling regimes allows us to understand the origin of the correlations in the two regimes separately, which helps elucidate the change in character of local moments from being effectively attractive around half-filling to effectively repulsive at low fillings. The first quantity we study is the  $g_2$  function of local moments, defined as,

$$g_2(r) \equiv \frac{\langle \hat{m}_z^2(r) \hat{m}_z^2(0) \rangle}{\langle \hat{m}_z^2(r) \rangle \langle \hat{m}_z^2(0) \rangle}. \quad (4.26)$$

Here,  $g_2(r)$  describes the probability of finding a moment at a distance  $r$  away from the origin given that there is a moment at  $r = 0$ . In the case where local moments are uncorrelated, so that  $\langle \hat{m}_z^2(r) \hat{m}_z^2(0) \rangle = \langle \hat{m}_z^2(r) \rangle \langle \hat{m}_z^2(0) \rangle$ ,  $g_2(r) = 1$ . In the situation where moments are effectively repulsive, or exhibit anti-bunching behavior, one would expect to observe a suppression of  $g_2$ , such that  $g_2(r) < 1$ . For a separation  $r$  of one lattice site, we can rewrite  $g_2(r = 1)$  in terms of the measured nearest-neighbor

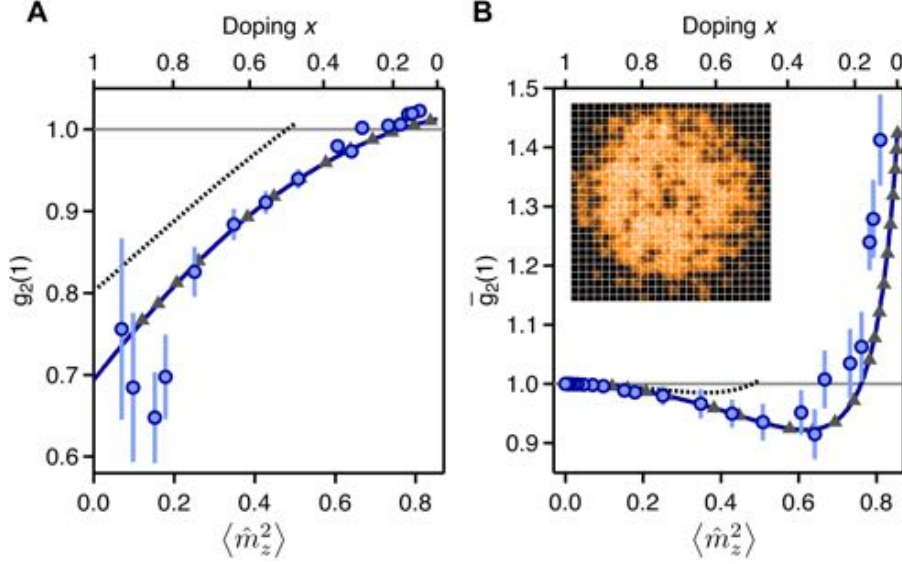


Figure 4-21:  $g_2(1)$  and  $\bar{g}_2(1)$  as functions of the average local moment for  $U/t = 7.2(1)$  and fixed temperature. (a) The  $g_2$  correlator for moments at a spatial separation of one site,  $g_2(1)$ , as a function of the average moment itself,  $\langle \hat{m}_z^2 \rangle$ . (b) The  $g_2$  correlator for anti-moments at a spatial separation of one site,  $\bar{g}_2(1)$ , as a function of the average moment,  $\langle \hat{m}_z^2 \rangle$ . The blue circles represent the experimental data extracted from  $C_m(1)$  and  $\langle \hat{m}_z^2 \rangle$  in Fig. 4-15(a), and the error bars represent the  $1\sigma$  statistical uncertainty in the measurement. The blue solid lines (gray triangles) represent numerical predictions for  $g_2(1)$  and  $\bar{g}_2(1)$  at  $U/t = 7.2$  and  $k_B T/t = 1.22$  from NLCE (DQMC). The black dotted lines denote the predictions for the two-component non-interacting fermi gas at fixed temperature corresponding to the same entropy per particle at half-filling as the fully interacting system. The doping axis,  $x = 1 - \langle \hat{n} \rangle$ , at the top of the figures is obtained from NLCE predictions for the total density as a function of average moment at  $k_B T/t = 1.22$  and  $U/t = 7.2$ . None of the theoretical predictions, nor the value of the doping, are adjusted for the finite experimental imaging fidelity. Inset to (b) An exemplary image demonstrating the bunching between neighboring doublons and holes (anti-moments) around half-filling. Figure reproduced from [38].

moment correlation function,

$$g_2(1) = 1 + \frac{C_m(1)}{\langle \hat{m}_{z,i}^2 \rangle \langle \hat{m}_{z,j}^2 \rangle}. \quad (4.27)$$

Fig. 4-21(a) shows the resulting measured value of  $g_2(1)$  as a function of  $\langle \hat{m}_z^2 \rangle$  (blue circles), obtained using Eq. 4.27, the measured nearest-neighbor moment correlation data in Fig. 4-15(a), and the measured values of the average moment. We compare our experimental data to calculations from both NLCE and DQMC (solid line and

gray triangles, respectively, in the figure) performed at a temperature of  $k_B T/t = 1.22$ , corresponding to the temperature of the experimental system obtained through both the average moment and nearest-neighbor spin correlations at half-filling. As was the case for the correlation data in Fig. 4-15, we find good agreement between the experimental measurements and the numerical predictions over the full range of fillings. Of special interest in this case is the strong suppression of  $g_2(1)$  below one at low fillings (or low average moments) observed in both the experiment and the numerics, which indicates a strong anti-bunching behavior between moments at low fillings. Thus,  $g_2(1)$  correctly captures the behavior we wanted to isolate in this low filling regime.

The suppression of  $g_2(1)$  below unity can be understood from the fact that, at low fillings, the average moment approximately measures the average total density,  $\langle \hat{m}_z^2 \rangle = \langle \hat{n} \rangle - 2 \langle \hat{d} \rangle \approx \langle \hat{n} \rangle$ . This approximation is valid when the doublon density is low,  $\langle \hat{d} \rangle \ll 1$ , which occurs at low average total densities. In this regime,  $g_2(1)$ , as it is written in Eq. 4.26, can be approximately understood as a  $g_2$  function for the total density,

$$g_2(r) \approx \frac{\langle \hat{n}(r)\hat{n}(0) \rangle}{\langle \hat{n}(r) \rangle \langle \hat{n}(0) \rangle}. \quad (4.28)$$

Eq. 4.28, however, immediately reminds us of the density  $g_2$  function for a spin-polarized, non-interacting Fermi gas discussed in section 2.1.2. In that example, we found that there was a strong suppression of  $g_2$ , as a function of  $k_F r$ , at zero separation ( $k_F r = 0$ ), reflecting the influence of Pauli blocking between same-spin fermions at short distances. We also found that this suppression of  $g_2$  extended from  $k_F r = 0$  to  $k_F r \sim 1$ , meaning that the effects of Pauli blocking can be observed not only at zero separation, where both Fermions are in the same spatial location, but also up to a distance  $r \sim 1/k_F \sim 1/n^{1/2}$ , corresponding to a separation on the order of the average inter-particle spacing. This real-space manifestation of Pauli blocking is sometimes referred to as the Pauli hole. Compared to the non-interacting case, however, where we parameterized the  $g_2$  function using the unit-less quantity  $k_F r$ , and conceptualized varying  $k_F r$  by keeping  $k_F \sim n^{1/2}$  fixed and varying the separation

$r$ , the data shown in Fig. 4-21(a) are taken at a fixed separation, one lattice site, and the filling is varied, which is equivalent to varying the density, and therefore  $k_F$ . In this sense, the data for  $g_2(1)$  with varying filling are directly related to the discussion of  $g_2(k_F r)$  in section 2.1.2 for the non-interacting gas, because one can picture the average local moment (or filling) axis, as a scan of  $k_F r$  with  $r$  fixed, and  $k_F \sim n^{1/2}$  changing. Therefore, the observed suppression of  $g_2(1)$  at low average local moment (or small  $k_F r$ ) can be interpreted as an *in situ* observation of the fermionic Pauli hole. Previous experiments have indirectly observed the effects of this Fermionic anti-bunching through the suppression of particle density fluctuations [200, 160, 169], as well as correlations in momentum space [196, 112]. However, a direct, *in situ* observation of the real-space Pauli hole in the  $g_2$  function had not previously been observed.

Of course, unlike the situation discussed in section 2.1.2, the real experimental system contains two different spin states. For the non-interacting spin mixture with equal densities of the two spin-states, one would expect the suppression of the  $g_2$  function for the *total* density at zero separation ( $k_F r = 0$ ) to be reduced by a factor of two, relative to the single component case, due to the fact that opposite spin states do not experience Pauli suppression. The black dotted line shown in Fig. 4-21(a) represents a direct calculation of  $g_2(1)$  for the non-interacting two-component gas on a square lattice using a fixed temperature corresponding to the same value of the entropy per particle at half-filling as the interacting system. The suppression of  $g_2(1)$  at low average moments in this case is purely due to effects from Pauli blocking between same-spin fermions. However, both the experimental data and the numerical calculations of the full, interacting system show a further suppression of  $g_2(1)$  beyond what is expected from Pauli blocking alone. This is because on-site repulsive interactions between opposite-spin atoms leads to anti-correlations between these opposite spin states, which, in addition to Pauli blocking for similar-spin atoms, further suppresses  $g_2(1)$  below the purely non-interacting case. In this sense, the observed hole in  $g_2(1)$  can be thought of as a combined Pauli and correlation hole.

Because  $\langle \hat{m}_z^2 \rangle \approx \langle \hat{n} \rangle$  at low fillings, we can interpret the negative correlations

seen in  $C_m(1)$  as a combination of Pauli suppression and repulsive interactions. Near half-filling on the other hand, where  $\langle \hat{m}_z^2 \rangle \sim 1$ , and double-occupancies are no longer negligible, this picture breaks down, and we must examine a different quantity which better captures the observed bunching behavior to guide our intuition. To motivate this quantity, we note that, near half-filling, there is a roughly uniform background of singly occupied sites in the Mott-insulating regime, for  $U/t = 7.2(1)$ , due to the strong on-site repulsive interactions (section 4.3). Because spatial uniformity in the local moment does not contribute to the connected part of the correlations in  $C_m(1)$ , the non-trivial correlations in the half-filling regime should mainly arise from sites which are not singly occupied, corresponding to occupation by either holes or doublons, so that a measurement of the local moment at such sites yields zero. These imaged holes (which in reality are either actual holes or doublons) create spatial inhomogeneity around half-filling, and are therefore the likely cause for the non-trivial correlations in this regime. This motivates us to consider then the  $g_2$  function of these imaged holes, or anti-moments, which can be represented by the operator  $1 - \hat{m}_{z,i}^2$ . We define this  $g_2$  for anti-moments, analogous to Eq. 4.26, as,

$$\bar{g}_2(r) \equiv \frac{\langle (1 - \hat{m}_z^2(r)) (1 - \hat{m}_z^2(0)) \rangle}{\langle 1 - \hat{m}_z^2(r) \rangle \langle 1 - \hat{m}_z^2(0) \rangle}. \quad (4.29)$$

Just like Eq. 4.27 for the  $g_2$  of moments, we can rewrite Eq. 4.29 in terms of the measured nearest-neighbor moment correlation function,  $C_m(1)$ ,

$$\bar{g}_2(r) = 1 + \frac{C_m(1)}{(1 - \langle \hat{m}_{z,i}^2 \rangle) (1 - \langle \hat{m}_{z,j}^2 \rangle)}. \quad (4.30)$$

Fig. 4-21(b) shows the experimentally measured values of  $\bar{g}_2(1)$  (blue circles) as a function of the average local moment  $\langle \hat{m}_z^2 \rangle$ , as well as numerical calculations of this quantity from both NLCE and DQMC (blue solid line and gray triangles, respectively) performed at the temperature  $k_B T/t = 1.22$ . Both the numerics and the experimental data agree reasonably well over the full range of fillings explored here, and show the same behavior. As we expected intuitively,  $\bar{g}_2(1)$  shows a strong enhancement

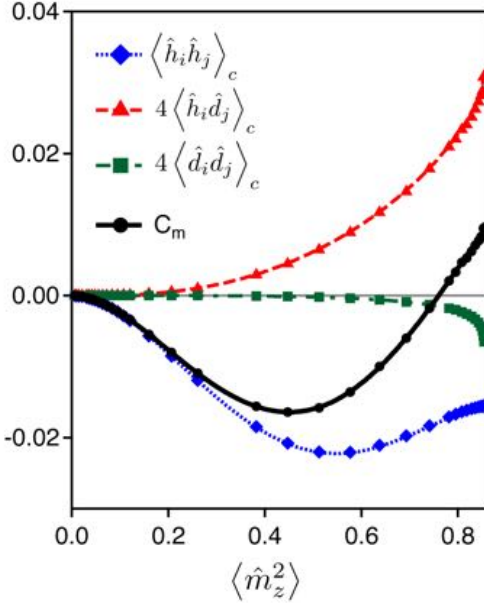


Figure 4-22: Relative contributions to  $C_m(1)$  as functions of the average local moment at  $U/t = 7.2$  and  $k_B T/t = 1.22$ . Plotted here are the hole-hole correlator (blue curve),  $\langle \hat{h}_i \hat{h}_j \rangle_c$ , the doublon-hole correlator (red curve),  $4 \langle \hat{h}_i \hat{d}_j \rangle_c$ , and the doublon-doublon correlator (green curve),  $4 \langle \hat{d}_i \hat{d}_j \rangle_c$ , as functions of the average local moment,  $\langle \hat{m}_z^2 \rangle$ . Also plotted is the moment correlation function itself (black curve),  $C_m(1)$ , given by the sum of these three separate contributions (Eq. 4.9). The solid lines are isothermal 9<sup>th</sup>-order numerical predictions from NLCE, and the symbols are predictions from DQMC. Near half-filling, the doublon-hole correlations dominate, and the moment correlation function is positive. At low fillings, the hole-hole correlations dominate, and the moment correlation function is negative. Figure reproduced from [38].

above unity near half-filling (the peak average moment), representing an effective attraction, or bunching, between anti-moments in this high filling regime. Thus,  $\bar{g}_2(1)$  is the correct quantity to examine that captures the desired behavior of the positive correlations in  $C_m(1)$  around half-filling.

In order to understand the observed effective attraction between anti-moments near half-filling, we can examine Eq. 4.9, which decomposes the nearest-neighbor moment correlations into three separate contributions: correlations between holes, correlations between doublons and holes, and correlations between doublons. As we

discussed in section 4.4.1, the contributions to  $C_m(1)$  from both  $\langle \hat{h}_i \hat{h}_j \rangle_c$  and  $\langle \hat{d}_i \hat{d}_j \rangle_c$  should be negative due to the combination of Pauli exclusion and repulsive on-site interactions. It follows then that the positive correlations observed in  $C_m(1)$ , and therefore the effective attraction between anti-moments observed in  $\bar{g}_2(1)$ , must arise from positive correlations, or effective attraction, between neighboring doublons and holes,  $\langle \hat{h}_i \hat{d}_j \rangle_c$ . We can quantitatively verify this intuitive argument by examining NLCE and DQMC calculations of each of these three correlator contributions to  $C_m(1)$ . Fig 4-22 shows the numerical calculations of  $\langle \hat{h}_i \hat{h}_j \rangle_c$ ,  $4 \langle \hat{d}_i \hat{d}_j \rangle_c$ , and  $4 \langle \hat{h}_i \hat{d}_j \rangle_c$  as functions of the average local moment, performed at the temperature  $k_B T/t = 1.22$  and  $U/t = 7.2$ , as well as the sum of these three terms representing  $C_m(1)$  according to Eq. 4.9. As expected,  $\langle \hat{h}_i \hat{h}_j \rangle_c$  is negative over the full range of fillings due to Pauli exclusion and strong repulsive interactions. This is also true for  $4 \langle \hat{d}_i \hat{d}_j \rangle_c$ , although this term carries significantly less weight due to the fact that occurrences of neighboring doublons are strongly suppressed in the Mott-insulating regime (section 4.4.1), since occurrences of single double occupancies are already suppressed there. The nearest-neighbor doublon-hole correlator  $4 \langle \hat{h}_i \hat{d}_j \rangle_c$  on the other hand shows strong positive correlations, meaning that doublons and holes effectively attract each other at half-filling.

This attraction between neighboring doublons and holes can be understood from the double-well model discussed in section 2.2.1, and the presence of super-exchange which causes antiferromagnetic nearest-neighbor spin correlations at half-filling. This building block of the Fermi-Hubbard model was realized and studied experimentally in [162]. Specifically, at large but finite values of the on-site interactions,  $U/t > 1$ , finite tunneling  $t$  admixes neighboring doublon-hole pairs into the spin singlet ground state with an amplitude  $2t/U$ . Thus, neighboring doublon-hole pairs should occur in the antiferromagnetic ground state with a probability  $4(t/U)^2$ , and the amount that this state can lower its energy with respect to, for example, the higher energy spin triplet states, is  $4t^2/U$ . In other words, the presence of antiferromagnetic nearest-neighbor spin correlations should go hand in hand with correlated doublon-hole pairs, because these pairs give the system an outlet with which it can lower its

energy through particle delocalization, as opposed to the situation where neighboring atoms are ferromagnetically aligned and delocalization is prevented because of Pauli blocking. It then seems reasonable that, given the relatively strong nearest-neighbor antiferromagnetic spin correlations observed at half-filling in Fig 4-15(b),(d), which are stronger than expected for the non-interacting system due to super-exchange, one should expect a non-negligible admixture of correlated nearest-neighbor doublon-hole pairs in the system. In the experimental site-resolved images, these neighboring doublon-hole pairs appear as neighboring anti-moments (or imaged holes) due to the parity-projected imaging. The inset to Fig. 4-21(b) shows a typical site-resolved image of the local moment where several instances of neighboring anti-moments can be observed. Because the significant number of occurrences of these neighboring anti-moments resemble an effective attraction between anti-moments, we thus understand the bunching behavior seen in  $\bar{g}_2(1)$  as arising from neighboring doublon-hole pairs associated with the physics of super-exchange. This also explains the large difference between the interacting curve in Fig. 4-21(b) and the calculation for  $\bar{g}_2(1)$  performed on a two-component non-interacting spin mixture on a square lattice (black dotted line in the figure). That is, because the non-interacting system inherently lacks this super-exchange physics, the enhancement of  $\bar{g}_2(1)$  above unity in this case is essentially negligible. It follows then that the observed positive moment correlations in the half-filling regime represent a non-trivial connection between the spin degree of freedom, where we observed antiferromagnetic correlations, and the charge degree of freedom. Such a connection warrants further studies into the role that doublon-hole correlations play, for example, in both the spin and charge transport properties of the Hubbard model. Connecting back to the anti-bunching behavior of moments observed at low fillings in  $g_2(1)$ , we now understand the change in sign of  $C_m(1)$  as the filling is varied as a competition between Pauli blocking and repulsive interactions at low fillings, which causes anti-bunching behavior, and super-exchange at half-filling, which causes bunching between neighboring doublons and holes.

Because the site-resolved experimental data used to measure  $C_s(1)$  and  $C_m(1)$  contains not only nearest-neighbor information, but also the full spatial correlation

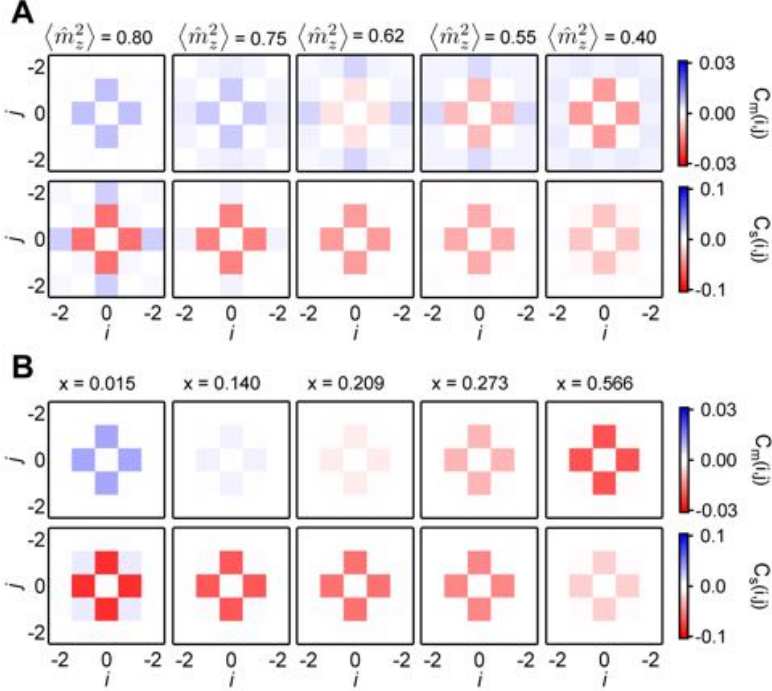


Figure 4-23: Charge and spin spatial correlation matrices as functions of  $\langle \hat{m}_z^2 \rangle$  at  $U/t = 7.2(1)$ . (a) The experimentally measured moment correlation function (top row),  $C_m(i, j)$ , and spin correlation function (bottom row),  $C_s(i, j)$ , at  $U/t = 7.2(1)$  and  $k_B T/t = 1.1(1)$ , for several different values of  $\langle \hat{m}_z^2 \rangle$ . Here,  $(i, j)$  represents the index of the site correlated with the origin. The correlation values measured at symmetric points on the square lattice (e.g.  $(\pm 1, 0)$  and  $(0, \pm 1)$ ) are averaged together. (b) The moment correlation function (top row),  $C_m(i, j)$ , and spin correlation function (bottom row),  $C_s(i, j)$ , of the 2D Fermi-Hubbard model at  $U/t = 7.2$  and  $k_B T/t = 1.00$ , for several different values of the doping,  $x = 1 - \langle \hat{n} \rangle$ , obtained using calculations from DQMC. In both (a) and (b), the non-zero, on-site charge and spin correlations at  $(0, 0)$  are omitted for simplicity, since these are directly determined from the value of the average local moment itself. Figure reproduced from [38].

information, we can access both spin and charge correlations between sites with arbitrary spatial separation. This simply requires generalizing the definitions of the charge and spin correlation functions in Eqs. 4.5 and 4.10, respectively, to arbitrary spatial separation, and then appropriately analyzing the experimental site-resolved images to obtain the desired correlation function at the desired spatial separation. Using the same radial averaging technique used to generate Fig. 4-15(a),(b), we can therefore examine the behavior of these longer-distance spin and charge correlations as functions of filling in the lattice. Fig. 4-23(a) shows the dependence on spatial sep-

aration of the experimentally measured charge and spin correlation functions,  $C_m(i, j)$  and  $C_s(i, j)$ , at several different values of the average local moment. The  $(i, j)$  notation used here represents the value of the correlation functions at a spatial separation  $i\hat{x} + j\hat{y}$ , although we can make use of the lattice translational symmetry to average together the values of the correlators obtained at symmetric points. For example, the  $(1, 1)$  correlator is averaged together with the  $(1, -1)$ ,  $(-1, 1)$ , and  $(-1, -1)$  correlators. In order to interpolate between different values of the average local moment, we fit the average moment dependence of the measured  $C_m(i, j)$  and  $C_s(i, j)$ , at each separation  $(i, j)$  after averaging over symmetric points, to a 6<sup>th</sup> order polynomial spline. We can compare the experimental results with calculations of  $C_m(i, j)$  and  $C_s(i, j)$  at various fillings made using NLCE and DQMC, as shown in Fig. 4-23(b). Both the experimental data and the numerical predictions show non-zero antiferromagnetic spin correlations near half-filling which extend slightly beyond nearest-neighbor, even at the temperatures achieved for this work,  $k_B T/t \approx 1.2$ . At even lower temperatures, one should expect to observe such significant antiferromagnetic correlations at even longer distances [180, 27, 152]. At such low temperatures, however, where the spin correlation length can extend over multiple sites, one must be careful not to confuse changes in the spin correlation strength due to a finite correlation length at finite temperature, with changes in the spin correlation strength due to changes in the filling of the sample over the same distance arising from spatial inhomogeneities in the underlying trapping potential. For example, from Fig. 4-14(d), the average local moment changes by  $\approx 25\%$  only  $\sim 3$  sites away from the half-filling point due to the intensity variation in the optical lattice beams. From Fig. 4-15(b), this corresponds to a decrease in the nearest-neighbor spin correlations by approximately a factor of two. Thus, one must be careful to disentangle a change in the spin correlations three sites away,  $C_s(0, 3)$ , for example, due to this 25% change in the filling, from changes in  $C_s(0, 3)$  due to effects of finite temperature. Such complications can be avoided by simply flattening out the underlying trapping potential using, for example, a correctly shaped repulsive potential projected onto the atoms through the microscope objective [152]. At the temperatures studied here, such effects do not appear to be

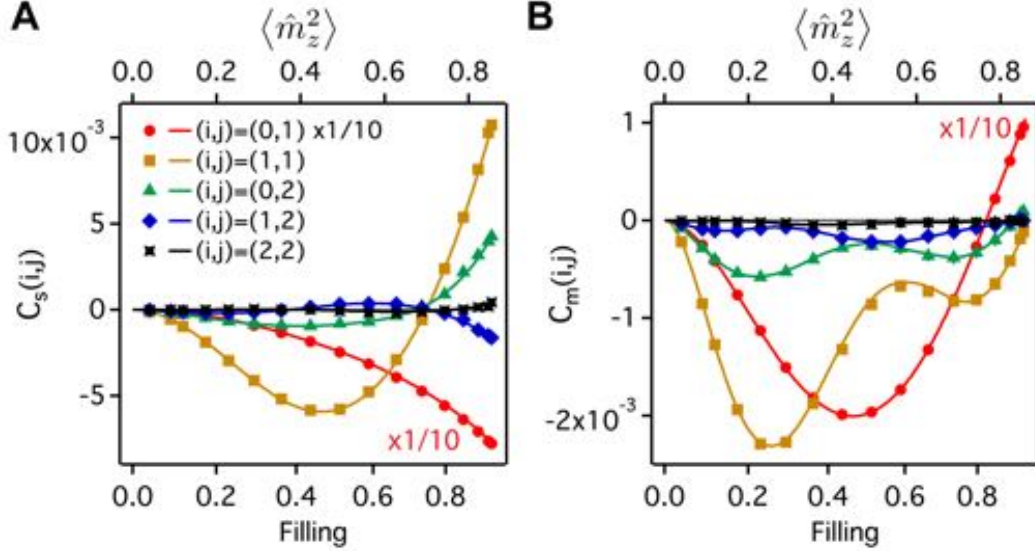


Figure 4-24: Spin and charge correlation functions of the 2D Fermi-Hubbard model versus filling,  $\langle \hat{n} \rangle = \langle \hat{n}_\uparrow + \hat{n}_\downarrow \rangle$ , for different values of the spatial separation between lattice sites, at  $U/t = 7.2$ . Shown here are isothermal numerical predictions for (a) the spin correlation function,  $C_s(i,j)$ , and for (b) the moment correlation function,  $C_m(i,j)$ , as a function of the total filling (bottom horizontal axes),  $\langle \hat{n} \rangle$ , at a temperature of  $k_B T/t = 1.00$ . The top horizontal axes convert the total filling to the average local moment,  $\langle \hat{m}_z^2 \rangle$ , at  $k_B T/t = 1.00$  and  $U/t = 7.2$ , which is the quantity actually measured in the experiment. Here,  $(i,j)$  represents the index of the site being correlated with the origin  $(0,0)$ , so that  $(i,j) = (0,1)$  denotes the nearest-neighbor correlation function (i.e.  $C_s(1)$  and  $C_m(1)$ ),  $(i,j) = (1,1)$  represents correlations between next-nearest-neighbor sites, separated along the diagonal of the square lattice, etc. The symbols shown in the figures are results from DQMC, and the solid lines represent 9<sup>th</sup>-order results from NLCE. As is evident from the plots, the DQMC and 9<sup>th</sup>-order NLCE results for  $C_s(i,j)$  and  $C_m(i,j)$  agree with each other over the various spatial separations shown, and over the full range of fillings at this particular temperature,  $k_B T/t = 1.00$ . Figure reproduced from [38].

significant. As can be seen in Fig. 4-23(a),(b), we find, in addition to non-zero longer-distance spin correlations at half-filling, that as the doping in the system increases, the antiferromagnetic spin correlations present at half-filling decrease in their magnitude, and become essentially homogeneously negative at each separation  $(i,j)$ . In contrast, the moment correlation function  $C_m(i,j)$  shows the previously discussed sign change at the nearest-neighbor separation, but does not show significant correlations beyond nearest-neighbor.

To examine the behavior of  $C_m(i,j)$  and  $C_s(i,j)$  more closely, we show in Fig. 4-

24(a),(b) NLCE and DQMC predictions for these correlators as functions of filling (and average moment) at a temperature  $k_B T/t = 1.00$  and  $U/t = 7.2$ , up to a maximal distance of  $(i, j) = (2, 2)$ . This figure clearly shows the sign change of the nearest-neighbor ( $(i, j) = (0, 1)$ ) moment correlator, and quantifies the magnitude of the difference between  $C_m(0, 1)$  and the longer-distance moment correlators. At this temperature, the peak magnitude of the next strongest moment correlator,  $C_m(1, 1)$ , is approximately an order of magnitude smaller than the peak magnitude of  $C_m(0, 1)$ . This demonstrates that the observed moment correlations, in both the low and high filling regimes, are very short-ranged. The spin correlations on the other hand,  $C_s(i, j)$ , show the previously discussed weakening of the magnitude of the correlation strength with decreasing filling at the nearest-neighbor distance ( $(i, j) = (0, 1)$ ). In contrast, the next-nearest-neighbor spin correlator  $C_s(1, 1)$  changes sign from positive at half-filling to negative at lower fillings, resembling the filling dependence of  $C_m(0, 1)$ . In fact, at sufficiently low filling, the spin correlator  $C_s(i, j)$  becomes negative for each of the  $(i, j)$  that are shown. Intuitively this makes sense because, as the filling becomes sufficiently low, so that double occupancies become negligible and the effects of interactions diminish, the spin correlation function  $C_s(i, j)$  of the real system can be expected to more closely resemble the spin correlations of a non-interacting two-component mixture. In the non-interacting case, the spin correlations are isotropically negative due to the fact that  $C_s(i, j)$  contains the Pauli suppressed density correlations of each spin state separately (see also section 2.1.2 of [37]).

The majority of the discussion regarding correlation functions has so far focused on a single value of the Hubbard parameters,  $U/t = 7.2(1)$ , where the strength of both the spin and charge correlations is expected to be maximal at a fixed temperature. We can, however, also study the effects of different values of the Hubbard parameters  $U/t$  on the nearest-neighbor spin and charge correlations,  $C_s(1)$  and  $C_m(1)$ , at, for example, fixed filling, e.g. half-filling. This can be done experimentally by varying the depth of the optical lattice used in the final lattice configuration to achieve the desired  $U/t$  value. Fig. 4-25 shows the experimental results for  $C_s(1)$  and  $C_m(1)$  as functions of  $U/t$ , measured at half-filling (blue circles) using the same method that

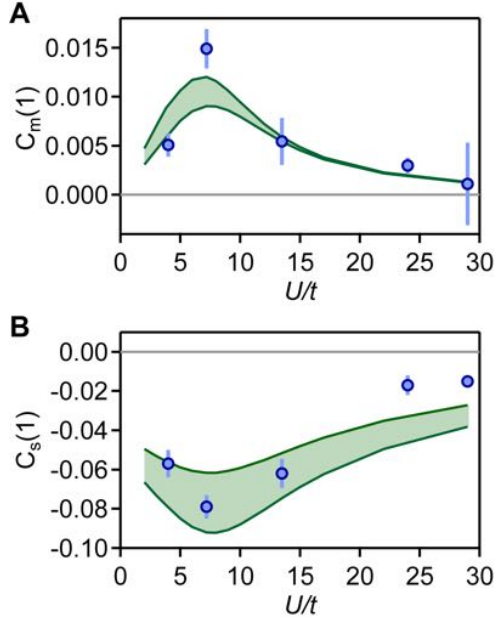


Figure 4-25: Nearest-neighbor spin and charge correlation functions versus  $U/t$  at half-filling and fixed temperature,  $k_B T/t$ . The blue circles in the figures represent the experimentally measured values of  $C_m(1)$  (a) and  $C_s(1)$  (b) at half-filling, for different values of the Hubbard parameters  $U/t$ . The error bars represent the  $1\sigma$  statistical uncertainty in the measurements. The experimental data in (a) and (b) are compared to isothermal 9<sup>th</sup>-order NLCE predictions for  $C_m(1)$  and  $C_s(1)$  as functions of  $U/t$  at  $k_B T/t = 0.89$  (lower solid green lines in the figures) and  $k_B T/t = 1.22$  (upper solid green lines in the figures). The green shaded areas between the solid lines represent the intermediate temperature region,  $0.89 < k_B T/t < 1.22$ , for the numerical predictions. This is the same temperature range used in Fig. 4-15(a),(b) for the spin and charge correlation functions versus the average moment. At a fixed value of the temperature, the correlations are strongest around  $U/t = 8$ . Figure reproduced from [38].

was used for  $U/t = 7.2(1)$ . We can compare our measurements with calculations from NLCE of  $C_s(1)$  and  $C_m(1)$  at various  $U/t$  values, performed at half-filling and fixed temperature (isothermal curves). The NLCE results are shown as the green solid lines in Fig. 4-25. The temperature range depicted here is the same range used for the correlation measurements performed at  $U/t = 7.2(1)$ , shown in Fig. 4-15,  $k_B T/t = 0.89 - 1.22$ . Both the numerics and the data demonstrate that both  $C_s(1)$  and  $C_m(1)$  reach their peak magnitude near  $U/t \approx 8$ , as we argued qualitatively in section 4.4. Additionally, our data for both the spin and charge correlations are reasonably consistent with the isothermal numerical predictions within the temperature range  $k_B T/t = 0.89 - 1.22$ . However, at large values of  $U/t$  ( $U/t > 20$ ) we find

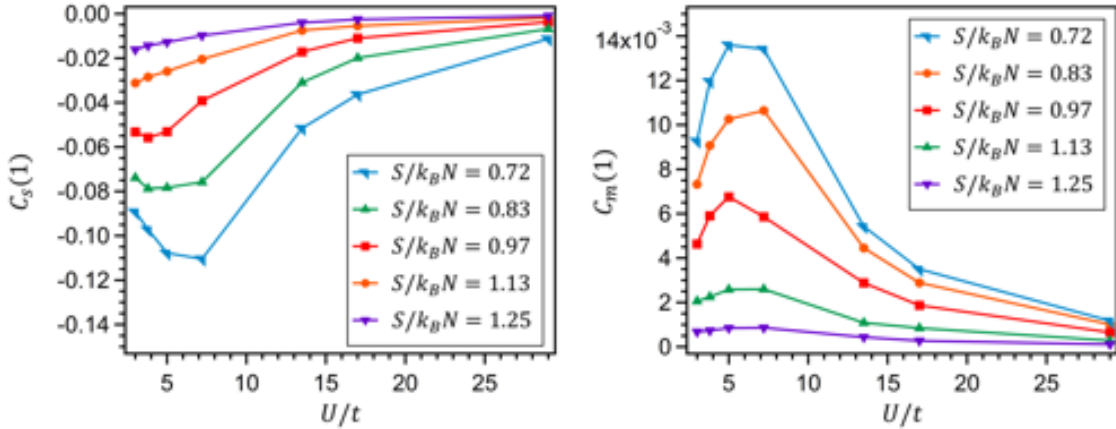


Figure 4-26: Nearest-neighbor spin and charge correlation functions versus  $U/t$  at half-filling and fixed entropy per particle,  $S/k_B N$ . The different curves represent isentropic, 9<sup>th</sup>-order NLCE predictions for  $C_s(1)$  and  $C_m(1)$  (symbols) of the 2D Fermi-Hubbard model at half-filling as a function of the Hubbard parameters  $U/t$ , for several different values of the entropy per particle in the range  $0.72 \leq S/k_B N \leq 1.25$ . This entropy range represents typical values of the entropy per particle which are achieved in the experimental data discussed in this thesis. The lines shown in the plots simply connect the discrete set of  $U/t$  values given by the numerics, and are there to guide the eye. It is worth comparing the behavior of the isentropic predictions shown here for  $C_s(1)$  and  $C_m(1)$  to the isothermal predictions shown in Fig. 4-25. These isentropic curves are generated using the NLCE data from [38].

that the spin correlations deviate from these isothermal curves. This deviation could be the result of technical issues associated with higher values of  $U/t$ , which correspond to larger lattice depths, or may point to the idea that, assuming the system is prepared adiabatically with the desired lattice depth, the preparation is actually isentropic, rather than isothermal. We will discuss the latter point in more depth in chapter 5, when we describe our measurements of spin transport, where we find that the system preparation is approximately isentropic rather than isothermal. For this to hold however, the technical issues associated with higher values of  $U/t$  must be addressed. These include possible technical heating from, for example, lattice laser intensity noise, which can become more significant at larger values of  $U/t$ , where the lattice laser powers are significantly larger. Additionally, one must ensure that the system is truly reaching thermal equilibrium at the larger lattice depths. That is, because the lattice depth changes the absolute scale of the tunneling strength  $t$ , the

time scales become much slower at larger lattice depths, so that one must give the system ample time to equilibrate in both the spin and charge degrees of freedom. The equilibration time of the system in both the spin and charge sectors was studied in detail in [180] by measuring the peak detected moment, as well as the nearest-neighbor and next-nearest-neighbor spin correlations at half-filling as functions of the lattice loading time. Spending significantly more time at larger lattice powers, however, can also lead to increased technical heating. Once these issues are addressed, the sample preparation in this experiment generally seems most consistent with isentropic preparation, as we will discuss subsequently. For comparison, we show in Fig. 4-26 the NLCE predictions for  $C_s(1)$  and  $C_m(1)$  at half-filling as a function of  $U/t$  at fixed entropy per particle, for several different values of the entropy per particle  $S/k_B N$ , in order to highlight the differences between isothermal and isentropic curves for these correlation functions.

For future reference, we also include, in Fig. 4-27, NLCE and DQMC calculations of the spin and moment correlations  $C_s(i, j)$  and  $C_m(i, j)$  at half-filling and  $U/t = 7.2$  as functions of temperature,  $k_B T/t$ , for  $(i, j) = (0, 1)$ ,  $(1, 1)$ , and  $(0, 2)$ . As can be seen from this figure, both numerical techniques agree with each other very well down to temperatures of  $k_B T/t \approx 0.2$  over all correlation distances, and to temperatures  $k_B T/t < 0.1$  for the nearest-neighbor correlation functions. This is maybe not so surprising, given that the numerics do not encounter the fermion sign problem at half-filling. However, the experimentally relevant point that these curves demonstrate is that, because the numerics can estimate the correlation signals so well at half-filling down to temperatures significantly below those achieved experimentally in this work ( $k_B T/t \sim 1.2$ ), we can reliably use these numerical calculations to estimate the system temperature. That is, within the range  $0.1 < k_B T/t < 2$ , where these correlation signals are reasonably sensitive to changes in the temperature, we can measure the strength of the nearest-neighbor spin and charge correlations at half-filling and  $U/t = 7.2$ , and compare the experimental measurement with the numerical predictions to obtain the temperature. As we discussed previously, this method of measuring the temperature works very well at  $k_B T/t \sim 1.2$ , and agrees with temper-

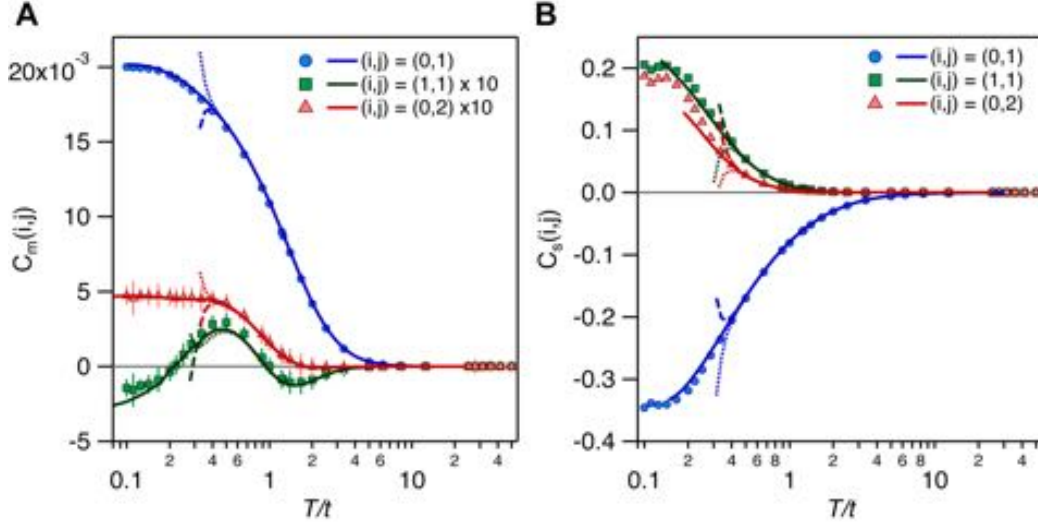


Figure 4-27: Charge and spin correlation functions of the half-filled 2D Fermi-Hubbard model versus temperature,  $k_B T/t$ , for different values of the spatial separation between lattice sites, at  $U/t = 7.2$ . Shown here are numerical predictions for (a) the moment correlation function,  $C_m(i,j)$ , and for (b) the spin correlation function,  $C_s(i,j)$ , at half-filling, as a function of the system temperature,  $k_B T/t$ . Here,  $(i,j)$  represents the index of the site being correlated with the origin  $(0,0)$ , so that  $(i,j) = (0,1)$  denotes the nearest-neighbor correlation function (i.e.  $C_m(1)$  and  $C_s(1)$ ), and  $(i,j) = (1,1)$  represents correlations between next-nearest-neighbor sites, separated along the diagonal of the square lattice. The symbols shown in the figures are results from DQMC, and the dotted, dashed, and solid lines represent 8<sup>th</sup>-order, 9<sup>th</sup>-order, and re-summed results from NLCE, respectively. As is evident from the plots, the DQMC and re-summed NLCE results for  $C_m(i,j)$  and  $C_s(i,j)$  agree with each other at half-filling over the various spatial separations down to temperatures of  $\sim k_B T/t = 0.2$ . Figure reproduced from [38].

ature estimates based on the average moment at half-filling. Additionally, it allows us to extend the range over which we can perform thermometry to temperatures below  $k_B T/t \sim 1$ , where the average moment at half-filling is no longer a sensitive thermometer. Practically speaking,  $C_s(1)$  at half-filling alone is likely the better thermometer, compared to  $C_m(1)$  at half-filling, because the signal is ten times larger. However, technically speaking  $C_s(1)$  requires both the spin-dependent and normal single-site imaging (unlike  $C_m(1)$ , which only requires normal single-site imaging), so depending on experimental stability and the number of images required to obtain the desired signal to noise, one could use either correlator (or both). Finally, to provide a complete picture of the temperature dependence of the correlation signals, we show in Fig. 4-

28 NLCE and DQMC predictions for the three correlators ( $\langle \hat{h}_i \hat{h}_j \rangle_c$ ,  $\langle \hat{h}_i \hat{d}_j \rangle_c$ , and  $\langle \hat{d}_i \hat{d}_j \rangle_c$ ) which make up the moment correlator  $C_m(i, j)$  at half-filling and  $U/t = 7.2$ , as functions of the temperature  $k_B T/t$ , for spatial separations  $(i, j) = (0, 1)$ ,  $(1, 1)$ , and  $(0, 2)$ . This figure once again emphasizes how the charge correlations at half-filling are very local, even down to temperatures of  $k_B T/t \sim 0.1$ . That is, as can be seen in Fig. 4-28(a),(b), even at the lowest temperatures shown, the next-nearest-neighbor signals in both  $\langle \hat{h}_i \hat{h}_j \rangle_c$ ,  $\langle \hat{h}_i \hat{d}_j \rangle_c$  are suppressed by roughly an order of magnitude relative to the nearest-neighbor correlators. The behavior of the doublon-doublon correlator  $\langle \hat{d}_i \hat{d}_j \rangle_c$  is not as drastic, but the absolute signal strength is still significantly weaker than either  $\langle \hat{h}_i \hat{h}_j \rangle_c$  or  $\langle \hat{h}_i \hat{d}_j \rangle_c$ . This general behavior lies in contrast with the spin correlator  $C_s(i, j)$  (Fig. 4-27(b)), where, at the lowest temperatures shown,  $C_s(1, 1)$  and  $C_s(0, 2)$  are within a factor of two of  $C_s(0, 1)$ , and as the temperature is lowered further, the spin correlation length diverges [150]. In appendix A, we show NLCE predictions for several isothermal and isentropic curves of  $\langle \hat{h}_i \hat{h}_j \rangle_c$ ,  $\langle \hat{h}_i \hat{d}_j \rangle_c$ , and  $\langle \hat{d}_i \hat{d}_j \rangle_c$  at half-filling, as functions of the Hubbard parameters  $U/t$ .

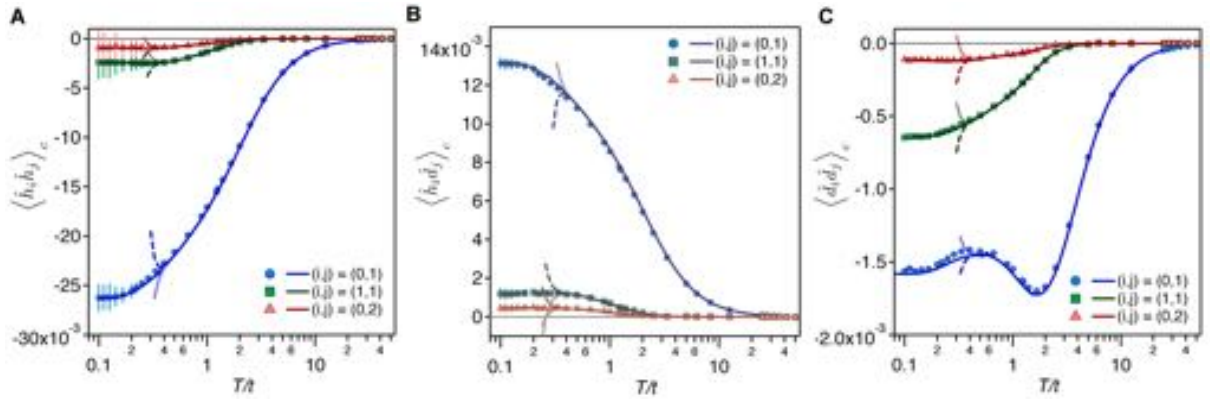


Figure 4-28: Hole-hole, hole-doublon, and doublon-doublon correlation functions of the half-filled 2D Fermi-Hubbard model versus temperature,  $k_B T/t$ , for different values of the spatial separation between lattice sites, at  $U/t = 7.2$ . Shown here are numerical predictions for (a) the hole-hole correlation function,  $\langle \hat{h}_i \hat{h}_j \rangle_c$ , for (b) the hole-doublon correlation function,  $\langle \hat{h}_i \hat{d}_j \rangle_c$ , and for (c) the doublon-doublon correlation function,  $\langle \hat{d}_i \hat{d}_j \rangle_c$ , at half-filling, as a function of the system temperature,  $k_B T/t$ . Here,  $(i, j)$  represents the index of the site being correlated with the origin  $(0, 0)$ , so that  $(i, j) = (0, 1)$  denotes the nearest-neighbor correlation function, and  $(i, j) = (1, 1)$  represents correlations between next-nearest-neighbor sites, separated along the diagonal of the square lattice. The symbols shown in the figures are results from DQMC, and the dotted, dashed, and solid lines represent 8<sup>th</sup>-order, 9<sup>th</sup>-order, and re-summed results from NLCE, respectively. As is evident from the different plots, the two numerical techniques (DQMC and re-summed NLCE) agree with each other extremely well regarding their predictions for these equilibrium correlation functions at half-filling over the different spatial separations, and over a very large range of temperatures. Figure reproduced from [38].



# Chapter 5

## Measuring Transport Properties of the Half-Filled Fermi-Hubbard Model

In this chapter, we discuss our experimental research regarding the transport properties of the 2D Fermi-Hubbard model. Specifically, we examine spin transport within the spin-balanced, half-filled Hubbard model, and measure both the spin diffusion coefficient and the spin conductivity, transport coefficients which characterize the response of the system to a spin-dependent force, as functions of the Hubbard parameters  $U/t$ . The experiment described in this chapter represents one of the first direct measurements of the spin transport coefficients of the 2D Fermi-Hubbard model, quantities which are difficult to measure experimentally in the cuprates, and which are highly challenging to calculate theoretically [202, 24, 127, 159, 122, 211, 115]. The results are summarized in the following publication:

*M. A. Nichols, L. W. Cheuk, M. Okan, T. R. Hartke, E. Mendez, T. Senthil, E. Khatami, H. Zhang, and M. W. Zwierlein, “Spin Transport in a Mott Insulator of Ultracold Fermions,” *Science* **363**, 383 (2019) [164]. Included in Appendix D.*

We begin the chapter with a brief introduction to how transport properties have been studied previously in ultracold atomic systems with experiments on both bosons and fermions. We then summarize the experimental implementation of our spin transport technique using our quantum gas microscope, and describe the calibrations of all

relevant experimental parameters. Subsequently, we discuss the results of our studies of both the spin diffusion coefficient,  $D_S$ , and the spin conductivity,  $\sigma_S$ , as functions of the Hubbard parameters  $U/t$ , where we find that for sufficiently strong on-site interactions,  $U \gg t$ , spin transport is driven by a combination of super-exchange and doublon-hole-assisted tunneling. We also describe our measurement of the  $U/t$ -dependent uniform spin susceptibility,  $\chi$ , an equilibrium property of the system which allows us to compare our different transport measurements using the Einstein relation,  $\sigma_S = D_S\chi$ . Additionally, we show how  $\chi$  can be used to obtain an estimate of the temperature or entropy of the system through a comparison to equilibrium calculations of the half-filled Hubbard model, at the desired value of  $U/t$ , made using NLCE. This equilibrium thermometry allows us to directly compare our experimental transport measurements to novel NLCE calculations of  $\sigma_S$  and  $D_S$ , where the only free parameter for the theoretical predictions is the experimental entropy per particle. We find good qualitative agreement between the experimental data and the theoretical predictions, but observe some quantitative differences. Therefore, we provide a brief summary of the challenges associated with such a theoretical calculation, and motivate possible reasons why the numerics deviate from the experimental measurements. Finally, we give a short outlook which describes how the experimental technique discussed here can be generalized in various ways, including measurement of the full frequency-dependent AC conductivity, and measurement of the spin transport coefficients in the presence of, for example, finite doping or finite spin-imbalance. Extending these transport measurements in this way can potentially reveal important aspects of the complex interplay between the spin and charge degrees of freedom in the 2D Fermi-Hubbard model.

## 5.1 Introduction and Summary of Previous Studies

Much of the continued interest in the high- $T_c$  superconducting cuprates arises from their unique (and useful) transport properties, and from the fact that much of the observed transport phenomena in these materials, even in their normal (not super-

conducting) state, cannot be explained via conventional means. For example, the combination of Fermi liquid theory with the Boltzmann kinetic equation, which describes the behavior of interacting electronic systems using a quasi-particle picture of transport, successfully explains the transport properties of a wide class of conventional materials, like standard metals. One common characteristic of these Fermi liquid type materials is that the charge resistivity  $\rho$  scales with the square of the temperature of the system,  $\rho \sim T^2$ , at low temperatures [148, 46]. Another commonality is that the resistivity should eventually saturate with increasing temperature [83]: because the mean-free-path cannot be smaller than the lattice, or interatomic spacing, a limit often called the Mott-Ioffe-Regel (MIR) limit [107, 158], the resistivity in these conventional materials cannot exceed the maximum value determined by the minimum of the mean-free-path. In the cuprates, and other materials which exhibit strong correlations between electrons, however, a simple Fermi liquid description of the dynamical properties of the system is no longer sufficient [206]. That is, many strongly interacting electronic systems demonstrate anomalous scalings of the charge resistivity with temperature [206, 217, 28], including a linear in  $T$  scaling,  $\rho \sim T$ , observed in the bad metallic state of the cuprates [104]. Additionally, the resistivity in many such materials does not saturate with increasing temperature, and can even violate the MIR limit [59, 83]. Because the strong electronic correlations in these materials forces a breakdown of a Fermi liquid description of their transport properties, a variety of other theoretical approaches have been proposed to better portray their observed anomalous characteristics [230, 7, 232, 92, 90]. In fact, it has even been proposed that many of the unusual transport phenomena observed in the normal state of the cuprates arise from a decoupling of the spin and charge degrees of freedom, caused by the presence of strong interactions between particles [8, 139]. Such behavior has been observed and studied previously in the context of one-dimensional strongly interacting systems [142, 93, 74, 14].

We are still, however, not totally certain about the physical mechanisms underlying many of the unusual phenomena observed in these materials. Such understanding is made more complicated by the fact that it can be difficult to disentangle effects

caused by couplings to phonons or impurities in the material, from effects due to the inherent strong interactions between electrons. This has motivated the study of transport in strongly interacting ultracold atomic systems, which are simultaneously clean and highly-controllable, and for which there exists a simple yet relevant Hamiltonian description of the system [63]. In this regard, much initial effort has been put, for example, into studying particle transport between two large reservoirs coupled via a narrow channel [25, 229, 131, 130], a mesoscopic geometry resembling the two-terminal configuration used to study electronic transport in real materials. There has also been much initial work studying bulk transport of fermionic atoms in optical lattices, without the aid of single-site resolution. For instance, suppression in the motion of a spin-polarized, band-insulating sample of fermionic atoms in a 3D lattice was observed, caused by Pauli blocking between atoms [172]. Upon introduction of a separate bosonic species of atoms to the sample, which could collide with the fermionic atoms, the mobility of the fermions in the lattice was seen to increase due to the finite scattering rate with the bosons negating the effects of Pauli, before it again began to decrease once the collision rate with the bosonic atoms was too strong [172]. Transport was also studied in an interacting, two-component Fermi gas in a 3D optical lattice by examining the center of mass dynamics after a quench in the displacement of the trap center, as a function of the on-site interactions between atoms in the attractive Hubbard model [219]. Several years later, with increased experimental control over these lattice systems, transport in the form of expansion dynamics of a two-component band insulator was studied using fermionic atoms in a homogeneous 3D optical lattice, as a function of the Hubbard parameters,  $U/t$ , on both the repulsive and attractive sides of the interaction energy [204]. Subsequently, charge transport was studied within the 3D Fermi-Hubbard model by preparing an initial spin-polarized metallic sample in equilibrium at a given tunneling strength  $t$ , and then initiating dynamics by applying a Raman pulse to suddenly transfer some atoms in the sample to a different spin state which could interact with the original state with on-site interaction energy  $U$  [243]. This Raman pulse also introduced a non-zero momentum to the transferred atoms, so that they moved with respect to the

initial cloud, and so the evolution of the mobility and quasi-momentum distributions of the different spin states was studied as the two clouds moved through and collided with each other, as a function of temperature and interaction strength  $U$ , revealing behavior consistent with bad-metallic type relaxation dynamics [243]. However, without the aid of single-site resolution, it has proven very difficult in these types of lattice experiments to quantitatively study the near-equilibrium transport properties of the Hubbard model, and to relate the observed dynamics to the linear response transport coefficients of the underlying equilibrium Hamiltonian.

The advent of quantum gas microscopy [16, 209, 40, 85, 179, 169, 58, 27], with the power of its single atom imaging and control, enabled many important studies of transport in both 1D and 2D Bose-Hubbard systems [70, 95, 184], including the observation of light-cone like spreading of particle correlations after a quench in the Hubbard parameters [35], the observation of magnon bound state dynamics in a unit-filling, two-component, 1D Bose-Hubbard chain [71], and an examination of the many-body localization transition within the 2D Bose-Hubbard model in the presence of site-resolved random disorder [44]. On the fermionic side of things, quantum gas microscopy has enabled a recent study of the AC optical charge conductivity in the 3D Fermi-Hubbard model using a dilute, harmonically trapped sample under the influence of an applied periodic drive [9]. Similar high-resolution imaging (without single-atom detection) has also enabled a recent two-terminal measurement of the charge conductance between two reservoirs through a 1D mesoscopic lattice located within a narrow channel [138]. However, it was not until this work [164], and the work of [26], that the strengths of quantum gas microscopy have been applied to address the unique transport behavior of the 2D Fermi-Hubbard model, the system most relevant to the high- $T_c$  cuprates, and to directly measure the transport coefficients, in the spirit of linear response, in both the spin and charge degrees of freedom, and in several regions of the model's phase diagram. Such simultaneous measurements in both the spin and charge sectors are very relevant to the cuprates, whose currently un-understood transport properties in the normal state may, in fact, arise from the complex interplay between these two degrees of freedom [8, 139], and where spin

transport measurements in particular are very challenging. In the next sections, we describe how we implement spin transport within the 2D Fermi-Hubbard model in our experiment, and describe the results of our measurements of the spin conductivity and the spin diffusion coefficient at half-filling, as a function of the Hubbard parameters  $U/t$ .

## 5.2 Experimental Implementation

In this section, we describe the details of our experimental implementation of the transport measurements discussed in section 5.4. To prepare an initial ultracold sample of  $^{40}\text{K}$ , we use the same experimental protocol for this work as was used in previous work on the equilibrium properties of the Hubbard model, which is described in detail in sections 3.3 and 4.2. Specifically, we first sympathetically cool the  $^{40}\text{K}$  atoms in the state  $|F = 9/2, m_F = 9/2\rangle$  through collisions with bosonic  $^{23}\text{Na}$  atoms in the state  $|F = 2, m_F = 2\rangle$ , while both species are trapped in a plugged magnetic quadrupole trap located  $\sim 2$  mm below the imaging plane. The  $^{23}\text{Na}$  atoms are evaporatively cooled directly using forced microwave evaporation, which transfers atoms from the  $|F = 2, m_F = 2\rangle$  state to the magnetically un-trapped  $|F = 1, m_F = 1\rangle$  state. After all the  $^{23}\text{Na}$  atoms are removed from the system with the microwave evaporation, we transfer the  $^{40}\text{K}$  atoms to the crossed ODT (see section 3.1.2), and subsequently bring the atoms from the  $|F = 9/2, m_F = 9/2\rangle$  state to the lowest energy state,  $|F = 9/2, m_F = -9/2\rangle$ , using a 10 ms Landau-Zener RF sweep at low magnetic fields,  $\approx 4$  G, produced using a small bias field applied along the  $x$ -direction. Once the atoms are in  $|F = 9/2, m_F = -9/2\rangle$  in the crossed ODT, we then increase the magnetic field to  $\approx 151$  G using a homogeneous field along the  $z$ -direction, that is produced using the Feshbach coil (see section 3.1.1) run in a Helmholtz configuration. To compensate gradients along the  $x$ ,  $y$ , and  $z$ -directions produced by inhomogeneities in the Feshbach field, we drive small currents in the slicer coil, which is run in an anti-Helmholtz configuration, as well two clover-leaf coils (labeled clover  $x$  and clover  $y$ ) located in the upper part of the chamber, near the solid immersion lens (see sec-

tion 3.1.4). For this work, we use only single clover-leaf coils (one for  $x$ , one for  $y$ ), which are located in the upper portion of the chamber, and not the corresponding coils in the lower half of the chamber. Nor do we make use of the second clover-leaf coil in the upper half of the chamber, which is located on the opposite side of the solid immersion lens along the same direction (e.g. there are two clover-leaf coils in the  $x$ -direction, on opposite sides of the solid immersion lens, that are both in the upper half of the vacuum chamber). That is, we use only single coils for both  $x$  and  $y$  clovers, although this can easily be changed in the future if larger gradient strengths are required. In this configuration, the final magnetic field, produced predominantly by the Feshbach coil, still points along the vertical,  $z$ -direction, and the gradient of this field along the  $z$ -direction is canceled using a vertical magnetic gradient from the slicer coil, whereas the gradients of this field along the  $x$  and  $y$ -directions are canceled using opposing horizontal gradients in the  $z$ -magnetic field produced by the clover  $x$  and clover  $y$  coils. We are also careful here to avoid over-compensation of the vertical gradient, which can happen if the vertical gradient due to gravity is mistaken for a vertical magnetic gradient. Accidentally compensating for gravity using a magnetic gradient can result in spatial separation in the optical trap between different spin states that have different magnetic moments, which can significantly affect the efficiency of further evaporative cooling stages.

At this 151 G field, we then transfer the atoms from the  $|F = 9/2, m_F = -9/2\rangle$  state to the  $|F = 9/2, m_F = -3/2\rangle$  state using a consecutive series of Landau-Zener sweeps ( $|9/2, -9/2\rangle \rightarrow |9/2, -7/2\rangle$ ,  $|9/2, -7/2\rangle \rightarrow |9/2, -5/2\rangle$ , etc...), produced by a single RF sweep with a large enough span to cover all the relevant  $m_F$  changing transitions, and a total RF sweep duration of 90 ms. Once all the atoms are in the  $|9/2, -3/2\rangle$  state, we create a 50:50 spin mixture of atoms in  $|9/2, -3/2\rangle$  and  $|9/2, -1/2\rangle$  using a series of ten non-adiabatic RF sweeps of 10 ms duration each, which are centered on the  $|9/2, -3/2\rangle \leftrightarrow |9/2, -1/2\rangle$  resonance. This spin mixture is energetically stable against  $m_F$  changing collisions at low temperatures and at the 151 G field, and has a scattering length for  $s$ -wave collisions very near the background value due to an absence of nearby Feshbach resonances at this field (see appendix C

of [37]). After we have prepared the spin mixture in the crossed ODT, we optically transport the atoms to the surface of the imaging system using the same experimental protocol that was described in section 4.2. That is, the atoms are moved in the crossed ODTs by sweeping the RF frequency of the ODT AODs to a position  $\sim 40\mu\text{m}$  below the substrate. The atoms are then transferred from the crossed ODTs to a combination of the accordion beam and the dimple, which is used to further compress the 2D layer of atoms while simultaneously moving it closer to the surface. For the spin transport measurements discussed in this chapter, the atoms are moved using the accordion to a position  $\approx 12.8\mu\text{m}$  below the surface of the substrate, where they are subsequently transferred to a single vertical layer of the shallow angle beam. This vertical position is different from previous experiments, such as those discussed in chapter 4, where the atoms were transferred to a single vertical layer of the shallow angle beam located  $\approx 7.9\mu\text{m}$  below the substrate. We decided to work in a layer which is further from the substrate surface for this work due to noticeable effects from surface potentials at the  $\approx 7.9\mu\text{m}$  position (see appendix A of [168]). A discussion of the procedure to re-optimize the single-site imaging for operation in the  $\approx 12.8\mu\text{m}$  position is given in section 3.2.1.

When the atoms have been transferred from the accordion beam to the shallow angle beam, and the accordion beam has been turned off, a final stage of optical evaporation is performed on the spin mixture in the combined shallow angle and dimple beams. To increase the efficiency of this final stage of evaporative cooling, a magnetic gradient is applied along the  $x$ -direction (the propagation direction of the shallow angle beam) to preferentially push atoms out along this axis, which has weaker confinement than either the vertical direction, in which there is a lattice, or the  $y$ -direction (the transverse direction of the shallow angle beam). The gradient for the evaporation is produced using the clover  $x$  coil, by increasing the current running through this coil beyond the value required to compensate the magnetic gradient from the Feshbach field along this direction. We then optically evaporate the spin mixture of atoms in the single 2D layer to quantum degeneracy by simultaneously lowering the powers of the shallow angle and dimple beams. However, because we

used a magnetic gradient for this evaporation, and because the two spin states used,  $|9/2, -3/2\rangle$  and  $|9/2, -1/2\rangle$ , have a significant differential magnetic moment at 151 G, the resulting spin mixture we obtain at the final evaporation depth is no longer a 50:50 mixture. That is, the atoms in the state  $|9/2, -3/2\rangle$  are preferentially pushed out of the trap by the applied magnetic gradient due to the larger magnetic moment of this state relative to  $|9/2, -1/2\rangle$ . The preferential removal of  $|9/2, -3/2\rangle$  atoms leads to a highly spin-imbalanced sample at the end of the evaporation, where  $\approx 85\%$  of the remaining atoms are in  $|9/2, -1/2\rangle$ , and  $\approx 15\%$  of the remaining atoms are in  $|9/2, -3/2\rangle$ . To ensure the final sample is a balanced 50:50 mixture, at this stage in the experimental sequence we remix the spin mixture using a second series of ten non-adiabatic RF sweeps of 10 ms duration each, centered on the  $|9/2, -3/2\rangle \leftrightarrow |9/2, -1/2\rangle$  resonance, after we have turned off the applied gradient by lowering the current in the clover  $x$  coil back to its compensating value. Although such a re-mixture of the spin states can add significant entropy to the sample once it has reached quantum degeneracy, it was the simplest method to reliably ensure we could study a balanced mixture for the spin transport measurements, at the expense of an increase in the sample temperature. Since our measurements were some of the first spin transport measurements performed on the half-filled 2D Hubbard model, and the final results were interesting even at increased temperatures, it didn't really matter if we reached temperatures of  $k_B T/t \sim 1$  (the temperature achieved for the equilibrium measurements of chapter 4) versus  $k_B T/t \sim 2$  (the actual temperature obtained for this work) at  $U/t = 8$ , for instance: the sacrifice in temperature was worth the reliability of a stable 50:50 spin mixture. We have subsequently improved this evaporation technique since the publication of these results in [164] by applying half of a Landau-Zener RF sweep of 15 ms duration which ends at the  $|9/2, -3/2\rangle \leftrightarrow |9/2, -1/2\rangle$  resonance position in the final  $\sim 151$  G magnetic field configuration, which includes the small applied magnetic gradient along the  $x$ -direction. At the end of the adiabatic RF sweep, the RF power is left on at the resonant frequency position. This dresses the bare atomic states with RF photons, such that the two dressed eigenstates at resonance are both equal superpositions of the two bare atomic states, with an

energy difference set by the RF Rabi frequency. Because the two dressed eigenstates are both equal superpositions of the bare atomic states, they both have the same magnetic moment. And since these dressed eigenstates are populated adiabatically by the half Landau-Zener sweep, this allows us to directly optically evaporate the spin mixture in the presence of a magnetic gradient (for efficient evaporation) without polarizing the sample. Thus, we leave the RF knife on at the resonance frequency as we lower the powers of the shallow angle and dimple beams for the evaporative cooling. At the end of the evaporation, we then reverse the half Landau-Zener sweep using a second 15 ms adiabatic sweep from the resonance frequency position back to the original RF frequency which is significantly detuned from resonance, and where the dressed eigenstates states are approximately given by the bare atomic states. We can then turn the RF off and lower the applied magnetic gradient, so that we're left with a quantum degenerate sample which is spin balanced, and which does not require the additional spin mixing stage that is used for the experiment discussed in the remainder of this chapter. With this RF-dressed evaporation in the presence of a magnetic gradient, we can achieve temperatures that are a factor of  $\approx 2$  lower than those achieved for [164] (Fig. 5-7), using the same spin mixture with the large differential magnetic moment that is required for spin transport. Future experiments could further improve upon this final evaporative cooling stage by employing the use of one of the two nearby *s*-wave Feshbach resonances between  $|9/2, -3/2\rangle$  and  $|9/2, -1/2\rangle$  at 138 G and 220 G, respectively (see appendix C of [37]), in order to enhance the scattering length between the two spin states during evaporation.

After the final stage of evaporative cooling, the sample is cold and spin balanced and the magnetic gradients are all compensated, and so we transfer the atoms in  $|9/2, -1/2\rangle$  to the state  $|9/2, +1/2\rangle$  using a final 20 ms Landau-Zener RF sweep. This final sweep does not add any additional entropy, and leaves us with a spin-balanced quantum degenerate sample of atoms in  $|9/2, -3/2\rangle$  and  $|9/2, +1/2\rangle$  at  $\approx 151$  G, within a single 2D layer at the focal plane of the imaging system,  $12.8\ \mu\text{m}$  from the substrate surface. At this field, the magnetic moments of these two spin states are  $-0.808(5)$  MHz/G and  $-0.303(6)$  MHz/G, respectively, corresponding to a

differential magnetic moment of  $-0.505 \text{ MHz/G}$ , and an average magnetic moment of  $-0.556 \text{ MHz/G}$ . Thus, the ratio of the differential magnetic moment between the two spin states to their average magnetic moment is  $\approx 0.91$  at an offset field of  $\approx 151 \text{ G}$ . Such a large ratio between the differential and the average magnetic moments was the original motivation for using these two particular spin states to study spin transport. That is, one desires a large differential magnetic moment to create a large differential force applied to the two spin states by a fixed magnetic gradient (see section 5.4). However, one does not want to apply such a strong magnetic gradient that atoms are actually pushed out of the trap before the spin distributions can be separated for spin transport. Therefore, one wants a spin mixture with a large differential magnetic moment to create a large differential force, and a small average magnetic moment to minimize the average force applied to the atoms by the gradient. For the  $151 \text{ G}$  offset field used here, these two spin states represent one of the optimal mixtures for this purpose. In principle, the ratio of the differential to the average magnetic moment could be further improved using different offset fields or even other stable spin mixtures at offset fields other than  $151 \text{ G}$ , but for the purposes of this work, these two spin states at this offset field provide sufficient conditions for studying spin transport.

Upon creation of the quantum degenerate mixture of  $|9/2, -3/2\rangle$  and  $|9/2, +1/2\rangle$  atoms in the shallow angle and dimple beams, the atoms are subsequently transferred into a single layer of a shallow, square optical lattice, formed using the  $x$  and  $y$  retro-reflected lattice beams, with a depth of  $3E_R$  along the  $x - y$  direction. Once the lattice has reached this initial shallow depth, we project a blue-detuned, repulsive box potential onto the atoms through the microscope objective. This potential is created using  $739 \text{ nm}$  broadband light, whose spectrum has a full width at half max (FWHM) of  $\sim 1 \text{ nm}$ , which is projected onto the atoms using a digital micromirror device (DMD) in the image plane of the single-site imaging system (see section 3.1.2). A detailed description of the DMD setup (both the light source and the DMD projection optical path), as well as a detailed characterization of the final box potential we project onto the atoms, are given in sections 4.3 and 4.4 of [168]. In general terms,

the box potential we project has a Gaussian profile centered on the atomic sample, with a square,  $22 \times 22$  site dark region cut out from the center of this Gaussian profile. The edges of the square are aligned to the axes of the optical lattice, and provide sharp walls ( $\sim 0.5$  sites wide from the maximum wall height to 50% of the max height), which prevent atoms trapped within the box from escaping during the transport dynamics. As this box potential is turned on, the Gaussian profile isolates the dark central region by pushing unwanted atoms far away, so that they are no longer in contact with the isolated box, and additionally, at the final power used in the experiment, prevents these unwanted atoms from entering the box region during the spin transport dynamics. The optical power of the box potential is increased linearly from zero to the final power used in the experiment over a 300 ms duration. We chose the final optical power of this repulsive potential to be the minimum power necessary to prevent atoms from entering or escaping the central square region during the transport dynamics. We have, however, verified that increasing the total power in this optical potential by 30% has no measurable effect on the values of the spin transport coefficients we extract. This is important to check, because too much optical power in the projected potential can have a noticeable effect on the dynamics (see section 5.3.1 of [168]) due to near-detuned light (739 nm versus the 767 nm wavelength of the  $^{40}\text{K}$  D2 line) present in the dark square region which arises from imperfect imaging of the DMD chip onto the plane of the atoms (see section 4.4 of [168]). As the power in the box potential is increased, we simultaneously lower the powers of the shallow angle and dimple beams to zero in order to transfer the atoms entirely to the combined potentials of the optical lattice and the box. The final atom number (or the final density) in the box is controlled by the depth of the final optical evaporation in the shallow angle and dimple beams, since this determines how many atoms are transferred into the initial  $3E_R$  lattice. By varying the depth of the final optical evaporation, we can, for example, prepare samples both above and below half-filling (see Fig. 5-6) if so desired.

For the measurements of the spin diffusion coefficient that we discuss in sections 5.4.1 and 5.4.2, we prepare the system in equilibrium in a lattice potential

which is tilted to one side by the presence of an applied magnetic gradient. Because the different spin states have very different magnetic moments, the magnitude of the tilt of the lattice which the two spin states experience in the presence of the magnetic gradient is also very different. Ultimately, this allows us to create initial equilibrium spin density profiles which are perturbed, in the sense of linear response, from the profiles one would expect in a homogeneous system, and which therefore have a significant spatial gradient in the total spin density (see section 5.4.1). To do this, after the box potential reaches its final depth in the  $3E_R$  lattice, and after the shallow angle and dimple beams have been turned off, we apply a magnetic field gradient of strength  $0.94(2)$  G/cm along the  $y$ -lattice direction by increasing the current running through both the clover  $x$  and clover  $y$  coils from the respective values which compensate the Feshbach field gradients, using a linear ramp of 300 ms duration. Because the gradients provided by each of the coils separately do not strictly point along the lattice axes, a combination of the two coils must be used. A description of how the gradient is aligned to the lattice axes using the combined clover coils, as well as how the magnitude of the applied gradient is calibrated, is given in section 5.2.2. By turning on the applied gradient while the lattice is shallow, the atoms can still move around with sufficient mobility (i.e. with a large enough tunneling amplitude) that they can quickly adjust to the differential force arising from the magnetic gradient, and rearrange the spin distributions. Once the magnetic gradient has reached its final value of  $0.94(2)$  G/cm using the ramp of the current in the clover coils, the depths of the lattices along the  $x$  and  $y$  directions are increased adiabatically using a linear ramp of their respective powers to a final depth corresponding to the desired value of the Hubbard parameters  $U/t$ . This linear lattice ramp is performed with a duration of at least 250 ms, where the ramp time is adjusted according to the final lattice depth in order to ensure adiabaticity. After the lattices reach their final depth, the system is in equilibrium in the tilted lattice potential. We can initiate spin dynamics for the measurement of the diffusion coefficient by quenching the magnetic gradient from  $0.94(2)$  G/cm to zero, and returning the currents running through the clover coils to their respective values which compensate the Feshbach field gradients within

2 ms. The speed with which the gradient is turned off (or on) is limited by the response time of one of the power supplies used to power the clover coils. To detect the spin profiles at various times during the dynamics, we freeze the atomic distribution at a given time by increasing the  $x$  and  $y$  lattice depths to  $\sim 100E_R$  within 2 ms. We then perform either the normal single-site imaging procedure in order to image the site-resolved local moment, or the spin-dependent imaging procedure discussed in sections 4.4.2 and 5.2.4 in order to image the singles density of one of the two spin states. During the lattice ramp from  $\sim 100E_R$  to  $\sim 1000E_R$ , which is used for single-site imaging (see section 4.2), the DMD potential is ramped down to zero over 20 ms so that it is off for the Raman sideband imaging.

For the direct spin conductivity measurements discussed in section 5.4.4, we adiabatically prepare the system in equilibrium in a homogeneous lattice, without an applied magnetic gradient, so that the initial total spin density (before we start the dynamics) is homogeneous in the box. That is, for this experiment, after the box potential has reached its final power, the  $x$  and  $y$  lattice depths are linearly increased in an adiabatic manner from  $3E_R$  to their final depths, corresponding to the desired value of  $U/t$ . The ramp speeds used here are the same as those used for the diffusive measurements, and are adjusted according to the final lattice depth in order to ensure the system is prepared adiabatically. Once the system has reached equilibrium at the desired Hubbard parameters  $U/t$ , we apply the same magnetic gradient which we use for the diffusive measurements, 0.94(2) G/cm, by running excess current in the clover coils, beyond what is required to compensate the Feshbach field gradients. In this conductivity experiment, however, the gradient is turned on within 2 ms to quench the gradient strength, and to apply a sudden spin-dependent force which separates the two spin distributions in the box as time evolves. We can then measure the spin density distributions as a function of time after turning on the magnetic gradient, to monitor their spatial separation, by freezing the atomic distribution at a given time during the dynamics with a sudden increase in the lattice depths along the  $x$  and  $y$  directions within 2 ms to  $\sim 100E_R$ . Once the atomic motion is frozen at  $\sim 100E_R$ , we can perform either the normal single-site fluorescence imaging, or the spin-dependent

imaging, in order to access the desired quantities. As with the diffusive measurement, the DMD potential is ramped to zero while the lattices are increased to  $\sim 1000E_R$  for single-site imaging.

### 5.2.1 Calibrating the Hubbard Parameters

The Hubbard parameters  $U$  and  $t$  were calibrated for this work using the same modulation spectroscopy technique discussed in detail in section 4.2.1. In this case,  $U$  was calibrated using modulation spectroscopy on a small ( $\sim 500$  total atoms), balanced mixture of atoms in the states used for studying spin transport,  $|F = 9/2, m_F = -3/2\rangle$  and  $|F = 9/2, m_F = +1/2\rangle$ , in the absence of the 739 nm projected box potential created by the DMD, and at the same magnetic field used in the experiment ( $\sim 150$  G). We removed the projected potential for this calibration to ensure that our interpretation of the modulation spectra, which should be determined strictly by the lattice depth and the scattering length between the two spin states, was not influenced by the presence of local AC stark shifts from the 739 nm light. To determine  $t$ , we again used the modulation spectroscopy technique discussed in section 4.2.1 to measure the bandgap between the ground and first-excited energy bands in the lattice. This was performed on a spin-polarized sample in order to minimize interaction effects, where 85% of the atoms were in the  $|9/2, 1/2\rangle$  state, and 15% of the atoms were in the  $|9/2, -3/2\rangle$  state. Such a highly spin-polarized sample was created by performing the final stage of optical evaporation in the presence of a magnetic gradient, which predominantly removes the spin state with the larger magnetic moment, and then turning off the RF sweeps which remix the spin states to make the final 50 : 50 mixture (see section 5.2) utilized for the transport measurements. We then used the bandgap measured from the modulation spectroscopy, in combination with a lattice band calculation, to determine the lattice depth. The calibrated depth was subsequently used in a tight-binding calculation to extract the tunneling amplitude  $t$ .

### 5.2.2 Calibrating the Magnetic Gradient Strength

Studying spin transport using a magnetic gradient to create a spin-dependent force requires one to have control over both the direction and the magnitude of the gradient. For the experiment described in this chapter, we wanted the magnetic gradient to be co-aligned with one of the lattice axes (in this case the  $y$ -lattice direction) to simplify the interpretation and analysis of the data. However, generalizing this work to study transport along other directions, i.e.  $45^\circ$  with respect to the lattice axes, might be a useful method to probe transport in interesting regimes of the Fermi-Hubbard model, such as the pseudogap regime, which, in the cuprates, can exhibit anisotropic transport phenomena [49, 139]. Aligning the gradient to the lattice axes can be done two different ways. The first, and simplest, method is to prepare a dilute two-component mixture in the box potential, whose edges are aligned to the lattice, in equilibrium in the presence of a gradient. Under the tilt produced by the gradient, the atoms will be forced to the edges of the box in a manner which depends on the direction of the tilt. Since the magnetic gradient is formed by shifting the fields produced by the  $x$  and  $y$  clover coils to values away from those which compensate the magnetic gradients produced by the Feshbach coil (see section 5.2), the direction of the gradient can be controlled by adjusting the relative strengths of the gradients produced by each of the clover coils. Once the atoms have moved to the edges of the box with the tilt, one can image the local moment over several different experimental realizations, and measure the average distribution of atoms in the box. One can then finely adjust the relative strength of the gradients produced by each clover coil until the atoms are symmetrically distributed along one particular edge of the box. The second method one can use to align the gradient direction is to perform microwave spectroscopy. Specifically, one can prepare a large sample, without the box potential, in a deep 2D lattice ( $\sim 100E_R$ ), so that the atomic motion is essentially frozen. One can then apply the magnetic gradient using the clover coils so that there is a significant magnetic field difference across the cloud in one direction. Subsequently, one can apply a small microwave sweep or a microwave pulse to transfer atoms from

the  $F = 9/2$  to the  $F = 7/2$  manifold. Because of the magnetic gradient however, only those atoms in resonance with the sweep or pulse will be transferred to the  $F = 7/2$  manifold. Once some of the atoms have been shelved in  $F = 7/2$ , one can apply a light pulse resonant on the  $F = 9/2 \rightarrow F' = 11/2$  transition, which removes all the atoms remaining in  $F = 9/2$ . When the atoms which were hidden in  $F = 7/2$  are subsequently imaged using the single-site Raman imaging, one should, in principle, observe a stripe of atoms which were resonant with the microwave transition [151]. One can then finely adjust the gradients produced by the two clover coils until the stripe is aligned along one of the lattice axes. We made use of both methods for this work, and found similar results for each.

For the experiment discussed in this chapter, we align the gradient using the  $x$  and  $y$  clover coils to point along the  $y$ -direction. Once the gradient is aligned, however, we must calibrate its magnitude in order to accurately measure the uniform spin susceptibility and the spin conductivity (see sections 5.4.1 and 5.4.4, respectively), which both depend on the spatial gradient in the differential chemical potential between the two atomic spin states, set by the magnetic gradient. Specifically, we calibrate the magnitude of the gradient using a large, dilute, spin-polarized atomic sample in the hyperfine state  $|F = 9/2, m_F = -9/2\rangle$ , which has a magnetic moment of 1.402 MHz/G at an offset magnetic field of 150 G. After preparing the spin-polarized cloud in a single vertical layer of a shallow square optical lattice ( $\approx 3E_R$ ), the lattice is quickly ramped to the pinning depth ( $\sim 100E_R$ ), in the same manner used for spin-selective imaging, in order to restrict atomic motion and localize the atoms. After freezing the atomic distribution, a magnetic field gradient  $\nabla B$  is turned on along the  $y$  direction, whose magnitude is set by the overall offset from the field used to compensate the Feshbach field gradients, which can be controlled. The spatially varying magnetic field due to the applied gradient yields a spatially varying microwave resonance frequency for the transfer of atoms from the  $|F = 9/2, m_F = -9/2\rangle$  hyperfine state to the  $|F = 7/2, m_F = -7/2\rangle$  hyperfine state. This then leads to a direct relation between the frequency of this resonance, and the spatial position of atoms in the sample along the direction of the gradient. Therefore, a short pulse of microwave

radiation near the frequency of this resonance will only transfer atoms to the other hyperfine state if they are positioned in the stripe of space where this particular frequency is resonant with the magnetic field. The finite duration of the microwave pulse in time creates a finite width of the pulse in frequency space, which leads to a finite width in real space of the stripe of atoms transferred to the other hyperfine state. For a fixed pulse time then, the width of the stripe of transferred atoms depends on the strength of the magnetic field gradient. After some atoms have been transferred to the  $|F = 7/2, m_F = -7/2\rangle$  hyperfine state using the short microwave pulse, a pulse of light resonant with the  $F = 9/2 \rightarrow F' = 11/2$  optical transition removes atoms left in the  $|F = 9/2, m_F = -9/2\rangle$  hyperfine state. The depth of the optical lattice is subsequently increased to the imaging depth, and a single-site resolved fluorescence image is taken of the remaining atoms, revealing the spatial location of the atoms which were resonant with the microwave pulse.

In order to avoid any issues arising from magnetic field fluctuations, a differential measurement is performed where two short microwave pulses with a fixed frequency difference and durations of  $300\mu\text{s}$  are used to transfer atoms in two different spatial locations to the other hyperfine state. By measuring the spatial separation of the two stripes of atoms which were successfully transferred to  $F = 7/2$  by the microwave pulses, using the site resolved fluorescence images and the known lattice spacing, we can obtain a direct measure of the relationship between real space and the frequency difference of the two microwave pulses. Fig. 5-1 shows an example single-site fluorescence image which demonstrates the observation of the two stripes generated from two microwave pulses separated by  $18\text{ kHz}$  in the presence of a gradient. This frequency difference between the two pulses can then be varied, and the average spacing between the two transferred stripes of atoms can be measured as a function of this frequency difference. The results of this measurement at one particular gradient strength are shown in Fig. 5-2. A linear fit to the data yields the slope of the dependence of the stripe spacing on the frequency difference between the two pulses, so that with knowledge of the magnetic moments of both the  $|F = 9/2, m_F = -9/2\rangle$  and  $|F = 7/2, m_F = -7/2\rangle$  hyperfine states used in the microwave transfer at the  $150\text{ G}$

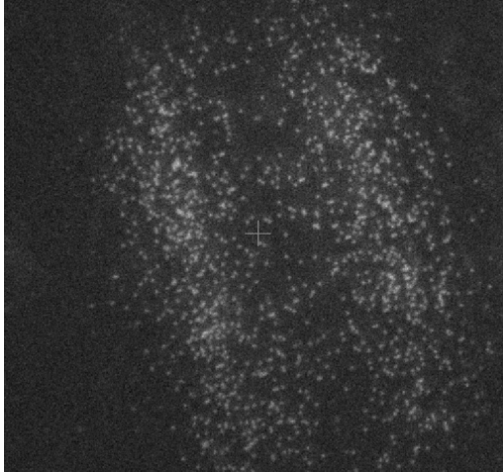


Figure 5-1: Creating stripes in a large, dilute sample of  ${}^4\text{K}$  atoms to calibrate an applied magnetic gradient. A spin-polarized sample of atoms in  $|F = 9/2, m_F = -9/2\rangle$  is held in a single vertical layer of a  $\sim 100E_R$  deep lattice, so that the atomic motion is effectively frozen. A magnetic gradient along the  $y$ -direction is applied using the clover coils, so that the Zeeman shift of the  $|F = 9/2, m_F = -9/2\rangle \rightarrow |F = 7/2, m_F = -7/2\rangle$  microwave transition is spatially dependent along  $\hat{y}$ . Two short,  $300\ \mu\text{s}$  microwave pulses with fixed frequency difference are then applied simultaneously to transfer some of the atoms in the lattice to  $|F = 7/2, m_F = -7/2\rangle$  in a spatially dependent manner. The atoms remaining in  $F = 9/2$  are then removed using a resonant light pulse on the  $F = 9/2 \rightarrow F' = 11/2$  optical transition, so that only those atoms successfully transferred to  $F = 7/2$  by the microwave pulses are subsequently imaged using the single-site fluorescence imaging. Due to the applied magnetic gradient, and the short duration of the microwave pulses, the distribution of transferred atoms resembles two spatially separated stripes.

offset field, we can extract the value of the magnetic field gradient. For the data shown in Fig. 5-2, we measure a magnetic field gradient of strength  $1.98(4)$  G/cm. The gradient strength used for the spin transport measurements discussed in section 5.4 is half the value of that used for the calibration shown in Fig. 5-2, and is therefore  $0.94(2)$  G/cm. The hyperfine states of the atoms used for the spin diffusion and spin conductivity experiments are  $|F = 9/2, m_F = -3/2\rangle$  and  $|F = 9/2, m_F = 1/2\rangle$ , which have magnetic moments of  $-0.808(5)$  MHz/G and  $-0.303(6)$  MHz/G, respectively, at the offset magnetic field of 150 G (the error bars in the magnetic moments come from the uncertainty in the determination of the offset field). The gradient strength used for the transport measurements then translates to an energy offset of  $41.1(8)$  Hz/site and  $15.4(3)$  Hz/site for the two spin states, respectively.

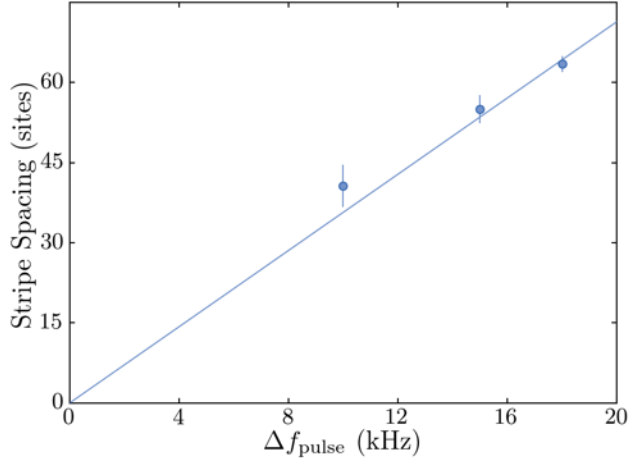


Figure 5-2: Calibration of the applied magnetic gradient using microwave spectroscopy. Plotted is the average observed spatial separation of the stripes from Fig. 5-1 (in units of lattice sites), as a function of the frequency difference between the two simultaneously applied microwave pulses. The stripe separation is obtained by integrating the observed site-resolved, parity-projected density in a given image along the  $x$ -direction (orthogonal to the applied gradient) to obtain a one-dimensional profile along the direction of the magnetic gradient. The resulting 1D profile is then fit to a sum of two gaussian distributions with different center positions, in order to extract the central locations of the two stripes along the  $y$ -direction, and therefore their spatial separation. The error bars represent the  $1\sigma$  statistical uncertainty of the measurement. The solid line denotes a linear fit to the data, where the offset of the fit is fixed to zero at zero frequency difference between the microwave pulses. From the slope of the fit, and the known magnetic moments of the atoms, one can extract the magnitude of the applied gradient, which is measured here to be  $1.98(4)$  G/cm.

This microwave spectroscopy based calibration of the magnetic gradient agrees with a separate calibration based on lattice modulation spectroscopy of a two-component Mott-insulating sample. Without the gradient present, modulating the lattice intensity at a frequency  $U/h$  drives resonant tunneling between neighboring sites which are occupied by single atoms in opposite spin states. Thus, this technique is typically used to calibrate the Hubbard parameter  $U$  (see sections 4.2.1 and 5.2.1), where the observable is typically the average singles density of the Mott-insulating sample, which drops at the modulation resonance due to the creation of neighboring doublons and holes from the original singly-occupied sites. If one were to perform this same experiment in the presence of a small linear tilt (due to, for example, a magnetic gradient) of the lattice potential, however, corresponding to an energy offset  $\Delta$  be-

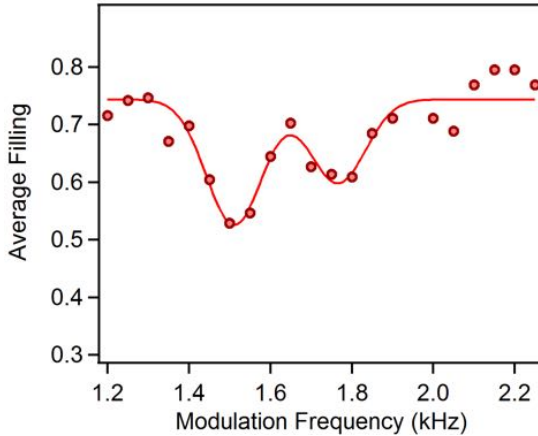


Figure 5-3: Calibration of the applied magnetic gradient using lattice modulation spectroscopy. A linear tilt along the  $y$ -lattice direction is applied, using a magnetic gradient produced by the clover coils, to a fermionic Mott insulator of  $|F = 9/2, m_F = -7/2\rangle$  and  $|F = 9/2, m_F = -5/2\rangle$  atoms, with on-site interaction energy  $U$  and a 150 G vertical offset field, at a lattice depth of  $16E_R$  along the  $y$ -direction, and  $\sim 50E_R$  along the  $x$ -direction. The intensity of the  $y$ -lattice beam is then modulated sinusoidally for 800 modulation cycles with 3% modulation amplitude. Plotted is the average filling measured in the central  $16 \times 16$  region of the sample after the modulation, as a function of the modulation frequency. Dips in the average filling are observed when the modulation frequency is resonant with either  $(U + \Delta)/h$  or  $(U - \Delta)/h$ , where  $\Delta$  is the energy offset between neighboring sites along the  $y$ -direction, since at this frequency the modulation resonantly generates neighboring doublon-hole pairs, which deplete the average local moment in the center of the sample. The solid line represents a fit to the data of a sum of two Gaussian distributions with different peak locations, in order to determine the two resonances.

tween neighboring sites, where  $\Delta < U$ , the  $U/h$  modulation resonance is split into two separate resonances corresponding to  $(U + \Delta)/h$  and  $(U - \Delta)/h$  [146]. The higher frequency resonance,  $(U + \Delta)/h$ , corresponds to an atom tunneling to a neighboring site which is offset in energy by  $+\Delta$  (i.e. it moves up the hill), and which is occupied by a single atom of the opposite spin state, so that they interact with energy  $U$ . The modulation thus supplies the energy required to generate this state from a state originally comprised of two neighboring singly occupied sites. The lower frequency resonance,  $(U - \Delta)/h$ , corresponds to the opposite process, where an atom tunnels to a neighboring site which is offset in energy by  $-\Delta$  (i.e. it moves down the hill), and which is occupied by a single atom of the opposite spin state, so that they interact with energy  $U$ . To suppress the  $U/h$  resonance corresponding to atoms

forming doublon-hole pairs along the direction orthogonal to the applied tilt, we increase the lattice depth along that direction to  $\sim 50E_R$ , so that tunneling, even in the presence of the modulation, is strongly suppressed along this direction as long as the amplitude of the modulation is small (e.g. 3% of the depth of the shallower lattice). An example modulation spectrum performed on a Mott-insulating sample consisting of atoms in the states  $|F = 9/2, m_F = -7/2\rangle$  and  $|F = 9/2, m_F = -5/2\rangle$ , in a linear magnetic gradient at a 150 G offset field, and with a lattice depth of  $16E_R$  along the gradient direction is shown in Fig. 5-3. Plotted is the average filling, or average singles density, of a  $16 \times 16$  region in the center of the sample as a function of the lattice modulation frequency. From the separation of the two peaks, corresponding to  $2\Delta/h$ , we can determine the energy offset between neighboring sites due to the linear magnetic gradient (127 Hz for the data shown in Fig. 5-3). Given the average magnetic moment of the two spin states used to create the Mott-insulating sample at the 150 G offset field, we can then back out the magnitude of the applied magnetic gradient. The calibration of the gradient strength obtained through this technique agrees, to within the experimental uncertainty, with the calibration that uses the microwave spectroscopy method shown in Fig. 5-2.

### 5.2.3 Calibrating the Harmonic Trapping Frequencies

In order to ensure that the spin dynamics studied here are not strongly influenced by the presence of an underlying harmonic trapping potential arising from spatial variation of the lattice intensity in a Gaussian lattice beam, we must calibrate the strength of the underlying harmonic confinement in the lattice, and compare it to the other relevant energy scales. Typically, this is done using dipole, or breathing mode, oscillation measurements, where the trap frequency is suddenly quenched from some initial value to the desired configuration using, for example, the intensity of the light forming the trap. This quench excites breathing mode oscillations in the trapping potential of interest, which can be observed as oscillations in the width of the atomic distribution that occur at twice the harmonic trapping frequency. However, these simple breathing mode oscillations can be significantly affected by the presence

of a periodic lattice potential along the direction of the oscillations, and therefore become more difficult to interpret in this case. The presence of on-site interactions between opposite spin states can also have a significant impact on the behavior of these collective oscillations. One way to get around these issues is to calibrate each lattice beam independently using a non-interacting gas. For instance, one can prepare a non-interacting system (a fermi gas in a single spin state) in a trap formed from a single lattice beam, which, in our experiment, would create both a vertical lattice, and an in-plane lattice along the direction of propagation of the beam (i.e. the atoms would be trapped in 1D tubes). One could then quench the depth of the lattice to excite breathing mode oscillations along the direction orthogonal to the in-plane lattice (i.e. along the direction of the 1D tubes), and subsequently measure the width of the atomic distribution using single-site imaging as a function of time after the quench. This would then allow one to measure twice the trap frequency along the transverse direction of this lattice beam. Such a technique was used, for example, in [77, 180] (see the supplementary materials) to calibrate the transverse trap frequency of each beam independently. However, there is an additional contribution to the trap frequency along a given direction which comes from the longitudinal confinement of the orthogonal lattice beam. That is, the total trapping frequency along a given direction in the final, full lattice configuration is a combination of the transverse trapping of one lattice beam, and the longitudinal trapping of the second beam, which is not directly measured in this technique. We thus sought a more precise method of calibrating the final harmonic trapping potential along the direction of interest for the dynamics (the direction of the magnetic gradient), which the atoms experience in the full lattice configuration.

Specifically, for the spin transport data described in this chapter, the trap frequency along the direction of the magnetic field gradient, i.e. the direction of flow of the spin current, is calibrated by preparing a small balanced mixture of atoms ( $\sim 500$  atoms total) in the states  $|F = 9/2, m_F = -9/2\rangle$  and  $|F = 9/2, m_F = -7/2\rangle$ , which have magnetic moments of  $1.402\text{ MHz/G}$  and  $1.22\text{ MHz/G}$ , respectively, at an offset magnetic field of  $150\text{ G}$ . Restricting the atom number ensures that the size

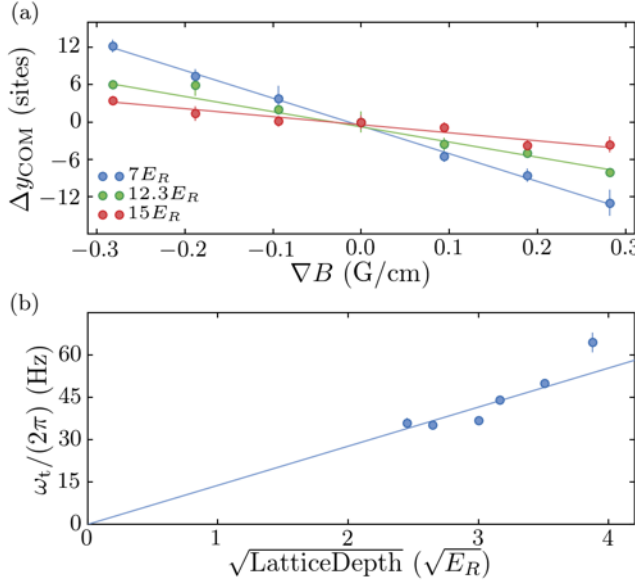


Figure 5-4: Calibration of the harmonic trapping frequency of the underlying potential of the optical lattice. (a) Shift in the center of mass (COM) of the atomic cloud (in units of lattice sites) from its initial position due to an applied magnetic field gradient along the  $y$ -direction, for different lattice depths. The circles represent the experimental data for different values of the lattice depth: blue circles are the COM of the sample at  $7E_R$ , green circles are for  $12.3E_R$ , and red circles are for  $15E_R$ . The solid lines denote a linear fit to the experimental data. The slope of this line is used to extract the value of the trapping frequency,  $\omega_t$ . (b) The measured harmonic trapping frequency,  $\omega_t$ , of the lattice as a function of the square root of the lattice depth,  $\sqrt{V/E_R}$ , where  $V/E_R$  is the lattice depth in units of  $E_R$ . The blue circles denote the experimentally measured trapping frequency, and the solid line represents a linear fit to the data to extract the slope of the dependence of  $\omega_t$  on  $\sqrt{V/E_R}$ .

of the atomic cloud ( $\sim 6 \mu\text{m}$  radius) is sufficiently small compared to the waists of the lattice beams ( $\approx 135 \mu\text{m}$ ) that only the harmonic properties of the lattices are probed. The balanced mixture is prepared adiabatically in a single plane of the optical lattice, and a small magnetic field gradient is applied simultaneously along the  $y$ -direction to shift the zero of the overall harmonic trap arising from the combination of the two lattice beams. The preparation of the atomic sample in the combined harmonic potential of the lattice and linear potential of the magnetic field gradient is done slowly, over a time scale of 1000 ms, so that the sample has had sufficient time to find the new zero of the total potential. By measuring the shift of the center of mass of the cloud as a function of the applied magnetic field gradient, the harmonic

trapping frequency due to the lattice potential can be extracted. Indeed, in the presence of a magnetic field gradient, a linear potential of the form  $y\bar{\mu}\nabla B$  is combined with the harmonic potential of the lattice,  $\frac{1}{2}m\omega^2y^2$ , where  $\nabla B$  denotes the magnetic field gradient along the  $y$ -direction and  $\bar{\mu}$  represents the average magnetic moment of the two spin states. This shifts the zero of the overall harmonic confinement by an amount  $\Delta y = \frac{\bar{\mu}\nabla B}{m\omega^2}$ . Therefore, by measuring the average center of mass of the cloud as a function of the applied gradient,  $\nabla B$  (which is independently calibrated, see section 5.2.2), as shown in Fig. 5-4(a), and extracting the slope of this linear dependence using a linear fit to the data, one can extract the quantity  $\frac{\bar{\mu}}{m\omega^2}$ . Using the known average magnetic moment, 1.311 MHz/G, and the mass of  $^{40}\text{K}$ , one can then obtain the trapping frequency of the full lattice potential along the direction of the applied gradient. The measured trap frequency along the direction of flow of spin current is shown in Fig. 5-4(b) as a function of  $\sqrt{V/E_R}$ , the square root of the depth of the optical lattice measured in terms of the recoil energy. For the purposes of this measurement, the lattice along the spin transport direction and that of the orthogonal direction are chosen to be of equal depth, so that the system is in the same 2D geometry used for the data discussed in section 5.4. A linear fit to the data shown in Fig. 5-4(b) yields a slope,  $\frac{\omega/2\pi}{\sqrt{V}}$ , of  $13.9(1)$  Hz/ $\sqrt{E_R}$ , and shows that for the range of lattice depths used in the experiment ( $\sim 7E_R$  to  $\sim 15E_R$ ), the harmonic trap frequency along the gradient direction varies over the range  $2\pi \times 37(2)$  Hz to  $2\pi \times 64(3)$  Hz.

Given this range of harmonic trapping frequencies experienced by the atoms in the box potential, one can ask how the presence of such a trap might affect the observed spin dynamics, and the measurement of the spin transport coefficients. For a half-filled system in the strongly interacting, Heisenberg limit,  $t/U \ll 1$ , the spins on neighboring lattice sites interact with an antiferromagnetic effective super-exchange coupling  $J_{ex} = 4t^2/U$  [54, 135]. This energy scale sets the rate of spin diffusion in this regime, since it is the only relevant energy scale in the  $t/U \ll 1$  limit which allows neighboring spins to communicate through interaction. In the presence of an underlying harmonic trapping potential, however, this exchange coupling is modified

and becomes site-dependent, due to the spatially-dependent energy offset between neighboring sites arising from the harmonic potential with trap frequency  $\omega$ . Specifically, the super-exchange coupling at site index  $j = y/a$  along the  $y$ -direction,  $J_{ex,j}$ , in the presence of a harmonic potential of the form  $\frac{1}{2}m\omega^2y^2$ , becomes [70]

$$J_{ex,j} = \frac{4t^2U}{U^2 - (\frac{1}{2}m\omega^2a^2)^2(2j-1)^2}. \quad (5.1)$$

From the trap frequency calibration, the harmonic trapping frequency along the gradient direction, over the range of lattice depths used for the data discussed in section 5.4, varies from  $2\pi \times 37(2)$  Hz to  $2\pi \times 64(3)$  Hz. At the highest lattice depth studied in this experiment, where  $\omega = 2\pi \times 64(3)$  Hz, the calibrated on-site interaction energy is  $U/h = 1077(30)$  Hz. For the maximum box size used in the experiment,  $L = 22$  sites, corresponding to a maximal site index of  $j = 11$  (the box is centered on the zero of the harmonic potential), the variation of  $J_{ex,j}$  across the sample is  $< 1\%$ . In this sense then, we are justified in ignoring the influence of the harmonic potential on the spin dynamics. Of course, in doing this, one must also ensure that the spatial variation of the density of the sample, which arises from the harmonic potential changing the local chemical potential in the sense of the LDA, is sufficiently small that the system is near half-filling across the entire sample. Otherwise, one can no longer claim to study dynamics in the linear response regime around a certain filling. For the experiment discussed in this chapter, which does not actively compensate the underlying trapping potential of the lattice, this is the dominant effect, rather than the spatial variation in the exchange coupling, and it limits the maximum box size one can reliably study to  $L \sim 22$  sites.

#### 5.2.4 Spin-Dependent Imaging Errors

To study spin transport, we must examine the dynamics of the site-resolved, average total spin density  $\langle \hat{S}_{z,j} \rangle = \langle \hat{n}_{\uparrow,j} - \hat{n}_{\downarrow,j} \rangle / 2 = \langle \hat{n}_{\uparrow,j}^s - \hat{n}_{\downarrow,j}^s \rangle / 2 = \langle \hat{n}_{\uparrow,j}^s \rangle / 2 - \langle \hat{n}_{\downarrow,j}^s \rangle / 2$ , where  $\hat{n}_{\uparrow,j}^s$  and  $\hat{n}_{\downarrow,j}^s$  are the singles densities of the two individual spin states, defined in Eq. 4.11. Measuring the average total spin density thus requires us to measure the

site-resolved average singles densities of the two spin states separately, for which we must use the spin-dependent imaging technique discussed in detail in section 4.4.2. For the experiments discussed in this chapter, the spin sensitive imaging is performed in the exact same manner as was described in section 4.4.2 (with the same experimental parameters used), except that the specific spin states studied are different. In this case, we use the two states  $|F = 9/2, m_F = -3/2\rangle$  and  $|F = 9/2, m_F = +1/2\rangle$  to study transport, rather than  $|F = 9/2, m_F = -9/2\rangle$  and  $|F = 9/2, m_F = -7/2\rangle$  that were used previously. To image state  $|F = 9/2, m_F = -3/2\rangle$  ( $|F = 9/2, m_F = +1/2\rangle$ ), we use a microwave sweep to transfer the atoms to the state  $|F = 7/2, m_F = -5/2\rangle$  ( $|F = 7/2, m_F = +3/2\rangle$ ), respectively, where they are effectively hidden, and the remaining, non-transferred atoms are selectively removed using a 5 ms light pulse resonant on the  $F = 9/2 \rightarrow F' = 11/2$  imaging transition. As was discussed previously, this spin removal step is performed after the atomic distribution has been frozen at  $\sim 100E_R$ , and before we increase the lattice depth to  $\sim 1000E_R$  for single-site Raman imaging.

In the situation where the spin-resolved imaging fidelity is not perfect, the quantities we actually observe,  $\hat{\tilde{n}}_{\sigma,j}^s$ , are modified forms of the normal spin-resolved singles densities,  $\hat{n}_{\sigma,j}^s$ , as defined in Eq. 4.17. As we discussed in section 4.4.2, the spin-imaging errors  $\epsilon_{1,\sigma}$  and  $\epsilon_{2,\sigma}$ , which represent unintended loss of the atoms being imaged and imperfect removal of the other spin state, respectively, are approximately spin-independent, and can be written as  $\epsilon_{1,\sigma} \approx \epsilon_1$  and  $\epsilon_{2,\sigma} \approx \epsilon_2$ . In this case, the observed total spin density becomes,

$$\begin{aligned}
\langle \hat{\tilde{S}}_{z,j} \rangle &= \frac{\langle \hat{\tilde{n}}_{\uparrow,j}^s \rangle - \langle \hat{\tilde{n}}_{\downarrow,j}^s \rangle}{2} \\
&= \left[ (1 - \epsilon_1) \langle \hat{n}_{\uparrow,j} \rangle + \epsilon_2 \langle \hat{n}_{\downarrow,j} \rangle - (1 - \epsilon_1 + \epsilon_2) \langle \hat{d}_j \rangle \right] / 2 \\
&\quad - \left[ (1 - \epsilon_1) \langle \hat{n}_{\downarrow,j} \rangle + \epsilon_2 \langle \hat{n}_{\uparrow,j} \rangle - (1 - \epsilon_1 + \epsilon_2) \langle \hat{d}_j \rangle \right] / 2 \\
&= (1 - \epsilon_1 - \epsilon_2) \frac{(\langle \hat{n}_{\uparrow,j} \rangle - \langle \hat{n}_{\downarrow,j} \rangle)}{2} \\
&= (1 - \epsilon_1 - \epsilon_2) \langle \hat{S}_{z,j} \rangle . \tag{5.2}
\end{aligned}$$

Including the finite imaging fidelity,  $f$ , associated with atom loss during the single-site Raman imaging process (see section 4.4.2), the observable total spin density becomes,

$$\left\langle \hat{S}_{z,j} \right\rangle = f(1 - \epsilon_1 - \epsilon_2) \left\langle \hat{S}_{z,j} \right\rangle. \quad (5.3)$$

Thus, any observable quantity which depends directly on  $\left\langle \hat{S}_{z,j} \right\rangle$ , including sums or derivatives of this quantity, must be corrected for the spin imaging fidelity factor  $f(1 - \epsilon_1 - \epsilon_2)$ . Using the techniques discussed in detail in section 4.4.2, the calibrated values of  $f$ ,  $\epsilon_1$ , and  $\epsilon_2$  are found to be  $f = 93(2)\%$ ,  $\epsilon_1 - \epsilon_2 = 0.11(1)$ , and  $\epsilon_1 + \epsilon_2 = 0.15(2)$  for the data presented in this chapter. We also note here that the spin-imaging error associated with imperfect non-detection of doublons,  $\epsilon_d$ , which is described in Eq. 4.23, cancels out when we examine the total spin density  $\left\langle \hat{S}_{z,j} \right\rangle$ , since it is common to the measurements of the singles densities of both spin states, and therefore cancels in the subtraction required to obtain the total spin density,  $\left\langle \hat{S}_{z,j} \right\rangle = \left\langle \hat{n}_{\uparrow,j}^s - \hat{n}_{\downarrow,j}^s \right\rangle / 2$ , just like the doublon operator  $\hat{d}_j$  cancels.

### 5.3 Thermoelectric Effects

When examining dynamics in an interacting, many-body lattice system, one must be careful to take into account possible thermoelectric effects which could, for example, generate thermal gradients across the sample during the dynamics due to coupling between the different diffusive transport eigenmodes (e.g. coupling between the spin and heat modes) [122]. Such thermoelectric effects could alter the interpretation of the observed spin dynamics, and would therefore affect the determination of the transport coefficients  $D_S$  and  $\sigma_S$  from observed spin currents.

There are two potential sources which can give rise to these types of thermoelectric effects during the spin transport dynamics: the spin thermoelectric susceptibility, defined as

$$\zeta_S \equiv \left. \frac{\partial \left\langle \hat{S}_z \right\rangle}{\partial T} \right|_{\mu_\uparrow, \mu_\downarrow}, \quad (5.4)$$

and the spin Seebeck coefficient  $S_S$ . The spin thermoelectric susceptibility,  $\zeta_S$ , is a static, thermodynamic quantity which describes the magnitude of induced gradients in the total spin density,  $\nabla \langle \hat{S}_{z,j} \rangle$ , arising from the presence of temperature gradients,  $\nabla T$ . That is,  $\nabla \langle \hat{S}_{z,j} \rangle = \zeta_S \nabla T$ . For the spin-balanced system at half-filling studied in the experiment described in this chapter, the spin thermoelectric susceptibility is zero. This follows from the fact that the Fermi-Hubbard model on a square lattice is particle-hole symmetric about half-filling,  $\mu_\uparrow = \mu_\downarrow = U/2$  (see section 2.2). Specifically, under such a particle-hole transformation,  $\hat{n}_{\sigma,j} \rightarrow 1 - \hat{n}_{\sigma,j}$ . At the symmetry point, half-filling, we must have that  $\langle \hat{n}_{\sigma,j} \rangle = \langle 1 - \hat{n}_{\sigma,j} \rangle$ , since the particle-hole transformation must map this symmetry point onto itself. From this it directly follows that  $\langle \hat{n}_{\sigma,j} \rangle = 0.5$  for  $\sigma = (\uparrow, \downarrow)$  at all temperatures. Therefore, at half-filling, we have that  $\langle \hat{S}_{z,j} \rangle = \langle \hat{n}_{\uparrow,j} \rangle / 2 - \langle \hat{n}_{\downarrow,j} \rangle / 2 = 0$ , regardless of the temperature  $k_B T/t$ , meaning the spin thermoelectric susceptibility must be zero,  $\zeta_S = 0$ . The spin Seebeck coefficient,  $S_S$ , on the other hand, describes the coupling between the diffusive heat transport mode and the diffusive spin transport mode [122],

$$\begin{pmatrix} \mathbf{J}_H \\ \mathbf{J}_S \end{pmatrix} = - \begin{pmatrix} \kappa & P_S \\ S_S & \sigma_S \end{pmatrix} \begin{pmatrix} \nabla T \\ \nabla(\mu_\uparrow - \mu_\downarrow) \end{pmatrix}. \quad (5.5)$$

Here,  $\mathbf{J}_H$  represents the heat current,  $\mathbf{J}_S$  is the spin current,  $\kappa$  is the thermal conductivity,  $\sigma_S$  is the spin conductivity, and  $P_S$  is the spin Peltier coefficient. The Peltier coefficient is related to the Seebeck coefficient via the Onsager relation,  $P_S = TS_S$ . Thus, not only can a spin-dependent force, which arises from a gradient in the differential chemical potential  $(\mu_\uparrow - \mu_\downarrow)$ , generate a spin current, but so too can a gradient in the temperature. Fortunately, for the spin-balanced system at half-filling studied here, the off-diagonal elements in Eq. 5.5 must vanish, meaning  $S_S = P_S = 0$ . This follows from spin-rotational invariance at this point,  $\mu_\uparrow = \mu_\downarrow = U/2$ . That is, under a  $180^\circ$  spin-rotation, the transport behavior of the system must remain unchanged due to the symmetry between the two spin states. However, under such a rotation  $\hat{S}_z \rightarrow -\hat{S}_z$ . It therefore follows that the spin Seebeck coefficient (and therefore the Peltier coefficient) must vanish at this point, since such a rotation would reverse the

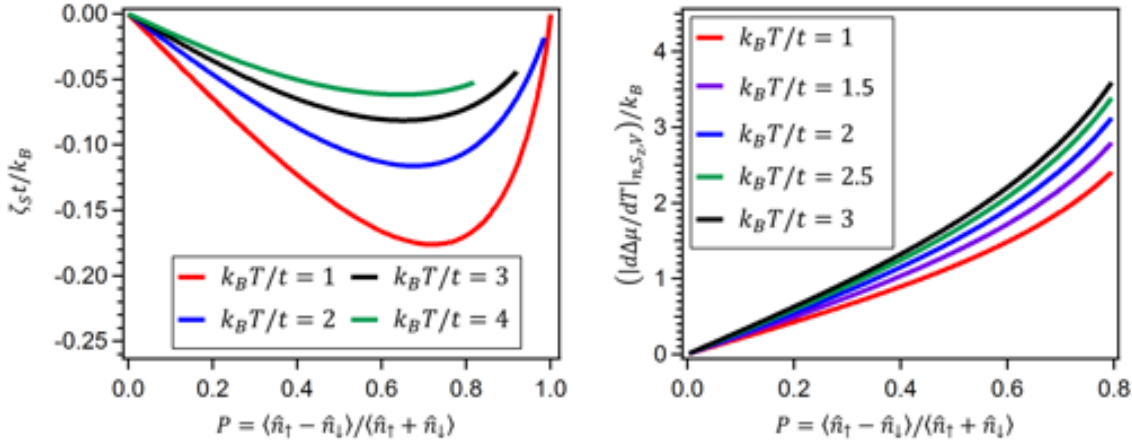


Figure 5-5: Spin thermoelectric susceptibility and spin Seebeck Coefficient versus polarization,  $(\hat{n}_\uparrow - \hat{n}_\downarrow)/(\hat{n}_\uparrow + \hat{n}_\downarrow)$ , of the half-filled 2D Fermi-Hubbard model. Shown are theoretical estimates of these quantities obtained from 9<sup>th</sup>-order NLCE calculations performed on a spin-imbalanced 2D Fermi-Hubbard system. (a) The spin thermoelectric susceptibility (Eq. 5.4) at half-filling,  $\langle \hat{n}_\uparrow + \hat{n}_\downarrow \rangle = 1$ , as a function of the sample polarization,  $P = (\hat{n}_\uparrow - \hat{n}_\downarrow)/(\hat{n}_\uparrow + \hat{n}_\downarrow)$ , for several different temperatures in the range  $1 \leq k_B T/t \leq 4$ , at  $U/t = 8$ . (b) The Kelvin formula for the spin Seebeck coefficient (Eq. 5.7) at half-filling,  $\langle \hat{n}_\uparrow + \hat{n}_\downarrow \rangle = 1$ , as a function of the sample polarization,  $P$ , for several different temperatures in the range  $1 \leq k_B T/t \leq 3$ , at  $U/t = 8$ . At low polarizations,  $0 \leq P \leq 0.2$ , both the spin thermoelectric susceptibility and the spin Seebeck coefficient are relatively small for the temperature range shown, and can typically be ignored. At larger polarizations, however, these thermoelectric effects can play a significant role in determining the spin transport properties of the system. The plots shown here are generated using spin-imbalanced NLCE data produced for [164].

sign of the spin current, but would leave the Seebeck coefficient and temperature gradient term unchanged. In other words, because there is nothing to distinguish between the two spin states, there is no way for the system to know which direction the spin current should flow in the presence of a temperature gradient. Thus, because both  $\zeta_S$  and  $S_S$  are zero, we can safely ignore all thermoelectric effects for the spin-balanced system at half-filling. This assumes, however, that all experiments are performed in the linear-response regime, so that  $\zeta_S$  and  $S_S$  both remain zero to leading order, even in the presence of small system perturbations.

These arguments break down, however, as soon as the system is no longer spin-balanced, even if it is half-filled,  $\langle \hat{n}_\uparrow + \hat{n}_\downarrow \rangle = 1$ . To estimate the magnitude of these thermoelectric effects in the presence of finite spin-imbalance, we can examine both

the spin thermoelectric susceptibility, Eq. 5.4, and the spin Seebeck coefficient  $S_S$  at half-filling,  $\langle \hat{n}_\uparrow + \hat{n}_\downarrow \rangle = 1$ , and non-zero polarization, defined as,

$$P \equiv \left\langle \frac{\hat{n}_\uparrow - \hat{n}_\downarrow}{\hat{n}_\uparrow + \hat{n}_\downarrow} \right\rangle. \quad (5.6)$$

Because  $\zeta_S$  is a thermodynamic quantity, it can be calculated using numerical techniques such as NLCE. Fig. 5-5 shows the NLCE predictions for  $\zeta_S$  at  $U/t = 8$  and half-filling,  $\mu_{avg} = (\mu_\uparrow + \mu_\downarrow)/2 = U/2$ , as a function of the polarization  $P$  of the sample, for several different temperatures,  $1 \leq k_B T/t \leq 4$ . At the lowest temperature shown here,  $k_B T/t = 1$ , and for polarizations  $P < 0.2$ , the magnitude of the spin thermoelectric susceptibility is small,  $|\zeta_S t/k_B| < 0.064$ . That is, in order to generate a small spin density gradient,  $\nabla \langle \hat{S}_z \rangle$ , of strength  $0.01a^{-1}$ , where  $a$  is the lattice spacing, one would require a temperature gradient  $k_B \nabla T > 0.16ta^{-1}$ , which is an extremely large temperature change between neighboring sites, at least in the sense that  $0.16t$  is not much smaller than the system temperature  $k_B T = t$ . Thus, at  $U/t = 8$ ,  $\langle \hat{n}_\uparrow + \hat{n}_\downarrow \rangle = 1$ , and at typical temperatures achieved in our experiment, the spin thermoelectric susceptibility can be safely ignored for small sample polarizations,  $P < 0.2$ . This is good news for future experiments which may want to explore the behavior of the spin transport coefficients  $D_S$  and  $\sigma_S$  at finite spin-imbalance (see section 5.5). Estimating the spin Seebeck coefficient  $S_S$  with finite spin-imbalance, on the other hand, is not quite as straight forward. There are several approximate formulas for  $S_S$ , however, which allow one to roughly estimate the magnitude of this coefficient, called the Mott-Heikes approximation [175, 208] and the Kelvin formula [182, 11, 126]. The Kelvin formula, for example, approximates  $S_S$  by expressing it in terms of thermodynamic quantities, which can be calculated using numerical techniques such as NLCE,

$$|S_{S,Kelvin}| = \left( \frac{\partial(\mu_\uparrow - \mu_\downarrow)}{\partial T} \right)_{n,S_z,V}, \quad (5.7)$$

where  $\mu_\uparrow - \mu_\downarrow = \Delta\mu$  is the differential chemical potential. Fig. 5-5 shows the NLCE predictions for this quantity, Eq. 5.7, at  $U/t = 8$  and half-filling,  $\mu_{avg} = (\mu_\uparrow +$

$\mu_\downarrow)/2 = U/2$ , as a function of the polarization  $P$  of the sample, for several different temperatures,  $1 \leq k_B T/t \leq 3$ . For sufficiently small sample polarizations  $P$ , this quantity is negligible, and approaches zero at zero polarization, as expected. However, as the polarization increases, this quantity can become significant, and must be taken into account if it is comparable in strength to the corresponding spin conductivity at the same  $U/t$ , total density, and polarization. The calculations shown in this figure are provided as a reference for future transport experiments whose goal is to explore the effects of finite spin imbalance (see section 5.5). A discussion of diffusive transport phenomena in the presence of thermoelectric couplings can be found in [91].

## 5.4 Results

In this section, we discuss the results of our experimental study of spin transport in the 2D Fermi-Hubbard model using a Mott insulator of spin-balanced ultracold fermions. This system is realized using  $^{40}\text{K}$  atoms in a square optical lattice, which are also confined by a box potential projected onto the 2D plane of atoms using a DMD. We apply the box potential to ensure that the system is closed, so that no atoms can escape or enter the system during the dynamics, which means the density within the box is constant in time. A detailed description of the experimental setup can be found in sections 3.1 and 5.2. For this work, we examine the situation where the density in the box is at half-filling,  $\langle \hat{n}_\uparrow + \hat{n}_\downarrow \rangle = 1$ . At this density, when the interactions in the system are strong,  $U \gg t$ , the system is Mott-insulating, a state characterized by minimal particle fluctuations and lattice sites which are predominantly occupied by single atoms instead of holes or doublons (see sections 4.2.2 and 4.3). We pick this regime to examine spin transport for two reasons. The first is that charge transport is strongly suppressed in this regime due to the strong interactions which inhibit particle fluctuations (this is an insulating state in the traditional sense of the word). Because of this, we can isolate the transport of spin in this regime, which need not behave in the same insulating way as the charge. This is because neighboring spins can interact with each other via super-exchange, the same process which gives rise to

antiferromagnetism (and nearest-neighbor antiferromagnetic correlations) in the 2D Fermi-Hubbard model, as we discussed in detail in section 4.4. Thus, in the same spirit as the mapping to the Heisenberg model, the Mott-insulating regime of the 2D Fermi-Hubbard model suppresses charge fluctuations and charge transport, but allows for spin transport through, for example, super-exchange. The second reason we focus on the half-filled case is more a matter of practicality: near half-filling the density is reasonably uniform within the box, even in the presence of a gradient which tilts the lattice potential along one direction. This allows us to make sure that we can probe the system in the spirit of linear response, because the distribution of atoms in the tilted potential (which we use to study dynamics) acts as a small perturbation to the distribution of atoms in the flat, homogeneous potential. Away from half-filling, however, in a dilute metallic sample for instance, a small tilt of the lattice can cause all the atoms to move towards one edge of the box (see Fig. 5-6(b) for example). When this occurs, the density distribution can become very inhomogeneous, so that it no longer resembles the dilute, homogenous, un-tilted scenario, which means that probing this system in the spirit of linear response becomes challenging.

This is not the first instance of using ultracold atomic systems to study spin transport, however. In fact, the transport of spin has been previously studied in bulk systems (with no lattice) of strongly interacting Fermi gases in both 3D [213, 214, 17, 228] and 2D [128, 145], as well as in a quantum point contact [131]. In the bulk 2D and 3D cases, the spin diffusivity was found to attain the quantum limit set by  $\hbar/m$ . In essence, this is because the diffusion coefficient,  $D_S$ , scales as  $D_S \approx vl$ , where  $v$  is the average speed of particles in the gas, and  $l$  is the mean free path. For the unitary Fermi gas, the scattering length is no longer the relevant length scale, and is replaced by the thermal de Broglie wavelength,  $\lambda$ , which, in the degenerate regime, scales as  $\lambda \sim 1/k_F$ , where  $k_F$  is the Fermi wavevector. The mean free path at unitarity should thus be given by  $l \sim 1/k_F$ . The average speed  $v$ , on the other hand, is on the order of the Fermi velocity,  $\hbar k_F/m$ , for the degenerate Fermi gas. Thus, the spin diffusion coefficient of the degenerate unitary Fermi gas should scale as  $D_S \approx vl \approx \hbar/m$ . In the lattice, the particle mass  $m$  becomes the effective mass, set my the lattice

band structure. In the tight binding limit, we can write the approximate scale of this effective mass as  $m = \hbar^2/ta^2$ , where  $t$  is the tunneling amplitude and  $a$  is the lattice spacing. As we will discuss in section 5.4.2, the effective spin mass, for the purposes of spin transport in the lattice, becomes significantly larger than what one might expect from the bare effective mass,  $m = \hbar^2/ta^2$ , and scales, in the strongly interacting limit, as  $mU/t$ .

In the next sections, we will discuss our measurements of both the spin diffusion coefficient  $D_S$  and the spin conductivity  $\sigma_S$  in the half-filled, repulsive Hubbard model, as functions of the Hubbard parameters  $U/t$ . These two transport coefficients characterize the response of the system to a DC (time-independent) spin-dependent force (the analog of a voltage or electric field in condensed matter systems), which we control using an applied magnetic gradient, and are related through the Nernst-Einstein equation,

$$\sigma_S = D_S \chi, \quad (5.8)$$

where  $\chi$  represents the uniform spin susceptibility. This equation gives us two ways to measure the spin conductivity of the system. We can measure the conductivity directly, for instance, by applying a spin-dependent force to a homogeneous Mott insulator, and observing the resulting spin current as a function of the Hubbard parameters  $U/t$  (section 5.4.4). Or, we can measure the spin diffusion coefficient  $D_S$ , as well as the uniform spin susceptibility  $\chi$ , which is a thermodynamic, equilibrium property of the system, and then make use of Eq. 5.8 to obtain an independent measure of the spin conductivity. To measure the spin diffusion coefficient, we can initialize the system with an inhomogeneous spin density distribution,  $\langle \hat{S}_{z,j} \rangle$ , to perturb the system slightly from its equilibrium distribution in a homogeneous system. Then, we could let this perturbation relax, in the absence of any spin-dependent force, in order to observe the resulting spin current in the system, and obtain the spin diffusivity from this current. Given Eq. 5.8, both methods of measuring the spin conductivity of the system should agree (and they will, as we will show subsequently), assuming that we are truly probing the system in linear response.

The technique we use in this experiment to create the spin-dependent force necessary to generate spin currents in the lattice is to apply a magnetic gradient, and to use hyperfine states of  $^{40}\text{K}$  with different magnetic moments. Because of this differential magnetic moment, the two spin states observe different potential landscapes in the presence of the magnetic gradient, which results in a differential (or spin-dependent) force applied to the spins by the magnetic tilt of the lattice potential. We can explicitly write down the Hamiltonian which describes this Hubbard system in the presence of a magnetic gradient along one direction,

$$\hat{H} = -t \sum_{\langle i,j \rangle, \sigma} \left( \hat{c}_{\sigma,i}^\dagger \hat{c}_{\sigma,j} + h.c. \right) + U \sum_i \hat{n}_{\uparrow,i} \hat{n}_{\downarrow,i} - \mu_\uparrow \sum_i \hat{n}_{\uparrow,i} - \mu_\downarrow \sum_i \hat{n}_{\downarrow,i} \\ + \Delta_\uparrow \sum_i i_x \hat{n}_{\uparrow,i} + \Delta_\downarrow \sum_i i_x \hat{n}_{\downarrow,i}. \quad (5.9)$$

Here, we have explicitly written out the chemical potentials of both states,  $\mu_\uparrow$  and  $\mu_\downarrow$ , in anticipation of the spin-dependent effects of the magnetic gradient. The only real difference between this Hamiltonian and the usual 2D Fermi-Hubbard model on a square lattice is the presence of the  $\Delta_\uparrow$  and  $\Delta_\downarrow$  terms, which represent a linear tilt of the lattice potential along one direction (if we decide to apply the magnetic gradient), which is different for the two spin states used in the experiment. For these two linear gradient terms,  $i_x$  represents the  $x$ -coordinate of lattice site  $i$ . In writing the tilt in this way, we are simply changing the coordinate system used: in the lab, the gradient actually points along what we normally call the  $y$ -direction, or the  $y$ -lattice direction. Here, and in the remainder of this chapter, because we do not otherwise distinguish between the  $x$  and  $y$  lattice directions, we call the direction of the gradient  $-\hat{x}$  for simplicity. The resulting tilted lattice potentials that the two different spin states experience are depicted in Fig. 5-6(a). From the calibration of the magnetic gradient discussed in section 5.2.2, the tilts  $\Delta_\uparrow$  and  $\Delta_\downarrow$  that the two spins used in this experiment experience are given by  $\Delta_\uparrow/h = 41.1(8)$  Hz/site and  $\Delta_\downarrow/h = 15.4(3)$  Hz/site. In comparison, the typical interaction energy scale for our experiment is  $U/h \sim 1$  kHz, and the typical tunneling strength is  $t/h \sim 100$  Hz. In

this sense,  $\Delta_{\uparrow,\downarrow} \ll U$ , and  $\Delta_{\uparrow,\downarrow} \lesssim t$  over the range of Hubbard parameters explored here, which is why we can think of the gradient as a relatively small perturbation to the otherwise homogeneous system.

### 5.4.1 Equilibrium Properties of the Tilted Potential

Before we discuss our measurements of the spin diffusion coefficient and the spin conductivity (see sections 5.4.2 and 5.4.4), it is worth understanding and exploring the equilibrium behavior of the 2D Fermi-Hubbard model at half-filling in the presence of the differential tilt of the lattice potential,  $\Delta_{\uparrow} - \Delta_{\downarrow} > 0$ , which is depicted in Fig. 5-6(a). Experimentally, we can realize this system by adiabatically preparing the atoms in the optical lattice simultaneously with the magnetic gradient. To understand the equilibrium distribution of atoms in the box, we can make use of the LDA to encompass the effect of the tilt into the chemical potential. That is, within the LDA, the tilted lattice leads to a local chemical potential  $\mu_{\sigma,j}$ , for  $\sigma = (\uparrow, \downarrow)$ , which decreases linearly, with a slope  $\Delta_{\sigma}$ , with increasing site-index  $i_x$  along the  $x$ -direction of the box. Thus, the local chemical potential of each spin state is highest on the left half of the box, and so one might expect that the total density of atoms,  $\langle \hat{n}_{\uparrow} + \hat{n}_{\downarrow} \rangle$  is also largest here, and that it decreases monotonically with increasing site-index  $i_x$ . For samples both above and below half-filling, this intuitive explanation applies, and the total density (or local moment) obeys this behavior. Fig. 5-6(b),(d) shows raw, site-resolved fluorescence images of the local moment of samples prepared adiabatically below half-filling and above half-filling, respectively, in the presence of the magnetic gradient. The imaged holes in the right half of the box in Fig. 5-6(b) correspond, predominantly, to actual holes, and the imaged holes (or anti-moments) in the left half of the box in Fig. 5-6(d) correspond, predominantly, to doublons. Thus, one can use single-site images of the system in a gradient, like these, to ensure the density of the system is properly set to half-filling at the center of the box, when this is required for transport: at half-filling, the density distribution must be symmetric about the center of the box. Anything slightly above half-filling results in an excess of doublons on the left half, and anything below half-filling results in an excess of holes on the right half.

At half-filling, however, the Mott gap of order  $U$  present in the strongly interacting regime,  $U \gg t$ , suppresses the formation of doublons and holes in the system, at least when  $\Delta_{\uparrow,\downarrow} \ll U$ , so that the Mott-insulating state maintains its roughly uniform distribution of singly-occupied sites, even in the presence of the tilt. In other words, the total density, and therefore the site-resolved local moment, remains homogeneous throughout the box in the presence of the tilt. Fig. 5-6(c) shows a raw, single-site fluorescence image of a Mott-insulating state at half-filling in the box, demonstrating this behavior. The average moment, acquired from several independent experimental realizations after integrating the moment along the direction orthogonal to the applied gradient, is shown in Fig. 5-6(e) as a function of the site-index  $i_x$  in the box. Like Fig. 5-6(c), this profile also demonstrates the relatively homogeneous density of singly-occupied sites in the half-filled, tilted system with strong on-site interactions. One can think of this, in some sense, as a direct demonstration of the incompressibility of the Mott insulator: its insulating character is derived from the strong on-site interactions, which reduce particle fluctuations, and also prevent the accumulation of particles on the left half of the box that would otherwise occur in a standard conducting state. This observation also opens up the intriguing possibility of using this technique to study the dielectric breakdown of the Mott-insulating state in the Hubbard model [220, 167, 166, 56, 10, 57, 244]. Specifically, if one were to increase the magnitude of the gradient so that it was comparable to the on-site interaction energy,  $\Delta_{\uparrow,\downarrow} \sim U$ , the gradient in the system could overcome the strong interactions, and one might expect this insulating behavior to break down, so that doublons would accumulate on the left half of the box, and holes would accumulate on the right half of the box.

Although, for our experimental parameters where  $\Delta_{\uparrow,\downarrow} \ll U$ , the total density remains homogeneous in the tilted potential, the density distributions of the individual spin states do not. Fig. 5-6(f),(h) shows single-site fluorescence images of the two spin states, labeled  $|\uparrow\rangle$  and  $|\downarrow\rangle$ , obtained through the spin-dependent imaging technique discussed in sections 4.4.2 and 5.2.4. These images reveal that, within the uniform background of singly occupied sites in the Mott-insulating state, the individual spin

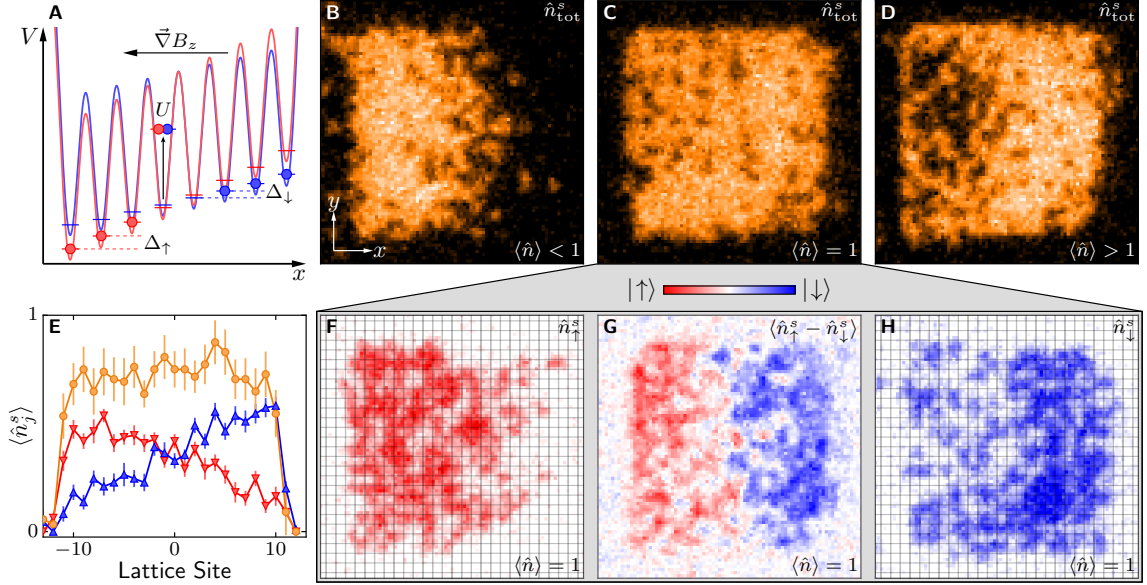


Figure 5-6: Separating the two spin states in a homogeneous 2D Fermi-Hubbard system. (a) An illustration of the tilted lattice potentials experienced by the two different spin states,  $|\uparrow\rangle$  (red) and  $|\downarrow\rangle$  (blue), in the presence of a magnetic gradient. (b),(c),(d) Single raw fluorescence images of the local moment for  $\langle \hat{n} \rangle < 1$  (b),  $\langle \hat{n} \rangle = 1$  (c), and  $\langle \hat{n} \rangle > 1$  (d), which have all been prepared in equilibrium in the tilted lattice potential (a). For (b), (c), and (d),  $t/U = 0.114(7)$ ,  $t/U = 0.067(4)$ , and  $t/U = 0.114(7)$ , respectively. (e) The average local moment,  $\langle \hat{m}_{z,j}^2 \rangle$ , (gold circles), along the direction of the gradient, along with the corresponding average singles-density of  $|\uparrow\rangle$  atoms (red triangles),  $\langle \hat{n}_{\uparrow,j}^s \rangle$ , and  $|\downarrow\rangle$  atoms (blue triangles),  $\langle \hat{n}_{\downarrow,j}^s \rangle$ , obtained from four independent experimental realizations for each quantity, at  $t/U = 0.026(2)$ . These data are not corrected for the finite spin-dependent imaging fidelity. (f) A raw fluorescence image of the  $|\uparrow\rangle$  atoms, obtained through spin-dependent imaging. (g) Six averaged fluorescence images of  $|\uparrow\rangle$  atoms minus six averaged fluorescence images of  $|\downarrow\rangle$  atoms. (h) A raw fluorescence image of the  $|\downarrow\rangle$  atoms. For (f), (g), and (h),  $t/U = 0.067(4)$  and  $\langle \hat{n} \rangle = 1$ . Figure reproduced from [164].

states have actually separated from each other spatially. Such behavior is confirmed in Fig. 5-6(g), which shows the average fluorescence image of  $|\uparrow\rangle$  atoms minus that of the  $|\downarrow\rangle$  atoms (using spin-dependent imaging), taken from six separate experimental realizations for each spin state. We can also measure the average site-resolved singles-density of each spin state,  $\langle \hat{n}_{\sigma,j}^s \rangle = \langle \hat{n}_{\sigma,j} - \hat{n}_{\uparrow,j} \hat{n}_{\downarrow,j} \rangle$ , taken from multiple experimental realizations, and then integrated along the direction orthogonal to the applied gradient to yield the spin-resolved singles density as a function of site-index along the  $x$ -direction. This is shown in Fig. 5-6(e) for both spin states,  $\sigma = (\uparrow, \downarrow)$ .

For the profiles shown in this figure, and for the spin-resolved singles density profiles,  $\langle \hat{n}_{\sigma,j}^s \rangle$ , shown in the remainder of this chapter, we typically take  $\sim 10$  site-resolved images of each spin state, and locally average the observed signal at each site in the box (similar to the site-resolved correlation analysis in section 4.4.3) to obtain a full 2D map of the average singles density of each spin state (we can also do this with the local moment) at each site. We then average this site-resolved density along the  $y$ -direction, for each value of the site-index  $j$  along the  $x$ -direction, to obtain a 1D profile of  $\langle \hat{n}_{\sigma,j}^s \rangle$  as a function of the site-index  $j$ . To simplify notation, any site-index,  $j$ , in a given quantity from this point forward will refer to the position of the site along the  $x$ -direction of the box. By imaging either the  $|\uparrow\rangle$  atoms, the  $|\downarrow\rangle$  atoms, or both through the local moment, we can access  $\langle \hat{n}_{\sigma,j}^s \rangle$  for either spin state, meaning we can locally measure  $\langle \hat{S}_{z,j} \rangle = \langle \hat{n}_{\uparrow,j}^s - \hat{n}_{\downarrow,j}^s \rangle / 2$  in the box. Or, we can access  $\langle \hat{n}_j^s \rangle \equiv \langle \hat{m}_{z,j}^2 \rangle$  using the normal single-site imaging technique to observe the total singles density in the box as a function of position along the gradient.

From the profiles of  $\langle \hat{n}_{\sigma,j}^s \rangle$  shown in Fig. 5-6(e) and the images in Fig. 5-6(f-h), it is clear the  $|\uparrow\rangle$  atoms prefer to occupy sites on the left half of the box, and the  $|\downarrow\rangle$  atoms prefer to occupy sites on the right half of the box [237]. The effect of the magnetic gradient on the Mott insulator then is to spatially separate the two spin states, while maintaining a fairly uniform background of singly-occupied sites. Intuitively this follows from the fact that  $\Delta_{\uparrow} > \Delta_{\downarrow}$ , so that the system can best lower its energy by letting the  $|\uparrow\rangle$  atoms predominantly occupy sites on the left half of the box. Although the  $|\downarrow\rangle$  atoms can also lower their energy by predominantly occupying sites on the left half of the box, the fact that those sites are better occupied by  $|\uparrow\rangle$  atoms (in the energetic sense), combined with the strong on-site interactions present in the Mott insulator, means that the  $|\downarrow\rangle$  atoms must occupy sites predominantly on the right half of the sample, even though these sites have a slightly higher potential energy.

Because the system was prepared in equilibrium in the tilted lattice potential, and because the magnetic gradient successfully pushed the two spin distributions apart in the box, we can use the fact that we can directly access the total spin density profile,

$\langle \hat{S}_{z,j} \rangle = \langle \hat{n}_{\uparrow,j}^s - \hat{n}_{\downarrow,j}^s \rangle / 2$ , from the difference of the two singles-density profiles of the two spin states, to measure the uniform spin susceptibility  $\chi$  of the unperturbed system in the spirit of linear response. This is because  $\chi$ , which represents the spin density response function and is a thermodynamic property of the system, can be written as,

$$\chi = \left( \frac{\partial \langle \hat{S}_{z,j} \rangle}{\partial \Delta\mu} \right)_{n,T}, \quad (5.10)$$

where  $\Delta\mu = \mu_{\uparrow} - \mu_{\downarrow}$  is the differential chemical potential. One can think of  $\chi$  as the response of the spin density (or the local magnetization) of the system to an applied Zeeman field, a potential which shifts the energies of the two spin states with respect to one another. This relative energy shift is incorporated into a differential chemical potential  $\Delta\mu$  between the two spins. Calculations of the uniform spin susceptibility in the half-filled 2D Fermi-Hubbard model can be found in, for example, [120], as a function of temperature  $k_B T/t$  for several values of  $U/t$ . Ultimately, this equation will allow us to access  $\chi$  directly from the total spin density profiles measured experimentally in the presence of the magnetic gradient. Specifically, using the LDA, we can convert the derivative with respect to the differential chemical potential,  $\partial/\partial\Delta\mu$ , to a spatial derivative with respect to the site-index  $j$  along the direction of the gradient:

$$\chi t a^2 = \frac{\partial \langle \hat{S}_{z,j} \rangle}{\partial j} \frac{t}{\partial \Delta\mu / \partial j}. \quad (5.11)$$

Eq. 5.11 is a dimensionless expression for the uniform spin susceptibility written in terms of experimentally measurable quantities. That is,  $t$  is calibrated from the lattice depth calibration (section 5.2.1),  $\partial \Delta\mu / \partial j$  is obtained from the LDA and is directly proportional to  $\Delta_{\uparrow} - \Delta_{\downarrow}$ , which is also calibrated independently (section 5.2.2), and  $\partial \langle \hat{S}_{z,j} \rangle / \partial j$  can be obtained by fitting the slope of the observed equilibrium spin density profile,  $\langle \hat{S}_{z,j} \rangle$ , in the presence of the gradient, using the  $\sim 7 - 10$  sites centered around the center of the box for the linear fit. By measuring each of these quantities for different values of the Hubbard parameters  $t/U$ , we can thus access  $\chi t a^2$  for the unperturbed system, in the spirit of linear response. The data we obtain

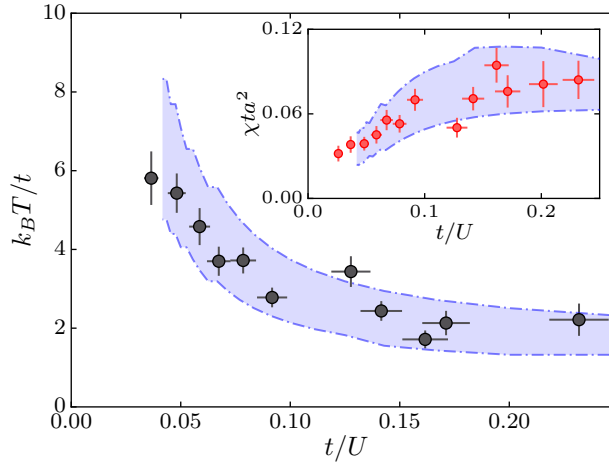


Figure 5-7: Measured temperature,  $k_B T/t$ , and uniform spin susceptibility,  $\chi ta^2$ , versus  $t/U$ . Plotted is the experimentally measured, unit-less, uniform spin susceptibility  $\chi ta^2$  (inset), shown in red circles, of the half-filled 2D Fermi-Hubbard model, as a function of the Hubbard parameters  $t/U$ . From the measured values of  $\chi ta^2$ , one can extract  $k_B T/t$  by comparing the measurements to numerical calculations, from NLCE, of  $\chi ta^2$  for different temperatures, at half-filling and the same value of  $t/U$ . The temperatures thus obtained are shown in the main figure as gray circles. The error bars in the plots (both vertical and horizontal) represent  $1\sigma$  statistical uncertainties in the measurements, where the horizontal error bars arise from the uncertainties in the calibrations of the Hubbard parameters. The blue shaded regions in both figures represent isentropic 9<sup>th</sup>-order NLCE calculations of the respective quantity versus  $t/U$ , performed at half-filling, for entropies per particle in the range  $1.0 \leq S/k_B N \leq 1.2$ , a regime where the numerics are expected to be essentially exact. From the agreement of the measured temperatures with the isentropic calculations, it follows that the experimental data is consistent with isentropic system preparation, at an entropy per particle of  $S/k_B N = 1.1(1)$ . Figure reproduced from [164].

from this measurement are shown in the inset to Fig. 5-7, as a function of  $t/U$ . Note, however, that because  $\chi$  is proportional to  $\partial \langle \hat{S}_{z,j} \rangle / \partial j$ , we must correct the measured values for the finite spin-imaging fidelity, using the correction factor  $f(1 - \epsilon_1 - \epsilon_2)$  (see section 5.2.4).

The uniform spin susceptibility at half-filling is a thermodynamic quantity which can be calculated directly, as a function of  $t/U$ , using numerical techniques like NLCE, which are performed on homogeneous systems in equilibrium. Thus, by comparing our measured values of  $\chi$  with the predictions from theory, we can use  $\chi$  as a thermometer to determine the temperature of the system as a function of  $t/U$ . This

process is performed in the same spirit as our discussion in chapter 4, where we used both the average local moment at half-filling, and the nearest-neighbor spin correlation function at half-filling as thermometers, by comparing the measured values of these quantities to calculations from theory. For the temperature range explored in the work discussed in this chapter, the NLCE calculations of  $\chi$  at half-filling are expected to be essentially exact over the full range of  $t/U$  values [120, 121, 38]. The temperatures we obtain from the uniform spin susceptibility are shown in Fig. 5-7 as a function of  $t/U$ . These temperature estimates agree with estimates based on a comparison of the average local moment measured at half-filling at the center of the box (where  $\langle \hat{n}_\uparrow \rangle = \langle \hat{n}_\downarrow \rangle = 0.5$ ) to NLCE calculations of the same quantity performed on a homogeneous system. As the data in Fig. 5-7 show, the measured system temperature is not constant as a function of  $t/U$ . This is because the preparation of the experimental system at a given value of  $t/U$  is performed at constant entropy rather than constant temperature. To see this, also shown in Fig. 5-7 are NLCE predictions for the isentropic temperature curves at half-filling, as functions of  $t/U$ , as well as isentropic curves for the uniform spin susceptibility as a function of  $t/U$ . The range of entropies per particle calculated from NLCE which are shown in this figure is  $S/k_B N = 1.0 - 1.2$ . The agreement of the measured temperatures and spin susceptibilities with these isentropic predictions provide an estimate of the experimental entropy per particle realized for this work,  $S/k_B N = 1.1(1)$ . The entropy per particle obtained from this equilibrium measurement fixes the only free parameter for a subsequent comparison of the experimentally measured values of the spin transport coefficients,  $D_S$  and  $\sigma_S$ , at half-filling, with independent theoretical estimates of these quantities (see section 5.4.5).

In addition to the form for  $\chi$  given by Eq. 5.10, the uniform spin susceptibility can also be directly related to the spin structure factor  $S_{\mathbf{q}=0}$  using the fluctuation-dissipation theorem [132], which more properly elucidates its relation to the antiferromagnetic properties of the system,

$$\chi = \frac{S_{\mathbf{q}=0}}{k_B T}, \quad (5.12)$$

where  $S_{\mathbf{q}=0}$  is directly related to the spin correlations present in the system,

$$S_{\mathbf{q}=0} = \sum_j \left( \langle \hat{S}_{z,i} \hat{S}_{z,j} \rangle - \langle \hat{S}_{z,i} \rangle \langle \hat{S}_{z,j} \rangle \right). \quad (5.13)$$

The sum here is over all sites  $j$  in the 2D lattice (including  $j = i$ ). We can write the spin structure factor explicitly in terms of the average local moment, using the fact that  $\langle \hat{m}_z^2 \rangle = 4 \langle \hat{S}_z^2 \rangle$ , and the spin correlation functions (generalized for arbitrary separation), as defined in Eq. 4.10 for the nearest-neighbor case:

$$S_{\mathbf{q}=0} = \frac{\langle \hat{m}_z^2 \rangle}{4} - |C_S(1)| + |C_S(1.4)| + \dots \quad (5.14)$$

In writing Eq. 5.14, we have already taken into account the fact that the spin correlation functions alternate sign, in an antiferromagnetic manner, according to their distance from the origin. The term  $C_S(1.4)$  written in this equation represents the next-nearest-neighbor spin correlation function (a separation of  $\sqrt{2}$  sites). At finite temperature, where the correlation functions decay with increasing distance, Eq. 5.14 can be thought of as an expansion for the spin structure factor in terms of the dominant correlation quantities, which therefore also applies to the uniform spin susceptibility. In fact, if one were to experimentally measure the site-resolved spin correlation functions for all separations at the center of the box (or in a homogeneous, un-tilted system), as well as the average local moment there, one could obtain an independent estimate of  $\chi$  to check the equivalence of these two forms for the uniform spin susceptibility. Or, assuming that both forms are equally valid (which they should be), and that the two independent experimental techniques to obtain  $\chi$  are equivalent, one could use the measurement of  $\chi$  based on Eq. 5.10, combined with the measurement of the spin structure factor, Eq. 5.14, obtained from summing all the measured spin correlations and the average local moment, to obtain a measure of the temperature of the system through Eq. 5.12 which does not require a comparison to predictions from theory.

Studying the local spin correlations in this equilibrium tilted lattice system is in

and of itself an interesting future experiment to perform. In addition to providing local information about the temperature of the system, such a measurement should reveal interesting behavior in this tilted potential. Specifically, because the magnetic gradient and the strong interactions spatially separate the distributions of the two spin states in the box, the local polarization,  $P_j \equiv \langle \hat{n}_{\uparrow,j} - \hat{n}_{\downarrow,j} \rangle / \langle \hat{n}_{\uparrow,j} + \hat{n}_{\downarrow,j} \rangle$  increases with increasing distance from the center of the box, and reaches a maximum value near the box edges. If the magnetic gradient is sufficiently strong, but still satisfies  $\Delta_{\uparrow,\downarrow} < U$ , so that the spatial separation of the two spin distributions is large enough, one should actually expect a change in the sign of the nearest-neighbor spin correlation function from negative at half-filling and zero polarization at the center of the box to positive at half-filling but large polarization near the box edges. That is, the nearest-neighbor spin correlations should change in character from antiferromagnetic to ferromagnetic as a function of position in the box, if the gradient is large enough. This situation was studied theoretically using DQMC in [18] for a tilted 2D Fermi-Hubbard system similar to the one realized experimentally here, where the antiferromagnetic to ferromagnetic change in the nearest-neighbor spin correlations was observed for large gradients. Although this is not the regime studied in the experiment described in this chapter, since we operate in the linear response regime, it is an interesting direction for future experiments. Extending such measurements of the locally resolved spin correlations to study their behavior during dynamical spin transport would also be an interesting direction for future experiments, and could reveal, for example, information about thermalization of the spin degree of freedom after a quench.

### 5.4.2 Measuring the Spin Diffusion Coefficient

The samples prepared in equilibrium in the tilted lattice potential reveal total spin density distributions  $\langle \hat{S}_{z,j} \rangle$  which have been perturbed slightly with respect to those one would obtain in a homogeneous system, where  $\langle \hat{S}_{z,j} \rangle = 0$  everywhere. Because the strength of the perturbation of the spin density profiles is controllable using the magnitude of the applied magnetic gradient, we can ensure that the density

perturbation is sufficiently small so as to be in the linear response regime. That is, by preparing a system near, but slightly away from the equilibrium distribution of the homogeneous system using a sufficiently weak magnetic gradient, we can probe the transport properties of the homogeneous system in linear response. We use this fact to measure the spin diffusion coefficient of the half-filled Hubbard model by preparing the system in equilibrium in the tilted lattice potential at a given value of  $t/U$ , so that there is a finite spatial gradient in the spin density, and then quickly turning off the magnetic gradient to initialize spin transport. We then monitor the relaxation of the initial spin density profile as a function of time after the quench, and observe as the system slowly re-establishes quasi-equilibrium in the now homogeneous potential. Fig. 5-8(a-f) shows the measured profiles of  $\langle \hat{n}_{\sigma,j}^s \rangle(\tau)$ , for  $\sigma = (\uparrow, \downarrow)$ , and  $\langle \hat{S}_{z,j} \rangle(\tau)$  at several different times  $\tau$  after the turn-off of the gradient for  $t/U = 0.23(1)$ . These profiles are obtained in the same manner as those for the equilibrium case (section 5.4.1), with typically  $\sim 10$  independent experimental realizations dedicated to imaging each spin state, and with the averaging performed in the same way. The various profiles in this figure demonstrate that the initially prepared spin density gradient relaxes, as time evolves, towards the equilibrium profile of the homogeneous box (where  $\langle \hat{S}_{z,j} \rangle = 0$  everywhere). The fact that the spin density gradient relaxes indicates that there must be a flux of spin across the center of the box. In other words, there must be a spin current  $J_S$  present at the box center during the spin density gradient decay.

In order to obtain this spin current from the observed spin density profiles,  $\langle \hat{S}_{z,j} \rangle(\tau)$ , we define a quantity called the spin density imbalance, which is defined at a time  $\tau$  after the quench of the gradient,

$$\mathcal{I}(\tau) \equiv \sum_L \langle \hat{S}_{z,j} \rangle(\tau) - \sum_R \langle \hat{S}_{z,j} \rangle(\tau). \quad (5.15)$$

Here,  $\sum_{L,R}$  represents summation over all sites on the left half ( $L$ ) and right half ( $R$ ) of the box. Essentially,  $\mathcal{I}(\tau)$  characterizes how much the spin density distribution has been pushed to one side of the box or the other, and is defined in such a way that

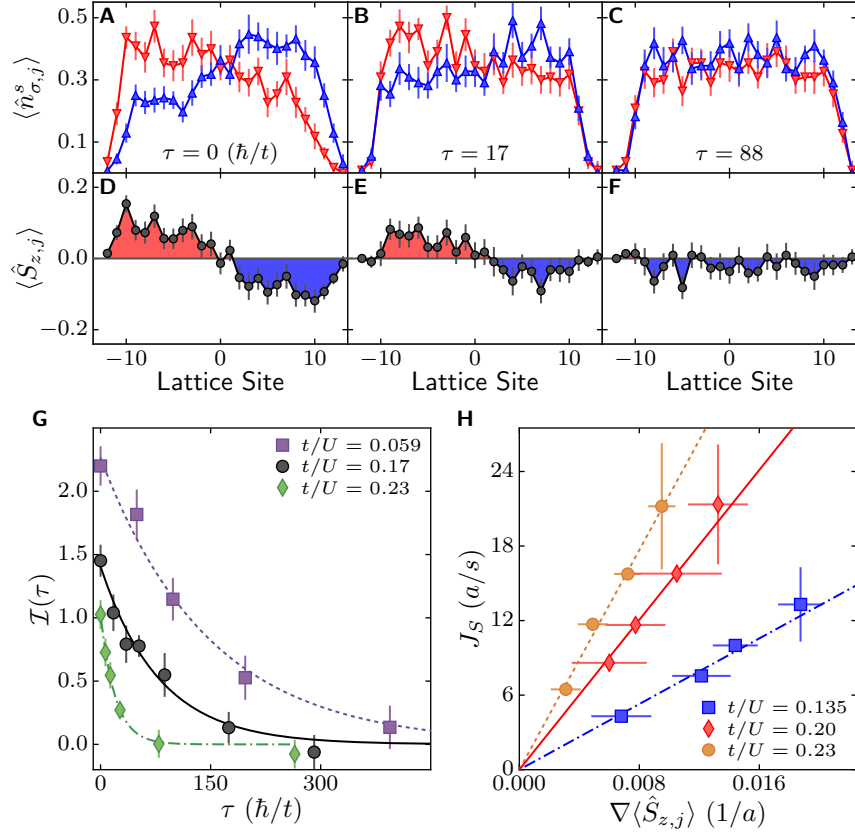


Figure 5-8: Relaxation dynamics after removing the tilt of the lattice potential. The average profiles (a-c) of  $\langle \hat{n}_{\sigma,j}^s \rangle$  (red) and  $\langle \hat{n}_{\sigma,j}^s \rangle$  (blue), and  $\langle \hat{S}_{z,j} \rangle$  (d-f), at different times  $\tau$  after suddenly removing the tilt, for  $t/U = 0.23(1)$ . (g) Time evolution of  $I(\tau)$  after the quench, for several different values of  $t/U$ , and corresponding exponential fits to the data. (h)  $J_S$  at  $j = 0$  as a function of  $\nabla \langle \hat{S}_{z,j}(\tau) \rangle$  at  $j = 0$ , for several different values of  $t/U$ , with corresponding linear fits to the data. The measurements are not corrected for the spin-dependent imaging fidelity. Figure reproduced from [164].

its time derivative determines the spin current flowing across the center of the box. Specifically, the spin current at the box center (defined as  $j = 0$ ) can be obtained via,

$$J_S(\tau) = -\frac{a}{2} \frac{d}{dt} I(t) \Big|_{\tau}, \quad (5.16)$$

where  $a$  here is the lattice spacing. To see this, one can examine the continuity equation for the spin density operator,

$$\frac{d}{d\tau} \hat{S}_{z,j} = \frac{i}{\hbar} [\hat{H}, \hat{S}_{z,j}]. \quad (5.17)$$

Plugging the Fermi-Hubbard Hamiltonian into Eq. 5.17 yields,

$$\frac{d}{d\tau} \hat{S}_{z,j} = \frac{it}{\hbar} \sum_{\langle i \rangle, \sigma} \sigma (\hat{c}_{\sigma,j}^\dagger \hat{c}_{\sigma,i} - \hat{c}_{\sigma,i}^\dagger \hat{c}_{\sigma,j}), \quad (5.18)$$

where the summation,  $\sum_{\langle i \rangle, \sigma}$ , is performed over the two nearest-neighbor site indices  $\langle i \rangle$  about site  $j$ , and the spin eigenvalues are  $\sigma = (1/2, -1/2)$  for  $|\uparrow\rangle$  and  $|\downarrow\rangle$  atoms, respectively. Taking the time derivative of both sides of Eq. 5.15 gives,

$$\begin{aligned} \frac{d\mathcal{I}}{d\tau} &= \frac{d}{d\tau} \left( \sum_{j<0} \langle \hat{S}_{z,j} \rangle - \sum_{j\geq 0} \langle \hat{S}_{z,j} \rangle \right) \\ &= \left\langle \sum_{j<0} \frac{d}{d\tau} \hat{S}_{z,j} - \sum_{j\geq 0} \frac{d}{d\tau} \hat{S}_{z,j} \right\rangle. \end{aligned} \quad (5.19)$$

Plugging the time derivative of the spin operator obtained from Eq. 5.18 into Eq. 5.19, and making use of the fact that no particles can enter or leave the box then yields,

$$\begin{aligned} \frac{d\mathcal{I}}{d\tau} &= \frac{2it}{\hbar} \left\langle \sum_{\sigma} \sigma (\hat{c}_{\sigma,-1}^\dagger \hat{c}_{\sigma,0} - \hat{c}_{\sigma,0}^\dagger \hat{c}_{\sigma,-1}) \right\rangle \\ &= -\frac{2}{a} J_S, \end{aligned} \quad (5.20)$$

where the average spin current at the center of the box is defined as,

$$J_S = \frac{-ita}{\hbar} \left\langle \sum_{\sigma} \sigma (\hat{c}_{\sigma,-1}^\dagger \hat{c}_{\sigma,0} - \hat{c}_{\sigma,0}^\dagger \hat{c}_{\sigma,-1}) \right\rangle, \quad (5.21)$$

so that we finally obtain Eq. 5.16. As it is currently defined in Eq. 5.21, the spin current has units of  $a$  per unit time. This is simply a matter of convention, and is written in these units so that the average spin current, when it is related to the spin diffusion coefficient and the spin density gradient, can be written as  $J_S = D_S \nabla \langle \hat{S}_{z,j} \rangle$ , where  $\langle \hat{S}_{z,j} \rangle$  is unit-less by convention.

Fig. 5-8(g) shows the observed time dependence of the measured spin density imbalance for several values of  $t/U$ . As this figure demonstrates, the spin density imbalance we observe exponentially decays to zero after a sufficiently long time. Such

behavior is found for all values of  $t/U$  studied here. The decay to zero imbalance is consistent with the relaxation of the spin density profiles towards the equilibrium distribution in the homogeneous box: in the homogeneous case, where the spin density is zero everywhere, one should measure zero imbalance. Because of the simple behavior of the data, we fit the spin density imbalance to an exponential decay of the form,

$$\mathcal{I}(\tau) = A_D e^{-\tau/\tau_D}, \quad (5.22)$$

where the initial amplitude  $A_D$  and the  $1/e$  decay time  $\tau_D$  are free fit parameters. Examples of these fit curves are also shown in Fig. 5-8(g). As one can see, the data are well described by this functional form of the decay. Because of this, we can use Eq. 5.22 and the fit parameters we obtain as a simple method of taking the time derivative of the spin density imbalance,  $d\mathcal{I}/d\tau$ . We have verified that this method of obtaining  $d\mathcal{I}/d\tau$  (which produces much smaller error bars) is consistent with an estimate of the time derivative obtained from various numerical derivative methods applied to the data. Thus, from the fit to the decay of the spin density imbalance, we can directly access the spin current  $J_S(\tau)$  flowing across the center of the box. As a side note, one thing which is worth pointing out about the imbalance curves in Fig. 5-8(g) is that, as the value of  $t/U$  decreases, the imbalance takes longer to decay, which is consistent with the idea that the super-exchange energy scale  $4t^2/U$ , in units of the tunneling time  $\hbar/t$ , becomes smaller, so that the rate at which spin information can diffuse in the system must become slower. Additionally, as  $t/U$  decreases, the initial amplitude of the imbalance also increases. This follows from the fact that the uniform spin susceptibility  $\chi$  increases with decreasing  $t/U$  at a fixed temperature. Thus, since from Eq. 5.11,  $\chi$ , in absolute units, is proportional to  $\partial \langle \hat{S}_{z,j} \rangle / \partial j$ ,  $\partial \langle \hat{S}_{z,j} \rangle / \partial j$  must increase with decreasing  $t/U$  at a fixed temperature and fixed gradient strength, which means the imbalance must also increase with decreasing  $t/U$  and fixed gradient strength, simply from the geometric relationship between the imbalance and the slope of the spin density profile. Although our measurements are performed at constant entropy rather than constant temperature, and from Fig. 5-7,

$\chi ta^2$  decreases marginally with decreasing  $t/U$  at fixed entropy,  $\chi$  in absolute units increases since  $t$  in absolute units decreases significantly at deeper lattice depths, which is how we change the value of  $t/U$ . The decrease in  $t$  at lower  $t/U$  values then more than compensates for the decrease in  $\chi ta^2$  with decreasing  $t/U$  at constant entropy, and therefore still leads to an increase in the imbalance at lower  $t/U$  values.

To obtain the spin diffusion coefficient from the spin current  $J_S(\tau)$ , we can examine the relationship between the spin current we obtain from  $(d\mathcal{I}/dt)|_{t=\tau}$ , and the spatial gradient in the spin density profile at the box center,  $\nabla \langle \hat{S}_{z,j=0} \rangle$ . We obtain the latter by fitting a line, using the  $\sim 7 - 10$  sites around the box center, to the spin density profile measured at each time  $\tau$  during the dynamics,  $\langle \hat{S}_{z,j} \rangle(\tau)$ , in order to extract the slope,  $(d\langle \hat{S}_{z,j} \rangle / dj)|_{j=0}$ , as a function of  $\tau$ . Since we can access both  $J_S(\tau)$  and  $\nabla \langle \hat{S}_{z,j=0} \rangle(\tau)$  at various values of  $\tau$  and at a given value of  $t/U$ , we can examine how one quantity depends on the other over a large range of values. This is shown in Fig. 5-8(h) for several values of  $t/U$ . From such plots, we observe experimentally, to within the uncertainty in the measurement, that the spin current  $J_S$  is linearly proportional to the gradient in the spin density  $\nabla \langle \hat{S}_{z,j=0} \rangle$ . A linear relationship between the spin current and the spin density gradient is in fact what one would expect to observe in a diffusive system, where the proportionality constant between the two is the spin diffusion coefficient,  $D_S$ , so that  $J_S = D_S \nabla \langle \hat{S}_{z,j=0} \rangle$ . We can independently verify that the dynamics are consistent with diffusion by varying the box size  $L$  along the direction of the initial magnetic gradient, and studying the power-law dependence of the  $1/e$  decay time  $\tau_D$  on  $L$  at a given value of  $t/U$ . This is discussed in detail in section 5.4.3, and the results are consistent with the observed linear relationship between the spin current and the spin density gradient shown in Fig. 5-8(h).

Because the dynamics are consistent with diffusive transport, meaning  $J_S = D_S \nabla \langle \hat{S}_{z,j=0} \rangle$ , we can extract  $D_S$  by measuring both the spin current and the spin density gradient at the same time  $\tau$ , and taking the ratio. Since the signal to noise ratio is best at early times,  $\tau = 0$ , where there is still a measurable slope in the spin density gradient, we measure the initial current from the slope of the spin density

imbalance decay at  $\tau = 0$ , and divide it by the initial slope of the spin density profile measured at the center of the box. Coincidentally, this is the same slope of the equilibrium profile ( $\tau = 0$ ) used to extract the uniform spin susceptibility from Eq. 5.11. From the fit function, Eq. 5.22, and the relationship between the spin current and the time derivative of the spin density imbalance, Eq. 5.16, the initial spin current is given in terms of the fit parameters by  $J_S(\tau = 0) = aA_D/2\tau_D$ . Thus, the unit-less spin diffusion coefficient,  $\hbar D_S/ta^2$ , can be expressed in terms of experimentally accessible quantities as,

$$\frac{\hbar D_S}{ta^2} = \frac{\hbar A_D}{2\tau_D t} \frac{1}{\left( \partial \langle \hat{S}_{z,j} \rangle / \partial j \right) \Big|_{j=0, \tau=0}}. \quad (5.23)$$

By measuring all of these quantities at each value of the Hubbard parameters  $t/U$ , we can obtain the spin diffusion coefficient of the half-filled, homogeneous Hubbard model as a function of  $t/U$ . The results of these measurements for  $D_S$  are shown as the gray circles in Fig. 5-9. The unit-less expression for the diffusion coefficient,  $\hbar D_S/ta^2$ , can be thought of as an expression for  $D_S$  in terms of the quantum scale for mass diffusion in a lattice,  $D_0 = \hbar/m$ , where  $m$  here represents the scale of the effective mass in a tight-binding limited band structure,  $m = \hbar^2/ta^2$ . From the data shown in Fig. 5-9, it is clear that the measured spin diffusion coefficient, in the limit of strong interactions,  $t/U \leq 0.125$ , is suppressed significantly below this quantum diffusive limit set by the bare effective mass in the lattice. Additionally, in this strongly interacting limit, we observe that  $D_S/D_0 = \hbar D_S/ta^2$  is linearly proportional to  $t/U$ , meaning  $D_S \propto t^2/U$  for  $t/U \lesssim 0.125$ . This behavior is emphasized in the inset to Fig. 5-9, which magnifies the data in this strongly interacting regime.

The fact that  $D_S \propto t^2/U$  in the strongly interacting regime can be, at least partially, understood by considering two different, but related, effects. First, in the half-filled Mott insulator, charge fluctuations are suppressed due to the strong, repulsive, on-site interactions, but neighboring spins interact antiferromagnetically with a coupling strength set by the super-exchange energy,  $J_{ex} = 4t^2/U$ . The antiferromagnetic coupling between neighboring spins gives rise to, for example, the antiferromagnetic nearest-neighbor spin correlations discussed in section 4.4.3. This regime is often

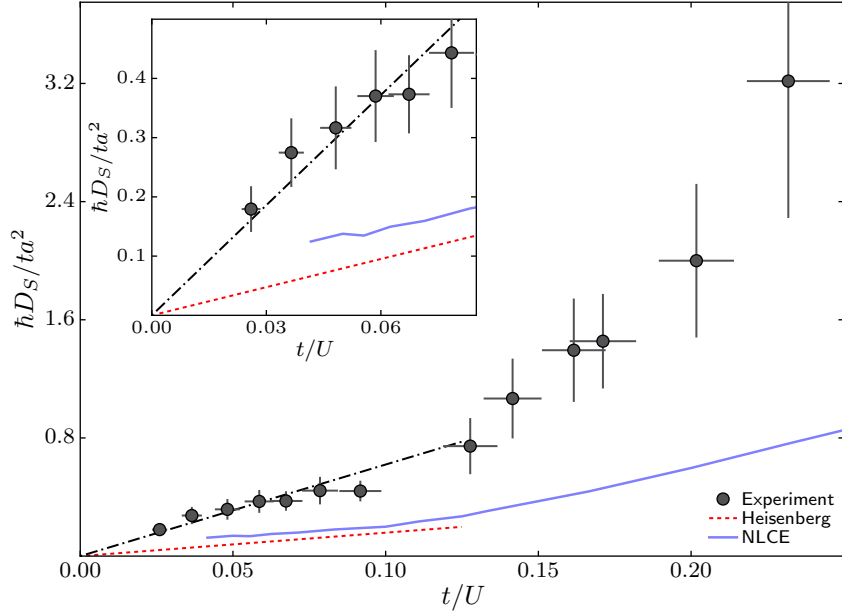


Figure 5-9:  $D_s$  of the half-filled homogeneous 2D Fermi-Hubbard model versus  $t/U$ . The gray circles represent experimental measurements of  $\hbar D_s / ta^2$  for the half-filled system, as a function of  $t/U$ , obtained by measuring the spin current resulting from the release of an initially equilibrated, inhomogeneous spin density distribution, into a homogeneous lattice potential (Eq. 5.23). The vertical and horizontal error bars represent the  $1\sigma$  statistical uncertainty in the measurements and the calibrations of  $t/U$ , respectively. The black dot-dashed line is a linear fit to the data points satisfying  $t/U < 0.09$ , where the offset is fixed to zero. The dashed red line is a prediction for the spin diffusion coefficient of the 2D Heisenberg model at high temperatures (Eq. 5.30),  $k_B T \gg 4t^2/U$ , and the blue solid line is an estimate of  $\hbar D_s / ta^2$  obtained from isentropic 8<sup>th</sup>-order NLCE calculations of real-time spin current-current correlation functions (Fig. 5-14) for the 2D Fermi-Hubbard model, at an entropy per particle of  $1.1k_B$  (see section 5.4.5). The inset is a magnified view of the data in the strongly interacting regime, with  $t/U < 0.09$ . Figure reproduced from [164].

called the Heisenberg limit of the half-filled Fermi-Hubbard model, due to a mapping between the isotropic Heisenberg and the Hubbard models which exists in this limit. Under this mapping, the charge degree of freedom is projected out, leaving an effective Hamiltonian describing the spin degree of freedom, the isotropic Heisenberg model, where neighboring spins interact with coupling  $J_{ex}$  [54],

$$H = \frac{4t^2}{U} \sum_{\langle i,j \rangle} \mathbf{S}_i \cdot \mathbf{S}_j. \quad (5.24)$$

Because the only energy scale for the spin interactions in this limit is the exchange coupling  $J_{ex}$ , the effective mass for spin must be set by  $J_{ex}$  rather than by  $t$ , which determines the lattice effective mass  $m = \hbar^2/ta^2$ . Thus, we can consider the effective spin mass,  $m_S \sim \hbar^2/J_{ex}a^2 \sim mU/t$  [95], which is significantly larger than the bare lattice effective mass for  $U \gg t$ . We can then examine the bound for quantum limited spin diffusion,  $D_S \sim \hbar/m_S$ , set by the spin mass, which gives  $D_S \sim t^2/U$ , the scaling we expected due to super-exchange, and the scaling we observe experimentally. There is a second effect, however, that can also give rise to the same  $t^2/U$  scaling, and which can increase the rate of spin diffusion in the system, the presence of doublon-hole fluctuations in the 2D Fermi-Hubbard model which are not captured by the Heisenberg picture. These fluctuations arise from states with energy greater than  $U$  [127], and can arise from both quantum and thermal processes. The quantum doublon-hole fluctuations arise from the admixture of correlated doublon-hole pairs into the wave function at finite values of  $U/t$ , and are ultimately connected to the effective antiferromagnetic super-exchange interactions between neighboring spins. These correlated doublon-hole pairs at half-filling give rise to, for example, the bunching of anti-moments in this regime, which we previously observed experimentally, and which we discussed in section 4.4.3. Doublon-hole fluctuations can also arise from thermal processes, where the finite temperature of the system can thermally excite doublons with energy  $U$ , which simultaneously leaves behind a hole in the process at half-filling. We explored the effects of temperature on the generation of doublons and holes in the Mott-insulating regime in section 4.3.4, where we observed that even temperatures of  $k_B T/U \sim 0.3 - 0.5$  can generate significant thermal doublon-hole excitations in the system. Because we operate, in this experiment, at finite values of  $t/U$  and at finite temperature ( $S/k_B N = 1.1(1)$ ), both sources can have a significant effect on the system. Specifically, the presence of a finite density of doublons and holes in the system can increase the rate of spin diffusion relative to what one would expect from super-exchange alone. That is, a spin can move directly to a neighboring site which is empty because there is no repulsive interaction energy cost incurred by the presence of an opposite spin atom, or Pauli blocking due to a

same spin atom. In the case of a doublon next to a singly-occupied site of either spin, the two can trade places resonantly without incurring an energy cost or experiencing Pauli. Spins can thus move directly through both holes and doublons at a rate set by the tunneling strength  $t$ , which is much faster than the super-exchange rate set by  $J_{ex}$ . However, in considering the impact of these doublon-hole fluctuations on the diffusion coefficient, one must consider their relative contribution, which is set by the amplitude with which these states are admixed into the wave function of the system, that itself is proportional to  $t/U$  in the strongly interacting regime. The overall scaling of the contribution of these quantum and thermal doublon-hole fluctuations to the spin diffusion coefficient in the strongly interacting limit is therefore also given by  $t^2/U$ , just like the contribution from super-exchange. At weaker interactions, on the other hand, outside of the strongly interacting regime,  $t/U > 0.125$ , Fig. 5-9 shows that the experimental spin diffusion coefficient  $D_S/D_0$  increases faster with increasing  $t/U$  than one would expect from this initial linear scaling. This can be due, in part, to the relative increase in the importance of other energy scales besides  $J_{ex}$  which occurs when  $t$  is no longer much smaller than  $U$ , and the system becomes more metallic and less Mott-insulating.

We can obtain a quantitative measure of the linear behavior of the spin diffusion coefficient,  $D_S/D_0$ , at  $t/U < 0.125$  and at our experimental entropy per particle,  $S/k_B N = 1.1(1)$ , by fitting the data in this regime to a line. For a fit constrained to go to  $D_S/D_0 = 0$  at  $t/U = 0$ , we obtain  $\hbar D_S = 6.2(5)a^2t^2/U$ . If we leave the offset in the linear fit as a free parameter, we obtain a slope of  $4.9(1.4)$  for the dependence of  $D_S/D_0$  on  $t/U$ , which is consistent with the zero-offset slope,  $6.2(5)$ , to within the experimental uncertainty in the fit parameter. However, in this case the fit yields a non-zero offset of  $D_S/D_0 \approx 0.07$  at  $t/U = 0$ . There are two potential reasons for measuring such a non-zero offset. The first is technical, and is due to a finite heating rate of the system in the optical lattice. Because the dynamics become very slow, in absolute units of time, in the  $t/U \rightarrow 0$  limit, the effects of lattice heating can become non-negligible in this regime. For example, in the  $t/U \rightarrow 0$  limit, where the super-exchange coupling also goes to zero, meaning

the timescales for the dynamics ( $\tau_D$  for instance) should become extremely long, the finite heating rate increases the temperature of the system as a function of time, which reduces the uniform spin susceptibility and leads to an effective decay of the spin density imbalance in the system (even in the absence of dynamics initiated by turning off the gradient). This leads to a shorter decay time  $\tau_D$  than one might expect physically in this regime. In fact, because heating can cause effective decay of the observed spin density imbalance, even when spin dynamics are absent, this can lead to a finite, non-zero, observed diffusion coefficient  $D_S$  at  $t/U = 0$ . We discuss the effects of lattice heating in more detail in section 5.4.6, where we find that it limits the lowest value of  $t/U$  we can reliably study in the experiment. A second, more physical, potential source of the non-zero offset in  $D_S/D_0$  obtained from the linear fit is the fact that the system preparation at different values of  $t/U$  is approximately isentropic. Because of this isentropic preparation, the temperature  $k_B T/t$  increases with decreasing  $t/U$ , which increases the density of thermally excited doublons and holes. As we previously discussed, these thermal doublons and holes increase the rate of spin diffusion in the system since the spins can move around with less impediment in this case. If the increase in thermal doublon-hole fluctuations arising from the isentropic relation between  $k_B T/t$  and  $t/U$  at half-filling compensates for the reduction in quantum doublon-hole pairs caused by reducing  $t/U$ , then the density of doublons and holes at half-filling can remain non-negligible, even for strong interactions,  $U/t \gg 1$ . Fig. 5-10 shows NLCE calculations of the isentropic density of doublons,  $\langle \hat{n}_\uparrow \hat{n}_\downarrow \rangle$ , as a function of  $U/t$  for the half-filled, homogeneous 2D Fermi-Hubbard model, for entropies per particle in the range  $0.64 \leq S/k_B N \leq 1.31$ . The wiggles observed at large  $U/t$  in this curve are unphysical, and simply arise from the fact that the NLCE calculations are performed at constant temperature instead of constant entropy, and only a discrete set of temperature points are available in the NLCE data [120] (see the discussion of Fig. 4-4 in section 4.2.2). For the entropy per particle of our experimental data,  $S/k_B N = 1.1(1)$ , this figure demonstrates that the doublon density can remain significant, even at large  $U/t$ . This fact, combined with the fact that a non-zero density of doublons and holes can increase the rate of spin

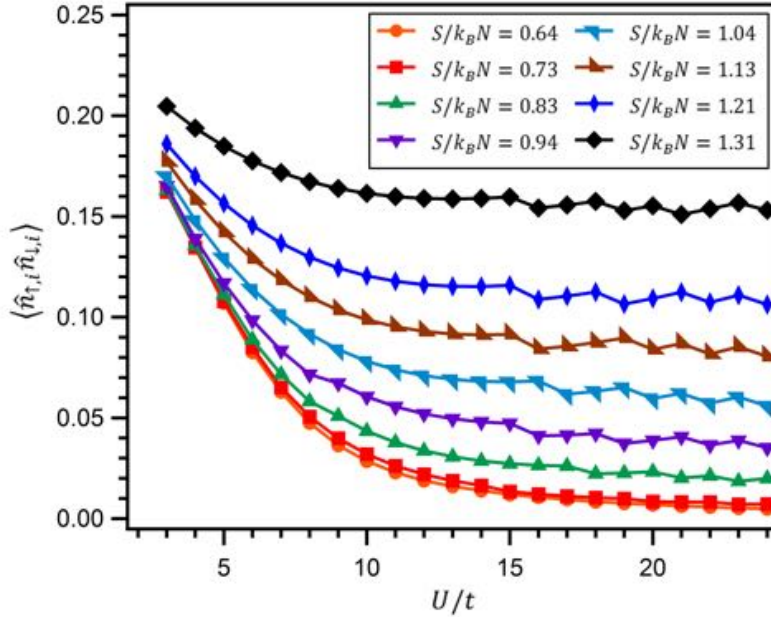


Figure 5-10: Average doublon density at half-filling and fixed entropy per particle versus  $U/t$ . The different curves represent isentropic, 9<sup>th</sup>-order NLCE predictions for the average density of doubly-occupied sites,  $\langle \hat{n}_{\uparrow,i} \hat{n}_{\downarrow,i} \rangle$ , of the 2D Fermi-Hubbard model at half-filling, as a function of the Hubbard parameters  $U/t$ , for several different entropies in the range  $0.64 \leq S/k_B N \leq 1.31$ . This entropy range represents typical values of the entropy per particle which are achieved in the experimental data discussed in this thesis (see, for example, Fig. 5-7). The variations observed at large values of  $U/t$  are artifacts which arise from the fact that the NLCE calculations are performed at fixed temperature, rather than fixed entropy, and only a discrete set of temperatures on a logarithmically uniform grid are given in the NLCE calculations. Despite this, it is clear from these calculations that, at typical experimental entropies, the density of doubly occupied sites in the system can remain non-zero, even out to relatively large values of the Hubbard parameters, e.g.  $U/t = 24$ . The curves are generated using the NLCE data provided in the supplement of [120].

diffusion in the system, ultimately also points toward a non-zero offset measured for the spin diffusion coefficient  $D_S/D_0$  at small values of  $t/U$ .

### 5.4.3 Examining the Dynamics as a Function of the System Size

We can examine the diffusive behavior of the spin dynamics more carefully by studying the functional dependence of the imbalance decay time,  $\tau_D$ , on the system size  $L$ . Specifically, for a diffusive system in the absence of a spin-dependent force, the decay

time should satisfy the relation  $\tau_D \propto L^2$ . If, in reality, the dynamics are actually sub- or super-diffusive, then the power-law scaling of the decay time with the system size  $L$  changes to  $\tau_D \propto L^\alpha$ , where  $\alpha < 2$  for super-diffusive dynamics and  $\alpha > 2$  for sub-diffusive dynamics. This follows from the continuity equation for the average spin density (written here as a function of a continuous spatial variable  $x$ , and ignoring operator notation),

$$\frac{dS_z(x, \tau)}{d\tau} = -\nabla \cdot \mathbf{J}_S, \quad (5.25)$$

and the diffusion equation  $\mathbf{J}_S = -D_S \nabla S_z(x, \tau)$ . That is, plugging the diffusion equation into Eq. 5.25 yields, for a diffusion coefficient which does not depend strongly on the spin density,

$$\frac{dS_z(x, \tau)}{d\tau} = D_S \nabla^2 S_z(x, \tau). \quad (5.26)$$

This assumption about the lack of spin density dependence of the diffusion coefficient is not necessary for this argument, but simply makes things most clear by allowing us to write Eq. 5.26. Examining the left hand side of Eq. 5.26, it is clear that the time derivative of the spin density should scale as  $1/\tau_D$ . On the other hand, the second spatial derivative on the right hand side of the equation should scale as  $1/L^2$ . Thus, for the diffusive case one should expect that  $\tau_D \propto L^2$ . For the sub- or super-diffusive cases, the second spatial derivative on the right hand side of Eq. 5.26 can be replaced, for example, by fractional spatial derivatives (i.e. no longer an integer number of spatial derivatives), which would reproduce the system size scaling expected for those cases.

To verify that the dynamics we observe are consistent with diffusion then, we can simply change the system size  $L$  using the DMD to project box potentials with variable width along the direction of the gradient, and perform the usual diffusion experiment at half-filling for these different box sizes. That is, we can prepare the system in equilibrium at a fixed value of  $t/U$  and in a fixed initial gradient, then turn the gradient off, and monitor the dynamics by measuring the total imbalance  $\mathcal{I}(\tau)$  from the average spin density profiles. Fitting the decay of the imbalance to a decaying exponential for different box sizes along the direction of the initial gradient

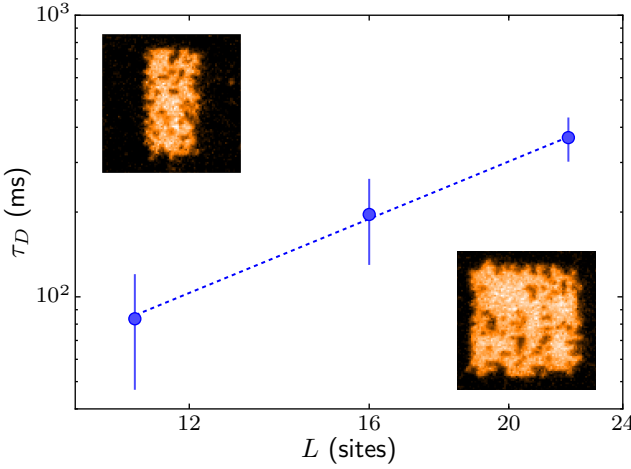


Figure 5-11: Dependence of the relaxation time,  $\tau_D$ , on the system size  $L$ . The blue circles represent experimental measurements of the  $1/e$  decay time,  $\tau_D$ , of the imbalance,  $\mathcal{I}(\tau)$ , after suddenly removing the applied magnetic gradient from an initially equilibrated, tilted Fermi-Hubbard system at half-filling, as a function of the box width  $L$  (in units of lattice sites) along the direction of the initial gradient. The errors bars are the  $1\sigma$  statistical uncertainties in the measurements, and the data are taken at the Hubbard parameters  $t/U = 0.079(5)$ . The dashed blue line represents a power-law fit to the data of the form  $\ln(\tau_D) = \alpha \ln(L) + \beta$ , where  $\alpha$  and  $\beta$  are the free parameters. The fit yields an exponent of  $\alpha = 2.1(6)$  for the power-law dependence of  $\tau_D$  on  $L$ , which is consistent with diffusive dynamics. The images in the inset to the figure are exemplary raw fluorescence images of the site-resolved local moment in the smallest ( $L = 11$ ) and largest ( $L = 22$ ) box sizes used for the data in the plot. For all values of  $L$  shown, the box width in the orthogonal direction is kept constant at 22 sites. Figure reproduced from [164].

then allows us to extract  $\tau_D$  as a function of the system size  $L$ , which is set by the box width. The results of this are shown in Fig. 5-11 on a double-logarithmic plot for  $t/U = 0.079(5)$ , along with raw images in the inset of the total singles density of the initially prepared systems at both the smallest and the largest box sizes. For this experiment, we keep the box width along the direction orthogonal to the applied gradient constant. This is done simply to provide more statistics for the averaging process, and helps improve the signal to noise ratio at small box sizes. We then fit the data shown in Fig. 5-11 to a line, whose slope determines the power-law dependence of  $\tau_D$  on  $L$ . Specifically, we use a fit of the form  $\ln(\tau_D) = \alpha \ln(L) + \beta$ , where  $\alpha$  and  $\beta$  are free parameters in the fit, and  $\alpha$  represents the desired power-law. From the fit to the data, we find that  $\alpha = 2.1(6)$ , which is consistent, to within the uncertainty in

the measurement, with diffusive behavior of the spin dynamics, where  $\alpha = 2$ . This agrees with the diffusive behavior discussed in section 5.4.2, where we observed a linear relationship between the spin current and the gradient in the spin density, as one would expect from Fick's law for diffusion.

Of course, the error bar in the measured value of  $\alpha$  is still somewhat large compared to the value of  $\alpha$  itself, and it would be an interesting experiment in and of itself to examine more scrupulously the behavior of the dynamics by measuring this quantity more precisely. One could hope, for example, to reduce the error bar in the measured value of  $\alpha$  slightly by reducing the error in each of the measured values of  $\tau_D$ . This simply requires taking more data for each value of  $L$  to average down the fit parameters to the decay of the imbalance. Practically speaking, however, based on the stability of the experiment and the amount of data this would require, this might only help to reduce the overall error in  $\alpha$  by a factor of  $\sim 2$  (which is of course still a significant gain). The more practical way to obtain a more precise fit to the slope of the data in Fig. 5-11 would be to increase the range of box sizes studied in order to increase the overall range in the measured values of  $\tau_D$ . Unfortunately, however, this is challenging in the current experimental setup because, at small values of  $L$ , the signal to noise ratio in the measurement decreases significantly due to the fact that there are simply fewer sites used to measure the imbalance from the spin density profile, which decreases the absolute magnitude of the initial imbalance for a fixed gradient strength. Thus, many more experimental realizations are required to achieve the same signal to noise ratio at small values of  $L$ , which eventually becomes impractical at sufficiently small  $L$ . Experimentally, we found this to occur around system sizes of  $L = 11$ , the smallest box size shown in Fig. 5-11. Additionally, at small system sizes, one begins to worry about finite-size effects, which also place a lower bound on the values of  $L$  one can use. At larger values of  $L$  on the other hand, such as  $L > 22$ , one must worry about inhomogeneities in the density distribution arising from the spatial variation in the intensity of the lattice beams. That is, at large enough  $L$ , the underlying harmonic confinement arising from the Gaussian nature of the lattice beams becomes significant, and has a noticeable effect on the total density. This would then

mean that the system could deviate significantly from half-filling across the size of the sample, which would affect the interpretation of the results. Experimentally, we found, at the lattice depth corresponding to  $t/U = 0.079(5)$ , that this occurs around  $L = 25$ , where we observed significant curvature of the total singles density due to the underlying trapping potential. Therefore, we do not consider box sizes greater than  $L = 22$  for Fig. 5-11. One could increase the maximum  $L$  that can be studied reliably by compensating for the underlying harmonic confinement of the lattice using a correctly calibrated anti-confining potential that is projected onto the atoms in the box using the DMD. This would flatten out the potential in the center of the box, and would allow one to access box sizes  $L > 22$ . Such trap shaping was not done for the data discussed in this chapter, but is certainly possible in future work.

#### 5.4.4 Measurement of the Conductivity

To measure the spin conductivity,  $\sigma_S$ , we can make use of the Nernst-Einstein equation, Eq. 5.8, which relates  $\sigma_S$  to the uniform spin susceptibility, which we measured in Fig. 5-7, and the spin diffusion coefficient, which we measured in Fig. 5-9. Multiplying the results of these two measurements thus gives us an estimate of  $\sigma_S$  for the half-filled Fermi-Hubbard model, as a function of  $t/U$ . However, we can actually perform an additional experiment to measure  $\sigma_S$  directly, and compare the result with what we would obtain from Eq. 5.8 and the results of sections 5.4.1 and 5.4.2. Specifically, rather than adiabatically preparing the atoms in the optical lattice simultaneously with the magnetic gradient, we can prepare instead an initial, equilibrium, homogeneous system of atoms in the lattice by leaving the magnetic gradient turned off during the preparation process. In this situation, the initial spin density profile,  $\langle \hat{S}_{z,j} \rangle (\tau = 0)$ , is homogeneous, so that the initial spin density gradient is zero,  $\nabla \langle \hat{S}_{z,j} \rangle (\tau = 0) = 0$ . We can then initiate spin transport in this configuration by quickly switching on the magnetic gradient at time  $\tau = 0$ . Because the dynamics in this conductivity experiment occur in the presence of a spin-dependent force arising from the magnetic gradient, the spin current at a given time  $\tau$  is no longer purely

determined by the diffusive contribution,  $-D_S \nabla \langle \hat{S}_{z,j} \rangle$ , but one must take into account the spin-analog of Ohm's law, which typically relates an induced charge current to an applied electric field via the charge conductivity. In the spin case, the analog of the applied electric field is the DC spin-dependent force,  $F_S \equiv -\frac{1}{a} (\Delta_\uparrow - \Delta_\downarrow) \hat{x}$ , so that the total current at time  $\tau \geq 0$  is given by  $J_S(\tau) = -D_S \nabla \langle \hat{S}_{z,j} \rangle + \sigma_S F_S$ . At early times,  $\tau \sim 0$ , however, when the system has not had time to respond to the applied spin-dependent force, and the spin density gradient remains negligible, the spin current is determined strictly by the spin conductivity and the applied force,  $J_S(\tau \sim 0) \approx \sigma_S F_S$ . Therefore, by measuring the initial spin current induced at the center of the box through the time derivative of the spin density imbalance,  $d\mathcal{I}/d\tau$ , similar to what we did for the diffusive measurements in section 5.4.2, we can directly obtain  $\sigma_S$ , since the spin-dependent force  $F_S$  is independently calibrated using the known values of  $\Delta_\uparrow - \Delta_\downarrow$ .

To measure the initial spin current,  $J_S(\tau = 0)$ , we measure the spin density imbalance  $\mathcal{I}(\tau)$  at various times  $\tau$  after the turn-on of the magnetic gradient using the spin density profiles  $\langle \hat{S}_{z,j} \rangle(\tau)$ . Because the initial spin-density profile is homogeneous, the initial imbalance is zero in the absence of a spin density gradient. As time evolves, however, the imbalance increases as the two spin distributions separate spatially in the box under the applied force. As the spin distributions separate, the spin density gradient at the center of the box increases, and the diffusive contribution to the total spin current,  $-D_S \nabla \langle \hat{S}_{z,j} \rangle$ , begins to counteract the spin current from the applied force, which means the spin density imbalance increases at a slower rate. Eventually, after a sufficiently long time, the diffusive term and the conduction term balance each other out, and the spin density imbalance saturates. This is demonstrated in Fig. 5-12, which shows the time evolution of the imbalance for several values of  $t/U$ . Like the diffusive case in Fig. 5-8(g), these data sets are well described by exponential behavior (in this case exponential saturation rather than exponential decay), so that we can fit the data to an exponential function of the form,

$$\mathcal{I}(\tau) = R_\sigma \tau_\sigma (1 - e^{-\tau/\tau_\sigma}), \quad (5.27)$$

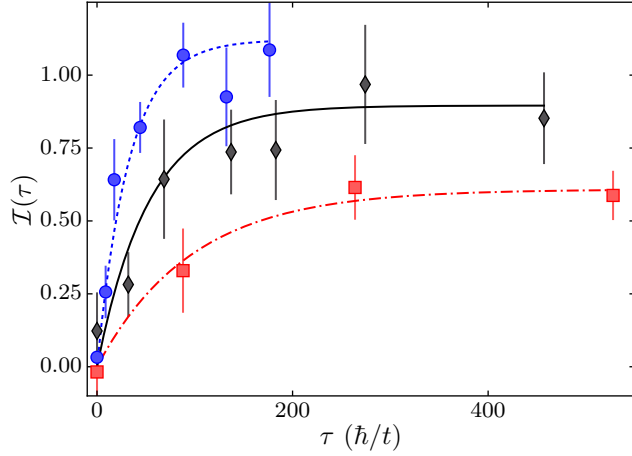


Figure 5-12: Time dependence of the imbalance in the box after quenching the magnetic gradient to a finite value from zero. Plotted is the imbalance,  $\mathcal{I}(\tau)$ , as a function of time  $\tau$  after the sudden application of a magnetic gradient to an initially homogeneous, half-filled, Fermi-Hubbard system in equilibrium. As time evolves, the imbalance, which starts near zero, begins to increase towards positive values due to the applied spin-dependent force, which generates a spin current and separates the two spin distributions in the box. Eventually, the spin current generated by this applied force is balanced out by the diffusive contribution to the spin current, arising from the non-zero gradient in the spin density which is created. When this happens, the imbalance stops increasing and eventually saturates. The red squares represent the dynamics which occur at  $t/U = 0.026(2)$ , the black diamonds represent  $t/U = 0.091(5)$ , and the blue circles represent  $t/U = 0.23(1)$ . The error bars are the  $1\sigma$  statistical uncertainties in the measurements. The dot-dashed red line, solid black line, and dotted blue line are exponentially saturating fits to the  $t/U = 0.026(2)$ ,  $t/U = 0.091(5)$ , and  $t/U = 0.23(1)$  data, respectively. Figure reproduced from [164].

in order to extract the initial slope of the imbalance,  $R_\sigma$ , and the  $1/e$  time constant for the saturation,  $\tau_\sigma$ . Examples of the results of these fits to the data are also shown in Fig. 5-12. The fitting process is carried out ultimately because it is a simpler, less noisy way of extracting the time derivative of the imbalance at time  $\tau = 0$ ,  $R_\sigma$ .

We can then use Eq. 5.16, the functional form of the fit, Eq. 5.27, and the fact that  $J_S(\tau = 0) = \sigma_S F_S$  to express the unit-less spin conductivity,  $\hbar\sigma_S$ , in terms of experimentally accessible quantities,

$$\hbar\sigma_S = \frac{\hbar R_\sigma}{2} \frac{1}{\Delta_\uparrow - \Delta_\downarrow}. \quad (5.28)$$

The fact that the spin conductivity is directly proportional to  $R_\sigma$ , which comes from

the spin density imbalance and ultimately requires the use of spin-dependent imaging, means that the experimentally measured values of  $\hbar\sigma_S$  from Eq. 5.28 must be corrected for the finite spin imaging fidelity using the correction factor  $f(1 - \epsilon_1 - \epsilon_2)$  (section 5.2.4). Interestingly, the spin diffusion coefficient  $D_S$  measured using Eq. 5.23 is insensitive to the spin imaging fidelity. This is because both the measured value of  $A_D$  and the measured slope in the spin density,  $(\partial \langle \hat{S}_{z,j} \rangle / \partial j) \Big|_{j=0,\tau=0}$ , in Eq. 5.23 are proportional to this fidelity factor, so that in taking the ratio of the two, the correction factor cancels out.

By measuring the time-dependence of the spin density imbalance at different values of  $t/U$ , and obtaining  $R_\sigma$  from fitting the data, we can directly measure the spin conductivity of the half-filled Hubbard model as a function of the Hubbard parameters  $t/U$ . The results of these measurements are shown as red squares in Fig. 5-13. The gray circles in this figure represent the estimate of the spin conductivity made using the Nernst-Einstein equation, Eq. 5.8, and the experimental measurements of the spin diffusion coefficient and the uniform spin susceptibility. We can explicitly write the spin conductivity using the Nernst-Einstein equation, Eq. 5.8, in terms of the experimentally measured quantities that were used to obtain  $D_S$  and  $\chi$  in Eqs. 5.23 and 5.11, respectively,

$$\hbar\sigma_S = \frac{\hbar A_D}{2\tau_D} \frac{1}{\Delta_\uparrow - \Delta_\downarrow}. \quad (5.29)$$

Upon examination of the data in Fig. 5-13, it is clear that the two independent methods of measuring  $\sigma_S$  agree with each other over the full range of  $t/U$  values explored, to within the experimental uncertainty in the measurements. Although this is not unexpected because of the Nernst-Einstein equation, it is at least a good experimental check that the system behaves as we expect, and that we are truly probing the system in linear response. We have also independently verified that we operate in the linear response regime by reducing the magnitude of the applied gradient by a factor of two for the measurement of the diffusion coefficient. This reduced the observed signal proportionally, but gave the same result for the value of  $D_S$  at the same  $t/U$ , to within the experimental uncertainty.

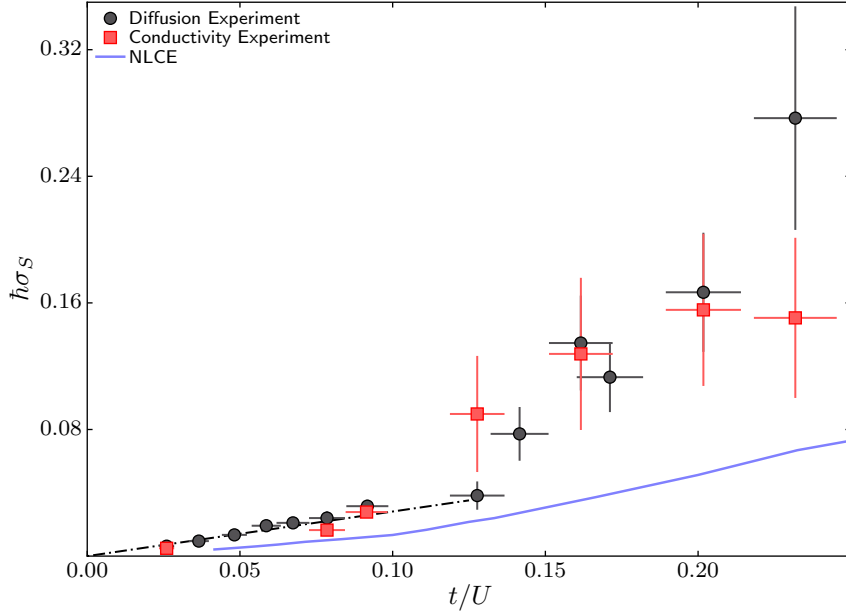


Figure 5-13: DC spin conductivity of the half-filled 2D Fermi-Hubbard model versus  $t/U$ . The experimentally measured values of  $\hbar\sigma_s$  at half-filling, obtained by applying a magnetic gradient to an initially homogeneous system in equilibrium and measuring the initial spin current, are shown in red squares. The gray circles represent a second experimental measurement of  $\hbar\sigma_s$  using the Nernst-Einstein relation (Eq. 5.8), the  $D_s$  data shown in Fig. 5-9, and the  $\chi$  data from Fig. 5-7. The black dot-dashed line is a linear fit to the data points (both gray and red) satisfying  $t/U < 0.09$ . The error bars, both vertical and horizontal, are the  $1\sigma$  statistical uncertainty of the measurements, where the horizontal error bars arise from the uncertainty in the calibration of the Hubbard parameters. The experimental data have been corrected for the finite spin-dependent imaging fidelity (see section 5.2.4). The blue solid line represents a prediction for  $\hbar\sigma_s$  obtained from isentropic, 8<sup>th</sup>-order NLCE calculations of the real-time spin current-current correlation functions for the 2D Fermi-Hubbard model (Fig. 5-14) at an entropy per particle of  $1.1k_B$ . Figure reproduced from [164].

The observed spin conductivity,  $\hbar\sigma_s$ , of the half-filled Hubbard model shown in Fig. 5-13 is linear in  $t/U$  in the strongly interacting regime,  $t/U < 0.125$ . We can fit the data in this region ( $t/U < 0.09$ ) to a line, where the offset is constrained to be zero at  $t/U = 0$ , which yields a spin conductivity of the form,  $\hbar\sigma_s = 0.28(2)t/U$ . Leaving the offset as a free parameter in the fit in this case does not change the value of the slope we obtain. We can understand the linear dependence of  $\hbar\sigma_s$  on  $t/U$  in several ways. From the Nernst-Einstein equation, for example,  $\sigma_s = D_s\chi$ . In the strongly interacting limit,  $D_s \sim t^2/U$ , as we discussed in section 5.4.2. On the other hand,  $\chi$

in this limit scales as  $\chi \sim 1/t$ , so that  $\sigma_S = D_S \chi \sim t/U$ . We can also understand this scaling from the Drude form of the conductivity,  $\sigma = ne^2\tau/m$ , where  $n$  is the total density of atoms,  $e = 1$  is the elementary charge of our neutral atom system, and  $\tau^{-1}$  is the scattering rate for particles undergoing transport. For a degenerate electron gas, the maximum scattering rate is set by the Fermi energy,  $\tau^{-1} = E_F/\hbar$ . In 2D, however,  $E_F \sim \hbar^2 n/m$ , so that,  $\tau^{-1} \sim \hbar n/m$  and therefore  $\sigma = n\tau/m \sim 1/\hbar$ . This limit on the conductivity,  $\hbar\sigma \sim 1$ , is often called the Mott-Ioffe-Regel (MIR) limit for charge conductance in a metal [107, 158], and arises when the mean-free-path for collisions between quasi-particles reaches the minimum possible value set by the lattice spacing  $a$ . In comparison, the spin conductivity of the half-filled Hubbard model we measure experimentally is suppressed significantly below what one would expect for the MIR limit based on the Drude formalism. However, if we replace the bare effective lattice mass  $m$  in the Drude equation for the conductivity with the heavier effective spin mass,  $m_S \sim mU/t$  (see section 5.4.2), then, using the previous arguments, where  $\tau^{-1} = E_F/\hbar \sim \hbar n/m$  (the lattice mass in the Fermi energy remains unchanged), one obtains,  $\hbar\sigma_S \sim t/U$ , and recovers the scaling we observe experimentally. The fact that the observed spin conductivity is suppressed below the MIR limit in the strongly interacting regime is not so surprising in the end, because in this limit, the notion of quasi-particles is not well defined, meaning the Drude-Boltzmann theory typically used to derive the MIR limit is not applicable.

Examining Fig. 5-13, as we increase the value of  $t/U$  in the system, and exit the strongly interacting regime where  $\hbar\sigma_S = 0.28(2)t/U$ , we find that the spin conductivity increases faster than this initial linear scaling would predict. This behavior is analogous to the behavior of the spin diffusion coefficient for  $t/U > 0.125$  (see Fig. 5-9), and arises for the same reasons: as  $t/U$  increases beyond the strongly interacting limit, the system becomes more metallic and less Mott-insulating, and the super-exchange coupling is no longer the relevant energy scale which governs the dynamics and the effective spin mass  $m_S$ . Thus, one should no longer expect the conductivity to be linear in  $t/U$  in this regime, and this is what we observe in the data, as an enhancement in the spin conductivity beyond the strongly interacting prediction.

### 5.4.5 Comparing the Experimental Data to Theory

We can gain some intuition about the behavior of the spin transport coefficients of the half-filled Hubbard model by comparing our experimental results for these quantities as functions of  $t/U$  with predictions from theory. For the spin diffusion coefficient  $D_S$ , for example, we understand physically that  $D_S$  should be proportional to  $t^2/U$  in the strongly interacting limit,  $t/U \ll 1$ , as we discussed in section 5.4.2, but it is unclear how much of the observed spin diffusion in this regime comes from nearest-neighbor spin interactions arising from super-exchange, versus diffusion arising from doublon-hole-assisted tunneling, for example. To isolate the amount of spin diffusion arising from nearest-neighbor spin interactions, we can compare our experimental results with a prediction for the spin diffusion coefficient of the 2D Heisenberg model at "infinite" temperature, where  $k_B T \gg J_{ex} = 4t^2/U$ . For the temperatures examined in this experiment, corresponding to an entropy per particle of  $S/k_B N = 1.1(1)$  (see Fig. 5-7), this is not such an unreasonable assumption. The analytic leading order result for the spin diffusion coefficient of the 2D Heisenberg model in a high-temperature series expansion in powers of  $J_{ex}/k_B T$  is given by [19, 212, 24],

$$\hbar D_S = 4\sqrt{\frac{\pi}{20}} \frac{a^2 t^2}{U} \approx 1.6 \frac{a^2 t^2}{U}. \quad (5.30)$$

The dashed red line in Fig. 5-9 compares this high-temperature Heisenberg prediction directly with our experimental data for  $D_S/D_0$ . The next leading term in the expansion is suppressed relative to Eq. 5.30 by a factor of  $\frac{J_{ex}}{k_B T} = 4 \frac{t/U}{k_B T/t}$  [212], which we can ignore in the  $t/U \ll 1$  limit. This Heisenberg result for  $D_S$ , Eq. 5.30, predicts the correct linear dependence of  $\hbar D_S/ta^2$  on  $t/U$  that we observe experimentally in the strongly interacting regime, but predicts a slope for this dependence of  $\approx 1.6$ , which is of the same order of magnitude, but still lower than both experimentally observed slopes, 6.2(5) and 4.9(1.4), obtained from fits with the offset constrained to go to zero, and with the offset as a free parameter, respectively. This fact is not so surprising, however, since we know that the Heisenberg model only captures the effects of super-exchange between neighboring spins, and does not capture any contri-

butions from charge fluctuations in the Fermi-Hubbard model, such as spin diffusion driven by doublon-hole-assisted tunneling. Be that as it may, it does provide initial insight into the relative importance of Heisenberg physics in driving spin diffusion at our experimental temperatures in the half-filled Fermi-Hubbard model.

We can go a step further, however, beyond the high-temperature Heisenberg prediction for spin transport, and compare our experimental data with a more unbiased theoretical estimate of the spin transport coefficients in the thermodynamic limit, i.e. an estimate which does not require one to ignore the charge fluctuations of the Hubbard model. Specifically, we can compare our experimental results for  $\sigma_S$  and  $D_S$  of the half-filled Hubbard model with predictions for these quantities based on NLCE calculations [194, 223] of real-time spin current-current correlation functions. Performing numerical calculations of these correlation functions in real-time, instead of imaginary-time, allows the NLCE to avoid any issues associated with analytic-continuation of the calculations from imaginary-time, which is a necessary step to calculate dynamical quantities in other numerical techniques such as DQMC. Additionally, because the NLCE technique calculates properties of the Hubbard model directly in the thermodynamic limit, it is relatively insensitive to finite-size effects in the numerics. These aspects of the numerical technique have allowed recent studies to successfully use NLCE to examine dynamical properties of non-equilibrium systems after a quench [238, 149, 82]. However, the numerics performed for this work [164] represent one of the first applications of NLCE to the calculation of real-time correlation functions in the equilibrium 2D Fermi-Hubbard model, in order to directly extract dynamical properties of the Hamiltonian, like the transport coefficients. This is not to say that NLCE is the only technique which can be used to obtain accurate estimates of transport coefficients in the Hubbard model. In fact, two other techniques, the finite-temperature Lanczos method (FTLM) [109, 125] and dynamical mean-field theory (DMFT) [129] were recently used in [26] to estimate the charge resistivity in the doped Hubbard model as a function of temperature,  $k_B T/t$ , at  $U/t = 7.4$ .

To access the transport coefficients, the NLCE calculates the uniform spin current-current correlation function,  $\langle J_S(\tau)J_S(0) \rangle$ , at half-filling, fixed temperature  $k_B T/t$ ,

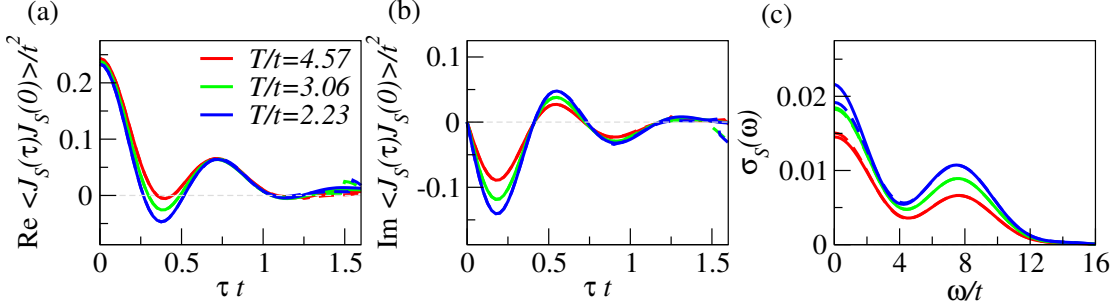


Figure 5-14: NLCE calculations of real-time spin current-current correlation functions and the AC spin conductivity. Plotted are isothermal 8<sup>th</sup>-order NLCE calculations of the half-filled 2D Fermi-Hubbard model at  $U/t = 8$ , for (a) the real-part of the real-time spin current-current correlation function,  $\text{Re} \langle J_S(\tau)J_S(0) \rangle /t^2$ , for (b) the imaginary-part of the real-time spin current-current correlation function,  $\text{Im} \langle J_S(\tau)J_S(0) \rangle /t^2$ , and for (c) the AC spin conductivity,  $\sigma_s(\omega)$ , which is obtained from the Fourier transforms of the quantities shown in (a) and (b). The different colors represent different temperatures for the calculations: red is  $k_B T/t = 4.57$ , green is  $k_B T/t = 3.06$ , and blue is  $k_B T/t = 2.23$ . The solid and dashed lines in (a) and (b) represent different re-summation methods for the numerics (Wynn and Euler, respectively [223]), which begin to disagree with each other around times of  $\tau \sim \hbar/t$ , signaling a lack of convergence in the NLCE beginning around this time. The solid and dashed lines in (c) represent calculations of  $\sigma_s(\omega)$  based on Eq. 5.31 and 5.32, respectively, which deviate from each other near the DC limit due to limited access of the numerics to finite times for the quantities in (a) and (b). Figure reproduced from [164].

and fixed  $U/t$  in the 2D Fermi-Hubbard model at equilibrium, where  $J_S$ , the spin current operator for current flowing along the  $x$ -direction in the box, is defined in Eq. 5.21, and  $\tau$  is real time. In units where  $\hbar = a = k_B = 1$ , the uniform ( $\mathbf{q} = 0$ ), AC spin conductivity,  $\sigma_S(\omega)$ , which describes the response of the spin current to an applied spin-dependent force at frequency  $\omega$  (i.e. the current response function), is directly related to the Fourier transform of the real-time spin current-current correlation function,  $\langle J_S(\tau)J_S(0) \rangle$ , via a Kubo formula [133, 134, 148, 115],

$$\text{Re } \sigma_S(\omega) = \frac{(1 - e^{-\beta\omega})}{\omega} \text{Re} \int_0^\infty d\tau e^{i\omega\tau} \langle J_S(\tau)J_S(0) \rangle, \quad (5.31)$$

where  $\beta = 1/T$ . Equivalently, the conductivity can be written as,

$$\text{Re } \sigma_S(\omega) = \frac{-2}{\omega} \text{Im} \int_0^\infty d\tau e^{i\omega\tau} \text{Im} \langle J_S(\tau)J_S(0) \rangle, \quad (5.32)$$

where the real and imaginary parts of the spin current-current correlation function are related to one another through a Kramers-Kronig relation, and the NLCE can directly calculate both as a function of  $\tau$ , at a given temperature and value of  $U/t$ . Fig. 5-14(a),(b) shows NLCE calculations of the real and imaginary parts of  $\langle J_S(\tau)J_S(0) \rangle$ , respectively, for the half-filled Hubbard model at  $U/t = 8$  and several different temperatures. From the correlation function calculations shown in this figure, one can plug the numerical data into Eqs. 5.31 or 5.32 in order to obtain the AC conductivity,  $\sigma_S(\omega)$ . The results of this process, conducted on the data in Fig. 5-14(a),(b), are shown in Fig. 5-14(c), as a representative example of the numerical calculations of  $\sigma_S(\omega)$  for several temperatures at a given  $U/t$ . To obtain the spin diffusion coefficient  $D_S$  from these calculations, one first takes the  $\omega \rightarrow 0$  limit of  $\sigma_S(\omega)$  to obtain the DC conductivity, then uses the Nernst-Einstein relation,  $\sigma_S = D_S\chi$ , where  $\chi$  is exactly calculated for the half-filled Hubbard model at the same  $U/t$  and the same temperature using an independent NLCE calculation (see section 5.4.1). At the finite temperatures examined in the current experiment, it is safe to ignore any Drude contribution to the spin conductivity [115], which occurs when there is a non-zero value of the real-time current-current correlation function at long times,  $\tau \rightarrow \infty$ . We can therefore picture the full AC conductivity  $\sigma_S(\omega)$  using just the "regular" part, which ignores the Drude weight, and is determined by Eqs. 5.31 and 5.32. Although the experiment discussed in this chapter examines only the DC conductivity (the  $\omega \rightarrow 0$  limit of Eqs. 5.31 and 5.32), the NLCE can access the full AC conductivity, since it is measured using the Fourier transform of the quantity which the numerics calculate directly, the current correlation function. The information provided for  $\omega > 0$  thus gives us an idea of the full frequency-dependent response, and is useful for future experiments aimed at measuring the AC conductivity of the Fermi-Hubbard model at half-filling (see outlook in section 5.5).

We can directly compare these NLCE estimates for the DC spin transport coefficients with our experimental measurements using the experimentally determined entropy per particle,  $S/k_B N = 1.1(1)$  (see section 5.4.1), as the only fixed parameter. The NLCE results for the spin diffusion coefficient and the spin conductivity at an en-

tropy per particle of  $S/k_B N = 1.1$  are shown as the blue curves in Figs. 5-9 and 5-13, respectively, as functions of  $t/U$ . From these figures, it is clear that the NLCE results qualitatively capture the general behavior of the experimental data as a function of  $t/U$ . That is, the numerics show the same linear scaling of both  $D_S/D_0$  and  $\hbar\sigma_S$  with  $t/U$  in the strongly interacting limit, as well as the same deviations from this initial linear scaling at higher values of  $t/U$ , outside the strongly interacting regime. However, the quantitative predictions of the numerics are systematically smaller than the experimental results for both  $D_S/D_0$  and  $\hbar\sigma_S$ . This underestimation of the transport coefficients by the numerics is potentially due to the fact that the numerics can only access the real-time spin current-current correlation function,  $\langle J_S(\tau)J_S(0) \rangle$ , up to times  $\tau \sim \hbar/t$ . For longer times, the numerical calculations no longer converge, and accurate estimates of the correlation function are no longer possible. This can be seen directly in Fig. 5-14(a),(b), where the various re-summation methods [223] used by the numerics to calculate the real and imaginary parts of  $\langle J_S(\tau)J_S(0) \rangle$  no longer agree with each other after times  $\tau \sim \hbar/t$ , indicating a lack of convergence in the NLCE. Practically speaking then, a finite cutoff time,  $\tau_{cutoff}$ , must be applied to the numerical data for  $\langle J_S(\tau)J_S(0) \rangle$ , before one can take the Fourier transform for Eqs. 5.31 and 5.32. The cutoff is chosen at a time  $\tau$  where the convergence of the numerics is still good, so that  $\tau_{cutoff} \sim \hbar/t$ . This finite cutoff time set by the tunneling strength  $t$  can lead to systematic errors when trying to estimate the transport coefficients, especially at DC, since an accurate estimate of the DC values of the Fourier transform requires knowledge of the time-dependent correlation function out to, in principle, infinite time. Additionally, due to the effects of Heisenberg physics and super-exchange interactions between neighboring spins in the strongly interacting limit, one would expect real-time spin current correlations up to times  $\tau \sim \hbar/J_{ex}$ , which can be significantly longer than the cutoff time  $\tau_{cutoff} \sim \hbar/t$ , and are therefore not captured by the numerics. Despite this fact, however, the numerics still qualitatively agree with the behavior of the experimental data, as can be seen in Figs. 5-9 and 5-13, and come within a factor of  $\sim 2$  of quantitative agreement. Because the numerics systematically miss the contributions to the transport coefficients due to cur-

rent correlations arising from super-exchange and Heisenberg physics, it is reasonable to assume that the NLCE predictions at least provide a lower bound for these quantities [164], although the actual magnitude of the systematic error is tough to estimate. Intuitively speaking for the moment, it is maybe not so unreasonable to think then that the actual theoretical value of  $D_S/D_0$  in the strongly interacting limit, for example, where we have the prediction from the Heisenberg model, is actually some combination of the Heisenberg prediction (red line in Fig. 5-9), which captures the super-exchange driven diffusion, but ignores the charge fluctuation induced diffusion, and the NLCE prediction (blue line in Fig. 5-9), which systematically underestimates the Heisenberg driven diffusion, but captures the contributions from processes related to  $t$ . Regardless of this though, it is clear that calculating these transport coefficients numerically for the 2D Fermi-Hubbard model, even at half-filling, is extremely challenging. In this sense, the experimental data represent a measurement of intrinsic properties of the Hamiltonian which are difficult to access theoretically, and therefore provide a useful benchmark for any theoretical predictions made in the future.

It is also worth noting here the finite width of the frequency-dependent conductivity  $\sigma_S(\omega)$  about  $\omega = 0$  which is observed in the NLCE predictions (Fig. 5-14). Although the observed width can arise from technical reasons, such as the finite cut-off time required for the numerics, which can lead to Fourier broadening, it can also arise from physical properties of the system, such as a finite momentum relaxation rate arising from, for example, umklapp scattering, a process where the lattice absorbs some portion of the net momentum in a collision between particles (which means momentum is not conserved in lattice systems). One can account for the existence of such a finite momentum relaxation rate by generalizing the diffusion equation  $\mathbf{J}_S = -D_S \nabla S_z(x, \tau)$ , which, as it stands on its own, inherently assumes that the presence of a spin density gradient instantaneously induces a spin current. We know, however, that a spin current should, in principle, take some finite time to equilibrate after the creation of a gradient in the spin density. For a finite momentum relaxation rate,  $\Gamma$ , then, which allows for this type of time delay between the generation of a spin density gradient and an equilibrated spin current, one simple way to generalize

the diffusion equation is [26],

$$\frac{\partial \mathbf{J}_S(x, \tau)}{\partial \tau} = -\Gamma (D_S \nabla S_z(x, \tau) + \mathbf{J}_S(x, \tau)) \quad (5.33)$$

Combining Eq. 5.33 with the continuity equation for the spin density,  $\partial S_z(x, \tau)/\partial \tau = -\nabla \cdot \mathbf{J}_S$ , then provides a closed set of differential equations for both the spin current and the spin density. To obtain an equation for the spin density alone, one can take an additional time derivative of both sides of the continuity equation, then take the spatial Fourier transform of all quantities in both the continuity equation and Eq. 5.33 to eliminate the spin current. After doing this, one arrives at a single differential equation for the spin density at momentum  $k$ ,

$$\frac{\partial^2 S_z(k, \tau)}{\partial \tau^2} + \Gamma \frac{\partial S_z(k, \tau)}{\partial \tau} + \Gamma D_S k^2 S_z(k, \tau) = 0. \quad (5.34)$$

Upon examination of this equation, it is clear that it is the same differential equation which governs the dynamics of a damped harmonic oscillator, where the oscillator damping rate is  $\Gamma/2$  and the resonance frequency is  $\omega_0 = \sqrt{\Gamma D_S} k$ . Such an equation applies to the situation where the system is not driven, so that the dynamics do not occur in the presence of a spin dependent force. This would apply, for example, to the diffusive measurements described in section 5.4.2. For the driven case, such as the conductivity measurements of section 5.4.4, one simply needs to include the spin analog of Ohm's law (the spin conductivity times the applied spin dependent force) in the quantity in parentheses on the right-hand-side of Eq. 5.33, which ends up as a driving term on the right-hand-side of Eq. 5.34. The drive can, in general, also be time-dependent. Thus, we can easily understand the behavior of the system with a finite momentum relaxation rate  $\Gamma$  using the intuition developed from the driven, damped harmonic oscillator. Specifically, in the situation where there is no drive, and the system is over-damped, meaning  $\Gamma \gg \sqrt{\Gamma D_S} k$ , one recovers the usual diffusive behavior, where the spin density perturbation decays exponentially according to the spin diffusion coefficient,  $S_z(k, \tau) \sim e^{-D_S k^2 \tau}$ , and the momentum relaxation rate drops out. Such behavior resembles, for instance, the exponential decay of the

spin density imbalance that we observe experimentally (see Fig. 5-8(g)), and is consistent with our analysis in section 5.4.2, where we observed that the system was well described by a purely diffusive model. This makes sense, because our experiment effectively operates in the over-damped limit due to the fact that we only examine very long wavelength perturbations to the spin density, corresponding to the small  $k$ , or (nearly) uniform limit. The observed diffusive behavior does not, however, preclude the observation of the finite width of the AC conductivity observed in the NLCE calculations: just like a driven, damped harmonic oscillator, the width of the response, i.e. the width of the conductivity peak, is set by the damping rate,  $\Gamma$ . Thus, in the over-damped limit where we appear to operate experimentally,  $\Gamma \gg \sqrt{\Gamma D_S} k$ , one can have a non-zero (albeit undetermined) value of the momentum relaxation rate  $\Gamma$ , which sets the finite width in the frequency dependent conductivity,  $\sigma_S(\omega)$ , while remaining completely insensitive to the actual value of  $\Gamma$  in the experimental dynamics, where it effectively drops out. A more detailed discussion of this generalized hydrodynamic description of the system is given in [26].

#### 5.4.6 Effects of Heating

Because the spin dynamics studied here occur at a rate set by the super-exchange energy  $4t^2/U$ , the time scales over which the dynamics occur, in absolute units, can get very long (on the order of seconds) at small values of  $t/U$ . It is thus necessary to verify that the dynamics we observe, and the values of the transport coefficients we obtain, are not significantly effected by heating of the sample caused by, for example, lattice intensity noise, which can occur over the time scales of the experiment (see Fig. 4-20). Specifically, we want to check that the effects of heating of the sample during the dynamics are sufficiently small that their impact on the observed transport coefficients is less than the typical respective experimental uncertainty in the measured values of  $\sigma_S$  and  $D_S$ . To do this, we simply prepare a sample in equilibrium at a given  $U/t$  in the presence of the magnetic gradient, as we described in sections 5.2 and 5.4.2 regarding our measurements of the diffusion coefficient  $D_S$ . This creates a finite initial imbalance,  $\mathcal{I}(0)$ , in the system. However, rather than turning the magnetic

gradient off to initiate dynamics as we did for the diffusion coefficient measurements, to observe the effects of heating we leave the gradient on so that the system stays in equilibrium, and hold the atoms in the lattice for a variable time at the depth corresponding to the desired value of  $U/t$ . We then measure the total imbalance  $\mathcal{I}(\tau)$  from the spin density profiles as a function of the total hold time  $\tau$ . The finite heating rate experienced by the sample leads to an effective decrease in the total imbalance  $\mathcal{I}(\tau)$ , which can mimic the decay observed in the dynamics experiments due to the spin diffusion we purposefully induce. This can be understood from the fact that an increase in the sample temperature leads to a reduction of the uniform spin susceptibility (see Fig. 2-6). Because the observed total imbalance decreases monotonically with decreasing slope in the spin density,  $\partial \langle \hat{S}_{z,j} \rangle / \partial j$ , for a fixed system size, and because the uniform spin susceptibility is directly proportional to this equilibrium slope (Eq. 5.11), it follows that a decrease in  $\chi$  caused by an increase in the temperature translates directly into a reduction of the total imbalance  $\mathcal{I}(\tau)$ . Thus, a finite lattice heating rate leads to an imbalance which decreases as a function of hold time  $\tau$ .

Measuring the effects of lattice heating on  $\mathcal{I}(\tau)$  at several values of  $t/U$ , we find that the decay is well-approximated by an exponential, just like the decay caused by the induced dynamics for the measurement of  $D_S$ . We thus fit the heating-induced decay of  $\mathcal{I}(\tau)$  to a decaying exponential of the form,

$$\mathcal{I}(\tau) = A_H e^{-\tau/\tau_{heating}}, \quad (5.35)$$

where  $A_H$  is the initial amplitude of the imbalance, and  $\tau_{heating}$  is the decay time associated with the heating rate. At larger lattice depths, this decay time decreases somewhat due to the increased lattice intensities at higher depths, which can lead to increased heating caused by intensity noise. Additionally, because the timescales of the spin dynamics become significantly slower at larger lattice depths, meaning the measured decay times of the imbalance in the diffusion experiments become much longer, the imbalance decay due to lattice heating becomes more significant. We thus

specifically examine the effects of lattice heating at the highest lattice depth used for the data discussed in section 5.4.2, which corresponds to  $t/U = 0.026(2)$ . At this depth, we measure a heating decay time  $\tau_{heating} = 4.8(6)$  s, which is roughly a factor of three longer than the diffusive evolution decay time measured at this depth,  $\tau_D = 1.5(4)$  s. Assuming, in the worst case scenario, that the observed diffusive decay time  $\tau_D$  is actually a combination of the real diffusive decay time,  $\tau_{real}$ , and the heating time  $\tau_{heating}$ ,

$$\frac{1}{\tau_D} = \frac{1}{\tau_{real}} + \frac{1}{\tau_{heating}}, \quad (5.36)$$

then the correction to the real decay time at this lattice depth is approximately a 30% change due to heating. Thus, because the spin diffusion coefficient  $D_S$  is proportional to  $1/\tau_D$ , this corresponds to a  $\approx 30\%$  correction to the measured diffusion coefficient, which is comparable to the uncertainty in the measured value of  $D_S$  at this lattice depth. Since the ratio of  $\tau_{heating}$  to  $\tau_D$  improves significantly at shallower lattice depths,  $t/U > 0.026$ , and since the effects of heating are comparable to the experimental uncertainty at the most sensitive lattice depth  $t/U = 0.026$ , we find that we can safely ignore the effects of lattice heating, relative to the experimental uncertainties in the measured values of  $D_S$ , over the full range of  $t/U$  values studied here. We have also verified this by directly measuring the heating decay times at several intermediate values of  $t/U$ . Therefore, we make no attempt to correct any of the experimental data for heating effects, since this would require one to make several significant assumptions about the quantitative effects of heating on a strongly interacting, dynamical many-body system, which lies beyond the scope of this work. However, the heating rate can lead to a non-zero offset in the observed diffusion coefficient at very small values of  $t/U \ll 1$  due to heating-induced decay of the imbalance in this regime, even in the atomic limit  $t/U \rightarrow 0$ . We are therefore fundamentally limited in the smallest value of  $t/U$  we can reliably study experimentally in the presence of finite lattice heating.

## 5.5 Outlook

The experiment described in this chapter [164], in conjunction with another recent study [26] that examines the charge resistivity of the doped Hubbard model, represents one of the first experimental, ultracold atoms studies of the intrinsic transport coefficients in the low temperature region of the 2D Fermi-Hubbard model, probed in linear response. Because such measurements represent a real challenge for theory, the experimental techniques developed for this work are powerful tools that truly embody the spirit of quantum simulation of complex many-body quantum systems. Additionally, since there are very few experimental measurements of the transport coefficients in the 2D Fermi-Hubbard model, there is much unexplored territory within the Hubbard phase diagram. By generalizing the measurement techniques discussed here then, one can easily extend this work in many ways, allowing one to examine transport in other interesting regimes of the Hubbard model, or to study the dependence of the transport coefficients on other parameters in the Hamiltonian. We briefly describe here several interesting extensions of this experiment, and how we are pursuing some of these through ongoing work (as this thesis is being written) in the lab.

One immediate path we would like to explore is the temperature dependence of the spin resistivity,  $\rho_S = 1/\sigma_S$ , at half-filling and at  $U/t = 8$ , an interaction regime where the antiferromagnetic spin correlations are strongest (see section 4.4.3). At high temperatures,  $k_B T > U$ , where charge fluctuations are very significant, and the spin correlations are essentially negligible, one might expect similar behavior between the spin and charge resistivities, since there isn't much to distinguish between them in this regime. At intermediate temperatures,  $J_{ex} < k_B T < U$ , preliminary NLCE calculations suggest  $\rho_S$  could display a linear scaling with temperature, behavior reminiscent of the temperature dependence of the charge resistivity in the bad metallic regime of the cuprates. In contrast to the charge resistivity, however, at lower temperatures,  $k_B T \sim J_{ex}$ , magnetic ordering of the spins could significantly lower the spin resistance below the expectation based on its intermediate temperature scaling. That

is, antiferromagnetic ordering of the spins at low temperatures (once charge fluctuations have already been frozen out) means there is an increased likelihood of spins to encounter nearest-neighbor sites that are singly-occupied by atoms of the opposite spin state. When neighboring sites are antiferromagnetically ordered, super-exchange between these spins allows for the propagation of spin information, and therefore increases spin conduction. When neighboring sites are occupied by atoms in the same spin state, on the other hand, Pauli blocking between like-spin atoms inhibits spin conduction. Thus, as the temperature is lowered, and antiferromagnetic correlations are enhanced in the system, one might expect to see non-trivial behavior in the spin resistance as a function of temperature at half-filling.

Other interesting directions to pursue include examining the effects of doping the system away from half-filling. One could, for example, prepare a system near optimal doping (where the superconducting critical temperature is largest), and study the spin resistivity (as a function of temperature at a fixed value of  $U/t$  for instance) in a regime where residual superconducting fluctuations or a strange metallic state could be present, which could have a non-trivial influence on the conduction of spin. In such a regime, it would also be interesting to examine the directional dependence of both the spin and charge conductivities (e.g. conduction along the lattice bonds versus  $45^\circ$  to the lattice bonds), in order to investigate potential pseudogap behavior. Generalizing the measurement technique to simultaneously measure the charge conductivity, in addition to the spin conductivity, in the doped Hubbard model could thus prove a powerful method to better understand the complex interplay between these two degrees of freedom in this regime. Such interplay between these sectors not only influences the equilibrium properties of the Hamiltonian, as we discussed in detail in section 4.4.3, but could also manifest itself in exciting new ways in the transport properties of the system. To access both quantities experimentally, one could, for example, before taking a spin-resolved single-site image of the system, freeze the lattice along the direction of the current, the  $x$ -direction, which locks in the relevant information, then lower the depth of the orthogonal lattice, the  $y$ -direction, while simultaneously increasing the box size in the  $y$ -direction using the DMD (the box

length in the  $x$ -direction would remain unchanged) to allow the atoms to expand along  $y$  while maintaining their respective positions along  $x$ . A large enough 1D expansion like this would allow the system to become sufficiently dilute that the likelihood of encountering double occupancies would be negligible. Once the system has become dilute along the  $y$ -direction, one would then freeze the atoms with this lattice, and continue with the usual spin-resolved imaging procedure. In this way, one could avoid the parity-projection effect, since essentially all the double occupancies would be eliminated, which would allow one to directly access the total density of either spin state, and therefore the overall total density in the system at various times during the dynamics. Thus, one could measure the spin current, as we have discussed in this chapter, as well as the charge current (set by the total density of particles), to extract both the spin and charge conductivities in various regions of the Hubbard phase diagram.

Another degree of freedom one can study is the dimensionality of the system. For instance, one could examine the spin and charge dynamics in 1D, where strong interactions can separate these two degrees of freedom, leading to drastically different propagation behavior in the spin and charge sectors [142, 93, 74, 14]. Measuring simultaneous spin and charge dynamics in reduced dimensionality, using, for instance, an expansion along the direction orthogonal to the dynamics, could thus allow one to investigate the physics of this spin-charge separation in a controlled, cold atoms-based environment. In 2D, on the other hand, one could also examine spin diffusion in higher spin systems, such as the  $SU(3)$ -symmetric Fermi-Hubbard model (see citations in section 4.4.2), using multiple stable hyperfine states in  ${}^{40}\text{K}$  (e.g.  $|F = 9/2, m_F = -9/2\rangle$ ,  $|F = 9/2, m_F = -7/2\rangle$ , and  $|F = 9/2, m_F = -5/2\rangle$ ). Higher spin systems could exhibit interesting new spin transport phenomena at low temperatures due to the emergence of exotic new phases in such systems.

We would also like to investigate the effects of spin imbalance on the spin transport coefficients of the Hubbard model, for the half-filled situation where  $\langle \hat{n}_\uparrow + \hat{n}_\downarrow \rangle = 1$ . Spin imbalance itself is interesting for several reasons. One is that, for large enough polarization,  $P = \langle \hat{n}_\uparrow - \hat{n}_\downarrow \rangle / \langle \hat{n}_\uparrow + \hat{n}_\downarrow \rangle$ , thermoelectric effects become significant,

which can couple the spin transport mode to the heat and density transport modes. This would make it possible then to induce heat gradients and heat currents from spin density gradients and spin currents. By studying the magnitude of these effects, one could hope to measure, for example, the various thermoelectric coupling parameters such as the spin Seebeck coefficient and the spin Peltier coefficient, which have not yet been studied experimentally in cold atoms Fermi-Hubbard systems. A more detailed discussion of thermoelectric effects in the presence of finite polarization at half-filling is given in section 5.3. Another interesting reason to study spin transport with finite spin-imbalance in the half-filled system actually arises from the mapping of the repulsive  $U > 0$  Hubbard model to the attractive  $U < 0$  Hubbard model on a bipartite lattice [98, 155]. Specifically, under the particle-hole transformation,

$$\hat{c}_{\downarrow,i} \longleftrightarrow (-1)^{i_x+i_y} \hat{c}_{\downarrow,i}^\dagger ; \quad \hat{c}_{\uparrow,i} \longleftrightarrow \hat{c}_{\uparrow,i}, \quad (5.37)$$

where  $i_x$  and  $i_y$  represent the  $x$  and  $y$  site indices, respectively, of lattice site  $i$ , the individual spin densities are mapped to  $\hat{n}_\uparrow \leftrightarrow \hat{n}_\uparrow$ ,  $\hat{n}_\downarrow \leftrightarrow (1 - \hat{n}_\uparrow)$ , and the repulsive Hubbard Hamiltonian is mapped to the attractive Hubbard Hamiltonian, where  $U \leftrightarrow -U$ . Additionally, under this mapping, the average chemical potential,  $\mu_{avg} = (\mu_\uparrow + \mu_\downarrow)/2$ , and the differential chemical potential,  $\Delta\mu = \mu_\uparrow - \mu_\downarrow$ , of the repulsive Hamiltonian are mapped to  $\bar{\mu}_{avg}$  and  $\bar{\Delta\mu}$  of the new Hamiltonian, where  $\bar{\mu}_{avg} = (\Delta\mu/2 - U/2)$  and  $\bar{\Delta\mu} = 2\mu_{avg} - U$ . Thus, spin-imbalance on the repulsive side ( $\Delta\mu \neq 0$ ) with  $\mu_{avg} = U/2$  (half-filling) gets mapped to doping on the attractive side ( $\bar{\mu}_{avg} \neq -U/2$ ) with zero imbalance,  $\bar{\Delta\mu} = 0$ . By studying then spin transport in the repulsive Fermi-Hubbard model using a spin-dependent force, which induces a spatial gradient in  $\Delta\mu$  on the repulsive side, one simultaneously measures charge transport on the attractive side, since a gradient in the differential chemical potential gets mapped onto a gradient in the total chemical potential on the attractive side. Therefore, measuring the spin conductivity of the repulsive model in the presence of finite spin imbalance at half-filling immediately gives you the charge conductivity of the attractive model with finite doping, since the spin transport experiment we

conduct on the repulsive side is equivalent to an analogous charge transport experiment on the attractive side. We could then hope to measure the spin resistance as a function of temperature, at a given  $U/t$  and half-filling, with finite polarization  $P = \langle \hat{n}_\uparrow - \hat{n}_\downarrow \rangle / \langle \hat{n}_\uparrow + \hat{n}_\downarrow \rangle$  in order to obtain the charge conductivity of the attractive model with finite doping as a function of temperature. As long as thermoelectric effects are small, one could then map out the charge conductivity of the attractive model as a function of temperature in various regimes of the attractive phase diagram.

We end this chapter with a short description of ongoing work in the lab, where we have been trying to extend our measurements of the DC spin conductivity and spin diffusion coefficient at half-filling in order to measure the full frequency dependent (AC) spin conductivity at half-filling, and at a fixed value of the Hubbard parameters  $U/t$ . To do this, we hope to generalize the measurement technique discussed in section 5.4.4, where we initially prepare the system in equilibrium in a homogenous lattice (no magnetic gradient applied) with the box potential projected onto the atoms using the DMD. To measure the DC conductivity, we then applied a constant spin-dependent force at time  $\tau = 0$  using a DC magnetic gradient, and measured the dynamics of the spin density imbalance  $\mathcal{I}(\tau)$  (Fig. 5-12). To access the AC conductivity then, we can instead apply an AC magnetic gradient to the system at time  $\tau = 0$ , which generates an AC spin-dependent force of the form

$$F_S(\tau, \omega) = -\frac{1}{a} (\Delta_\uparrow^0 - \Delta_\downarrow^0) \sin(\omega\tau) \hat{x}, \quad (5.38)$$

where  $\Delta_\uparrow^0 - \Delta_\downarrow^0$  represents the amplitude of the applied differential potential. In the language of the damped harmonic oscillator description of the spin density (with non-zero momentum relaxation rate  $\Gamma$ ) given by Eq. 5.34, this spin-dependent force becomes an AC driving term on the right-hand-side of Eq. 5.34, making it a driven, damped harmonic oscillator. If we then measure the spin density imbalance  $\mathcal{I}(\tau)$  in this driven system as a function of time after turning on the drive, we observe a sinusoidally oscillating imbalance. Fig. 5-15 shows an example of the dynamics of the spin density imbalance as a function of time  $\tau$  after turning on the oscillating

magnetic gradient. For this figure,  $U/t \approx 4.2$ , and we drive the system very slowly, at a frequency  $\omega \approx 0.03(t/\hbar)$ , a regime where the drive is sufficiently slow that the induced spin density gradient should easily be able to follow. Although, for all practical purposes, this is effectively the DC limit, as a proof of principle experiment it means we are able to induce an oscillating spin density imbalance with a decent signal to noise ratio. As we improve this technique (making sure everything behaves as we expect, for instance) and as we calibrate the system (including the gradients, to ensure we apply a symmetric drive along the  $x$ -direction), we can begin to increase the drive frequency to study the response of the system over a larger range of frequencies. For instance, based on the NLCE AC conductivity predictions (Fig. 5-14), one should expect a peak in the system response at a drive frequency near the on-site interaction energy,  $U/h \sim 1\text{ kHz}$ . At higher frequencies, one might even hope to observe anomalous scaling of the AC conductivity [197].

To connect the observed response in the spin density  $S_z(x, \tau)$  directly to the spin conductivity, we can, instead of separately integrating the two halves of the box to obtain the spin density imbalance  $\mathcal{I}(\tau)$  (Eq. 5.15), take a discrete spatial Fourier transform of the spin density in the box of size  $L$  to obtain  $S_z(k, \tau)$ . This is a slightly simpler approach because the response of the spin density at momentum  $k$  and frequency  $\omega$  is determined, in linear response, by the spin density response function,  $\chi(k, \omega)$ , also called the spin susceptibility. That is, we have that,

$$S_z(k, \omega) = \chi(k, \omega)\delta V(k, \omega), \quad (5.39)$$

where  $\delta V(k, \omega)$  represents the discrete spatial Fourier transform of the applied spin-dependent potential at frequency  $\omega$ , which is simply the linear differential potential between the two spin states, determined by the applied magnetic gradient (i.e. Eq. 5.38 converted to a potential). Since we in principle know the applied potential  $\delta V(k, \omega)$  from the calibration of the magnetic gradients, by measuring the amplitude and phase of the spin density response,  $S_z(k, \omega)$ , with respect to our drive (after any transient response of the system has decayed), we can obtain both the real and imag-

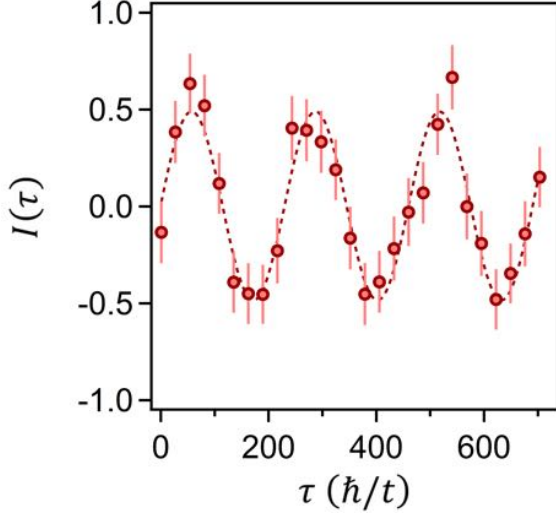


Figure 5-15: AC response of the spin density imbalance under a sinusoidal drive. Plotted is the measured imbalance (red circles),  $I(\tau)$ , in the box after turning on a sinusoidally oscillating spin dependent force,  $F_s(\tau, \omega)$ , at a frequency  $\omega$ , beginning at time  $\tau = 0$ . Before the drive is turned on, the system is initially homogeneous, spin-balanced at half-filling, and in equilibrium in the box at  $U/t = 4.2$ , corresponding to a lattice depth of  $7.6E_R$ . The initial phase of the drive is zero, so that  $F_s(0, \omega) = 0$ , the drive frequency is  $\omega \approx 0.03(t/\hbar)$ , where  $t/\hbar \approx 144$  Hz, and the amplitude of the drive is approximately 70% of the spin-dependent force applied in the DC experiments, corresponding to a gradient of  $\approx 0.66$  G/cm. The error bars represent the  $1\sigma$  statistical uncertainty in the measurements, and the dashed red line is a sinusoidal fit to the data, where the amplitude and phase are left as free parameters.

inary parts of the spin susceptibility  $\chi(k, \omega)$ . A measurement of  $\chi(k, \omega)$  then allows us to obtain the AC spin conductivity through the relation,

$$\text{Re } \sigma_S(\omega) = \lim_{k \rightarrow 0} \frac{\omega}{k^2} \text{Im } \chi(k, \omega). \quad (5.40)$$

Eq. 5.40 follows from the continuity equation for the spin density,  $\partial S_z(x, \tau)/\partial \tau = -\nabla \cdot \mathbf{J}_S$ , after Fourier transforming both sides of the equation in both space and time, and using the linear response relationship, Eq. 5.39, as well as the corresponding linear response relationship for the spin current,  $J_S(k, \omega)$ . Therefore, by driving the system at different frequencies  $\omega$ , and measuring the amplitude and phase of the response in the spin density relative to our applied drive, we can map out the full AC spin conductivity of the half-filled Hubbard model at a given temperature and  $U/t$ . As

this thesis is being written, this work is still ongoing and details of the technique are still being perfected.

# Chapter 6

## Summary and Outlook

Previously in this thesis, we presented the results from several experiments that examined different aspects of the behavior of ultracold fermionic atoms in a square optical lattice, a pristine, isolated, and highly controllable model system which realizes the two dimensional Fermi-Hubbard model. The different experiments covered two main areas of research: the first involved equilibrium measurements of thermodynamic properties of the system, such as spatial spin or charge correlations, and the second involved near-equilibrium transport studies that examined spin transport coefficients for the Hubbard model at half-filling. This chapter provides a brief summary of these results, and gives a short outlook towards future research directions one could pursue with the fermionic quantum gas microscope depicted here.

We began the thesis by providing a detailed description of our quantum gas microscope for  $^{40}\text{K}$ , which allows us to simulate the 2D Fermi-Hubbard model on a square lattice with full experimental control over all Hamiltonian parameters, and which also allows us to observe the system *in situ* with sufficient spatial resolution to detect single atoms and single lattice sites. We introduced the different components of the experiment which give us the ability to prepare cold, degenerate samples in the focal plane of our high-resolution imaging system, and we subsequently described our fluorescence imaging technique based on Raman sideband cooling, with which we can detect single atoms on single sites in the lattice with high-fidelity. Similar imaging techniques have been employed by other research groups around the world for the

same purpose of quantum gas microscopy of fermionic atoms [85, 179, 169, 58, 27]. We then discussed the experimental details behind our spin-dependent imaging technique, which allows to us observe each spin state in the lattice separately, and which therefore provides us with access to spatial correlations in the spin degree of freedom.

In chapter 4, we introduced the local moment observable, which characterizes the density of singly-occupied sites in the system, and we discussed some of its thermodynamic properties within the 2D Fermi-Hubbard model, including the fact that its variance can be directly determined from its average value. We then described our site-resolved observation of different paradigmatic states of the Hubbard model, including metallic, Mott-insulating, and band-insulating states, and examined how they distinguish themselves through manifestly different behavior in the average local moment and its variance. We found that, through a comparison with numerical calculations such as NLCE or DQMC, the average local moment itself at half-filling can be used as an accurate thermometer to estimate the temperature of the system within a temperature range below the Mott gap, but above the Néel temperature, where thermal charge fluctuations are present. Subsequently, we examined local, spatial spin and charge correlations in a trapped Mott-insulating sample, which, given the single-site resolution of our quantum gas microscope, allowed us to directly measure the nearest-neighbor spin and charge correlators of the system as functions of doping. At half-filling, we observed significant nearest-neighbor antiferromagnetic spin correlations, beyond what one would naively expect for a non-interacting two-component Fermi gas, with simultaneous correlated bunching between doublons and holes, which revealed a non-trivial connection between the spin and charge degrees of freedom within the Fermi-Hubbard model at this density. Upon doping the system, we observed that the nearest-neighbor spin correlations weakened monotonically with increasing doping, and that the nearest-neighbor charge correlations changed in character from bunching behavior to anti-bunching behavior, due to the competition between an effective doublon-hole attraction, which dominates near half-filling, and an interaction enhanced Pauli-correlation hole, a real space manifestation of Pauli blocking, which leads to an effective repulsion between particles, and dominates at

low fillings. With finite antiferromagnetic spin correlations present in the system at low temperatures, we also found that the nearest-neighbor spin correlator at half-filling could be used as a sensitive thermometer, through comparisons with numerical calculations of this quantity, which could allow one to estimate the temperature of the sample at relatively low temperatures, where the thermal charge fluctuations are frozen out, and the average local moment at half-filling is no longer a sensitive probe.

At even lower temperatures than those achieved for the work discussed in this thesis, e.g. the Néel temperature or below, the spin correlations at half-filling and  $U/t \sim 8$  are expected to become much longer ranged than a single site of separation, and can even approach the finite size of the sample [152]. In the presence of finite doping at such low temperatures, numerical calculations are impeded by the fermionic sign problem, which can allow current experiments to access parameter regimes that are not well understood theoretically. For the experiment discussed in this thesis, one route towards achieving these low temperatures could involve the successful implementation of entropy redistribution, using an optical potential projected onto the atoms by the DMD to shape the underlying trap formed by the optical lattice [20, 99, 152, 43]. In this way, one can enhance the local storage of entropy in large annular metallic regions, while maintaining a smaller, homogeneous region of interest in the center of the sample, where the local entropy is much lower, and which has the desired density. Another option is to increase the number of spin states present in the lattice, where the entropy requirements to observe magnetically ordered states are more experimentally accessible. As discussed in section 4.4.2, one could potentially generate a balanced three-spin system with fermionic  $^{40}\text{K}$  that is approximately  $SU(3)$  symmetric. This could allow one to examine spatial spin correlations in a spin-1 Hubbard model with single-site imaging, which could host a variety of novel magnetic phases [102, 36, 94, 188].

In chapter 5, we described a new technique that we developed, in conjunction with a similar technique (applied to the charge degree of freedom) developed in [26], which allowed us to examine spin transport, in the linear response regime, within a homogeneous, two-dimensional Fermi-Hubbard system at half-filling, with single atom

resolution. We observed that the spin transport dynamics behaved diffusively, and we independently measured both the spin diffusion coefficient, and the spin conductivity at half-filling, as functions of the relative strength between the on-site interactions and the nearest-neighbor tunneling amplitude. These two transport coefficients are related to one another through an Einstein relation, and we found that our independent measurements of these two quantities were consistent with such behavior. In the strongly interacting Mott regime, we observed that spin diffusion was driven by super-exchange and doublon-hole-assisted tunneling. Upon lowering the relative strength of the interactions, however, thereby creating a more metallic sample, we observed that other energy scales, beyond just the super-exchange scale, came into play, which enhanced the conduction of spin in this regime. These measurements of the spin transport coefficients of the 2D Fermi-Hubbard model at half-filling represent one of the first of their kind, since similar experiments in the cuprates are inherently challenging due to difficulties in controlling and manipulating spin currents in these materials. We were thus able to benchmark novel, independent NLCE calculations of the transport coefficients, and found good qualitative agreement between experiment and theory, but observed quantitative differences due to the significant theoretical challenges associated with calculating transport properties of the system in the DC limit.

At the end of chapter 5, we provided a detailed look at various extensions and generalizations of the spin transport measurements discussed there, which could allow one to examine transport in many different regimes of the Fermi-Hubbard phase diagram, a research topic with many open questions and relatively few experimental answers. One of the most immediate and simplest generalizations mentioned there involves a measurement of the AC spin conductivity at half-filling using a sinusoidally alternating magnetic gradient. Such a technique could allow one to map out the full frequency-dependence of the spin conductivity at a fixed value of the Hubbard parameters  $U/t$ , in order to look for deviations from theoretical predictions (e.g. Fig. 5-14), or to search for anomalous scaling of the AC conductivity at high frequencies [197]. Another interesting direction would be to examine the impact of

dimensionality on transport, and to study the crossover from one to two dimensions, which one can control using the depth of the optical lattice along one of the directions. In 1D, for example, the Fermi-Hubbard model is known to feature spin-charge separation [142, 74, 14, 96], which should manifest itself in fundamentally different propagation modes for the spin and charge degrees of freedom. In the 2D case, one could also study the effects of finite doping away from half-filling, where superconducting fluctuations or a strange metallic phase might be present [139, 26]. Through simultaneous measurements of, for instance, the temperature dependence of the spin and charge conductivities in the doped regime, one could look for the different ways these phases manifest themselves through transport [171, 49, 139], in order to better understand the complex interplay between the spin and charge degrees of freedom in the doped 2D Fermi-Hubbard model.

An alternative research direction that would be very interesting to pursue, through both equilibrium measurements and transport studies, would be to make use of the fact that the experiment also utilizes bosonic  $^{23}\text{Na}$ . Currently the Na is used only as a sympathetic coolant for K, which is removed from the system before the K atoms are loaded into the optical traps. However, one could leave extra Na atoms around, and trap both species in the optical dipole traps, where the Bose-Fermi mixture could then be optically transported to the substrate surface. Practically speaking, this might be useful for reaching lower temperatures for the K atoms, through further sympathetic cooling at the substrate surface in the final stage of optical evaporation, immediately prior to preparation in the square optical lattice. Additionally, one could even imagine preparing both species in the lattice, in order to study interacting Bose-Fermi mixtures with single-site resolution. For this purpose, we have recently assembled a D1 laser cooling system for Na, which could potentially allow us to perform site-resolved fluorescence imaging of  $^{23}\text{Na}$  using sub-Doppler cooling in a D1 gray molasses [47]. We could then image both species with single-site resolution, which would prove a powerful tool for studying the rich phase diagram of interacting Bose-Fermi mixtures in a lattice [1]. For instance, due to the interspecies interactions, the fermionic atoms could pair with the bosons, resulting in a system of composite

fermions that could host a variety of novel phases [140]. In two dimensions, it has also been predicted that such a system could host a super-solid phase characterized by simultaneous crystalline and phase order [29]. The recently demonstrated creation of ultracold ground state NaK molecules [176, 178] also leaves the possibility for studying lattice models in two dimensions that possess long-range and anisotropic interactions, using the power of single-site resolution afforded from quantum gas microscopy.

In conclusion, the experimental apparatus discussed in this thesis offers an extremely flexible and versatile platform for studying strongly correlated, Hubbard-type many-body systems, with the unprecedented level of control that quantum gas microscopy can offer. In addition to providing insight into the physics of strongly correlated electronic systems like the cuprates, such a platform, with the many tools available to ultracold atomic systems (e.g. spin orbit coupling, artificial gauge fields, or Feshbach resonances to alter the sign of the interspecies interaction), can be used to realize and observe novel and exotic many-body phenomena that have not yet been seen in nature. There are many possible research directions to pursue, and so many open questions waiting to be answered, that the future looks extremely bright for this experiment, and in general for the field of fermionic quantum gas microscopy.

## Appendix A

# Isothermal and Isentropic Numerical Calculations of the Hole-Hole, Hole-Doublon, and Doublon-Doublon Correlation Functions at Half-Filling Versus $U/t$

This appendix contains both isothermal and isentropic NLCE calculations of the nearest-neighbor correlation functions  $\langle \hat{h}_i \hat{h}_j \rangle_c$ ,  $\langle \hat{h}_i \hat{d}_j \rangle_c$ , and  $\langle \hat{d}_i \hat{d}_j \rangle_c$ , within the spin-balanced 2D Fermi-Hubbard model at half-filling, as functions of the Hubbard parameters  $U/t$ . The weighted sum of these correlators together make up the nearest-neighbor local moment correlator discussed in chapter 4, via  $C_m(1) = \langle \hat{h}_i \hat{h}_j \rangle_c + 4 \langle \hat{h}_i \hat{d}_j \rangle_c + 4 \langle \hat{d}_i \hat{d}_j \rangle_c$ . Interestingly, as can be seen from the different figures, all of the correlation functions, in both the isothermal and isentropic cases, appear to weaken in magnitude monotonically with increasing  $U/t$ . The weighted sum of these terms, however, in the form of  $C_m(1)$ , is maximized around  $U/t \approx 8$ , as is shown in Figs. 4-25 and 4-26. The different curves shown in this appendix were generated using the NLCE data produced for [38], and are provided here for future reference.

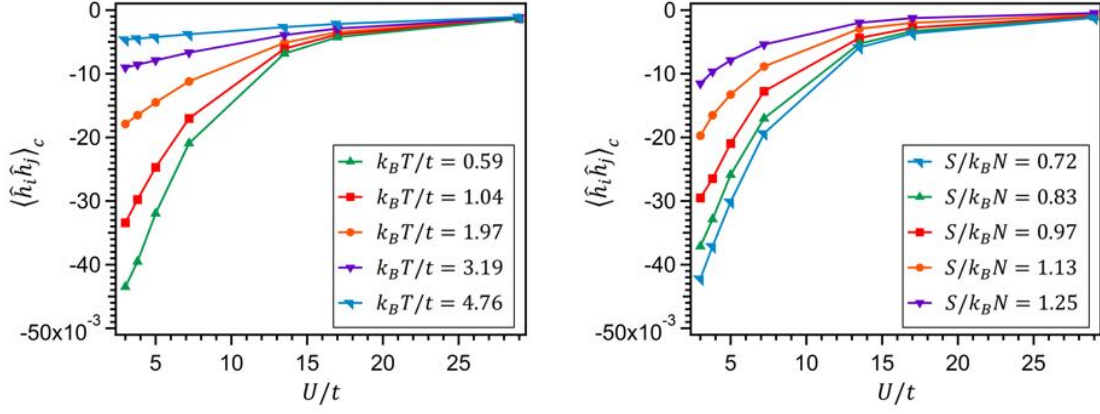


Figure A-1: Nearest-neighbor hole-hole correlation function versus  $U/t$  at half-filling for fixed temperature and fixed entropy per particle,  $S/k_B N$ . The left figure shows isothermal, 9<sup>th</sup>-order NLCE calculations (symbols) of  $\langle \hat{h}_i \hat{h}_j \rangle_c$  for the spin-balanced 2D Fermi-Hubbard model at half-filling, as a function of  $U/t$ , for several temperatures in the range  $0.59 \leq k_B T/t \leq 4.76$ . The right figure shows isentropic, 9<sup>th</sup>-order NLCE calculations (symbols) of  $\langle \hat{h}_i \hat{h}_j \rangle_c$  at half-filling, as a function of  $U/t$ , for several different values of the entropy per particle in the range  $0.72 \leq S/k_B N \leq 1.25$ . The lines shown in the plots are a guide to the eye. These different curves are generated using the NLCE data from [38].

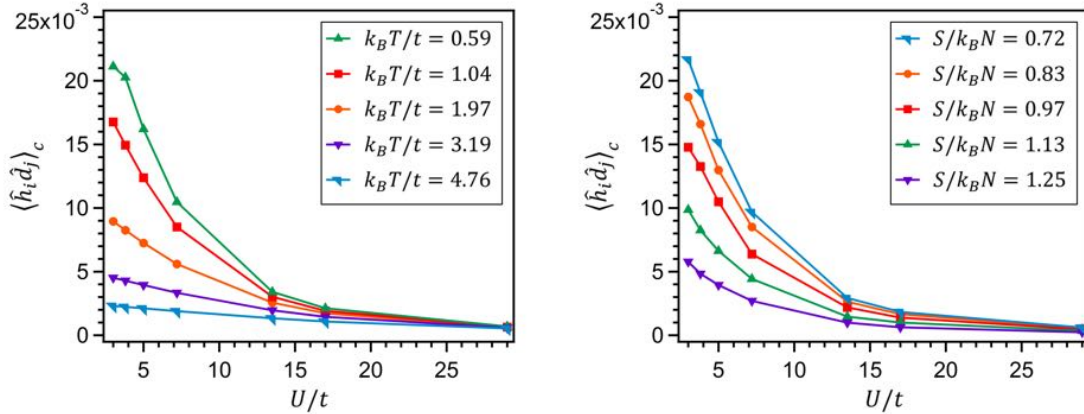


Figure A-2: Nearest-neighbor hole-doublon correlation function versus  $U/t$  at half-filling for fixed temperature and fixed entropy per particle,  $S/k_B N$ . The left figure shows isothermal, 9<sup>th</sup>-order NLCE calculations (symbols) of  $\langle \hat{h}_i \hat{d}_j \rangle_c$  for the spin-balanced 2D Fermi-Hubbard model at half-filling, as a function of  $U/t$ , for several temperatures in the range  $0.59 \leq k_B T/t \leq 4.76$ . The right figure shows isentropic, 9<sup>th</sup>-order NLCE calculations (symbols) of  $\langle \hat{h}_i \hat{d}_j \rangle_c$  at half-filling, as a function of  $U/t$ , for several different values of the entropy per particle in the range  $0.72 \leq S/k_B N \leq 1.25$ . The lines shown in the plots are a guide to the eye. These different curves are generated using the NLCE data from [38].

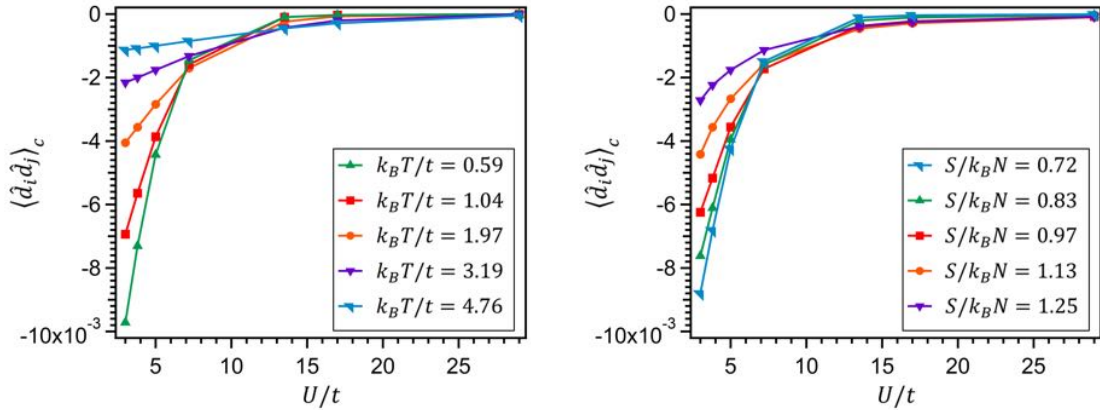


Figure A-3: Nearest-neighbor doublon-doublon correlation function versus  $U/t$  at half-filling for fixed temperature and fixed entropy per particle,  $S/k_B N$ . The left figure shows isothermal, 9<sup>th</sup>-order NLCE calculations (symbols) of  $\langle \hat{d}_i \hat{d}_j \rangle_c$  for the spin-balanced 2D Fermi-Hubbard model at half-filling, as a function of  $U/t$ , for several temperatures in the range  $0.59 \leq k_B T/t \leq 4.76$ . The right figure shows isentropic, 9<sup>th</sup>-order NLCE calculations (symbols) of  $\langle \hat{d}_i \hat{d}_j \rangle_c$  at half-filling, as a function of  $U/t$ , for several different values of the entropy per particle in the range  $0.72 \leq S/k_B N \leq 1.25$ . The lines shown in the plots are a guide to the eye. These different curves are generated using the NLCE data from [38].



## Appendix B

# Observation of 2D Fermionic Mott Insulators of $^{40}\text{K}$ with Single-Site Resolution

This appendix contains a reprint of the following paper [39]:

L. W. Cheuk, M. A. Nichols, K. R. Lawrence, M. Okan, H. Zhang, and M. W. Zwierlein, “Observation of 2D Fermionic Mott Insulators of  $^{40}\text{K}$  with Single-Site Resolution,” Phys. Rev. Lett. **116**, 235301 (2016).



## Observation of 2D Fermionic Mott Insulators of $^{40}\text{K}$ with Single-Site Resolution

Lawrence W. Cheuk, Matthew A. Nichols, Katherine R. Lawrence, Melih Okan, Hao Zhang, and Martin W. Zwierlein  
*Department of Physics, MIT-Harvard Center for Ultracold Atoms, and Research Laboratory of Electronics,  
MIT, Cambridge, Massachusetts 02139, USA*

(Received 31 March 2016; published 10 June 2016)

We report on the site-resolved observation of characteristic states of the two-dimensional repulsive Fermi-Hubbard model, using ultracold  $^{40}\text{K}$  atoms in an optical lattice. By varying the tunneling, interaction strength, and external confinement, we realize metallic, Mott-insulating, and band-insulating states. We directly measure the local moment, which quantifies the degree of on-site magnetization, as a function of temperature and chemical potential. Entropies per particle as low as  $0.99(6)k_B$  indicate that nearest-neighbor antiferromagnetic correlations should be detectable using spin-sensitive imaging.

DOI: 10.1103/PhysRevLett.116.235301

Strongly correlated fermions present a fundamental challenge to many-body physics, as no general method exists to predict what phenomena will emerge [1]. Ultracold gases of fermionic atoms have shown promise as a clean, highly controllable platform for studying such systems [2,3]. One prominent example is the realization of strongly coupled fermionic superfluids, enabled by the enhanced interactions that arise near a Feshbach resonance [4,5]. Another class of strongly correlated systems well suited for simulation with ultracold atoms is lattice models, in which the kinetic and interaction energies can be set to comparable strengths [3,6]. One such model is the Fermi-Hubbard model, believed to capture the essential aspects of high-temperature superconductivity [7,8].

The realization of the Fermi-Hubbard model at low entropies has been a longstanding goal in ultracold atom experiments. Mott-insulating behavior has been observed in three dimensions (3D) via reduction of double occupancies and compressibility [9–12]. Short-range antiferromagnetic correlations above the Néel temperature were observed via Bragg scattering and dimerized lattices [13–15]. Recently, the equation of state of the Fermi-Hubbard model has been measured in two dimensions (2D) for spin 1/2 and in 3D for higher spin values [16,17]. However, these experiments relied on conventional imaging techniques that do not allow site-resolved measurements of microscopic quantities.

Such microscopic measurements first became possible in bosonic systems through the development of quantum gas microscopes with single-site resolution, and have enabled studies of ordering, spatial structures, and correlations in the Bose-Hubbard model [18–21]. Recently, the ability to perform single-site imaging has been extended to the two workhorse fermionic isotopes of alkali atoms,  $^6\text{Li}$  and  $^{40}\text{K}$  [22–26]. While  $^6\text{Li}$  has faster lattice dynamics due to its smaller mass,  $^{40}\text{K}$  features a larger fine structure splitting, which is beneficial for implementing spin-dependent potentials and spin-orbit coupling.

After initial demonstrations of site-resolved imaging of nondegenerate Fermi gases, the goal has been to apply

these imaging techniques to low-entropy degenerate gases in order to study quantum many-body phenomena. Within the past few months, Pauli blocking was directly observed in a spin-polarized gas of  $^6\text{Li}$  [26], and the metallic, Mott-insulating, and band-insulating states of the 2D Fermi-Hubbard model have been directly detected, both in  $^6\text{Li}$  [27], and, as reported in this paper, in  $^{40}\text{K}$ . In this Letter, we also demonstrate the formation of local moments at half filling as the temperature is lowered.

Our system is described by the single-band 2D Hubbard Hamiltonian with two spin states on a square lattice,

$$\hat{H} = -t \sum_{\langle i,j \rangle, \sigma} (\hat{c}_{i\sigma} \hat{c}_{j\sigma}^\dagger + \text{H.c.}) + U \sum_i \hat{n}_{i\uparrow} \hat{n}_{i\downarrow} + \sum_{i,\sigma} (V_i - \mu_0) \hat{n}_{i\sigma},$$

where  $\hat{c}_{i\sigma}$  ( $\hat{c}_{i\sigma}^\dagger$ ) is the fermion annihilation (creation) operator for spin  $\sigma = \{\uparrow, \downarrow\}$  on site  $i$ ,  $n_{i\sigma} = \hat{c}_{i,\sigma}^\dagger \hat{c}_{i,\sigma}$  is the number operator on site  $i$ , and angle brackets indicate summation over nearest neighbors.  $U$  and  $t$  denote the on-site interaction energy and nearest-neighbor hopping amplitude, respectively, while  $\mu_0$  is the chemical potential and  $V_i$  is the on-site energy due to the overall trapping potential. The trapping potential is approximated by  $V_i = \frac{1}{2} m \omega^2 d_i^2 a^2$ , where  $m$  is the atomic mass,  $\omega$  is the global trapping frequency,  $d_i$  is the distance in lattice sites from the center of the trap, and  $a$  is the lattice spacing.

Despite the simplicity of the Hamiltonian, this model is theoretically intractable and has been solved only in special cases. At weak interactions ( $U/8t < 1$ ) or when the average filling is well below unity, the system is metallic. If the chemical potential is high enough to fill all available states, the system becomes a band insulator, with two opposite-spin atoms per site. At strong interactions ( $U/8t \gg 1$ ) and at half filling, another insulating state, the Mott insulator, appears when the temperature  $k_B T \ll U$ . At temperatures well below the superexchange scale of  $4t^2/U$ , long-range antiferromagnetic correlations arise. It is conjectured that  $d$ -wave superconductivity emerges upon doping a magnetically ordered

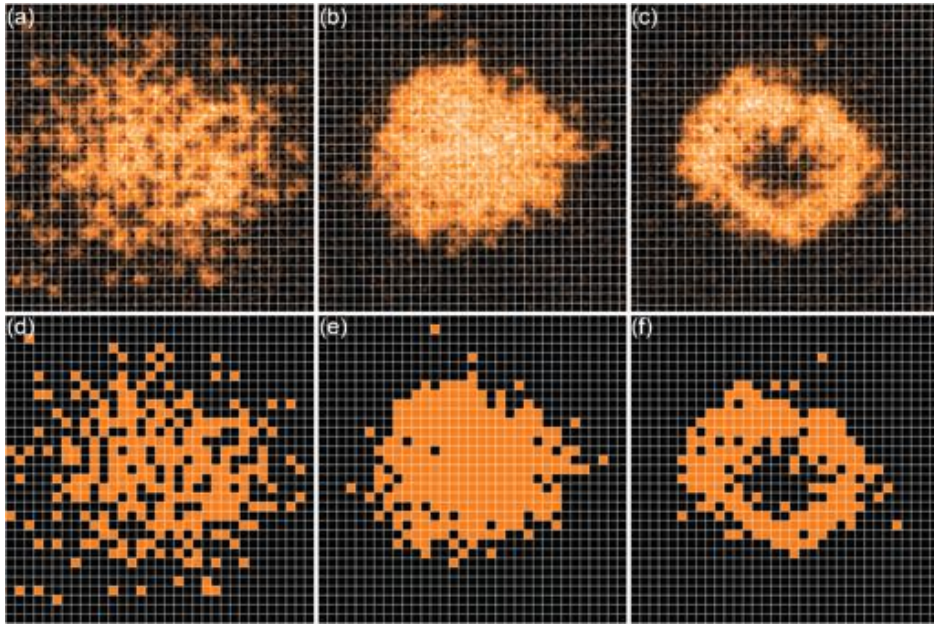


FIG. 1. Metallic, Mott-insulating, and band-insulating states under the quantum gas microscope: observed fluorescence images, showing (a) the metallic state, with  $\mu_0/h = 280(40)$  Hz,  $\omega = 2\pi \times 111(3)$  Hz, and  $U/8\bar{t} = 0.33(4)$  with  $U/h = 540(60)$  Hz; (b) the Mott-insulating state, with  $\mu_0/h = 624(22)$  Hz,  $\omega = 2\pi \times 115(3)$  Hz, and  $U/8\bar{t} = 12.3(8)$  with  $U/h = 1350(50)$  Hz; and (c) the band-insulating state, with  $\mu_0/h = 1450(40)$  Hz,  $\omega = 2\pi \times 181(3)$  Hz, and  $U/8\bar{t} = 2.6(1)$  with  $U/h = 1007(40)$  Hz. [(d)–(f)] Reconstructed detected site occupations corresponding to (a)–(c), respectively.

Mott insulator [7,8]. Within the local density approximation (LDA), the overall harmonic confining potential leads to a spatially varying local chemical potential, and thus metallic, Mott-insulating, and band-insulating states can coexist within the same sample [28,29].

To realize this model, we begin by sympathetically cooling  $^{40}\text{K}$  atoms with  $^{23}\text{Na}$  atoms in a magnetic trap. The  $^{40}\text{K}$  atoms are then transferred into an optical dipole trap, and an equal mixture of hyperfine states  $|F = 9/2, m_F = -9/2\rangle$  and  $|9/2, -7/2\rangle$  is created. After evaporation and transport, we obtain a highly oblate layer of  $\sim 300$   $^{40}\text{K}$  atoms in the  $x$ - $y$  plane  $7\ \mu\text{m}$  underneath the imaging system. Subsequently, we ramp up a square optical lattice in the  $x$ - $y$  plane, with lattice spacing  $a = 541$  nm, to a depth of either  $6E_R$ ,  $12E_R$ , or  $18E_R$ , where  $E_R = (\hbar^2/2m)(\pi/a)^2$ . The laser beams that create the  $x$ - $y$  lattice also interfere to form a lattice along  $z$  with  $3\ \mu\text{m}$  spacing, where only one layer is populated. We use the lattice depth to tune the Hubbard parameters  $t$  and  $U$ , without utilizing any Feshbach resonances. For this work, the magnetic field is set to 4.5 G, where the scattering length is  $170a_0$ ,  $a_0$  being the Bohr radius. While the lattice is ramped up, the radial confinement within the plane is brought to the desired value. For imaging, the lattice depth is quickly increased to  $\sim 1000E_R$ , while an additional lattice along the  $z$  direction with spacing 532 nm is also applied.

We detect the occupation on each lattice site using Raman sideband cooling, which cools the atoms while scattering enough photons to produce a fluorescence image [22]. This imaging technique, combined with an image reconstruction algorithm, allows us to determine the occupation of a given lattice site with a measured imaging fidelity of 95%. Because pairs of atoms residing on the same site are lost during imaging due to light-assisted collisions [30], only the parity of the occupation is detected. Additionally, this imaging

method does not distinguish between the two spin states. The average detected occupation at site  $i$  is thus given by  $n_{\text{det}}(i) = \langle \hat{n}_{\text{det}}(i) \rangle$ , where  $\hat{n}_{\text{det}}(i) = \hat{n}_{i\uparrow} + \hat{n}_{i\downarrow} - 2\hat{n}_{i\uparrow}\hat{n}_{i\downarrow}$ .

We directly observe the metallic, Mott-insulating, and band-insulating states using three configurations of lattice depths and radial confinements. The three different samples are prepared identically until the 2D lattice ramp, where both the depth of the lattice and the radial confinement are adjusted. In Fig. 1 we show the site-resolved fluorescence images and the reconstructed detected site occupations. In Fig. 2 we show profiles of the corresponding radially averaged parity-projected densities  $n_{\text{det}}$  and their variances. The Mott-insulating and band-insulating states are both expected to show suppressed variance in  $n_{\text{det}}$ . In particular, the variance is suppressed in Mott-insulating regions due to the charge gap, which is  $U$  at half filling; in the band-insulating regions, it is suppressed instead by Pauli blocking. In the metallic regions the variance is not suppressed, and in the case of half filling it equals 0.25, since a site is equally likely to be empty, doubly occupied, or singly occupied by an atom of either spin state. The variance can either be directly measured, or obtained via  $\langle \hat{n}_{\text{det}}^2 \rangle - \langle \hat{n}_{\text{det}} \rangle^2 = n_{\text{det}}(1 - n_{\text{det}})$ . This is due to the operator identity  $\hat{n}_{i\sigma}^2 = \hat{n}_{i\sigma}$  for fermions, which implies  $\langle \hat{n}_{\text{det}}^2 \rangle = \langle \hat{n}_{\text{det}} \rangle$ , and more generally all moments of  $n_{\text{det}}$  can be found from  $n_{\text{det}}$  itself.

The metallic state, with peak occupation 0.7 and peak variance  $\sim 0.25$ , is shown in Figs. 1(a), 1(d), 2(a), and 2(d). Here, the lattice depth is  $6E_R$  and the radial confinement is  $\omega = 2\pi \times 111(3)$  Hz. This corresponds to  $U/8\bar{t} = 0.33(4)$ , where  $\bar{t} = \sqrt{t_x t_y}$  is the mean hopping amplitude, with  $t_x$  ( $t_y$ ) being the mean hopping amplitude along the  $x$  ( $y$ ) direction [39]. In order to observe the Mott insulator, shown in Figs. 1(b), 1(e), 2(b), and 2(e), we increase the interaction to  $U/8\bar{t} = 12.3(8)$  by increasing the lattice depth to  $18E_R$

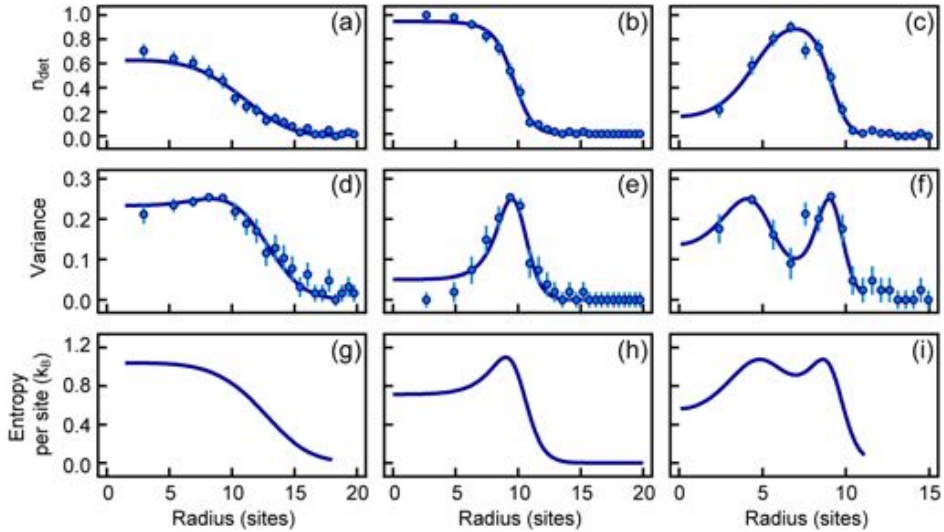


FIG. 2. Radially averaged detected site occupation [(a)–(c)], variance [(d)–(f)], and entropy [(g)–(i)], with theoretical curves. [(a), (d), and (g)] Metallic state, with  $\mu_0/h = 280$  (40) Hz and  $k_B T/U = 1.46(18)$ ; average entropy per particle  $S/N = 1.7(1)k_B$ . [(b), (e), and (h)] Mott-insulating central region, with  $\mu_0/h = 624$  (22) Hz and  $k_B T/U = 0.09(1)$ ;  $S/N = 1.23(6)k_B$ . [(c), (f), and (i)] Band-insulating center and Mott-insulating annular region, with  $\mu_0/h = 1450$  (40) Hz and  $k_B T/U = 0.18(2)$ ;  $S/N = 0.99(6)k_B$ . The profiles were fitted to numerical linked cluster expansion (NLCE) data with  $U/\bar{t} = 3$  for (a), (d), and (g) and to high-temperature series expansion (HTSE) for (b), (e), and (h). For (c), (f), and (i), profiles were fitted to NLCE data with  $U/\bar{t} = 21$ , shown in solid.

and the trap confinement to  $\omega = 2\pi \times 115$  (3) Hz. The detected site occupation flattens to 0.98(2) at the trap center, with a corresponding variance less than 0.03. To observe the band insulator, shown in Figs. 1(c), 1(f), 2(c), and 2(f), we

increase the global chemical potential, by increasing the trap confinement to  $\omega = 2\pi \times 181$  (3) Hz, while reducing the interaction to  $U/8\bar{t} = 2.6(1)$ , by lowering the lattice depth to  $12E_R$ . At the center the detected density is depleted and the

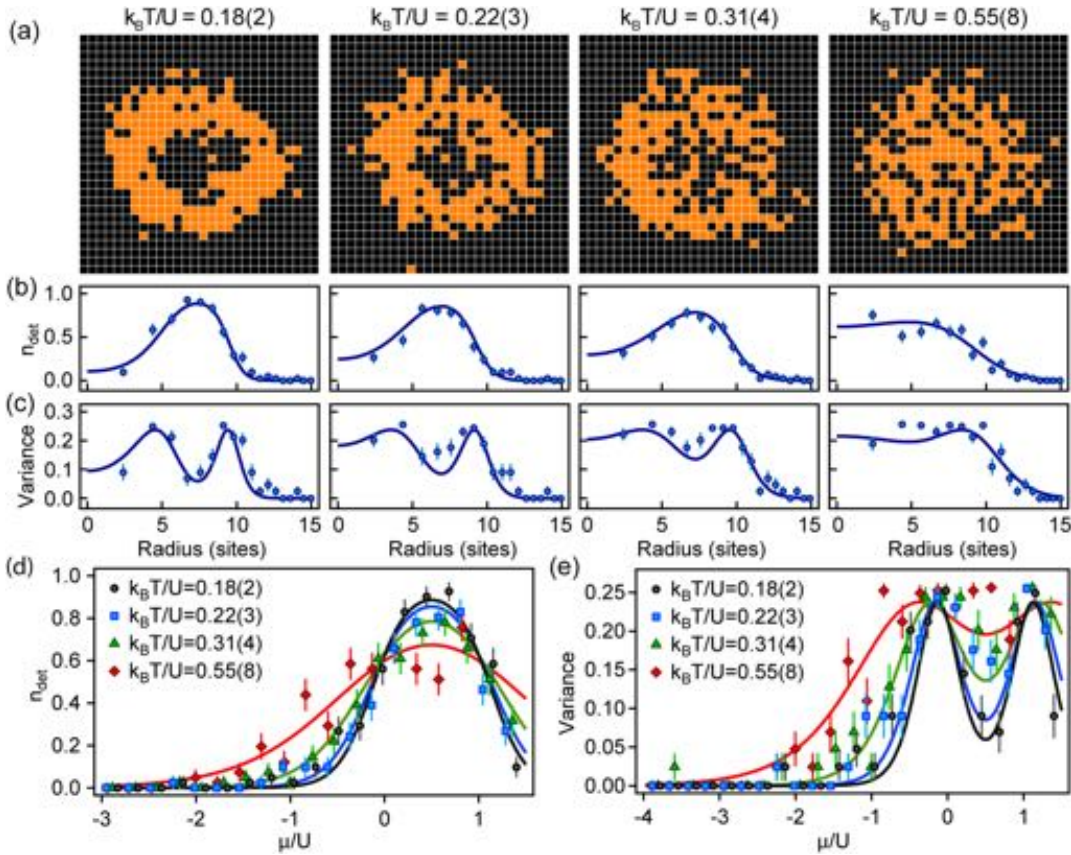


FIG. 3. Heating of Mott and band insulators. (a) Site-resolved images, (b) density profiles, and (c) variances for temperatures  $k_B T/U = 0.18(2), 0.22(3), 0.31(4), 0.55(8)$  (left to right) at fixed  $U/8\bar{t} = 2.6(1)$  and  $\omega = 2\pi \times 183$  (3) Hz, with fitted curves from HTSE (solid). [(d) and (e)] Radially averaged observed filling and variance, respectively, for all four temperature values as a function of chemical potential, calculated from the fitted global chemical potential.

variance is suppressed, indicating a band-insulating region with two atoms per site. Because of the varying local chemical potential across the trap, a surrounding Mott-insulating annular region is also visible. The metallic regions that border the insulating regions are clearly evidenced by the increased variance.

To characterize the atomic clouds, we fit the radially averaged parity-projected density  $n_{\text{det}}$  to the equation of state of the spin-balanced Hubbard model obtained either through NLCE data [31], for  $U/8t = 0.33(4), 2.6(1)$ , or from the HTSE in  $t/k_B T$  [32], for  $U/8t = 12.3(8)$ . From these fits, we extract temperatures of  $k_B T/U = 0.55(9), 0.09(1), 0.18(2)$  for the three configurations shown in Figs. 2(a), 2(d), and 2(g); 2(b), 2(e), and 2(h); and 2(c), 2(f), and 2(i), respectively. From the fits, we deduce the local entropy per site, shown in Figs. 2(g)–2(i), and the trap-averaged entropy per particle. These curves illustrate redistribution of entropy between the different regions of the trap. There is a local reduction of entropy in the Mott and band-insulating regions, with a corresponding increase of entropy in the metallic rings. Additionally, we observe that the average entropy per particle is  $1.7(1)k_B$ ,  $1.23(6)k_B$ , and  $0.99(6)k_B$  for the three configurations.

In order to explore the effects of temperature, we heat samples at  $U/8t = 2.6(1)$  and confinement of  $\omega = 2\pi \times 181(3)$  Hz by varying the hold time in the lattice up to 3 s. In Fig. 3(a), we show the reconstructed site occupations for four temperatures from  $k_B T/U = 0.18(2)$  to  $0.55(8)$ . As the temperature increases, singly occupied sites are created in the band-insulating region as  $k_B T$  approaches  $\mu_0$ , while double occupancies and holes appear in the Mott-insulating region as  $k_B T$  approaches  $U$ . The radially averaged density profiles, shown in Fig. 3(b), are fitted with HTSE to extract the temperature and chemical potential. In Fig. 3(c), we show the measured variance for the samples from Fig. 3(a). The variance is suppressed in insulating regions at low temperatures, but approaches 0.25 throughout the sample at high temperatures. To extract trap-independent properties, we use the fitted value of  $\mu_0$  and the trap frequency  $\omega$  to determine the local chemical potential  $\mu = \mu_0 - \frac{1}{2}m\omega^2 d_i^2 a^2$ . Under the LDA, the local properties are equivalent to those of a homogeneous system at the same chemical potential. Radial profiles can then be converted to profiles with varying  $\mu/U$ , as shown in Figs. 3(d) and 3(e) for the site occupation and variance, respectively.

While the detected site occupation  $n_{\text{det}}$  does not allow one to obtain the total density  $\langle \hat{n}_\downarrow + \hat{n}_\uparrow \rangle$  or the double occupancy  $\langle \hat{n}_\downarrow \hat{n}_\uparrow \rangle$  separately, it directly gives the local moment  $\langle m_z^2 \rangle = \langle (\hat{n}_\uparrow - \hat{n}_\downarrow)^2 \rangle = \langle \hat{n}_\uparrow + \hat{n}_\downarrow - 2\hat{n}_\uparrow \hat{n}_\downarrow \rangle = \langle \hat{n}_{\text{det}} \rangle$  [33]. In the strong coupling limit  $U \gg t$  and at half filling, as the temperature is lowered below  $\sim U$ , the local moment is expected to approach unity as the system enters the Mott-insulating state. At even lower temperatures, near the superexchange scale  $t^2/U$ , the moment is expected to slightly decrease, signaling reduced localization as magnetic

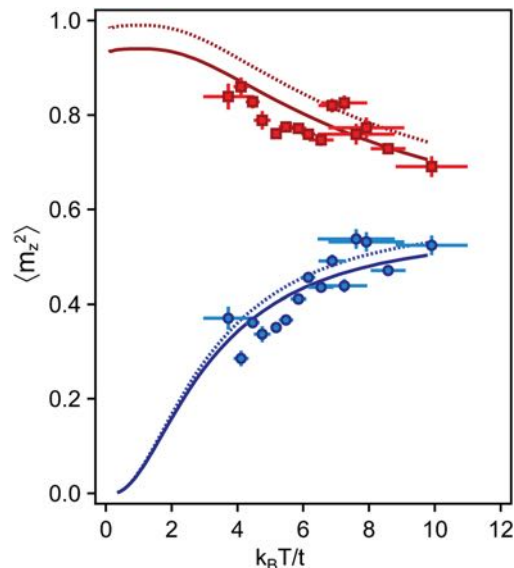


FIG. 4. Local moment  $\langle m_z^2 \rangle$  as a function of temperature at  $U/8t = 2.6(1)$  for  $\mu/U = 0.5$  (red squares) and  $\mu/U = -0.25$  (blue circles). The local moments are extracted from 117 samples. For each sample, the temperature and global chemical potential are determined by fitting to HTSE in the outer regions where  $n_{\text{det}} < 0.25$ . NLCE data at  $U/t = 21$  with and without adjustment for imaging fidelity are shown in solid and dotted lines, respectively.

interactions become important [34]. The moment, directly given by  $n_{\text{det}}$ , can thus show signatures of superexchange, albeit at temperatures lower than those accessed in the current work. In Fig. 4, we show the local moment at half filling ( $\mu = U/2$ ) as a function of temperatures for the same parameters as in Fig. 3. To determine the half-filling point, the detected occupation is fitted to HTSE in the outer regions of the sample where  $n_{\text{det}} < 0.25$ , from which we extract the temperature and global chemical potential  $\mu_0$ . At half filling, a measurement of the local moment also yields the double occupancy via  $\langle \hat{n}_\uparrow \hat{n}_\downarrow \rangle = (1 - \langle m_z^2 \rangle)/2$ . We also show the measured temperature dependence of the moment at  $\mu = -U/4$ . Note that  $\langle m_z^2 \rangle$  is symmetric about  $\mu = U/2$ , a consequence of the particle-hole symmetry of the Fermi-Hubbard model on a bipartite lattice. Thus, the behavior of the moment versus temperature at  $\mu = -U/4$  is representative of the metallic regions both below and above half filling. After correction for imaging fidelity, the data for both values of  $\mu$  are consistent with the NLCE predictions.

In summary, we have directly observed with single-site resolution the Mott-insulating, band-insulating, and metallic states of the 2D Hubbard model using fermionic  $^{40}\text{K}$  in an optical lattice. We measure entropies as low as  $0.99(6)k_B$  per particle, indicating that short-range antiferromagnetic spin correlations should be present [31,35,36]. The Mott insulator provides a well-controlled initial state for further studies, such as the properties of one-dimensional Hubbard chains and dynamics of magnetic

polarons [8,37]. Additionally, the presence of  $^{23}\text{Na}$  in our system, combined with the recently demonstrated creation of ground state  $^{23}\text{Na}^{40}\text{K}$  molecules [38], opens the possibility to study lattice models with long-range and anisotropic interactions at the single-site level.

The authors thank David Reens and Thomas Lompe for experimental support, and Zoran Hadzibabic for a critical reading of the manuscript. This work was supported by the NSF, AFOSR-PECASE, AFOSR-MURI on Exotic Phases of Matter, ARO-MURI on Atomtronics, a grant from the Army Research Office with funding from the DARPA OLE program, and the David and Lucile Packard Foundation. K. R. L. was supported by the Fannie and John Hertz Foundation and the NSF GRFP. M. A. N. was supported by the DoD through the NDSEG Fellowship Program.

- 
- [1] M. Troyer and U.-J. Wiese, *Phys. Rev. Lett.* **94**, 170201 (2005).
  - [2] *Proceedings of the International School of Physics “Enrico Fermi,” Course CLXIV, Varenna, 2006*, edited by M. Inguscio, W. Ketterle, and C. Salomon (IOS Press, Amsterdam, 2008).
  - [3] I. Bloch, J. Dalibard, and W. Zwerger, *Rev. Mod. Phys.* **80**, 885 (2008).
  - [4] *The BCS-BEC Crossover and the Unitary Fermi Gas*, edited by W. Zwerger (Springer, New York, 2011), Vol. 836.
  - [5] M. W. Zwierlein, in *Novel Superfluids*, edited by K.-H. Bennemann and J. B. Ketterson (Oxford University Press, Oxford, 2014), Vol. 2.
  - [6] T. Esslinger, *Annu. Rev. Condens. Matter Phys.* **1**, 129 (2010).
  - [7] P. W. Anderson, *Science* **235**, 1196 (1987).
  - [8] P. A. Lee, N. Nagaosa, and X.-G. Wen, *Rev. Mod. Phys.* **78**, 17 (2006).
  - [9] R. Jördens, N. Strohmaier, K. Günter, H. Moritz, and T. Esslinger, *Nature (London)* **455**, 204 (2008).
  - [10] U. Schneider, L. Hackermüller, S. Will, T. Best, I. Bloch, T. A. Costi, R. W. Helmes, D. Rasch, and A. Rosch, *Science* **322**, 1520 (2008).
  - [11] S. Taie, R. Yamazaki, S. Sugawa, and Y. Takahashi, *Nat. Phys.* **8**, 825 (2012).
  - [12] P. M. Duarte, R. A. Hart, T.-L. Yang, X. Liu, T. Paiva, E. Khatami, R. T. Scalettar, N. Trivedi, and R. G. Hulet, *Phys. Rev. Lett.* **114**, 070403 (2015).
  - [13] D. Greif, T. Uehlinger, G. Jotzu, L. Tarruell, and T. Esslinger, *Science* **340**, 1307 (2013).
  - [14] R. A. Hart, P. M. Duarte, T.-L. Yang, X. Liu, T. Paiva, E. Khatami, R. T. Scalettar, N. Trivedi, D. A. Huse, and R. G. Hulet, *Nature (London)* **519**, 211 (2015).
  - [15] D. Greif, G. Jotzu, M. Messer, R. Desbuquois, and T. Esslinger, *Phys. Rev. Lett.* **115**, 260401 (2015).
  - [16] E. Cocchi, L. A. Miller, J. H. Drewes, M. Koschorreck, D. Pertot, F. Brennecke, and M. Köhl, *Phys. Rev. Lett.* **116**, 175301 (2016).
  - [17] C. Hofrichter, L. Riegger, F. Scazza, M. Höfer, D. R. Fernandes, I. Bloch, and S. Fölling, [arXiv:1511.07287](https://arxiv.org/abs/1511.07287) [*Phys. Rev. X* (to be published)].
  - [18] W. S. Bakr, A. Peng, M. E. Tai, R. Ma, J. Simon, J. I. Gillen, S. Fölling, L. Pollet, and M. Greiner, *Science* **329**, 547 (2010).
  - [19] J. F. Sherson, C. Weitenberg, M. Endres, M. Cheneau, I. Bloch, and S. Kuhr, *Nature (London)* **467**, 68 (2010).
  - [20] M. Endres, M. Cheneau, T. Fukuhara, C. Weitenberg, P. Schauß, C. Gross, L. Mazza, M. C. Banuls, L. Pollet, I. Bloch, and S. Kuhr, *Science* **334**, 200 (2011).
  - [21] M. Cheneau, P. Barmettler, D. Poletti, M. Endres, P. Schauß, T. Fukuhara, C. Gross, I. Bloch, C. Kollath, and S. Kuhr, *Nature (London)* **481**, 484 (2012).
  - [22] L. W. Cheuk, M. A. Nichols, M. Okan, T. Gersdorf, V. V. Ramasesh, W. S. Bakr, T. Lompe, and M. W. Zwierlein, *Phys. Rev. Lett.* **114**, 193001 (2015).
  - [23] E. Haller, J. Hudson, A. Kelly, D. A. Cotta, B. Peaudecerf, G. D. Bruce, and S. Kuhr, *Nat. Phys.* **11**, 738 (2015).
  - [24] M. F. Parsons, F. Huber, A. Mazurenko, C. S. Chiu, W. Setiawan, K. Wooley-Brown, S. Blatt, and M. Greiner, *Phys. Rev. Lett.* **114**, 213002 (2015).
  - [25] G. J. A. Edge, R. Anderson, D. Jervis, D. C. McKay, R. Day, S. Trotzky, and J. H. Thywissen, *Phys. Rev. A* **92**, 063406 (2015).
  - [26] A. Omran, M. Boll, T. A. Hilker, K. Kleinlein, G. Salomon, I. Bloch, and C. Gross, *Phys. Rev. Lett.* **115**, 263001 (2015).
  - [27] D. Greif, M. F. Parsons, A. Mazurenko, C. S. Chiu, S. Blatt, F. Huber, G. Ji, and M. Greiner, *Science* **351**, 953 (2016).
  - [28] V. W. Scarola, L. Pollet, J. Oitmaa, and M. Troyer, *Phys. Rev. Lett.* **102**, 135302 (2009).
  - [29] T. Paiva, R. Scalettar, M. Randeria, and N. Trivedi, *Phys. Rev. Lett.* **104**, 066406 (2010).
  - [30] M. T. DePue, C. McCormick, S. L. Winoto, S. Oliver, and D. S. Weiss, *Phys. Rev. Lett.* **82**, 2262 (1999).
  - [31] E. Khatami and M. Rigol, *Phys. Rev. A* **84**, 053611 (2011).
  - [32] J. Oitmaa, C. Hamer, and W. Zheng, *Series Expansion Methods for Strongly Interacting Lattice Models* (Cambridge University Press, Cambridge, 2006).
  - [33] J. E. Hirsch, *Phys. Rev. B* **31**, 4403 (1985).
  - [34] T. Paiva, R. T. Scalettar, C. Huscroft, and A. K. McMahan, *Phys. Rev. B* **63**, 125116 (2001).
  - [35] J. P. F. LeBlanc and E. Gull, *Phys. Rev. B* **88**, 155108 (2013).
  - [36] S. Chiesa, C. N. Varney, M. Rigol, and R. T. Scalettar, *Phys. Rev. Lett.* **106**, 035301 (2011).
  - [37] C. Weitenberg, M. Endres, J. F. Sherson, M. Cheneau, P. Schausz, T. Fukuhara, I. Bloch, and S. Kuhr, *Nature (London)* **471**, 319 (2011).
  - [38] J. W. Park, S. A. Will, and M. W. Zwierlein, *Phys. Rev. Lett.* **114**, 205302 (2015).
  - [39] See Supplemental Material <http://link.aps.org/supplemental/10.1103/PhysRevLett.116.235301> for determination of Hubbard parameters.

## Appendix C

# Observation of Spatial Charge and Spin Correlations in the 2D Fermi-Hubbard Model

This appendix contains a reprint of the following paper [38]:

L. W. Cheuk\*, M. A. Nichols\*, K. R. Lawrence, M. Okan, H. Zhang, E. Khatami, N. Trivedi, T. Paiva, M. Rigol, and M. W. Zwierlein, “Observation of Spatial Charge and Spin Correlations in the 2D Fermi-Hubbard Model,” *Science* **353**, 1260 (2016).

also in two dimensions. Realization of the paradigmatic quantum phase transition from such an artificial valence bond solid to a Heisenberg antiferromagnet (41) therefore seems within reach of present experiments.

Recently, we became aware of similar experimental results in two dimensions (42, 43).

## REFERENCES AND NOTES

- P. W. Anderson, *Science* **235**, 1196–1198 (1987).
- K. L. Hur, T. M. Rice, *Ann. Phys.* **324**, 1452–1515 (2009).
- A. Auerbach, *Interacting Electrons and Quantum Magnetism* (Springer Science & Business Media, 1994).
- T. Giamarchi, *Quantum Physics in One Dimension* (Clarendon, 2004).
- T. Esslinger, *Ann. Rev. Condens. Matter Phys.* **1**, 129–152 (2010).
- R. Jördens, N. Strohmaier, K. Günter, H. Moritz, T. Esslinger, *Nature* **455**, 204–207 (2008).
- U. Schneider et al., *Science* **322**, 1520–1525 (2008).
- R. Jördens et al., *Phys. Rev. Lett.* **104**, 180401 (2010).
- S. Taie, R. Yamazaki, S. Sugawa, Y. Takahashi, *Nat. Phys.* **8**, 825–830 (2012).
- P. M. Duarte et al., *Phys. Rev. Lett.* **114**, 070403 (2015).
- D. Greif et al., *Science* **351**, 953–957 (2016).
- L. W. Cheuk et al., *Phys. Rev. Lett.* **116**, 235301 (2016).
- C. Hofrichter et al., *Phys. Rev. X* **6**, 021030 (2016).
- E. Cocco et al., *Phys. Rev. Lett.* **116**, 175301 (2016).
- S. Trotzky, Y.-A. Chen, U. Schnorrberger, P. Cheinet, I. Bloch, *Phys. Rev. Lett.* **105**, 265303 (2010).
- D. Greif, T. Uehlinger, G. Jotzu, L. Tarruell, T. Esslinger, *Science* **340**, 1307–1310 (2013).
- D. Greif, G. Jotzu, M. Messer, R. Desbuquois, T. Esslinger, *Phys. Rev. Lett.* **115**, 260401 (2015).
- R. A. Hart et al., *Nature* **519**, 211–214 (2015).
- S. Murmann et al., *Phys. Rev. Lett.* **115**, 215301 (2015).
- L. W. Cheuk et al., *Phys. Rev. Lett.* **114**, 193001 (2015).
- M. F. Parsons et al., *Phys. Rev. Lett.* **114**, 213002 (2015).
- E. Haller et al., *Nat. Phys.* **11**, 738–742 (2015).
- G. J. A. Edge et al., *Phys. Rev. A* **92**, 063406 (2015).
- A. Omran et al., *Phys. Rev. Lett.* **115**, 263001 (2015).
- G. Zürn et al., *Phys. Rev. Lett.* **110**, 135301 (2013).
- J. Sirker, A. Klümper, *Phys. Rev. B* **66**, 245102 (2002).
- E. V. Gorelik et al., *Phys. Rev. A* **85**, 061602 (2012).
- B. Scialla et al., *Phys. Rev. A* **88**, 063629 (2013).
- F. H. L. Essler, H. Frahm, F. Göhmann, A. Klümper, V. E. Korepin, *The One-Dimensional Hubbard Model* (Cambridge Univ. Press, 2005).
- Supplementary text is available as supplementary materials on Science Online.
- J. Seby-Straley, M. Anderlini, P. Jessen, J. Porto, *Phys. Rev. A* **73**, 033605 (2006).
- S. Fölling et al., *Nature* **448**, 1029–1032 (2007).
- F. Werner, O. Parcollet, A. Georges, S. R. Hassan, *Phys. Rev. Lett.* **95**, 056401 (2005).
- R. Olf, F. Fang, G. E. Marti, A. MacRae, D. M. Stamper-Kurn, *Nat. Phys.* **11**, 720–723 (2015).
- J.-S. Bernier et al., *Phys. Rev. A* **79**, 061601 (2009).
- T.-L. Ho, Q. Zhou, *Proc. Natl. Acad. Sci. U.S.A.* **106**, 6916–6920 (2009).
- A. M. Rey et al., *Europhys. Lett.* **87**, 60001 (2009).
- S. Trebst, U. Schollwöck, M. Troyer, P. Zoller, *Phys. Rev. Lett.* **96**, 250402 (2006).
- S. Nascimbéne et al., *Phys. Rev. Lett.* **108**, 205301 (2012).
- M. Lubasch, V. Murg, U. Schneider, J. I. Cirac, M.-C. Bañuls, *Phys. Rev. Lett.* **107**, 165301 (2011).
- T. Senthil, A. Vishwanath, L. Balents, S. Sachdev, M. P. A. Fisher, *Science* **303**, 1490–1494 (2004).
- M. F. Parsons et al., *Science* **353**, 1253–1256 (2016).
- L. W. Cheuk et al., *Science* **353**, 1260–1264 (2016).

## ACKNOWLEDGMENTS

We acknowledge help by K. Kleinlein and M. Lohse during the setup of the experiment and financial support by Max-Planck-Gesellschaft and the European Union [Ultracold Quantum Matter (UQUAM) and Quantum Simulation of Many-Body Physics in Ultracold Gases (QUSIMGAS)]. The data that support the plots

within this paper and other findings of this study are available from the corresponding author upon reasonable request.

## SUPPLEMENTARY MATERIALS

[www.sciencemag.org/content/353/6305/1257/suppl/DC1](http://www.sciencemag.org/content/353/6305/1257/suppl/DC1)  
Supplementary Text  
Figs. S1 to S5  
Table S1  
References (44–51)  
17 May 2016; accepted 18 August 2016  
10.1126/science.aag1635

## QUANTUM SIMULATION

# Observation of spatial charge and spin correlations in the 2D Fermi-Hubbard model

**Lawrence W. Cheuk,<sup>1\*</sup> Matthew A. Nichols,<sup>1\*</sup> Katherine R. Lawrence,<sup>1</sup> Melih Okan,<sup>1</sup> Hao Zhang,<sup>1</sup> Ehsan Khatami,<sup>2</sup> Nandini Trivedi,<sup>3</sup> Thereza Paiva,<sup>4</sup> Marcos Rigol,<sup>5</sup> Martin W. Zwierlein<sup>1†</sup>**

Strong electron correlations lie at the origin of high-temperature superconductivity. Its essence is believed to be captured by the Fermi-Hubbard model of repulsively interacting fermions on a lattice. Here we report on the site-resolved observation of charge and spin correlations in the two-dimensional (2D) Fermi-Hubbard model realized with ultracold atoms. Antiferromagnetic spin correlations are maximal at half-filling and weaken monotonically upon doping. At large doping, nearest-neighbor correlations between singly charged sites are negative, revealing the formation of a correlation hole, the suppressed probability of finding two fermions near each other. As the doping is reduced, the correlations become positive, signaling strong bunching of doublons and holes, in agreement with numerical calculations. The dynamics of the doublon-hole correlations should play an important role for transport in the Fermi-Hubbard model.

**A** central question in the study of cuprate high-temperature superconductors is how spin and charge correlations give rise to the wealth of observed phenomena. Antiferromagnetic order present in the absence of doping quickly gives way to superconductivity upon doping with holes or electrons (1), suggesting the viewpoint of competing phases. On the other hand, antiferromagnetic correlations can also occur in the form of singlet bonds between neighboring sites. In fact, it has been proposed (2) that superconductivity could result, upon doping a Mott insulator, from the condensation of such resonating valence bonds. It has also been argued (1) that the pseudogap and “strange metal” regions are supported by a liquid of spin-singlets. This argument has spurred the simultaneous examination of nearest-neighbor spin and charge correlations, which might reveal the underlying mechanisms of pairing and transport.

In recent years, ultracold atomic gases have been established as pristine quantum simulators of strongly correlated many-body systems (3–5). The Fermi-Hubbard model is of special importance, thanks to its paradigmatic role for the study of high-critical temperature cuprates. At low temperatures and away from half-filling, solving the Fermi-Hubbard model theoretically

is very challenging because of the fermion sign problem. Central properties of Fermi-Hubbard physics—from the reduction of double occupancy (6, 7) and of compressibility (8, 9) as the repulsion is increased, to short-range antiferromagnetic correlations (10–12) and the equation of state (9, 13, 14)—have been observed in ultracold atom experiments. The recently developed Fermi gas microscopes (13, 15–19) have led to the direct observation of two-dimensional (2D) fermionic Mott insulators, band insulators, and metals with single-atom, single-site-resolved detection (20, 21). The strength of this technique, however, is on full display when single-site detection is used to directly measure correlations in the gas, as has been achieved with bosons (22–24).

<sup>1</sup>Department of Physics, MIT-Harvard Center for Ultracold Atoms, and Research Laboratory of Electronics, Massachusetts Institute of Technology (MIT), Cambridge, MA 02139, USA.

<sup>2</sup>Department of Physics and Astronomy, San José State University, San José, CA 95192, USA. <sup>3</sup>Department of Physics, The Ohio State University, Columbus, OH 43210, USA. <sup>4</sup>Instituto de Física, Universidade Federal do Rio de Janeiro, Caixa Postal 68.528, 21941-972 Rio de Janeiro, RJ, Brazil. <sup>5</sup>Department of Physics, The Pennsylvania State University, University Park, PA 16802, USA.

\*These authors contributed equally to this work. †Corresponding author. Email: zwierlein@mit.edu

In our study, we used a Fermi gas microscope of  $^{40}\text{K}$  atoms to directly observe charge and spin correlations in the 2D Fermi-Hubbard model (15, 21). Spin correlations displaying antiferromagnetic behavior have also been observed very recently with fermionic  $^6\text{Li}$  in one (25) and two (26) dimensions. We employ the local resolution to simultaneously obtain correlations in the entire range from zero doping (half-filling) to full doping (zero filling), as the density varies in the underlying trapping potential. The microscope measures the parity-projected density on a given lattice site—that is, doubly occupied sites (doublons) appear empty. For a two-spin mixture of fermions in the lowest band of the optical lattice, the parity-projected density is described by the magnetic moment operator (27)  $\hat{m}_{z,i}^2 = (\hat{n}_{\uparrow,i} - \hat{n}_{\downarrow,i})^2$ , where  $\hat{n}_{\sigma,i} = \hat{c}_{\sigma,i}^\dagger \hat{c}_{\sigma,i}$  is the number operator and  $\hat{c}_{\sigma,i}$  ( $\hat{c}_{\sigma,i}^\dagger$ ) are fermion annihilation (creation) operators for spin  $\sigma = \uparrow, \downarrow$  on site  $i$ . Many repeated measurements yield the average local moment on each site (Fig. 1, A and D), which is a thermodynamic quantity that quantifies the interaction energy. This is evident when one rewrites the interaction energy term  $U\hat{n}_{\uparrow,i}\hat{n}_{\downarrow,i}$  as  $\frac{U}{2}(\hat{n}_{\uparrow,i} + \hat{n}_{\downarrow,i} - \hat{m}_{z,i}^2)$ . The Fermi-Hubbard Hamiltonian can be written in terms of local moments as

$$\hat{H} = -t \sum_{\langle i,j \rangle, \sigma} (\hat{c}_{\sigma,i}^\dagger \hat{c}_{\sigma,j} + \text{h.c.}) - \frac{U}{2} \sum_i \hat{m}_{z,i}^2 - \mu \sum_i (\hat{n}_{\uparrow,i} + \hat{n}_{\downarrow,i}) \quad (1)$$

which is a form that highlights the particle-hole symmetry of the Hamiltonian. Here,  $\langle i,j \rangle$  denotes nearest-neighbor sites  $i$  and  $j$ ,  $t$  is the nearest-neighbor hopping amplitude,  $U$  is the on-site interaction energy, and  $\mu$  is the chemical potential. At moderate temperatures and depending on the fillings  $n_i = \langle \hat{n}_{\uparrow,i} + \hat{n}_{\downarrow,i} \rangle$ , this model can yield metallic, band insulating, or Mott insulating states. At half-filling ( $n_i = 1$ ) and at temperatures below the superexchange scale  $4t^2/U$ , quasi-long-range antiferromagnetic correlations arise. For a fixed temperature, these correlations are expected to be maximal when  $U \approx 8t$ , where the interaction energy equals the single-particle bandwidth. Upon doping, a pseudogap phase emerges; at even lower temperatures, one expects a d-wave superconducting state (1). Although the superexchange scale is about a factor of 2 lower than the temperatures achieved here, site-resolved detection of short-range correlations should already reveal precursory signs of physics at this energy scale.

Figure 1A shows a typical measurement of the site-resolved average local magnetic moment from ~90 individual experimental realizations at  $U/t = 7.2(1)$ . Atoms are confined in a radially symmetric trapping potential. Under the local density approximation, this results in a varying local chemical potential and, thus, a spatially varying filling  $n$  throughout the sample. We prepared samples where the maximum filling, which occurs in the center of the trap, lies above  $n = 1$ . From radially averaged profiles (Fig. 1D), the half-filling point is identified as the radial position where the moment reaches its maximum. This follows from the

particle-hole symmetry of the moment operator  $\hat{m}_{z,i}^2$ , a property that holds for all of its averages and cumulants (27).

Because the local moment satisfies the operator identity  $(\hat{m}_{z,i}^2)^2 = \hat{m}_{z,i}^2$ , fluctuations of the local moment do not yield additional information.

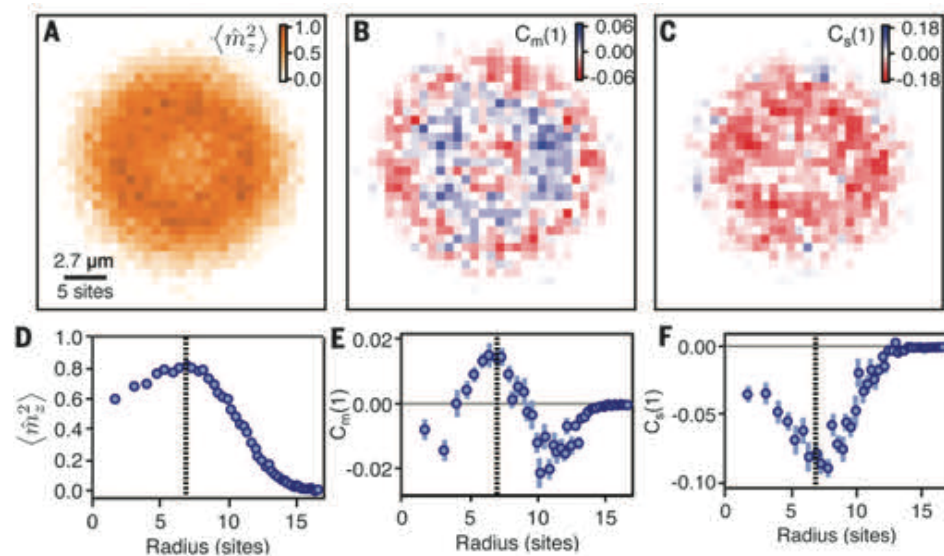


**Fig. 1. Local moment and nearest-neighbor charge and spin correlations.** An ultracold atom realization of the Fermi-Hubbard model for  $U/t = 7.2(1)$  is shown. (A to C) Local moment, nearest-neighbor moment correlator, and nearest-neighbor spin correlator, respectively, as functions of position, averaged over ~90 shots. The spatial variations reflect the varying local doping due to the underlying trapping potential. (D to F) Radial averages of (A), (B), and (C), respectively. The half-filling point is marked by vertical dotted lines.

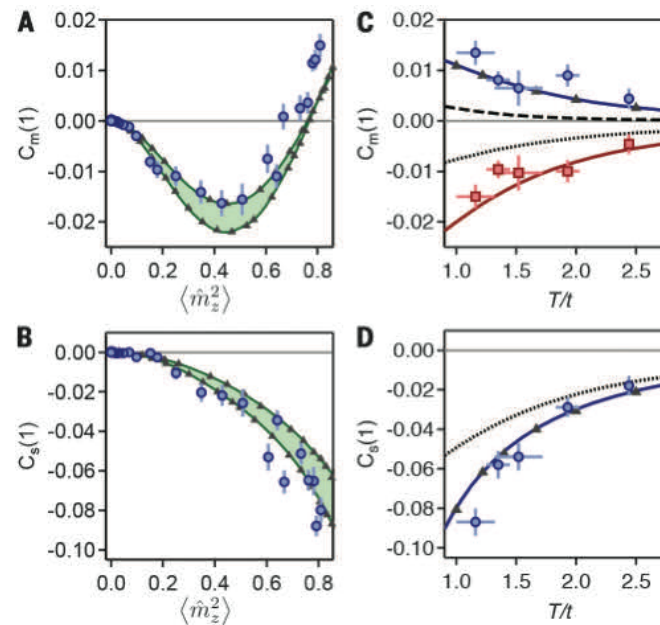


**Fig. 2. Spin and moment correlators as functions of doping and temperature for  $U/t = 7.2(1)$ .** (A and B) Nearest-neighbor moment correlator [ $C_m(1)$ ] (A) and spin correlator [ $C_s(1)$ ] (B) as functions of the local moment, denoted by blue circles. Results from NLCE (and DQMC) for temperatures  $T/t = 0.89$  and  $1.22$  are shown in green lines (and gray triangles), with the intermediate temperature range indicated by green shading. (C) The maximum and minimum of the moment correlator as functions of temperature are denoted by blue circles and red squares, respectively. Corresponding results are obtained from NLCE (solid blue line and solid red line, respectively), and from DQMC for the correlator at half-filling (gray triangles). (D) Nearest-neighbor spin correlator at half-filling as a function of temperature (blue circles). Solid blue line, NLCE results; gray triangles, DQMC results; black dotted line, noninteracting gas. For all graphs, theory curves are not adjusted for the experimental imaging fidelity of 95%.

However, correlations of the moment between different sites do (27). We experimentally measured the moment correlator at a separation of one site,  $C_m(1)$ , defined as

$$C_m(1) = \frac{1}{4} \sum_{j \in \text{nn}_i} \left[ \langle \hat{m}_{z,i}^2 \hat{m}_{z,j}^2 \rangle - \langle \hat{m}_{z,i}^2 \rangle \langle \hat{m}_{z,j}^2 \rangle \right] \quad (2)$$

where the sum is over all four nearest neighbors. The locally resolved correlator  $C_m(1)$  at each site  $i$  and its radial average are shown in Fig. 1, B and E, respectively.  $C_m(1)$  displays nonmonotonic behavior, changing sign as the filling is lowered.

The local moment correlator, however, is not sensitive to the sign of the spin  $S_{z,i} = \frac{1}{2}(\hat{n}_{\uparrow,i} - \hat{n}_{\downarrow,i})$ . One important spin-sensitive correlator is  $\langle \hat{S}_{z,i} \hat{S}_{z,j} \rangle$ , which can reveal antiferromagnetic ordering, expected to occur at half-filling and at low temperatures. This correlator can be expressed as  $\frac{1}{2} \sum_{\sigma} \langle \hat{p}_{\sigma,i} \hat{p}_{\sigma,j} \rangle - \frac{1}{4} \langle \hat{m}_{z,i}^2 \hat{m}_{z,j}^2 \rangle$  (28), where  $\hat{p}_{\sigma,i} = \hat{n}_{\sigma,i} - \hat{n}_{\uparrow,i} \hat{n}_{\downarrow,i}$ , which we measured by removing one spin state via resonant light, before imaging. All terms can be obtained experimentally in separate runs and are averaged separately. Analogous to the nearest-neighbor moment correlator  $C_m(1)$ , we define the nearest-neighbor spin correlator at site  $i$

$$C_s(1) = \sum_{j \in \text{nn}_i} (\langle \hat{S}_{z,i} \hat{S}_{z,j} \rangle - \langle \hat{S}_{z,i} \rangle \langle \hat{S}_{z,j} \rangle) \quad (3)$$

Figure 1, C and F, show the locally resolved nearest-neighbor spin correlation  $C_s(1)$  and its corresponding radial average, respectively. The fact that  $C_s(1)$  is negative suggests antiferromagnetic correlations, as expected (29–31). However, even without interactions, Pauli-blocking of like spins suppresses  $C_s(1)$ . One can see this by noting

that  $C_s(1)$  contains density correlations of either spin species separately [ $\langle \hat{n}_{\sigma,i} \hat{n}_{\sigma,j} \rangle - \langle \hat{n}_{\sigma,i} \rangle^2$ ], which are negative even for the noninteracting gas thanks to Pauli suppression. For the lowest temperatures reached, we observed a maximum absolute spin correlation of about a factor of 2 larger than that of a noninteracting Fermi gas.

Figure 2, A and B, show the nearest-neighbor moment and spin correlations versus the measured local moment  $\langle \hat{m}_z^2 \rangle$ . This representation allows for comparison with theory under minimal assumptions. As a thermodynamic quantity, the moment can replace the role of the chemical potential  $\mu$ . All thermodynamic variables can then be viewed as functions of the local moment, the spin correlation at half-filling,  $U$ , and  $t$ . In fact, the local spin correlation at half-filling is itself a thermometer that does not require any fit (32). Also shown in Fig. 2, A and B, are numerical linked-cluster expansion (NLCE) (33) and determinantal quantum Monte Carlo (DQMC) (34) calculations (28), which display similar behavior as the experimental data. Note that there are no free parameters; the temperature  $T/t = 1.16(16)$  is obtained from the spin correlation at half-filling.

As expected, the antiferromagnetic spin correlations are maximum at half-filling and decrease in absolute value with increased doping. Moment correlations instead are negative at low to intermediate fillings, crossing zero around a moment of 0.75 (doping  $\approx 0.21$ ) before turning positive toward half-filling. This implies that moments change their character from effectively repulsive (antibunching) to effectively attractive (bunching). The antibunching and bunching behaviors in the moments, as well as the antiferromagnetic spin correlations, become more pronounced as the temperature is lowered. Figure 2C shows the moment

correlation at half-filling (maximum positive value), as well as its minimum value versus temperature. The spin correlator at half-filling (minimum value) (Fig. 2D) displays a similar temperature dependence, reaching  $-0.09$  at the lowest temperatures in our experiment. This is about 30% of the maximum spin correlation expected for the spin- $\frac{1}{2}$  Heisenberg model at zero temperature in two dimensions (35).

To interpret the moment correlations, one may recast them in terms of the two-point correlator

$$g_2(r) = \frac{\langle \hat{m}_z^2(r) \hat{m}_z^2(0) \rangle}{\langle \hat{m}_z^2(r) \rangle \langle \hat{m}_z^2(0) \rangle} \quad (4)$$

which measures the probability of finding two moments a distance  $r$  from each other. In the absence of correlations,  $g_2 = 1$ . At low filling, for which the doublon density is negligible and the moment  $\langle \hat{m}_z^2 \rangle = \langle \hat{n} \rangle - 2\langle \hat{n}_{\uparrow} \hat{n}_{\downarrow} \rangle \approx n$  is essentially the density,  $g_2(r)$  measures density correlations. These are nontrivial even for the spin-polarized noninteracting Fermi gas, where fermion statistics lead to anticorrelations at short distances, reflecting the fact that two fermions cannot occupy the same site. This leads to Pauli suppression of  $g_2$  that persists to a distance on the order of the average interparticle spacing, a feature known as the Pauli hole. Although implications of this fermion antibunching have been observed in the suppression of density fluctuations (36, 37) and momentum space correlations (38, 39), the real space suppression  $g_2(r)$  has not been observed in situ before. In a noninteracting two-spin mixture, the anticorrelations are halved, as only two identical fermions experience the Pauli hole. However, repulsive interactions between opposite spins also suppress  $g_2(r)$ , leading to a combined Pauli and correlation hole.

In Fig. 3A, we show the directly measured  $g_2(1)$  as a function of moment at an intermediate interaction of  $U/t = 7.2$ . The strong suppression of  $g_2(1)$  at low fillings (large interparticle spacing) is observed and is stronger than Pauli suppression alone, reflecting short-range anticorrelations due to repulsive interactions. The data are well described by NLCE and DQMC calculations (Fig. 3A).

Whereas  $g_2(r)$  measures the probability of finding two moments a distance  $r$  from each other, near half-filling, where  $\langle \hat{m}_z^2 \rangle \sim 1$ , the correlations arise mainly from sites where the moment is zero (i.e., sites with holes and doublons). The number of holes and doublons, which appear empty after imaging, is given by  $\langle 1 - \hat{m}_z^2 \rangle$ . The corresponding two-point correlation function  $\bar{g}_2(r)$  of these antimoments is thus

$$\bar{g}_2(r) = \frac{\langle (1 - \hat{m}_z^2(r))(1 - \hat{m}_z^2(0)) \rangle}{\langle 1 - \hat{m}_z^2(r) \rangle \langle 1 - \hat{m}_z^2(0) \rangle} \quad (5)$$

In Fig. 3B, we show that  $\bar{g}_2(1)$  is strongly enhanced near half-filling beyond the uncorrelated value of 1.  $\bar{g}_2(1)$  thus reveals the strong bunching of holes and doublons. There are three contributions

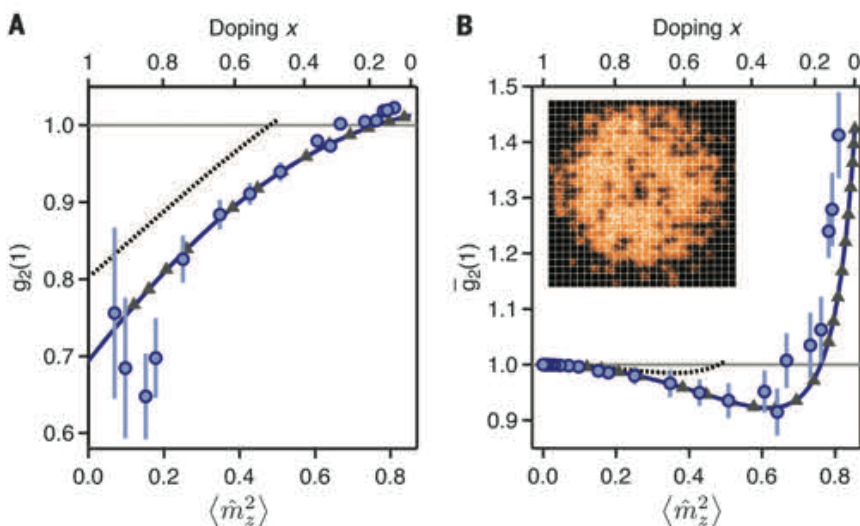
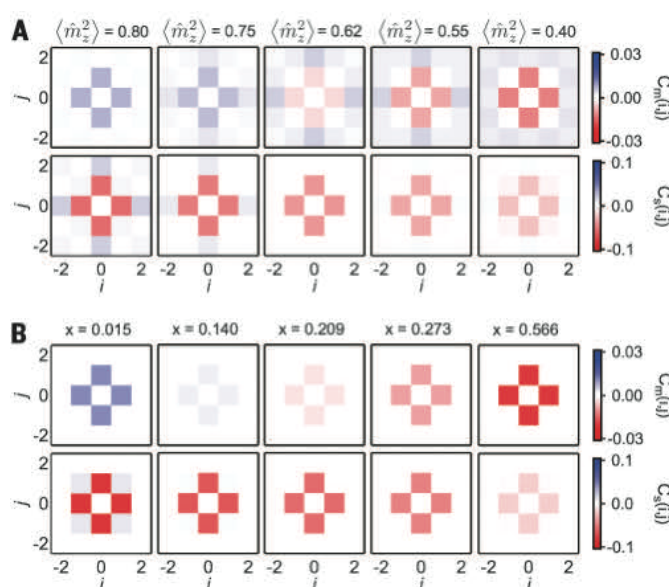


**Fig. 3. Two-point correlation functions.**  $g_2$  is the correlation function for moments and  $\bar{g}_2$  for antimoments at a separation of one lattice site for  $U/t = 7.2(1)$ . (A)  $g_2(1)$  for moments. (B)  $\bar{g}_2(1)$  for antimoments. Blue circles, experimental data; blue solid line, NLCE theory; gray triangles, DQMC theory. Both NLCE and DQMC calculations are performed at  $T/t = 1.22$ , and neither are adjusted for the experimental imaging fidelity of 95%. Black dotted lines, noninteracting gas. The doping  $x$  as a function of local moment is determined from NLCE theory at  $T/t = 1.22$ , without adjustment for imaging fidelity. (Inset) Typical image showing neighboring antimoments (imaged holes) near half-filling.

**Fig. 4. Spin and moment correlations as functions of distance and doping.** (A) Moment and spin correlations for  $U/t = 7.2(1)$  are shown in the top and bottom rows, respectively, at various values of the local moment. Correlation values are averaged over symmetric points. The moment correlator  $C_m(0,1)$  changes sign near a local moment of  $\langle \hat{m}_z^2 \rangle \approx 0.75$ . The anticorrelation of spins  $C_s(0,1)$  is observed to weaken upon increasing doping (decreasing moment). In contrast, the next-nearest-neighbor spin correlator  $C_s(1,1)$  changes from positive at zero doping to negative at large doping. (B) Moment and spin correlations obtained from DQMC theory for  $U/t = 7.2(1)$  and  $T/t = 1.00$  are shown in the top and bottom rows, respectively, at various values of doping  $x$ . The nonzero value of the moment and spin correlators at distance  $(i,j) = (0,0)$  are omitted for clarity. They are both local quantities determined by the value of the moment. NLCE and DQMC results for the correlators at all distances shown are in good agreement (28).



to  $\bar{g}_2(1)$ : correlations between pairs of holes, between pairs of doublons, and between holes and doublons. One expects neighboring holes and neighboring doublons to show negative correlations due to Pauli suppression and strong repulsion. Hence, the bunching behavior must originate from positive correlations between neighboring doublon-hole pairs. This expectation is confirmed by NLCE and DQMC calculations (28).

The strong doublon-hole correlation near half-filling in the presence of antiferromagnetic correlations can be qualitatively captured by a simple two-site Hubbard model, experimentally realized in (40). In the strongly interacting limit ( $U \gg t$ ), the doublon density vanishes and the ground state is a spin singlet. However, at intermediate interaction strengths, tunneling admixes a doublon-hole pair into the ground state wave function, with an amplitude  $\sim t/U$ . Thus, short-range singlet correlations at moderate  $U/t$  occur naturally together with nearest-neighbor doublon-hole correlations.

At a separation of one lattice site, we have revealed the competition between the combined Pauli- and interaction-driven repulsion of singly occupied sites and the effective attraction of doublons and holes, which manifests itself in a sign change of the correlator. The ability of the microscope to measure at a site-resolved level also allows investigation of longer-distance correlations. In Fig. 4, A and B, we show the moment and spin correlations  $C_m(i,j)$  and  $C_s(i,j)$ , respectively, as a function of separation distance  $i\hat{x} + j\hat{y}$ . Near half-filling, even at the temperatures of this graph ( $T/t \approx 1.2$ ), antiferromagnetic spin correlations beyond the next neighbor are visible. With increased doping, they give way to a more isotro-

pic negative spin correlation. For example,  $C_s(1,1)$  changes sign from positive at half-filling to negative at large dopings. This resembles the effect of Pauli suppression that is already present for non-interacting fermions. For the moment correlator, we clearly observe the sign change of  $C_m(1,0)$  at a doping of  $x \approx 0.21$  and that the correlations do not extend substantially beyond one site.

The measurement of nonlocal moment correlations also results in direct access to the associated potential energy fluctuations ( $\Delta E_{\text{pot}}$ ). From the Fermi-Hubbard Hamiltonian in Eq. 1, we find that

$$\begin{aligned} \Delta E_{\text{pot}}^2 &= \frac{1}{4} U^2 \left( \langle \hat{M}^2 \rangle - \langle \hat{M} \rangle^2 \right) \\ &= \frac{1}{4} U^2 \sum_{ij} \left( \langle \hat{m}_{z,i}^2 \hat{m}_{z,j}^2 \rangle - \langle \hat{m}_{z,i}^2 \rangle \langle \hat{m}_{z,j}^2 \rangle \right) \end{aligned} \quad (6)$$

where  $\hat{M} = \sum_i \hat{m}_{z,i}^2$  is the total moment operator. At half-filling, the contribution to the fluctuations from the nearest-neighbor moment correlations is thus  $U^2 C_m(1) \approx 0.8t^2$  for  $T/t \approx 1$  and  $U/t = 7.2(1)$ . This suggests that doublon-hole correlations can arise from coherent tunneling of particles bound in spin singlets.

Away from half-filling, both NLCE and DQMC calculations are currently limited to a temperature range around  $T/t \approx 0.5$ , not far below what is reached experimentally in this work. Further reduction in experimental temperatures will provide a valuable benchmark for theoretical techniques, especially away from half-filling, where the sign problem arises. The clear importance of doublon-hole correlations will prompt further studies of their dynamics, especially away from

half-filling, which could elucidate their role for the transport properties of a possible strange metal phase and potential pseudogap behavior.

## REFERENCES AND NOTES

- P. A. Lee, N. Nagaosa, X.-G. Wen, *Rev. Mod. Phys.* **78**, 17–85 (2006).
- P. W. Anderson, *Science* **235**, 1196–1198 (1987).
- M. Inguscio, W. Ketterle, C. Salomon, Eds., *Ultracold Fermi Gases*, Proceedings of the International School of Physics “Enrico Fermi,” Course CLXIV, Varenna, 20 to 30 June 2006 (IOS Press, 2008).
- I. Bloch, J. Dalibard, W. Zwerger, *Rev. Mod. Phys.* **80**, 885–964 (2008).
- T. Esslinger, *Annu. Rev. Condens. Matter Phys.* **1**, 129–152 (2010).
- R. Jördens, N. Strohmaier, K. Günter, H. Moritz, T. Esslinger, *Nature* **455**, 204–207 (2008).
- S. Taie, R. Yamazaki, S. Sugawa, Y. Takahashi, *Nat. Phys.* **8**, 825–830 (2012).
- U. Schneider et al., *Science* **322**, 1520–1525 (2008).
- P. M. Duarte et al., *Phys. Rev. Lett.* **114**, 070403 (2015).
- D. Greif, T. Uehlinger, G. Jotzu, L. Tarruell, T. Esslinger, *Science* **340**, 1307–1310 (2013).
- R. A. Hart et al., *Nature* **519**, 211–214 (2015).
- D. Greif, G. Jotzu, M. Messer, R. Desbuquois, T. Esslinger, *Phys. Rev. Lett.* **115**, 260401 (2015).
- E. Cocchi et al., *Phys. Rev. Lett.* **116**, 175301 (2016).
- C. Hofrichter et al., *Phys. Rev. X* **6**, 021030 (2016).
- L. W. Cheuk et al., *Phys. Rev. Lett.* **114**, 193001 (2015).
- E. Haller et al., *Nat. Phys.* **11**, 738–742 (2015).
- M. F. Parsons et al., *Phys. Rev. Lett.* **114**, 213002 (2015).
- A. Omran et al., *Phys. Rev. Lett.* **115**, 263001 (2015).
- G. J. A. Edge et al., *Phys. Rev. A* **92**, 063406 (2015).
- D. Greif et al., *Science* **351**, 953–957 (2016).
- L. W. Cheuk et al., *Phys. Rev. Lett.* **116**, 235301 (2016).
- M. Endres et al., *Science* **334**, 200–203 (2011).
- M. Endres et al., *Appl. Phys. B* **113**, 27–39 (2013).
- R. Islam et al., *Nature* **528**, 77–83 (2015).
- M. Boll et al., *Science* **353**, 1257–1260 (2016).
- M. F. Parsons et al., *Science* **353**, 1253–1256 (2016).
- E. Kapit, E. Mueller, *Phys. Rev. A* **82**, 013644 (2010).
- See the supplementary materials on Science Online.
- J. E. Hirsch, *Phys. Rev. B* **31**, 4403–4419 (1985).
- E. Khatri, M. Rigol, *Phys. Rev. A* **84**, 053611 (2011).
- J. P. F. LeBlanc, E. Gull, *Phys. Rev. B* **88**, 155108 (2013).
- M. J. H. Ku, A. T. Sommer, L. W. Cheuk, M. W. Zwierlein, *Science* **355**, 563–567 (2012).
- M. Rigol, T. Bryant, R. R. P. Singh, *Phys. Rev. Lett.* **97**, 187202 (2006).
- R. Blankenbecler, D. J. Scalapino, R. L. Sugar, *Phys. Rev. D Part. Fields* **24**, 2278–2286 (1981).
- T. Paiva, R. Scalettari, M. Randeria, N. Trivedi, *Phys. Rev. Lett.* **104**, 066406 (2010).
- C. Sanner et al., *Phys. Rev. Lett.* **105**, 040402 (2010).
- T. Müller et al., *Phys. Rev. Lett.* **105**, 040401 (2010).
- T. Rom et al., *Nature* **444**, 733–736 (2006).
- T. Jeltes et al., *Nature* **445**, 402–405 (2007).
- S. Murmann et al., *Phys. Rev. Lett.* **114**, 080402 (2015).

## ACKNOWLEDGMENTS

We thank S. Todadri, M. Randeria, and M. Greiner and his research group for fruitful discussions. This work was supported by the NSF, an Air Force Office of Scientific Research Presidential Early Career

Award for Scientists and Engineers and Multidisciplinary University Research Initiative (MURI) on Exotic Quantum Phases, an Army Research Office MURI on Atomtronics, and the David and Lucile Packard Foundation. M.A.N. was supported by the U.S. Department of Defense through the National Defense Science and Engineering Graduate Fellowship Program. K.R.L. was supported by the Fannie and John Hertz Foundation and the NSF Graduate Research Fellowship Program. N.T. acknowledges funding from

NSF Division of Materials Research grant 1309461 and partial support by a grant from the Simons Foundation (343227) and thanks S. Todadri for hospitality at MIT during her sabbatical. T.P. acknowledges support from Brazilian National Council for Scientific and Technological Development, Fundação de Amparo à Pesquisa do Estado do Rio de Janeiro, and Instituto Nacional de Ciência e Tecnologia on Quantum Information. M.R. was supported by the U.S. Office of Naval Research.

## SUPPLEMENTARY MATERIALS

[www.sciencemag.org/content/353/6305/1260/suppl/DC1](http://www.sciencemag.org/content/353/6305/1260/suppl/DC1)  
Supplementary Text  
Figs. S1 to S6  
References (41–47)

10 June 2016; accepted 18 August 2016  
10.1126/science.aag3349

## POLYMER SCIENCE

# Quantifying the impact of molecular defects on polymer network elasticity

Mingjiang Zhong,<sup>1,2\*</sup> Rui Wang,<sup>2\*</sup> Ken Kawamoto,<sup>1\*</sup>  
Bradley D. Olsen,<sup>2†</sup> Jeremiah A. Johnson<sup>1†</sup>

Elasticity, one of the most important properties of a soft material, is difficult to quantify in polymer networks because of the presence of topological molecular defects in these materials. Furthermore, the impact of these defects on bulk elasticity is unknown. We used rheology, disassembly spectrometry, and simulations to measure the shear elastic modulus and count the numbers of topological “loop” defects of various order in a series of polymer hydrogels, and then used these data to evaluate the classical phantom and affine network theories of elasticity. The results led to a real elastic network theory (RENT) that describes how loop defects affect bulk elasticity. Given knowledge of the loop fractions, RENT provides predictions of the shear elastic modulus that are consistent with experimental observations.

**M**olecular defects fundamentally govern the properties of all real materials (1–3). The language of crystallography has been successfully used to describe defects and to model their impact in materials with a degree of periodicity, such as silicon, steel, block copolymers, and liquid crystals. However, understanding defects in amorphous materials presents a continued challenge. In polymer networks, the relevant defects are largely of a topological nature: The properties of these amorphous materials depend primarily upon the way the molecules in the material are connected. Understanding the correlation between the network topology and properties is one of the greatest outstanding challenges in soft materials.

Polymer networks can have a wide range of shear elastic moduli ( $G'$ ) from  $\sim 10^2$  to  $\sim 10^7$  Pa (4, 5), with different applications requiring moduli across this entire range. Covalent polymer networks are generally formed via kinetically controlled processes; consequently, they possess cyclic topological defects. The classical affine and phantom network theories of network elasticity neglect the presence of such defects (4, 5); they rely on idealized end-linked networks (Fig. 1A) that consider only acyclic tree-like structures, which leads to overestimation of  $G'$  (6, 7). In practice,  $G'$  is frequently calculated according to the equation

$G' = Cv_{\text{eff}}kT$ , where  $kT$  is the thermal energy,  $v_{\text{eff}}$  is the density of elastically effective chains, and  $C$  is a constant that has a value of 1 for the affine network model and  $1 - 2/f$  for the phantom network model (where  $f$  is the functionality of the network junctions). Because polymer networks include elastically defective chains,  $v_{\text{eff}}$  is never known precisely, and thus neither theory is able to accurately fit experimental data; a controversy continues over which theory, if either, is correct. Thus, despite decades of advances in polymer network design, our inability to quantitatively calculate the effects of defects on shear elastic modulus and to measure the corresponding defect densities in real polymer networks precludes quantitative prediction of  $G'$  and validation of the affine and phantom network models (4, 8–12).

To understand how molecular structure affects  $G'$  and to use this knowledge to create a predictive theory of elasticity, it is first necessary to quantify the density of topological defects in a polymer network and to determine the impact of these defects on the mechanical properties of the network. Cyclic defects, created from intrajunction reactions during network formation, are chemically and spectroscopically almost identical to noncyclic junctions, making them difficult to distinguish and quantify (5, 13–16). We have developed symmetric isotopic labeling disassembly spectrometry (SILDAs) as a strategy to precisely count the number of primary loops (Fig. 1B), the simplest topological defects, in polymer networks formed from  $A_2 + B_3$  and  $A_2 + B_4$  reactions (17–20). Furthermore, we have developed Monte Carlo

simulations and kinetic rate theories that show that cyclic defects in these polymer networks are kinetically linked, such that experimental measurement of only the primary loops determines the densities of all higher-order defects including secondary (Fig. 1C) and ternary loops (Fig. 1D) (21). Here, we measured loop fractions and  $G'$  for a series of hydrogels, thus providing quantitative relationships between these parameters. With this information, we examined the classical affine and phantom network theories of elasticity, and we derived a modified phantom network theory—real elastic network theory (RENT)—that accounts for topological molecular defects.

To rigorously determine how molecular topological defects affect elasticity, it is necessary to measure the topological defect density and modulus in the same gel. A class of stable yet chemically degradable gels was developed from bis-azido-terminated polyethylene glycol (PEG) (number-average molecular weight  $M_n = 4600$ , dispersity index  $D = 1.02$ ) polymers with non-labeled or isotopically labeled segments near their chain ends,  $A_{2H}$  and  $A_{2D}$ , respectively (22) (structures are shown in Fig. 1A; for synthesis and characterization details, see figs. S1 to S3 and figs. S17 to S34). Such labeling provides a convenient method for precise measurement of primary loops by SILDAs (19). The PEG molecular weight ensures that the polymer solutions used to form gels are well below the entanglement regime (5, 12). The labeled ( $A_{2D}$ ) and non-labeled ( $A_{2H}$ ) polymers (referred to herein as “ $A_2$  monomers”) were mixed in a 1:1 molar ratio, and this mixture was allowed to react with a tris-alkyne ( $B_3$ ) or a tetra-alkyne ( $B_4$ ) (structures are shown in Fig. 1A) in propylene carbonate solvent to provide end-linked gels via copper-catalyzed azide-alkyne cycloaddition (23, 24). When the reactive group stoichiometry—azide and alkyne in this case—was carefully controlled to be 1:1, spectroscopic analysis demonstrated that dangling functionalities (unreacted azides or alkynes) could be minimized (19) such that their impact on elasticity is negligible. Gels with varied fractions of topological defects were synthesized by varying the initial concentrations of  $A_2$  and  $B_3$  or  $B_4$  monomers (22).

For measurement of the shear elastic modulus as a function of gel preparation conditions, gel samples 1.59 mm thick were formed in situ in Teflon molds under an inert atmosphere (fig. S4). Gel disks (diameter 12 mm) were punched (Fig. 1A) and loaded onto an oscillatory shear rheometer equipped with parallel-plate geometry. Propylene carbonate was chosen as the solvent

<sup>1</sup>Department of Chemistry, Massachusetts Institute of Technology, Cambridge, MA 02139, USA. <sup>2</sup>Department of Chemical Engineering, Massachusetts Institute of Technology, Cambridge, MA 02139, USA.

\*These authors contributed equally to this work. †Corresponding author. Email: bdolsen@mit.edu (B.D.O.); jaj2109@mit.edu (J.A.J.)

## Appendix D

# Spin Transport in a Mott Insulator of Ultracold Fermions

This appendix contains a reprint of the following paper [164]:

M. A. Nichols, L. W. Cheuk, M. Okan, T. R. Hartke, E. Mendez, T. Senthil, E. Khatami, H. Zhang, and M. W. Zwierlein, “Spin Transport in a Mott Insulator of Ultracold Fermions,” *Science* **363**, 383 (2019).

## QUANTUM SIMULATION

# Spin transport in a Mott insulator of ultracold fermions

Matthew A. Nichols<sup>1,2,3</sup>, Lawrence W. Cheuk<sup>2,4</sup>, Melih Okan<sup>1,2,3</sup>, Thomas R. Hartke<sup>1,2,3</sup>, Enrique Mendez<sup>1,2,3</sup>, T. Senthil<sup>1</sup>, Ehsan Khatami<sup>5</sup>, Hao Zhang<sup>1,2,3</sup>, Martin W. Zwierlein<sup>1,2,3\*</sup>

**Strongly correlated materials are expected to feature unconventional transport properties, such that charge, spin, and heat conduction are potentially independent probes of the dynamics. In contrast to charge transport, the measurement of spin transport in such materials is highly challenging. We observed spin conduction and diffusion in a system of ultracold fermionic atoms that realizes the half-filled Fermi-Hubbard model. For strong interactions, spin diffusion is driven by super-exchange and doublon-hole-assisted tunneling, and strongly violates the quantum limit of charge diffusion. The technique developed in this work can be extended to finite doping, which can shed light on the complex interplay between spin and charge in the Hubbard model.**

In materials, electrons are the elementary carriers of both spin and charge, and one might thus expect that the properties of spin and charge conduction are always closely related. However, strong electron correlations can lead to the separation of charge and spin degrees of freedom, such as in one-dimensional systems (1–3). The unusual transport properties of the cuprate high-temperature superconductors in the normal state have been proposed to arise from decoupled spin and charge transport (4, 5). The simplest model believed to capture the essential features of the cuprate phase diagram, the Fermi-Hubbard model, features spin-charge separation in one dimension (6). In two dimensions, relevant for the cuprates, strong correlations render calculations of transport properties highly challenging (7–13). Simultaneous measurements of transport in both the charge and spin sectors would thus be of great relevance. However, in the cuprates, creating and manipulating spin currents is difficult.

Cold-atom quantum simulators can be used to experimentally study the Fermi-Hubbard model in a pristine, isolated environment, with full control of all Hubbard parameters (14). The advent of quantum gas microscopes for fermionic atoms (15–20), with their single-atom, single-lattice site resolution, has enabled precision measurements of the equation of state (21, 22) and of spin and charge correlations (23–25) of the two-dimensional (2D) Fermi-Hubbard model. These microscopes are poised for the study of transport, as already demonstrated with bosonic atoms (26–31). Previ-

ous measurements of fermionic charge transport were performed without the aid of single-atom resolution (32–34). However, it has proven difficult to directly connect the observed dynamics of lattice systems to the transport coefficients of the underlying Hamiltonian. Recently, the optical charge conductivity of a dilute, harmonically trapped 3D Fermi-Hubbard system has been measured (35), as well as the charge conductance through a mesoscopic lattice in a wire geometry (36).

Here, we explored spin transport in the repulsive 2D Fermi-Hubbard model using ultracold fermionic <sup>40</sup>K atoms on a square lattice confined by a uniform box potential. A natural region in the Hubbard phase diagram where spin and charge transport could differ is near the Mott insulator at half-filling, where charge transport is strongly suppressed, whereas spin transport can occur via super-exchange. Previous experiments have studied spin transport in strongly interacting Fermi gases without a lattice, both in three dimensions (37–40) and in two dimensions (41, 42). In those studies, spin diffusion was observed to attain the quantum limit of  $\sim \hbar/m$ , where  $\hbar$  is Planck's constant  $\hbar$  divided by  $2\pi$  and  $m$  is the particle mass. Here, we measure both the spin diffusion coefficient  $D_S$  and the spin conductivity  $\sigma_S$ . These transport coefficients dictate the response of the system to a spin-dependent force and are related through the Einstein relation,  $\sigma_S = D_S \chi$ , where  $\chi$  is the uniform spin susceptibility, which can be measured independently.

The 2D Fermi-Hubbard model is realized by evaporatively cooling <sup>40</sup>K atoms to quantum degeneracy and preparing them in an equal mixture of the hyperfine states  $|\uparrow\rangle \equiv |F=9/2, m_F=-3/2\rangle$  and  $|\downarrow\rangle \equiv |F=9/2, m_F=1/2\rangle$  in a single layer of a highly oblate optical dipole trap (43). A sample with uniform filling is produced by projecting a repulsive optical potential through the microscope objective (Fig. 1A), which isolates a uniform  $22 \times 22$  site region of the system (44). The sample is subsequently prepared adiabatically

in a square optical lattice, where it is described by the single-band Hubbard Hamiltonian

$$\begin{aligned} \hat{H} = & -t \sum_{\langle i,j \rangle, \sigma} (\hat{c}_{\sigma,i}^\dagger \hat{c}_{\sigma,j} + \text{h.c.}) + \\ & U \sum_i \hat{n}_{\uparrow,i} \hat{n}_{\downarrow,i} - \mu_\uparrow \sum_i \hat{n}_{\uparrow,i} \\ & - \mu_\downarrow \sum_i \hat{n}_{\downarrow,i} + \Delta_\uparrow \sum_i i_x \hat{n}_{\uparrow,i} \\ & + \Delta_\downarrow \sum_i i_x \hat{n}_{\downarrow,i} \end{aligned} \quad (1)$$

Here,  $t$  and  $U$  denote the nearest-neighbor tunneling amplitude and on-site interaction energy, respectively;  $\langle i,j \rangle$  represents nearest-neighbor sites  $i$  and  $j$ ;  $\mu_\uparrow$  ( $\mu_\downarrow$ ) is the chemical potential of atoms in state  $|\uparrow\rangle$  ( $|\downarrow\rangle$ );  $i_x$  represents the  $x$ -coordinate of lattice site  $i$ ; and  $\Delta_\uparrow$  ( $\Delta_\downarrow$ ) represents a possible spin-dependent tilt of the potential along the  $x$ -direction for state  $|\uparrow\rangle$  ( $|\downarrow\rangle$ ). The operators  $\hat{c}_{\sigma,i}^\dagger$  ( $\hat{c}_{\sigma,i}$ ) are the fermion creation (annihilation) operators for spin  $\sigma = \uparrow, \downarrow$  on lattice site  $i$ , and  $\hat{n}_{\sigma,i} = \hat{c}_{\sigma,i}^\dagger \hat{c}_{\sigma,i}$  is the number operator on site  $i$ . To measure the spin transport coefficients  $\sigma_S$  and  $D_S$  at half-filling, we apply a spin-dependent force derived from a magnetic gradient along  $-\hat{x}$  (Fig. 1A). The magnetic gradient gives rise to a linear tilt in the potential energy of  $\Delta_\uparrow/h = 41.1 (\pm 0.8)$  Hz per site and  $\Delta_\downarrow/h = 15.4 (\pm 0.3)$  Hz per site. This tilt has the same sign for atoms of both spins but differs in magnitude. The Hubbard parameters  $t$  and  $U$  have typical values given by  $t/h \sim 100$  Hz and  $U/h \sim 1$  kHz, and their ratio is varied using the depth of the optical lattice.

We first measure the spin diffusion coefficient by preparing the sample adiabatically in the presence of the magnetic gradient. The equilibrium density profile can be understood through the local density approximation (LDA). Under LDA, the local chemical potential  $\mu_{\sigma,i}$  decreases linearly along the  $x$ -direction with slope  $\Delta_\sigma$ , for  $\sigma = \uparrow, \downarrow$ . For a weakly interacting system, one expects the densities of both spins to decrease monotonically along  $\hat{x}$ . This is observed in fluorescence images of samples below and above half-filling, shown in Fig. 1, B and D, respectively. In Fig. 1D, doubly occupied sites appear as holes because of light-assisted collisions during the imaging process (45), so that the left side of the box region, where the density is highest, appears empty. At half-filling, however, the large charge gap of order  $U$  present in the Mott-insulating regime suppresses the formation of double occupancies as long as  $\Delta_{\uparrow,\downarrow} \ll U$ , so that the average density remains homogeneous throughout the sample (Fig. 1, C and E). This directly demonstrates the incompressibility of the Mott-insulating state, which, in an isolated system, suppresses the transport of charge. Spin transport, on the other hand, is not impeded, as spins are free to move.

Indeed, although the total density is insensitive to position, the individual spin densities reveal the effect of the gradient. As shown in Fig. 1E, as well as through images of the individual

<sup>1</sup>Department of Physics, Massachusetts Institute of Technology, Cambridge, MA 02139, USA. <sup>2</sup>MIT-Harvard Center for Ultracold Atoms, Cambridge, MA 02139, USA. <sup>3</sup>Research Laboratory of Electronics, Massachusetts Institute of Technology, Cambridge, MA 02139, USA.

<sup>4</sup>Department of Physics, Harvard University, Cambridge, MA 02138, USA. <sup>5</sup>Department of Physics and Astronomy, San José State University, San José, CA 95192, USA.

\*Corresponding author. Email: zwierlein@mit.edu

spin states in Fig. 1, F to H, we observe that  $|\uparrow\rangle$  spins accumulate toward  $-\hat{x}$ , whereas  $|\downarrow\rangle$  spins accumulate toward  $+\hat{x}$  (46). The incompressibility of the Mott insulator forces  $|\downarrow\rangle$  spins to occupy the right half of the sample at the expense of an increase in potential energy due to the tilt. The thermodynamic properties, in-

cluding individual spin densities and double occupancies, of such a tilted fermionic Hubbard system have been studied theoretically using determinant quantum Monte Carlo (DQMC) for weak to intermediate interactions ( $0.08 < t/U < 1$ ) and gradient strengths comparable to those used in the present work (47). Experimentally, we use

this separation of the individual spin densities to measure the entropy of the sample; that is, from the equilibrated total spin density profile  $\langle \hat{S}_{z,j} \rangle = (1/2)(\hat{n}_{\uparrow,j} - \hat{n}_{\downarrow,j})$  in the tilted potential (we retain only the site index along  $\hat{x}$ ), we can obtain the uniform spin susceptibility  $\chi = \partial \langle \hat{S}_{z,j} \rangle / \partial \Delta\mu$ , where  $\Delta\mu = \mu_{\uparrow} - \mu_{\downarrow}$ , of the unperturbed system in linear

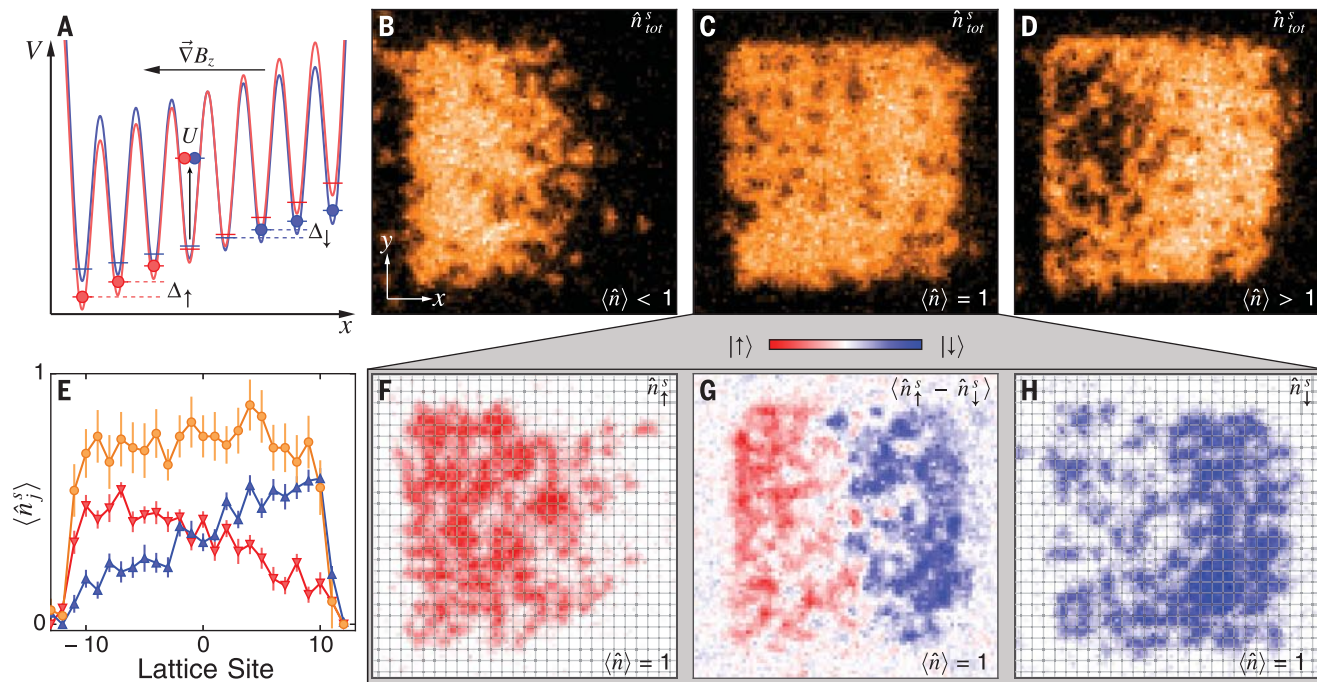


**Fig. 1. Creating spin textures in a homogeneous Fermi-Hubbard system.** (A) A diagram of the optical potentials used to confine the atoms, and the tilted lattice potential experienced by the two spin states  $|\uparrow\rangle$  (red) and  $|\downarrow\rangle$  (blue) in the presence of a magnetic field gradient. (B to D) Raw fluorescence images of the parity-projected total density  $\hat{n}_{\text{tot}}^s$  for total densities  $\langle \hat{n} \rangle < 1$ ,  $\langle \hat{n} \rangle = 1$ , and  $\langle \hat{n} \rangle > 1$ , respectively, which have been prepared adiabatically in the presence of the magnetic gradient;  $t/U = 0.114 (\pm 0.007)$ ,  $0.067 (\pm 0.004)$ , and  $0.114 (\pm 0.007)$  for (B), (C), and (D), respectively. (E) The average singles

densities,  $\langle \hat{n}_{\text{tot},j}^s \rangle$  (gold),  $\langle \hat{n}_{\uparrow,j}^s \rangle$  (red), and  $\langle \hat{n}_{\downarrow,j}^s \rangle$  (blue) over four independent realizations at  $t/U = 0.026 (\pm 0.002)$ , averaged along the  $y$ -direction from the reconstructed detected site occupations. Error bars represent  $1\sigma$  statistical uncertainty. The average singles densities shown have not been corrected for finite detection fidelity. (F) A single raw image of  $\hat{n}_{\uparrow}^s$  at  $t/U = 0.067 (\pm 0.004)$ . (G) Fluorescence of  $|\uparrow\rangle$  minus fluorescence of  $|\downarrow\rangle$  averaged over six images for the same configuration as (F). (H) A single image of  $\hat{n}_{\downarrow}^s$  for the same configuration as (F).

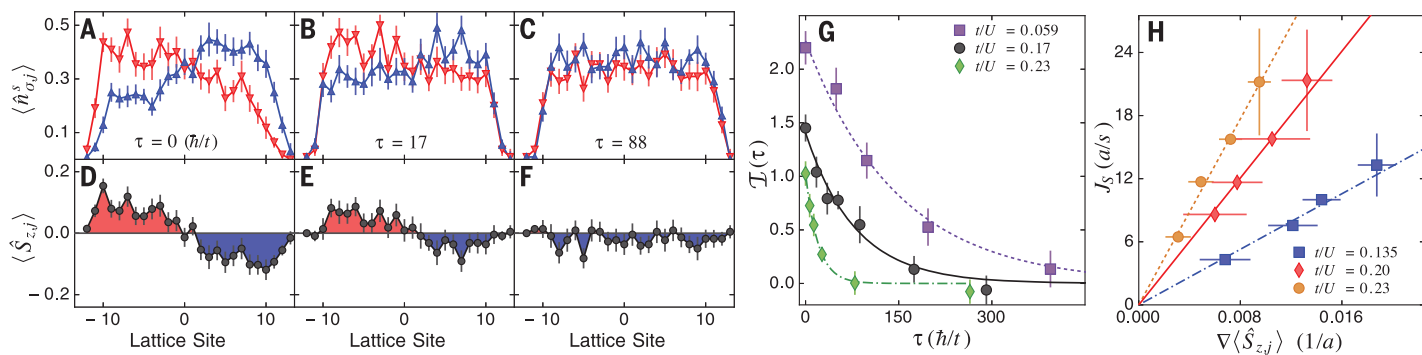


**Fig. 2. Observation of spin relaxation after sudden gradient removal.**

(A to F) Time evolution of the average singles densities  $\langle \hat{n}_{\uparrow,j}^s(\tau) \rangle$  (red) and  $\langle \hat{n}_{\downarrow,j}^s(\tau) \rangle$  (blue) (upper panels), and of the spin density  $\langle \hat{S}_{z,j}(\tau) \rangle$  (lower panels), after removing the magnetic field gradient for  $t/U = 0.23 (\pm 0.01)$  at times  $\tau(h/t) = 0, 17$ , and  $88$ . (G) Imbalance  $\mathcal{I}(\tau)$  for  $t/U = 0.059 (\pm 0.005)$ ,  $t/U = 0.17 (\pm 0.01)$ , and  $t/U = 0.23 (\pm 0.01)$  and exponential fits to the data. All error bars in (A) to (G) represent  $1\sigma$  statistical uncertainty. (H) Spin current  $J_S$  at  $j = 0$

as a function of the spatial gradient in  $\langle \hat{S}_{z,j}(\tau) \rangle$  at  $j = 0$  for  $t/U = 0.135 (\pm 0.009)$ ,  $t/U = 0.20 (\pm 0.01)$ , and  $t/U = 0.23 (\pm 0.01)$  and corresponding linear fits to the data. The error bars along the horizontal axis represent  $1\sigma$  statistical uncertainty in the measurement of the spatial gradient in  $\langle \hat{S}_{z,j}(\tau) \rangle$ . Vertical error bars are representative for each curve, derived from the uncertainty in the exponential fit to the imbalance  $\mathcal{I}(\tau)$ , and are proportional to the magnitude of the spin current. The data in (A) to (H) have not been corrected for finite detection fidelity.

response (44). By comparing the measured values of  $\chi$  with calculations from the numerical linked-cluster expansion (NLCE) technique (48), we can determine the entropy per particle  $S/k_B N$  (where  $k_B$  is the Boltzmann constant). We find an entropy per particle of  $S/k_B N = 1.1 (\pm 0.1)$ , a regime where NLCE is expected to converge at half-filling over the range of  $t/U$  explored here (23, 49, 50).

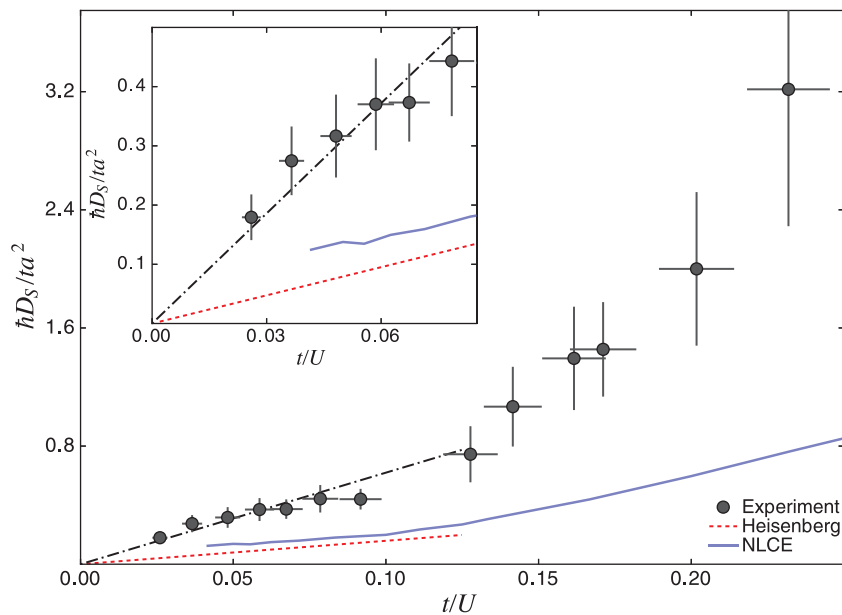
The equilibrated samples with a spin density gradient provide the starting point for subsequent measurements. Because the initial spin density gradient is small, it acts as a small perturbation to the untilted scenario, ensuring that we are probing properties of the homogeneous system in linear response. After the sample has been prepared at a fixed value of  $t/U$ , the magnetic gradient is suddenly switched off. Following this quench, the system begins to relax back to equilibrium, where  $\langle \hat{S}_{z,j} \rangle = 0$  everywhere. Figure 2, A to F, shows the decay of the spin density gradient after the quench for  $t/U = 0.23 (\pm 0.01)$ . This relaxation implies that a spin current  $J_S$  must be present. To obtain  $J_S$  from the measured spin profiles, we define the spin density imbalance,  $\mathcal{I}(\tau)$ , at time  $\tau$  after the quench as

$$\mathcal{I}(\tau) = \sum_L \langle \hat{S}_{z,j}(\tau) \rangle - \sum_R \langle \hat{S}_{z,j}(\tau) \rangle \quad (2)$$

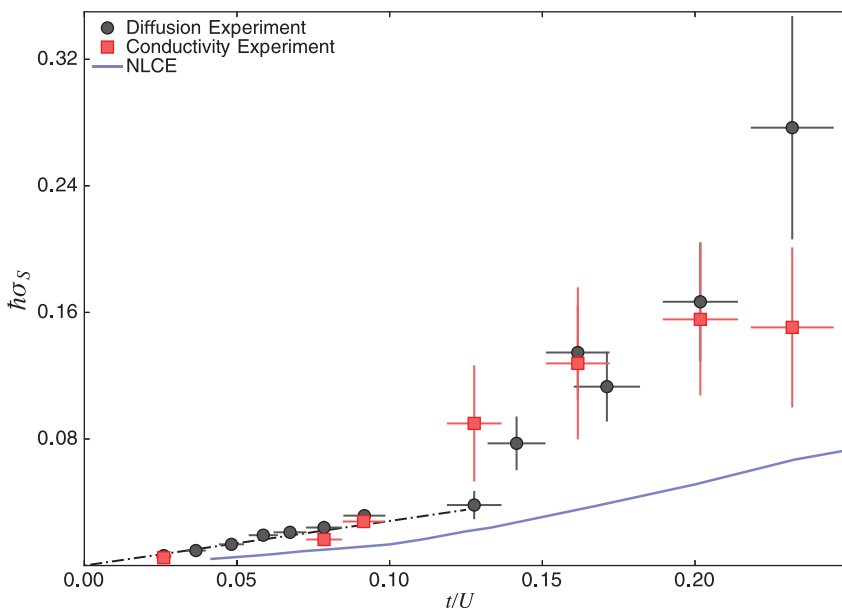
where  $\sum_{L,R}$  denotes summation over the left and right halves of the box. Using the continuity equation for the spin density, one can relate  $\mathcal{I}(\tau)$  to the spin current  $J_S$  at the center of the box ( $j = 0$ ) via  $J_S(\tau) = -(a/2)(d/dt)\mathcal{I}(t)|_v$ , where  $a$  is the lattice spacing.

Figure 2G shows  $\mathcal{I}(\tau)$  measured for several values of  $t/U$ . For all values of  $t/U$  explored,  $\mathcal{I}(\tau)$  decays to zero. We have verified that the effects of lattice heating during this decay are negligible relative to the experimental uncertainty in the measurement (44).  $\mathcal{I}(\tau)$  is then fitted to an exponential curve, and the spin current  $J_S$  is obtained through the time derivative of the fit. To connect  $J_S$  with the spin transport coefficients, we first examine the dependence of  $J_S$  on the spin density gradient at the center of the box,  $\nabla \langle \hat{S}_{z,j=0} \rangle$ . By extracting both quantities for a fixed  $t/U$  at various times  $\tau$ , we have access to the dependence of  $J_S$  on  $\nabla \langle \hat{S}_{z,j=0} \rangle$  over a large range of values (Fig. 2H). We find that to within experimental error,  $J_S$  is linearly proportional to  $\nabla \langle \hat{S}_{z,j=0} \rangle$ . This implies that the spin dynamics are diffusive, so that  $J_S = D_S \nabla \langle \hat{S}_{z,j=0} \rangle$ , where  $D_S$  is the spin diffusion coefficient. The diffusive nature of the dynamics is also independently probed by a measurement of the power-law dependence of the decay time of  $\mathcal{I}(\tau)$ , at a fixed value of  $t/U$ , on the system size  $L$  (44).

Figure 3 shows the measured spin diffusion coefficient  $D_S$  of the half-filled, homogeneous Hubbard model as a function of  $t/U$ , in units of the quantum scale for mass diffusion  $D_0 = \hbar/m$ , where  $m = \hbar^2/ta^2$  is the effective mass in the tight-binding limit. For all data in the strongly interacting regime ( $t/U \leq 0.125$ ), the spin diffusion coefficient lies below the scale of quantum-limited mass diffusion  $D_0$ . In this range, the dependence



**Fig. 3. Spin diffusion coefficient of the half-filled Fermi-Hubbard system versus  $t/U$ .** The experimentally measured spin diffusion coefficient  $\hbar D_S/ta^2 = D_S/D_0$  at half-filling (black circles) versus the Hubbard parameters  $t/U$ , and a linear fit to data points with  $t/U < 0.09$  (black dot-dashed line). The vertical error bars represent the  $1\sigma$  statistical error in the measurement; the horizontal error bars represent the  $1\sigma$  statistical error in the calibrated value of  $t/U$ . The blue solid line represents isentropic results for  $D_S/D_0$  obtained from NLCE calculations of the real-time spin current-current correlation function for the Hubbard model (44), with an entropy per particle of  $1.1k_B$ . With a finite temporal cutoff of  $\sim \hbar/t$  for the real-time correlation functions, the NLCE theory is expected to provide a lower bound to the true diffusivity. For comparison, a prediction for the spin diffusion coefficient of the 2D Heisenberg model at high temperatures,  $k_B T \gg J_{ex}$ , where  $T$  is the temperature, is shown (dashed red line) (8, 51, 52). Inset: A close-up view of the spin diffusion coefficient at half-filling for  $t/U < 0.09$ , where it is expected to scale approximately linearly with  $t^2/U$ .



**Fig. 4. Spin conductivity of the half-filled Fermi-Hubbard system versus  $t/U$ .** The measured spin conductivity at half-filling from the initial spin current in an applied magnetic gradient (red squares) and from the measured spin diffusion coefficient using the Einstein relation  $\sigma_S = D_S \chi$  (black circles). A linear fit to data points with  $t/U < 0.09$  is represented by the black dot-dashed line. The vertical error bars represent the  $1\sigma$  statistical uncertainty of the measurements; the horizontal error bars represent the  $1\sigma$  statistical error in the calibrated value of  $t/U$ . The data have been corrected for finite detection fidelity associated with the imaging process of the two spin states (44). The blue solid line is the result obtained for  $\hbar \sigma_S$  at constant entropy using an NLCE calculation of the real-time spin current-current correlation function for the Hubbard model, with an entropy per particle of  $1.1k_B$  (44).

of  $D_S/D_0$  on  $t/U$  is linear, implying  $D_S \propto t^2/U$ . From a linear fit constrained to go to zero diffusion at  $t/U = 0$  (Fig. 3), we obtain  $\hbar D_S = 6.2 (\pm 0.5) \times a^2 t^2/U$ . This  $t^2/U$  scaling can be partially understood by considering the Heisenberg limit of the half-filled Fermi-Hubbard model, where spins interact with an exchange coupling  $J_{\text{ex}} = 4t^2/U$  called the super-exchange energy. Because  $J_{\text{ex}}$  sets the energy scale in this limit, the effective spin mass is given by  $m_S \sim \hbar^2/J_{\text{ex}}a^2 \sim mU/t$  (29). Spin excitations are thus parametrically more massive than  $m$ . For quantum-limited transport, the spin diffusion coefficient  $D_S$  is given by  $\hbar/m_S$ , giving rise to the  $t^2/U$  scaling. Although this argument gives the correct scaling, the Heisenberg prediction for the spin diffusion coefficient at temperatures much larger than  $J_{\text{ex}}$  is

$$\hbar D_S = \frac{4\sqrt{\pi/20}a^2 t^2}{U} \approx \frac{1.6a^2 t^2}{U} \quad (3)$$

(8, 51, 52), lower than experimentally observed (Fig. 3). This is not surprising, as the Heisenberg model does not capture quantum or thermal doublon-hole fluctuations of the Fermi-Hubbard model, which arise from states with energies greater than  $U$  (9). Doublon-hole fluctuations can increase spin diffusion because spins can move directly from occupied to empty sites, or can trade places with doublons; both processes occur at a rate set by  $t$ . Because doublon-hole fluctuations are admixed into the wave function of the system with an amplitude proportional to  $t/U$  in the strongly interacting regime, the overall scaling of this mechanism is again proportional to  $t^2/U$ . As shown in Fig. 3, for weaker interaction strengths ( $t/U > 0.125$ ), the diffusivity  $D_S/D_0$  increases faster with  $t/U$  than what is given by this initial linear slope.

To gain further insight, we developed a method to calculate the spin conductivity and diffusivity through real-time current-current correlation functions within the NLCE technique (44). This method avoids the ill-posed problem of analytic continuation from imaginary time, as required in DQMC, and is immune to finite-size effects. These calculations thus give unbiased estimates of transport coefficients in the thermodynamic limit. When comparing the experimental data to the calculations, the only fixed parameter is the entropy per particle, which is independently determined from the measured uniform spin susceptibility. As shown in Fig. 3, the theoretical estimate of the spin diffusivity (blue curve) captures the essential behavior of the experimental data as a function of  $t/U$ . However, the theoretical calculations systematically underestimate the experimental diffusion coefficient. One possible source of this discrepancy arises from limited access to real-time correlation functions for times longer than  $\sim\hbar/t$ . In practice, a cutoff on the order of  $\sim\hbar/t$  is used when calculating the direct current (DC) transport coefficients, which can lead to systematic errors. For example, in the Heisenberg limit, one expects real-time correlations to extend out to times  $\sim\hbar/J_{\text{ex}}$ , which can be much longer

than  $\hbar/t$ . It is therefore notable that even with access to real-time correlations only up to times  $\sim\hbar/t$ , the NLCE estimates agree qualitatively with the experimental data, and also quantitatively to within a factor of  $\sim 2$ . Although it is difficult to estimate the magnitude of the systematic error, we expect the NLCE estimates to provide a lower bound for  $D_S$  (44).

In addition to the spin diffusion coefficient  $D_S$ , we also independently measure the spin conductivity  $\sigma_S$ . To do this, we first prepare an equilibrated system at half-filling without a potential tilt. We then switch on the tilt suddenly, which induces a spin current in the system. Because  $\nabla\langle S_{z,j} \rangle = 0$  at time  $\tau = 0$ , the diffusive contribution to the spin current is negligible initially; in analogy with Ohm's law, which relates a charge current to an applied electric field using the charge conductivity, the initial spin current  $J_S(\tau = 0)$  is directly proportional to the applied spin-dependent force,  $-(1/a)(\Delta_\uparrow - \Delta_\downarrow)\hat{x}$ , where the spin conductivity  $\sigma_S$  is the constant of proportionality. Therefore, by measuring the spin current at the center of the box under the known spin-dependent tilt, the spin conductivity can be obtained. The measured spin conductivities at various interaction strengths  $t/U$  are shown in Fig. 4. A second way to obtain the conductivity is through the Einstein relation  $\sigma_S = D_S\chi$ , where the spin diffusion coefficient  $D_S$  and the uniform spin susceptibility  $\chi$  are both obtained from the data used in Fig. 3. The values of  $\hbar\sigma_S$  obtained in this way are also shown in Fig. 4. We find that these two independent methods of measuring the spin conductivity agree with each other to within experimental uncertainty.

We observe that the spin conductivity is linear with  $t/U$  in the strongly interacting regime ( $t/U \leq 0.125$ ), and find that  $\sigma_S = 0.28 (\pm 0.02) \times t/U\hbar$  from a linear fit constrained to yield zero conductivity at  $t/U = 0$  (Fig. 4). The measured spin conductivities drop far below the Mott-Ioffe-Regel limit for charge in a metal (53, 54),  $\sigma_0 = ne^2\tau/m = e^2/\hbar$ , derived for a scattering rate  $\tau^{-1} = E_F/\hbar$  given by the Fermi energy  $E_F$ , where the elementary charge of our system is  $e = 1$ . It therefore appears once again as if the effective mass of the carriers of spin is  $m_S \sim mU/t$ . A breakdown of the Mott-Ioffe-Regel limit is naturally expected in our regime where quasiparticles are ill-defined and Drude-Boltzmann theory does not apply. As  $t/U$  increases, the observed spin conductivity grows beyond the initial linear scaling with  $t/U$ , in analogy with the diffusion coefficient. NLCE predictions for  $\hbar\sigma_S$  at half-filling (blue curve in Fig. 4) capture the behavior of the spin conductivity with  $t/U$  qualitatively, but are systematically lower than the experimental data, for the same potential reasons discussed previously in the context of the diffusion coefficient. Given the substantial challenges associated with calculating the DC limit of the spin conductivity, the experimental data provide a valuable benchmark for future theoretical calculations.

Our study of spin transport can be readily extended in many ways. For example, one can

explore the temperature dependence of the spin resistivity, which could display linear behavior reminiscent of charge transport in bad metals. One can also investigate the effect of doping away from half-filling (e.g., at optimal doping), where superconducting fluctuations or a strange metal phase could be present in experimentally attainable conditions. Through simultaneous measurements of both the spin and charge dynamics, such experiments could elucidate the intricate interplay between these two degrees of freedom in the Fermi-Hubbard model.

## REFERENCES AND NOTES

- T. Giannetti, *Quantum Physics in One Dimension* (Clarendon, 2004).
- O. M. Auslaender et al., *Science* **308**, 88–92 (2005).
- A. J. Heeger, S. Kivelson, J. R. Schrieffer, W. P. Su, *Rev. Mod. Phys.* **60**, 781–850 (1988).
- P. W. Anderson, *Phys. Today* **50**, 42–47 (1997).
- P. A. Lee, N. Nagaosa, X.-G. Wen, *Rev. Mod. Phys.* **78**, 17–85 (2006).
- E. H. Lieb, F. Y. Wu, *Phys. Rev. Lett.* **20**, 1445–1448 (1968).
- D. J. Scalapino, S. R. White, S. Zhang, *Phys. Rev. B* **47**, 7995–8007 (1993).
- J. Bonča, J. Jaklić, *Phys. Rev. B* **51**, 16083–16087 (1995).
- P. Kopietz, *Phys. Rev. B* **57**, 7829–7834 (1998).
- S. Mukerjee, V. Oganesyan, D. Huse, *Phys. Rev. B* **73**, 035113 (2006).
- H. Kim, D. A. Huse, *Phys. Rev. A* **86**, 053607 (2012).
- A. P. Snyder, T. N. De Silva, *Phys. Rev. A* **86**, 053610 (2012).
- C. Karrasch, D. M. Kennes, J. E. Moore, *Phys. Rev. B* **90**, 155104 (2014).
- T. Esslinger, *Annu. Rev. Condens. Matter Phys.* **1**, 129–152 (2010).
- L. W. Cheuk et al., *Phys. Rev. Lett.* **114**, 193001 (2015).
- E. Haller et al., *Nat. Phys.* **11**, 738–742 (2015).
- M. F. Parsons et al., *Phys. Rev. Lett.* **114**, 213002 (2015).
- A. Omran et al., *Phys. Rev. Lett.* **115**, 263001 (2015).
- G. J. A. Edge et al., *Phys. Rev. A* **92**, 063406 (2015).
- P. T. Brown et al., *Science* **357**, 1385–1388 (2017).
- E. Cocchi et al., *Phys. Rev. Lett.* **116**, 175301 (2016).
- C. Hofferberth et al., *Phys. Rev. X* **6**, 021030 (2016).
- L. W. Cheuk et al., *Science* **353**, 1260–1264 (2016).
- M. Boll et al., *Science* **353**, 1257–1260 (2016).
- M. F. Parsons et al., *Science* **353**, 1253–1256 (2016).
- M. Cheneau et al., *Nature* **481**, 484–487 (2012).
- T. Fukuhara et al., *Nat. Phys.* **9**, 235–241 (2013).
- T. Fukuhara et al., *Nature* **502**, 76–79 (2013).
- S. Hild et al., *Phys. Rev. Lett.* **113**, 147205 (2014).
- P. M. Preiss et al., *Science* **347**, 1229–1233 (2015).
- J. Y. Choi et al., *Science* **352**, 1547–1552 (2016).
- N. Strohmaier et al., *Phys. Rev. Lett.* **99**, 220601 (2007).
- U. Schneider et al., *Nat. Phys.* **8**, 213–218 (2012).
- W. Xu, W. R. McGehee, W. N. Morong, B. DeMarco, arXiv:1606.06695v5 [cond-mat.quant-gas] (28 August 2018).
- R. Anderson, F. Wang, P. Xu, V. Venu, S. Trotzky, F. Chevy, J. H. Thywissen, arXiv:1712.09965v2 [cond-mat.quant-gas] (28 May 2018).
- M. Lebrat et al., *Phys. Rev. X* **8**, 011053 (2018).
- A. Sommer, M. Ku, G. Roati, M. W. Zwierlein, *Nature* **472**, 201–204 (2011).
- A. Sommer, M. Ku, M. W. Zwierlein, *New J. Phys.* **13**, 055009 (2011).
- A. B. Bardon et al., *Science* **344**, 722–724 (2014).
- G. Veltolina et al., *Nat. Phys.* **13**, 704–709 (2017).
- M. Koschorreck, D. Pertot, E. Vogt, M. Köhl, *Nat. Phys.* **9**, 405–409 (2013).
- C. Luciuk et al., *Phys. Rev. Lett.* **118**, 130405 (2017).
- L. W. Cheuk et al., *Phys. Rev. Lett.* **116**, 235301 (2016).
- See supplementary materials.
- M. T. DePue, C. McCormick, S. L. Winoto, S. Oliver, D. S. Weiss, *Phys. Rev. Lett.* **82**, 2262–2265 (1999).
- D. M. Weld et al., *Phys. Rev. Lett.* **103**, 245301 (2009).
- G. G. Batrouni, R. T. Scalettar, *Phys. Rev. A* **96**, 033632 (2017).
- M. Rigol, T. Bryant, R. R. P. Singh, *Phys. Rev. Lett.* **97**, 187202 (2006).
- E. Khatami, M. Rigol, *Phys. Rev. A* **84**, 053611 (2011).
- E. Khatami, M. Rigol, *Phys. Rev. A* **86**, 023633 (2012).

51. H. S. Bennett, P. C. Martin, *Phys. Rev.* **138**, A608–A617 (1965).
52. A. Sokol, E. Gagliano, S. Bacci, *Phys. Rev. B* **47**, 14646–14649 (1993).
53. A. F. Ioffe, A. R. Regel, *Prog. Semicond.* **4**, 237–291 (1960).
54. N. F. Mott, *Philos. Mag.* **26**, 1015–1026 (1972).
55. M. A. Nichols, Replication data for: Spin transport in a Mott insulator of ultracold fermions. Harvard Dataverse (2018); <https://doi.org/10.7910/DVN/OOFNFT>.

#### ACKNOWLEDGMENTS

We thank W. S. Bakr, M. Greiner, and their research groups for fruitful discussions. **Funding:** Supported by NSF, AFOSR, an AFOSR MURI on Exotic Quantum Phases, ARO, ONR, the David and

Lucile Packard Foundation, and Gordon and Betty Moore Foundation grant GBMF5279. E.K. was supported by NSF grant DMR-1609560. The computations were performed in part on the Teal computer cluster of the Department of Physics and Astronomy of San José State University and in part on the Spartan high-performance computing facility at San José State University supported by NSF grant OAC-1626645. T.S. was supported by NSF grant DMR-1608505 and partially through a Simons Investigator Award from the Simons Foundation. **Author contributions:** M.A.N., L.W.C., M.O., T.R.H., E.M., H.Z., and M.W.Z. planned and performed the experiment and analyzed the data. E.K. performed the NLCE simulations. All authors contributed to the interpretation of the data and the preparation of the manuscript. **Competing**

**interests:** The authors declare no competing financial interests. **Data and materials availability:** All data shown in this work can be found in an online database (55).

#### SUPPLEMENTARY MATERIALS

[www.sciencemag.org/content/363/6425/383/suppl/DC1](http://www.sciencemag.org/content/363/6425/383/suppl/DC1)

Supplementary Text

Figs. S1 to S6

References (56–61)

26 February 2018; accepted 20 November 2018

Published online 6 December 2018

10.1126/science.aat4387

# Bibliography

- [1] Alexander Albus, Fabrizio Illuminati, and Jens Eisert. Mixtures of bosonic and fermionic atoms in optical lattices. *Phys. Rev. A*, 68:023606, Aug 2003.
- [2] B. P. Anderson and M. A. Kasevich. Loading a vapor-cell magneto-optic trap using light-induced atom desorption. *Phys. Rev. A*, 63:023404, Jan 2001.
- [3] M.H. Anderson, J.R. Ensher, M.R. Matthews, C.E. Wieman, and E.A. Cornell. Observation of Bose-Einstein condensation in a dilute atomic vapor. *Science*, 269:198–201, 1995.
- [4] P. W. Anderson. Theory of magnetic exchange interactions: Exchange in insulators and semiconductors. In F. Seitz and D. Turnbull, editors, *Solid State Physics*, volume 14, pages 99–214, New York, 1963. Academic Press Inc.
- [5] P. W. Anderson. Model for the electronic structure of amorphous semiconductors. *Phys. Rev. Lett.*, 34:953–955, Apr 1975.
- [6] P. W. Anderson. The resonating valence bond state in  $\text{La}_2\text{CuO}_4$  and superconductivity. *Science*, 235:1196–1198, 1987.
- [7] P. W. Anderson. Hidden fermi liquid: The secret of high- $T_c$  cuprates. *Phys. Rev. B*, 78:174505, Nov 2008.
- [8] Philip W. Anderson. When the electron falls apart. *Physics Today*, 50:42–47, 1997.
- [9] Rhys Anderson, Fudong Wang, Peihang Xu, Vijin Venu, Stefan Trotzky, Frédéric Chevy, and Joseph H. Thywissen. Conductivity spectrum of ultracold atoms in an optical lattice. *Phys. Rev. Lett.*, 122:153602, Apr 2019.
- [10] Camille Aron. Dielectric breakdown of a mott insulator. *Phys. Rev. B*, 86:085127, Aug 2012.
- [11] Louis-François Arsenault, B. Sriram Shastry, Patrick Sémond, and A.-M. S. Tremblay. Entropy, frustration, and large thermopower of doped mott insulators on the fcc lattice. *Phys. Rev. B*, 87:035126, Jan 2013.
- [12] N. W. Ashcroft and N. D. Mermin. *Solid State Physics*. Brooks/Cole, Cengage Learning, Belmont, CA, 1st edition, 1976.

- [13] Assa Auerbach. *Interacting Electrons and Quantum Magnetism*. Springer-Verlag, New York, 1994.
- [14] O. M. Auslaender, H. Steinberg, A. Yacoby, Y. Tserkovnyak, B. I. Halperin, K. W. Baldwin, L. N. Pfeiffer, and K. W. West. Spin-charge separation and localization in one dimension. *Science*, 308(5718):88–92, 2005.
- [15] W. S. Bakr, A. Peng, M. E. Tai, R. Ma, J. Simon, J. I. Gillen, S. Fölling, L. Pollet, and M. Greiner. Probing the superfluid-to-Mott insulator transition at the single-atom level. *Science*, 329(5991):547–550, 2010.
- [16] Waseem S. Bakr, Jonathon I. Gillen, Amy Peng, Simon Fölling, and Markus Greiner. A quantum gas microscope for detecting single atoms in a Hubbard-regime optical lattice. *Nature*, 462(7269):74–77, 2009.
- [17] A. B. Bardon, S. Beattie, C. Luciuk, W. Cairncross, D. Fine, N. S. Cheng, G. J. A. Edge, E. Taylor, S. Zhang, S. Trotzky, and J. H. Thywissen. Transverse demagnetization dynamics of a unitary fermi gas. *Science*, 344(6185):722–724, 2014.
- [18] G. George Batrouni and Richard T. Scalettar. Interaction-induced gradients across a confined fermion lattice. *Phys. Rev. A*, 96:033632, Sep 2017.
- [19] Herbert S. Bennett and Paul C. Martin. Spin diffusion in the heisenberg paramagnet. *Phys. Rev.*, 138:A608–A617, Apr 1965.
- [20] Jean-Sébastien Bernier, Corinna Kollath, Antoine Georges, Lorenzo De Leo, Fabrice Gerbier, Christophe Salomon, and Michael Köhl. Cooling fermionic atoms in optical lattices by shaping the confinement. *Phys. Rev. A*, 79:061601, Jun 2009.
- [21] R. Blankenbecler, D. J. Scalapino, and R. L. Sugar. Monte carlo calculations of coupled boson-fermion systems. i. *Phys. Rev. D*, 24:2278–2286, Oct 1981.
- [22] Immanuel Bloch, Jean Dalibard, and Wilhelm Zwerger. Many-body physics with ultracold gases. *Rev. Mod. Phys.*, 80(3):885–964, 2008.
- [23] Martin Boll, Timon A. Hilker, Guillaume Salomon, Ahmed Omran, Jacopo Nespolo, Lode Pollet, Immanuel Bloch, and Christian Gross. Spin- and density-resolved microscopy of antiferromagnetic correlations in fermi-hubbard chains. *Science*, 353(6305):1257–1260, 2016.
- [24] J. Bonča and J. Jaklič. Spin diffusion of the t-j model. *Phys. Rev. B*, 51:16083–16087, Jun 1995.
- [25] Jean-Philippe Brantut, Jakob Meineke, David Stadler, Sebastian Krinner, and Tilman Esslinger. Conduction of ultracold fermions through a mesoscopic channel. *Science*, 337(6098):1069–1071, 2012.

- [26] Peter T. Brown, Debayan Mitra, Elmer Guardado-Sanchez, Reza Nourafkan, Alexis Reybaut, Charles-David Hébert, Simon Bergeron, A.-M. S. Tremblay, Jure Kokalj, David A. Huse, Peter Schauß, and Waseem S. Bakr. Bad metallic transport in a cold atom fermi-hubbard system. *Science*, 363(6425):379–382, 2019.
- [27] Peter T. Brown, Debayan Mitra, Elmer Guardado-Sanchez, Peter Schauß, Stanimir S. Kondov, Ehsan Khatami, Thereza Paiva, Nandini Trivedi, David A. Huse, and Waseem S. Bakr. Spin-imbalance in a 2d fermi-hubbard system. *Science*, 357(6358):1385–1388, 2017.
- [28] J. A. N. Bruin, H. Sakai, R. S. Perry, and A. P. Mackenzie. Similarity of scattering rates in metals showing t-linear resistivity. *Science*, 339(6121):804–807, 2013.
- [29] H. P. Büchler and G. Blatter. Supersolid versus phase separation in atomic bose-fermi mixtures. *Phys. Rev. Lett.*, 91:130404, Sep 2003.
- [30] Thomas Busch, Berthold-Georg Englert, Kazimierz Rzażewski, and Martin Wilkens. Two cold atoms in a harmonic trap. *Foundations of Physics*, 28(4):549–559, Apr 1998.
- [31] Yuan Cao, Valla Fatemi, Ahmet Demir, Shiang Fang, Spencer L. Tomarken, Jason Y. Luo, Javier D. Sanchez-Yamagishi, Kenji Watanabe, Takashi Taniguchi, Efthimios Kaxiras, Ray C. Ashoori, and Pablo Jarillo-Herrero. Correlated insulator behaviour at half-filling in magic-angle graphene superlattices. *Nature*, 556:80–84, 2018.
- [32] Yuan Cao, Valla Fatemi, Shiang Fang, Kenji Watanabe, Takashi Taniguchi, Efthimios Kaxiras, and Pablo Jarillo-Herrero. Unconventional superconductivity in magic-angle graphene superlattices. *Nature*, 556:43–50, 2018.
- [33] Sudip Chakravarty, Bertrand I. Halperin, and David R. Nelson. Low-temperature behavior of two-dimensional quantum antiferromagnets. *Phys. Rev. Lett.*, 60:1057–1060, Mar 1988.
- [34] Sudip Chakravarty, Bertrand I. Halperin, and David R. Nelson. Two-dimensional quantum heisenberg antiferromagnet at low temperatures. *Phys. Rev. B*, 39:2344–2371, Feb 1989.
- [35] M. Cheneau, P. Barmettler, D. Poletti, M. Endres, P. Schauß, T. Fukuhara, C. Gross, I. Bloch, C. Kollath, and S. Kuhr. Light-cone-like spreading of correlations in a quantum many-body system. *Nature*, 481:484–487, 2012.
- [36] R. W. Cherng, G. Refael, and E. Demler. Superfluidity and magnetism in multicomponent ultracold fermions. *Phys. Rev. Lett.*, 99:130406, Sep 2007.
- [37] Lawrence W. Cheuk. *Quantum Gas Microscopy of Strongly Correlated Fermions*. Ph.d. thesis, Massachusetts Institute of Technology, 2017.

- [38] Lawrence W. Cheuk, Matthew A. Nichols, Katherine R. Lawrence, Melih Okan, Hao Zhang, Ehsan Khatami, Nandini Trivedi, Thereza Paiva, Marcos Rigol, and Martin W. Zwierlein. Observation of spatial charge and spin correlations in the 2d fermi-hubbard model. *Science*, 353(6305):1260–1264, Sep 2016.
- [39] Lawrence W. Cheuk, Matthew A. Nichols, Katherine R. Lawrence, Melih Okan, Hao Zhang, and Martin W. Zwierlein. Observation of 2d fermionic mott insulators of  $^{40}\text{K}$  with single-site resolution. *Phys. Rev. Lett.*, 116:235301, Jun 2016.
- [40] Lawrence W. Cheuk, Matthew A. Nichols, Melih Okan, Thomas Gersdorf, Vinay V. Ramasesh, Waseem S. Bakr, Thomas Lompe, and Martin W. Zwierlein. Quantum-gas microscope for fermionic atoms. *Phys. Rev. Lett.*, 114:193001, May 2015.
- [41] Cheng Chin, Rudolf Grimm, Paul Julienne, and Eite Tiesinga. Feshbach resonances in ultracold gases. *Rev. Mod. Phys.*, 82(2):1225, 2010.
- [42] J.K. Chin, D.E. Miller, Y. Liu, C. Stan, W. Setiawan, C. Sanner, K. Xu, and W. Ketterle. Evidence for superfluidity of ultracold fermions in an optical lattice. *Nature*, 443(7114):961–964, 2006.
- [43] Christie S. Chiu, Geoffrey Ji, Anton Masurenko, Daniel Greif, and Markus Greiner. Quantum state engineering of a hubbard system with ultracold fermions. *Phys. Rev. Lett.*, 120:243201, Jun 2018.
- [44] Jae-yoon Choi, Sebastian Hild, Johannes Zeiher, Peter Schauß, Antonio Rubio-Abadal, Tarik Yefsah, Vedika Khemani, David A. Huse, Immanuel Bloch, and Christian Gross. Exploring the many-body localization transition in two dimensions. *Science*, 352(6293):1547–1552, 2016.
- [45] Eugenio Cocchi, Luke A. Miller, Jan H. Drewes, Marco Koschorreck, Daniel Pertot, Ferdinand Brennecke, and Michael Köhl. Equation of state of the two-dimensional hubbard model. *Phys. Rev. Lett.*, 116:175301, Apr 2016.
- [46] Piers Coleman. *Introduction to Many-Body Physics*. Cambridge University Press, Cambridge, 2015.
- [47] Giacomo Colzi, Gianmaria Durastante, Eleonora Fava, Simone Serafini, Giacomo Lamporesi, and Gabriele Ferrari. Sub-doppler cooling of sodium atoms in gray molasses. *Phys. Rev. A*, 93:023421, Feb 2016.
- [48] Ph. Courteille, R.S. Freeland, D.J. Heinzen, F.A. van Abeelen, and B.J. Verhaar. Observation of a Feshbach resonance in cold atom scattering. *Phys. Rev. Lett.*, 81:69–72, 1998.
- [49] Andrea Damascelli, Zahid Hussain, and Zhi-Xun Shen. Angle-resolved photoemission studies of the cuprate superconductors. *Rev. Mod. Phys.*, 75:473–541, Apr 2003.

- [50] K. B. Davis, M.-O. Mewes, M. R. Andrews, N. J. van Druten, D. S. Durfee, D. M. Kurn, and W. Ketterle. Bose-Einstein condensation in a gas of sodium atoms. *Phys. Rev. Lett.*, 75(22):3969–3973, 1995.
- [51] B. DeMarco and D.S. Jin. Onset of Fermi degeneracy in a trapped atomic gas. *Science*, 285:1703–1706, 1999.
- [52] M. T. DePue, C. McCormick, S. L. Winoto, S. Oliver, and D. S. Weiss. Unity occupation of sites in a 3D optical lattice. *Phys. Rev. Lett.*, 82:2262, 1999.
- [53] Raimundo R. dos Santos. Introduction to quantum Monte Carlo simulations for fermionic systems. *Brazilian Journal of Physics*, 33:36 – 54, 03 2003.
- [54] L.-M. Duan, E. Demler, and M. D. Lukin. Controlling spin exchange interactions of ultracold atoms in optical lattices. *Phys. Rev. Lett.*, 91:090402, Aug 2003.
- [55] Pedro M. Duarte, Russell A. Hart, Tsung-Lin Yang, Xinxing Liu, Thereza Paiva, Ehsan Khatami, Richard T. Scalettar, Nandini Trivedi, and Randall G. Hulet. Compressibility of a fermionic mott insulator of ultracold atoms. *Phys. Rev. Lett.*, 114:070403, 2015.
- [56] Martin Eckstein, Takashi Oka, and Philipp Werner. Dielectric breakdown of mott insulators in dynamical mean-field theory. *Phys. Rev. Lett.*, 105:146404, Sep 2010.
- [57] Martin Eckstein and Philipp Werner. Dielectric breakdown of mott insulators – doublon production and doublon heating. *Journal of Physics: Conference Series*, 427:012005, mar 2013.
- [58] G. J. A. Edge, R. Anderson, D. Jervis, D. C. McKay, R. Day, S. Trotzky, and J. H. Thywissen. Imaging and addressing of individual fermionic atoms in an optical lattice. *Phys. Rev. A*, 92:063406, Dec 2015.
- [59] V. J. Emery and S. A. Kivelson. Superconductivity in bad metals. *Phys. Rev. Lett.*, 74:3253–3256, Apr 1995.
- [60] M. Endres, M. Cheneau, T. Fukuhara, C. Weitenberg, P. Schauß, C. Gross, L. Mazza, M. C. Bañuls, L. Pollet, I. Bloch, and S. Kuhr. Observation of correlated particle-hole pairs and string order in low-dimensional mott insulators. *Science*, 334(6053):200–203, 2011.
- [61] M. Endres, M. Cheneau, T. Fukuhara, C. Weitenberg, P. Schauß, C. Gross, L. Mazza, M. C. Bañuls, L. Pollet, I. Bloch, and S. Kuhr. Single-site- and single-atom-resolved measurement of correlation functions. *Appl. Phys. B*, 113(1):27–39, 2013.

- [62] Philipp T. Ernst, Sören Götze, Jasper S. Krauser, Karsten Pyka, Dirk-Sören Lühmann, Daniela Pfannkuche, and Klaus Sengstock. Probing superfluids in optical lattices by momentum-resolved bragg spectroscopy. *Nature Physics*, 6:56–61, 2010.
- [63] T. Esslinger. Fermi-Hubbard physics with atoms in an optical lattice. *Annu. Rev. Condens. Matter Phys.*, 1:129–152, 2010.
- [64] T.S Evans and D.A Steer. Wick’s theorem at finite temperature. *Nuclear Physics B*, 474(2):481 – 496, 1996.
- [65] Richard Feynman. Simulating physics with computers. *International Journal of Theoretical Physics*, 21(6):467–488, 1982.
- [66] R. S. Fishman and M. Jarrell. f-sum rule for the spin conductivity in itinerant magnets. *Journal of Applied Physics*, 91(10):8120–8122, 2002.
- [67] R. W. Floyd and L. Steinberg. An adaptive algorithm for spatial grayscale. *Proceedings of the Society of Information Display*, 17(2):75–77, 1976.
- [68] J. Friedel. Metallic alloys. *Il Nuovo Cimento*, 7(2):287–311, Sep 1958.
- [69] A. Fuhrmanek, R. Bourgain, Y. R. P. Sortais, and A. Browaeys. Light-assisted collisions between a few cold atoms in a microscopic dipole trap. *Phys. Rev. A*, 85:062708, Jun 2012.
- [70] Takeshi Fukuhara, Adrian Kantian, Manuel Endres, Marc Cheneau, Peter Schauß, Sebastian Hild, David Bellem, Ulrich Schollwöck, Thierry Giamarchi, Christian Gross, Immanuel Bloch, and Stefan Kuhr. Quantum dynamics of a mobile spin impurity. *Nature Physics*, 9:235–241, 2013.
- [71] Takeshi Fukuhara, Peter Schauß, Manuel Endres, Sebastian Hild, Marc Cheneau, Immanuel Bloch, and Christian Gross. Microscopic observation of magnon bound states and their dynamics. *Nature*, 502(7469):76–79, 2013.
- [72] Murray Gell-Mann and Francis Low. Bound states in quantum field theory. *Phys. Rev.*, 84:350–354, Oct 1951.
- [73] Christian Thomas Joachim Gersdorf. *A Quantum Gas Microscope for Fermionic Atoms*. Master’s thesis, ETH Zürich, 2012.
- [74] Thierry Giamarchi. *Quantum Physics in One Dimension*. Clarendon Press, 2004.
- [75] S. R. Granade, M. E. Gehm, K. M. O’Hara, and J. E. Thomas. All-optical production of a degenerate Fermi gas. *Phys. Rev. Lett.*, 88:120405, 2002.
- [76] Daniel Greif, Gregor Jotzu, Michael Messer, Rémi Desbuquois, and Tilman Esslinger. Formation and dynamics of antiferromagnetic correlations in tunable optical lattices. *Phys. Rev. Lett.*, 115:260401, Dec 2015.

- [77] Daniel Greif, Maxwell F. Parsons, Anton Maziurenko, Christie S. Chiu, Sebastian Blatt, Florian Huber, Geoffrey Ji, and Markus Greiner. Site-resolved imaging of a fermionic mott insulator. *Science*, 351(6276):953–957, 2016.
- [78] Daniel Greif, Thomas Uehlinger, Gregor Jotzu, Leticia Tarruell, and Tilman Esslinger. Short-range quantum magnetism of ultracold fermions in an optical lattice. *Science*, 340(6138):1307–1310, 2013.
- [79] Markus Greiner. *Ultracold quantum gases in three-dimensional optical lattice potentials*. Ph.d. thesis, Ludwig Maximilian University of Munich, 2003.
- [80] Markus Greiner, Olaf Mandel, Tilman Esslinger, Theodor W. Hänsch, and Immanuel Bloch. Quantum phase transition from a superfluid to a mott insulator in a gas of ultracold atoms. *Nature*, 415:39–44, 2002.
- [81] R. Grimm. Ultracold fermi gases in the bec-bcs crossover: a review from the innsbruck perspective. In M. Inguscio, W. Ketterle, and C. Salomon, editors, *Ultracold Fermi Gases, Proceedings of the International School of Physics "Enrico Fermi", Course CLXIV, Varenna, 20 - 30 June 2006*. IOS Press, Amsterdam, 2008.
- [82] Elmer Guardado-Sánchez, Peter T. Brown, Debayan Mitra, Trithep Devakul, David A. Huse, Peter Schauß, and Waseem S. Bakr. Probing the quench dynamics of antiferromagnetic correlations in a 2d quantum ising spin system. *Phys. Rev. X*, 8:021069, Jun 2018.
- [83] O. Gunnarsson, M. Calandra, and J. E. Han. Colloquium: Saturation of electrical resistivity. *Rev. Mod. Phys.*, 75:1085–1099, Oct 2003.
- [84] Z. Hadzibabic, C. A. Stan, K. Dieckmann, S. Gupta, M.W. Zwierlein, A. Goyert, and W. Ketterle. Two species mixture of quantum degenerate Bose and Fermi gases. *Phys. Rev. Lett.*, 88:160401, 2002.
- [85] E. Haller, J. Hudson, A. Kelly, D. A. Cotta, B. Peaudecerf, G. D. Bruce, and S. Kuhr. Single-atom imaging of fermions in a quantum-gas microscope. *Nat. Phys.*, 11:738–742, 2015.
- [86] S. E. Hamann, D. L. Haycock, G. Klose, P. H. Pax, I. H. Deutsch, and P. S. Jessen. Resolved-sideband Raman cooling to the ground state of an optical lattice. *Phys. Rev. Lett.*, 80:4149, 1998.
- [87] Dian-Jiun Han, Steffen Wolf, Steven Oliver, Colin McCormick, Marshall T. DePue, and David S. Weiss. 3D Raman sideband cooling of cesium atoms at high density. *Phys. Rev. Lett.*, 85:724–727, Jul 2000.
- [88] A. Brooks Harris and Robert V. Lange. Single-particle excitations in narrow energy bands. *Phys. Rev.*, 157:295–314, May 1967.

- [89] R. A. Hart, P. M. Duarte, Tsung-Lin Yang, X. Liu, T. Paiva, E. Khatami, R. T. Scalettar, N. Trivedi, D. A. Huse, and R. G. Hulet. Observation of anti-ferromagnetic correlations in the Hubbard model with ultracold atoms. *Nature*, 519:211–214, 2015.
- [90] S. A. Hartnoll, A. Lucas, and S. Sachdev. *Holographic Quantum Matter*. MIT Press, Cambridge, MA, 2018.
- [91] Sean A. Hartnoll. Theory of universal incoherent metallic transport. *Nature Physics*, 11:54–61, 2015.
- [92] Sean A. Hartnoll and Andreas Karch. Scaling theory of the cuprate strange metals. *Phys. Rev. B*, 91:155126, Apr 2015.
- [93] A. J. Heeger, S. Kivelson, J. R. Schrieffer, and W. P. Su. Solitons in conducting polymers. *Rev. Mod. Phys.*, 60(3):781–850, 1988.
- [94] Michael Hermele, Victor Gurarie, and Ana Maria Rey. Mott insulators of ultracold fermionic alkaline earth atoms: Underconstrained magnetism and chiral spin liquid. *Phys. Rev. Lett.*, 103:135301, Sep 2009.
- [95] Sebastian Hild, Takeshi Fukuhara, Peter Schauß, Johannes Zeiher, Michael Knap, Eugene Demler, Immanuel Bloch, and Christian Gross. Far-from-equilibrium spin transport in heisenberg quantum magnets. *Phys. Rev. Lett.*, 113:147205, Oct 2014.
- [96] Timon A. Hilker, Guillaume Salomon, Fabian Grusdt, Ahmed Omran, Martin Boll, Eugene Demler, Immanuel Bloch, and Christian Gross. Revealing hidden antiferromagnetic correlations in doped hubbard chains via string correlators. *Science*, 357(6350):484–487, 2017.
- [97] J. E. Hirsch. Two-dimensional hubbard model: Numerical simulation study. *Phys. Rev. B*, 31:4403–4419, 1985.
- [98] A. F. Ho, M. A. Cazalilla, and T. Giamarchi. Quantum simulation of the hubbard model: The attractive route. *Phys. Rev. A*, 79(3):033620, 2009.
- [99] Tin-Lun Ho and Qi Zhou. Universal Cooling Scheme for Quantum Simulation. *arXiv e-prints*, page arXiv:0911.5506, Nov 2009.
- [100] Christian Hofrichter, Luis Riegger, Francesco Scazza, Moritz Höfer, Diogo Rio Fernandes, Immanuel Bloch, and Simon Fölling. Direct probing of the mott crossover in the  $SU(n)$  fermi-hubbard model. *Phys. Rev. X*, 6:021030, Jun 2016.
- [101] W. Hofstetter, J. I. Cirac, P. Zoller, E. Demler, and M. D. Lukin. High-temperature superfluidity of fermionic atoms in optical lattices. *Phys. Rev. Lett.*, 89:220407, Nov 2002.

- [102] Carsten Honerkamp and Walter Hofstetter. Ultracold fermions and the  $SU(n)$  hubbard model. *Phys. Rev. Lett.*, 92:170403, Apr 2004.
- [103] Florian Gerhard Huber. *Site-Resolved Imaging with the Fermi Gas Microscope*. Ph.d. thesis, Harvard University, 2014.
- [104] N E Hussey. Phenomenology of the normal state in-plane transport properties of high- $t_c$  cuprates. *Journal of Physics: Condensed Matter*, 20(12):123201, feb 2008.
- [105] Jakub Imriška, Mauro Iazzi, Lei Wang, Emanuel Gull, Daniel Greif, Thomas Uehlinger, Gregor Jotzu, Leticia Tarruell, Tilman Esslinger, and Matthias Troyer. Thermodynamics and magnetic properties of the anisotropic 3D Hubbard model. *Phys. Rev. Lett.*, 112:115301, 2014.
- [106] S. Inouye, M. R. Andrews, J. Stenger, H. J. Miesner, D. M. Stamper-Kurn, and W. Ketterle. Observation of Feshbach resonances in a Bose-Einstein condensate. *Nature*, 392(6672):151–154, 1998.
- [107] A. Ioffe and A. Regel. Non-crystalline, amorphous and liquid electronic semiconductors. *Prog. Semicond.*, 4:237–291, 1960.
- [108] R. Islam, R. Ma, P. M. Preiss, M. E. Tai, A. Lukin, M. Rispoli, and M. Greiner. Measuring entanglement entropy in a quantum many-body system. *Nature*, 528(15750):77–83, 2015.
- [109] J. Jaklič and P. Prelovšek. Finite-temperature properties of doped antiferromagnets. *Advances in Physics*, 49(1):1–92, 2000.
- [110] D. Jaksch, C. Bruder, J. I. Cirac, C. W. Gardiner, and P. Zoller. Cold bosonic atoms in optical lattices. *Phys. Rev. Lett.*, 81:3108–3111, Oct 1998.
- [111] M. Jarrell and J. E. Gubernatis. Bayesian inference and the analytic continuation of imaginary-time quantum monte carlo data. *Physics Reports*, 269(3):133–195, 1996.
- [112] T. Jeltes, J. M. McNamara, W. Hogervorst, W. Vassen, V. Krachmalnicoff, M. Schellekens, A. Perrin, H. Chang, D. Boiron, A. Aspect, and C. I. Westbrook. Comparison of the hanbury brown–twiss effect for bosons and fermions. *Nature*, 445(05513):402–405, 2007.
- [113] S. Jochim, M. Bartenstein, G. Hendl, J. Hecker-Denschlag, R. Grimm, A. Mosk, and M. Weidemüller. Magnetic field control of elastic scattering in a cold gas of fermionic lithium atoms. *Phys. Rev. Lett.*, 89:273202, 2002.
- [114] Robert Jördens, Niels Strohmaier, Kenneth Günter, Henning Moritz, and Tilman Esslinger. A Mott insulator of fermionic atoms in an optical lattice. *Nature*, 455(7210):204–207, 2008.

- [115] C. Karrasch, D. M. Kennes, and J. E. Moore. Transport properties of the one-dimensional hubbard model at finite temperature. *Phys. Rev. B*, 90:155104, Oct 2014.
- [116] A. M. Kaufman, B. J. Lester, and C. A. Regal. Cooling a single atom in an optical tweezer to its quantum ground state. *Phys. Rev. X*, 2:041014, Nov 2012.
- [117] Andrew J. Kerman, Vladan Vuletić, Cheng Chin, and Steven Chu. Beyond optical molasses: 3D raman sideband cooling of atomic cesium to high phase-space density. *Phys. Rev. Lett.*, 84:439, 2000.
- [118] W. Ketterle, D.S. Durfee, and D.M. Stamper-Kurn. Making, probing and understanding Bose-Einstein condensates. In M. Inguscio, S. Stringari, and C.E. Wieman, editors, *Bose-Einstein condensation in atomic gases, Proceedings of the International School of Physics Enrico Fermi, Course CXL, Varenna, 7-17 July 1998*, pages 67–176. IOS Press, Amsterdam, 1999.
- [119] W. Ketterle and M.W. Zwierlein. Making, probing and understanding ultracold Fermi gases. In M. Inguscio, W. Ketterle, and C. Salomon, editors, *Ultracold Fermi Gases, Proceedings of the International School of Physics "Enrico Fermi", Course CLXIV, Varenna, 20 - 30 June 2006. Reprinted in Rivista del Nuovo Cimento, 31(5), 247 (2008)*. IOS Press, Amsterdam., 2008.
- [120] Ehsan Khatami and Marcos Rigol. Thermodynamics of strongly interacting fermions in two-dimensional optical lattices. *Phys. Rev. A*, 84:053611, 2011.
- [121] Ehsan Khatami and Marcos Rigol. Effect of particle statistics in strongly correlated two-dimensional hubbard models. *Phys. Rev. A*, 86:023633, Aug 2012.
- [122] Hyungwon Kim and David A. Huse. Heat and spin transport in a cold atomic fermi gas. *Phys. Rev. A*, 86:053607, Nov 2012.
- [123] C. Klempert, T. van Zoest, T. Henninger, O. Topic, E. Rasel, W. Ertmer, and J. Arlt. Ultraviolet light-induced atom desorption for large rubidium and potassium magneto-optical traps. *Phys. Rev. A*, 73:013410, Jan 2006.
- [124] Michael Köhl, Henning Moritz, Thilo Stöferle, Kenneth Günter, and Tilman Esslinger. Fermionic atoms in a three dimensional optical lattice: Observing Fermi surfaces, dynamics, and interactions. *Phys. Rev. Lett.*, 94:080403, 2005.
- [125] J. Kokalj and Ross H. McKenzie. Thermodynamics of a bad metal–mott insulator transition in the presence of frustration. *Phys. Rev. Lett.*, 110:206402, May 2013.
- [126] J. Kokalj and Ross H. McKenzie. Enhancement of thermal expansion of organic charge-transfer salts by strong electronic correlations. *Phys. Rev. B*, 91:205121, May 2015.

- [127] Peter Kopietz. Spin conductance, dynamic spin stiffness, and spin diffusion in itinerant magnets. *Phys. Rev. B*, 57:7829–7834, Apr 1998.
- [128] Marco Koschorreck, Daniel Pertot, Enrico Vogt, and Michael Köhl. Universal spin dynamics in two-dimensional fermi gases. *Nature Physics*, 9(7):405–409, 2013.
- [129] G. Kotliar, S. Y. Savrasov, K. Haule, V. S. Oudovenko, O. Parcollet, and C. A. Marianetti. Electronic structure calculations with dynamical mean-field theory. *Rev. Mod. Phys.*, 78:865–951, Aug 2006.
- [130] Sebastian Krinner, Tilman Esslinger, and Jean-Philippe Brantut. Two-terminal transport measurements with cold atoms. *Journal of Physics: Condensed Matter*, 29(34):343003, jul 2017.
- [131] Sebastian Krinner, Martin Lebrat, Dominik Husmann, Charles Grenier, Jean-Philippe Brantut, and Tilman Esslinger. Mapping out spin and particle conductances in a quantum point contact. *Proceedings of the National Academy of Sciences*, 113(29):8144–8149, 2016.
- [132] R Kubo. The fluctuation-dissipation theorem. *Reports on Progress in Physics*, 29(1):255–284, jan 1966.
- [133] Ryogo Kubo. Statistical-mechanical theory of irreversible processes. i. general theory and simple applications to magnetic and conduction problems. *Journal of the Physical Society of Japan*, 12(6):570–586, 1957.
- [134] Ryogo Kubo. *Lectures in Theoretical Physics*, volume 1 (Boulder). Wiley-Interscience, New York, 1959 pp. 120-203.
- [135] A. B. Kuklov and B. V. Svistunov. Counterflow superfluidity of two-species ultracold atoms in a commensurate optical lattice. *Phys. Rev. Lett.*, 90:100401, Mar 2003.
- [136] J. P. F. LeBlanc, Andrey E. Antipov, Federico Becca, Ireneusz W. Bulik, Garnet Kin-Lic Chan, Chia-Min Chung, Youjin Deng, Michel Ferrero, Thomas M. Henderson, Carlos A. Jiménez-Hoyos, E. Kozik, Xuan-Wen Liu, Andrew J. Millis, N. V. Prokof'ev, Mingpu Qin, Gustavo E. Scuseria, Hao Shi, B. V. Svistunov, Luca F. Tocchio, I. S. Tupitsyn, Steven R. White, Shiwei Zhang, Bo-Xiao Zheng, Zhenyue Zhu, and Emanuel Gull. Solutions of the two-dimensional hubbard model: Benchmarks and results from a wide range of numerical algorithms. *Phys. Rev. X*, 5:041041, 2015.
- [137] J. P. F. LeBlanc and Emanuel Gull. Equation of state of the fermionic two-dimensional hubbard model. *Phys. Rev. B*, 88:155108, 2013.
- [138] Martin Lebrat, Pjotrs Grišins, Dominik Husmann, Samuel Häusler, Laura Corman, Thierry Giamarchi, Jean-Philippe Brantut, and Tilman Esslinger. Band

and correlated insulators of cold fermions in a mesoscopic lattice. *Phys. Rev. X*, 8:011053, Mar 2018.

- [139] Patrick A. Lee, Naoto Nagaosa, and Xiao-Gang Wen. Doping a Mott insulator: Physics of high-temperature superconductivity. *Rev. Mod. Phys.*, 78(1):17, 2006.
- [140] M. Lewenstein, L. Santos, M. A. Baranov, and H. Fehrmann. Atomic bose-fermi mixtures in an optical lattice. *Phys. Rev. Lett.*, 92:050401, Feb 2004.
- [141] Elliott Lieb and Daniel Mattis. Theory of ferromagnetism and the ordering of electronic energy levels. *Phys. Rev.*, 125:164–172, Jan 1962.
- [142] Elliott H. Lieb and F. Y. Wu. Absence of mott transition in an exact solution of the short-range, one-band model in one dimension. *Phys. Rev. Lett.*, 20:1445–1448, Jun 1968.
- [143] E. Y. Loh and J. E. Gubernatis. Stable numerical simulations of models of interacting electrons in condensed-matter physics. In W. Hanke and Y. V. Kopaev, editors, *Modern Problems in Condensed Matter Sciences*, volume 32, pages 177–235, Amsterdam, 1992. North-Holland.
- [144] E. Y. Loh, J. E. Gubernatis, R. T. Scalettar, S. R. White, D. J. Scalapino, and R. L. Sugar. Sign problem in the numerical simulation of many-electron systems. *Phys. Rev. B*, 41:9301–9307, May 1990.
- [145] C. Luciuk, S. Smale, F. Böttcher, H. Sharum, B. A. Olsen, S. Trotzky, T. Enss, and J. H. Thywissen. Observation of quantum-limited spin transport in strongly interacting two-dimensional fermi gases. *Phys. Rev. Lett.*, 118:130405, Mar 2017.
- [146] Ruichao Ma, M. Eric Tai, Philipp M. Preiss, Waseem S. Bakr, Jonathan Simon, and Markus Greiner. Photon-assisted tunneling in a biased strongly correlated bose gas. *Phys. Rev. Lett.*, 107:095301, Aug 2011.
- [147] A. H. MacDonald, S. M. Girvin, and D. Yoshioka.  $\frac{t}{U}$  expansion for the hubbard model. *Phys. Rev. B*, 37:9753–9756, Jun 1988.
- [148] G. D. Mahan. *Many-Particle Physics*. Springer, New York, 3 edition, 2000.
- [149] Krishnanand Mallayya and Marcos Rigol. Quantum quenches and relaxation dynamics in the thermodynamic limit. *Phys. Rev. Lett.*, 120:070603, Feb 2018.
- [150] Efstratios Manousakis. The spin-1/2 heisenberg antiferromagnet on a square lattice and its application to the cuprous oxides. *Rev. Mod. Phys.*, 63:1–62, Jan 1991.
- [151] G. Edward Marti, Ross B. Hutson, Akihisa Goban, Sara L. Campbell, Nicola Poli, and Jun Ye. Imaging optical frequencies with 100  $\mu$ Hz precision and 1.1  $\mu$ m resolution. *Phys. Rev. Lett.*, 120:103201, Mar 2018.

- [152] Anton Mazurenko, Christie S. Chiu, Geoffrey Ji, Maxwell F. Parsons, Márton Kanász-Nagy, Richard Schmidt, Fabian Grusdt, Eugene Demler, Daniel Greif, and Markus Greiner. A cold-atom fermi–hubbard antiferromagnet. *Nature*, 545:462–466, 2017.
- [153] N. D. Mermin and H. Wagner. Absence of ferromagnetism or antiferromagnetism in one- or two-dimensional isotropic heisenberg models. *Phys. Rev. Lett.*, 17:1133–1136, Nov 1966.
- [154] Martin Miranda, Ryotaro Inoue, Yuki Okuyama, Akimasa Nakamoto, and Mikio Kozuma. Site-resolved imaging of ytterbium atoms in a two-dimensional optical lattice. *Phys. Rev. A*, 91:063414, Jun 2015.
- [155] Debayan Mitra, Peter T. Brown, Elmer Guardado-Sánchez, Stanimir S. Kondov, Trithep Devakul, David A. Huse, Peter Schauß, and Waseem S. Bakr. Quantum gas microscopy of an attractive fermi–hubbard system. *Nature Physics*, 14:173–177, 2018.
- [156] G. Modugno, F. Ferlaino, R. Heidemann, G. Roati, and M. Inguscio. Production of a fermi gas of atoms in an optical lattice. *Phys. Rev. A*, 68:011601, Jul 2003.
- [157] C. Monroe, D. M. Meekhof, B. E. King, S. R. Jefferts, W. M. Itano, D. J. Wineland, and P. Gould. Resolved-sideband Raman cooling of a bound atom to the 3D zero-point energy. *Phys. Rev. Lett.*, 75:4011–4014, Nov 1995.
- [158] N. F. Mott. Conduction in non-crystalline systems ix. the minimum metallic conductivity. *The Philosophical Magazine: A Journal of Theoretical Experimental and Applied Physics*, 26(4):1015–1026, 1972.
- [159] Subroto Mukerjee, Vadim Oganesyan, and David Huse. Statistical theory of transport by strongly interacting lattice fermions. *Phys. Rev. B*, 73:035113, Jan 2006.
- [160] Torben Müller, Bruno Zimmermann, Jakob Meineke, Jean-Philippe Brantut, Tilman Esslinger, and Henning Moritz. Local observation of antibunching in a trapped fermi gas. *Phys. Rev. Lett.*, 105:040401, Jul 2010.
- [161] A. Muramatsu. Quantum Monte Carlo for lattice fermions. In M. P. Nightingale and C. J. Umrigar, editors, *Quantum Monte Carlo Methods in Physics and Chemistry*, pages 343–373, Dordrecht, 1999. NATO Science Series, Kluwer Academic Press.
- [162] Simon Murmann, Andrea Bergschneider, Vincent M. Klinkhamer, Gerhard Zürn, Thomas Lompe, and Selim Jochim. Two fermions in a double well: Exploring a fundamental building block of the hubbard model. *Phys. Rev. Lett.*, 114:080402, Feb 2015.
- [163] Karl D. Nelson, Xiao Li, and David S. Weiss. Imaging single atoms in a three-dimensional array. *Nat. Phys.*, 3(8):556–560, 2007.

- [164] Matthew A. Nichols, Lawrence W. Cheuk, Melih Okan, Thomas R. Hartke, Enrique Mendez, T. Senthil, Ehsan Khatami, Hao Zhang, and Martin W. Zwierlein. Spin transport in a mott insulator of ultracold fermions. *Science*, 363(6425):383–387, Jan 2019.
- [165] J. Oitmaa, C. Hamer, and W. Zheng. *Series Expansion Methods for Strongly Interacting Lattice Models*. Cambridge University Press, Cambridge, England, 2006.
- [166] Takashi Oka and Hideo Aoki. Ground-state decay rate for the zener breakdown in band and mott insulators. *Phys. Rev. Lett.*, 95:137601, Sep 2005.
- [167] Takashi Oka, Ryotaro Arita, and Hideo Aoki. Breakdown of a mott insulator: A nonadiabatic tunneling mechanism. *Phys. Rev. Lett.*, 91:066406, Aug 2003.
- [168] Melih Okan. *Controlling Ultracold Fermions under a Quantum Gas Microscope*. Ph.d. thesis, Massachusetts Institute of Technology, 2018.
- [169] Ahmed Omran, Martin Boll, Timon A. Hilker, Katharina Kleinlein, Guillaume Salomon, Immanuel Bloch, and Christian Gross. Microscopic observation of pauli blocking in degenerate fermionic lattice gases. *Phys. Rev. Lett.*, 115:263001, Dec 2015.
- [170] R. Onofrio, C. Raman, J. M. Vogels, J.R. Abo-Shaeer, A. P. Chikkatur, and W. Ketterle. Observation of superfluid flow in a Bose-Einstein condensed gas. *Phys. Rev. Lett.*, 85:2228–2231, 2000.
- [171] J. Orenstein and A. J. Millis. Advances in the physics of high-temperature superconductivity. *Science*, 288(5465):468–474, 2000.
- [172] H. Ott, E. de Mirandes, F. Ferlaino, G. Roati, G. Modugno, and M. Inguscio. Collisionally induced transport in periodic potentials. *Phys. Rev. Lett.*, 92:160601, Apr 2004.
- [173] Thereza Paiva, R. T. Scalettar, Carey Huscroft, and A. K. McMahan. Signatures of spin and charge energy scales in the local moment and specific heat of the half-filled two-dimensional hubbard model. *Phys. Rev. B*, 63:125116, Mar 2001.
- [174] Thereza Paiva, Richard Scalettar, Mohit Randeria, and Nandini Trivedi. Fermions in 2d optical lattices: Temperature and entropy scales for observing antiferromagnetism and superfluidity. *Phys. Rev. Lett.*, 104:066406, Feb 2010.
- [175] Gunnar Pálsson and Gabriel Kotliar. Thermoelectric response near the density driven mott transition. *Phys. Rev. Lett.*, 80:4775–4778, May 1998.

- [176] Jee Woo Park, Sebastian A. Will, and Martin W. Zwierlein. Ultracold dipolar gas of fermionic  $^{23}\text{Na}^{40}\text{K}$  molecules in their absolute ground state. *Phys. Rev. Lett.*, 114:205302, May 2015.
- [177] Jee Woo Park, Cheng-Hsun Wu, Ibon Santiago, Tobias G. Tiecke, Sebastian Will, Peyman Ahmadi, and Martin W. Zwierlein. Quantum degenerate bose-fermi mixture of chemically different atomic species with widely tunable interactions. *Phys. Rev. A*, 85:051602, May 2012.
- [178] Jee Woo Park, Zoe Z. Yan, Huanqian Loh, Sebastian A. Will, and Martin W. Zwierlein. Second-scale nuclear spin coherence time of ultracold  $^{23}\text{Na}^{40}\text{K}$  molecules. *Science*, 357(6349):372–375, 2017.
- [179] Maxwell F. Parsons, Florian Huber, Anton Mazurenko, Christie S. Chiu, Widagdo Setiawan, Katherine Wooley-Brown, Sebastian Blatt, and Markus Greiner. Site-resolved imaging of fermionic  $^6\text{Li}$  in an optical lattice. *Phys. Rev. Lett.*, 114:213002, May 2015.
- [180] Maxwell F. Parsons, Anton Mazurenko, Christie S. Chiu, Geoffrey Ji, Daniel Greif, and Markus Greiner. Site-resolved measurement of the spin-correlation function in the fermi-hubbard model. *Science*, 353(6305):1253–1256, 2016.
- [181] Y. S. Patil, S. Chakram, L. M. Aycock, and M. Vengalattore. Nondestructive imaging of an ultracold lattice gas. *Phys. Rev. A*, 90:033422, Sep 2014.
- [182] Michael R. Peterson and B. Sriram Shastry. Kelvin formula for thermopower. *Phys. Rev. B*, 82:195105, Nov 2010.
- [183] L. Pezzè, L. Pitaevskii, A. Smerzi, S. Stringari, G. Modugno, E. de Mirandes, F. Ferlaino, H. Ott, G. Roati, and M. Inguscio. Insulating behavior of a trapped ideal fermi gas. *Phys. Rev. Lett.*, 93:120401, Sep 2004.
- [184] Philipp M. Preiss, Ruichao Ma, M. Eric Tai, Alexander Lukin, Matthew Rispoli, Philip Zupancic, Yoav Lahini, Rajibul Islam, and Markus Greiner. Strongly correlated quantum walks in optical lattices. *Science*, 347(6227):1229–1233, 2015.
- [185] C. Raman, J.R. Abo-Shaeer, J. M. Vogels, K. Xu, and W. Ketterle. Vortex nucleation in a stirred Bose-Einstein condensate. *Phys. Rev. Lett.*, 87:210402, 2001.
- [186] Vinay Venkatesh Ramasesh. *Towards a Quantum Gas Microscope for Fermionic Atoms*. Bachelor’s thesis, Massachusetts Institute of Technology, 2012.
- [187] Vinay Venkatesh Ramasesh. *Construction of a Quantum Gas Microscope for Fermionic Atoms*. Master’s thesis, Massachusetts Institute of Technology, 2013.

- [188] Ákos Rapp and Achim Rosch. Ground-state phase diagram of the repulsive  $\text{su}(3)$  hubbard model in the gutzwiller approximation. *Phys. Rev. A*, 83:053605, May 2011.
- [189] C. A. Regal, M. Greiner, and D. S. Jin. Observation of resonance condensation of fermionic atom pairs. *Phys. Rev. Lett.*, 92(4):040403, 2004.
- [190] Cindy Regal. *Experimental Realization of BCS-BEC Crossover Physics with a Fermi Gas of Atoms*. Ph.d. thesis, University of Colorado, Boulder, 2005.
- [191] Alexander Reischl, Erwin Müller-Hartmann, and Götz S. Uhrig. Systematic mapping of the hubbard model to the generalized  $t-j$  model. *Phys. Rev. B*, 70:245124, Dec 2004.
- [192] Robert C. Richardson. The pomeranchuk effect. *Rev. Mod. Phys.*, 69:683–690, Jul 1997.
- [193] Keno Riechers, Klaus Hueck, Niclas Luick, Thomas Lompe, and Henning Moritz. Detecting friedel oscillations in ultracold fermi gases. *The European Physical Journal D*, 71(9):232, Sep 2017.
- [194] Marcos Rigol, Tyler Bryant, and Rajiv R. P. Singh. Numerical linked-cluster approach to quantum lattice models. *Phys. Rev. Lett.*, 97:187202, Nov 2006.
- [195] Marcos Rigol, Tyler Bryant, and Rajiv R. P. Singh. Numerical linked-cluster algorithms. ii.  $t-j$  models on the square lattice. *Phys. Rev. E*, 75:061119, Jun 2007.
- [196] T. Rom, Th. Best, D. van Oosten, U. Schneider, S. Fölling, B. Paredes, and I. Bloch. Free fermion antibunching in a degenerate atomic Fermi gas released from an optical lattice. *Nature*, 444(7120):733–736, 2006.
- [197] M. J. Rozenberg, G. Kotliar, H. Kajueter, G. A. Thomas, D. H. Rapkine, J. M. Honig, and P. Metcalf. Optical conductivity in mott-hubbard systems. *Phys. Rev. Lett.*, 75:105–108, Jul 1995.
- [198] J. J. Sakurai. *Modern Quantum Mechanics*. Pearson Education, Inc., 2nd edition, 2011.
- [199] Guillaume Salomon, Joannis Koepsell, Jayadev Vijayan, Timon A. Hilker, Jacopo Nespolo, Lode Pollet, Immanuel Bloch, and Christian Gross. Direct observation of incommensurate magnetism in hubbard chains. *Nature*, 565(7737):56–60, 2019.
- [200] Christian Sanner, Edward J. Su, Aviv Keshet, Ralf Gommers, Yong-il Shin, Wujie Huang, and Wolfgang Ketterle. Suppression of density fluctuations in a quantum degenerate fermi gas. *Phys. Rev. Lett.*, 105:040402, Jul 2010.

- [201] D.J. Scalapino. The case for  $d_{x^2-y^2}$  pairing in the cuprate superconductors. *Physics Reports*, 250(6):329 – 365, 1995.
- [202] Douglas J. Scalapino, Steven R. White, and Shoucheng Zhang. Insulator, metal, or superconductor: The criteria. *Phys. Rev. B*, 47:7995–8007, Apr 1993.
- [203] V. W. Scarola, L. Pollet, J. Oitmaa, and M. Troyer. Discerning incompressible and compressible phases of cold atoms in optical lattices. *Phys. Rev. Lett.*, 102:135302, 2009.
- [204] U. Schneider, L. Hackermüller, J. P. Ronzheimer, S. Will, S. Braun, T. Best, I. Bloch, E. Demler, S. Mandt, D. Rasch, and A. Rosch. Fermionic transport and out-of-equilibrium dynamics in a homogeneous hubbard model with ultracold atoms. *Nat. Phys.*, 8:213–218, 2012.
- [205] U. Schneider, L. Hackermüller, S. Will, Th Best, I. Bloch, T. A. Costi, R. W. Helmes, D. Rasch, and A. Rosch. Metallic and insulating phases of repulsively interacting fermions in a 3D optical lattice. *Science*, 322(5907):1520–1525, 2008.
- [206] A. J. Schofield. Non-fermi liquids. *Contemporary Physics*, 40(2):95–115, 1999.
- [207] F. Schreck, L. Khaykovich, K. L. Corwin, G. Ferrari, T. Bourdel, J. Cubizolles, and C. Salomon. Quasipure Bose-Einstein condensate immersed in a Fermi sea. *Phys. Rev. Lett.*, 87:080403, 2001.
- [208] B Sriram Shastry. Electrothermal transport coefficients at finite frequencies. *Reports on Progress in Physics*, 72(1):016501, dec 2008.
- [209] Jacob F. Sherson, Christof Weitenberg, Manuel Endres, Marc Cheneau, Immanuel Bloch, and Stefan Kuhr. Single-atom-resolved fluorescence imaging of an atomic Mott insulator. *Nature*, 467(7311):68–72, 2010.
- [210] Avinash Singh and Haranath Ghosh. Stability of the doped antiferromagnetic state of the  $t - t'$  hubbard model. *Phys. Rev. B*, 65:134414, Mar 2002.
- [211] Andrew P. Snyder and Theja N. De Silva. Spin diffusion of lattice fermions in one dimension. *Phys. Rev. A*, 86:053610, Nov 2012.
- [212] A. Sokol, E. Gagliano, and S. Bacci. Theory of nuclear spin-lattice relaxation in  $\text{la}_2\text{cu}_{1-x}\text{o}_4$  at high temperatures. *Phys. Rev. B*, 47:14646–14649, Jun 1993.
- [213] Ariel Sommer, Mark Ku, Giacomo Roati, and Martin W. Zwierlein. Universal spin transport in a strongly interacting fermi gas. *Nature*, 472(7342):201–204, 2011.
- [214] Ariel Sommer, Mark Ku, and Martin W. Zwierlein. Spin transport in polaronic and superfluid fermi gases. *New J. Phys.*, 13:055009, 2011.

- [215] D. M. Stamper-Kurn, H. J. Miesner, S. Inouye, M. R. Andrews, and W. Ketterle. Collisionless and hydrodynamic excitations of a Bose-Einstein condensate. *Phys. Rev. Lett.*, 81(3):500–503, 1998.
- [216] Jürgen Stein. Flow equations and the strong-coupling expansion for the hubbard model. *Journal of Statistical Physics*, 88(1):487–511, Jul 1997.
- [217] G. R. Stewart. Non-fermi-liquid behavior in *d*- and *f*-electron metals. *Rev. Mod. Phys.*, 73:797–855, Oct 2001.
- [218] Thilo Stöferle, Henning Moritz, Christian Schori, Michael Köhl, and Tilman Esslinger. Transition from a strongly interacting 1d superfluid to a mott insulator. *Phys. Rev. Lett.*, 92:130403, Mar 2004.
- [219] Niels Strohmaier, Yosuke Takasu, Kenneth Günter, Robert Jördens, Michael Köhl, Henning Moritz, and Tilman Esslinger. Interaction-controlled transport of an ultracold fermi gas. *Phys. Rev. Lett.*, 99:220601, Nov 2007.
- [220] Y. Taguchi, T. Matsumoto, and Y. Tokura. Dielectric breakdown of one-dimensional mott insulators  $\text{sr}_2\text{cu}\text{o}_3$  and  $\text{src}\text{uo}_2$ . *Phys. Rev. B*, 62:7015–7018, Sep 2000.
- [221] S. Taie, R. Yamazaki, S. Sugawa, and Y. Takahashi. An  $\text{su}(6)$  mott insulator of an atomic fermi gas realized by large-spin pomeranchuk cooling. *Nat. Phys.*, 8:825–830, 2012.
- [222] M. Takahashi. Half-filled hubbard model at low temperature. *Journal of Physics C: Solid State Physics*, 10(8):1289–7301, apr 1977.
- [223] Baoming Tang, Ehsan Khatami, and Marcos Rigol. A short introduction to numerical linked-cluster expansions. *Computer Physics Communications*, 184(3):557 – 564, 2013.
- [224] J. D. Thompson, T. G. Tiecke, A. S. Zibrov, V. Vuletić, and M. D. Lukin. Coherence and Raman sideband cooling of a single atom in an optical tweezer. *Phys. Rev. Lett.*, 110:133001, 2013.
- [225] S. Trotzky, P. Cheinet, S. Fölling, M. Feld, U. Schnorrberger, A. M. Rey, A. Polkovnikov, E. A. Demler, M. D. Lukin, and I. Bloch. Time-resolved observation and control of superexchange interactions with ultracold atoms in optical lattices. *Science*, 319(5861):295–299, 2008.
- [226] Matthias Troyer and Uwe-Jens Wiese. Computational complexity and fundamental limitations to fermionic quantum monte carlo simulations. *Phys. Rev. Lett.*, 94:170201, May 2005.
- [227] Andrew G. Truscott, Kevin E. Strecker, William I. McAlexander, Guthrie B. Partridge, and Randall G. Hulet. Observation of Fermi pressure in a gas of trapped atoms. *Science*, 291:2570–2572, 2001.

- [228] G. Valtolina, F. Scazza, A. Amico, A. Burchianti, A. Recati, T. Enss, M. Inguscio, M. Zaccanti, and G. Roati. Exploring the ferromagnetic behaviour of a repulsive fermi gas through spin dynamics. *Nat. Phys.*, 13:704–709, 2017.
- [229] Giacomo Valtolina, Alessia Burchianti, Andrea Amico, Elettra Neri, Klejdja Xhani, Jorge Amin Seman, Andrea Trombettoni, Augusto Smerzi, Matteo Zaccanti, Massimo Inguscio, and Giacomo Roati. Josephson effect in fermionic superfluids across the bec-bcs crossover. *Science*, 350(6267):1505–1508, 2015.
- [230] C. M. Varma, P. B. Littlewood, S. Schmitt-Rink, E. Abrahams, and A. E. Ruckenstein. Phenomenology of the normal state of cu-o high-temperature superconductors. *Phys. Rev. Lett.*, 63:1996–1999, Oct 1989.
- [231] J.M. Vogels, K. Xu, C. Raman, J. R. Abo-Shaeer, and W. Ketterle. Experimental observation of the bogoliubov transformation for a Bose-Einstein condensed gas. *Phys. Rev. Lett.*, 88:060402, 2002.
- [232] J. Vučičević, D. Tanasković, M. J. Rozenberg, and V. Dobrosavljević. Bad-metal behavior reveals mott quantum criticality in doped hubbard models. *Phys. Rev. Lett.*, 114:246402, Jun 2015.
- [233] Vladan Vuletić, Cheng Chin, Andrew J. Kerman, and Steven Chu. Degenerate Raman sideband cooling of trapped cesium atoms at very high atomic densities. *Phys. Rev. Lett.*, 81:5768–5771, Dec 1998.
- [234] John Weiner, Vanderlei S. Bagnato, Sergio Zilio, and Paul S. Julienne. Experiments and theory in cold and ultracold collisions. *Rev. Mod. Phys.*, 71:1–85, Jan 1999.
- [235] Christof Weitenberg. *Single-Atom Resolved Imaging and Manipulation in an Atomic Mott Insulator*. Ph.d. thesis, Ludwig Maximilian University of Munich, 2011.
- [236] Christof Weitenberg, Manuel Endres, Jacob F. Sherson, Marc Cheneau, Peter Schausz, Takeshi Fukuhara, Immanuel Bloch, and Stefan Kuhr. Single-spin addressing in an atomic mott insulator. *Nature*, 471(7338):319–324, 03 2011.
- [237] David M. Weld, Patrick Medley, Hirokazu Miyake, David Hucul, David E. Pritchard, and Wolfgang Ketterle. Spin gradient thermometry for ultracold atoms in optical lattices. *Phys. Rev. Lett.*, 103:245301, Dec 2009.
- [238] I. G. White, B. Sundar, and K. R. A. Hazzard. Quantum dynamics from a numerical linked cluster expansion. *ArXiv e-prints*, October 2017.
- [239] S. R. White, D. J. Scalapino, R. L. Sugar, E. Y. Loh, J. E. Gubernatis, and R. T. Scalettar. Numerical study of the two-dimensional hubbard model. *Phys. Rev. B*, 40:506–516, Jul 1989.

- [240] G. C. Wick. The evaluation of the collision matrix. *Phys. Rev.*, 80:268–272, Oct 1950.
- [241] Sebastian Will. *Interacting Bosons and Fermions in Three-Dimensional Optical Lattice Potentials*. Ph.d. thesis, Johannes Gutenberg University Mainz, 2011.
- [242] Cheng-Hsun Wu. *Strongly Interacting Quantum Mixtures of Ultracold Atoms*. Ph.d. thesis, Massachusetts Institute of Technology, 2013.
- [243] W. Xu, W. R. McGehee, W. N. Morong, and B. DeMarco. Bad-metal relaxation dynamics in a fermi lattice gas. *ArXiv e-prints*, Aug 2018.
- [244] H. Yamakawa, T. Miyamoto, T. Morimoto, T. Terashige, H. Yada, N. Kida, M. Suda, H. M. Yamamoto, R. Kato, K. Miyagawa, K. Kanoda, and H. Okamoto. Mott transition by an impulsive dielectric breakdown. *Nature Materials*, 16:1100–1105, 2017.
- [245] Y. Yu, N. R. Hutzler, J. T. Zhang, L. R. Liu, J. D. Hood, T. Rosenband, and K.-K. Ni. Motional-ground-state cooling outside the lamb-dicke regime. *Phys. Rev. A*, 97:063423, Jun 2018.
- [246] M. W. Zwierlein, J. R. Abo-Shaeer, A. Schirotzek, C. H. Schunck, and W. Ketterle. Vortices and superfluidity in a strongly interacting Fermi gas. *Nature*, 435:1047–1051, 2005.
- [247] M.W. Zwierlein, C.A. Stan, C.H. Schunck, S.M.F. Raupach, A.J. Kerman, and W. Ketterle. Condensation of pairs of fermionic atoms near a Feshbach resonance. *Phys. Rev. Lett.*, 92:120403, 2004.